Study of Turbulent Single-Phase Heat Transfer and Onset of Nucleate Boiling in High Aspect Ratio Mini-Channels to Support the MITR LEU Conversion

by

Eric Christopher Forrest
S.M. Nuclear Science and Engineering, Massachusetts Institute of Technology, 2009
S.B. Nuclear Science and Engineering, Massachusetts Institute of Technology, 2009

SUBMITTED TO THE DEPARTMENT OF NUCLEAR SCIENCE AND ENGINEERING IN PARTIAL FULFILLMENT OF THE REQUIREMENTS FOR THE DEGREE OF

DOCTOR OF PHILOSOPHY IN NUCLEAR SCIENCE AND ENGINEERING

AT THE

MASSACHUSETTS INSTITUTE OF TECHNOLOGY

JUNE 2014

Signature of Author:_____
Department of Nuclear Science and Engineering
May 16, 2014

Certified by:_____
Lin-Wen Hu
Associate Director, MIT Nuclear Reactor Laboratory
Thesis Supervisor

Certified by:_____
Jacopo Buongiorno
Associate Professor of Nuclear Science and Engineering
Thesis Supervisor

Certified by:_____
Thomas J. McKrell
Research Scientist, Nuclear Science and Engineering
Thesis Supervisor

Certified by:_____
Neil E. Todreas
Professor Emeritus, Nuclear Science and Engineering
Thesis Reader

Accepted by:_____
Mujid S. Kazimi
TEPCO Professor of Nuclear Engineering
Chair, Department Committee on Graduate Students

Study of Turbulent Single-Phase Heat Transfer and Onset of Nucleate Boiling in High Aspect Ratio Mini-Channels to Support the MITR LEU Conversion

by

Eric Christopher Forrest

Submitted to the Department of Nuclear Science and Engineering on May 16, 2014 in partial fulfillment for the requirements of the degree of

DOCTOR OF PHILOSOPHY
in NUCLEAR SCIENCE AND ENGINEERING

ABSTRACT

Heat transfer in high aspect ratio mini-channels has important applications for materials test reactors using plate-type fuel. These fuel plates typically possess coolant channels with hydraulic diameters on the order of 4 mm or less. The single and two-phase heat transfer in such channels has not been well-characterized, especially in regard to the onset of nucleate boiling. While surface effects are known to dramatically influence the incipience of boiling, they have not been widely considered under forced convection. Since the limiting safety system setting for the MITR is the onset of nucleate boiling, there is considerable interest in better characterizing the phenomenon in such channels.

This study presents a first-of-a-kind, two-phase flow facility designed to measure the single-phase heat transfer coefficient and onset of nucleate boiling in a high aspect ratio mini-channel over a wide range of flow conditions while also permitting high speed visualization of the entire surface. The single-phase heat transfer coefficient is measured for mass fluxes ranging from 750 kg/m^2-sec up to 6000 kg/m^2-sec and for subcoolings ranging from 20 °C to 70 °C. The onset of nucleate boiling superheat and heat flux are measured for mass fluxes ranging from 750 kg/m^2-sec to 3000 kg/m^2-sec and for subcoolings ranging from 10 °C to 45 °C. Measurements are supported with high speed videography to visualize bubble incipience when conditions permit. The influence of surface wettability on the incipience point is also investigated by performing tests on a surface oxidized at high temperature in air.

Using a boundary layer analysis along with experimental data obtained in the study, a semi-analytical correlation is developed to predict the single-phase heat transfer coefficient in high aspect ratio rectangular channels. The correlation accounts for effects from secondary flows and heating asymmetry, and is suitable for both the transition and fully turbulent flow regimes. The new correlation predicts the Nusselt number with a mean absolute error of 4.9% in the range of $2.2<Pr<5.5$ and $4000<Re<70{,}000$. The onset of nucleate boiling heat flux on the reference surface is adequately predicted with the correlation of Bergles and Rohsenow, as long as the appropriate single-phase heat transfer prediction is used. However, the oxidized surface displays a modest increase in the incipient heat flux due to the improved wettability. This effect is not captured in the correlation of Bergles and Rohsenow, but is accounted for in other correlations such as that of Davis and Anderson.

Surface science measurements are presented for prototypical materials test reactor fuel surfaces to quantify effects of roughness, oxidation, and surface contamination on wettability. Overall, surface cleanliness is found to have a profound effect on wettability, and in turn, is expected to influence boiling incipience.

THESIS SUPERVISOR: Lin-Wen Hu, Ph.D., PE
Associate Director and Principal Research Scientist, MIT Nuclear Reactor Laboratory

THESIS SUPERVISOR: Jacopo Buongiorno, Ph.D.
Associate Professor of Nuclear Science and Engineering

THESIS SUPERVISOR: Thomas J. McKrell, Ph.D.
Research Scientist, Nuclear Science and Engineering

THESIS READER: Neil E. Todreas, Sc.D.
Professor Emeritus, Nuclear Science and Engineering

Acknowledgements

First and foremost, I owe thanks and acknowledgement to the Lord, our God, for all the blessings he has bestowed upon me. I have been granted tremendous opportunities throughout my life, for which I am grateful.

I wish to extend my gratitude and thanks to my thesis supervisor Dr. Lin-Wen Hu for her continued guidance on this project. Her support, despite the numerous technical hurdles, enabled such an ambitious undertaking. I also owe special thanks to my thesis supervisor Professor Jacopo Buongiorno, not only for his guidance on this project, but his continued mentoring since my time as an undergraduate at the Institute. My success is in no small part due to the attention and concern he has paid to his students. I very much appreciate Dr. Thomas McKrell taking on the significant responsibility of thesis co-advisor. His advice and expertise contribute substantially to the skill development of any student he supervises.

I am incredibly fortunate to have Professor Neil Todreas as a reader for this thesis. It is a rare privilege to receive comments and feedback from one of the continuing leaders in the field of nuclear thermal hydraulics. I also greatly appreciate Professor Emilio Baglietto taking on the role of thesis committee chair and providing feedback throughout the study.

The drafting and fabrication of the test section in this study would have been extremely challenging were it not for the skills and expertise of Yakov Ostrovsky. His assistance in this process was invaluable. David Carpenter's aid with the LabVIEW programming was instrumental in building the user interface and control systems for the experimental facility. I was also fortunate to have a very skilled undergraduate student, Sarah Don, working on the project as a UROP and assisting with surface characterization. Her level of enthusiasm and professionalism has been greatly appreciated.

I would also like to acknowledge Dr. Koroush Shirvan for his considerable assistance with STAR-CCM+ and RELAP5. Dr. Shirvan's extensive working knowledge of codes and simulation tools truly makes him an asset to NSE. Floyd Dunn at Argonne National Laboratory has also been an extremely helpful resource with respect to the RELAP5 simulations for the MITR.

Special thanks are due to Dr. David Dombrowski, Dr. Roland Schulze, and Dr. Cheng Liu for hosting me at Los Alamos National Laboratory for a summer. Not only did I garner valuable experience with the GTRI Convert program, but this experience enabled me to undertake a unique and relevant study, some results of which are presented in Appendix E.

I have received advice and feedback on various aspects of this study from a number of people, including Dr. Tom Newton (MIT NRL), Dr. Gordon Kohse (MIT NRL), Paul Menadier (MIT NRL), Professor Pete Griffith (MIT MechE), Dr. Matteo Bucci (CEA), Erik Wilson (ANL), Eric Shaber (INL), Jared Wight (B&W), and others. The range of feedback from such a wide range of expertise is greatly appreciated.

Thank you to Adam Grein at NRL, and John and Ray at the NRL Machine Shop, for helping me get set up on machine shop equipment and allowing me to borrow tools whenever needed. I also would like to acknowledge the continued use of tools, supplies, and equipment from the Massachusetts Broken Stone Company. The ease of access to this wide range of tools and equipment expedited construction of the experimental facility.

The Schlumberger-Doll Research Center has kindly allowed continued access to its confocal microscope at no charge, which was essential for the surface roughness measurements. Kurt Broderick of the MIT Microsystems Technology Laboratory is also recognized for providing SEM access. Lowel Lighting is kindly acknowledged for donating the LED lighting systems, along with offering professional assistance, to obtain the lighting required for high speed video capture. Thanks are due to Bren Phillips and Rosie Sugrue for their assistance with proof-of-concept high speed video measurements using the LED lighting system.

My gratitude goes out to the administrators in NSE and NRL, who work tirelessly in the background with no expectation of recognition or reward for their efforts. Specifically, I would like to acknowledge Clare Egan, Heather Barry, Pete Brenton, and Jennifer Gwinn in NSE, among others, for always making sure academic requirements were met, RA's were processed, and tuition had been paid. I would like to acknowledge Mary Young and Rose Rizzo at NRL for always understanding the funding dilemmas of a project of this scope, and processing the seemingly endless invoices associated with experimental parts and equipment.

I am also grateful to the many mentors, collaborators, and colleagues I have had throughout the years since starting at MIT. I have learned a great deal from these individuals, and developed skills and expertise that could not be learned elsewhere. In this regard, I would like to thank Professor Michael Rubner, Professor Robert Cohen, Professor Alan Hatton, Phil Sharpe, Mike Curry, Pete Skrabis, Wes Williams, Erik Williamson, Hyungdae Kim, Greg DeWitt, Bao Truong, Craig Gerardi, Tim Lucas, Stefano Passerini, Reza Azizian, Sung Joong Kim, and In-Cheol Bang, among others.

I would like to thank my family and friends for their support through my many years at the Institute. Special thanks to Morgan, and to my brothers Drew and Brett, for their encouragement and support during the thesis writing process. My late great grandfather, Richard Robinson (MIT S.B. 1933), certainly set the bar high, and his support of my undergraduate education will forever be appreciated. Lastly, this thesis would not have been possible were it not for the wish of my late mother, Lisa, to see me complete my doctoral degree.

The experimental program of this study was funded by the National Nuclear Security Administration's Global Threat Reduction Initiative. Research was performed under appointment to the U.S. Department of Energy Nuclear Nonproliferation Safeguards Graduate Fellowship Program sponsored by the National Nuclear Security Administration's Office of Nonproliferation and International Security. Financial assistance was also provided through the U.S. NRC Nuclear Education Graduate Fellowship, the American Nuclear Society Graduate Scholarship Award, and the Theos J. Thompson Memorial Fellowship.

Dedicated to my mother, Lisa. Were it not for your strength, compassion, courage, and kindness, this thesis would not have been possible.
You will be missed.

Table of Contents

List of Figures

List of Tables

Nomenclature

Symbol	*Description*	*Units*
A	surface area	m^2
A	heat equivalent of work (=1 for SI units)	-
a	Fitted constant	-
A_{flow}	flow area	m^2
A.R.	aspect ratio	-
$\vec{B}$	magnetic field vector	T
B	magnetic field strength	T
b	intercept	varies
b	fitted constant	-
BE	binding energy	eV
C_d	drag coefficient	-
C_f	skin friction coefficient	-
$Cs,_f$	surface-fluid interaction parameter	-
c	concentration	ppm or mg/L
c	fitted constant	-
c_p	specific heat capacity	J/(kg K)

Symbol	*Description*	*Units*
$\mathcal{D}$	diffusion coefficient	m^2/sec
D	minimum channel dimension	m
D_{eq}	equivalent diameter; typically same as D_{hyd}	m
D_H	heated diameter; based on heated perimeter	m
D_{hyd}	hydraulic diameter	m
D_L	laminar equivalent diameter	m
$\vec{E}$	electric field vector	V/m
E_f	energy per fission	J or MeV
E_s	surface energy	mJ/m^2
f	Darcy friction factor	-
f	function	-
f	frequency	sec^{-1}
f_0	source frequency	sec^{-1}
f_r	rotation frequency	sec^{-1}
f_s	frequency of vortex shedding	sec^{-1}
G	mass flux	$kg/(m^2\ sec)$
G	Gibbs free energy	J
g	acceleration due to gravity	m/s^2
h	Planck's Constant	eV-sec
h	heat transfer coefficient	$W/(m^2\ K)$
h	specific enthalpy	J/kg

Symbol	***Description***	***Units***
$h_{1\phi}$	single-phase heat transfer coefficient	W/(m^2 K)
h_{fg}	heat of vaporization	J/kg
I	current	A
I_p	primary current	A
I_s	applied current	A
I	electron intensity	counts/sec
$\mathcal{K}$	mass transfer coefficient	m/sec
$K_{discharge}$	discharge coefficient	-
K	pressure form loss coefficient	-
$K_{Doppler}$	Doppler flow coefficient	m^3
$K_{turbine}$	turbine meter flow coefficient	m
KE	kinetic energy	eV
k	thermal conductivity	W/(m K)
k_H	Henry's Law constant	Pa
L	length	m
L_c	characteristic length	m
L_H	heated length	m
L_p	Laplace length	m
L_{PT}	distance between pressure taps	m
$\vec{l}$	length vector	m
M	molar mass	g/mol
m	slope	varies

Symbol	***Description***	***Units***
m	mass	kg
$\dot{m}$	mass flow rate	kg/sec
N	number density	m^{-3}
N	number of measurements	-
N_A	Avogadro's number	mol^{-1}
n	number	-
P	Pressure	Pa or bar
P_E	electrical power	W
P_H	heated perimeter	m
P_w	wetted perimeter	m
ΔP	pressure drop or differential pressure	Pa
Q	volumetric flow rate	m^3/sec or gpm
$\dot{Q}$	heat rate	W
q''	heat flux	W/m^2
q'''	volumetric heat generation rate	W/m^3
q''_{CHF}	critical heat flux	W/m^2
q''_{ONB}	onset of nucleate boiling heat flux	W/m^2
R	electrical resistance	ohm
R	specific gas constant	J/(kg K)
R	channel outlet subcooling ratio	-
R^2	coefficient of determination	-
R_a	arithmetic roughness	μm

Symbol	*Description*	*Units*
R_p	Glättungstiefe	μm
$R_{th,c}$	thermal contact resistance	$(m^2 K)/W$
R_z	peak roughness	μm
$\vec{r}$	position vector	m
r	radius of curvature	m
r	roughness factor	-
r_b	bubble radius	m
r_c	cavity radius	m
S	Seebeck coefficient	V/K
T	temperature	ºC or K
T_0	reference temperature	ºC or K
T_∞	free stream temperature	ºC or K
T_b	bulk fluid temperature	ºC or K
T_{int}	interface temperature	ºC or K
T_{sat}	saturation temperature	ºC or K
T_w	wall (surface) temperature	ºC or K
ΔT_b	wall bulk superheat, T_w-T_b	ºC or K
ΔT_{sat}	wall saturation superheat, T_w-T_{sat}	ºC or K
ΔT_{sub}	subcooling, T_{sat}-T_b	ºC or K
t	thickness	m
t_{gap}	gap thickness	m

Symbol	*Description*	*Units*
U	overall heat transfer coefficient	W/(m^2 K)
u	flow velocity magnitude in primary (z) direction	m/sec
$u+$	Dimensionless velocity	-
u_∞	free stream velocity magnitude	m/sec
u_τ	friction velocity	m/sec
V	volume	m^3
V_E	voltage	V
V_H	Hall voltage	V
$\vec{v}$	velocity vector	m/sec
v	y-component of velocity	m/sec
w	weight fraction	-
w	weight	-
w	width	m
W_{sl}	Work of adhesion	mJ/m^2
X	expected (true) value	varies
x	transverse (width) coordinate for three-dimensional space	m
x	position coordinate for one-dimensional space	m
x	dependent variable	varies
x	random variable	varies
Y_{peak}	surface peak height	μm
Y_{valley}	surface valley depth	μm

Symbol	*Description*	*Units*
y	thickness (depth) coordinate for three-dimensional space	m
y	independent variable	varies
$y+$	dimensionless distance from wall	-
y_b	height of bubble	m
y_{stag}	height of stagnation point	m
z	axial (length) coordinate for three-dimensional space	m
z^*	dimensionless heated position	-
$z+$	dimensionless hydrodynamic position	-
z_P	position from inlet pressure tap	m

-Greek Letters-

α	thermal diffusivity	m^2/sec
α	temperature coefficient of resistance	K^{-1}
α^*	inverse aspect ratio	-
β	dynamic receding contact angle	degrees
γ	isotopic fraction	-
γ	surface heat flux ratio	-
γ	half groove angle	degrees
γ	generalized interfacial tension	N/m
γ_{sv}	solid-vapor interfacial tension	N/m
γ_{sl}	solid-liquid interfacial tension	N/m

Symbol	*Description*	*Units*
δ_{crit}	critical wall thermal layer thickness for incipience condition	m
δ_{hyd}	velocity boundary layer thickness	m
δ_{crit}	superheated layer thickness	m
δ_{HC}	hydrocarbon contaminant thickness	nm
δ_{th}	thermal boundary layer thickness	m
$\delta_{th,eq}$	equivalent thickness of entire thermal layer assuming linear temperature drop	m
δ_{v}	viscous (laminar) sublayer thickness	μm
δ_{v}^{+}	Dimensionless viscous sublayer thickness	-
ε	uncertainty (typically at 95% confidence level)	varies
ε_{H}	eddy diffusivity of heat	m^2/sec
ε_{M}	eddy diffusivity of momentum	m^2/sec
ζ	temperature drop in plate	ºC or K
θ	contact angle, apparent contact angle	degrees
θ_A	static advancing (advanced) contact angle	degrees
θ_{eqm}	static equilibrium contact angle	degrees
θ_I	intrinsic contact angle	degrees
θ_N	angle to normal	degrees
θ_R	static receding (receded) contact angle	degrees
θ_r	receding contact angle	degrees
κ	von Kármán constant	-

Symbol	*Description*	*Units*
κ_θ	thermal wall layer analog to von Kármán constant	-
λ	mean free path	Å
μ_o	permeability of free space	N/A^2
μ	viscosity	Pa sec
ν	photon frequency	sec^{-1}
ν	kinematic viscosity	m^2/sec
ν_t	kinematic eddy viscosity	m^2/sec
υ	specific volume	m^3/kg
$\Delta\upsilon$	specific volume change	m^3/kg
ρ	density	kg/m^3
ρ	resistivity	ohm m
Σ_f	macroscopic fission cross section	cm^{-1}
σ	surface tension	N/m
σ_f	microscopic fission cross section	cm^2
σ_x	standard deviation	varies
$\sigma_{\bar{x}}$	standard deviation of the mean (standard error)	varies
$\tau_{transit}$	transit time of kinematic wave	sec
τ_w	wall shear stress	Pa
Φ	dissipation function	-
φ	heater inclination angle	degrees
ϕ	neutron flux	neutrons/ (cm^2 sec)

Symbol	*Description*	*Units*
ϕ^*	geometry function	-
ϕ_s	spectrometer work function	eV
ψ_θ	wall layer function	-

Symbol	*Description*
	-Subscripts-
1	first in series outer edge of laminar sublayer
1ϕ	single-phase
∞	free stream
avg	average
b	bulk
back	backside
c	cavity
crit	critical
ct	circular tube
cw	chilled water
E	electrical
elec	electric
eq	equivalent
eqm	equilibrium
ext	external

Symbol	*Description*
f	liquid at saturation temperature fluid
film	evaluated at film temperature
g	vapor at saturation temperature
H	heated
hyd	hydrodynamic hydraulic
i	index for i^{th} value
in	inlet
int	internal
iso	isothermal
JIS	Japanese Industrial Standard
l	liquid
lo	liquid only
loc	local conditions
m	two-phase mixture
meas	measured
melt	at melting point
max	maximum value
min	minimum value
OFI	at the onset of (excursive) flow instability
ONB	at the onset of nucleate boiling

Symbol	***Description***
out	outlet
ran	random
rc	rectangular channel
ref	reference condition reference wall
rms	root mean square
sat	at saturation condition
ss	stainless steel
surf	surface
sys	systematic
th	thermal
tot	total
v	vapor
ve	vapor embryo
w	wall

-Superscripts-

D	dispersive component
ND	nondispersive component
′	time-varying quantity

-Abbreviations-

AC	Alternating Current
ACS	American Chemical Society
AEC	Atomic Energy Commission
AES	Auger Electron Spectroscopy
ANPP	Army Nuclear Power Program
ANSI	American National Standards Institute
AR-XPS	Angle Resolved X-ray Photoelectron Spectroscopy
ASME	American Society of Mechanical Engineers
ASTM	American Society for Testing and Materials
at%	Atomic Percent
ATR	Advanced Test Reactor
B&W	Babcock and Wilcox
CAD	Computer-Aided Design
CEA	Commissariat à l'Energie Atomique et aux Énergies Alternatives
CHF	Critical Heat Flux
CTE	Coefficient of Thermal Expansion
CW	Chilled Water
DC	Direct Current
DI	Deionized
DNB	Departure from Nucleate Boiling
DO	Dissolved Oxygen
DU	Depleted Uranium

EDM	Electrical Discharge Machining
EDS	Energy-Dispersive X-ray Spectroscopy
ELF	Extremely Low Frequency
EMI	Electromagnetic interference
FBR	Fast Breeder Reactor
FFC	Fuel Fabrication Capability
FOV	Field of View
GTRI	Global Threat Reduction Initiative
HC	Hydrocarbon
HEU	High Enriched Uranium
HFBR	High Flux Beam Reactor
HFIR	High Flux Isotope Reactor
HIP	Hot Isostatic Press
HPRR	High Performance Research Reactor
IAEA	International Atomic Energy Agency
IAPWS	International Association for the Properties of Water and Steam
ISO	International Organization for Standardization
JHR	Jules Horowitz Reactor
JRR	Japanese Research Reactor
LANL	Los Alamos National Laboratory
LED	Light-Emitting Diode
LEU	Low Enriched Uranium
LSSS	Limiting Safety System Setting

LWR	Light Water Reactor
MAE	Mean Absolute Error
MCM	Thousands of Circular Mils
MITR	MIT Reactor
MTR	Materials Test Reactor
NIST	National Institute of Standards and Technology
NNSA	National Nuclear Security Administration
NPT	Nonproliferation Treaty
NRC	Nuclear Regulatory Commission
OFI	Onset of Flow Instability
OMRE	Organic Moderated Reactor Experiment
ONB	Onset of Nucleate Boiling
OSV	Onset of Significant Voiding
PBR	Prompt Burst Reactor
PID	Proportional-Integral-Differential
PTFE	Polytetrafluoroethylene
RERTR	Reduced Enrichment for Research and Test Reactors
RDD	Radioactive Dispersal Device
RMS	Root Mean Square
RSD	Relative Standard Deviation
RTD	Resistance Temperature Detector
SEM	Scanning Electron Microscopy
SLE	Special Limits of Error

SNM	Special Nuclear Material
SS	Stainless Steel
TC	Thermocouple
TCR	Temperature Coefficient of Resistance
TEFC	Totally Enclosed, Fan-Cooled
TOA	Take-Off Angle
U-10Mo	Uranium-10wt% Molybdenum Alloy
VAC	Volts, alternating current
VDC	Volts, direct current
VI	Virtual Instrument
WMD	Weapon of Mass Destruction
XPS	X-ray Photoelectron Spectroscopy
XRF	X-ray Fluorescence

Dimensionless Parameters

Dimensionless Parameter	***Physical Interpretation***	***Formula***
Biot Number (*Bi*)	Ratio of external thermal resistance to internal thermal resistance of a body	$Bi = \frac{hL_c}{k_s}$
Boiling Number (*Bo*)	Non-dimensional heat flux	$Bo = \frac{q''}{Gh_{fg}}$
Brinkman Number (*Br*)	Ratio of thermal dissipation to thermal conduction	$Br \equiv EcPr$
Colburn Factor (j_h)	Dimensionless heat transfer coefficient	$j_h = \frac{h}{\rho c_p u}\left(\frac{\mu c_p}{k}\right)^{2/3} \equiv \frac{Nu}{RePr^{1/3}}$
Colburn Factor ($j_{\mathcal{M}}$)	Dimensionless mass transfer coefficient	$j_{\mathcal{M}} = \frac{Sh}{ReSc^{1/3}}$
Confinement Number (*Co*)	Ratio of capillarity to buoyancy in a channel	$Co = \frac{\sqrt{\sigma/[g(\rho_l - \rho_v)]}}{D_h}$
Eckert Number (*Ec*)	Ratio of kinetic energy of flow to boundary layer enthalpy difference	$Ec = \frac{u^2}{c_p(T_s - T_b)}$
Eötvös Number (*Eo*)	Ratio of gravity force to surface tension force	$Eo = \frac{g(\rho_l - \rho_v)L_c^2}{\sigma}$

Dimensionless Parameter	***Physical Interpretation***	***Formula***
Froude Number (*Fr*)	Ratio of inertia to gravity force	$Fr = \frac{u^2}{gL_c}$
Graetz Number (*Gz*)	Ratio of advection to heat conduction in developing region of channel; measure of thermal development of flow in entrance	$Gz = \frac{\rho c_p u D_{hyd}^2}{kL} \equiv RePr\frac{D_{hyd}}{L}$
Grashof Number (*Gr*)	Ratio of buoyancy force to viscous force	$Gr = \frac{g\beta(T_w - T_\infty)}{\nu}$
Jakob Number (*Ja*)	Ratio of sensible heat to latent heat absorption during vaporization	$Ja = \frac{c_p(T_w - T_{sat})}{h_{fg}}$
Morton Number (*Mo*)	Captures effects of fluid properties on bubble shape in fluid flow	$Mo = \frac{g\mu_l^4(\rho_l - \rho_v)}{\rho_l^2\sigma^3}$
Nusselt Number (*Nu*)	Ratio of heat transfer by convection to heat transfer by conduction; Proportional to the boundary layer thickness	$Nu = \frac{hL_c}{k}$
Péclet Number (*Pe*)	Ratio of thermal advection to thermal diffusion	$Pe = \frac{uL_c}{\alpha} \equiv RePr$
Phase Change Number (N_{pch})	Scales rate of phase change to channel heat rate	$N_{pch} = \frac{q''L_H P_H(\rho_f - \rho_g)}{\rho_f\rho_g h_{fg} A_{flow} u_{in}}$
Prandtl Number (*Pr*)	Ratio of momentum diffusivity to thermal diffusivity	$Pr = \frac{\mu c_p}{k}$
Turbulent Prandtl Number (*Pr*)	Ratio of eddy diffusivity for momentum to eddy diffusivity for heat	$Pr_t = \frac{\varepsilon_M}{\varepsilon_H}$
Reynolds Number (*Re*)	Ratio of inertia to viscous force	$Re = \frac{\rho u L_c}{\mu}$
Modified Reynolds Number (*Re**)	Reynolds number to correlate friction pressure drop using laminar equivalent geometry function	$Re^* = \phi^* Re$

Dimensionless Parameter	***Physical Interpretation***	***Formula***
Schmidt Number (*Sc*)	Ratio of momentum diffusivity to mass diffusivity	$Sc = \frac{\mu}{\rho \mathcal{D}}$
Sherwood Number (*Sh*)	Ratio of convective to diffusive mass transport	$Sh = \frac{\mathcal{K} L_c}{\mathcal{D}}$
Stanton Number (*St*)	Ratio of heat transfer into fluid to heat capacity of fluid flow	$St = \frac{h}{\rho c_p v} \equiv \frac{Nu}{RePr}$
Strouhal Number (*Sl*)	Ratio of vibration frequency to the characteristic frequency of the body	$Sl = \frac{f_s L_c}{u}$
Subcooling Number (N_{sub})	Accounts for time lag effects in liquid region due to subcooling at inlet	$N_{sub} = \frac{(h_f - h_{in})(\rho_f - \rho_g)}{h_{fg}\rho_g}$
Weber Number (*We*)	Ratio of inertia to surface tension force	$We = \frac{\rho u^2 L_c}{\sigma}$

Chapter 1

Introduction

1.1. Motivation for the Study

The spread and possible use of weapons-grade nuclear material is a risk inherent to the growth of nuclear research, technology, and power production. However, the Nuclear Nonproliferation Treaty (NPT) guarantees the right of all parties to the treaty to research, develop, produce, and use nuclear energy for peaceful purposes. Over the past sixty years, hundreds of civilian research reactors have been constructed around the globe in accordance with the principles of Article IV of the NPT. These research reactors have not only been pivotal in training engineers and scientists in nuclear-related fields, but are also necessary for the production of radioisotopes for applications in medicine, industry, and agriculture. Research reactors capable of producing a high thermal neutron flux ($>10^{14}$ n/cm^2-sec) are paramount in the development and testing of advanced materials for the next generation of nuclear power reactors. As nuclear power becomes a vital component in ensuring the future energy security of the United States, the mission of these research reactors will become more important in supporting research and development of new nuclear technologies.

The crux is that many of these research reactors rely on high enriched uranium (HEU) fuel to achieve high performance in compact core configurations. The IAEA defines high enriched uranium as uranium, in any chemical form, with 20% or more of the uranium consisting of the isotope U-235 by weight [1]. HEU fuel is considered a direct use material by the IAEA,

as it has the potential to be used in a nuclear weapon. As such, HEU-fueled research reactors have been identified as a potential threat for diversion or theft of weapons-usable material.

The distinction between high enriched uranium and low enriched uranium was first introduced by the National Laboratories and Atomic Energy Commission around 1955, though the terms were not formally defined [2]. While weapons-grade uranium is typically defined as uranium with a U-235 isotopic content of 90% or greater by weight [3], enrichments below 90% may still be employed in a nuclear weapon. In fact, any uranium enriched to 20% or more in U-235 is considered "weapons-usable," though this metric is somewhat arbitrary. Appendix A provides a primer on nuclear proliferation as it pertains to the use of HEU in civilian programs.

While it is difficult to quantitatively assess the actual proliferation risk posed by research reactors operating with HEU fuel, the issue has incited policymakers, both in the United States and internationally, to push for removal of HEU from civilian programs. The Atoms for Peace Plan, originating from President Dwight Eisenhower's famous 1953 speech to the UN General Assembly, originally stipulated limiting U-235 enrichment to 20% for civilian programs. The international rise of non-state terrorist organizations in the 1970's led to increased concerns over civilian HEU use in foreign programs. The Nuclear Nonproliferation Act of 1978 called for reconsideration of the role of HEU in the civilian fuel cycle [4]. The Schumer Amendment to the Energy Policy Act of 1992 [5] mandated that countries receiving HEU fuel or targets from the United States must convert to LEU in their civilian programs as soon as is technically possible. In the past decade, prevention of nuclear terrorism has become a focal point of U.S. national security policy, with both Republican and Democratic presidents identifying nuclear terrorism as the single greatest threat facing the country [6,7].

Conversion of materials test reactors using HEU fuel, both domestically and abroad, is therefore an important policy issue. However, numerous technical obstacles exist in converting these reactors. These high performance research and test reactors were designed to use HEU fuel, and the technical challenge of not just enabling operation but also maintaining performance with LEU fuel is immense. In most cases, conversion must be achieved with minimal or no changes to reactor components or core geometry. The Global Threat Reduction Initiative is geared toward tackling these technical issues. This study directly supports GTRI programs through thermal hydraulic experiments and analyses to enable conversion of materials test reactors such as the MITR.

1.1.1. The Global Threat Reduction Initiative and RERTR

The National Nuclear Security Administration's (NNSA) Global Threat Reduction Initiative (GTRI) is aimed at preventing the use of civilian nuclear and radiological material in weapons of mass destruction (WMD). The GTRI has three primary initiatives to achieve this objective [8]:

- **Convert:** Conversion of domestic and international civilian research reactors and isotope production facilities from the use of HEU to LEU, development of new LEU fuels, and deployment of associated manufacturing capabilities needed for new LEU fuels in the U.S.
- **Protect:** Protection of high-priority nuclear and radiological materials worldwide from theft and sabotage.
- **Remove:** Removal or disposition of excess nuclear and radiological materials from civilian sites worldwide.

The Protection initiative has successfully improved physical security, protocols, and accountancy at numerous domestic and international civilian sites which possess special nuclear material (SNM) and radiological material. Radiological materials, such as Co-60, Sr-90, and Cs-137, have numerous applications benefiting society in medical, industrial, and agricultural sectors. These materials, however, could potentially be used to make a radiological dispersal device (RDD). Radiological material is more widespread and typically considered an easier target for theft or misuse than fissile material, an issue that the Protect initiative is addressing.

The Removal initiative has permanently removed excess and unsecured radiological materials worldwide. The initiative has also enabled the repatriation of U.S. and Russian-origin spent fuel (both HEU and LEU) from research reactors in other countries. The Removal initiative results in permanent threat reduction because potential targets for theft are eliminated.

The Conversion initiative, which the motivation for this thesis falls under, encompasses the Reduced Enrichment for Research and Test Reactors (RERTR) program, which began in 1978 at Argonne National Laboratory. RERTR has three technology components [9]:

- The development of advanced LEU fuels.
- Design and safety analyses for research reactor conversion.

- Development of targets and processes for the production of the medical isotope molybdenum-99 with LEU.

Currently, Mo-99, the principal parent nuclide used to obtain technetium-99m, is produced by neutron irradiation of HEU targets. Technetium-99m is the most widely used radioisotope in nuclear medicine, accounting for over 80% of all medical isotopes. [10]. The last component of the RERTR program, though not related to this study, is important for ensuring a consistent and economical supply of Mo-99 for medical use while reducing proliferation risk. Currently, LEU foils in place of HEU dispersion targets are being studied to maintain production capabilities of Mo-99 without increasing costs.

The RERTR program has converted or verified the shutdown of 72 HEU-fueled research and test reactors as of 2010 [8]. Despite the continued success of the program, 28 reactors that fall under the scope of the GTRI are unable to convert with existing high-density LEU fuels. 19 of these reactors, including the MIT Research Reactor (MITR) and five other high performance research reactors (HPRR's) in the U.S., have been identified as candidates for a 90 wt% uranium, 10 wt% molybdenum (U-10Mo), alloy monolithic fuel currently under development. These reactors and others internationally, are listed in Table 1. As seen in the table, these reactors consume over 475 kg of HEU annually, or more than nineteen significant quantities of HEU as defined by the IAEA. Conversion of these reactors would yield a substantial reduction in the amount of HEU in the civilian fuel cycle.

The experimental thermal hydraulic research in this study directly supports the second technical component of the RERTR program by measuring heat transfer phenomena and characteristics of a prototypic materials test reactor coolant channel. While fuel development and qualification is not the focus of this study, it is the lynchpin of the conversion program for HPRR's; without the very high density LEU fuel, the MITR and most other HPRR's will be unable to convert. Therefore, an overview of the fuel development program is provided in section 1.3.2.

Table 1: Candidate Research Reactors for Conversion Using the Proposed U-10Mo Fuel. HEU consumption values are approximate, and may vary. *Adapted from Ref. [11].*

Reactor	Location	Power	HEU Consumption
Western Design			
ATR	Idaho Falls, ID, USA (Idaho National Laboratory)	250 MW	120 kg/yr
HFIR	Oak Ridge, TN, USA (Oak Ridge National Laboratory)	100 MW	80 kg/yr
NBSR	Gaithersburg, MD, USA (NIST)	20 MW	13 kg/yr
MURR	Columbia, MI, USA (University of Missouri)	10 MW	24 kg/yr
MITR	Cambridge, MA, USA (MIT)	6 MW	5 kg/yr
ATRC*	Idaho Falls, ID, USA (Idaho National Laboratory)	5 kW	~0 kg/yr
JHR†	France	100 MW	N/A
BR2	Belgium	80 MW	29 kg/yr
RHF	France	57 MW	55 kg/yr
ORPHEE	France	14 MW	16 kg/yr
Russian Design			
MIR-M1	Russia	100 MW	62 kg/yr
VVR-M	Russia	18 MW	15 kg/yr
IVV-2M	Russia	15 MW	9 kg/yr
VVR-TS	Russia	15 MW	21 kg/yr
LWR-15	Czech Republic	10 MW	14 kg/yr
IR-8	Russia	8 MW	2 kg/yr
IRT-T	Russia	6 MW	6 kg/yr
IRT-MEPI	Russia	2.5 MW	1 kg/yr
CA.MIR-M1	Russia	~0 MW	~0 kg/yr

*Critical Assembly.

†Under construction; as of this writing, CEA intends to use 27% enriched U_3Si_2 fuel since U-10Mo fuel is not yet available [12].

1.1.2. Heat Transfer in Narrow Rectangular Channels

The use of closely spaced, plate-type fuel elements in the MITR and other materials test reactors results in coolant channel geometries which are rectangular and very narrow. Study of convective heat transfer, both single-phase and two-phase, in narrow rectangular channels is limited in comparison to circular geometries. The primary reason is that few high heat transfer applications use rectangular cooling geometries, as circular tubes are easier to fabricate than rectangular ducts, are more suited for service at elevated pressure, and typically offer lower overall thermal resistances for the system. In addition, experimental investigation of heat transfer in rectangular channels is more difficult in regard to fabrication, testing, and measurement.

The hydraulic diameter is a useful parameter when dealing with flow in non-circular conduits for the purpose of characterizing hydrodynamic and heat transfer phenomena:

$$D_{hyd} = \frac{4A_{flow}}{P_w} \tag{1}$$

In the case of a circular tube, the hydraulic diameter is equivalent to the tube diameter:

$$D_{hyd,c.t.} = \frac{4A_{flow}}{P_w} = \frac{4\pi D^2/4}{\pi D} = D_{c.t.} \tag{2}$$

The rectangular channels in materials test reactors are commonly characterized by very high aspect ratios. A schematic of a prototypic geometry is shown in Figure 1.

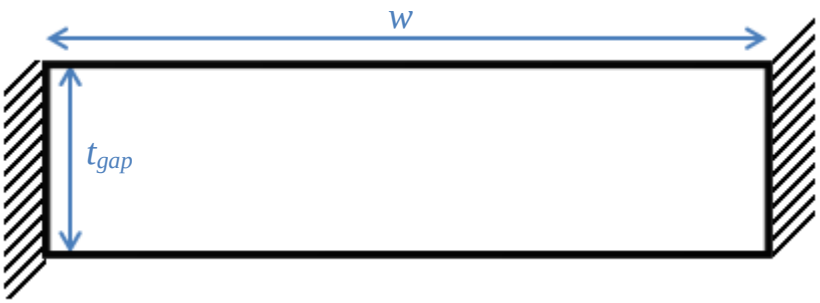

Figure 1: Rectangular Channel Geometry and Characteristic Dimensions.

Here w is the dimension of the long wall and t_{gap} is the dimension of the short wall. The aspect ratio for this geometry is defined as:

$$A.R. = \frac{w}{t_{gap}} \tag{3}$$

And the inverse of the aspect ratio is simply:

$$\alpha^* = \frac{t_{gap}}{w} \tag{4}$$

In the case that $w \gg t_{gap}$, $\alpha^* \to 0$ and the hydraulic diameter simplifies to:

$$D_{hyd,r.c.} = \frac{4A_{flow}}{P_w} = \frac{4wt_{gap}}{2w + 2t_{gap}} \xrightarrow{w \gg t_{gap}} 2t_{gap} \tag{5}$$

which is simply twice the coolant channel gap. In fact, the representation of the hydraulic diameter in equation (5) is the most appropriate for high aspect ratio, narrow rectangular channels, since hydrodynamic and heat transfer phenomena in the majority of the channel are independent of and not physically influenced by the edges [13]. This result is equivalent to that for a flat duct (parallel plates), where $\alpha^* = 0$. Therefore, experimental investigations of heat transfer in parallel plate geometries are relevant to narrow rectangular coolant channel geometries. In the case where the coolant channel geometry has some curvature, such as in the Materials Testing Reactor, the MITR-I core, ATR, HFIR, JHR, and others, the parallel plate approximation may still be suitable. If the radius of curvature, r, is much greater than the coolant channel gap ($r \gg t_{gap}$), then a parallel plate approximation is appropriate.

Narrow rectangular coolant channel geometries found in materials test reactors may also be characterized in relation to the capillary length scale, or Laplace constant, which is defined as:

$$L_p = \sqrt{\frac{\sigma}{g(\rho_l - \rho_v)}} \tag{6}$$

The Laplace constant is a relevant length scale for flow in conduits to determine the relative effect between gravity forces and surface tension forces. For very small channel geometries, flow phenomena, especially under two-phase conditions, may be markedly different than at the macro-scale. Additionally, friction pressure drop and heat transfer models developed for flows at the macro-scale may not be applicable in very small channels. For this reason, attempts have been made to classify coolant channel geometries in relation to expected effects from changes in length scale. Some of the earliest classifications simply denoted conventional channels as having a characteristic dimension larger than the Laplace constant, and non-conventional, or mini-channels, having a characteristic dimension on the order of the Laplace constant or smaller. Kew and Cornwell [14] established a more specific criterion by introducing a confinement number, defined as:

$$Co = \frac{\sqrt{\sigma/[g(\rho_l - \rho_v)]}}{D_{hyd}} \tag{7}$$

which is simply the Laplace constant divided by the hydraulic diameter of the channel. By examining studies of capillary flow, flooding, and heat transfer in vertical up-flow, in addition to their own experimental measurements, they determine that effects of confinement on flow and heat transfer are significant if:

$$Co > 0.5 \tag{8}$$

The physical interpretation of this result is that for confined flow, bubbles may not be considered as isolated. Rather, bubbles, formed from boiling or coalescence, completely fill the channel gap, and are physically constrained by the geometry.

Table 2: Channel Classification Based on Minimum Dimension. ***Adapted from Ref. [16].***

Channel Classification	Length Scale*
Conventional Channels	$D > 3$ mm
Mini-channels	200 μm $< D \leq 3$ mm
Microchannels	10 μm $< D \leq 200$ μm
Transitional Microchannels	1 μm $< D \leq 10$ μm
Transitional Nanochannels	0.1 μm $< D \leq 1$ μm
Nanochannels	$D \leq 0.1$ μm

*Here D represents the minimum channel dimension.

The value of the Laplace constant and confinement number of course depend on the fluid properties. Therefore, changing fluids, or even changing the operating temperature, could change the definition of a channel with fixed dimensions. Kandlikar has introduced a fixed metric classifying channels based on absolute channel dimensions [15, 16]. The classification is listed in Table 2. Based on this classification, the coolant channels in the MITR and similar materials test reactors are mini-channels.

For materials test reactors, natural convection, single-phase forced convection, onset of nucleate boiling (ONB), onset of significant voiding (OSV), two-phase convective heat transfer, onset of flow instability (OFI), and the critical heat flux (CHF) are all relevant heat transfer phenomena for either normal operation or potential accident scenarios. Figure 2 provides a representative flow boiling curve, summarizing some of the relevant thermal phenomena in a materials test reactor. Unfortunately, all of the aforementioned heat transfer phenomena have not been thoroughly studied in high aspect ratio mini-channels. While there has been enormous interest in microchannels for heat transfer applications in recent years, rectangular mini-channels have largely been overlooked. Growing interest in compact heat exchangers for power generation applications may lead to increased study in the future, though. At the present, the

majority of studies cover low mass flux conditions and fluids other than water. The onset of nucleate boiling, which is the criterion for the Limiting Safety Systems Setpoint (LSSS) in the MITR, is of little practical interest for most other applications, resulting in even fewer studies under relevant conditions, especially with regard to surface effects. A review of available literature on heat transfer in narrow rectangular channels is provided in Chapter 4 and Chapter 5.

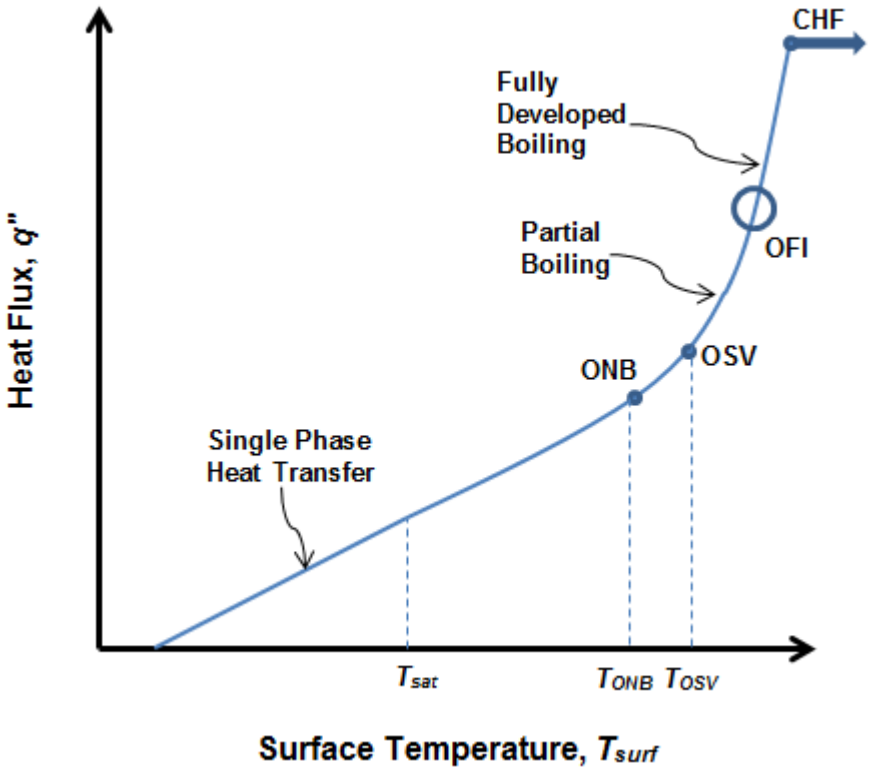

Figure 2: Typical Forced Convection Subcooled Boiling Curve, with Relevant Thermal Phenomena Listed. OFI may occur under certain conditions, with interconnected multiple channels being more susceptible to the Ledinegg-type instability.

1.2. Technical Objectives

Even with the development of advanced LEU fuels, HPRR's will suffer from a loss of performance once converted to LEU. Performance loss is primarily associated with a decrease in the thermal neutron flux, which is attributed to a harder neutron spectrum. The harder neutron spectrum is due to the higher U-238 content in the fuel, resulting in more resonance captures during down-scattering. Considering that generating a high thermal neutron flux is the primary feature of the MITR and similar reactors, experimental programs will be adversely affected. Specifically, the conversion of the MITR from HEU to LEU fuel is expected to result in a decrease of the thermal neutron flux by 20% or more.

A method to regain lost performance in the MITR and other HPRR's following conversion is by increasing the total core power. The total core power is related to the neutron flux by:

$$\dot{Q} = \int_V E_f \Sigma_f(\vec{r})\phi(\vec{r})dV \tag{9}$$

All else remaining the same, an increase in power will yield a proportional increase in the neutron flux. However, the maximum power is set by thermal hydraulic operating limits. Therefore, this study seeks to measure heat transfer characteristics of prototypic, high aspect ratio, rectangular coolant channels found in the MITR and similar materials test reactors (MTR's). Better estimates of heat transfer in these reactors can allow for removal of excess conservatism, allowing for system uprates and recapture of lost performance from the conversion.

In the case of the MITR, the upper thermal hydraulic operating limit is established by the Limiting Safety System Setting (LSSS) criterion, which is the onset of nucleate boiling (ONB). This means that ONB must not be encountered anywhere on the clad during routine 6 MW operation nor during natural convection with heat generation up to 100 kW [17]. Use of ONB as the LSSS criterion for the MITR is discussed in greater detail in Chapter 5.

1.2.1. Measurement of the Single-Phase Heat Transfer Coefficient

Boiling incipience strongly depends on the saturation wall superheat, among other factors. Current prediction methods of the cladding surface temperature in the MITR and other materials test reactors rely on the use of single-phase heat transfer correlations developed for circular tubes, which may not be appropriate for the coolant channel geometries found in materials test reactors. The influence of secondary flows and heating asymmetry may result in considerable disagreement in heat transfer coefficients between these channels and circular geometries. While studies have been performed in the past for turbulent single-phase heat transfer in high aspect ratio mini-channels, the studies are few in number and limited in scope. Additionally, the measurement uncertainty in some studies is high enough to preclude any sort of conclusion when comparing to circular tube predictions. However, even a 10% increase in the single-phase heat transfer coefficient can have a dramatic effect on the onset of nucleate boiling heat flux. Therefore, the first technical objective of this study is to measure the turbulent single-phase heat transfer coefficient in a prototypic MTR coolant channel geometry, at prototypic conditions, with high accuracy (±10% or better). Minimization of measurement uncertainty is critical; as such, a thorough overview of the experimental facility and instrumentation is provided in Chapter 2 and Chapter 3, along with a review of the state of the art in flow and temperature measurement, which are the leading contributors to measurement uncertainty in this type of experiment. Experimental results for the turbulent single-phase heat transfer coefficient, along with development of a new single-phase heat transfer correlation, are provided in Chapter 4.

1.2.2. Investigation of ONB from Plain and Oxidized Surfaces

The second major technical objective is to measure the heat flux and wall superheat at the onset of nucleate boiling. Studies of boiling incipience in the geometry of interest are even more limited than those for the turbulent single-phase heat transfer coefficient. The correlation of Bergles and Rohsenow [18], developed in 1962 for circular tubes and discussed in detail in Chapter 5, has been the mainstay in predicting the onset of nucleate boiling in the MITR. Assessment of the suitability of this correlation is paramount for any uprate analysis, as excess conservatism could potentially be recaptured. Determination of ONB is achieved using temperature measurement, pressure measurement, and supported with high speed video when conditions allow. Experimental results are presented in Chapter 5.

Another component of this objective involves the investigation of surface effects on the onset of nucleate boiling. Since effects such as wettability are known to have a profound impact on boiling incipience, tests are also conducted on a surface that has been oxidized in air, resulting in a decreased contact angle and improved wettability. A systematic characterization study is also carried out on the heat transfer surfaces and typical fuel component surfaces to support the heat transfer experiments. Not only are boiling surfaces thoroughly characterized with a variety of techniques, but effects of roughness, hydrocarbon contamination, and oxidation on the surface wettability of relevant fuel materials are explored. Expected influence on the onset of nucleate boiling is inferred, with results provided in Chapter 6.

1.3. Supplementary Background

While this study focuses on fundamental thermal hydraulic phenomenon in narrow channels, it is important to understand the system relevance, along with relevance to other research programs. For this reason, an overview of the MITR is provided in the next section. In addition, the fundamental necessity driving the conversion schedule is the fuel development; without the fuel, the conversion cannot take place. Therefore, a concise background on advanced fuel development for research and test reactors is provided in section 1.3.2.

1.3.1. Overview of the MITR

In the spring of 1958, construction of a research reactor was completed at the Massachusetts Institute of Technology. The reactor project had been undertaken in 1955 by Professor Manson Benedict and Theos Thompson. The reactor, designated as the MITR, first achieved criticality on July 21, 1958. Initially, the reactor operated at a power of 1 MW, though the core was designed for operation up to 5 MW. After upgrading the heat exchanger and cooling tower to accommodate higher heat removal from the primary system, 5 MW operation was attained. The reactor was moderated and cooled by heavy water, with a graphite reflector surrounding the 4 foot diameter by 7 foot high aluminum core tank. The fuel elements were an exact replica of those found in the Materials Testing Reactor, with the exception that the two outermost plates were not fueled [19]. The fuel consisted of 18 curved plates in a square assembly, with a coolant channel gap of 0.117". Each fuel plate was composed of high enriched U-Al alloy fuel, which was clad in aluminum. Thirty assembly positions existed in the core, with several of these positions used for experimental irradiation programs. A peak thermal neutron flux of 1.2×10^{14} n/cm^2-sec was achieved at the center of the core, with the maximum thermal flux accessible for experiments being 2×10^{13} n/cm^2-sec at the core periphery.

Spacing of fuel elements in the MITR core was sub-optimal, and it was soon realized that a more compact core configuration would allow for higher neutron fluxes. In the 1960's, concern over the ability of the MITR to compete with research reactors under development led to a desire for a significant core redesign. Experience with the High Flux Beam Reactor at Brookhaven National Laboratory offered insight into required design features necessary for a more compact core configuration. The MITR core redesign team was led by Theos Thompson,

which eventually settled on a design using light water as the coolant and moderator, with heavy water and graphite acting as reflectors. The original MITR core (now designated as the MITR-I) continued operation until May of 1974 when it was shut down to accommodate installation of the redesigned core. In addition to modification of the core, a new tank system was installed, with an inner tank to accommodate the core and light water coolant/moderator, surrounded by an exterior tank for the heavy water reflector. Changes were made to allow for greater flexibility and access to beam ports and in-core irradiation positions. In August of 1976, the new MITR core (designated as the MITR-II) first achieved criticality. A cut-away view of the MITR-II is shown in Figure 3.

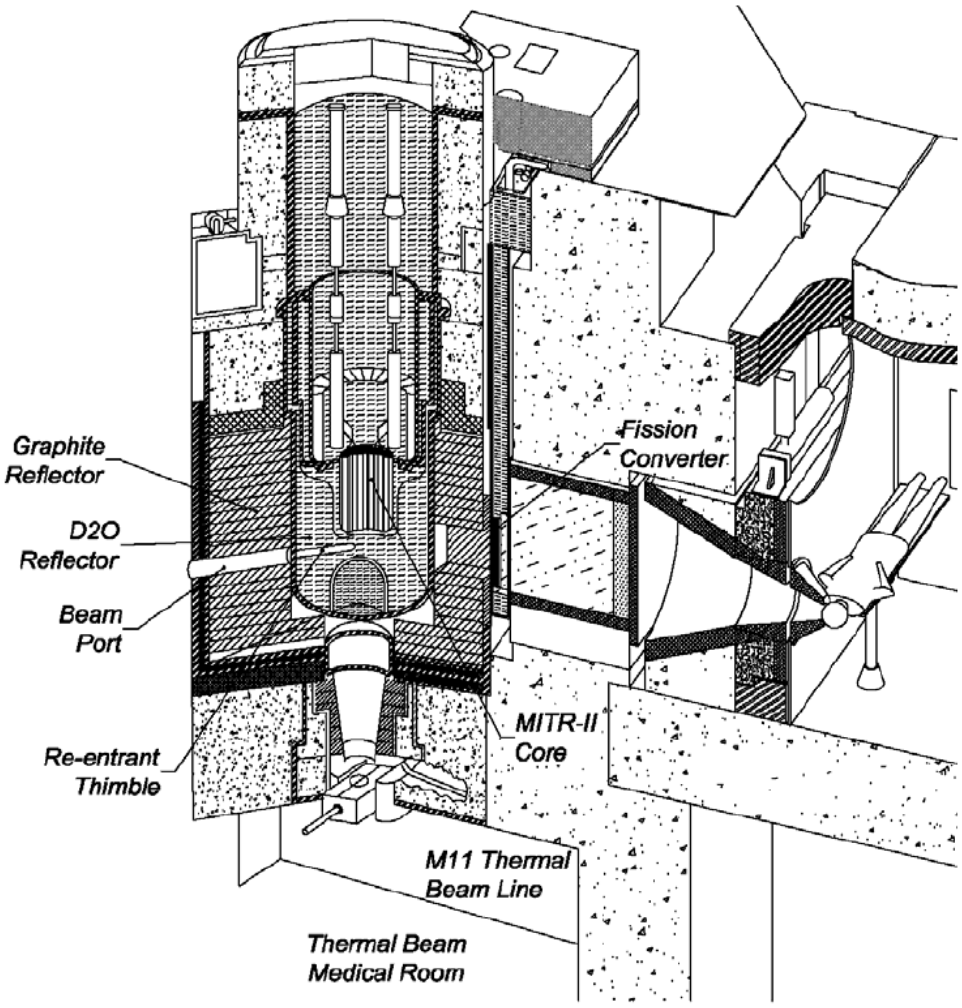

Figure 3: Cut-away View of the MITR-II Core Tank and Structural Components. *Source: Ref. [20].*

The MITR-II core began operation at 5 MW, with 6 MW operation starting in April of 2011 following approval of the uprate by the NRC. The MITR-II is classified as a tank-type reactor, with the top of the core tank at atmospheric pressure, and water flowing up through the core. General operating parameters and characteristics of the MITR-II are provided in Table 3. The fuel elements consist of 15 plates (uncurved) in a rhomboidal assembly. The fuel plates consist of high enriched UAl_x fuel in an aluminum matrix (cermet fuel), with 6061 aluminum serving as the cladding material. The fuel is unique in that the outer clad has longitudinal grooves, or micro-fins, milled into the surface to improve heat transfer to the coolant. The core consists of 27 assembly positions, with three typically being reserved for in-core experiments. Figure 4 shows the core and a single fuel assembly. In Figure 5, the core flow shroud, the fuel element storage ring, and instrumentation above the core can be seen.

The MITR has numerous irradiation facilities for materials testing, medical isotope production, medical therapy, education, and general research purposes such as neutron activation analysis and neutron radiography. Fast and thermal fluxes up to 1.2×10^{14} n/cm^2-sec and 5.0×10^{13} n/cm^2-sec, respectively, are available for experiments. The MITR is also one of the few sources for production of extremely uniform, high-quality n-type, neutron transmutation doped silicon for specialty semiconductor and power electronics applications. The MITR possesses a

Table 3: Steady-State Operating Parameters of the HEU MITR-II Core.

Parameter	Value
Nominal Power	6.0 MW
Power Density	70 kW/L
Heat Flux (Average at Fuel Meat)	277 kW/m^2
Maximum Inlet Pressure	1.99 bar
Nominal Outlet Temp.	53 °C
Nominal Core Flow Rate	125 kg/sec
Mass Flux (Average Channel)	2750 kg/m^2-sec
Flow Velocity (Average Channel)	2.8 m/sec

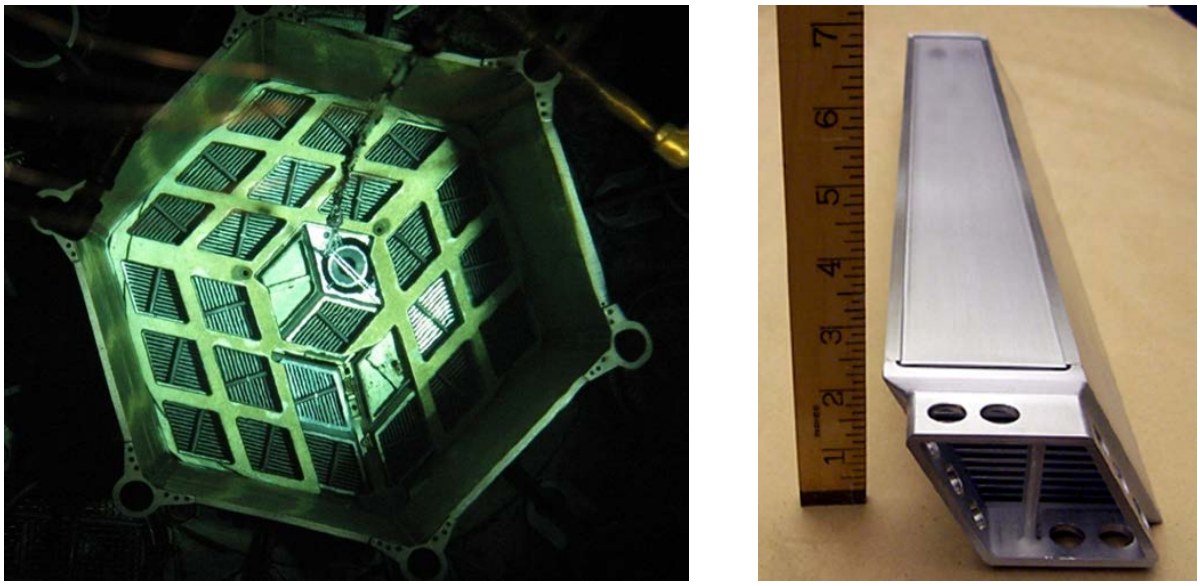

Figure 4: MITR-II Core (left) and a Single Fuel Assembly (right). *Source: Ref. [20]*.

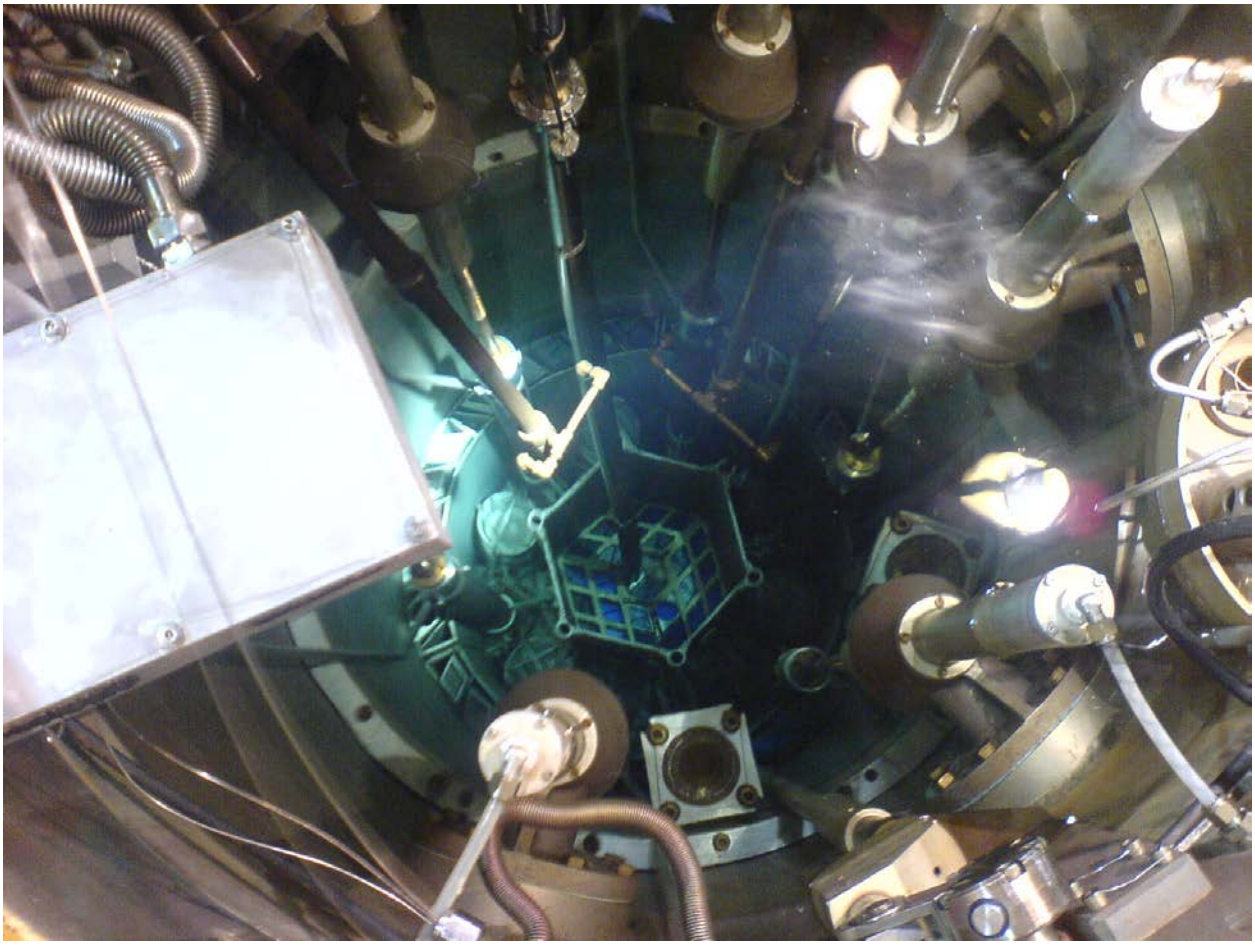

Figure 5: Photograph of the MITR-II Core Taken by the Author at the Top of the Core Tank. An in-core experiment is installed in the A-ring.

Table 4: MITR Experimental Facilities.

Facility	Description	Neutron Flux
In-Core	3 Spaces Available	
High Pressure Coolant Loops	High pressure loops capable of operating at up to 316 °C to simulate BWR and PWR conditions.	3.6×10^{13} n/cm^2-sec (*thermal*) 1.2×10^{14} n/cm^2-sec (*fast*)
High Temperature Irradiation Facility	>1000 °C in inert gas.	3.6×10^{13} n/cm^2-sec (*thermal*) 1.2×10^{14} n/cm^2-sec (*fast*)
Beam Ports	One 12” radial port Two 6” radial ports	4×10^{12}-1×10^{13} n/cm^2-sec (*thermal*)
	Four 4” radial ports One 6” through-port One 4” through-port	2.5×10^{12}-5.5×10^{12} (*thermal*)
Pneumatic Tubes	1PH1- 1” intermediate flux pneumatic tube	8×10^{12} n/cm^2-sec (*thermal*)
	2PH1- 2” High Flux Pneumatic Tube	5×10^{13} n/cm^2-sec (*thermal*)
Graphite Reflector Positions	Two vertical positions in reflector for sample irradiation.	4×10^{12}-1×10^{13} n/cm^2-sec (*thermal*)
Medical Rooms	Room with horizontal beam from fission converter.	5×10^{9} n/cm^2-sec (*epithermal*)
	Room beneath core with vertical thermal beam.	1×10^{10} n/cm^2-sec (*thermal*)

fission converter beam facility that has been used in clinical trials of boron-neutron capture therapy for the treatment of glioblastoma. The MITR also produces irradiated gold seeds for various other cancer treatments. Additionally, the available neutron flux in the MITR is similar to that found in a commercial PWR, which, combined with in core experimental loops capable of operating at PWR temperature and pressure, allows for testing of materials under prototypic PWR conditions. Table 4 summarizes the experimental facilities at the MITR.

The conversion of the MITR to LEU fuel will require the use of the U-10Mo fuel discussed previously. The currently proposed LEU fuel retains the longitudinal grooves of the HEU fuel, as seen in Figure 6. The implementation of LEU fuel will result in some changes to the fuel assemblies, most notably an increase in the number of plates per assembly from 15 to 18 and a decrease in the coolant channel gap. The differences between the HEU and LEU fuel are summarized in Table 5. A transitional core conversion strategy is planned for the U-10Mo fuel, which will introduce less excess reactivity during each fuel cycle and allow for monitoring a prediction of LEU fuel element performance by initially placing in lower flux positions within the core. The conversion will result in extended downtime for the MITR, in addition to significantly impacting the performance of in-core experiments due to the change in flux distribution and hardening of the neutron spectrum.

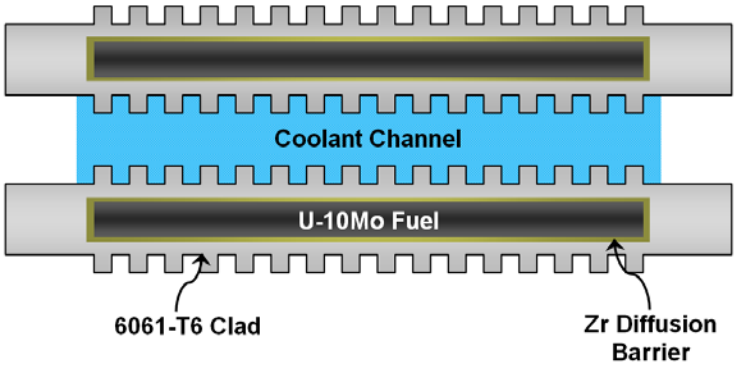

Figure 6: Schematic of Finned Coolant Channel Geometry for the LEU Fuel. The coolant channel geometry is actually a parallelogram due to the rhomboidal assembly, but can be represented as rectangular due to the high aspect ratio. Coolant flows up through each assembly (upflow). Micro-fins are not to scale.

Table 5: Comparison of Existing HEU and Proposed LEU Fuel for the MITR.

	HEU	**LEU**
Fuel Type	U-Al_x	U-10Mo Monolith
Enrichment	93%	19.75%
Active Fuel Length	0.584 m (23″)	0.584 m (23″)
Fuel Plates per Assembly	15	18
Radial peaking	2.0	1.76
Fuel Meat Thickness	0.762 mm (0.030”)	0.508 mm (0.020”)
Fuel Cladding Thickness	0.381 mm (0.015”)	0.254 mm (0.010”)
Coolant Gap	1.98 mm (0.078”)	1.83 mm (0.072”)

1.3.2. Development of Advanced LEU Fuels

Reactor fuel is typically classified by fuel geometry (e.g. rod, plate, etc.), cladding material, and fuel material. Materials test reactors almost exclusively employ fuel in a plate-type geometry, whether it be flat or in a curved configuration. The fuel is typically clad in aluminum or an aluminum alloy, with 6061 being commonplace. Dispersion fuels, either composed of the intermetallic uranium aluminide (UAl_x), or of the ceramic triuranium octaoxide (U_3O_8), embedded in an inert metallic matrix, have become the standard for MTR's. For example, the MITR and ATR rely on UAl_x in an aluminum matrix, while HFIR uses U_3O_8 in an aluminum matrix [21]. However, various other fuel materials have been used in the past or are being proposed for MTR fuel, the general classifications of which are summarized in Table 6.

Table 6: Classification of Fuels for Materials Test Reactors.

Chemical Form	Physical Form	Examples	Comments
ALLOY	Monolithic	U-Al; U-Mo; U-Zr; U-ZrH_x	High physical density of material; High *k*
	Dispersion	U-Mo-Al	Matrix allows for fission gas accumulation
CERAMIC	Monolithic	UO_2	High melting point; Good temperature stability
	Dispersion	U_3O_8-Al	"Cermet" fuel; Advantages of ceramic with better bulk *k*
INTERMETALLIC	Monolithic	U_3Si_x	Very high uranium loading achievable
	Dispersion	UAl_x-Al; U_3Si_x-Al	"Cermet" fuel; Good mix of properties; Porosity allows for fission gas accumulation

As seen in the table, the chemical and physical forms of fuel are not always mutually exclusive; many fuels can be fabricated as a monolith or dispersed in a matrix. The term "monolithic" refers to the fuel meat of an element consisting of a continuous medium. Dispersion fuels have the fuel material in powder form (particle size typically ~100 μm) in a metallic matrix, most commonly of aluminum, magnesium, or zirconium. Ceramic or intermetallic fuel in dispersion form is often referred to as cermet fuel. While monolithic fuels may offer higher physical densities, dispersion fuels typically have added porosity, enabling the accumulation of fission gases and helium in the fuel meat while reducing swelling of the fuel. In commercial power reactors, a gap between the fuel and the clad provides for fission gas accumulation. In MTR plate-type fuel, no such gap exists. One type of fuel that does not quite fit into the categories of Table 6 is Caramel fuel. Caramel fuel consists of miniature uranium oxide or alloy wafers sandwiched between plates with no interstitial matrix, allowing for fairly high density while accommodating fission gas buildup. CEA of France has led the development of Caramel fuel for research and test reactor applications.

Not only must criticality be maintained, but a similar level of performance in terms of neutron flux, reactivity, and burn-up must be achieved with the replacement LEU fuel. To summarize, the general fuel criteria for conversion to LEU are [22]:

- The safety margins and reliability of the fuel should not be lower than for the current design based on highly enriched fuel.
- Major modifications to the reactor should not be required.
- There should be no more than marginal loss of reactor performance (e.g. flux-per-unit power), nor increase in operation costs.

The macroscopic fission cross-section for U-235 may be defined as:

$$\Sigma_f^{U235} = N_{U235}\sigma_f^{U235} \tag{10}$$

where the U-235 atomic number density for an alloy or compound can be expressed as:

$$N_{U235} = \frac{\gamma_{U235} w_U \rho_{tot} N_A}{M_U} \tag{11}$$

where N_A is Avogadro's number, M_U is the molar mass of uranium, w_u is the weight fraction of uranium in the compound or alloy, and γ is the isotopic fraction, or enrichment, of U-235. To maintain the same U-235 number density at reduced enrichment, either a material of higher physical density must be used (i.e. $\rho_{tot} \uparrow$), or, an alloy or compound with a higher weight fraction of uranium must be used (i.e. $w_u \uparrow$), or both. However, increased capture from the higher fraction of U-238 results in lower reactivity and lower burn-up potential. The number density of U-235 in 20% enriched fuel must therefore be 12-15% higher than the number density of 93% enriched fuel to maintain adequate performance [22]. Pure uranium metal has a density of 19.1 g/cm^3, and effectively sets the upper achievable limit for the physical uranium density in reactor fuels. However, in practice, uranium metal is not suitable as a fuel material, due to poor phase stability, difficulties with fabrication, and susceptibility to corrosion. Alloying with other metals may resolve many of these issues by stabilizing uranium in the γ-phase, which is the most ductile and malleable, in addition to improving corrosion resistance and reducing grain size.

In the drive for higher uranium density at low enrichment, alloy fuel would appear to be the most attractive candidate. However, use of alloy fuel in nuclear reactors is not new; in fact, alloy fuels were the first fuels used in large-scale nuclear reactors, both for research and power production. In the 15 years following the Manhattan project, uranium metal and its alloys were studied extensively, with nearly every alloy imaginable being considered and explored for potential applications in nuclear reactors. Alloys of uranium and aluminum, uranium and beryllium, uranium and molybdenum, uranium and niobium, uranium and zirconium, and others, were studied extensively, and employed, during this period [23]. The world's first large-scale materials test reactor, aptly named the Materials Testing Reactor, utilized a uranium-aluminum alloy fuel clad with aluminum plate [24]. The reactor, located at the National Reactor Testing Station near Idaho Falls, started operation in 1952, and set the standard for materials test reactors to follow in terms of design and performance. Uranium-aluminum alloy fuel with aluminum cladding became the standard fuel type for research and test reactors, though high enrichments were typically employed to overcome the low physical density of the alloy and the relatively low uranium loadings that could be achieved. Typically, U-Al alloy fuel with up to 30% uranium content was used as it performed well, was easily fabricated and relatively inexpensive, and displayed good metallurgical properties [25]. As early as 1958, studies were being conducted to

increase the uranium loading in U-Al alloys for the purpose of substituting HEU fuel with LEU fuel for nonproliferation purposes [26].

When introduced in in mid-1960's, UAl_x and U_3O_8 dispersion (cermet) fuels were considered a significant advancement over the U-Al alloy fuels they were intended to replace. These dispersion fuels allowed for more uniform distribution of fissile material than U-Al alloy fuel, enabled the addition of burnable poisons (thereby increasing fuel burn-up potential), and could be fabricated with the standard picture-frame, hot-rolling technique [27]. Initially, these dispersion fuels were meant to act as low enriched replacements for existing high enriched U-Al alloy fuel. However, improved performance outweighed proliferation concerns, and reactors were designed and built with these dispersion fuels at high enrichment.

Another alloy fuel studied extensively in the late 1940's and through the 1950's was the uranium-molybdenum system, with molybdenum concentrations of 5-15 wt% being most prevalent. U-Mo fuels were primarily considered for service in light water power reactors and liquid metal cooled fast reactors, due to the good corrosion resistance of U-Mo and the very good performance of U-Mo under irradiation at elevated temperatures, outperforming U-Nb and U-Zr alloys. U-Mo alloy fuels have a successful history of in-core service, with the world's first nuclear power station at Obninsk in Russia utilizing U-Mo fuel. The 5 MW(e) graphite moderated, light water cooled power station began operation in 1954 using a U-9Mo powder fuel dispersed in a magnesium matrix. The fuel successfully attained burn-ups up to 35,000 MWd/MTHM [28]. U-Mo alloy was considered the most promising candidate for the blanket material of the first core in the Shippingport Atomic Power Station, until UO_2 was selected, which was poorly studied and had not been used extensively until that point [29]. The physical form for the Shippingport blanket was to be wafers sandwiched between plates, similar to Caramel fuel [30]. The Enrico Fermi Fast Breeder Reactor, the first large-scale fast breeder, achieved criticality in 1963 using U-10Mo alloy fuel [31]. Enriched to 26% in U-235, the alloy fuel was in the form of pins metallurgically bonded to zirconium cladding. U-Mo was also used for the blanket. The Dounreay Fast Reactor used various U-Mo alloy fuels with niobium as the cladding material, achieving burn-ups as high as 9 at% [32].

U-Mo alloy fuel enjoyed widespread use in prompt-burst reactors, which were initially conceived to confirm the effect of negative temperature reactivity coefficients. Second-generation prompt burst reactors needed higher fluxes for testing materials and components

under extreme irradiation, to simulate radiation fields that might be encountered during the detonation of a nuclear weapon. U-10Mo alloy fuel was employed because it could undergo repeated rapid temperature cycles of 500 °C with relatively small crystal growth and excellent phase stability [33]. The Super Kukla prompt-burst reactor used cast rings of U-10Mo fuel, enriched to 20% in U-235. The U-10Mo fuel had a 0.005" nickel plating for protection against stress corrosion, as it was exposed to air, and to contain fission products within the fuel [34]. The U-10Mo fuel performed well during the extreme conditions encountered during repeated 200 μsec bursts, where the neutron flux reached 4×10^{18} n/cm^2-sec and the rate of temperature change was as high as 1.6×10^{6} °C/sec at the fuel surface.

U-Mo alloy, clad in aluminum, has also been the fuel of choice in organic moderated reactors [35]. The 16 MW Organic Moderated Reactor Experiment (OMRE), which began operation in 1957 at the National Reactor Testing Station, tested various types of U-Mo alloy fuel in its different cores, including a U-10Mo alloy plate fuel, nickel plated and isostatically bonded to 1100 aluminum cladding [36]. The 46 MW Piqua Nuclear Generating Station in Ohio was an organic moderated and cooled reactor which started operation in 1963. The reactor fuel, enriched to 1.6% in U-235, was a U-3.5Mo-0.2Al/Si alloy, clad in aluminum [37]. The fuel geometry was annular, with a 0.001" thick nickel diffusion barrier between the metallurgically bonded U-Mo alloy and aluminum cladding, which was finned to improve heat transfer [38].

Given the extensive operating history summarized above, it is not surprising that the GTRI/RERTR program has chosen a uranium-molybdenum alloy, in monolithic form, for converting the High Performance Research Reactors in the United States to LEU fuel. The alloy will consist of 10 wt% molybdenum and 90 wt% uranium, enriched to slightly under 20% in U-235. Some of the mechanical property advantages of the U-10Mo alloy fuel are listed below.

U-10Mo Mechanical Property Advantages (*Source: Ref. [34]*):

1) *Strength*: The alloy has a yield strength of 130,000 psi (896 MPa).

2) *Dimensional Stability*: U-10Mo is not subject to ratcheting during thermal cycling. It has a very isotropic coefficient of linear expansion.

3) *Gamma Stability*: All gamma-stabilized uranium alloys are metastable at room temperature and subject to transformation when heated in the range of 300 °C. U-10Mo, however, is the most stable alloy presently known and is entirely satisfactory from this standpoint.

4) *Homogeneity*: U-10Mo is not subject to gross segregation. The microsegregation which does occur can be relieved readily by a short homogenization treatment.

5) *Familiarity*: More work has been done on the U-10Mo alloy than any other high strength uranium alloy.

U-Mo alloy dispersion fuel systems, specifically U-8Mo in an aluminum matrix, are also being studied as a backup fuel to the U-10Mo monolithic fuel. It is hoped that a dispersion form of the fuel will yield the benefits of the U-Mo alloy while mitigating some of the issues of fabricating the U-Mo alloy into plate-type elements. Selected physical properties of cladding and matrix materials are listed in Table 7. Properties of the U-Mo alloy fuels are compared to other fuels in Table 8. Properties are listed for unirradiated fuels at room temperature, unless otherwise noted. For dispersion fuels, the properties listed are for the dispersant, not the fuel matrix. Reference [39] has information on calculating thermophysical properties of fuel dispersed in a matrix.

Table 7: Properties of Cladding and Matrix Materials for Research and Test Reactors.

	T_{melt} (°C)	Density (g/cm^3)	k (W/m-K)	c_p (J/kg-K)	Thermal Expansion Coeff. (K^{-1})	Yield Strength[a] (MPa)	Status
1100-O Al	643[c]	2.71	222	904	2.36×10^{-5}	34.5	Extensive prior use as research and test reactor clad. Current use as fuel matrix material.
6061-O[b] Al	582[c]	2.70	180	896	2.36×10^{-5}	55.2	In use as cladding for research and test reactor fuel.
Zr	1852	6.53	16.7	285	5.80×10^{-6}	230	Widespread use in zircaloy for LWR cladding. Prior use as fuel matrix material.
Mg	648	1.74	159	1025	2.61×10^{-5}	90	Prior use as cladding and fuel matrix material.
316 SS	1370[c]	8.00	16.3	500	1.6×10^{-5}	290	Extensive prior use as clad material in early reactors. Limited use as fuel matrix material in some ANPP reactors.

[a]Yield strength is for annealed specimens, unless otherwise noted.
[b]While T6 temper is usually specified, hot-rolling and clad bonding are likely to remove any pre-existing temper.
[c]Solidus temperature.

Table 8: Physical Properties of Fuel Materials for Research and Test Reactors.

	T_{melt} (°C)	Theor. Density (g/cm^3)	Current U Loading[g]/ Max. U Loading (gU/cm^3)	Physical Form[e]	k (W/m-K)	c_p (J/kg-K)	Thermal Expansion Coeff. (K^{-1})	Yield Strength[a] (MPa)	Status
U metal	1132	19.1	19.11	α-phase (O)	26.8	115.6	$1.9x10^{-5}$	276	Typically not used; poor phase stability and corrosion.
U-Al alloy	640	3.56	1.1/1.9 (30/45wt% U)	-	151	-	$1.94x10^{-5}$	102.4 (forged)	Extensive prior use in research and test reactors.
U-ZrH_x	-	-	3.7	-	16.7	-	-	-	In use as TRIGA reactor fuel.
UAl_x in Al:		6.4	2.3/2.8		-	-	-	-	In use as research and test reactor fuel.
UAl_2	1688	8.1		FCC					
UAl_3	1349	6.7		SC					
UAl_4	732	6.0		O					
U_3O_8 in Al	1300[f]	8.40	3.2/3.8	O	18	-	-	-	In use as research and test reactor fuel.
UO_2	2875	10.96	9.1/9.1	FCC	~10	-	-	-	In use as LWR fuel.
U_3Si_2 in Al	1665	12.2	4.8/6.0	-	15	-	-	-	Qualified and approved by US NRC. Selected for use in JHR.
U_3Si in Al	930[f]	15.3	6.1/8.0	BCT	20	179.9	$1.6x10^{-5}$	-	Under development. Dropped from US program.
U-10Mo	1150	17.1	16.38	α+δ phase[d] (O+T)	12.1	142	$1.23x10^{-5}$	993 (γ-quench)	Prior use in FBR's, PBR's, OMR's. Under development for research and test reactors.
U-8Mo in Al or Mg	1133	17.5	8.0	α+δ phase[d] (O+T)	14.2	-	$1.38x10^{-5}$	-	Under development.

[a]Yield strength is for annealed specimens, unless otherwise noted.
[d]Metastable in γ-phase (BCC) with appropriate quenching heat treatment.
[e]FCC = Face Centered Cubic; HCP = Hexagonal Close Packed; O = Orthorhombic; SC = Simple Cubic; T=Tetragonal
[f]Decomposes.
[g]Current achievable uranium loadings for UAl_x-Al, U_3O_8-Al, and U_3Si_2 were developed and qualified under RERTR.

While U-10Mo alloy fuel has been used successfully in FBR's, OMR's, PBR's, and other reactor types, fabrication into plate-type fuel for research reactors presents a number of additional challenges. U-10Mo is somewhat more difficult to form into plate-type fuel using the standard picture-frame technique than it is for U-Al alloy fuels and Al-based dispersion fuels. However, the most significant challenge is development of an appropriate technique for cladding the U-10Mo alloy, which historically has been difficult, but not impossible, for other reactor applications such as the Enrico Fermi FBR [40]. The desire to use an aluminum alloy cladding material, due to its long history as cladding for MTR fuel elements, further exacerbates the U-10Mo cladding challenge. A direct metallurgical bond is considered a requisite to reduce thermal resistance between the fuel and coolant, and improve the integrity of the fuel elements.

However, the interdiffusion of aluminum with uranium is a well-known issue, first being studied in the 1950's and 1960's. Interdiffusion results in the formation of intermediate layers of UAl_2, UAl_3, and UAl_4 at the interface which can cause a non-uniform diffusion zone, porosity formation, distortion, and crack formation. The issue is much less significant when using U-Al alloy fuel because diffusion is possible only in the aluminum primary solid solution [41]. Interdiffusion occurs much more rapidly at elevated temperatures encountered during fabrication and in-core service. The resulting imperfections in the clad-fuel interface are of prime concern, as fission and helium gas formed during irradiation can cause preferential fuel swelling or even rupture in these locations. The interdiffusion problem is not limited to monolithic fuel, as U-Mo powder dispersed in aluminum results in interdiffusion between the U-Mo particles and aluminum matrix. A magnesium matrix has been used in past applications to mitigate this issue.

In addition to the interdiffusion problem, the choice of aluminum as a cladding material leads to other challenges due to its limited tensile strength, especially at elevated temperatures, and therefore a limited ability to constrain swelling of nuclear fuel. Use of aluminum cladding limits bonding techniques that may be used and also precludes the use of most heat treatments for the fuel following metallurgical bonding, due to the low melting point of aluminum and its alloys [42]. Additionally, the mismatch in strength, hardness, and hot-working temperatures of the aluminum and U-10Mo introduces additional fabrication issues. A much harder fuel meat material and softer clad can result in breakthrough of the cladding, especially if roll-fabrication processes are employed.

Irradiation testing of U-Mo mini-plates for the RERTR program initiated in 1997. Dispersion U-Mo fuels were initially tested at low temperature with very high burn-up. U-Mo monolithic mini-plates were first tested under the RERTR program in 2001. While initial irradiation tests looked promising, the interdiffusion issue later became readily apparent. Subsequent testing in France and Russia of full-size, prototypic fuel elements resulted in severe fuel failures, revealing the aluminum-uranium interaction issue which led to excessive swelling. Figure 7 shows a failed U-Mo dispersion fuel plate tested by CEA. Figure 2 shows a failed U-10Mo monolithic fuel plate where complete delamination has occurred.

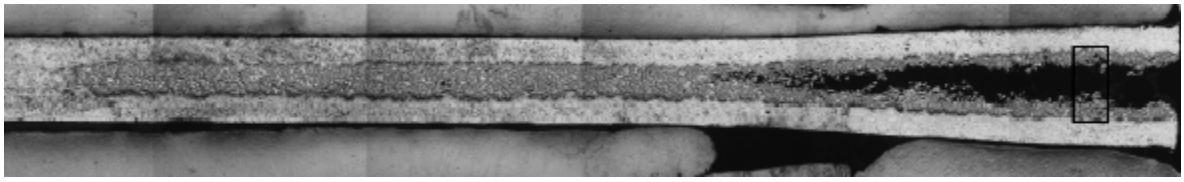

Figure 7: Micrograph of Failed IRIS-2 Plate. The plate consisted of atomized U-7Mo dispersion fuel in an aluminum matrix, clad in aluminum, loaded to 8.3 gU/cm^3. Peak cladding temperature and heat flux were 93 °C and 2380 kW/m^2, respectively. Failure was likely initiated by interdiffusion of U-Mo and Al. *Source: Ref. [11].*

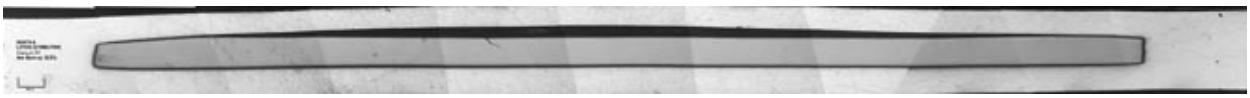

Figure 8: Micrograph of a U-10Mo Monolithic Fuel Plate from the RERTR-6 Test. The clad delaminated from the fuel following irradiation due to poor bond strength between the clad and fuel, likely due to interdiffusion. *Source: Ref. [11].*

Identification of the interdiffusion issue led to recommendation that a diffusion barrier be used. Nickel plating has been used successfully for aluminum-clad U-Mo alloy fuel in the past [36], and is the recommended diffusion barrier to prevent aluminum-uranium interdiffusion [41], though zirconium foil has also been used successfully. For the RERTR program, zirconium foil has been selected as the diffusion barrier for the monolithic U-Mo fuel, first being employed in 2006 [43].

The LEU fuel selected for conversion of the U.S. HPRR's, including the MITR, is the U-10Mo monolith, now incorporating 25 μm thick zirconium foil to act as an interdiffusion barrier, and clad in 6061 aluminum. The fuel plate fabrication consists of multiple steps, which are

summarized in Figure 9. U-10Mo foil is clad in zirconium foil using a co-rolling process. Prior to canning for the hot rolling, U-10Mo foil surfaces are immersed in a 30% nitric acid bath to remove oxidation. Zirconium foils are polished to remove oxidation prior to the hot rolling process. The rolling cans are welded closed within an inert argon gas glove box. For the hot rolling, the can is preheated to 650 °C. Following hot rolling, the entire assembly is annealed for 45 minutes at 650 °C. Cold rolling follows after opening the hot rolling can. The outer zirconium surface of the monolithic fuel is polished to remove any contamination and oxidation in preparation for the clad bonding process. Both hot isostatic pressing (HIP) and friction stir welding are being investigated for the final clad bonding process.

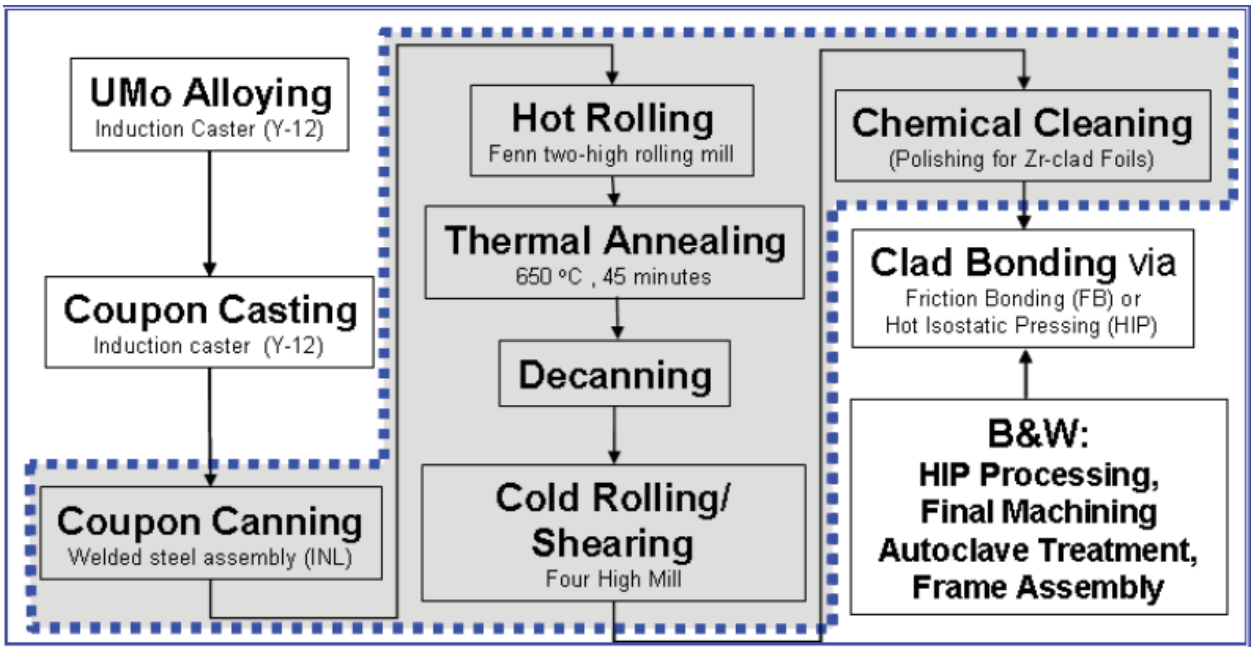

Figure 9: Monolithic Fuel Plate Processing Scheme. ***Source: Ref. [44].***

Hot isostatic pressing involves application of elevated temperatures and uniform pressures to facilitate diffusion bonding between components. The HIP process is also frequently used to reduce porosity in metals and ceramics. For details on the HIP process, refer to reference [45]. For the U-Mo fuel, the HIP process is utilized to bond the outer 6061 clad to the U-10Mo/Zr foil. The HIP process operates at 560 °C for 90 minutes, with an isostatic pressure of 100 MPa being provided by an inert argon environment. The entire fuel fabrication process is described in detail in reference [46]. Even with the implementation of a zirconium interdiffusion barrier, fuel development and qualification is ongoing, with recent challenges

delaying fuel availability until 2026. While U-10Mo fuel has performed well in past applications, the incredibly high burn-ups, high heat fluxes, narrow plate geometry, and use of aluminum cladding have resulted in inadequate fuel performance [11]. The problem is not so much an issue with the fuel, but rather an issue with the aluminum cladding and its ability to accommodate fission gas buildup. Alternative cladding materials, such as zirconium, zircaloy, niobium alloys, or molybdenum alloys could potentially alleviate many of the technical issues facing aluminum cladding, but such cladding materials may face additional licensing constraints.

Chapter 2

Design and Fabrication of a Prototypic Materials Test Reactor Coolant Channel

The primary challenge in undertaking the experimental program of this thesis revolved around the design and fabrication of a heated coolant channel representative of that found in materials test reactors, capable of operating under prototypic conditions. One reason for the limited amount of heat transfer data in narrow rectangular channels at high mass flux and high heat flux conditions is due to the difficulty of designing and building an apparatus for testing such a geometry. A limited number of studies have involved construction of similar experiments in the past, which are discussed in the next section. While modern advances in measurement, instrumentation, and control facilitate improvement in other experimental features compared to prior studies, the fundamental issues regarding test section design and fabrication remain. The successful design and construction of this facility required substantial innovation and ingenuity, along with extensive modeling and analysis. A full chapter is therefore devoted to the design, modeling, development, and fabrication of the prototypic test section used in this study.

2.1. Review of Comparable Experimental Geometries

One of the earliest detailed studies investigating heat transfer in narrow rectangular channels at prototypic flow conditions was that of Levy [47], which was specifically investigating single-phase heat transfer and burnout for materials test reactor applications. A photograph of the test section is shown in Figure 10. The test section consisted of a solid rectangular channel of stainless steel, which was heated resistively. This meant that the channel was heated on all four sides, and heat flux peaking occurred at the edges. In most materials test reactor coolant geometries, including the MITR, the edges are essentially unheated (though some gamma heating and heat conduction may occur), and the heated sides have an unfueled region near the edge.

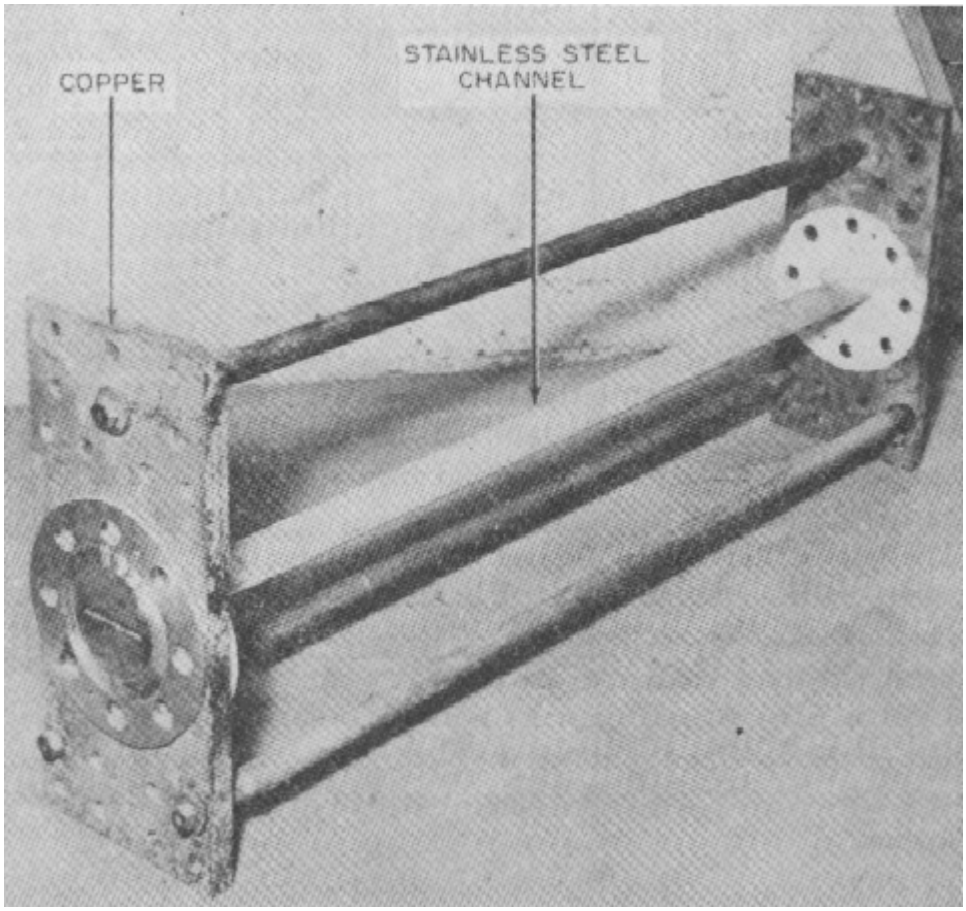

Figure 10: Stainless Steel Test Section from Levy's Experiment. The channel dimension was 0.1" x 2.5", with both 18" and 36" lengths tested. *Source: Ref. [47].*

A 1961 study [48] was conducted to support the design and construction of the High Flux Isotope Reactor (HFIR) at Oak Ridge National Laboratory. The study investigated single-phase heat transfer, friction pressure drop, and CHF in a prototypic channel. Both nickel and aluminum test sections were used, both of which were heated resistively. The test sections were therefore heated on all sides, but for the aluminum test section the edges were rounded, as seen in Figure 11, to attempt to alleviate the preferential heating at the edge encountered in Levy's experiment. A photograph of the test section is provided in Figure 12.

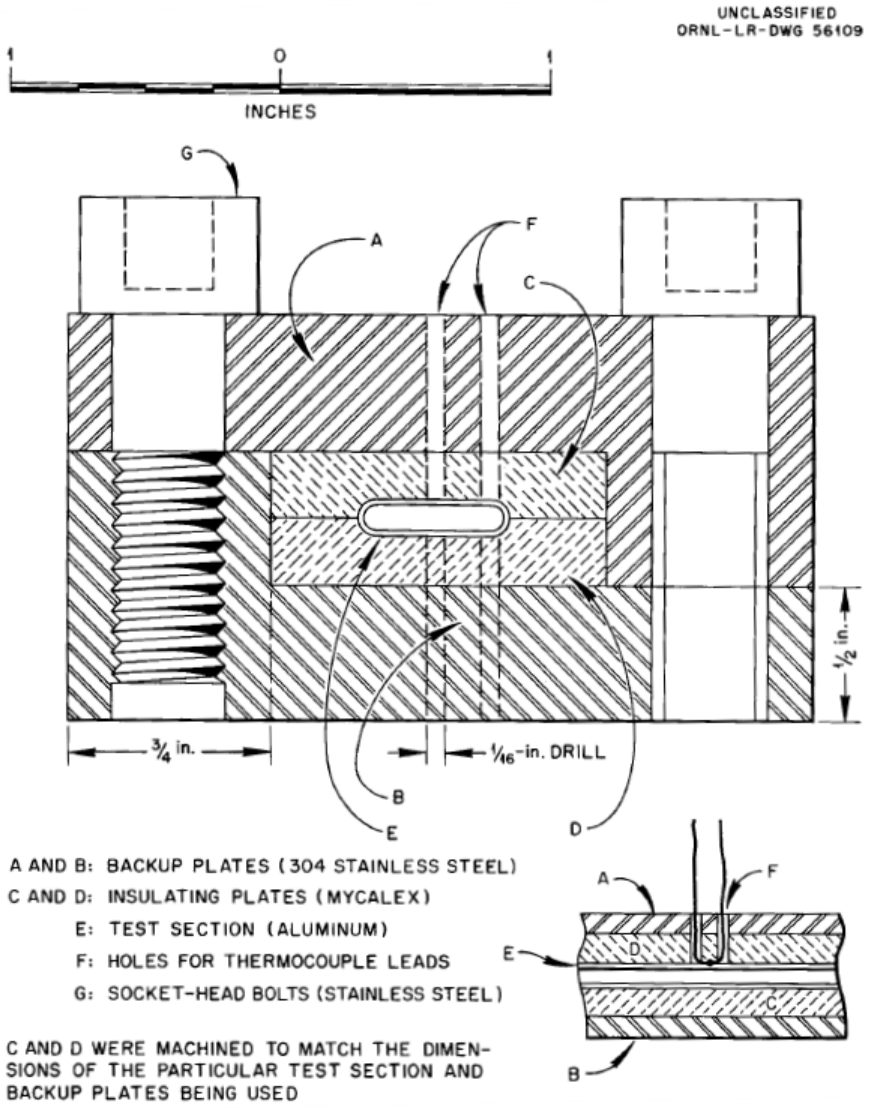

Figure 11: Cross-section of the Aluminum Test Section for the HFIR Heat Transfer Study. The aluminum channel was heated resistively, with the rounded edges implemented to reduce localized heat flux peaking. The channel dimension was nominally 0.050" x 0.50" with a heated length of 18". *Source: Ref. [48].*

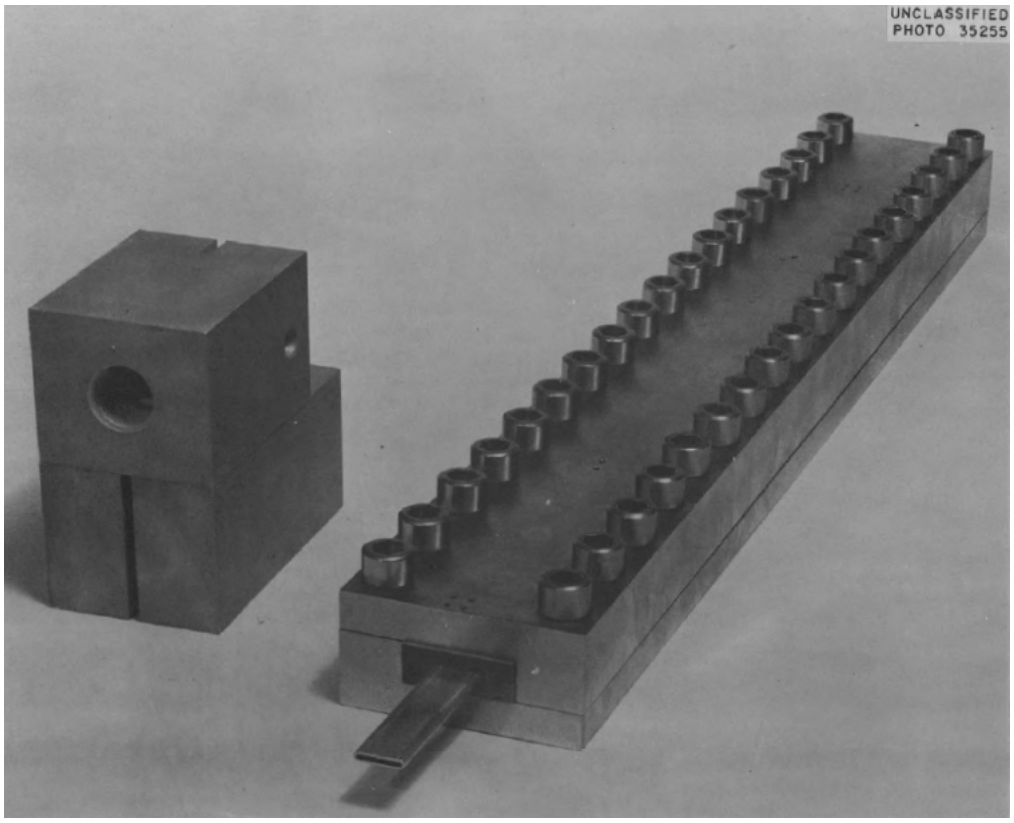

Figure 12: Photograph of Test Section Used in the HFIR Heat Transfer Study. ***Source: Ref. [48].***

Three studies were conducted for prototypic coolant channel geometries at MIT in the late 1960's and early 1970's, in direct support of the MITR core redesign. These three studies only intended to investigate single-phase heat transfer, and heat fluxes were therefore limited to about 100 kW/m^2 or less. All three of these experimental studies were undertaken in the MIT Heat Transfer Laboratory, a premier experimental heat transfer laboratory, with the support and service of its faculty, staff, and equipment. The studies also had extensive support from machine shop personnel.

The first MIT study [49], conducted by Spurgeon under the supervision of Theos Thompson and with support from Arthur Bergles, investigated single-phase heat transfer in smooth and finned channels. To quote Spurgeon, "The fabricational difficulty of the experimental test section cannot be overestimated…" The channels were made of stainless steel and heated resistively, as shown in Figure 13. The finned test section possessed fins twice the size and spacing of those currently found in the MITR, due to the difficulty of machining the smaller fins in stainless steel.

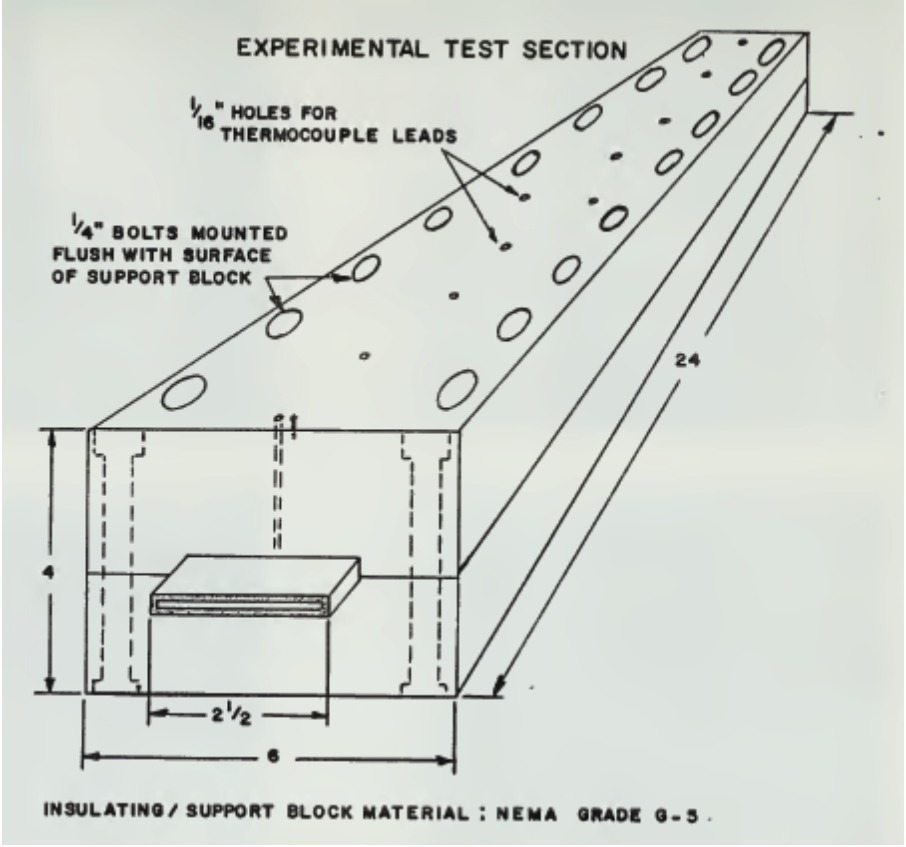

Figure 13: Schematic of Test Section to Study Single-Phase Heat Transfer for the MITR Core Redesign in the Late 1960's. The stainless steel channel was heated on all sides by passing current through the channel walls. The channel dimension was 0.090" x 2.50" with a heated length of 24". *Source: Ref. [49].*

The second of the thermal hydraulic studies carried out in support of the MITR core redesign [50], which received support from Bora Mikic, attempted a conduction heating approach to measure the single-phase heat transfer for finned channels. Specifically, an aluminum channel with prototypic microfins was employed, which was electrically insulated from the stainless steel plates on the back sides of the channel using very thin layers of polytetrafluoroethylene (PTFE). The stainless steel plates were heated resistively, with the intent that heat would flow somewhat uniformly through the PTFE and to the aluminum channel. However, the approach proved unsuccessful, yielding inconclusive results. Even at relatively low heat fluxes (<100 kW/m^2), uneven heating resulted in melting of the PTFE insulator.

The third study [51], conducted by Szymczak, reiterated the difficulty of test section fabrication, stating, "The difficulties in the experimental phase of the thesis cannot be overestimated." Szymczak once again attempted a conduction heating approach to measure the single-phase heat transfer coefficient, but this time employing cartridge heaters embedded in solid aluminum blocks which formed the coolant channel. A schematic of Szymczak's design is shown in Figure 14. The channel possessed prototypic microfins, but was only able to operate at relatively low heat fluxes, leading to high uncertainty in the measured heat transfer coefficients.

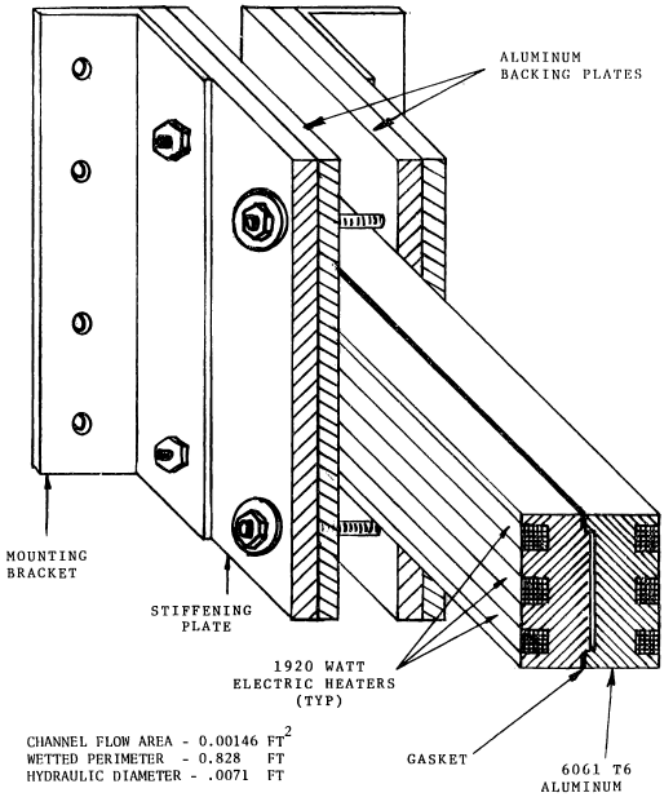

Figure 14: Schematic of Conduction Heater Test Section Used to Measure Single-Phase Heat Transfer for Micro-finned MITR Coolant Channels. The channel has a hydraulic diameter of 2.16 mm. *Source: Ref. [51]*.

While the MITR utilizes onset of nucleate boiling as the limiting safety system setpoint, the studies conducted at MIT did not measure this phenomena, due to the much higher required heat flux. In 1985, Sudo et al. built an apparatus to measure single-phase heat transfer and onset of nucleate boiling in support of the JRR-3 conversion to LEU fuel [52, 53]. The test section was heated on two sides (the edges were not heated), with viewing windows along the edges to

visually identify incipience. The channel was formed by two Inconel plates, which were heated resistively due to the high heat flux requirements for boiling incipience. The channel width was less than that encountered in the JRR-3, due to power supply limitations. A schematic of the test section is provided in Figure 15.

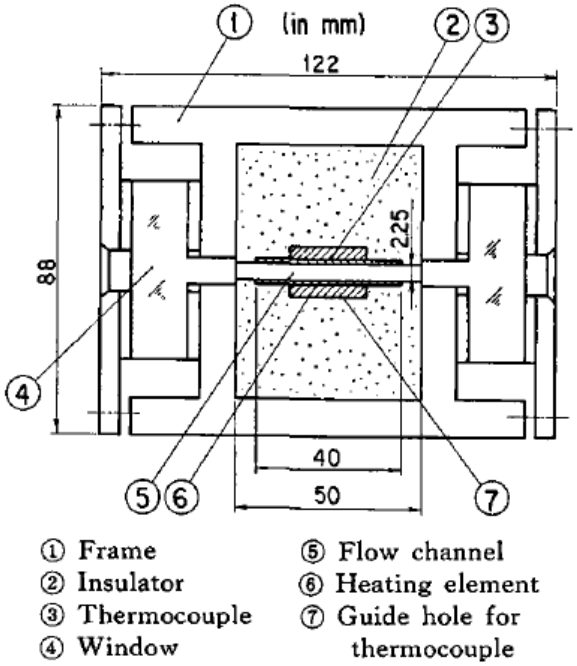

Figure 15: Cross-section of Test Section Employed by Sudo to Measure Single-Phase Heat Transfer and Onset of Nucleate Boiling for the JRR-3 Conversion. *Source: Ref. [52]*.

Several additional studies of onset of nucleate boiling in prototypic geometries have been conducted more recently. Belhadj et al. utilized a conduction heater design for their test section, but only investigated boiling onset for laminar flow, specifically for conditions where $Re<700$ [54]. As such, the test section operated at relatively low heat fluxes. Hong et al. [55] and Wang et al. [56] also investigate ONB in narrow rectangular channels, but their studies are limited to 840 kg/m^2-sec and 603 kg/m^2-sec, respectively. Once again, their test section designs required much lower heat fluxes and are not considered relevant to this study.

2.2. Test Section Design Parameters

The primary objective of this study is to measure single-phase heat transfer and onset of nucleate boiling in a prototypic materials test reactor coolant channel geometry, under typical steady-state operating conditions. Replication of the channel gap was considered pivotal to the study, as was maintaining the same aspect ratio of MTR coolant channels. These design criteria required that the test section possess a full-width channel. Additionally, visualization of boiling incipience using high speed video was desired, thereby necessitating a viewing window on the test section.

The requirement for a viewing window on the test section meant that the one-piece channel design, employed by Levy [47], Gambill [48], and in the prior MIT study by Spurgeon [49], would not be feasible. This would make test section fabrication substantially more complicated, though the issues encountered in the one-piece channel design (edge heating and power peaking in corners) might be avoided. Viewing from the side (along the channel gap) was initially considered, as this was the method employed by Sudo [53]. However, full-field visualization of the surface was preferred, in order to more accurately identify the location of incipience, and eliminate issues with capturing images along an extended focal plane, especially if multiple bubbles formed along the heated surface at the same distance from the inlet. Therefore, a viewing window on the front of the test section was set as another design criterion. This meant that the channel could be heated on one side only, which is not representative of a full channel in a MTR, but is representative of a side channel. However, heating from one side versus two sides is considered to have little, if any, effect on single-phase heat transfer and onset of nucleate boiling, which is discussed further in chapter 4 and chapter 5 (the effect on two-phase heat transfer, onset of flow instability (OFI), and CHF may be significant, though).

Some compromise was required in other areas when trying to match the test section to the characteristics of an MITR coolant channel. Where characteristics could not be matched exactly, an attempt was made to ensure that the test section represented a more conservative condition when compared to an actual MITR coolant channel, i.e., that would result in the onset of nucleate boiling occurring at a lower heat flux. The primary differences between the test section and an MITR coolant channel are highlighted in Table 9 and are discussed in this chapter.

Table 9: Parameters for the Test Section Employed in This Study Compared to the Proposed Unfinned Coolant Channel in MITR LEU Core.

PARAMETER	TEST SECTION	MITR COOLANT CHANNEL (unfinned)	COMMENTS
-Geometry-			
Channel Gap, t_{gap}	1.96 mm (0.077")	1.96 mm (0.077")	-
Channel Width, w	55.9 mm (2.20")	55.9 mm (2.20")	-
Hydraulic Diameter, D_{hyd}	3.91 mm (0.154")	3.91 mm (0.154")	Calculated using twice the gap thickness.
Aspect Ratio, $A.R.$	29:1	29:1	-
Inverse Aspect Ratio, α^*	0.035	0.035	Parallel plate approximation valid away from edges.
Heated Width, w_H	51 mm (2.00")	52.88 mm (2.082")	Heat spreading to "unheated" region will occur in actual coolant channel.
Channel Length, L	482.6 mm (19.00")	584.2 mm (23")	In MITR coolant channel, hydrodynamic and thermal boundary layers develop nearly simultaneously.
Heated Length, L_H	304.8 mm (12.00")	558.8 mm (22.0")	Heated length of test section designed to be twice the entry length of c.t. prediction.
Inclination, φ	90° (vertical upflow)	90° (vertical upflow)	-
- Other - Characteristics			
Heating Method	***Direct*** (Joule heating)	***Conduction*** (Nuclear heat source)	Conduction heating not feasible in test section for high heat fluxes. Expected effect on 1ϕ htc and ONB for unfinned plate is negligible.
Heating Profile	***One-sided Uniform Heat Flux*** (axial and transverse)	***Two-sided Varying Heat Flux*** (axial and transverse)	Two-sided heating not feasible in test section due to full-field visualization requirement. Effect on 1ϕ htc and ONB expected to be small; discussed further in Chapter 4 and Chapter 5.

PARAMETER	TEST SECTION	MITR COOLANT CHANNEL (unfinned)	COMMENTS
Surface Material	316 stainless steel	6061 Al	No effect on 1ϕ htc. Influence on ONB discussed in Chapter 5 and Chapter 6.
Inlet Pressure, P_{in}	up to 3.08 bar	1.99 bar	MITR inlet pressure achievable in test section.
Inlet Temp., T_{in}	up to 99 ºC	42 ºC	MITR inlet temperature achievable in test section.
Mass Flux, G	up to 7000 kg/m^2-sec	3300 kg/m^2-sec	MITR flow conditions achievable in test section.
Surface Heat Flux, q''	up to 3.8 MW/m^2	231 kW/m^2	Necessary heat fluxes achievable in test section.
Laplace Length, L_p	2.55 mm to 2.77 mm	2.68 mm to 2.72 mm	-
-Dimensionless- Parameter			
Prandtl Number, Pr	1.77 to 9.44	2.98 to 4.15	Both thermal and viscous diffusion are relevant to 1ϕ htc, but $\delta_{hy} > \delta_{th}$.
Reynolds Number, Re_{Dhyd}	2200 to 93,000	13,500 to 26,700	Fully turbulent flow expected.
Confinement Number, Co	0.65 to 0.71	0.68 to 0.69	Co>0.5, effects of confinement on boiling are significant.
Eötvös Number, Eo_{Dhyd}	2.00 to 2.36	2.07 to 2.13	Surface tension effects do not dominate, but are not negligible.
Morton Number, Mo	3.34×10^{-13} to 1.72×10^{-11}	1.69×10^{-12} to 4.82×10^{-12}	Similar bubble shape in MITR coolant channel and test section.
Froude Number, Fr_{Dhyd}	11 to 1390	151 to 273	Inertia force dominant over buoyancy.
Weber Number, We_{Dhyd}	24 to 3480	335 to 632	Inertia force dominant over surface tension.
Dimensionless Length, L_h/D_{hyd}	78	143	Fully developed flow based on ct. predictions.

The hydraulic diameter is used as the characteristic length, where noted, as recommended by Kandlikar [57].

In the MITR, the fueled width of the plates is 2.08 inches, which was approximated here as the heated width of the fuel plates (though in reality the heat may spread somewhat at the surface of the fuel plate). The fueled length of the plates in the MITR ranges from 22.00 to 22.75 inches. While a full width coolant channel was maintained in the test section, a full heated length was considered impractical, due to concerns over bowing of the heating surface and excessive power requirements, which is discussed in the next section. The hydrodynamic and heated lengths of the channel are the distances over which the velocity and temperature profiles fully develop, which, in turn, influences the boundary layer thickness and heat transfer. Flow development also strongly depends on the inlet configuration of a channel. The MITR core possesses upper and lower plenums, with nozzles directing flow at the entrance to each assembly (refer to Figure 4). In addition, the axial heating profile in the MITR is non-uniform, which will influence thermal boundary layer development in each channel. Since the inlet conditions, heating profile, and heated length of the MITR were not replicated, the objective was to achieve fully developed flow within the test section. Developing flow in the entrance region of coolant channels results in higher heat transfer due to a thinner boundary layer, whereas the lowest value of the heat transfer coefficient is observed for fully developed flow. Therefore, fully developed flow represents a conservative condition, and was sought when designing the test section for this study. Flow is considered fully developed hydrodynamically when the pressure gradient achieves a constant value. Flow is considered fully developed thermally when the Nusselt number at a given location from the inlet is within 5% of the expected Nusselt number an infinite distance from the inlet [58].

Unfortunately, limited data exists for hydrodynamic or thermally developing flow in narrow rectangular channels. The presence of secondary flows also influences the entry length. For the hydrodynamic entrance length in rectangular channels, flow in the entrance region may remain laminar for Reynolds numbers well above 2200 [59]. According to Bhatti and Shah [60], "no analytical or experimental results for thermally developing flow in rectangular ducts are available." They suggest using results for flat ducts (parallel plates) as an estimate if the inverse aspect ratio is close to zero, i.e. $\alpha^* \approx 0$. However, data for flat ducts (parallel plates) is also sparse. Therefore, circular tube correlations were used for design purposes, with the hydrodynamic entry length for turbulent flow estimated by [61]:

$$\frac{L_{hyd}}{D_{hyd}} = 1.359Re^{1/4} \tag{12}$$

and the thermal entry length for turbulent flow estimated as [62]:

$$\frac{L_{th}}{D_{hyd}} \approx 40 \tag{13}$$

The heated length of the test section was therefore designed to be twice the maximum expected entry length calculated from the circular tube relation in equation (13).

The entrance configuration has a strong effect on flow development, with sharp contractions generating vortices which may require 40 or more diameters to disappear. Initially, unheated calming regions at the inlet and exit of the test section were considered, but even a small disruption in the flanged connection could form vortices. Additionally, having calming sections matching the cross section of the test section would result in a prohibitively high pressure drop for the system. Instead, custom transition sections were designed for the inlet and outlet, to minimize pressure drop and vortex formation. The transition section consisted of a continuous nozzle which diverged from the one inch tube to the 2.20 inch channel width, and converged to the 0.077 inch channel gap. The length of the nozzle was chosen to allow a transition angle of approximately 30° between the tube and channel. Fabrication of the transition sections is described in section 2.5.

As seen in Table 9, the majority of relevant parameters for the test section encompass the characteristics encountered in the proposed unfinned MITR coolant channel geometry. However, some notable differences include the surface material, one versus two-sided heating, heat flux profile, and the heating method. The surface material has no influence on single-phase heat transfer (as long as the roughness is small), but the influence on onset of nucleate boiling can be significant, and is discussed further in Chapter 5 and Chapter 6. Selection of an appropriate heating method was carefully considered, and is discussed in the next section.

2.3. Test Section Power Considerations

Achieving the heat flux required for onset of boiling at high subcoolings and high mass fluxes, in a full-scale geometry, proved challenging. Initially, conduction heating methods were investigated, as this would most closely simulate the heating in actual fuel plates and would allow for a 6061 aluminum heat transfer surface, as in the core.

A method using cartridge heaters, similar to that employed by Szymczak [51], was first considered, but it is fairly simple to show that the required heat fluxes for this experiment (refer to the next section) are not attainable. The cartridge heater setup would consist of cartridge heaters embedded in a metal block of high thermal conductivity (aluminum or copper), metallurgically bonded to the boiling surface. As 6061 aluminum is the actual fuel cladding material, embedding the heaters directly in 6061 aluminum would eliminate the need for attaching a separate boiling surface. Cartridge heaters may be cylindrical or rectangular in profile, and typically consist of a nichrome resistance heating element in magnesium oxide insulation, surrounded by a metal sheath. The sheath material is usually stainless steel, or Incoloy for higher temperature service. The highest power density available for commercial cartridge heaters is 40 W/cm^2 at the sheath surface [63]. Therefore, to reach 3 MW/m^2 or greater, the cartridge heater or heaters would have to be embedded in a well-insulated block whose cross-section reduces substantially at the heat transfer surface. In addition, the temperature rise across the block in which the cartridge heaters are embedded would be quite large. Fourier's law of heat conduction gives us:

$$q'' = -k\nabla T \tag{14}$$

For a one-dimensional slab of uniform material, equation (14) may be simplified to:

$$q'' = -k\frac{\Delta T}{\Delta x} \tag{15}$$

For 6061-T6 aluminum, k=167 W/m-K. For q''=3 MW/m^2, this means, to a first approximation, that the temperature rise would be ~180 ºC per centimeter of separation between the cartridge heater and boiling surface. Any configuration would require at least several centimeters of

heating block material within which to embed the cartridge heater, resulting in a temperature rise higher than the melting point of aluminum. This does not even include the substantial thermal contact resistance between the cartridge sheath and heater block, or the thermal resistance imposed by the insulation between the cartridge sheath and nichrome heating element. Use of copper, with a higher melting point and higher thermal conductivity, would partly alleviate the issue, but would require the attachment of a separate boiling surface to the copper block, imposing even larger thermal resistances between the fluid and heating element. Therefore, the use of cartridge heaters was not viewed as a feasible heating option for the test section.

Use of a custom-fabricated strip heater bonded to a 6061 aluminum boiling surface was also considered. This sort of configuration would require a thin, electrically insulating interlayer between the electrical strip heater and the 6061 aluminum boiling surface. This method is similar to that attempted by Hollenberg [50], where current was passed through a stainless steel strip which was attached to the aluminum heating surface, separated by a thin layer of PTFE. However, even at low heat fluxes (<100 kW/m^2), Hollenberg experienced failure of his heater due to failure of the PTFE. With a thermal conductivity of ~0.2 W/m-K, the PTFE would have a temperature rise of 1500 ºC across a 100 μm thickness for q''=3 MW/m^2, which does not even account for contact resistance. Therefore, a ceramic with reasonably high thermal conductivity, such as magnesium oxide, would have to be employed in this sort of design to achieve the necessary heat fluxes in this experiment. However, even slight variations in the insulator thickness, along with defects in the metal to insulator bond, or differential thermal expansion issues could result in local hot spots and failure of the heater. Additionally, temperature measurement would be challenging, and subject to large uncertainties. Therefore, this method was ruled out as a heating option in this experiment.

Ultimately, a direct heating method using Joule heating (also called resistive or Ohmic heating) was selected for the test section, much like that used in the apparatuses of Levy [47], Gambill [48], Spurgeon [49], Sudo [53], and others. The primary advantage of a direct heating method is that it allows for very high power densities while minimizing the need for large temperature gradients. In addition, the total efficiency of the setup (fraction of heat going to fluid versus that lost to the surroundings) tends to be greater than for conduction heater setups. However, direct heating limits the range of materials that may be employed, and also presents the issue of electrochemical corrosion when water is used as the coolant. Electrochemical

corrosion will have little, if any, effect on single-phase heat transfer, but may have a large effect on ONB and CHF due to changes in the surface chemistry and wettability. However, selection of an appropriate heater material, and minimizing the required voltage, will help mitigate the effects of electrochemical corrosion.

2.3.1. Power Requirements

The required heat flux to achieve onset of nucleate boiling in the test section was estimated using the Dittus-Boelter equation (refer to chapter 4) and the Bergles-Rohsenow correlation (refer to chapter 5). A script written in MATLAB iteratively determined the ONB heat flux by calculating the predicted wall temperature for single-phase heat transfer, and determining when this temperature converged with that calculated from the Bergles and Rohsenow correlation. The results for varying mass flux and subcoolings at atmospheric pressure are shown in Figure 16. As seen in the figure, the expected ONB heat flux under nominal MITR operating conditions using Dittus-Boelter and Bergles and Rohsenow is over 1 MW/m^2. However, some sources in the literature indicate that the Bergles and Rohsenow correlation underpredicts the ONB heat flux, by as much as a factor of two, in predicting onset of nucleate boiling. Therefore, when designing the test section, significant margin was desired to accommodate the anticipated heat fluxes, account for heat loss, and also allow for testing at higher mass fluxes and possible testing beyond ONB in later studies. Therefore, a heat flux of 3 MW/m^2 was set as the minimum requirement for the test section.

The required power was determined by multiplying the required heat flux by the heated surface area, yielding a required power of 48.1 kW. Since Joule heating was selected as the heating method, the power (assuming no losses) is determined by:

$$P_E = IV_E \tag{16}$$

The current, voltage, and heater resistance are related by Ohm's Law:

$$V_E = IR_E \tag{17}$$

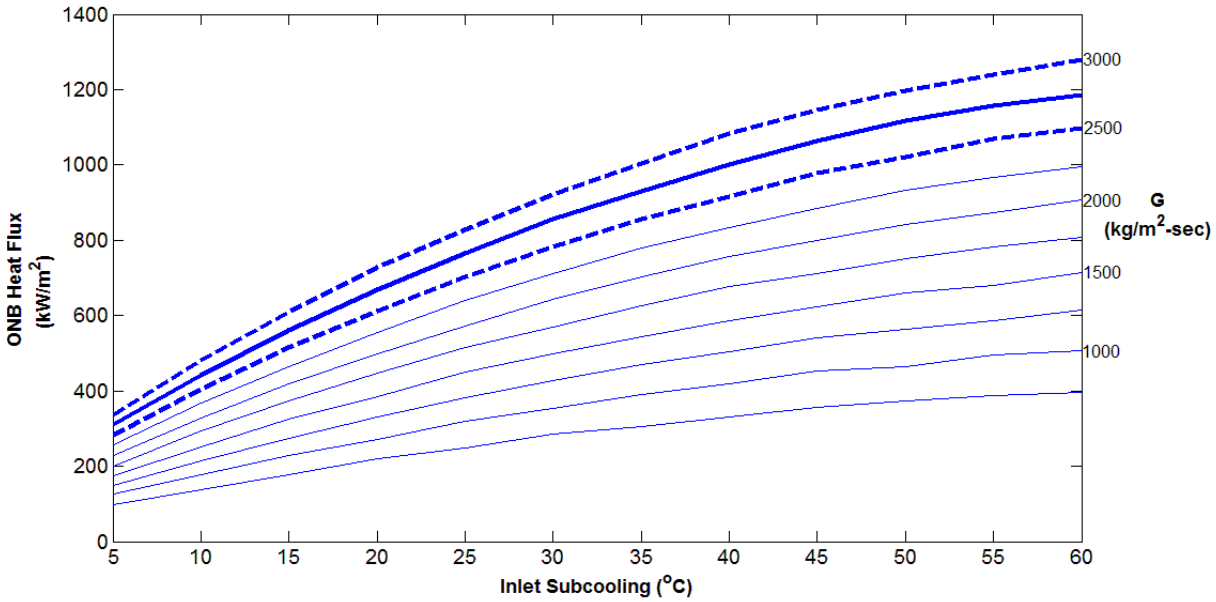

Figure 16: Expected Onset of Nucleate Boiling Heat Flux from Dittus-Boelter and Bergles and Rohsenow Prediction. Results are shown for a range of inlet mass fluxes and inlet subcoolings. The bold blue line denotes the current nominal average channel mass flux in the MITR.

6061 aluminum was desired for the heater plate material, but the very low electrical resistivity would require excessively high currents, precluding its use in the test section. Nichrome, Incoloy, and 316 stainless steel were considered, with 316 stainless steel ultimately being selected for the heater plate material due to its very good corrosion resistance in water under an applied potential and prior use in similar experiments. A heater plate thickness of 0.060" (1.52 mm) was specified to give the heater plate sufficient strength and rigidity while minimizing current draw.

A Magna-Power Electronics MSA16-4500 DC power supply, capable of delivering 4500 A at 16 V, was purchased to deliver power to the heater plate. The power supply was connected to the building AC electrical, requiring a three-phase, 480 VAC input. A platform was purpose built for the power supply to keep it stationary and keep it elevated off the floor to prevent water damage. With this power supply, the maximum power that could be delivered to the heater plate was current limited (4500 A at 13.1 V). The maximum achievable test section surface heat flux with this power supply, assuming no losses, is 3.8 MW/m^2.

Strong magnetic fields are associated with high currents, and are a cause for concern due to the potential for interference with instrumentation and adverse health effects. Health effects

of magnetic fields are an ongoing area of study, with no specific OSHA standards addressing extremely low frequency (ELF) magnetic fields [64]. However, consensus exists among some organizations as to limits on magnetic field exposure based on scientific evidence. For static magnetic fields, the International Commission on Non-Ionizing Radiation Protection recommends a peak occupational magnetic flux density limit of 2 T, a general public limit of 400 mT, and a pacemaker limit of 0.5 mT [65]. The time-weighted eight hour occupational exposure should not exceed 60 mT. The IEEE recommends a maximum permissible exposure limit of 118 mT for the general public [66]. The magnetic field generated by the test section may be calculated using Ampère's Law:

$$\oint \vec{B} \cdot d\vec{l} = \mu_0 I \tag{18}$$

Simplifying the problem to an infinite cylinder, the magnitude of the magnetic flux density at a distance, *r*, from the heater may be estimated as:

$$B = \frac{\mu_0 I}{2\pi r} \tag{19}$$

At maximum current, a magnetic flux density of 0.5 mT exists 0.56 meters away from the test section. Therefore, the hazard was clearly posted on the experiment, with a boundary around the facility to mark the presence of a potentially hazardous field to any individual with a pacemaker. In terms of magnetic interference with instrumentation, static magnetic fields, unlike electric fields, cannot be completely shielded against using a Faraday cage. Rather, a high permeability alloy, such as mu-metal, must be used to attenuate the field, which cannot be completely eliminated. However, mu-metal and other magnetic shielding alloys tend to be expensive. Therefore, magnetic interference was one criterion considered when selecting thermocouples for the test section, which is discussed in chapter 3.

2.3.2. Electrical Conductors and Connections

Connecting the test section to the power supply was not a trivial task. Ideally, no power would be lost in the lines and all would be delivered to the test section. However, even when

using copper conductors, some line losses exist, and if not sized properly, a hazardous situation involving conductor overheating and failure could result. The transfer of thousands of amps of current is only encountered in a limited number of applications, so experience and best practices for electrical connections were not immediately available. Initially water-cooled cables were considered, as they would allow for smaller and lighter conductors. However, the requirement of an active cooling system for the cables was considered to be a disadvantage, with corrosion and safety in the event of the cooling system failure being top concerns. A system involving overhead, air-cooled cables was also considered, in order to keep the cables off the floor to eliminate a potential trip hazard. However, the overall weight of such a configuration would have been over 0.5 tonne, which would be impractical to support from the ceiling.

A trip was taken to the Plasma Science and Fusion Center (PSFC) at MIT, where high currents are routinely encountered to generate intense magnetic fields. Large, solid copper busbars appeared to be the standard at the PSFC. Therefore, a configuration using two busbars was considered, and would have yielded the lightest and least expensive configuration for connecting the power supply to the test section. However, there was concern that two attached busbars would overly constrain the test section, so a configuration using a solid copper busbar on the positive leg, and flexible cables on the negative leg, was selected.

The required size for the cables and copper busbar was determined by setting a steady-state temperature limit for the surface of the conductors to 85 ºC. A one-dimensional heat transfer analysis was performed for the busbar and cables, incorporating the thermal resistance of the electrical insulation and using natural convection to ambient as the final heat sink. The results of the analysis are listed in Table 10. From the analysis, a busbar made of 101 copper (oxygen free electronic grade copper), measuring ¾" thick by 5" wide, was used for the positive leg, and four 2000 MCM welding cables were used for the negative leg. 2000 MCM welding cables are the largest standard cable size that is readily available, with each cable having a conductor diameter of 1.92". The cables are shown in Figure 17. Two large electrode clamps were machined from solid blocks of 101 copper, and used to connect the busbar and cables to the electrodes on the test section. Each clamp weighs approximately sixty pounds, with half of one clamp shown in Figure 18. An electrically and thermally conductive silver paste was used on all connections, in order to reduce electrical contact resistance and minimize local heating. The solid copper busbar had to be bent at a 90º angle to connect the terminal on the power supply to

the electrode on the heater plate. A hydraulic roll bender at Ramsay Welding & Fabrication in Woburn, Massachusetts was used to accomplish this task, with the result shown in Figure 19.

Figure 17: Welding Cables Used to Connect the Negative Electrode of the Power Supply to the Test Section.

Table 10: Characteristics of the Electrical Conductors for the Test Section.

	Positive Leg (+)	Negative Leg (-)
Conductor Type	Solid 101 copper busbar	2000 MCM copper welding cable
Number of Conductors	1	4
Conductor Dimensions	1.9 cm x 12.7 cm x 91.4 cm long (¾"× 5" × 3' long)	4.88 cm OD x 305 cm (1.92" OD × 10' long)
Total Weight	26.3 kg (58 lbs.)	108.9 kg (240 lbs.)
Total Resistance	6.46×10^{-6} Ω	1.65×10^{-5} Ω
Power Dissipation at 4500 A	0.13 kW	0.33 kW
Surface Heat Flux at 4500 A	537 W/m^2	562 W/m^2
Conductor Surface Temperature at 4500 A	81.2 ºC	82.9 ºC

Figure 18: Electrode Clamp Used to Connect the Conductors to the Test Section.

Figure 19: Copper Busbar for Connecting the Positive Electrode of the Power Supply. The bar was bent using a hydraulic roll bender.

2.4. Selection of Materials and Thermal Expansion Considerations

A significant constraint in designing and building the test section for this study was imposed by materials limitations. As previously discussed, 316 stainless steel was chosen for the heater plate, largely due to its electrical properties and ability to resist corrosion. The inlet and outlet transition sections, the test section body, and the backing plate were also constructed of 316 stainless steel, due to its strength and corrosion resistance. All gasketing and o-rings for sealing the test section were made of either PTFE or other fluoropolymers.

Several materials were considered for the test section window. Not only does the window allow for visualization, but in the final test section design the window thickness actually sets the interior channel gap. Therefore, changing the window for one of different thickness would allow adjustment of the channel gap size. Initially, fused quartz was favored for the window material, due to its clarity and ability to operate at high temperatures. However, fused quartz is expensive to grind to the appropriate shape and size, and the risk of catastrophic window failure presents a safety hazard. Additionally, a quartz window would be more susceptible to damage from thermal shock, thermal cycling, or overpressurization. Therefore, polymer materials were also considered, though only a limited number of polymers are transparent, capable of operation at elevated temperatures, and chemically inert enough to not contaminate the fluid stream. Polysulfone and polyetherimide (Ultem) met the requirements and were both considered. The properties of quartz, polysulfone, and Ultem are compared in Table 11. Both polysulfone and Ultem possess a yellow/amber tint, which is not a major issue with the black and white video captured from the high speed video camera. While Ultem has superior temperature resistance, it was found to be significantly less transparent that polysulfone. Therefore, polysulfone was selected for the window, with the provision that a quartz window could be manufactured later if the polysulfone window did not perform satisfactorily.

The test section design centered around selection of an appropriate material for the heater plate insulating block. The insulating block would serve to isolate the heater plate from the test section body, hold the heater plate in place during operation, act as a sealing surface for the back side of the test section, and enclose penetrations to the back side of the heater plate for temperature measurement. Therefore, the material would need to be electrically insulating, machinable, strong, resistant to creep, capable of high temperature operation, and ideally have

Table 11: Comparison of Materials Considered for the Test Section Window.

	Fused Quartz	Polysulfone	Polyetherimide (Ultem 1000)
Maximum Operating Temp. (continuous)	1100 ºC	150 ºC	171 ºC
Thermal Conductivity	1.4 W/m-K	0.259 W/m-K	0.220 W/m-K
Yield Strength	48 MPa*	70.3 MPa	110 MPa
Transparency	Excellent (clear)	Good (yellow tint)	Fair (amber tint)
Chemical Resistance	Excellent	Good	Very Good
Cost (Material + Fabrication)	High	Low	Low

*Ultimate tensile strength

a thermal expansion coefficient near that of stainless steel while also being thermally insulating. Macor, a machinable ceramic with properties similar to borosilicate, was first used as the insulator material. However, despite incorporating tolerances to account for thermal expansion at expected operating temperatures, the ceramic insulator failed after several tests. Failure was likely due to thermal shock; while appropriate tolerances were incorporated for thermal expansion under steady-state conditions, a rapid cooling transient likely resulted in brittle failure of the insulator. A portion of the failed Macor insulator is shown in Figure 20.

Figure 20: Section of Failed Macor Insulator.

As a result of the Macor insulator failure, significant effort was placed on identifying an appropriate replacement material for the insulator that would not be susceptible to thermal shock or brittle failure. PTFE is capable of high temperature operation and is electrically insulating. However, PTFE is not sufficiently rigid, and is very susceptible to creep at elevated temperatures. Therefore, glass-filled PTFE options were explored, with relevant properties of materials considered listed in Table 12.

Table 12: Properties of Glass-Filled PTFE Materials Compared to Macor.

	Macor Machinable Glass Ceramic	**25% Glass Fiber Filled PTFE**	**15% Glass Fiber, 5% MoS_2 Filled PTFE**
Cont. Service Temp.	800 ºC	260 ºC	288 ºC
Peak Operating Temp.	1000 ºC	288 ºC	316 ºC
Electrical Resistivity	$>10^{16}$ Ω-cm	$>10^{17}$ Ω-cm	10^{18} Ω-cm
Thermal Conductivity	1.46 W/m-K	0.250 W/m-K	0.250 W/m-K
Ultimate Tensile Strength	90 MPa	18 MPa	45 MPa
Compressive Strength	345 MPa	8.2 MPa (10% distortion)	11 MPa (10% distortion)
Elongation at Break, %	~0	250	240
Hardness	48 (Rockwell A)	58-63 (Shore D)	60-65 (Shore D)
Coefficient of Thermal Expansion[a]	9.30 μm/m-K (25 °C to 300 °C)	76-119 μm/m-K	100 μm/m-K
Maximum Linear Expansion	-	0.7% (30 °C to 150 °C)	1% (30 °C to 150 °C)
Permanent Deformation under Load	-	7%	7.5%
Machinability Rating (1=easy, 10=difficult)	-	4	4
Cost (Material + Fabrication)	High	Low	Intermediate

[a]For 316 stainless steel, CTE = 16.0 μm/m-K (0 °C to 315 °C).
[b]ASTM D-621.

The 15% glass fiber, 5% molybdenum disulfide filled PTFE composite was chosen for the replacement insulator. In addition to meeting the electrical, mechanical, and temperature requirements, the material is superior to Macor as a thermal insulator, substantially reducing heat loss out the back side of the test section. One significant drawback of the material, and of polymer materials in general, is that they have very high thermal expansion coefficients. There was no concern of brittle failure of the insulator from stresses imposed by thermal expansion, as was the case with the Macor insulator. However, distortion of the insulator was a possibility, so compensation of the tolerances for the plate to insulator fit and the insulator to flow chamber assembly fit were sought.

For this purpose, a two-dimensional heat conduction model was constructed in MATLAB using the Partial Differential Equation Toolbox. The model simulates a cross section of the test section, and incorporates components including the stainless steel body, stainless steel backing plate, PTFE gasket, 15% glass/5% MoS_2 filled PTFE insulator, and the heater plate. The heat equation in the structure is solved using finite element analysis, with the convective boundary condition applied on all open surfaces. A constant heat transfer coefficient to the coolant is applied at the surface of the heater plate, and natural convection to ambient is assumed for all other surfaces. The solution yields a full temperature distribution in the cross-section, and more importantly, gives an idea of the temperature distribution expected in the insulator for various operating conditions. Results for the two limiting cases are provided in Figure 21 and Figure 22. The first represents a high inlet subcooling case and the second represents a low inlet subcooling case. The high inlet subcooling is the limiting case, due to the much higher heat flux required for onset of nucleate boiling. The surface heat transfer coefficients were estimated using the Dittus-Boelter equation.

The results of the conduction heat transfer models were used to estimate the expected thermal expansion of the insulator and heater plate at operating conditions. Appropriate tolerances were then incorporated into the fabrication of the insulator block to allow for this thermal expansion, with the objective being a slip fit when the test section reached operational temperatures.

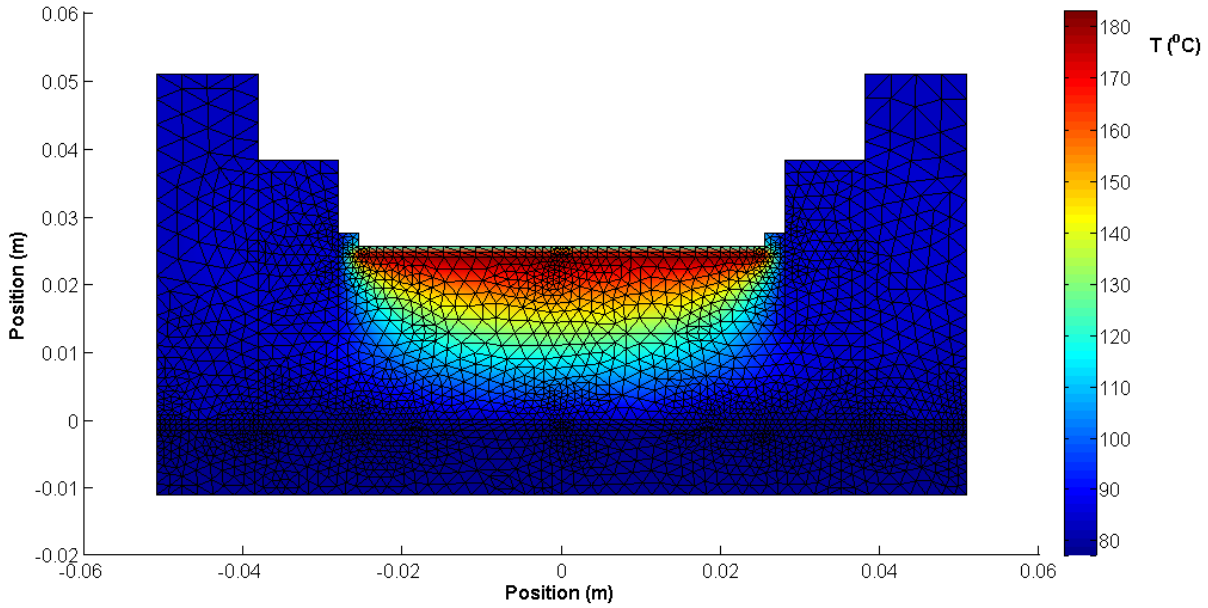

Figure 21: Temperature Distribution in Cross-Section of Test Section. $T_{b,in}$=40 °C, G=3000 kg/m²-sec, q''=1200 kW/m².

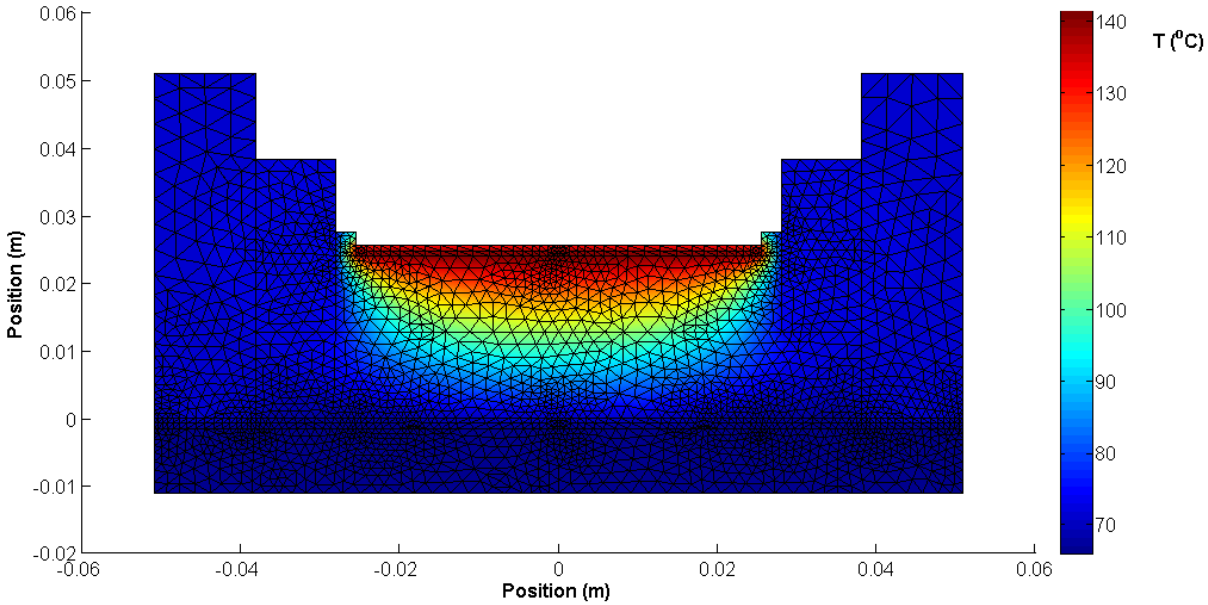

Figure 22: Temperature Distribution in Cross-Section of Test Section. $T_{b,in}$=90 °C, G=750 kg/m²-sec, q''=200 kW/m².

2.5. Test Section Computational Fluid Dynamics Model

With the intent of validating the experimental design, and later developing simulations to support experimental results in future work, a model of the test section coolant channel was constructed in STAR-CCM+. Direct import of the CAD model resulted in some difficulty, as gaps and allowances for thermal expansion resulted in discontinuities in the CFD model. Therefore, the coolant channel was implemented independently in STAR-CCM+ using the built-in drafting feature. The coolant channel model is shown in Figure 23.

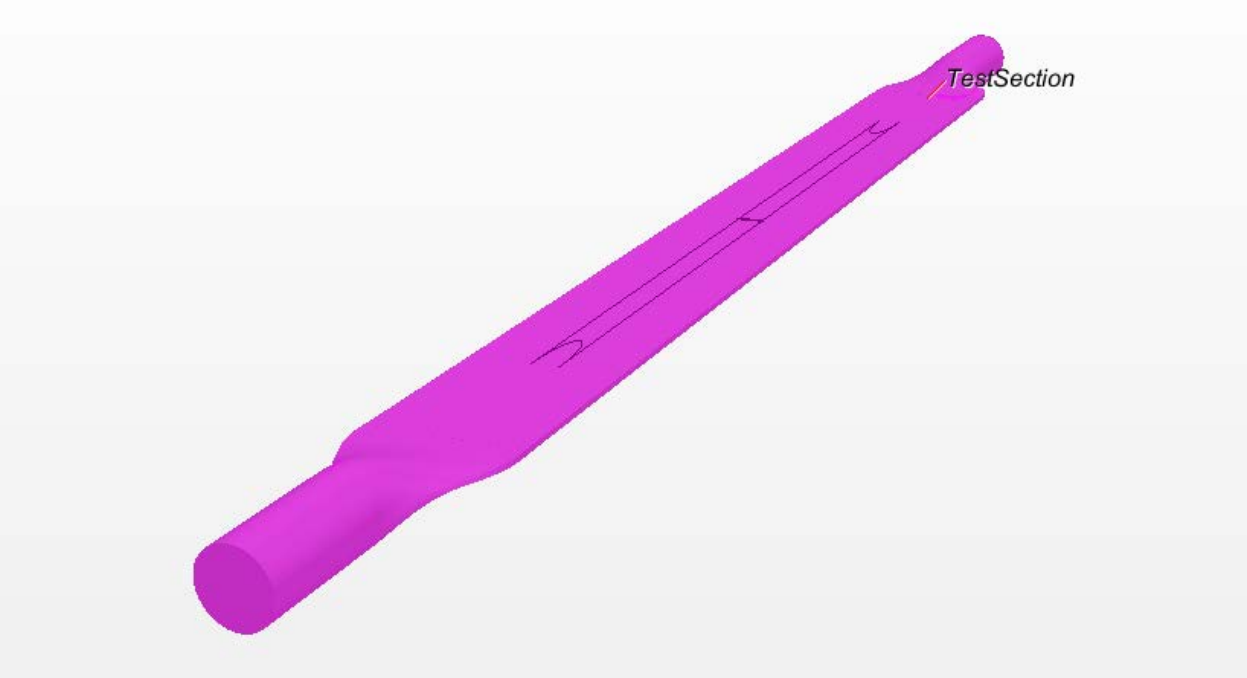

Figure 23: Test Section Coolant Channel Model Drawn in STAR-CCM+.

Unfortunately, it became readily apparent that the computing requirements to implement the number of cells needed to accurately model flow behavior in the long, high aspect ratio channel exceeded that of a single desktop machine. Figure 24 shows results for the finest mesh achievable with a single desktop machine of modest computing power. In addition, proper modeling of flow behavior and secondary flows in the narrow channel exceeded the scope of this study. Several other independent studies have been initiated to use computational fluid dynamics to investigate single-phase heat transfer in the narrow rectangular channel used in this study, and further exploration of this topic is recommended for future work.

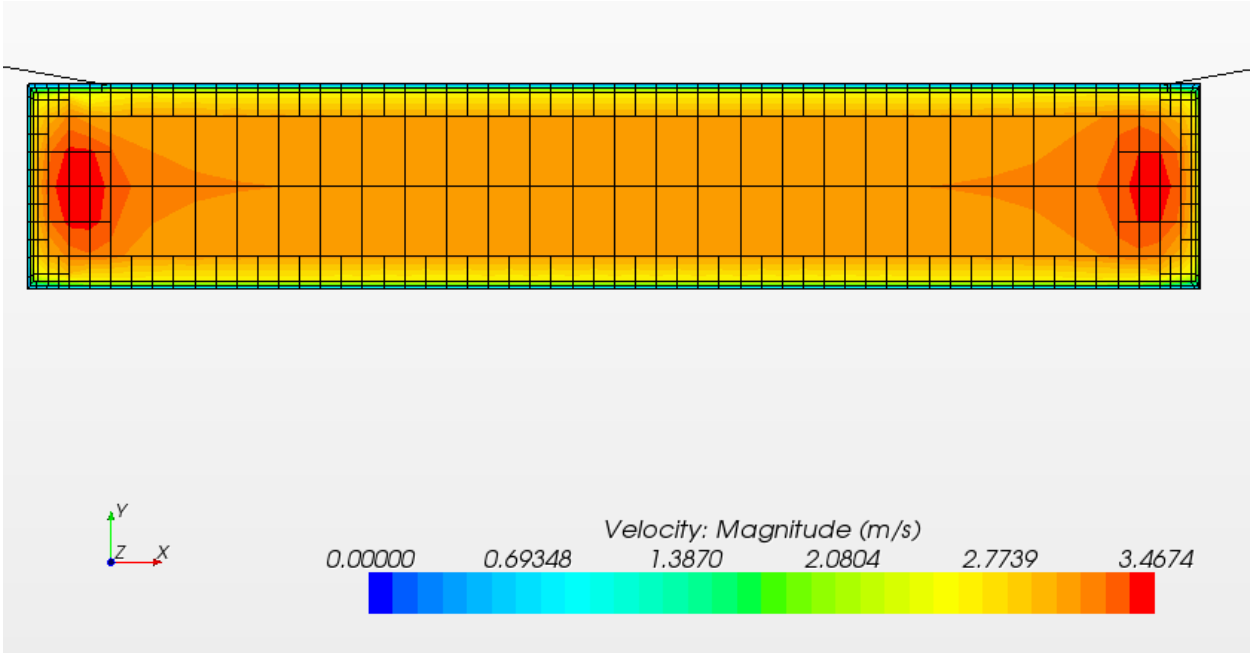

Figure 24: Cross-Section of Channel Showing Velocity Profile Calculated Using Standard κ-epsilon Model with a Coarse Mesh. Clearly, the mesh needs to be refined, and the models need closer attention, which was beyond the scope of this study.

2.6. Heater Plate Multi-Physics Modeling Using Finite Element Analysis

In order to verify that power was generated uniformly within the heater plate, and to optimize the electrode design, a multiphysics model of the heater plate was implemented in COMSOL. The heater plate CAD model, with attached electrodes and tie down studs, was directly imported into COMSOL. The heater plate, as it appears in the COMSOL graphical user interface, is shown in Figure 25. A coupled electrical and heat transfer model was employed, to determine the current density and associated heat flux and temperature distributions. A constant heat transfer coefficient, estimated from the Dittus-Boelter equation, was applied to the surface of the heater plate. A physics-controlled, very fine tetrahedral mesh was generated in the model using the automatic meshing feature. Various conditions were tested, with expected temperature profiles plotted at every thermocouple location.

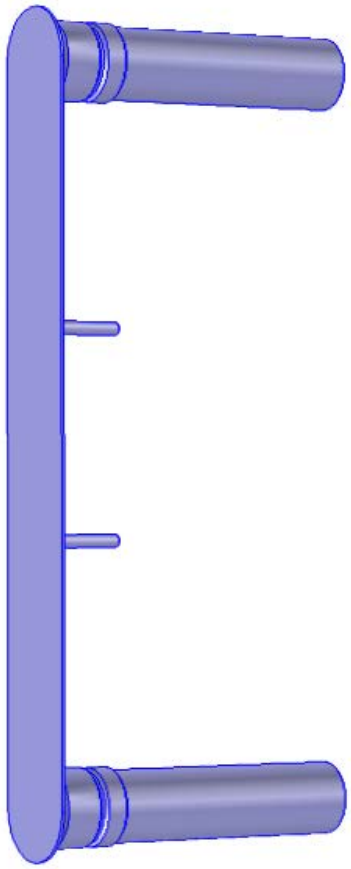

Figure 25: Three-Dimensional Model of Heater Plate Used in COMSOL.

Results for current density, heat flux, and temperature for two test cases are summarized in the following figures. The first case represents a typical voltage and current applied to the heater during single-phase heat transfer measurements. The second case is representative of power levels required for onset of nucleate boiling. Figure 26 shows the current density at the surface of the heater, Figure 27 provides the heat flux distribution, and Figure 28 shows the expected temperature distribution with the imposed surface heat transfer coefficient. As seen in the figures, power generation, and therefore the heat flux, is very uniform across the width of the plate. In addition, virtually no power is generated in the electrodes. However, there is some peaking at the electrode junction, which was unavoidable, but lessened by incorporating a chamfer on the electrode. In addition, there is a slight depression in the power generation at the tie down stud locations. Nonetheless, power generation and expected temperature profiles are reasonably uniform at temperature measurement locations.

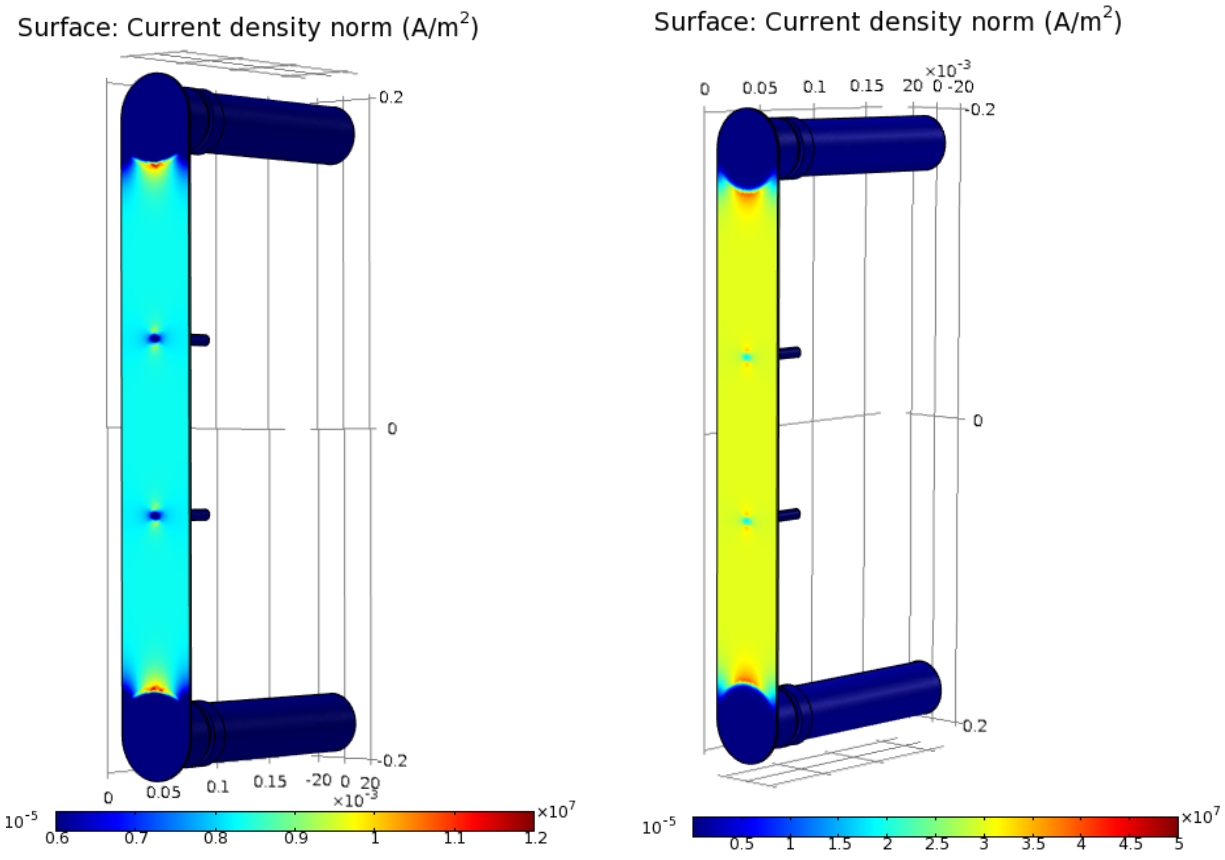

Figure 26: Current Density Distribution in Heater Plate for V_E=2.0 V, I=690 A (left) and V_E=7.5 V, I=2575 A (right). Note that the color scales are different for each case.

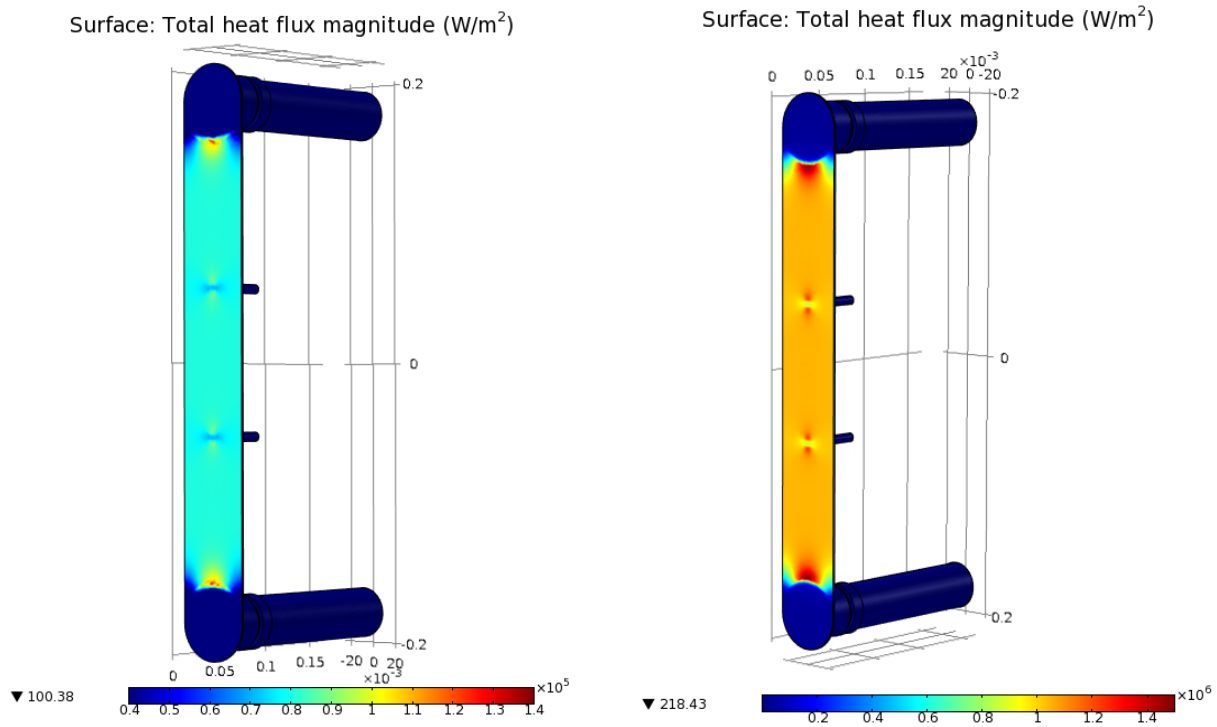

Figure 27: Surface Heat Flux Distribution in Heater Plate for V_E=2.0 V, I=690 A (left) and V_E=7.5 V, I=2575 A (right). Note that the color scales are different for each case.

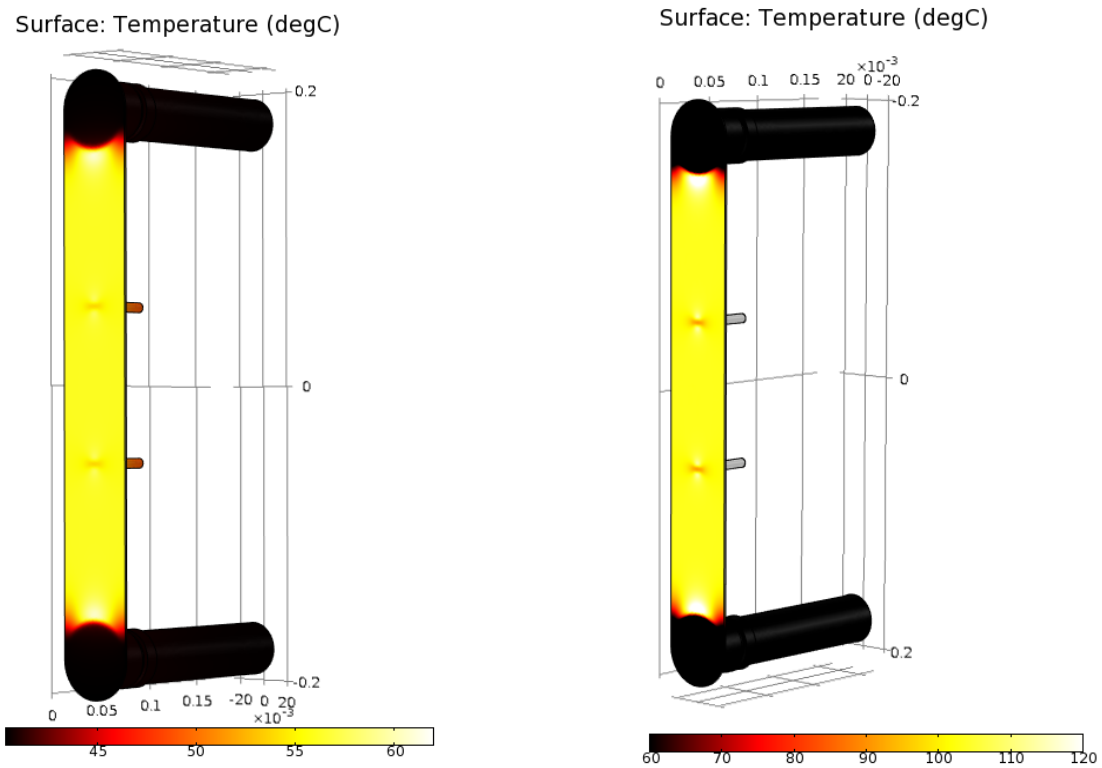

Figure 28: Temperature Distribution in Heater Plate for V_E=2.0 V, I=690 A (left) and V_E=7.5 V, I=2575 A (right), assuming a constant heat transfer coefficient at the surface exposed to the coolant flow and with $T_{b,in}$=40 °C. Note that the color scales are different for each case.

The expected surface temperature across the width of the heater is shown in Figure 29 and Figure 30. These cases are plotted for the axial midpoint, but line plots were also generated at all axial locations where thermocouples would be placed, with similar results being obtained. In reality, there might be some variation in the surface temperature across the width if the heat transfer coefficient varies in this direction.

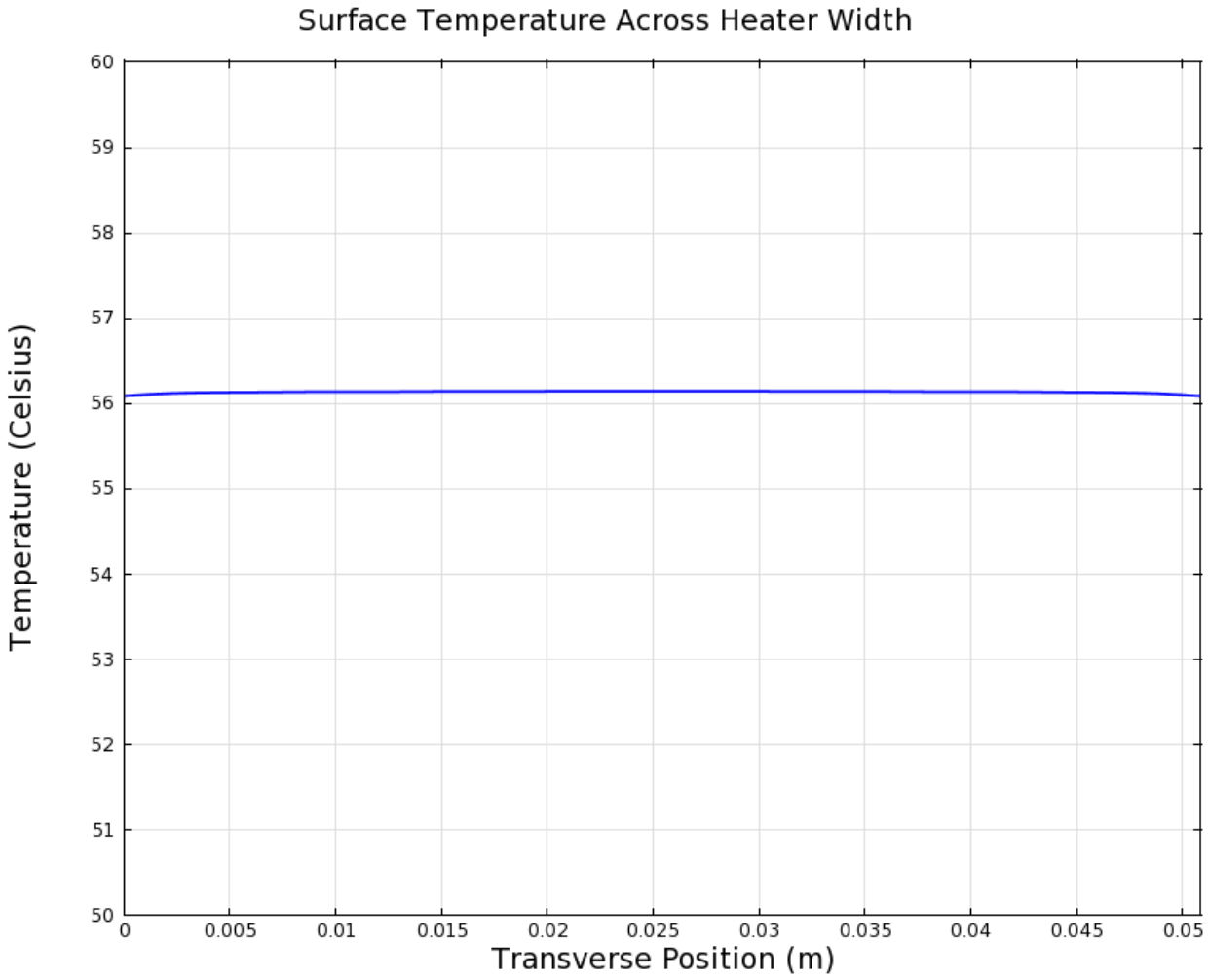

Figure 29: Simulated Surface Temperature Across Heater Width at Axial Midpoint (away from tie down studs) for V_E=2.0 V and I=690 A.

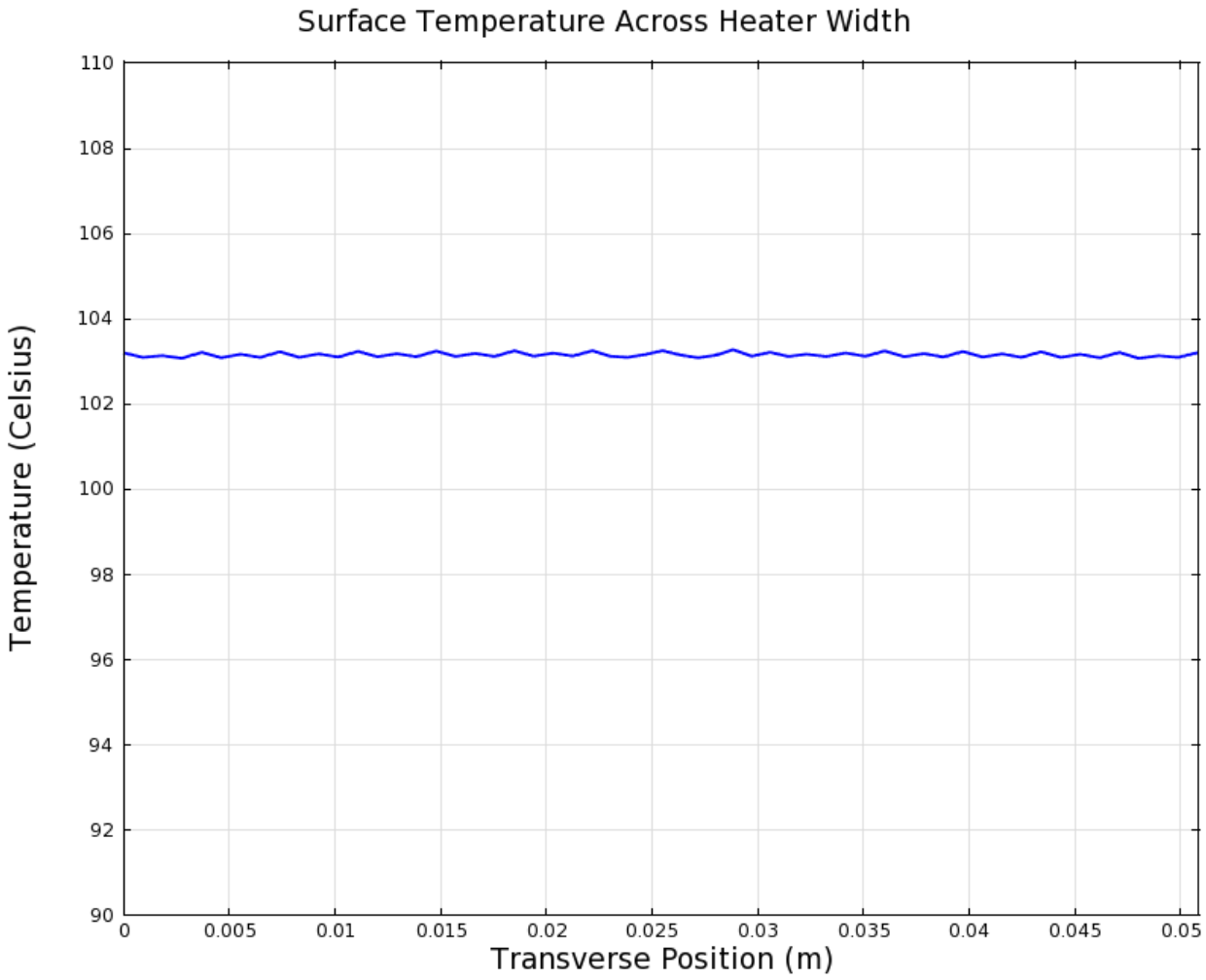

Figure 30: Simulated Surface Temperature Across Heater Width at Axial Midpoint (away from tie down studs) for V_E=7.5 V and I=2575 A.

The temperature drop along the thickness of the heater plate is an important parameter, since temperature measurement on the front side of the heater was not possible without disturbing the flow and affecting the channel gap. Therefore, the front side surface temperature had to be inferred from back side measurements. Even at low heat fluxes, the COMSOL model demonstrates that the temperature drop is significant and must be accounted for. In addition, the results show that a linear approximation of the temperature drop is not appropriate; heat generation within the plate must be accounted for to get an accurate result. Figure 31 shows a cross section of the heater plate, with a color plot of the temperature drop, showing it is relatively uniform along the width of the plate. Figure 32 and Figure 33 show the temperature drop calculated in the COMSOL model at the center of the heater plate for the two cases.

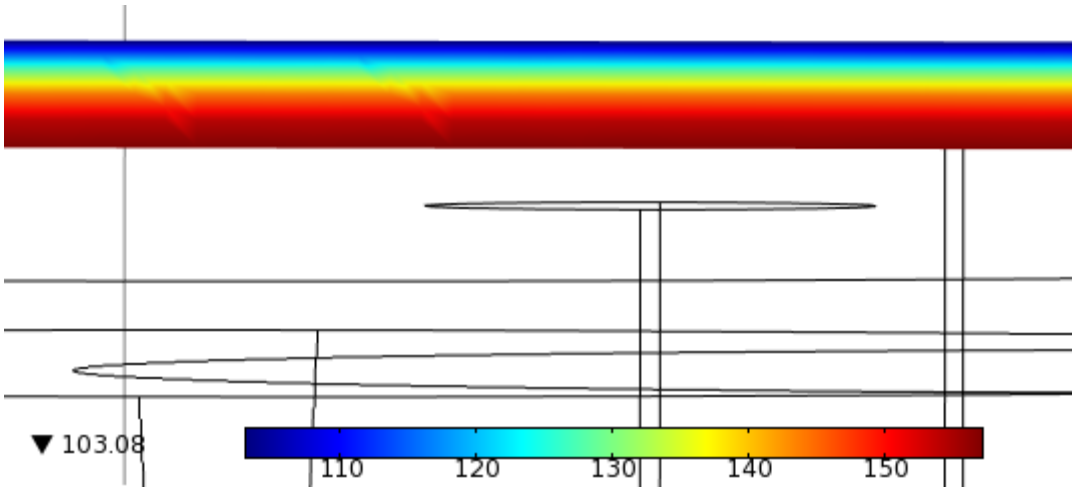

Figure 31: Cross-Section of Heater Plate Temperature Slice Showing Expected Drop from Backside to the Surface Exposed to the Coolant. V_E=7.5 V and I=2575 A.

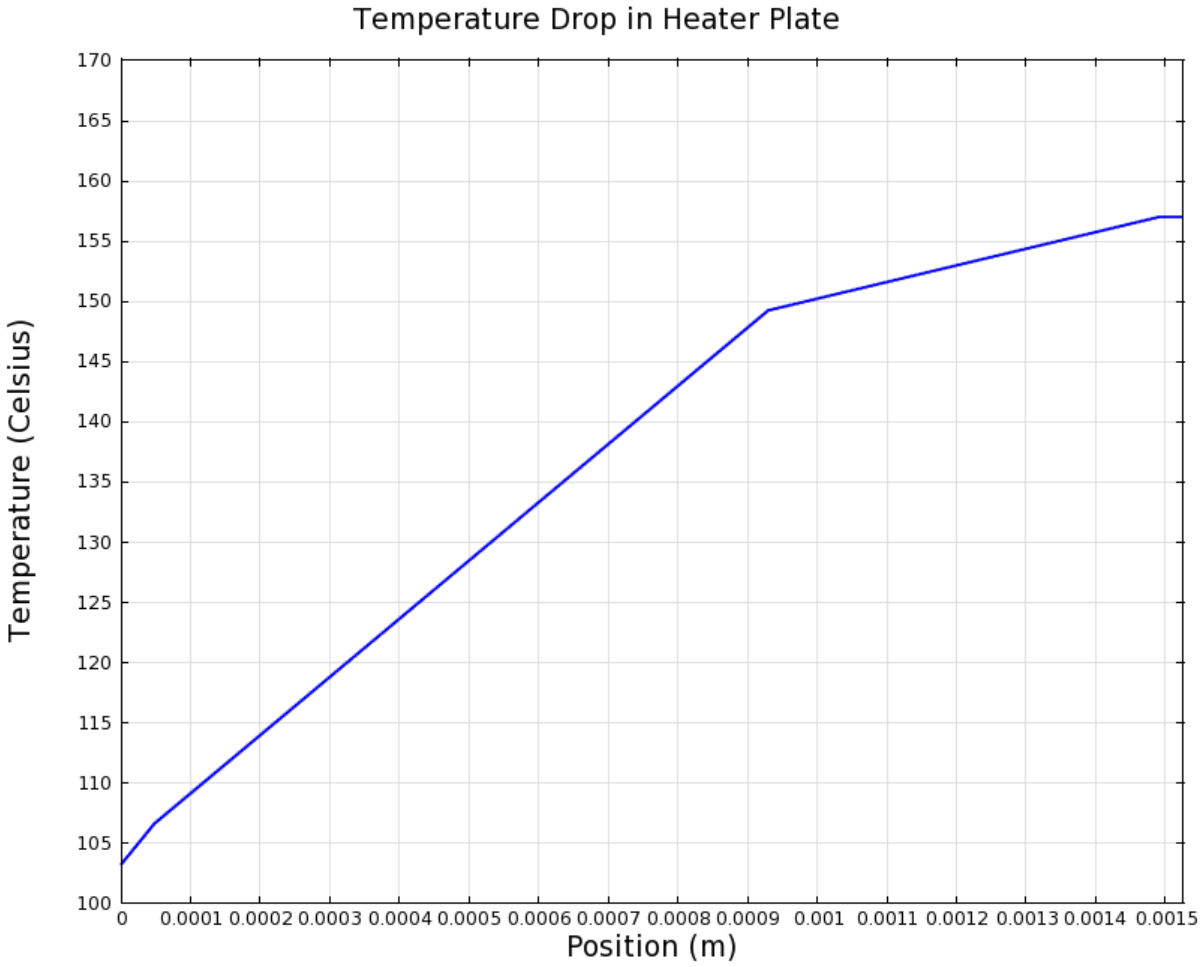

Figure 32: Simulated Temperature Drop Across Thickness of Plate at the Axial and Transverse Midpoint of the Heater Plate. The expected temperature drop is nearly identical at other locations away from the electrodes. V_E=7.5 V and I=2575 A.

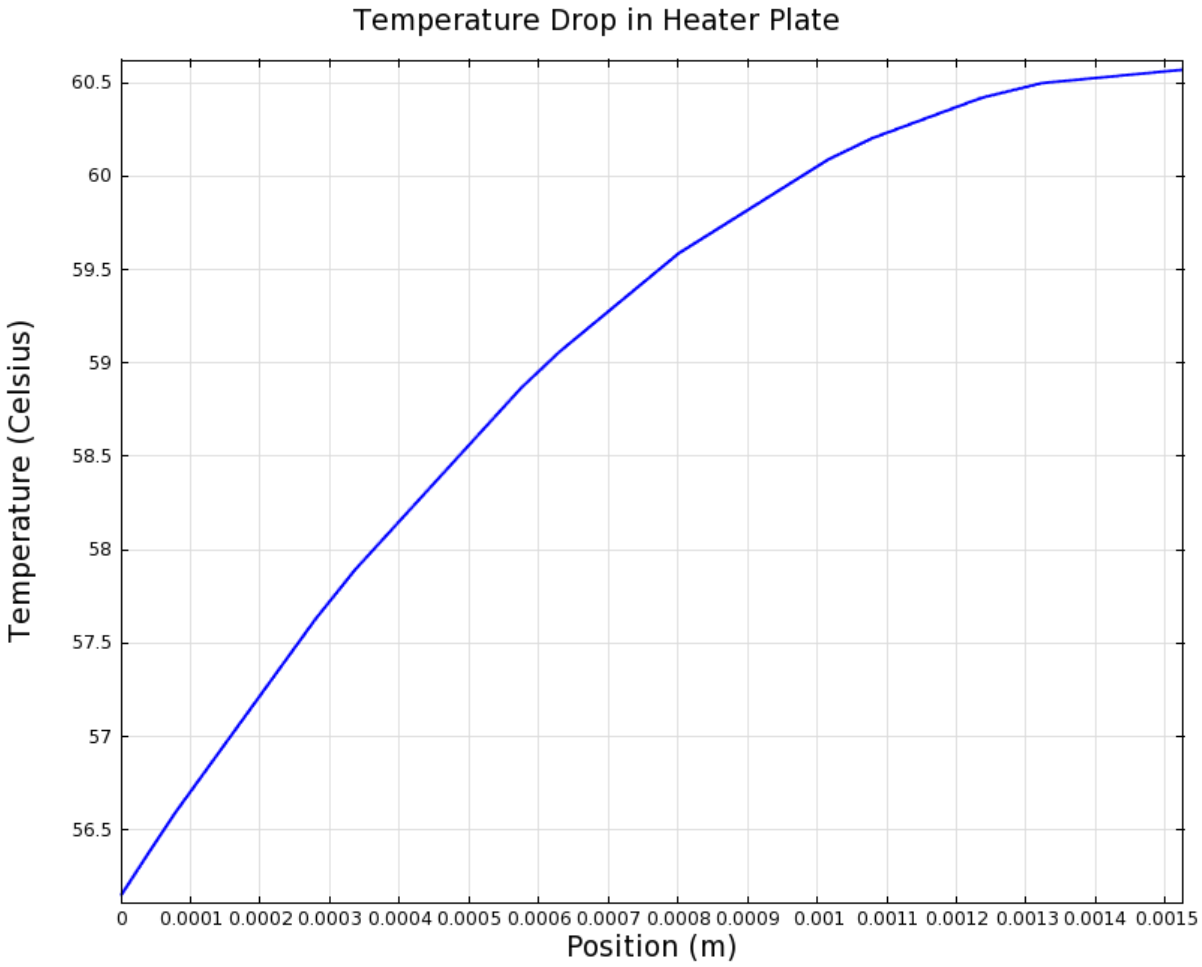

Figure 33: Temperature Drop Across Thickness of Plate at the Axial and Transverse Midpoint of the Heater Plate. The expected temperature drop is nearly identical at other locations away from the electrodes. V_E=2.0 V and I=690 A.

2.7. Test Section Fabrication

After several iterations, the final test section design was completed in SolidWorks, and is shown in Figure 34. Use of off-the-shelf components in an experimental apparatus is ideal, and enhances reliability while simultaneously reducing cost and lead time. However, specifications for the rectangular channel in this study required that nearly all test section components be custom-fabricated. The transition sections, test section body, backing plate, window, window frame, heater plate, insulator, and other parts were custom-machined for the test section.

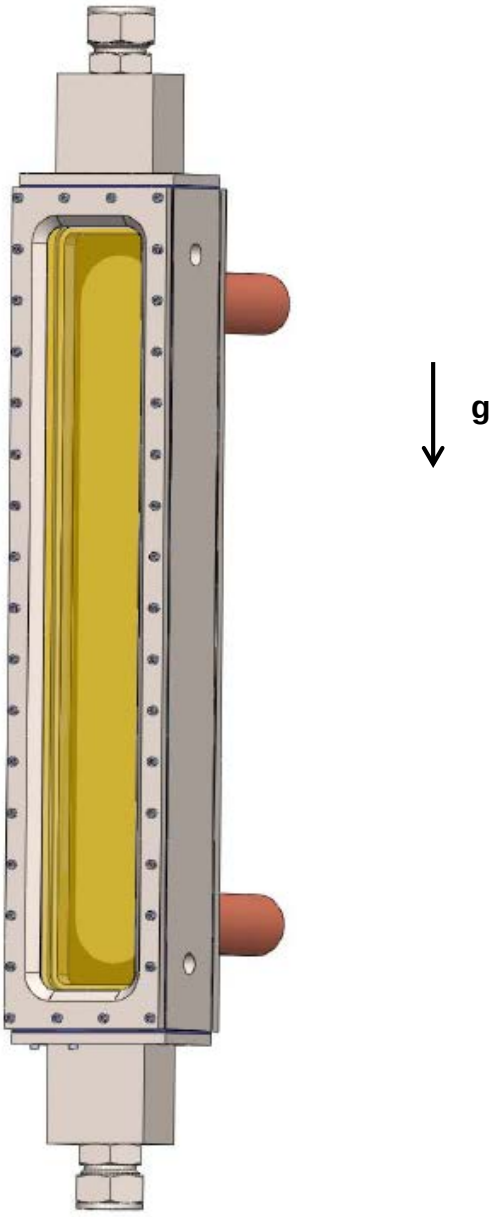

Figure 34: Final CAD Model of the Test Section Assembly.

The transition sections, discussed earlier, were fabricated by wire electric discharge machining (EDM) a converging/diverging channel into solid blocks of 316 stainless steel. Compression tube to butt weld adapters were then welded to the blocks for connection to one-inch tubing and flanges. A wire-frame model of the transition section is shown in Figure 35.

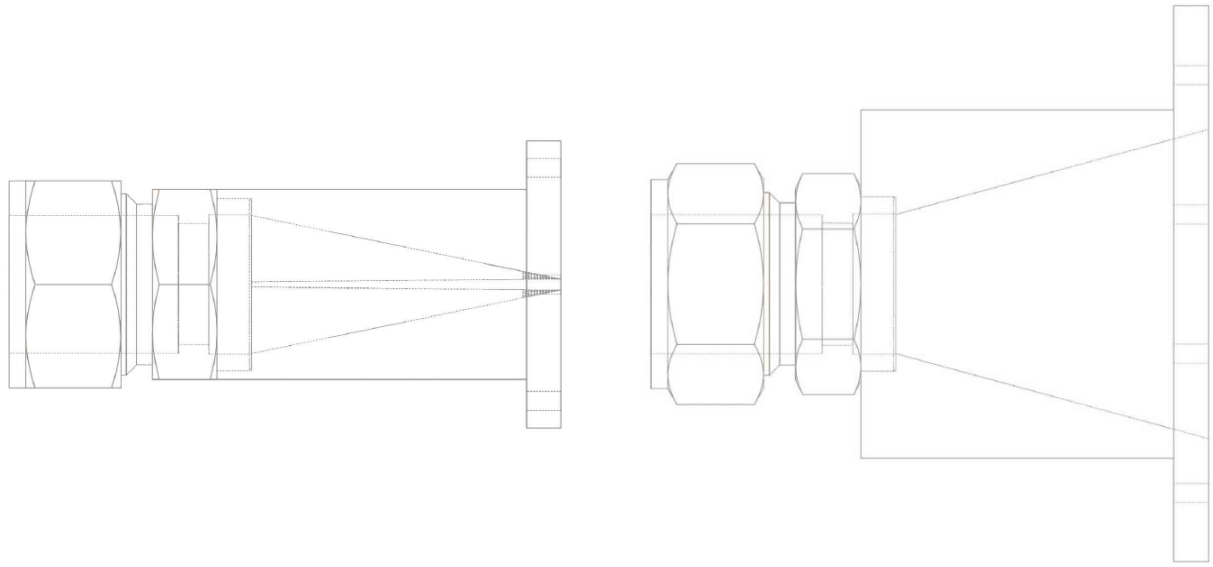

Figure 35: Wireframe Drawings of the Transition Section Viewed from the Side (left) and from the Top (right).

The test section body was also made from 316 stainless steel, with the channel being machined using wire EDM and the steps for the window and insulator machined using an end mill. A groove was incorporated into the step for the window to accommodate a Viton O-ring. The polysulfone window was milled and the surfaces polished to allow for viewing of the heater plate. A 316 stainless steel frame holds the window in place and provides pressure against the O-ring and a glass-filled PTFE gasket to seal the window.

The heater plate was fabricated from 316 stainless steel plate, 0.060" thick, which was vacuum brazed to two copper electrodes. The brazing surfaces were electroplated with nickel to facilitate the brazing process. The wetted portions of the copper electrodes were also electroplated with nickel to alleviate electrochemical corrosion during operation. Two stainless steel studs were vacuum brazed to the back of the heater plate, in order to constrain the heater and prevent bowing during operation. Nuts for the tie down studs were custom-fabricated from

G-10, for the purpose of keeping the heater plate electrically isolated. An O-ring groove was incorporated into the nuts to prevent leaking. An innovative design was incorporated for sealing the electrodes, which involved custom-fabricated, 316 stainless steel nuts. The electrode nuts not only held the plate flush with the insulator, but had two integral grooves for Viton O-rings, one to seal against the insulator and the other to seal against the electrode. The aforementioned parts can be seen in the exploded CAD model of the test section in Figure 36.

The glass/MoS_2 filled PTFE insulator was machined using standard tooling. In addition to electrically isolating the heater plate, the insulator provided support and was milled to maintain a flat and smooth channel while accounting for thermal expansion. Holes were drilled in the insulator to allow thermocouple access to the back of the heater plate. Small recesses were incorporated at the surface of the insulator to allow for injection of an electrically insulating, high thermal conductivity epoxy to improve thermal contact of the thermocouple probe to the heater plate. A 316 stainless steel backing plate holds the insulator in place, with a PTFE foam gasket sealing the insulator surface. Threaded holes were tapped into the backing plate to accommodate 1/16" custom PTFE compression fittings for thermocouple probe access. PTFE was used to provide an additional measure of electrical isolation, ensuring that the thermocouples did not act as a current pathway. The compression fittings seal the thermocouple probes and swage down on the sheath to provide additional contact pressure of the probe against the backside of the heater plate.

Flanged fittings enabled easy installation and removal of the test section into the two-phase flow facility, which is covered in the next chapter. Instrumentation and measurement of experimental parameters are also discussed in depth in the following chapter.

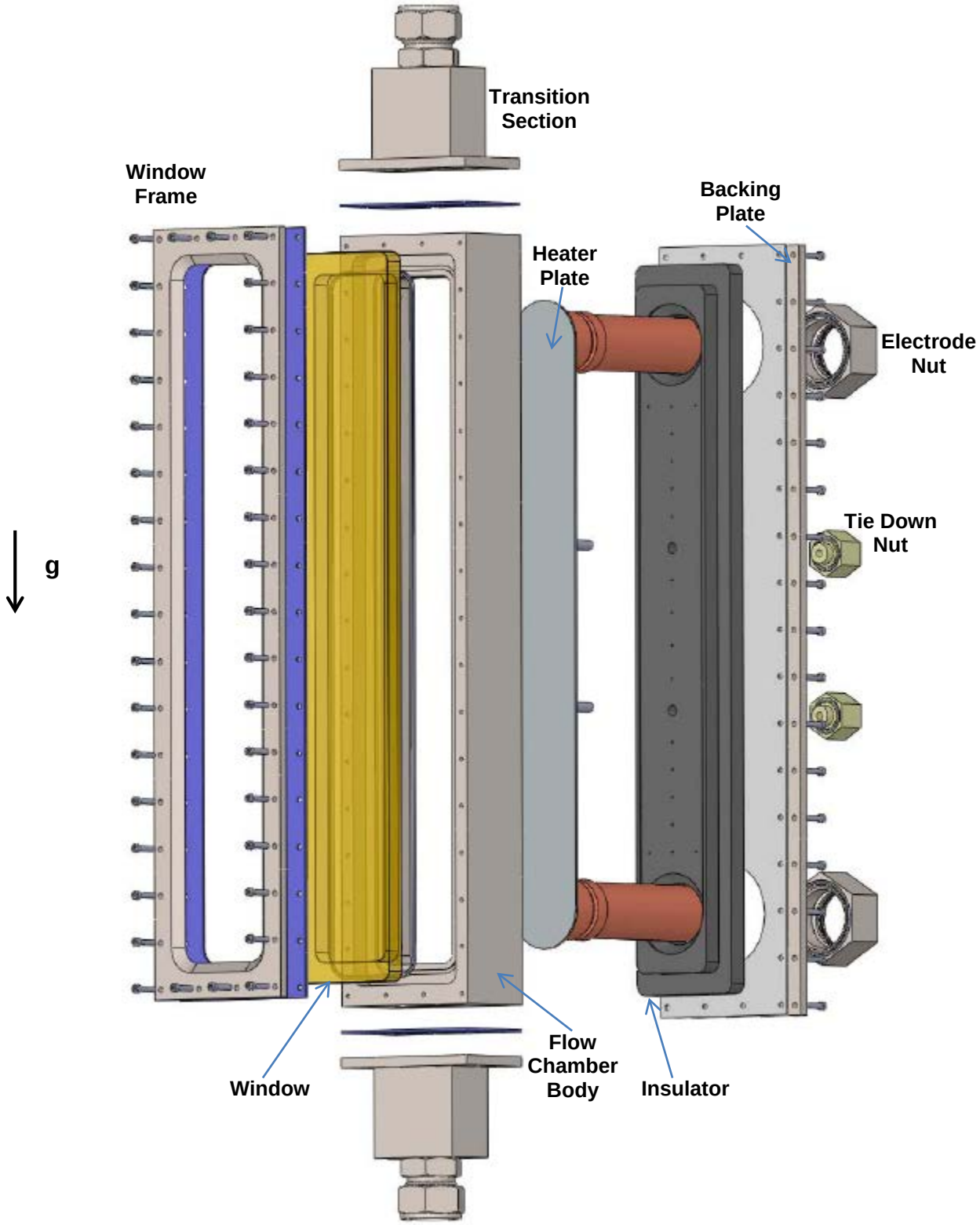

Figure 36: Exploded View of Test Section Showing All Major Parts.

Chapter 3

Design and Construction of a Two-Phase Flow Facility

3.1. Flow Facility Design Parameters

A heated thermal hydraulic loop was designed and built to accommodate the MTR test section described in Chapter 2. As the primary objective of this study involves accurately measuring single-phase heat transfer and onset of nucleate boiling at typical MITR conditions, the loop was purpose-built to operate at and beyond the steady-state flow conditions found in the MITR (refer to Table 3 in Section 1.1.3). The nominal operating parameters of the flow loop are listed in Table 13. The flow loop was designed in a modular fashion, to allow easy substitution of components if operating conditions outside of those listed in Table 13 were desired.

The loop is configured vertically and supported using 6105-T5 aluminum T-slotted framing. Aluminum T-slotted framing was chosen for its light weight, strength, machinability, and modularity. The robust support structure ensures consistent positioning of the piping and test section while providing support for heavy components such as the electrodes, accumulator, and heat exchanger. The entire loop was built on a 122 cm wide by 244 cm long platform elevated 11.5 cm above the floor and constructed of high density polyethylene, to provide space for wiring and cables, and keep important loop components dry in the event of flooding of the laboratory space. The non-conductive platform also isolates the user from ground if an energized component is accidentally contacted. The support structure is securely anchored to the concrete ceiling and to the elevated platform, which, in turn, is anchored to the concrete floor.

Table 13: Nominal Operating Parameters of the Thermal Hydraulic Test Facility. Test section and heater details are provided in the previous chapter.

PARAMETER	MINIMUM	MAXIMUM	NOTES
Operating Temperature	10 °C	99 °C	Minimum temperature set by chilled water system. Maximum temperature limited by flow meter electronics.
Operating Pressure	0.065 bar	3.08 bar	Set by test section (polymer window).
Flow Rate	4.54 L/min (1.2 gpm)	45.4 L/min (12 gpm)	Set by measurement range of flow meter.
Mass Flux (Test Section)	650 kg/m^2-sec	7000 kg/m^2-sec	Set by measurement range of flow meter.
Flow Velocity (Test Section)	0.68 m/sec	7.00 m/sec	Set by measurement range of flow meter.
Reynolds Number (Test Section)	2200	93,000	-
Prandtl Number	1.77	9.44	Using deionized water as the working fluid.

The primary loop consists of 1" (2.54 cm) outer diameter, 300 series stainless steel tubing connected using double-ferrule compression fittings. Connection to certain components required National Pipe Thread (NPT)-to-compression fitting adapters. The dissolved oxygen measurement loop consists of ½" (1.27 cm) stainless steel tubing. All other wetted parts consist of 300 series stainless steel or hard fluoroelastomers to reduce corrosion and contaminants in the de-ionized water stream. The tubing and a small number of fittings possessed some residual mill scale and grease, likely from fabrication and handling. Since the onset of nucleate boiling is sensitive to surface contamination, all tubing and fittings exposed to the primary working fluid were thoroughly cleaned before assembly. The cleaning procedure is described below.

Cleaning Procedure for Primary Loop Components

1) Soak with Fantastik® cleaner, scrub with nylon brush, and rinse with DI water.
2) Immerse in 65% nitric acid solution for 30 seconds followed by rinse with DI water.
3) Sonicate in acetone for 15 minutes.
4) Rinse with ethanol then DI water.
5) Dry with compressed nitrogen.

Tubing and fittings were then assembled, with the loop interior kept isolated from the environment to reduce ingress of dust and other contaminants.

The superstructure stands 3.34 meters high, with the hydraulic head of the loop being 2.18 meters. The total fluid transit length of the flow loop is 5.92 meters. Flanged connections were installed in the loop to allow easy removal and installation of the test section. The test section is electrically isolated from the loop using a flange isolation kit, since an electrical short of the 4500 A power supply to the loop and superstructure would present a hazardous condition. The loop (excluding the test section) and superstructure are grounded with 10 gauge wire to reduce the risk of electrocution from the pump, preheater, or instrumentation. An appropriately-sized safety relief valve was also installed on the flow loop to prevent over-pressurization in the event of pump overspeed or overcharging of the accumulator or fill tank. Valves were installed on the loop to isolate components and allow filling, pulling a vacuum, and venting of the loop during operation. The loop, heat exchanger, and test section were thermally insulated using polyethylene foam pipe insulation.

A photograph showing the loop, superstructure, support platform, and power supply is provided in Figure 37. Figure 38 provides a schematic of the loop and major components. All major components and systems are described in Section 3.2.

Figure 37: Photograph of the Two-Phase Flow Facility.

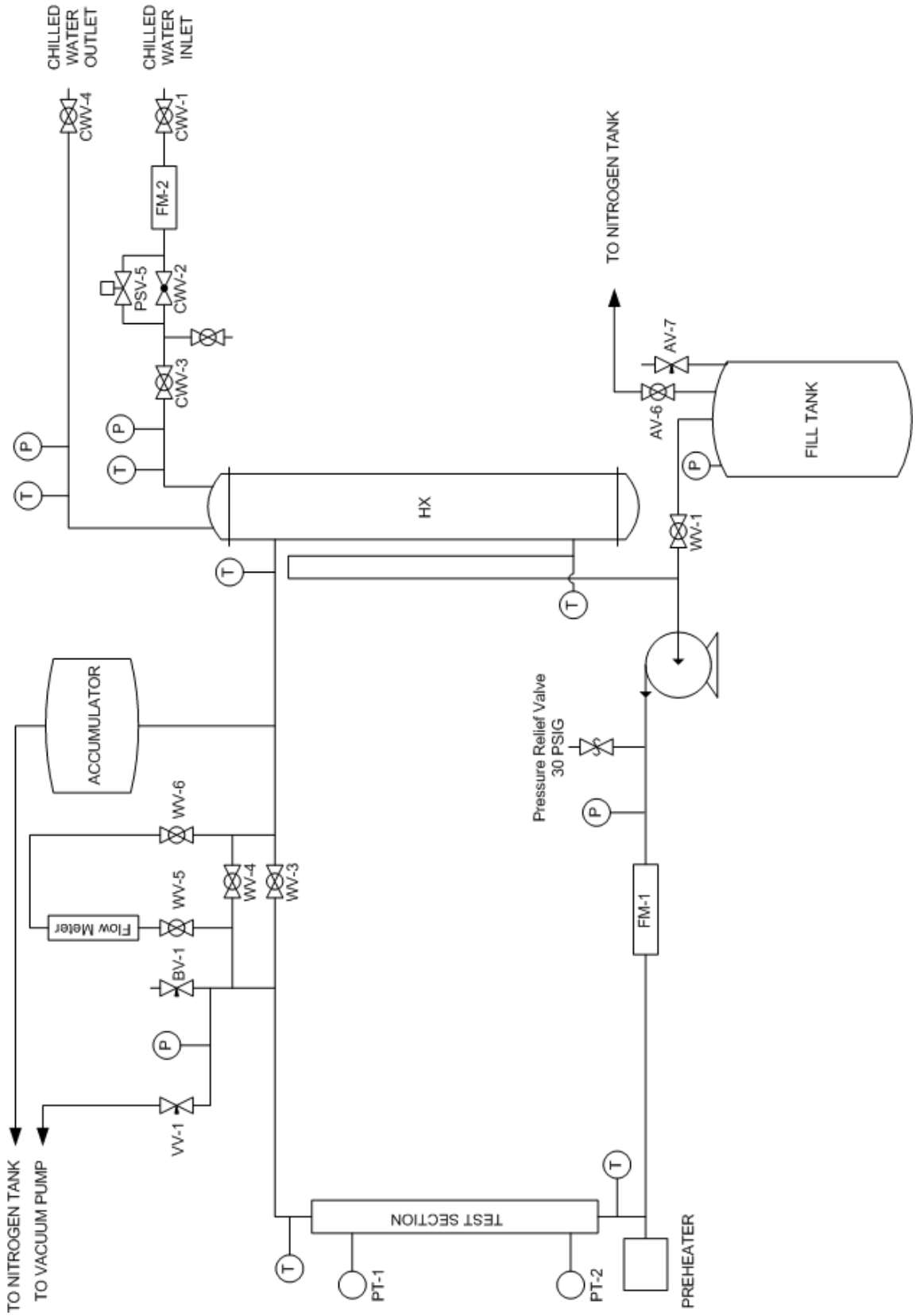

Figure 38: Schematic of the Two-Phase Flow Facility.

3.2. Components

The primary components of the flow loop are the pump, the preheater, the vacuum system, the accumulator and associated charging system, the heat exchanger, and the chilled water circuit. Table 14 provides maximum operating limits for components, fittings, piping, and instrumentation installed in the flow loop and associated systems.

Table 14: Operating Limits for Components of the Flow Loop and Associated Systems.

COMPONENT	MAXIMUM PRESSURE	MAXIMUM TEMEPRATURE	NOTES
-<u>Primary Loop</u>-			
1" Stainless Steel Tubing	110 bar at 22 °C	816 °C	-
½" Stainless Steel Tubing	117 bar at 22 °C	816 °C	-
Stainless Steel Compression Fittings	132 bar at 22 °C	650 °C	-
Class 150 Stainless Steel Pipe and Fittings	20 bar at 38 °C	427 °C	Values for flanges and flanged fittings (ANSI B16).
Ball Valves	69 bar at 93 °C	230 °C	With PTFE seat and seal.
Needle Valves	345 bar at 93 °C	230 °C	With PTFE packing.
Fill Tank	9.7 bar at 38 °C	230 °C	-
Centrifugal Pump	6.3 bar	121 °C	-
Primary Flow Meter	20 bar	99 °C	Higher temperatures may affect the solid state relay.
Rotameter	10.3 bar at 21 °C	93 °C	Rotameter is isolated from the primary loop during normal operation.

COMPONENT	MAXIMUM PRESSURE	MAXIMUM TEMEPRATURE	NOTES
Dissolved Oxygen Probe	7.5 bar	50 °C	DO probe is isolated from the primary loop during normal operation.
Preheater	132 bar at 22 °C	427 °C	-
Accumulator	14.8 bar	343 °C	Bellows is 316 stainless steel. Shell (not wetted) is carbon steel
Heat Exchanger	10.3 bar	232 °C	Maximum shell side pressure is 17.2 bar.
-Chilled Water Circuit-			
Class 150 Stainless Steel Pipe and Fittings	132 bar at 22 °C	427 °C	Values for flanges and flanged fittings (ANSI B16).
Chilled Water Flow Meter	20 bar	99 °C	Higher temperatures may affect the solid state relay.
Solenoid Valve	34.5 bar	50 °C	Maximum differential pressure is 3.5 bar.
Flow Sight	30 bar at 21 °C	82 °C	-
Flexible Hose (Cold Leg)	34.5 bar	88 °C	-
Flexible Hose (Hot Leg)	17.2 bar	232 °C	-
-Nitrogen System-			
Flexible Air Line	20 bar at 24 °C	93 °C	-
Brass Fittings and Valves	41.4 bar at 38 °C	204 °C	-
Backpressure Regulator	17.2 bar	-	-
Cylinder Regulator	276 bar inlet 13.8 bar outlet	-	-

3.2.1. Pump and Variable Speed Controller

Flow is driven by a Berkeley model SS1XS-1, high head, centrifugal pump with a stainless steel impeller. A one horsepower (0.75 kW), 460 VAC three-phase, TEFC (totally enclosed, fan cooled) motor powers the pump. A cutaway view of the pump along with a photo of the pump installed in the flow loop is shown in Figure 39.

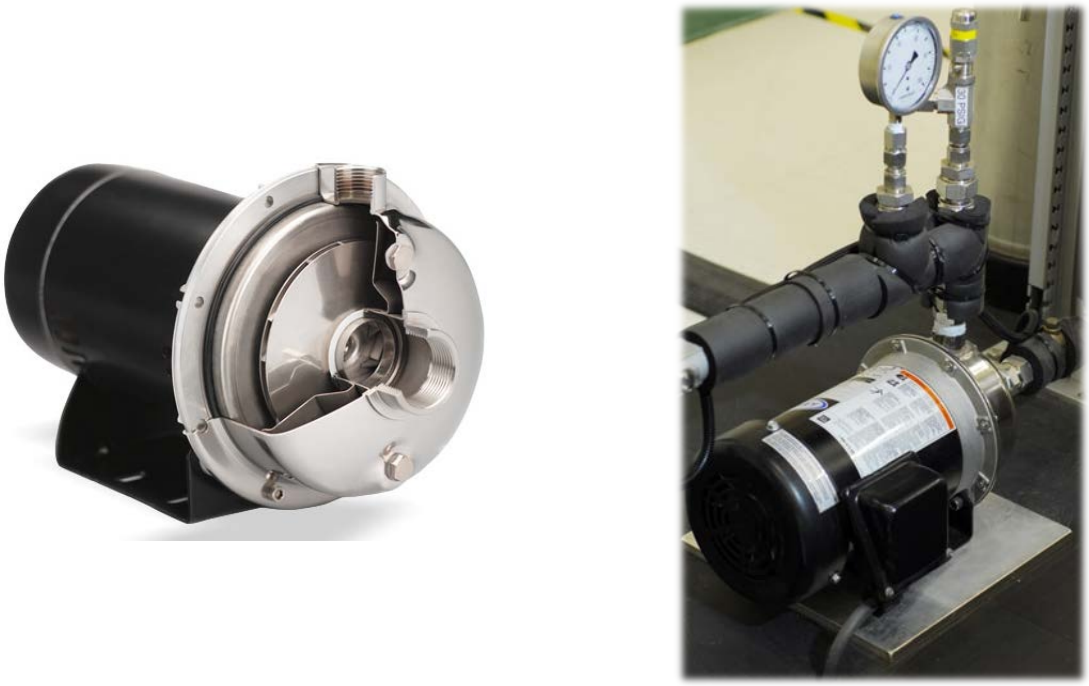

Figure 39: Cutaway View of the Pump Showing Impeller (left) and the Pump Installed on the Flow Loop (right).

The pump motor housing was properly grounded and the pump motor was connected to a Square D OmegaPak Class 8803 Type P, AC drive, constant torque, variable speed motor controller. Figure 40 shows the variable speed controller mounted in a metal enclosure. The variable speed controller was wired for remote operation, with a 0-10 V signal allowing for proportional output, and in turn, control of the pump speed. Figure 41 provides a performance chart for the pump operating at maximum speed.

Figure 40: Square D Variable Speed Controller in Metal Enclosure (cover removed).

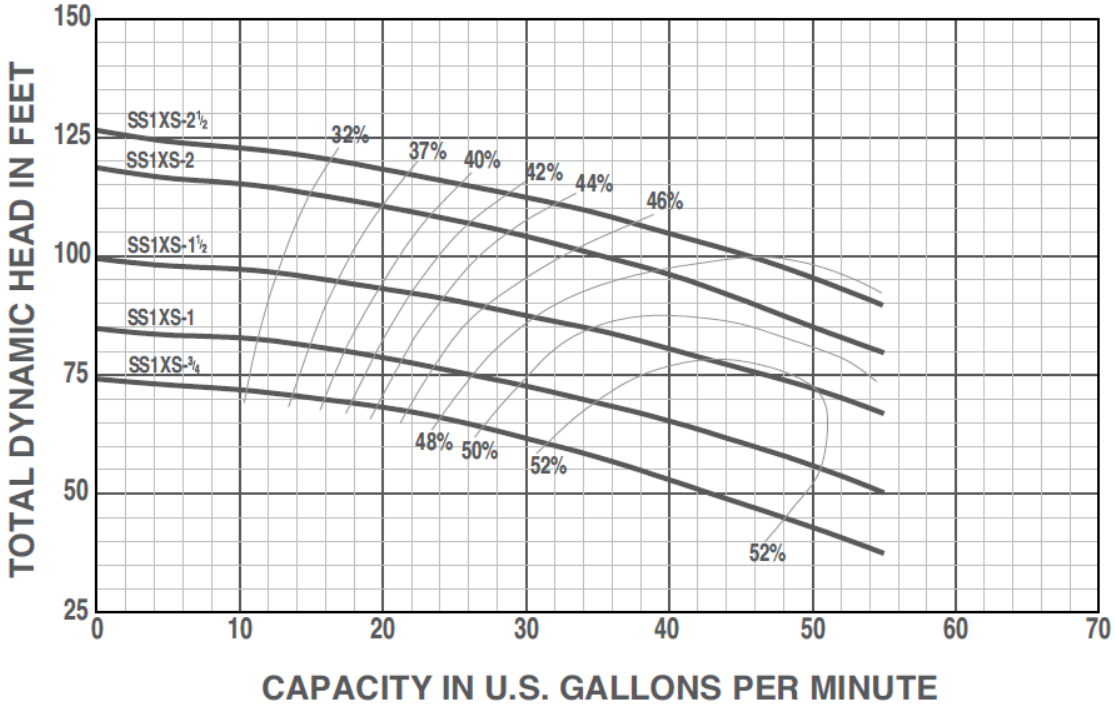

Figure 41: Pump Performance Curve at Maximum Speed. The 1 hp model is installed in the facility. *Source: Ref. [67].*

3.2.2. Preheater and Controller

A 120 VAC, 1.5 kW screw-plug immersion heater, manufactured by Tempco Electric Heater Corp., acts as a preheater for the test section. The preheater provides the ability to maintain an elevated inlet temperature when the test section is at low or no power, enables an inlet temperature closer to the saturation point without risking pump cavitation, and reduces the heat up time for the working fluid.

The preheater was wired to an OMEGA Engineering CS2110 benchtop controller. The benchtop controller relies on measurement of the bulk fluid temperature using a three-wire RTD placed downstream of the preheater, before the test section. The 120 VAC, 15 A (maximum) benchtop controller uses mechanical relays to control the power output to the preheater. The benchtop controller is capable of on/off or proportional-integral control. The on/off control mode with factory default settings provided unsatisfactory control, with noticeable periodic oscillation of the bulk fluid inlet temperature. As such, the controller was operated in the proportional-integral mode, with manual adjustment of the proportional band and cycle time to provide optimum control of the test section inlet temperature. The inlet temperature obtained with the on/off mode compared to the proportional-integral mode is plotted as a function of time in Figure 42. The preheater, as installed in the flow loop, and controller are shown in Figure 43.

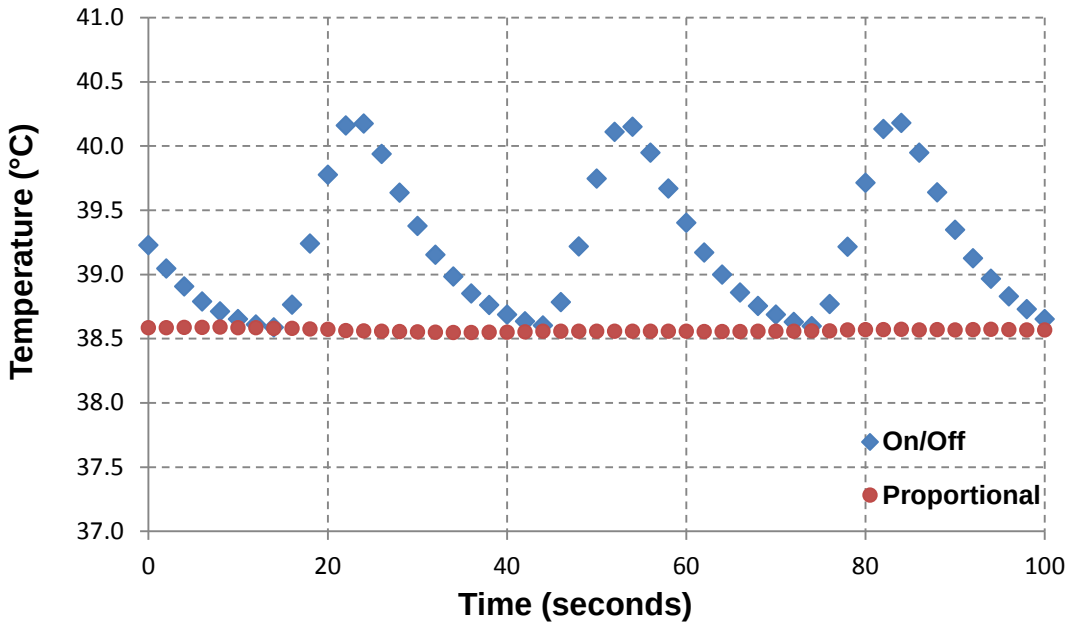

Figure 42: Test Section Inlet Temperature in On/Off and Proportional Control Mode. Proportional mode was used since on/off mode resulted in undesirable system oscillation.

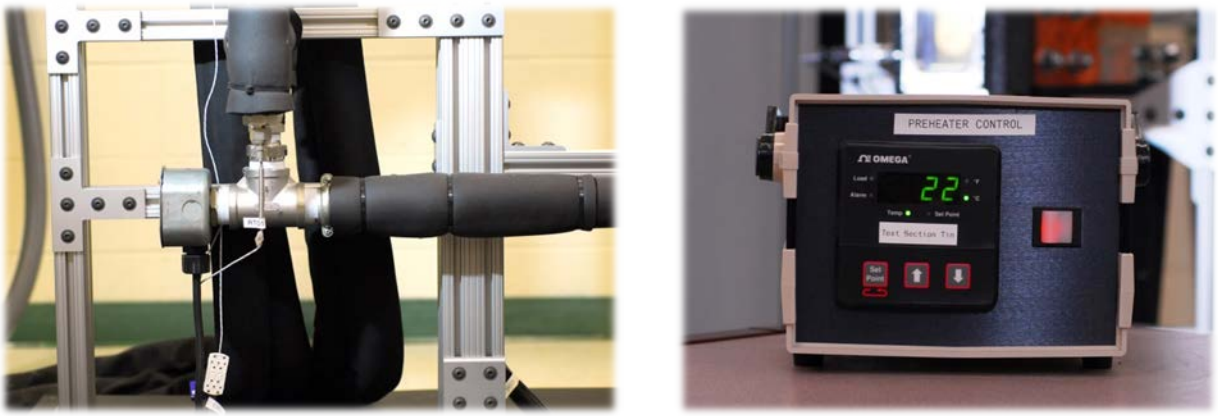

Figure 43: Preheater (left) and Controller (right).

3.2.3. Vacuum System

Non-condensable gases and entrapped air pockets can adversely affect pump performance and interfere with flow control and measurement. While the vertical setup of the loop aids with the removal of non-condensable gases and reduces the possibility of entrapped air pockets, a vacuum system was also required to completely remove entrapped air and facilitate charging of the loop with the working fluid. A Precision Model DD 20, 5 micron vacuum pump was attached to the loop with a vacuum line, and doubly isolated from the primary system to prevent possible backflow of vacuum pump oil and contamination of the working fluid if the line were not vented after use. A photograph of the vacuum pump, as installed on the loop, is shown in Figure 44.

Figure 44: Vacuum Pump Installed in the Flow Facility.

3.2.4. Accumulator and Charging System

A Flexicraft Industries Hydropad model HY12 accumulator was installed in the flow loop to act as a pressurizer, thermal expansion compensator, and pulsation dampener. The stainless steel, bellows-type accumulator provides two liters of liquid displacement, which is more than adequate for expected thermal expansion over the temperature ranges of interest. The metal bellows-type accumulator was chosen due to the virtually maintenance free design with a low likelihood of failure when compared to bladder-type accumulators. A cutaway view, along with a photograph of the accumulator installed on the flow loop, is shown in Figure 45.

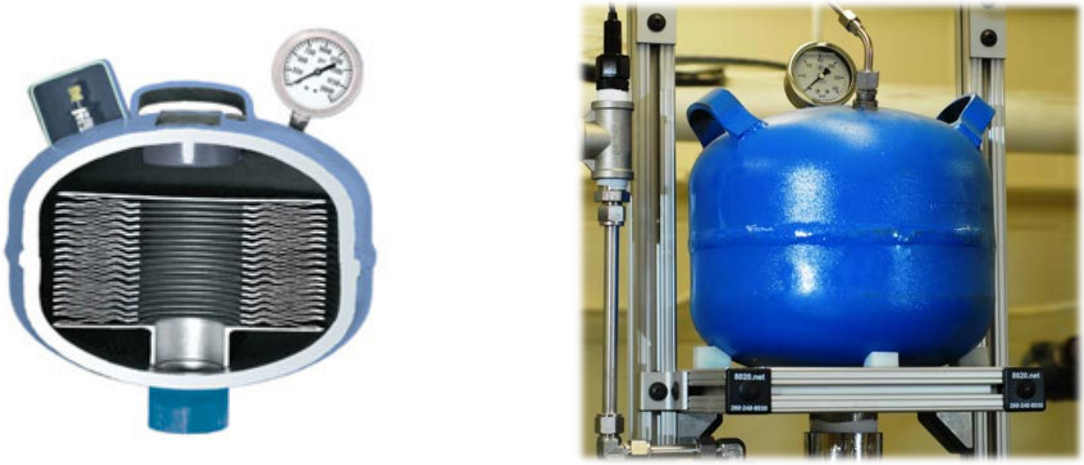

Figure 45: Cutaway View of the Accumulator (left) and the Accumulator Installed on the Flow Loop (right).

The accumulator is actively charged via a pneumatic system consisting of a compressed nitrogen cylinder, gas regulator, backpressure regulator, and safety relief valve, along with several isolation valves. The backpressure regulator ensures constant pressure in the event of variations in the compressed nitrogen temperature. The nitrogen system also charges the working fluid fill tank, facilitating easy filling of the primary system. The fill tank is connected to the primary loop and the nitrogen system using quick-disconnect fittings. The nitrogen system is shown in Figure 46, and the fill tank is shown in Figure 47.

Figure 46: Nitrogen System.

Figure 47: Fill Tank.

3.2.5. Heat Exchanger

A ThermaSys USSC-836 four pass, shell and tube heat exchanger was installed in the flow loop to maintain the loop temperature and act as a condenser. The U-tube heat exchanger design allows for thermal expansion/contraction of the tube bundle while preserving a large 1.11 m^2 heat transfer area. All wetted parts consist of 316L stainless steel. The heat exchanger was mounted vertically, with the working fluid (primary side) flowing through the shell and the chilled water flowing through the tubes. A cutaway view, along with a photo of the heat exchanger, is provided in Figure 48.

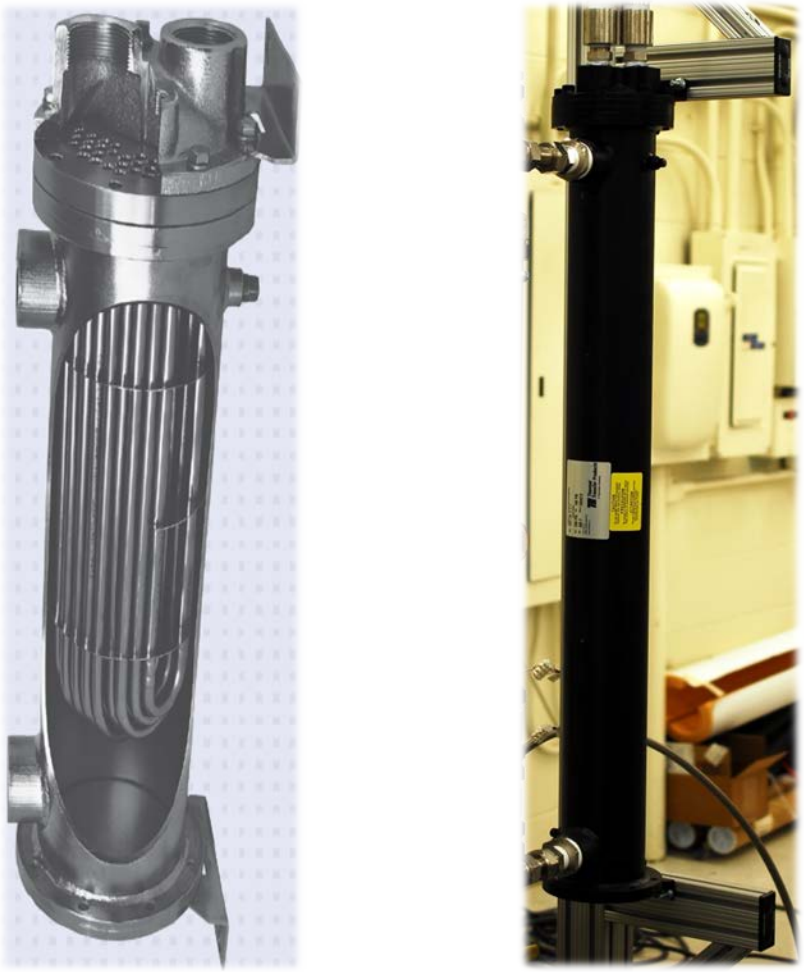

Figure 48: Cutaway View of the Shell and Tube Exchanger (left) and the Heat Exchanger Mounted in the Flow Loop with Insulation Removed (right).

3.2.6. Chilled Water Circuit

The building chilled water system serves as the heat sink for the two-phase flow loop. The nominal chilled water system parameters are listed in Table 15. The heat exchanger was connected to the building chilled water system using flexible hose and class 150 stainless steel pipe, and supported by pipe hangers anchored into the concrete ceiling, as shown in Figure 39. The inlet and outlet temperatures of the chilled water system are monitored using Type E thermocouples.

Table 15: Chilled Water System Parameters

PARAMETER	VALUE	NOTES
Inlet Pressure	11.35 bar (150 psig)	Maximum pressure under ideal conditions. Heavy load on CW system (summertime HVAC use) reduces available pressure.
Inlet Temperature	10 °C	Minimum temperature under ideal conditions. Heavy load on CW system increases temperature.
System Saturation Temperature	185.5 °C	-
Flow Rate	45.4 L/min (12 gpm)	Maximum flow rate under ideal conditions.

Figure 49: Chilled Water Circuit Connecting Heat Exchanger to Building Supply.

Chilled water flow is regulated using a manual needle valve in parallel with a solenoid valve. The manual valve allows for coarse control, up to the maximum chilled water system flow rate. The solenoid valve provides fine control over the chilled water flow rate. The solenoid valve (OMEGA Engineering FSV10 series) is connected to a driver module, which, in turn, is connected to a full PID process controller (OMEGA Engineering CNi852). The full PID controller relies on temperature measurements from a four-wire RTD at the outlet of the heat

exchanger on the primary system. A 0-5 VDC signal sent to the driver module results in a 0-29 VDC signal controlling the lift of the solenoid valve, and therefore, the flow rate of the chilled water system. The operator of the experiment need only enter the desired temperature set point for the primary system fluid temperature at the exit of the heat exchanger. The setup enables completely automated control of the primary system temperature, even if flow or power conditions are adjusted. A schematic of the solenoid valve, along with the valve installed on the chilled water circuit, is shown in Figure 50.

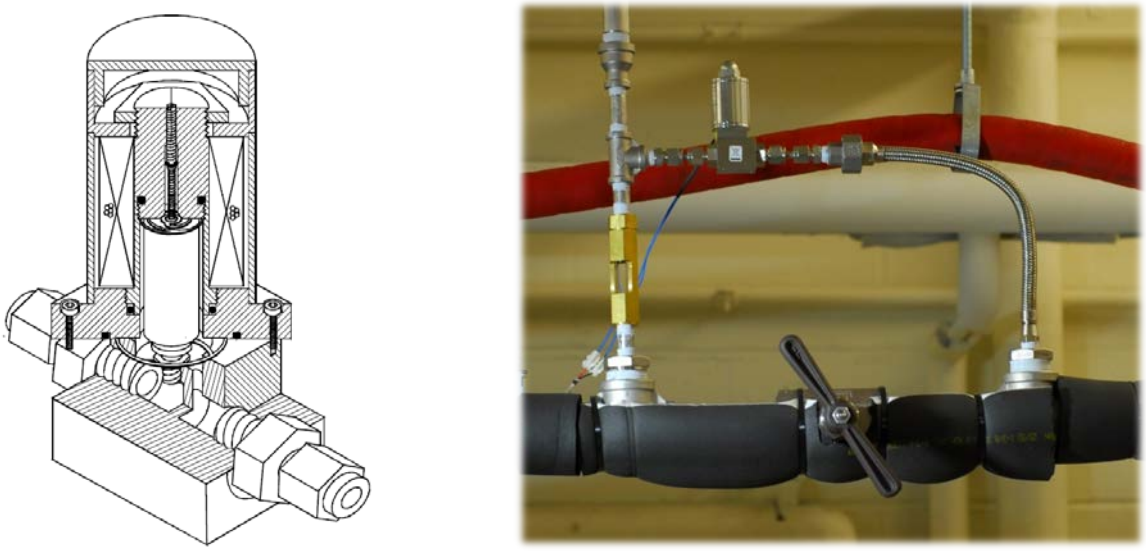

Figure 50: A Schematic of the Solenoid Valve (left) and the Valve Installed on the Chilled Water Circuit (right).

3.3. Measurement and Instrumentation

The flow loop and test section possess instrumentation to determine all necessary quantities, including flow rate, pressure, fluid temperature, the heater plate surface temperature, heat flux, and dissolved oxygen content. Each instrument was selected to measure variables over the operating range of the loop with minimal measurement error. Where applicable, shielded signal wire was used to connect instruments to the data acquisition system to reduce the possibility of electromagnetic interference (EMI). Each instrument is described in detail in the sections below.

3.3.1. Flow Measurement

Accurate measurement of the flow rate is crucial for any forced convection heat transfer experiment. Therefore, significant effort was placed in identifying an appropriate flow meter for the experiment. Typically, flow meters are calibrated to output the volumetric flow rate. The volumetric flow rate, *Q*, is defined as:

$$Q = uA_{flow} \tag{20}$$

Quantities such as the mass flow rate, mass flux, and Reynolds number may be determined from the volumetric flow rate, calculation of which is discussed in Section 3.6.

Several options were considered for measuring the flow rate in the primary system and chilled water circuit in order to optimize accuracy over the desired measurement range. Flow-constriction meters (specifically, Venturi meters), magnetic flow meters, Doppler flow meters, turbine flow meters, rotameters, and vortex meters were all investigated. Though many other techniques exist, such as positive-displacement, ultrasonic transit time, and thermal mass measurements, these were not considered.

Venturi Meters

Flow-constriction meters, such as Venturi meters, rely on the Bernoulli principle and the continuity equation to determine flow velocity. A typical Venturi tube is shown in Figure 51.

For inviscid, incompressible flow, the Bernoulli equation can be derived from the energy equation when there is no work or heat transfer:

$$\frac{P}{\rho} + \frac{u^2}{2} + gz = constant \tag{21}$$

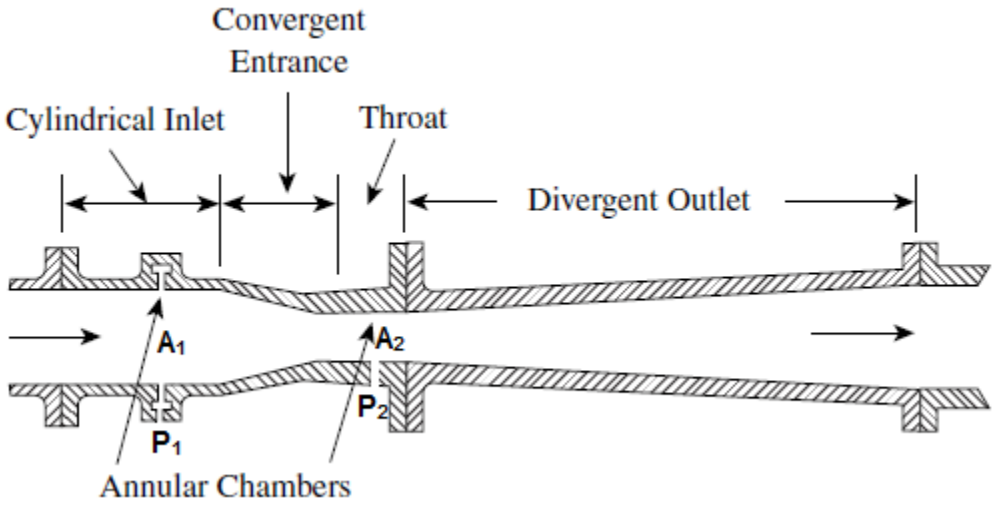

Figure 51: Schematic of Classic Venturi Meter. ***Source: Ref. [68].***

For a constant elevation, the volumetric flow rate for an ideal system may therefore be expressed as:

$$Q_{ideal} = \frac{A_2}{\sqrt{1-(A_2/A_1)^2}} \sqrt{2\frac{P_1 - P_2}{\rho}} \tag{22}$$

where the subscripts denote the positions shown in Figure 51. Therefore, the actual quantity being measured in a Venturi meter is the differential pressure. In an actual system, there will be some friction and form losses in the meter, thereby necessitating an empirical coefficient, called the discharge coefficient:

$$K_{discharge} = \frac{Q_{actual}}{Q_{ideal}} \tag{23}$$

The discharge coefficient depends strongly on the meter geometry and Reynolds number.

Venturi meters can be very accurate, have no moving parts, exhibit low overall pressure loss, and therefore would appear to be ideal for flow measurement. In practice, however, stated accuracies are typically only valid for high Reynolds numbers, typically *Re*>100,000 [68]. The accuracy is also strongly dependent on the flow being properly conditioned. Therefore, appropriate upstream and downstream straight pipe lengths and/or flow conditioners are required. In addition, since the discharge coefficient depends on the flow rate, turndown ratios for Venturi and other flow-constriction type meters tends to be small. The turndown ratio indicates the range over which a flow meter yields acceptable accuracy and is defined as the ratio of the maximum to minimum flow range for which the meter is designed. Venturi meters are relatively expensive for smaller pipe diameters, but become cost-effective options for diameters larger than 10 cm when compared to other types of flow meters. In conclusion, Venturi meters are suitable options for large diameter pipe systems with high Reynolds number where the range of measurement is small. However, Venturi meters were not considered appropriate for the thermal hydraulic test loop due to the need to measure flow over a wide range and at lower Reynolds numbers.

Magnetic Flow Meters

Magnetic flow meters utilize the principle of electromagnetic induction to determine the velocity of a fluid. In a magnetic flow meter, a magnetic field is applied perpendicular to the flow direction. Electrodes in contact with the fluid are placed in the pipe at 90° from the magnetic coils outside the pipe. The electric potential difference is then measured across the electrodes. The integral form of the Maxwell-Faraday equation gives us:

$$\oint \vec{E} \cdot d\vec{l} = -\iint \frac{\partial \vec{B}}{\partial t} \cdot d\vec{A} \tag{24}$$

And the electric potential is related to the electric field by:

$$V_E = \oint \vec{E} \cdot d\vec{l} \tag{25}$$

For a conductor moving through a stationary, non-fluctuating magnetic field, perpendicular to the plane where the electric potential is measured, equation (24) and equation (25) may be combined to yield:

$$\Delta V_E = -BL\frac{dl}{dt} = -BLu \tag{26}$$

Where B is the scalar magnetic field strength, L is the distance between electrodes, and v is the flow velocity. Magnetic flow meters therefore offer a means of measuring flow rate with no moving parts and virtually no pressure drop. Additionally, in practice, magnetic flow meters offer a very large turndown ratio, require minimal flow conditioning, are insensitive to whether flow is turbulent or laminar, and are priced similarly to other flow meters.

However, magnetic flow meters require that the fluid medium be conductive. Modern magnetic flow meters can measure fluids with conductivities as low as 10^{-7} siemens/cm. For experimental purposes, the deionized water to be used in the flow loop will have a resistivity of 15 MΩ-cm or greater, which corresponds to a conductance of 6.67×10^{-8} siemens/cm. Therefore, even magnetic flow meters with the highest sensitivities are not suitable for use in the primary flow loop, though they would be suitable for a tap water system, such as the chilled water circuit.

Doppler Flow Meters

Doppler flow meters are capable of determining flow velocity based upon the Doppler Effect, whereby a frequency shift in a transmitted ultrasonic signal may be related to the flow velocity:

$$u = K_{Doppler}(f_0 - f) \tag{27}$$

where f_0 is the source frequency, f is frequency at the receiver, and $K_{Doppler}$ is a constant which depends on the relative orientation of the transmitter and receiver along with speed of sound in the transducer. Doppler flow meters are non-contact, require minimal upstream and downstream

piping requirements, and are capable of very high turndown ratios. However, traditional Doppler flow meters require entrained particles or bubbles greater than 30 μm in diameter, which is not expected in this experiment. While variations have been developed for clean liquids by relying on reflection of ultrasonic signals off turbulent eddies, these meters were prohibitively expensive for the application.

Turbine Meters

Turbine meters are a well-established form of flow measurement, where a turbine, typically with an axis of rotation parallel to the flow, rotates with a frequency which is directly proportional to the flow rate:

$$Q = \frac{f_r}{K_{turbine}} \tag{28}$$

where f_r is the frequency of rotation and $K_{turbine}$ is the flow coefficient for the meter. Depending on the meter, the rotation frequency may be detected by mechanical sensors or inductance, reluctance, capacitive, or Hall effect pickup coils. The flow coefficient depends on the kinematic viscosity of the fluid, but meters are typically designed such that the effect is minimal over a reasonable range.

Turbine meters can achieve accuracy up to 0.5%, but this usually comes at a high cost. In addition, upstream and downstream piping requirements can be prohibitive, where 20 pipe diameters or more of straight pipe are required downstream of an elbow, and 50 diameters or more are recommended if swirling flow is present. Flow conditioners can reduce these piping requirements. Presence of entrained air, bubbles, or solid particles will affect the accuracy of the meter and lead to degradation and damage of the turbine. As the bearing and components experience wear over time, frequent recalibration of turbine meters is recommended. Turbine meters can also be sensitive to electrical noise, and should be installed away from sources of electromagnetic interference and signal conditioners should be installed as close to the meter output as possible. Turbine meters can achieve turndown ratios of 10:1 or more, though the optimum range for a typical turbine meter is $4{,}000<Re<20{,}000$ [69]. For these reasons, a turbine meter was not selected for the primary loop or chilled water circuit.

Rotameters

A rotameter relies on the balance of force between drag, buoyancy, and weight to determine volumetric flow rate. A float in a tapered channel rises in proportion to the flow rate, which is read off a scale on the channel. The float may be constructed of a variety of materials, thereby allowing for potential operation at high temperatures. In older models, the float rotated for stabilization, leading to the term "rotameter." The flow rate in a rotameter is calculated from the force balance on the float:

$$Q = A_{flow}\sqrt{\frac{2gV_{float}}{C_d A_{float}}\left(\frac{\rho_{float}}{\rho_f} - 1\right)} \tag{29}$$

where A_{float} is the cross-sectional area of the float, and A_{flow} is the flow area around the float. As seen in equation (29), the measured flow rate depends on the density of the fluid and the drag coefficient, C_d, which depends on the fluid viscosity. Viscosity and density depend on fluid temperature, meaning that rotameters are typically calibrated for a one fluid at a specific temperature. While floats are typically designed to minimize dependence on viscosity changes, density changes can have a significant effect on flow measurement. Additionally, rotameters must be installed vertically with upflow, and data logging is not straightforward (i.e. they are typically used as visual indicators). For these reasons, a rotameter was considered unsuitable for primary or chilled water flow measurement. However, a rotameter was selected for measurement of flow in the dissolved oxygen measurement loop, as this would be performed at constant temperature and isolated from the primary flow loop during normal operation. The specifications for the Blue-White Industries, model F-450, are listed in Table 16. A photograph of the rotameter, as installed in the dissolved oxygen measurement loop, is shown in Figure 52.

Vortex Flow Meters

Vortex flow meters rely on the generation of a von Kármán vortex street to determine the flow velocity. Meters contain a bluff body in the center of the flow stream, upon which flow separates and creates a regular, alternating pattern of vortices in the wake of the bluff body. This phenomenon is termed a von Kármán vortex street. The frequency of the vortex shedding from

Table 16: Specifications of the Rotameter Installed in the Dissolved Oxygen Meter Loop.

PARAMETER	VALUE
Minimum Flow Rate	0.4 L/min
Maximum Flow Rate	4.0 L/min
Maximum Pressure	10.34 bar at 21 °C
Maximum Temperature	93 °C
Output	Visual
Manufacturer's Stated Accuracy	±5% of reading

Figure 52: Rotameter Installed in the DO Loop.

the bluff body is determined by measuring the variation in pressure downstream of the body with a piezoelectric sensor. The frequency of shedding, f_s, and the flow velocity are related by the Strouhal number:

$$Sl = \frac{f_s L_c}{u} \tag{30}$$

which is defined as the ratio of the vibration frequency to the characteristic frequency of the body. Note that L_c is the characteristic dimension of the bluff body, not of the pipe itself. For well-designed systems, the Strouhal number remains quite constant over a wide range of Reynolds number, typically within 1% for $10{,}000<Re<10^6$ [70]. A schematic illustrating the measurement principle is shown in Figure 53.

Vortex flow meters have no moving parts and maintain calibration over extended operational periods. Vortex meters can handle clean fluids or fluids with suspended solids (e.g. colloids) with no effect on accuracy. However, very viscous liquids may be problematic, though this issue is not relevant in the current study. Vortex flow meters may be installed in any

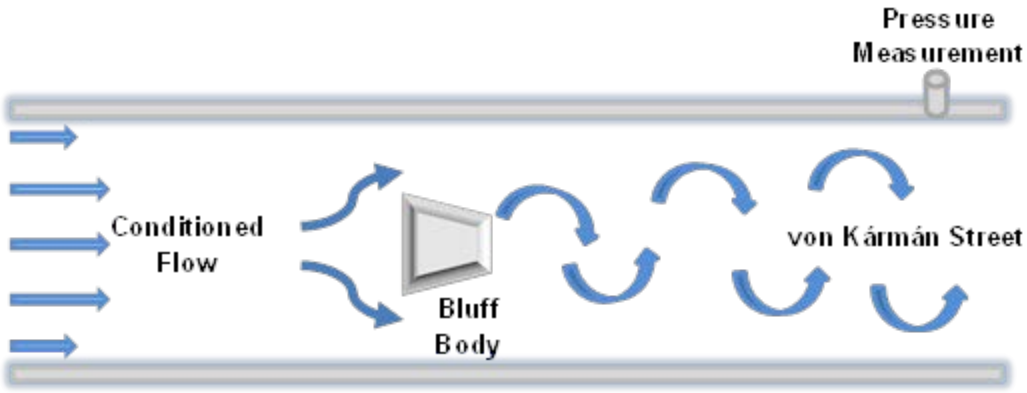

Figure 53: Schematic Showing Principle of Operation of a Vortex Flow Meter.

position, provided air is not trapped in the meter. Accuracies of 1% or better are achievable with appropriate flow conditioning. The drawback of this type of meter is that the flow over the bluff body must be turbulent for vortex shedding to occur, and measurement error increases for Re<10,000. Flashing and cavitation may also occur in the meter if backpressure is not sufficient, especially close to the saturation temperature of the fluid. This affects the flow measurement and leads to noise. Noise may also be introduced by pipe vibrations of similar frequency for which the meter is calibrated, though this can be avoided by properly supporting the piping system. Modern vortex meters have integrated signal conditioners and filters to address noise, and can also correct for flow which is not conditioned adequately.

The advantages and disadvantages of each method of flow measurement are listed in Table 17. From the table, it becomes clear that the only tenable options for the primary system were turbine meters or vortex meters, considering the necessary turndown ratio, the low conductivity of the fluid, and the desire to operate the system in a degassed state.

Ultimately the vortex meters were selected for measuring flow rate in the primary system and chilled water circuit due to concerns over wear, drift in calibration, and the expense of high accuracy turbine meters. Each vortex meter was appropriately sized for the expected flow conditions in each system. The specifications for the installed meters are listed in Table 18. Though the manufacturer's stated accuracy is less than desirable, the stated repeatability is excellent. Calibration of the meters (refer to Section 3.6) in the installed setup would thereby ensure an overall accuracy much higher than that stated. While these particular meters specify that no upstream or downstream straight pipe lengths are required, each meter was installed with at least 10 upstream and 10 downstream pipe lengths of equivalent diameter to the meter housing

Table 17: Summary of Flow Measurement Methods Considered for the Two-Phase Flow Loop.

Meter Type	Operation Principle	Turndown Ratio	Advantages	Disadvantages	Installation Considerations
Venturi Meters	Differential pressure measurement from Bernoulli principle	Typical 3:1 Maximum 5:1	No moving parts; High accuracy achievable	Small turndown ratio; High Reynolds number required for good accuracy	A least 10 straight pipe diameters upstream, 3 downstream
Magnetic Flow Meters	Velocity of conductor determined from EM induction	Typical 20:1 Maximum 100:1	No moving parts; High accuracy; Large turndown ratio	Requires minimum electrical conductivity of working fluid	Minimal flow conditioning required
Doppler Flow Meters	Velocity of entrained particle or bubble determined from Doppler shift	Typical 50:1 Maximum 200:1 or more	No moving parts; Large turndown ratio	Requires entrained particles or bubbles in working fluid	Minimal flow conditioning required
Turbine Meters	Rotation frequency of turbine proportional to flow rate	Typical 10:1	High accuracy achievable; Widely used	Sensitive to electrical noise; Wear of turbine and bearing affects calibration	At least 20 straight pipe diameters downstream of elbow; Flow straightener recommended to eliminate swirl
Rota-meters	Force balance on a float	Typical 10:1 Maximum 15:1	Simple; Visual indication of flow	Calibrated for specific fluid and temperature	Must be installed vertically
Vortex Meters	Frequency of vortex shedding from bluff body related to flow velocity	Typical 10:1 Maximum 20:1	No moving parts; Good accuracy	Flow must be turbulent	Upstream and downstream piping for best accuracy

to maximize accuracy. Specifically, the flow meter in the primary system was installed over 10 downstream pipe diameters from a concentric reducer, and over 30 diameters downstream of an elbow. Swirl was not considered an issue in meter installation as there were no out-of-plane pipe

bends upstream of the meter. Photos of the meters, as installed in the primary system and chilled water circuit are shown in Figure 54.

Table 18: Specifications for the Primary and Chilled Water Flow Meters.

	Primary Flow Meter	Chilled Water Flow Meter
Model	OMEGA Engineering FV102-SS	OMEGA Engineering FV103
Minimum Flow Rate	4.54 L/min (1.2 gpm)	9.46 L/min (2.5 gpm)
Maximum Flow Rate	45.4 L/min (12 gpm)	95.6 L/min (25 gpm)
Maximum Pressure	20 bar	20 bar
Maximum Temperature	99 °C	99 °C
Output	4-20 mA current signal	4-20 mA current signal
Manufacturer's Stated Accuracy	±5%	±5%
Manufacturer's Stated Repeatability	±0.25%	±0.25%

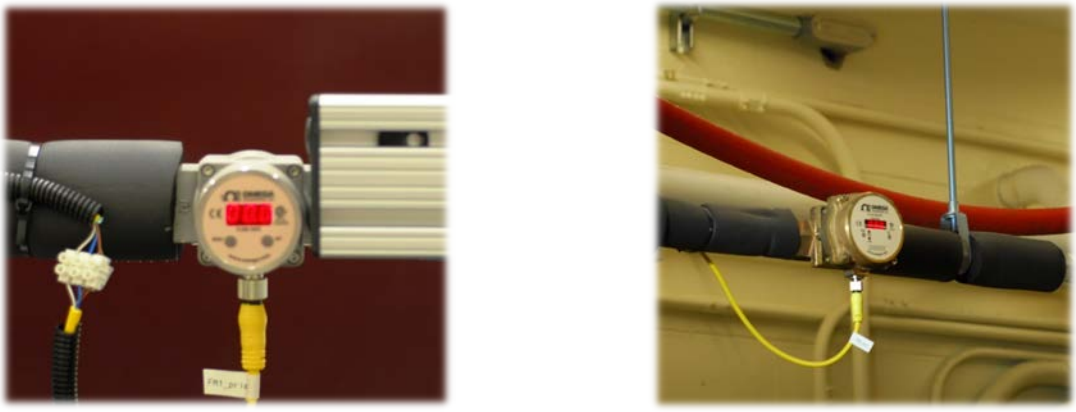

Figure 54: Vortex Flow Meter Installed in Primary Loop (left) and the Chilled Water Circuit (right).

3.3.2. Pressure Measurement

Pressure is measured at various points in the primary loop, chilled water circuit, and nitrogen system, as indicated in Figure 38. Pressure gauges of the bourdon-tube type are used for visual indication of the pressure downstream of the pump, near the primary system vent, on the fill tank, on the air side of the accumulator, on the nitrogen tank, and at the inlet and outlet of the heat exchanger on the chilled water side.

The absolute pressure is measured and recorded at the inlet and outlet of the test section with OMEGA Engineering PX329-050A5V pressure transducers for normal operation and PX329-200A5V pressure transducers for higher pressure operation. The specifications of the transducers are listed in Table 19. The pressure transducers utilize silicon strain gauges which are bonded to a stainless steel diaphragm. The tap size for pressure measurement is known to influence the measured value due to local disturbance of the boundary layer [71], with an infinitesimally small hole yielding the true value. However, there is a practical limit on how small of a hole may be drilled, and burrs have an even more drastic effect on pressure measurement than hole size alone. Therefore, for this study, plugs of PTFE were fabricated by hand for the pressure taps, with 1/16" (1.58 mm) holes drilled to measure the fluid pressure. Typically hole sizes of 0.5 mm to 3 mm are considered optimum for pressure measurement. The surface of the plugs were carefully finished to ensure the smoothest possible area around the hole.

While a prior study [72] investigated friction pressure drop in similar channels with and without longitudinal grooves, differential pressure measurement was still incorporated in this experiment for more accurate determination of pressure drop along the channel. A review of corresponding literature indicates that friction pressure drop for flat ducts is well-predicted by circular tube correlations, but pressure drop for rectangular channels may deviate by 20% or more using the standard hydraulic diameter and circular tube predictions [73]. Specifically, the aspect ratio of the channel has been shown to have an effect separate from the hydraulic diameter on friction pressure drop in turbulent flow. It was therefore desired to measure the pressure drop accurately. An OMEGA Engineering PX2300-10DI differential transducer was installed horizontally with pressure lines utilizing the same taps as the absolute pressure transducers. The specifications for the differential pressure transducer are found in Table 20. The differential pressure transducer was calibrated using ten points from a 0-10psi calibration device. A

photograph of the absolute and differential pressure transducers installed on the test section is shown in Figure 55.

Table 19: Absolute Pressure Transducer Specifications.

Parameter	Value	Notes
Model	OMEGA Engineering PX329	PX329-050A5V for low pressure operation and PX329-200A5V for high pressure calibration. NIST traceable calibration provided.
Pressure Range	0 bar to 13.79 bar (0- 200 psia)	Absolute Pressure.
Compensated Temperature Range	-20 °C to 85 °C	-
Output	0-5 VDC	-
Manufacturer's Stated Accuracy	±0.25% Full Scale	-
Total Error Band	±2% Full Scale	Includes linearity, hysteresis, repeatability, thermal hysteresis, thermal errors, and offset.

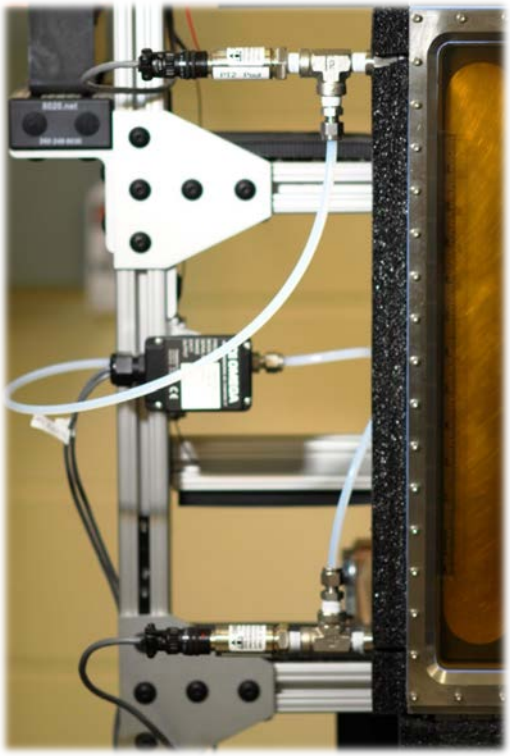

Figure 55: Absolute and Differential Pressure Transducers Installed on the Test Section. A 1/16" hole was used for the pressure tap to minimize measurement error.

Table 20: Differential Pressure Transducer Specifications.

Parameter	Value	Notes
Model	OMEGA Engineering PX2300-10DI	Calibrated in-house using a 0-10 psi source.
Differential Pressure Range	0 bar to 0.689 bar (0- 10 psi)	Differential Pressure.
Compensated Temperature Range	-1 °C to 65 °C	-
Output	4-20 mA	-
Manufacturer's Stated Accuracy	±0.25% Full Scale	-
Total Error Band	±2% Full Scale	Includes linearity, hysteresis, repeatability, thermal hysteresis, thermal errors, and offset.

3.3.3. Temperature Measurement

Accurate measurement of temperature is essential to the study, as both the heat flux and wall superheat are determined from temperature measurements. On the primary system, fluid temperature was measured at the inlet and outlet of both the test section and heat exchanger using four-wire resistance temperature detector (RTD's). Additional RTD's were placed at the inlet of the test section to provide feedback to the preheater controller, and at the exit of the heat exchanger to provide feedback to the chilled water flow controller. On the chilled water system, thermocouples were placed at the inlet and outlet of the heat exchanger to monitor temperature and as a check on the energy balance of the system. As discussed in Chapter 2, thermocouples were installed on the back side of the heater plate at various locations to determine the surface temperature. Thermocouples were chosen for this application due to the lower cost and wider availability of sizes. The RTD's and thermocouples are described in the following sections.

Resistance Temperature Detector (RTD)

Resistance temperature detectors enable accurate temperature measurement over a wide range of temperature measurement. RTD's rely on the relationship between electrical resistance of a conductor and the conductor temperature to determine the temperature of the conductor. For certain materials, the response may be nearly linear over a fixed range, and the resistance and temperature may be related by the temperature coefficient of resistance, α:

$$R(T) = R(T_0)[1 + \alpha \Delta T] \tag{31}$$

In the two-phase flow loop, four-wire RTD's were employed to negate the impact of lead resistance on the temperature measurement. Figure 56 provides a diagram for a four-wire RTD.

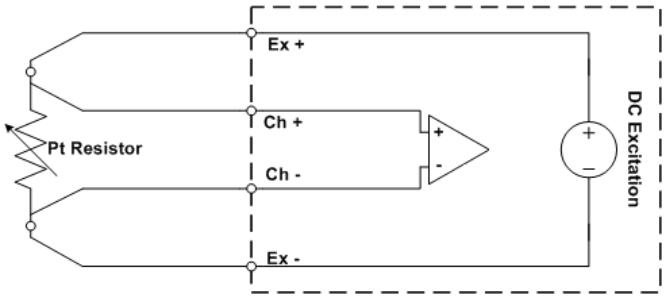

Figure 56: Wiring Diagram of Four-Wire RTD Circuit.

The specifications for the four-wire RTD's installed in the flow loop are listed in Table 21.

Table 21: Four-Wire RTD Specifications.

Parameter	
Model	OMEGA Engineering PR-11-3-100-1/8-6-E
Standards Met	DIN/IEC 60751
Temperature Range	-200 °C to 600 °C
Resistor Material	Wire wound, class A platinum
Nominal Resistance	100 Ω at 0 °C
TCR	0.00385 Ω/(Ω-K)
Manufacturer's Stated Accuracy	±0.15 °C

Thermoelectric Temperature Sensor (Thermocouple)

When two dissimilar metals are joined electrically, a small voltage is produced. More importantly, the amplitude of the voltage is proportional to the temperature at the junction. This phenomenon, called the Seebeck effect, enables temperature measurement using a variety of materials. The thermoelectric power, or Seebeck coefficient, *S*, is defined by [74]:

$$\vec{E} = S\boldsymbol{\nabla}T \tag{32}$$

Given that $\vec{E} = -\boldsymbol{\nabla}V_E$, the Seebeck coefficient may be expressed as:

$$S = -\frac{|\boldsymbol{\nabla}V_E|}{|\boldsymbol{\nabla}T|} \tag{33}$$

For small temperature differences, the Seebeck coefficient can be approximated as:

$$S = -\frac{\Delta V_E}{\Delta T} \tag{34}$$

which is how it often appears in practice.

However, other factors may influence the voltage produced by the Seebeck effect. If current flows through the circuit, cooling or heating will occur at the junction, depending on the direction of current flow and the materials employed. This evolution of heat, due to the Peltier effect, occurs in addition to any Joule (resistive) heating in the circuit. If a temperature gradient also exists along either of the conduction paths of the junction materials, cooling or heating will occur due to the Thomson effect. Lastly, a voltage will also be generated when connecting to the voltage measurement device, requiring a reference junction to determine the voltage generated at the measurement junction. An ice bath is commonly used to establish a known temperature at the reference junction. However, modern data acquisition systems may employ internal reference junctions, relying on RTD's or thermistors to measure the junction temperature, to eliminate the need for an external reference. In addition to the aforementioned sources of error when using thermocouples, impurities in the junction materials can have a significant effect on precision and accuracy.

While several effects lead to increased error when using thermocouples compared to RTD's, selection of the appropriate thermocouple type for the end application, use of special limits of error (SLE) wire, use of thermocouples manufactured in the same lot from the same stock material, and calibration of the thermocouple using the actual setup can lead to respectable accuracy and precision. Uncertainties of 0.1 °C to 0.2 °C are achievable with appropriate calibration over the temperature range of interest [75]. However, one commonly encounters users selecting thermocouples solely on desired temperature range, with no regard to the sensitivity, thermoelectric inhomogeneity, hysteresis, susceptibility to noise, drift due to oxidation, and maximum achievable accuracy of the thermocouple type. Type K, Type T, and Type J thermocouples are those most commonly encountered for the temperature ranges expected in this study. Note that some sources recommend against using Type K thermocouples for temperatures below about 300 °C [76]. Note that the Alumel element of Type K thermocouples undergoes a magnetic transformation around 150 °C, leading to significant variation in the Seebeck coefficient in this temperature range [75]. Type E thermocouples, though commonly encountered in cryogenic applications (because of their high sensitivity), are

under-utilized for precision temperature measurements up to 450 °C. Table 22 shows relevant properties of thermocouples considered for this study, and Figure 57 plots the sensitivity as a function of temperature for these thermocouples.

Table 22: Selected Characteristics of Thermocouples Considered for This Study.

	Type E	Type J	Type K	Type T
(+) Junction Material	Chromel (90%-10% Ni-Cr)	Iron	Chromel (90%-10% Ni-Cr)	Copper
(-) Junction Material	Constantan (55%-45% Cu-Ni)	Constantan (55%-45% Cu-Ni)	Alumel (94%-3%-2%-1% Ni-Mn-Al-Si)	Constantan (55%-45% Cu-Ni)
Operational Range	-253 °C to 1000 °C	-253 °C to 760 °C	-253 °C to 1370 °C	-253 °C to 400 °C
Recommended Range* (protected element)	-243 °C to 650 °C	-18 °C to 590 °C	300 °C to 1090 °C	-185 °C to 370 °C
Seebeck Coefficient [77]	58.5 μV/K at 0 °C	50.2 μV/K at 0 °C	39.4 μV/K at 0 °C	38.0 μV/K at 0 °C
Other Considerations	Non-magnetic; Annealed wire recommended	Magnetic	Magnetic; Curie point at 152.5 °C	Non-magnetic; High thermal conductivity

*Upper temperature limit may also depend on wire gauge.

Type E thermocouples have the highest Seebeck coefficient, and therefore the highest sensitivity, of any base metal thermocouple. This makes Type E thermocouples advantageous when electrical noise is a concern due to the higher signal-to-noise ratio [78]. In addition, since the test section passes considerable current and generates magnetic fields of appreciable strength, as described in Chapter 2, magnetic interference was deemed to be a potential concern. The elements in Type E thermocouples are non-magnetic; therefore Type E thermocouples are affected less by magnetic fields than Type K thermocouples. Type E thermocouple elements have modest thermal conductivities when compared to the undesirably high thermal conductivity of the copper element in Type T thermocouples, making Type E advantageous over Type T thermocouples in reducing heat conduction to the thermo-element. Inhomogeneity voltages are

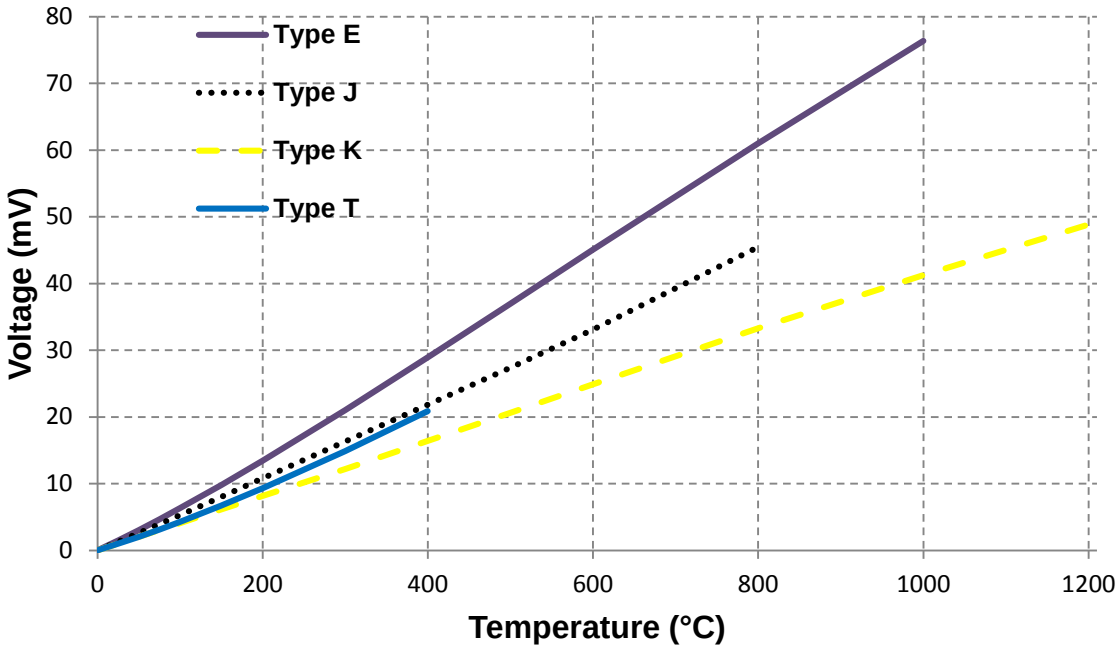

Figure 57: Temperature Sensitivity of Base Metal Thermocouples. Reference junction at 0 °C.

an issue with any thermocouple type, but can be kept especially low in Type E thermocouples with proper sourcing of materials. A publication by NIST states, "Thus, when its properties are compared with other thermocouples, the Type E thermocouple is the most suitable for general use from 20 or 30 K to 450 °C…" [75]. Therefore, Type E thermocouples were chosen for measuring the temperature on the backside of the heater plate.

Stainless steel sheathed thermocouples are employed to improve resistance to oxidation and isolate the thermo-elements from the environment. The sheathed elements are insulated with magnesium oxide. Considering that transient temperature response was not a priority, ungrounded thermocouples were selected to eliminate the possibility of leakage currents, which could affect the temperature measurement and also present a safety hazard. The specifications for the thermocouples used on the test section are listed in Table 23. Thermocouples were affixed to the back of the heater plate using a high thermal conductivity, electrically insulating epoxy to minimize thermal contact resistance and eliminate current leakage through the sheath. After allowing the epoxy to dry, measurement of electrical resistance between the thermocouple sheaths and the heater plate with a multimeter confirmed that a thin layer of epoxy isolated the sheath electrically from the plate. Custom-fabricated PTFE compression fittings seal the

pressure boundary and act as an additional safety measure to prevent shorting of the heater plate to the test section body.

Table 23: Specifications of the Thermocouples Used for Heater Plate Temperature Measurement.

Parameter	
Model	OMEGA Engineering TJC12-CXSS-062U
Specifications Met	ANSI MC 96.1, Special Limits of Error Wire
Type	E
Sheath Material	304 stainless steel
Sheath Diameter	1.57 mm (0.062")
Insulator	Magnesium oxide
Junction Type	Ungrounded
Output	mV signal
Manufacturer's Stated Accuracy	<±1.0 °C or 0.4% (0 °C to 900 °C)

3.3.4. Dissolved Oxygen Meter

Dissolved non-condensable gas content of liquids is known to have an effect on boiling [79], affecting incipience, the boiling heat transfer coefficient, and even CHF. While this study does not intend to characterize the effect in detail, it is desirable to maintain a consistent dissolved gas content across all tests. Therefore, measurement of the dissolved gas content was desired in the experimental apparatus. Total dissolved gas meters measure use a gas permeable membrane and pressure sensor to measure the partial pressures of non-condensable gases in a system. The dissolved concentration of each species may be determined from Henry's law:

$$P_i = k_{H,i} c_i \tag{35}$$

where P_i is the partial pressure, $k_{H,i}$ is Henry's constant, and c_i is the concentration of the i^{th} dissolved gas. The partial pressure of each species is related to the total pressure by Dalton's law:

$$P_{total} = \sum_{i=1}^{N} P_i \tag{36}$$

However, total dissolved gas meters were determined to be too costly for the application, so a dissolved oxygen meter was used instead. In a study by McAdams [80], he made the assumption that the ratio of dissolved nitrogen to dissolved oxygen was constant and the same as that in water saturated with air, which is reasonable since the Henry constant should not change with concentration. In this study, similar treatment is used, with the dissolved oxygen content used as a metric for the relative amount of total dissolved gases.

A Eutech Alpha DO 500 2-wire dissolved oxygen transmitter and dissolved oxygen probe with integral temperature sensor were installed in the flow loop to measure dissolved oxygen content. The measurement relies on a galvanic cell inside the probe, with a zinc anode and silver cathode immersed in a sodium chloride electrolyte to produce a voltage capable of reducing oxygen. A PTFE membrane, permeable to oxygen, separates the galvanic cell and electrolyte from the measurement medium. Oxygen is reduced at the cathode, generating a current which is proportional to the concentration of oxygen in the cell. A two-wire platinum resistance temperature detector measures the temperature in the cell to correct for changes in the permeability of the membrane with temperature.

A separate loop in which water flow could be bypassed was constructed to accommodate the dissolved oxygen probe. This allowed for better control of temperature and flow rate over the probe, and allowed isolation of the probe during normal operation. The specifications for the dissolved oxygen meter are listed in Table 24, with a photo of the meter in Figure 58.

Figure 58: Photograph of the DO Meter Installed in the Facility.

Table 24: Specifications of the Dissolved Oxygen Meter.

Parameter	
Model	Eutech DO 500
Maximum Pressure	7.5 bar
Range	0.0 mg/L to 19.99 mg/L
Temperature Compensation	0 °C to 50 °C
Resolution	0.01 mg/L
Output	4-20 mA current signal
Manufacturer's Stated Accuracy	±1.5% full scale

3.3.5. Test Section Voltage and Current Measurement

The voltage and current across the test section are measured to determine the electric power delivered to the heater. Two taps were spot welded on each electrode to measure the voltage across the heater plate. The taps were located as close to the heater plate as possible to minimize the effect of conductor losses.

The high currents associated with the heater plate made current measurement with a shunt resistor impractical. Instead, other measurement techniques allowing for complete galvanic isolation from the primary circuit were considered. Current sensing using the Hall effect allows for non-contact measurement of AC or DC current for high power applications with good accuracy. A schematic of the principle of operation is shown in Figure 59 for open-loop Hall effect current transducer technology. In an open-loop Hall effect transducer, a magnetic circuit surrounding the busbar concentrates the magnetic field. A semiconductor Hall sensor measures the field in the air gap of the magnetic circuit, outputting a voltage called the Hall voltage:

$$V_H \propto \vec{I_s} \times \vec{B} \tag{37}$$

where I_s is the current applied to the Hall sensor. The primary current, I_p, is related to the magnetic field by Ampère's Law in equation (18).

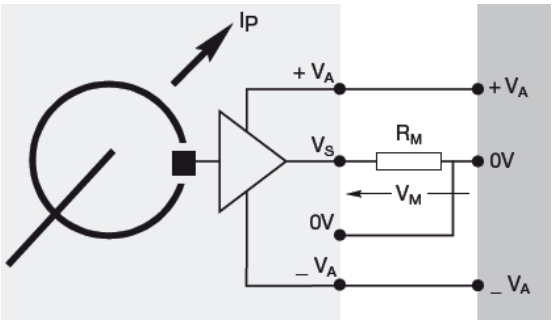

Figure 59: Principle of Operation of an Open-Loop Hall Effect Current Transducer.
Source: Ref. [81].

The Hall voltage is conditioned and amplified to yield a voltage output which is directly proportional to the primary current being measured. For this study, an LEM HAZ 6000-SB

current transducer using open-loop Hall effect technology was installed on the positive busbar. The specifications for the current transducer are listed in Table 25, and a photograph of the transducer installed in the experimental apparatus is provided in Figure 60.

Table 25: Specifications for the Current Transducer.

Parameter	
Model	LEM HAZ 6000-SB
Primary Current Measurement Range	±6000 A
Ambient Operating Temperature	-25 °C to 50 °C
Output	0 VDC to ±10 VDC
Manufacturer's Stated Accuracy	<±1%

Figure 60: Photograph of the Current Transducer Installed on the Positive Busbar.

3.3.6. High Speed Video Camera and Lighting System

A Phantom v12.1 high speed camera enables acquisition of bubble formation and departure from the heater surface. A Nikon AF Micro-NIKKOR 200mm lens with extension rings was attached to the camera to provide high magnification with a minimum focal distance. The maximum achievable spatial resolution of the setup approaches ~20 μm/pixel when using the entire 1280×800 CMOS sensor of the camera. A length scale on the viewing window of the test section allows in situ calibration of the setup, thereby enabling approximation of bubble diameter from high speed images.

While the Phantom v12.1 is capable of recording video up to 680,000 frames per second at the minimum pixel resolution, in actuality the maximum frame rate is limited by lighting. Ideally, the subject being recorded, a bubble or bubbles, would be backlit to enhance the brightness and contrast, thereby allowing for very high frame rates. In this experiment, the lighting presents a considerable challenge since the single window on the front side of the test section precludes the use of backlighting. Therefore, the captured image relies on light reflected off the subject and the surface behind the subject, inherently limiting the maximum achievable frame rate.

Selection of appropriate lighting systems was critical for visualization of the heater surface. Fluorescent lighting was immediately ruled out due to the expected presence of flicker, typically at 100/120 Hz, or twice the supply frequency. While this frequency of flicker is indistinguishable to the average human eye, it would be readily apparent with the high speed video system. Halogen lamps are usually flicker free regardless of power source due to the thermal inertia of the filament, but high operating temperatures require frequent bulb replacement and present a burn hazard if the lamps must be handled during operation. Light-emitting diode (LED) lamps offer long lamp life and reduced burn hazard due to lower operating temperatures. However, flicker may be present depending on the quality of the LED lamp and the power supply. Low quality LED lamps were tested and displayed appreciable flicker in proof-of-concept testing of the high speed camera. Flicker in LED lamps can be caused by poor rectification of the AC input or, in dimmable lights, the use of pulse-width modulation to achieve the dimming effect. Two Lowel Blender lighting systems were acquired and tested for flicker. No flicker was observed in high speed camera video captured up through 5000 fps (this was the maximum capture rate tested). The lighting systems proved effective and were employed in all

subsequent tests using the HSV camera. Specifications for the HSV camera and lighting setup are listed in Table 26. Figure 61 shows the camera and lighting systems in operation.

Table 26: Specifications of the High Speed Video Camera and Lighting System.

Parameter	
HSV Camera	Phantom v12.1
Lighting System	Lowel Blender LED Lamps (2)
Lens	Nikon AF Micro-NIKKOR 200mm
Maximum Surface Illuminance	13,400 lumens/m^2 at 0.5 m from lamps
Maximum Resolution	1280x800 pixels
Maximum Frame Rate in Setup	~5000 fps
Maximum Spatial Resolution	20 μm/pixel
FOV at Maximum Resolution	25.6 mm x 16.0 mm

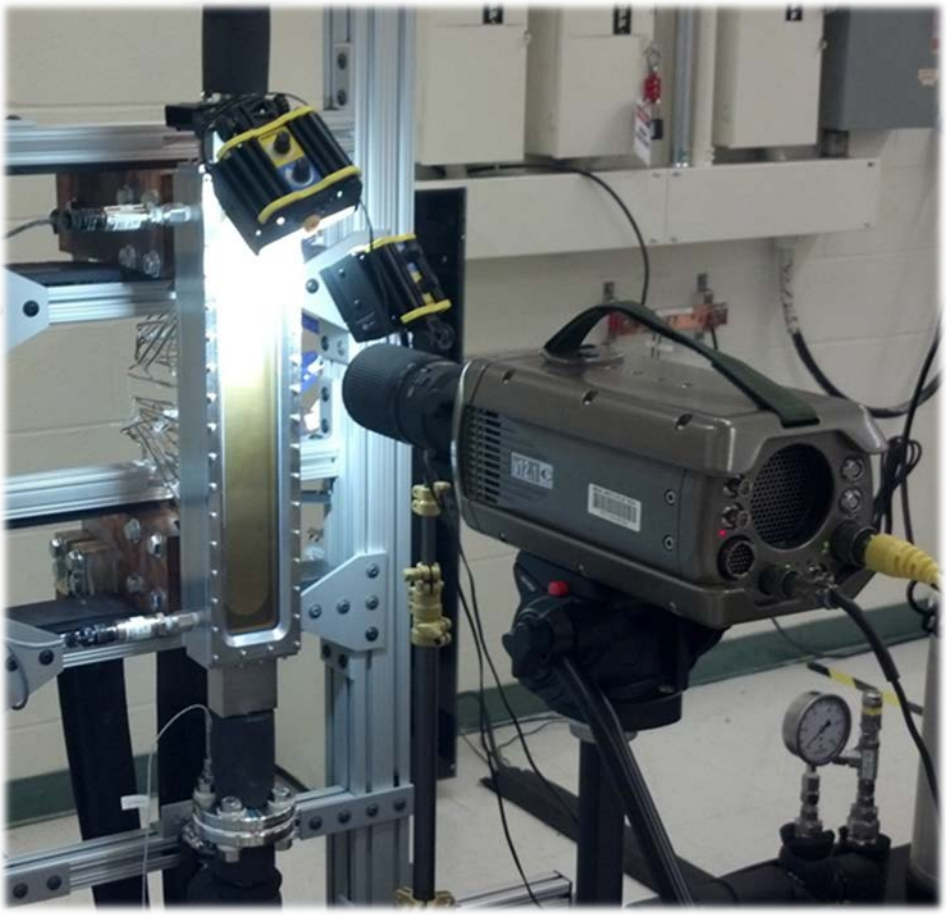

Figure 61: View of the Test Section, with the High Speed Video Camera and LED Lighting System.

3.4. Data Acquisition and Control Systems

Operation of the flow loop and test section requires monitoring and measurement of over 40 separate channels. An Agilent Technologies 34980A Multifunction Switch/Measure Unit serves as the main data acquisition and control system. Several additional modules were installed on the system to enable measurement and control of all desired parameters. A 34921A 40-Channel Armature Multiplexer allows for 40 voltage measurements, 4 current measurements, and has a built in thermocouple reference junction configured for common thermocouple types, eliminating the need for an external reference. A 34938A 20-Channel 5A Switch enables mechanical switching functions to control output of the power supply and pump controller. Lastly, a 34952A Multifunction Module provides 0-10V DC signals to control the variable speed controller output and the power supply output.

An electrical box was constructed to safely and securely house major wire junctions, DC power supplies for instrumentation, and control relays for the 75 kW DC power supply and pump controller. The exterior of the control box and data acquisition system are shown in Figure 62, and the interior of the control box is shown in Figure 63. A green LED was installed on the front of the electrical control box to indicate when the system is energized. An emergency shut-down button is located on the front of the control box, which enables immediate shutdown of the pump and 75 kW DC power supply, placing the power supply in an interlock state and de-energizing the experiment. Electrical control diagrams for the 75 kW DC power supply and pump controller are provided in Figure 64. Electronics for the chilled water solenoid valve are also located in the electrical control box.

Good wiring practices were employed to help reduce the possibility of ground loop currents, a common source of electrical noise and measurement error. Thermocouples were electrically isolated from all other instrumentation and power sources. Instruments requiring a reference ground share a common ground with the loop piping, which is connected at one point only (see Figure 65). Insulated grounding wire of appropriate gauge was used to ensure the voltage drop from instrument connections to the actual ground reference is essentially zero. Figure 66 shows the wiring diagram for all instrumentation in the flow loop and test section.

Figure 62: Data Acquisition System and Electrical Control Box.

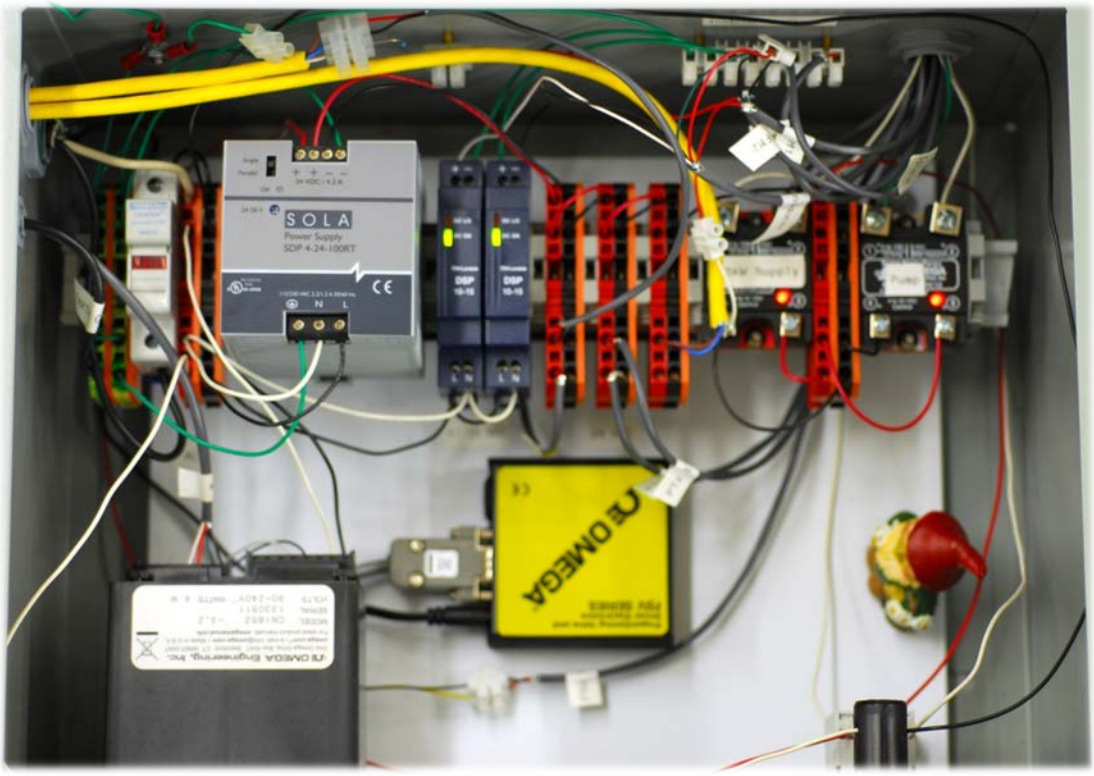

Figure 63: Interior of the Electrical Control Box Showing DC Power Supplies for Instrumentation and Relays for Switching.

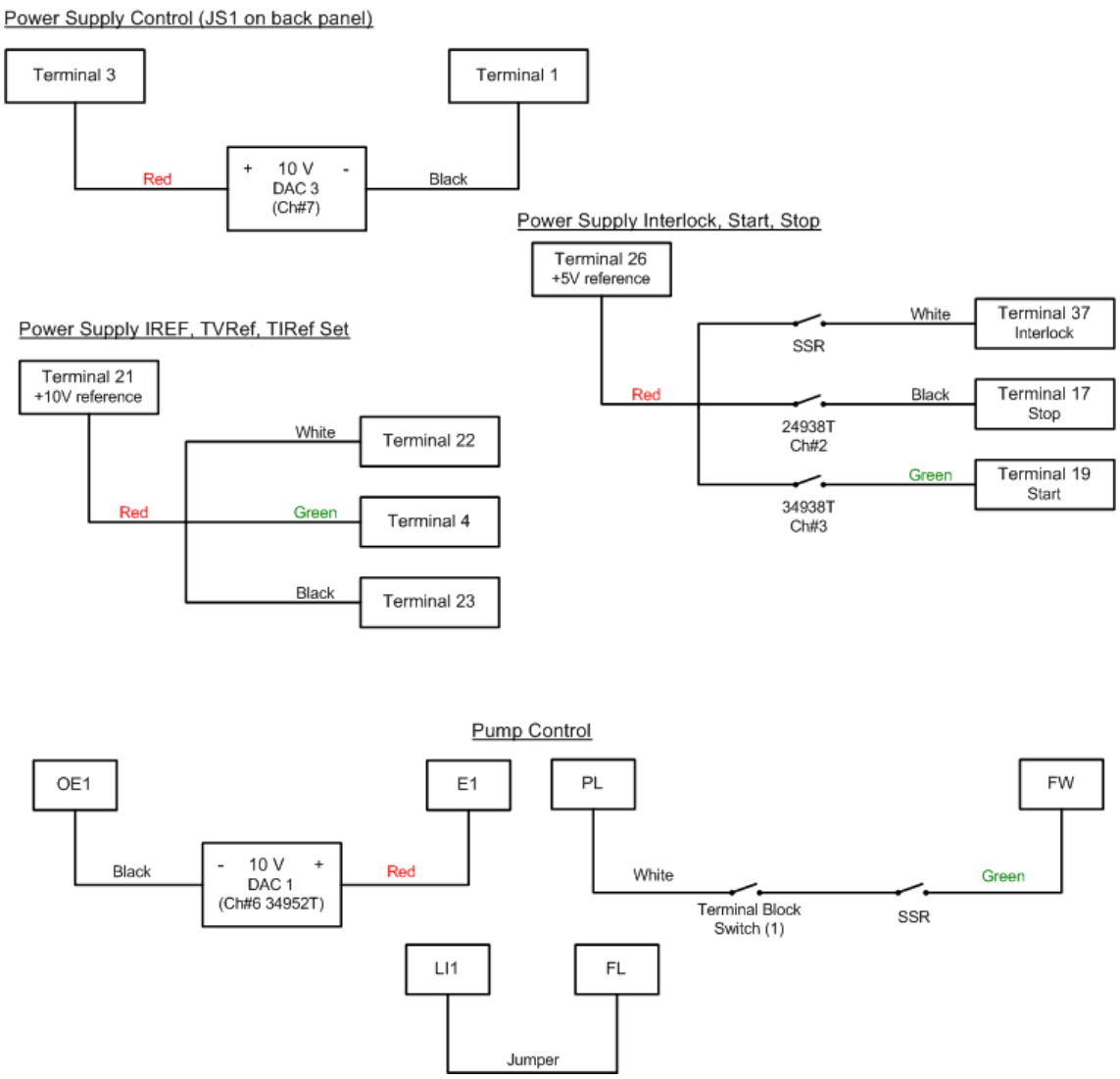

Figure 64: Detailed Wiring for 75 kW DC Power Supply and Pump Control.

Figure 65: Electrical Ground for Loop and Instrumentation Requiring a Voltage Reference.

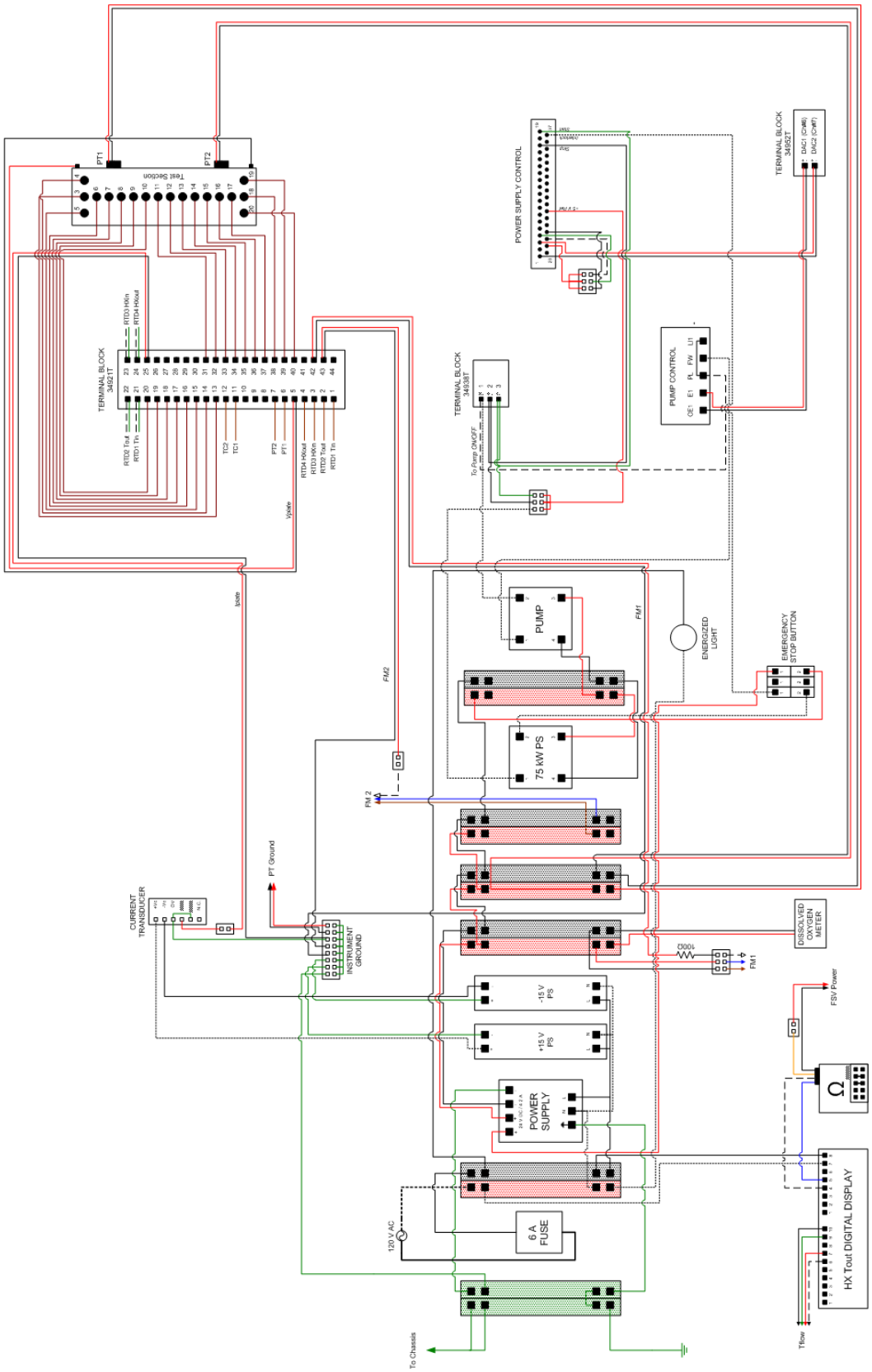

Figure 66: Electrical Diagram for Two-Phase Flow Loop Showing Wiring for Instrumentation.

3.5. LabVIEW Interface

The interface to monitor and control the two-phase flow facility was programmed using National Instruments LabVIEW 11.0. Pre-programmed "virtual instruments," or VI's, enabled communication with the Agilent data acquisition system via a USB connection. LabVIEW VI's were available from Agilent for thermocouples, RTD's, voltage and current measurement, and switching functions. Use of these pre-programmed VI's simplified programming requirements.

The graphical user interface is designed to be clear and intuitive, with important parameters such as mass flux and test section temperature displayed graphically. The interface provides for remote operation of the power supply and pump. The program also writes all measured parameters to a text file for post-processing. Integrated safety features include a minimum mass flux and maximum temperature set point, which automatically turn off the 75 kW DC power supply if these set points are passed. For example, if the pump trips and the measured flow rate drops below the set point, power to the test section will be cut off to prevent overheating and burnout of the test section from loss of flow. Similarly, if the backside of the heater plate exceeds the pre-set temperature limit due to occurrence of CHF, power will be cut off, stopping or at least limiting damage to the heater plate and test section. The front panel of the LabVIEW program for the two-phase flow facility is shown in Figure 67.

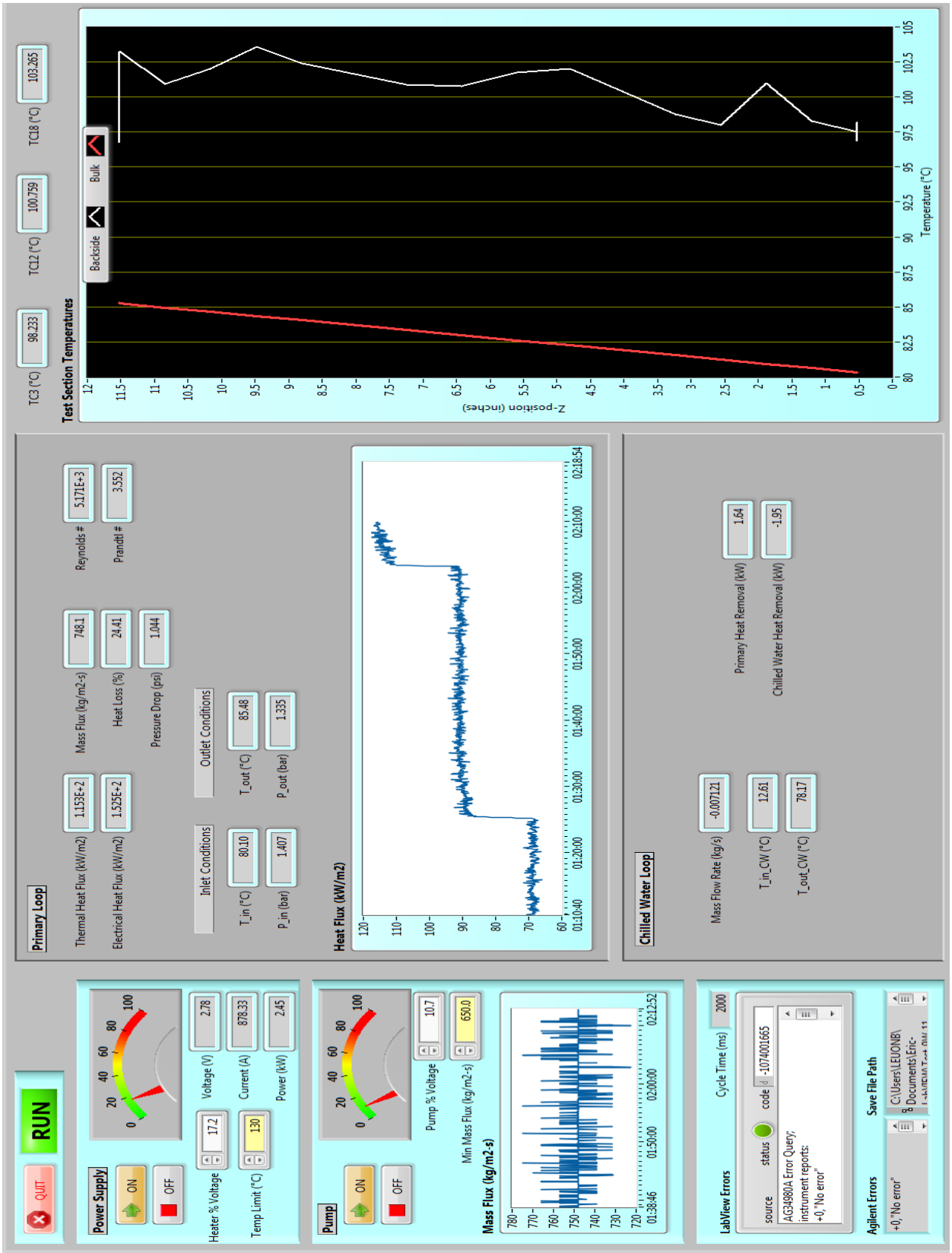

Figure 67: Front Panel of the LabVIEW Interface.

3.6. Equipment Calibration and Uncertainty Analysis

3.6.1. Method of Uncertainty Analysis

Experimental measurements and observations carry some associated uncertainty. Proper accounting and reporting of this uncertainty is crucial to any study; firm conclusions cannot be drawn from data without knowledge of the associated uncertainty. Uncertainty quantification and how it affects analysis of experimental data is an extensive field, with wide-ranging applications to every subject area in science and engineering. A concise summary of important concepts and relevant terminology is discussed here. For a detailed treatment of the topic, please see reference [82].

A measured value, such as voltage, temperature, length, etc. may be treated as a random variable with an associated uncertainty, $x \pm \varepsilon$. The uncertainty in each random variable may be broken into two components, the random component and the systematic component. The random component of uncertainty (also referred to as the random error or repeatability) arises from stochastic fluctuations in the measurement. These fluctuations may be a result of the measurement process itself (e.g. random electronic signal fluctuations due to noise) or a result of some inherent and uncontrollable random component of the quantity or phenomenon being measured. For instance, determination of the activity from a radioactive sample by count rate may have a random uncertainty component from electrical noise in the detector and also from the inherent probabilistic nature of the decay process.

The systematic component of uncertainty (also referred to as systematic error or bias) refers to an uncertainty that is fixed for a given set of conditions, i.e. it does not fluctuate randomly, even with repeated measurements. In an ideal experiment, the systematic component of uncertainty will be zero. The systematic uncertainty is a result of an imperfect experimental setup or non-ideal measurement conditions. Identifying sources of systematic uncertainty in an experiment is challenging, but once identified, the bias can either be eliminated or corrected for by applying a fixed correction to the measured value. Ideally, all possible sources of systematic uncertainty would be identified during the design phase of an experimental setup. In reality, some sources are not identified until operating an experiment, and others are never identified.

“Accuracy” and “precision” are two terms related to uncertainty of a measurement. Precision refers to the repeatability of a measurement, i.e. a precise measurement will have a

small random uncertainty component. Accuracy may refer to either the total uncertainty or only the bias in the measurement. When accuracy is used to refer to the total uncertainty, "trueness" may be used to refer to the bias in measurement. In the case of equipment manufacturer's stated accuracies in section 3.3, the term "accuracy" is taken to encompass the total uncertainty for the measured parameter. Repeatability refers to the random uncertainty of the instrument. The term "error" is often used interchangeably with "uncertainty", though in some contexts they are not equivalent.

Typically, more than one measurement is made of a single parameter in order to obtain a best estimate of that parameter. For N nominally identical measurements of x, the mean value is commonly used as the best estimate:

$$\bar{x} = \frac{1}{N}\sum_{i=1}^{N} x_i \tag{38}$$

$x_i - \bar{x}$ is representative of the random error associated with a single measurement, x_i. The difference between the mean value and the expected value (also called the true value, X) is representative of the systematic error, or bias. The total error for a single measured value, x_i, is simply the difference between the expected value and the measured value, $x_i - X$.

For most nominally identical, random measurements, the variation about the mean value can be correctly described by the normal, or Gaussian, distribution. This occurrence is in part explained by the Central Limit Theorem, since the uncertainty of the measured parameter is likely composed of many smaller, randomly distributed uncertainties. Note that for small sample sizes, the t-distribution is often more appropriate. In this study, the uncertainties of all measured parameters and observations are treated as normally distributed, unless otherwise noted. It is useful to use the standard deviation for a sample of nominally identical measurements to describe the variability of individual measurements in the sample:

$$\sigma_x = \left[\frac{\sum_{i=1}^{N}(x_i - \bar{x})^2}{N-1}\right]^{1/2} \tag{39}$$

The standard deviation is useful in characterizing the random component of the uncertainty of a single measurement, x_i. The standard error of the mean value is used to describe the expected deviation of a mean value of a set of measurements from the true value, and is defined as:

$$\sigma_{\bar{x}} = \frac{\sigma_x}{N^{1/2}} \tag{40}$$

The best method for expressing the total uncertainty of a measured parameter is somewhat debatable, as acceptable confidence limits and the appropriate means of combining random and systematic uncertainties are not well defined. The American Society of Mechanical Engineers (ASME) was the first to develop standards for uncertainty reporting in the 1950's. An ISO standard was introduced in 1995 [83] that replaces the "random error" and "systematic error" terminology with "Type A" and "Type B" uncertainties. This terminology is not employed in this study, though. Rather, the treatment of uncertainties in this study more closely reflects the policy introduced by the ASME and American National Standards Institute (ANSI) in 1985 [84, 85]. Specifically, the random uncertainty, $\pm\varepsilon_{ran}$, is taken to represent the experimentalist's 95% confidence range, or $\pm 1.96\sigma$. The ASME policy states the same for the systematic uncertainty, though one should note that defining confidence limits for bias is less straightforward than for random error, as systematic uncertainty is usually harder to classify statistically. The total uncertainty is the combination of the random component and systematic component summed in quadrature:

$$\varepsilon = \sqrt{\varepsilon_{sys}^2 + \varepsilon_{ran}^2} \tag{41}$$

It should be noted that the relation in equation (41) is a reasonable approximation but not rigorously justified [86].

At this point it is important to make the distinction between directly measured parameters and calculated parameters. In this study, many parameters are calculated from more fundamental measured quantities. In fact, the case can be made that the majority of parameters are derived from a voltage or current output. Thermocouple temperatures, for instance, are actually derived from a voltage measurement. Therefore, accurate and complete reporting of necessary

parameters requires that parameters are calculated correctly from measured quantities, and that the associated uncertainty from measured quantities is propagated in an appropriate manner. In this study, the uncertainty propagation formula introduced by Kline and McClintock [87] is used, as recommended by the ASME [84]. If some calculated quantity, $\boldsymbol{f}$, is a function of one or more independent measured variables, $x, \ldots, z$ (i.e., $\boldsymbol{f}=\boldsymbol{f}(x,\ldots, z)$), and each measured variable has an associated uncertainty ε, then the uncertainty of the calculated quantity may be expressed as:

$$\varepsilon_{\boldsymbol{f}} = \sqrt{\left(\frac{\partial \boldsymbol{f}}{\partial x}\right)^2 \varepsilon_x^2 + \cdots + \left(\frac{\partial \boldsymbol{f}}{\partial z}\right)^2 \varepsilon_z^2} \tag{42}$$

Note that since equation (42) is derived using Taylor expansions, ε is assumed to be small compared to each measured quantity. In addition, all of the measured variables that make up the function f are considered independent of one another. If the uncertainties of the variables are not independent, i.e. they are correlated, then the covariance term should be accounted for in the uncertainty, which may serve to increase or decrease the overall uncertainty in the calculated parameter. While Monte Carlo methods for uncertainty propagation are very useful in cases of complicated uncertainties where correlation of variables is not clear, standards of implementation are not as well-developed as those using the Kline-McClintock formula and the measurements in this study do not require their use.

In some situations, it may be more appropriate to quantify the uncertainty of an observed parameter from the statistical dispersion of a set of nominally identical observations, rather than using the total propagated uncertainty from fundamental measurements. Typically in these cases, the spread of nominally identical measurements far exceeds the predicted measurement uncertainty. For the purpose of this study, this type of uncertainty will be termed as the "stochastic uncertainty." Take, as an example, the measured critical heat flux from a wire during pool boiling. The heat flux and associated uncertainty may be calculated from the voltage, current, and diameter of the wire, which may yield an uncertainty in the heat flux of ±2% or so. However, the actual variation in CHF might be 20% or more. This seemingly inconsistent result may be attributed to the dependence of CHF on other variables which cannot be precisely controlled by the experimentalist. Local, and statistically random, variations in fluid flow and surface features can have a very strong effect on CHF. Therefore, reporting the stochastic

uncertainty is most appropriate because departure from nucleate boiling is a local phenomenon [88, 89]. Bubble departure diameter during flow boiling is another good example, as it depends on local surface and local flow conditions, which are typically beyond the control of the experimentalist. While the spatial resolution of the high speed video setup may be as low as 20 μm, the sample spread in measured bubble departure diameters for a set of nominally identical conditions could be an order of magnitude higher. Therefore, a stochastic uncertainty is more appropriate in quantifying the uncertainty of the measured bubble departure diameter.

Vendors and manufacturer's supply equipment with some guarantee of accuracy, which is listed in section 3.3 for the instrumentation used in this study. Ideally, the equipment will have a NIST-traceable calibration, with documentation certifying such. However, NIST-traceable calibrations are not always available, and usually come at an added cost. There is little reason to question stated accuracies from reputable vendors, but equipment calibration by the end user can remove doubts about accuracy when using older equipment or equipment that has been procured from secondary sources. In addition, calibration by the end user may be desired to reduce the overall uncertainty. Equipment manufacturers typically report a bounding uncertainty that may represent a total error band of more than 2σ. Also, equipment and instrumentation are usually designed to be plug and play and capable of operation in a wide range of applications and setups under varying conditions. Stated accuracies normally reflect expected accuracy under all possible conditions for which the instrument was designed. Therefore, calibration of the instrument in the intended setup by the end user can substantially improve the overall accuracy, and reduce final uncertainties in reported data. For this reason, thermocouples, RTD's, and the flow meters used in this study were calibrated by the author in their intended setup. These instruments together are responsible for the greatest uncertainties in calculated parameters, and reduction in their measurement error significantly improves the accuracy of the single-phase heat transfer coefficient, measured ONB heat flux, and measured ONB saturation superheat in this study.

3.6.2. Thermocouple and RTD Calibration

Thermocouples and RTD's were calibrated using the same data acquisition system that would be utilized in the flow facility. A three point calibration was conducted for all thermocouples and RTD's to minimize uncertainty in the associated temperature measurement.

The three temperature reference points were chosen to encompass the expected range of temperatures that the thermocouples and RTD's in the primary loop would encounter during testing. Specifically, the lower limit for both the RTD's and thermocouples was expected to be around 20 ºC, while the upper limit for the RTD's and thermocouples was expected to be 100 ºC and 180 ºC, respectively. While use of calibration points from the International Temperature Scale of 1990 [90] would have been ideal, it was not practical to replicate the defining points in the necessary temperature range (triple point of water, 0.01 °C, melting point of gallium, 29.76 °C, freezing point of indium, 156.60 °C, etc.). Instead, a deionized water ice bath at atmospheric pressure, boiling deionized water at atmospheric pressure, and boiling propylene glycol at atmospheric pressure were used as calibration points. The ice bath consisted of pure, finely crushed ice in equilibrium with deionized water. Ice baths are often used to approximate

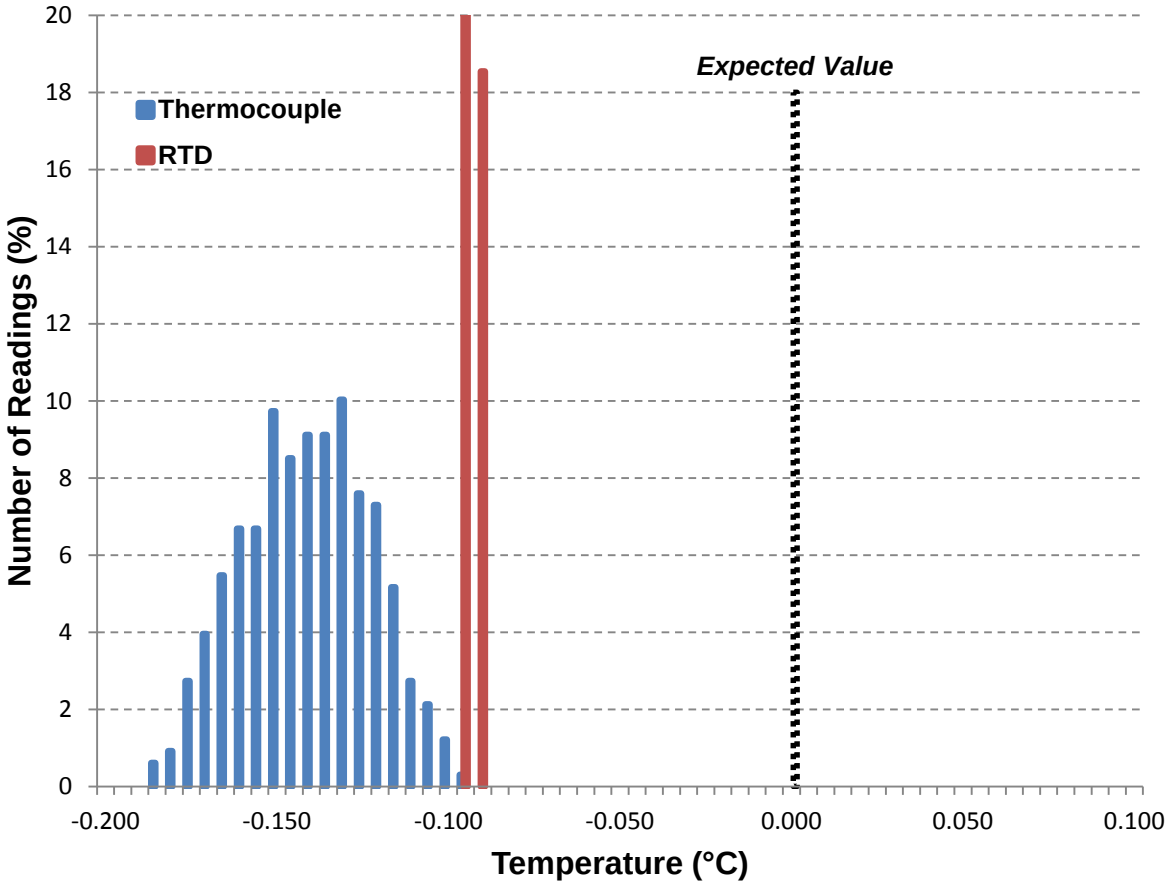

Figure 68: Histogram Showing Typical Thermocouple and RTD Response for Ice Bath Using Deionized Water. There is very little spread in the RTD measurements, despite the large number of measurements taken.

the triple point of water and are quite common for external thermocouple reference junctions, with an expected temperature of 0.0001 °C at atmospheric pressure. The ice bath temperature variation with local pressure is negligible for the purposes of this study, making it an excellent lower calibration point. Results for a thermocouple and RTD measuring the temperature of the ice bath are shown in Figure 68. Similar measurements were obtained for all the thermocouples installed in the test section and RTD's installed in the flow facility, with the results shown in Figure 68 being typical.

Measurements were also performed for the boiling of deionized water in an open beaker. The expected boiling point is based off the local pressure at the time of measurement, which varies slightly with elevation and atmospheric conditions. Typical results for an RTD and thermocouple are provided in Figure 69. Similar results were obtained with all other thermocouples and RTD's for the boiling of deionized water, with good agreement between measured and expected values.

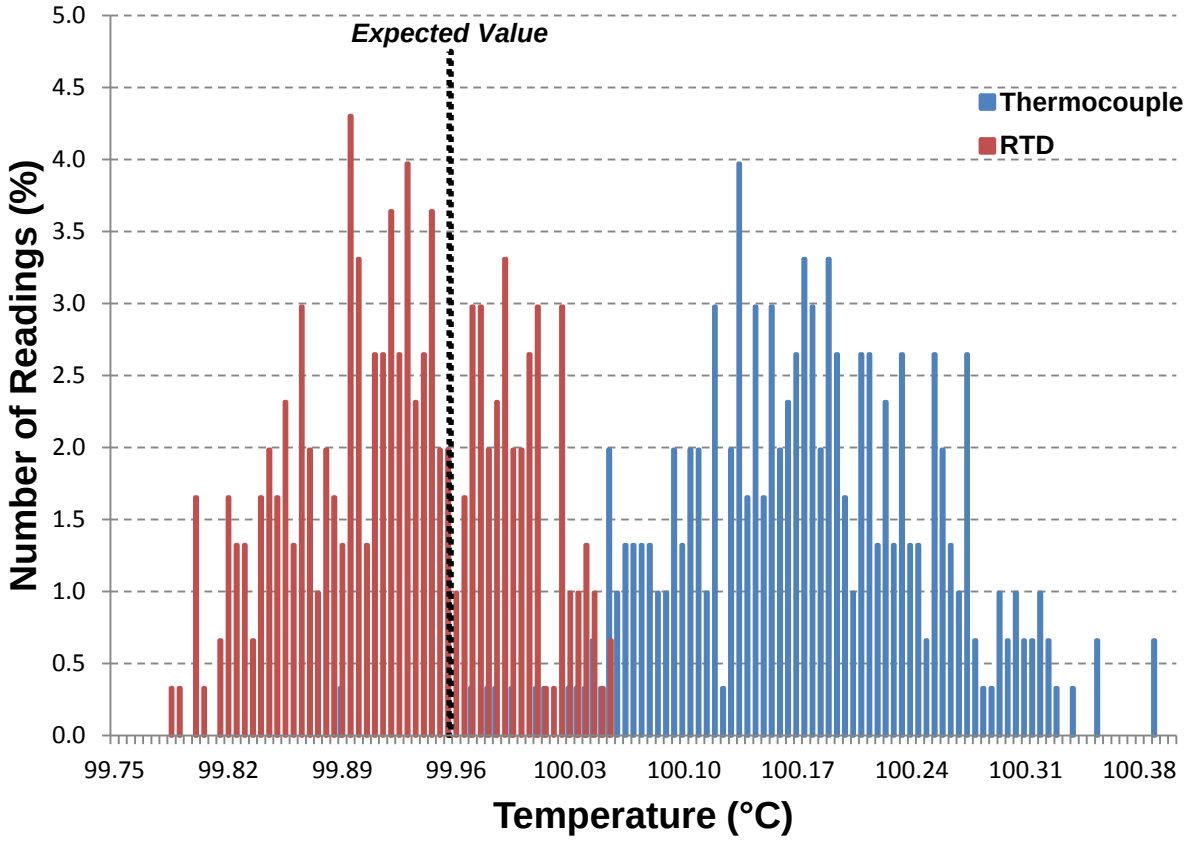

Figure 69: Histogram Showing Typical Thermocouple and RTD Response in Boiling Deionized Water.

The boiling point of propylene glycol has an expected value at atmospheric pressure of 188.2 °C, making it a relevant upper reference point for thermocouple measurements. However, the boiling point of propylene glycol was considered as a less reliable reference point, due to variation that can result from trace levels of impurities. Nonetheless, agreement was very good, with deviation between measured values and the expected value being about 0.3 °C or less.

While identification of the thermocouple and RTD bias from reference measurements hypothetically allows for corrections to the measured temperatures, three points were not considered adequate for re-fitting the response curves over the range of interest. However, the response of both the thermocouples and RTD's is expected to be monotonic with temperature over the range of interest. Therefore, the measurement uncertainties determined at the reference points are used as bounding values for the measurement uncertainty, with the total uncertainty calculated as shown in equation (41). The measurement uncertainty for each thermocouple and RTD was calculated, with the eventual installation location of each probe being tracked. This would allow for the individual assignment of measurement uncertainty to each probe, though for simplicity, the uncertainty that was associated with the least accurate thermocouple and the least accurate RTD was used. The maximum total uncertainties associated with RTD and thermocouple measurements were 0.297 °C and 0.156 °C, respectively.

Another important temperature parameter is the differential temperature measured between the inlet and outlet RTD. The differential temperature is used to determine the thermal power; i.e. the actual power transferred from the heater plate to the fluid. While the associated measurement uncertainty of each RTD could be used and the differential error calculated with equation (42), this would tend to over predict the uncertainty associated with this quantity. If RTD's are from the same lot, bias will tend to occur in the same direction away from the expected value, and differential error will be small. Therefore, the differential error between the inlet and outlet RTD for the aforementioned reference points was also recorded, resulting in a differential error of about 0.05 °C or less. As an additional check, agreement between the test section inlet and outlet RTD's was checked at the beginning of each flow test while the fluid was at ambient conditions and low flow. Observed differences were usually 0.02 °C or less.

At this point, it is important to note that while the uncertainty in temperature measurements was carefully accounted for, uncertainties associated with fluid properties other than the enthalpy were not considered. Fluid properties depend on temperature and pressure, and

therefore can have three sources of uncertainty: the temperature uncertainty, the pressure uncertainty, and the uncertainty associated with the original fluid property measurement. While the third source of error may be significant for poorly studied fluids or water at unusual conditions (e.g. around the critical point), property values of water at the temperatures and pressures of this study have been recorded with incredibly high accuracy. This study relies on the water and steam properties as formulated in IAPWS-IF97 [91]. For the conditions explored in this study, the property values from IAPWS-IF97 are essentially identical to those of IAPWS-95, with no discernable difference between values for the decimal precision used in calculations here. The variation of single-phase properties with pressure uncertainty is negligible for the conditions in this study. With the exception of the fluid enthalpy, it was assumed that some property evaluated at T had the same value at $T+\varepsilon_T$, which is a reasonable approximation, even for the viscosity. For the measured fluid temperature uncertainty in this study, the maximum expected variation in viscosity due to the temperature measurement uncertainty is 0.1% or less.

3.6.3. Flow Meter Calibration

While the flow meters which were procured for the primary loop and chilled water circuit had very good stated repeatability (low random uncertainty), as discussed in section 3.3.1, the manufacturer's stated accuracy (total uncertainty) was rather high. Therefore, calibration of the flow meters was considered as paramount in reducing the total uncertainty associated with flow measurements and, in turn, the thermal power measurement. The flow meters were calibrated using a steady state volumetric liquid flow measurement method. In these calibration tests, the flow meters were configured in their ultimate piping configuration with the same upstream and downstream straight pipe lengths. Flow was initiated, and once steady state was reached the flow was discharged into a calibrated container with marked graduations. A stopwatch recorded the time it took to reach each graduation. Several calibration measurements were performed for each meter over the intended range of flow measurement. The graduated container was large enough to minimize the fractional volume uncertainty, and the output of the meter was shown to be steady while the graduated container was filled. Calibration results for each flow meter are shown in Figure 70 and Figure 71. Note that the error bars in the measured output current and calculated flow rate are so small as to be obscured by the data markers.

A linear response is expected from the vortex meters, as mentioned in section 3.3.1. A best fit to the data points was obtained using the method of least squares. The results are shown in Figure 70 and Figure 71. Calculating the uncertainty of the resulting fitted function is important in determining the total uncertainty of the eventual mass flow rate measurements. Accounting for the uncertainty of a general fitted function, $y(x)$, when both data points x_i and y_i have non-negligible uncertainties is quite complicated and not definitive. In the case of a linear fitted function of the form $y=mx+b$, where all uncertainties in x_i are of equal magnitude and all uncertainties in y_i are of equal magnitude, the following equation may be used to express the equivalent uncertainty of y_i [92]:

$$\varepsilon_{y_i,eq} = \sqrt{\varepsilon_{y_i}^2 + \left(m\varepsilon_{x_i}\right)^2} \tag{43}$$

If the uncertainties in x, or in y, are not all equal, then the equivalent error will be different for each point along the curve. The uncertainty in the slope and intercept of the linear calibration curve can then be determined by:

$$\varepsilon_m = \varepsilon_{y_i,eq}\sqrt{\frac{\sum_{i=1}^{N} x_i^2}{N\sum_{i=1}^{N} x_i^2 - (\sum_{i=1}^{N} x_i)^2}} \tag{44}$$

$$\varepsilon_b = \varepsilon_{y_i,eq}\sqrt{\frac{N}{N\sum_{i=1}^{N} x_i^2 - (\sum_{i=1}^{N} x_i)^2}} \tag{45}$$

where N is the number of calibration points from which the linear curve is fitted. The 95% confidence bands for the straight line are then defined by:

$$y(x) = (m \pm \varepsilon_m)x + (b \pm \varepsilon_b) \tag{46}$$

The total uncertainty for flow measurements is then determined by the deviation between the value calculated by the calibration curve and the bounding value(s) predicted by equation (46).

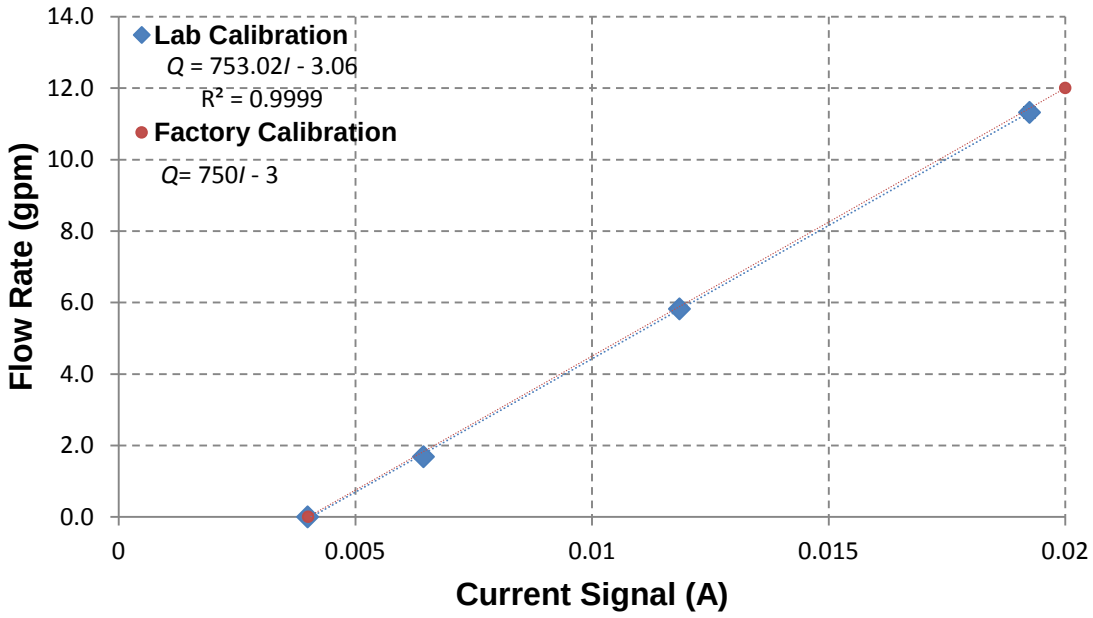

Figure 70: Four Point Calibration Curve for Primary Flow Meter. Note that the horizontal and vertical error bars are obscured by the data markers.

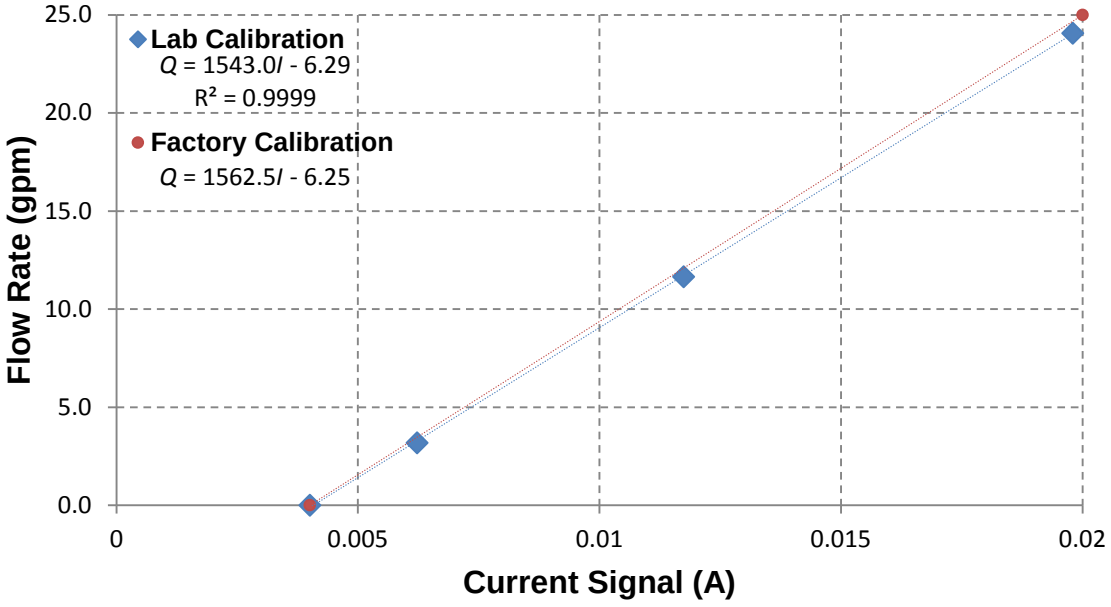

Figure 71: Four Point Calibration Curve for Chilled Water Flow Meter. Note that the horizontal and vertical error bars are obscured by the data markers.

3.6.4. Measurement Uncertainty of Other Equipment and Instrumentation

For all other equipment, the manufacturer's stated accuracy was used to determine the total measurement uncertainty, unless otherwise noted. For the current transducer, a small offset was corrected for with the no current condition used as a reference point. As an additional check, the output of the current transducer was compared to the digital ammeter on the power supply during operation, with agreement typically being within 10 A. The pressure transducers were ordered with a NIST-traceable calibration certificate, and the stated accuracy was used for all pressure measurements. The uncertainties of dimensional parameters are summarized in Table 27. Other fundamental uncertainties, estimated to the 95% confidence level, are summarized in Table 28. All other uncertainties that cannot be expressed in terms of a fixed value or fixed percentage for the measurement range are listed in Appendix B.

Table 27: Summary of Uncertainties for Dimensional Parameters.

PARAMETER	TOTAL UNCERTAINTY	NOTES
Gap Thickness, t_{gap}	$\pm 1.27\times10^{-5}$ m (±0.0005 inches)	From specified fabrication precision.
Heater Plate Thickness, t	$\pm 1.27\times10^{-5}$ m (±0.0005 inches)	From specified fabrication precision.
Flow Channel Width, w	$\pm 1.27\times10^{-4}$ m (±0.005 inches)	From specified fabrication precision.
Heated Width, w_H	$\pm 1.27\times10^{-4}$ m (±0.005 inches)	From specified fabrication precision.
Heated Length, L_h	$\pm 1.27\times10^{-4}$ m (±0.005 inches)	From specified fabrication precision.
Hydraulic Diameter, D_{hyd}	$\pm 2.54\times10^{-5}$ m	For $D_{hyd}=2\times t_{gap}$.
Wetted Perimeter, Pw	$\pm 2.55\times10^{-4}$ m	-
Flow Area, A_{flow}	$\pm 7.55\times10^{-7}$ m^2	-
Heated Surface Area, A_{surf}	$\pm 4.56\times10^{-5}$ m^2	-
Heater Plate Volume, V_{heat}	$\pm 2.15\times10^{-7}$ m^3	-

Table 28: Summary of Fundamental Measurement Uncertainties for the Thermal Hydraulic Facility and Test Section. Uncertainties represent 95% confidence bounds, unless otherwise noted.

PARAMETER	TOTAL UNCERTAINTY	NOTES
Primary Current, I_P	±1% FS = ±60 A	For current transducer. Excludes offset. Offset corrected for from zero current measurement.
Voltage Drop, V_E	±[0.005% of reading + 4×10^{-6}] V	Data acquisition system voltage channel.
Current Signal, I	5.5×10^{-5} A	Data acquisition system 4-20 mA channel.
Type E TC Temp., T_{back}	±0.297 °C	Total uncertainty of least accurate thermocouple on backside of heater plate.
RTD Temp., T_{in}, T_{out}	±0.156 °C	Total uncertainty of least accurate RTD used for inlet and outlet fluid temp. measurements.
Differential RTD Temp., ΔT	±0.052 °C	Maximum deviation + random uncertainty of inlet and outlet RTD.
Primary Mass Flow Rate, Q_p	ε_m = ±5.68 gpm/A ε_b = ±0.068 gpm	Uncertainty in slope and intercept of fitted calibration curve.
Chilled Water Mass Flow Rate, Q_{cw}	ε_m = ±11.80 gpm/A ε_b = ±0.143 gpm	Uncertainty in slope and intercept of fitted calibration curve.
Absolute Pressure, P	±0.25% FS = ±0.125 psia (±0.0086 bar)	Manufacturer's stated accuracy with NIST-traceable calibration. Includes linearity, repeatability, and hysteresis.
Differential Pressure, P	±0.25% FS = ±0.025 psia (±0.0017 bar)	Manufacturer's stated accuracy. Includes linearity, repeatability, and hysteresis.

3.6.5. Temperature Drop in Heater Plate

During the design phase of the experimental facility, it was well understood that use of the backside plate temperature measurement in place of the surface temperature would not be appropriate. Therefore, the temperature drop across the heater plate needed to be determined. What may not be readily obvious is that both the electric power and thermal power must be accounted for in such a problem, i.e. it is typically not safe to assume that the electrical power

generated is all transferred to the working fluid, with few exceptions. Exceptions include when a resistively heated element is entirely immersed in the working fluid, and heat transfer to the conductors is negligible, i.e. there are no other primary heat transfer paths. This can be determined from a simple Biot-type analysis. Additionally, if the voltage taps are not close to the heater, line losses may not be negligible, especially when high currents are involved.

In general, all heat transfer pathways should be accounted for, though they can usually be neglected if the product of the overall heat transfer coefficient and surface area are small, such that $\frac{(UA)_{prim}}{(UA)_{sec}} \gtrsim 100$. Despite the test section being covered in foam insulation during testing, it was found that approximately 5% to 10% of the electrical power was lost to the environment. Therefore, the heat flux to the working fluid (derived from the fluid enthalpy rise across the test section) was treated as a separate parameter and acts as a boundary condition. The temperature drop across the plate was calculated using the steady state heat equation in one dimension:

$$\frac{d}{dy}\left[k_{ss}\frac{dT}{dy}\right] + q'''_{elec} = 0 \tag{47}$$

where the variable y is taken to be the spatial coordinate into the heater plate, with the backside of the plate at y=0 and the working fluid surface at $y=t_{plate}$. While the temperature change across the plate will result in a small change in the stainless steel thermal conductivity with position, k_{ss} was instead calculated from the average plate temperature and treated as a constant with an associated uncertainty, so that the following equation could be used:

$$k_{ss}\frac{d^2T}{dy^2} + q'''_{elec} = 0 \tag{48}$$

The boundary conditions used to solve the equation are:

$$T|_{y=0} = T_{back} \tag{49}$$

$$-k_{ss}(dT/dy)|_{y=t_{plate}} = q''_{th} \tag{50}$$

where the first boundary condition is the Dirichlet-type, and the second is the Neumann-type. The solution to equation (48) with the above boundary conditions is:

$$T_w = T_{back} - q'''_{elec}\frac{t_{plate}^2}{2k_{ss}} + \frac{t_{plate}}{k_{ss}}\left(q'''_{elec}t_{plate} - q''_{th}\right) \tag{51}$$

Simulations from the COMSOL model discussed in section 2.6 verified that the one-dimensional assumption was accurate at all thermocouple locations, and that equation (51) is valid for calculating the temperature drop. The modeling in section 2.6 also verified the assumption that internal heat generation and the surface heat flux were essentially uniform.

3.6.6. Thermocouple Contact Resistance

During the design phase of the study, another potential source of bias was identified, though estimation of its magnitude was not straightforward. In order to keep the thermocouples electrically isolated, they were not metallurgically bonded to the back of the heater plate, thereby introducing the potential for non-negligible thermal contact resistance. Even if thermocouples are spot-welded to a surface, contact resistance may play a role, especially for high heat fluxes. Also, recall that the thermocouple junction is sheathed and ungrounded, so an additional, non-negligible thermal resistance may exist between the sheath tip and the actual junction. Thermal contact resistance depends on a number of factors, including local surface roughness and contact pressure. A thorough review of the topic, along with experimental measurements, can be found in reference [93]. Precise estimation is incredibly difficult, especially if contact pressure and local surface roughness are not known. Therefore, it typically must be measured for a specific configuration or setup.

While a thermally conductive epoxy was utilized to reduce the thermal contact resistance and ensure consistent contact, it was suspected that contact resistance was still resulting in a bias of at least a couple of degrees in temperature measurements. Therefore, a method was devised to measure the contact resistance of each thermocouple in the setup. All other factors being equal (mass flux, fluid temperature, etc.), the heat transfer coefficient should have no dependence on the heat flux, as long as the fluid remains in the liquid phase. However, a change in heat flux will change the measured temperature. By measuring the heat transfer coefficient at the same conditions while only varying the heat flux, one may solve for the thermal contact resistance of each thermocouple.

In practice, an increase in the heat flux will raise the film temperature, thereby affecting the local fluid properties near the wall, with the most notable being the viscosity. However, the wall viscosity effect on the heat transfer coefficient can be minimized by taking measurements at a temperature where the change in viscosity is smallest. A plot of the viscosity of liquid water with temperature at 1.01 bar is shown in Figure 72. The first derivative of viscosity with respect to temperature is also plotted. The effect of wall viscosity on the heat transfer coefficient, which is discussed in detail in Chapter 4, is typically formulated as:

$$h \propto \left(\frac{\mu_b}{\mu_{wall}}\right)^{0.14} \tag{52}$$

Therefore, the experiments to determine contact resistance were designed to keep the effect of changing wall viscosity on the heat transfer coefficient to 3% or less. As the magnitude of $d\mu/dT$, is quite large near room temperature, the tests were conducted at elevated temperatures, with reasonable heat fluxes to ensure the wall temperature rise was not too high.

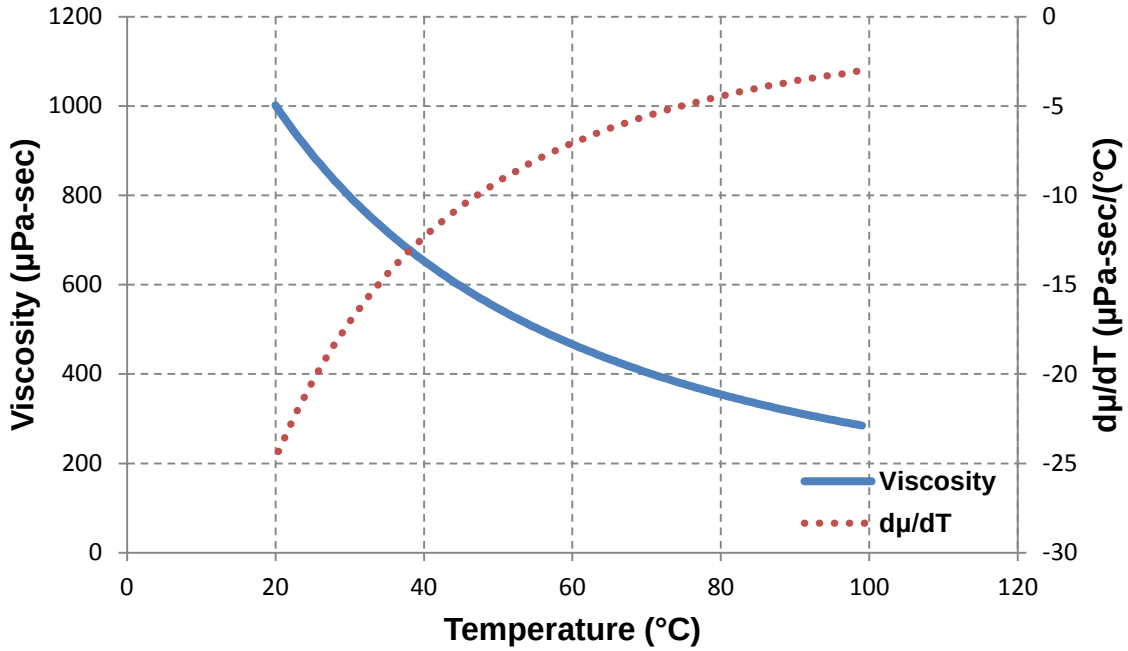

Figure 72: Viscosity of Water and First Derivative with Respect to Temperature at 1.01 bar.

To solve for the contact resistance, a minimum of two single-phase flow tests must be conducted (in the following analysis denoted as test 1 and test 2), with different thermal heat fluxes, $q''_{th,1}$ and $q''_{th,2}$. The following system of six equations with six unknowns can therefore be solved for each thermocouple location to determine the thermal contact resistance, $R_{th,c}$, at that point:

$$R_{th,c} = \frac{T_{back,1} - T_{meas,1}}{q''_{loss,1}} \quad (53) \qquad R_{th,c} = \frac{T_{back,2} - T_{meas,2}}{q''_{loss,2}} \quad (54)$$

$$q''_{th,1} = h(T_{w,1} - T_{b,1}) \quad (55) \qquad q''_{th,2} = h(T_{w,2} - T_{b,2}) \quad (56)$$

$$k_{ss,1}\frac{d^2T_1}{dy^2} + q'''_{elec,1} = 0 \quad (57) \qquad k_{ss,2}\frac{d^2T_2}{dy^2} + q'''_{elec,2} = 0 \quad (58)$$

The boundary conditions provided in equation (49) and equation (50) are used to solve the differential equations. Here T_{meas} corresponds to the measured temperature at that thermocouple location, and q''_{loss} represents the heat flux out the back of the heater plate:

$$q''_{loss,i} = \frac{\dot{Q}_{elec,i} - \dot{Q}_{th,i}}{A_{surf}} \quad (59)$$

The final result was calculated by hand and verified using Mathematica. The calculated contact resistance for a specific thermocouple is:

$$R_{th,c} = \frac{q''_{th,2}\left(\zeta_1 + T_{b,1} - T_{meas,1}\right) - q''_{th,1}\left(\zeta_2 + T_{b,2} - T_{meas,2}\right)}{q''_{loss,1}q''_{th,2} - q''_{loss,2}q''_{th,1}} \quad (60)$$

where

$$\zeta_i = q'''_{elec,i}\frac{t_{plate}^2}{2k_{ss,i}} - \left[q'''_{elec,i}t_{plate} - q''_{th,i}\right]\frac{t_{plate}}{k_{ss,i}} \quad (61)$$

with the subscript *i* denoting the corresponding test number. Several sets of tests were conducted, using various heat fluxes (100 kW/m^2, 200 kW/m^2, 300 kW/m^2). The mass flux was selected to ensure flow was fully turbulent. Even when conducting tests at different temperatures or mass fluxes, the measured thermal contact resistance across sets was consistent, with standard errors of 10% or less. Typical results for contact resistances are listed in Table 29. While it is difficult to specifically reference the case in this study, typical contact resistances for silicon epoxy bonded to aluminum are 2×10^{-5} to 9×10^{-5} m^2-K/W [94]. Therefore, the results for the epoxy-bonded thermocouple contact resistance in this study appear to be reasonable. For single-phase heat transfer experiments, the associated temperature drop due to contact resistance will therefore be around a couple of degrees Celsius. The thermal contact resistance was frequently verified to ensure no changes had taken place in the epoxy bond as a result of thermal cycling and fatigue. New thermal contact resistance values were determined for each thermocouple if the plate and/or thermocouples were changed in the setup.

Table 29: Typical Measured Thermal Contact Resistance for Thermocouples Experiencing Fully Developed Flow Conditions.

TC Designation	Average Value (m^2-K/W)	Standard Error
TC7	3.79×10^{-4}	±8.62%
TC8	4.40×10^{-4}	±2.77%
TC9	2.94×10^{-4}	±7.41%
TC10	3.25×10^{-4}	±5.41%
TC11	3.65×10^{-4}	±4.77%
TC12	2.99×10^{-4}	±7.49%
TC13	3.57×10^{-4}	±6.06%
TC14	3.87×10^{-4}	±4.47%
TC15	4.42×10^{-4}	±4.23%
TC16	3.52×10^{-4}	±5.61%

3.6.7. Isothermal Heat Loss

A commonly overlooked source of bias in flow experiments is heat loss from the fluid to structural components and the environment. Accounting for this heat loss can be important when the surface heat flux is determined via the enthalpy (temperature) rise in the test section. Even with insulation, heat loss from the fluid to piping and the environment could affect the measured thermal power. Non-circular geometries tend to be more problematic, as they are more difficult to effectively insulate. The issue worsens for bulk fluid temperatures well above ambient. While placement of fluid temperature sensors as close to the inlet and outlet of the test section reduces the effect on measurements, there must be an appropriate length of pipe at the test section outlet to ensure the fluid has mixed adequately once it reaches the temperature sensor. In addition, for our case, heat loss still occurs in the test section through the front window and the copper electrodes. While this source of measurement bias was identified during the design phase of the experiment, it was initially thought that it could be neglected.

The bias from fluid heat loss is considered separate from the electric heating losses. Recall that electric heating losses in this study are modeled as heat loss from the back side of the plate through the electric insulator, and are measured during experiments. For the purpose of this study, the heat loss from the fluid was treated as independent from the electric heat loss, and could therefore be accurately measured by conducting flow tests under isothermal conditions. One would expect the heat loss from the fluid to the environment to depend on the mass flux, fluid temperature, and ambient temperature. Therefore, isothermal tests were conducted for the entire range of mass fluxes and fluid temperatures that would be encountered in this study. The ambient temperature of the laboratory space was kept constant throughout testing. With no heat loss and neglecting the change in gravitational potential, one would expect the inlet and outlet enthalpies to be the same when no power is applied to the heater. Therefore, at zero power conditions and accounting for the differential RTD error, the difference between the measured inlet and outlet fluid temperatures may be attributed to heat loss from the fluid to the environment through piping and structural components. This temperature deviation and associated enthalpy change was recorded for each mass flux and bulk fluid condition for every heater installation. The deviation at each condition was then used to apply a correction to the measured thermal power for all experiments (including experiments to determine contact resistance), such that:

$$\dot{Q}_{th} = \dot{m}(h_{out} - h_{in}) + \dot{Q}_{iso} \tag{62}$$

where $\dot{Q}_{iso}$ is the magnitude of the isothermal heat loss. The isothermal heat loss was assumed to occur uniformly across the test section between the inlet and outlet RTD measurements. For fluid temperatures close to ambient, the isothermal heat loss was negligible, but it should be taken into account at elevated fluid temperatures, especially if the operating heat flux is low.

Chapter 4

Single-Phase Heat Transfer Experiments

4.1. Introduction

The primary mode of heat removal in materials test reactors is single-phase, forced convection from the surface of the fuel cladding to the coolant. This heat transfer process is best quantified using a heat transfer coefficient, *h*, which is defined in the following equation:

$$q'' = h(T_w - T_\infty) \tag{63}$$

where for internal flows, the free stream temperature, T_∞, is typically replaced by the bulk temperature, T_b. While equation (63) is often attributed to Isaac Newton and his famous 1701 article "Scala Graduum Caloris," this is technically incorrect as the concept of heat flux and the heat transfer coefficient did not exist at the time and were unknown to Newton [95]. It was actually Fourier who presented the concepts necessary for the above relation [96]. Nonetheless, equation (63) has long been referred to as Newton's Law of Cooling in engineering and heat transfer textbooks, and for the sake of clarity, will be referred to as such in this study.

Convective heat transfer represents the combined heat transfer due to advection and conduction within a fluid. However, a comprehensive understanding of this heat transfer process was not possible until the introduction of boundary layer theory. Ludwig Prandtl was the first to formally introduce the concept of boundary layers in fluid flow at the Third International Congress of Mathematicians in 1904 [97]. Prandtl's student, Heinrich Blasius, further

elaborated on the theory of boundary layers in his influential 1908 paper, "The Boundary Layers in Fluids with Little Friction" [98]. A thorough history of the development of boundary layer theory is available in reference [99].

Boundary layer theory is a central part of modern convective heat transfer analysis. Reference [100] provides a suitable introduction, while the classic text by Herrmann Schlichting [101] should be read for a detailed treatment of the subject. However, given the depth of the topic, only a brief synopsis of important ideas can be covered in this chapter.

The flow of a fluid parallel to a surface may be characterized by a layer near the surface in which the effects of viscosity are most apparent. This layer is referred to as the velocity boundary layer. Away from the surface, in the free stream, friction forces have little influence on the flow, and the fluid flows with velocity u_∞. Therefore, considering that a no-slip boundary condition exists at the wall, the boundary layer is the region in which the velocity gradient, $\partial u/\partial y$ (and therefore the shear stress) is the greatest. The demarcation of the boundary layer is arbitrarily chosen as the point where u=0.99u_∞. The boundary layer thickness, δ_{hyd}, is the distance from the wall to the streamline where u=0.99u_∞. Turbulent boundary layers may be further characterized by three regions: the viscous (laminar) sublayer, the buffer layer, and the core or turbulent region. In the viscous sublayer, flow remains laminar, and little mixing occurs. Therefore, the predominant means of heat transfer through the viscous sublayer is conduction. For internal flow in a hydraulically smooth channel, the dimensionless thickness of the viscous sublayer may be estimated using the following criterion:

$$\delta_v^+ = \frac{\delta_v u_\tau}{\nu} = 5 \tag{64}$$

Equation (64) estimates the thickness of the viscous sublayer to be between 5.80 μm to 71.0 μm for flow in the test section at operating conditions expected in the proposed MITR smooth coolant channel design.

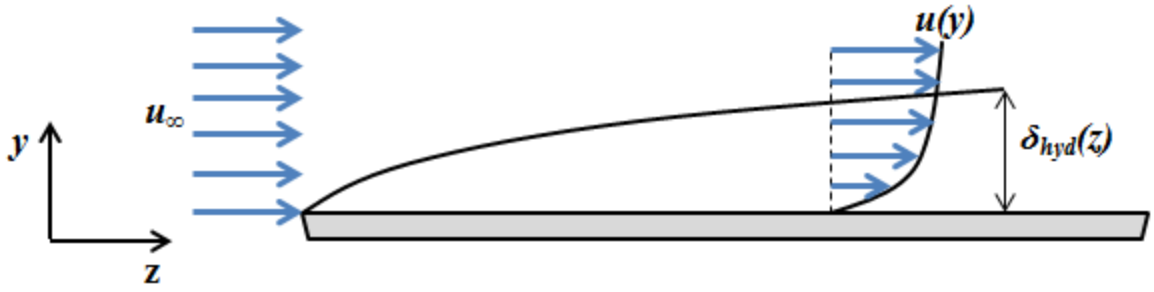

Figure 73: Schematic of Velocity Boundary Layer in Relation to Surface.

Similar to development of a velocity boundary layer, a thermal boundary layer also develops when heat is transferred between a surface and a fluid. The thermal boundary layer defines the region near the wall where the temperature gradient $\partial T(y)/\partial y$ is most significant. In the free stream, the temperature is constant with $T=T_\infty$. Similar to the velocity boundary layer thickness, the thermal boundary layer thickness, δ_{th}, is arbitrarily defined as the point where:

$$\frac{T_w - T(y)}{T_w - T_\infty} = 0.99 \tag{65}$$

As convective heat transfer involves both advection and heat conduction through the fluid, both δ_{th} and δ_{hyd} are relevant to the heat transfer process. An important parameter for characterizing the heat transfer process in fluid flows is the Prandtl number:

$$Pr = \frac{\nu}{\alpha} = \frac{\mu c_p}{k} \tag{66}$$

which is defined as the ratio of viscous diffusion to thermal diffusion. It is important to note that *Pr* also relates the velocity and thermal boundary layers, such that:

$$Pr \sim \frac{\delta_{hyd}}{\delta_{th}} \tag{67}$$

Therefore, the Prandtl number in forced convection is a direct measure of the ratio of thicknesses of the two boundary layers, and indicates the relative importance of momentum transfer to thermal diffusion in the convective heat transfer process.

An important measure of the mechanical similarity of flows is found in the dimensionless group called the Reynolds number:

$$Re = \frac{\rho u L_c}{\mu} \tag{68}$$

and is simply the ratio of inertial forces to viscous forces in flow. The last parameter needed, which contains the aforementioned convective heat transfer coefficient, *h*, is the Nusselt number:

$$Nu = \frac{h L_c}{k} \tag{69}$$

which, by definition, is inversely proportional to δ_{th}. For internal flows, which are the focus of this study, the characteristic length in equation (68) and equation (69) is taken to be the hydraulic diameter, D_{hyd}. It can be shown that for hydraulically smooth channels experiencing symmetric and uniform heating in the absence of dissipation (i.e. $Br<<1$), the above dimensionless parameters may be related by:

$$Nu = \boldsymbol{f}(Re, Pr) \tag{70}$$

Equation (70) forms the basis for correlating the heat transfer coefficient, *h*, to fluid properties and flow conditions, which are discussed in the following two sections.

4.1.1. Circular Tube Correlations

A wide variety of single-phase, forced convection heat transfer correlations for turbulent flow have been developed in the wake of the introduction of the boundary layer concept by Prandtl. The vast majority of these correlations have been developed from experimental or theoretical investigations of circular tube geometries. In general, they relate the Nusselt number to the Reynolds number and Prandtl number using a power function, a rational function, or some combination of the two. Some correlations also include the friction factor, in order to account for heat transfer effects of hydraulically rough channels. Correlations may also be typified on how the fluid properties are evaluated: at the bulk fluid temperature, the film temperature, the

wall temperature, or some combination thereof. A selection of circular tube correlations for turbulent, fully developed flow which are relevant to this study are summarized in this section. Note that throughout this study, if not specifically indicated, fluid properties should be evaluated at the bulk temperature.

The Dittus and Boelter Equations

In 1930, Dittus and Boelter presented equations for heat transfer within circular tubes based on empirical data, with a distinction between heating and cooling [102]. The original equation was not dimensionless as presented, and there was also a significant typographical error with the Reynolds number exponent, being 0.08 instead of 0.8. In dimensionless form, with the error corrected, the original Dittus and Boelter equations are:

$$Nu = 0.0241 Re^{0.8} Pr^{0.4} \quad \text{for heating of fluid} \tag{71}$$

$$Nu = 0.0264 Re^{0.8} Pr^{0.3} \quad \text{for cooling of fluid} \tag{72}$$

Dittus and Boelter intended the property values to be evaluated at the mean "stream," or bulk, temperature, i.e. the average of the inlet and outlet bulk temperatures. Dittus and Boelter note that the agreement is no better when evaluating properties at the tube surface temperature, nor at the average temperature between the tube surface and the stream.

In his 1942 textbook, McAdams presents the following equation, with little explanation of its development or origin, stating it is valid for Re>2100 and for fluid viscosity values no more than twice that of water [103]:

$$Nu = 0.023 Re^{0.8} Pr^{0.4} \tag{73}$$

The property values are once again evaluated at the bulk fluid temperature. Winterton [104] notes that equation (73) is often misrepresented as the Dittus-Boelter equation. Looking at the McAdams text, it is clearly not a typographical error, as McAdams presents the forms of the Dittus and Boelter equations on the preceding page (note that the leading coefficient in equation (73) was rounded up from the value of 0.0225 found in the 1933 edition of the text). Therefore, equation (73) should be attributed to McAdams, but for the sake of clarity and consistency with

other studies, it will be referred to in this study as the Dittus-Boelter equation. This is an important distinction, as prior MITR-II safety analyses have used equation (73), referring to it as the Dittus-Boelter equation.

The Film Temperature and Colburn's Correlation

In his 1933 paper [105], Colburn makes extensive use of a film temperature, which for viscous (laminar) flow is defined as:

$$T_{film} = T_{avg} + \frac{1}{4}(T_w - T_{avg}) \tag{74}$$

and for turbulent flow is defined as:

$$T_{film} = T_{avg} + \frac{1}{2}(T_w - T_{avg}) = \frac{T_w + T_{avg}}{2} \tag{75}$$

where T_{avg} is the average bulk temperature. The correlation proposed by Colburn from a fit to empirical data is:

$$\frac{hD_{hyd}}{k} = 0.023\left(\frac{GD_{hyd}}{\mu_{film}}\right)^{0.8}\left(\frac{c_p\mu_{film}}{k}\right)^{1/3} \tag{76}$$

where the subscript "film" denotes that the property is evaluated at the film temperature. In this case only the viscosity is evaluated at the film temperature, with other properties evaluated at the bulk temperature. A modified Colburn equation, proposed by Stoever [106], was recommended by the Phillips Reactor Safeguards Committee for the Materials Testing Reactor [107], and is presented as:

$$\frac{hD_{hyd}}{k_{film}} = 0.023\left(\frac{\rho_{film}uD_{hyd}}{\mu_{film}}\right)^{0.8}\left(\frac{c_p\mu_{film}}{k_{film}}\right)^{0.3} \tag{77}$$

Note that all fluid properties are evaluated at the film temperature, and the exponent on the Prandtl number has changed. This modified Colburn equation is relevant to the present study since it was used in the preliminary design study of the MITR-II [49], and has been used in analyses for similar materials test reactors such as the Brookhaven HFBR [108].

Wall Viscosity Effects and the Correlation of Sieder and Tate

Though the effect of wall viscosity had been previously considered by Dittus and Boelter, and accounted for in some respect through the use of a film temperature by Colburn, Sieder and Tate [109] considered the influence of varying fluid viscosity with temperature to be significant enough to warrant more attention. Sieder and Tate collected data for three oils, with different temperature coefficients of viscosity, at laminar and transition flow conditions. Data for turbulent flow conditions were taken from prior studies. They found that the term introduced in equation (52) applied equally well to both laminar and turbulent flow regimes. The fit for turbulent data was only presented graphically, with McAdams [103] later presenting it explicitly as:

$$Nu = 0.027 Re^{0.8} Pr^{1/3} \left(\frac{\mu_b}{\mu_{wall}} \right)^{0.14} \tag{78}$$

Note that all other properties are evaluated at the bulk temperature if not indicated. In the 1954 edition of his textbook [110], McAdams updates the coefficient from 0.027 to 0.023, noting that a leading coefficient of 0.023 correlates data better for air and for water. However, 0.027 is adopted in this study as this most closely matches a fit by this author to the data originally presented in the paper of Sieder and Tate.

More Recent Formulations

While the early correlations faired adequately for many applications, predicted heat transfer coefficients are typically expected to deviate by ±20% or more from actual values. Incorporating the friction factor and assuming constant physical properties, Petukhov [111] provides the following:

$$Nu = \frac{(f/8)RePr}{1.07 + 12.7\sqrt{f/8}(Pr^{2/3} - 1)} \tag{79}$$

where the values of 1.07 and 12.7 are approximations of otherwise variable constants, and properties are evaluated using the bulk temperature. Petukhov defines the friction factor for smooth tubes as:

$$f = [1.82log_{10}(Re) - 1.64]^{-2} \tag{80}$$

Petukhov recommends equation (79) for $10{,}000<Re<5\times10^6$ and $0.5<Pr<2000$.

Gnielinski [112] made a slight modification to the Petukhov correlation so that it could be extended down to the transition flow regime:

$$Nu = \frac{(f/8)(Re - 1000)Pr}{1 + 12.7\sqrt{f/8}(Pr^{2/3} - 1)} \tag{81}$$

where, for smooth tubes, the friction factor of equation (80) is recommended. Equation (81) is applicable for $2100<Re<5\times10^6$, and should be valid for the *Pr* range of eq. (79). The Gnielinski correlation has become the standard among thermal scientists for predicting single-phase heat transfer in circular tubes, and is the correlation against which others are often measured.

4.1.2. Correlations for Parallel Plates and Rectangular Channels

The suitability of using circular tube correlations to predict heat transfer in high aspect ratio, narrow rectangular channels is debatable. Nonetheless, the correlations discussed in the previous section continue to be used for design and safety analyses of materials test reactor coolant channels. A 1959 study by Levy et al. [47] was specifically aimed at investigating this issue with respect to materials test reactor coolant channels, with Levy noting that there was essentially no data available for such channels. Levy measured single-phase heat transfer and CHF, reporting turbulent forced convection heat transfer rates 30-45% below that predicted by Sieder-Tate, and 15-30% lower than that predicted most other circular tube correlations. Levy also found CHF to be significantly lower than that for circular tubes. The poor heat transfer

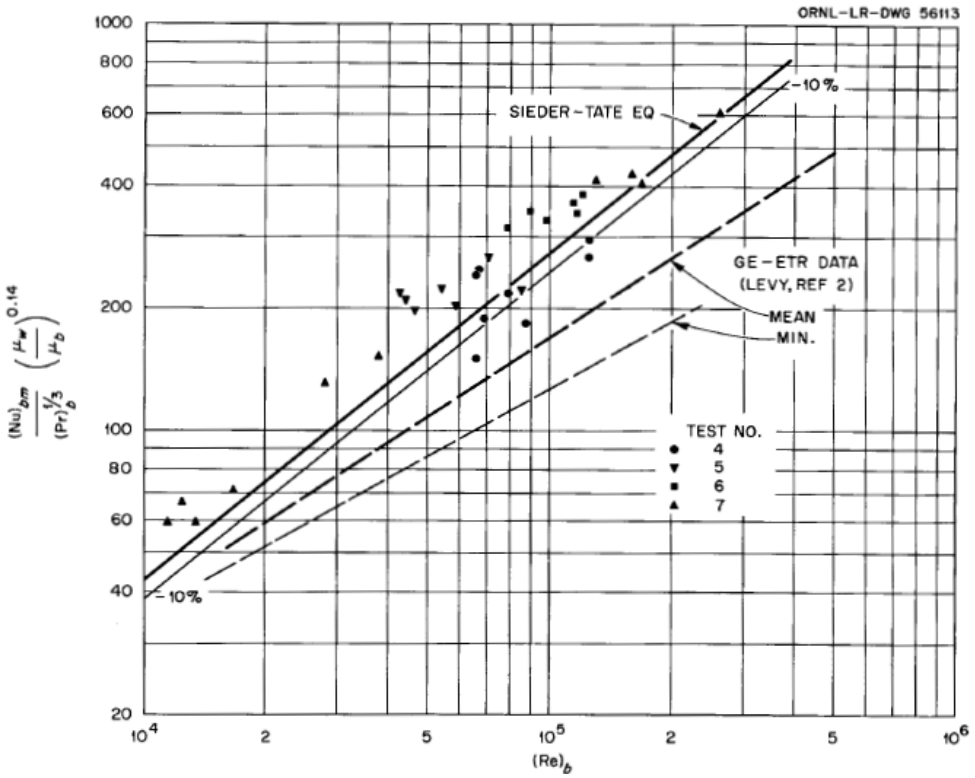

Figure 74: Single-Phase Heat Transfer Results from the Study by Gambill in Support of the HFIR Design. Results are Compared to the Sieder-Tate Correlation. *Source: Ref. [48].*

characteristics reported by Levy were the primary driver for a study by Gambill [48] in support of the High Flux Isotope Reactor (HFIR) design. In this study, Gambill identified potential issues with the setup used by Levy et al., such as heat flux peaking in the channel corners leading to premature burnout. As seen in Figure 74, Gambill's results are 10-20% greater than the predictions by the Sieder-Tate correlation (equation (78)).

Several studies investigating single-phase heat transfer in similar channels were conducted at MIT, with the experimental test sections mentioned in Chapter 2. Only one of these studies yielded results for smooth channels, finding the single-phase heat transfer coefficient to be 12% greater than that predicted by the modified Colburn correlation shown in equation (77). The summary of smooth channel results for this study is shown in Figure 75. A more recent study by Sudo et al. [52] investigated both laminar and turbulent flow for upflow and downflow in a narrow rectangular channel meant to simulate a coolant channel of the JRR-3 research reactor. Unlike previous experiments, the short edges of Sudo's channel were not heated, more closely replicating the actual heating geometry in materials test reactors. As seen in Figure 76, above *Re*=10,000, the spread of the data was approximately ±20%, making it difficult to draw

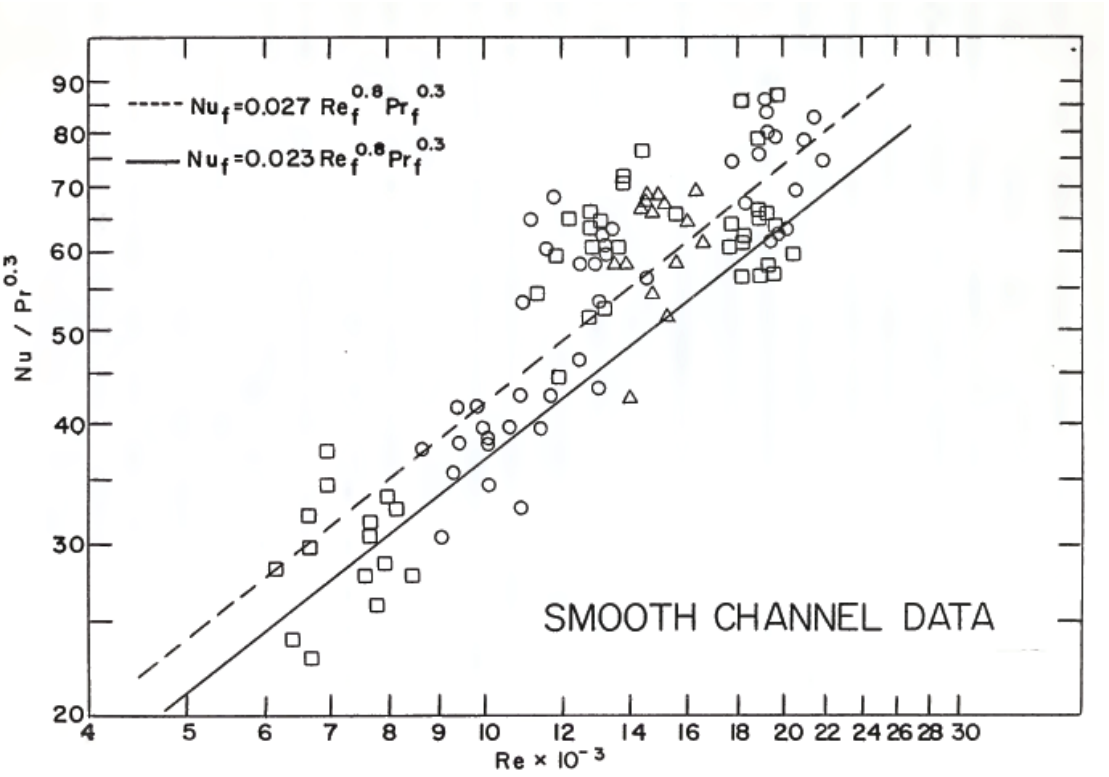

Figure 75: Single-Phase Heat Transfer Results for a Narrow Rectangular Channel from the Study by Spurgeon. Results are compared to the modified Colburn correlation. *Source: Ref. [49]*.

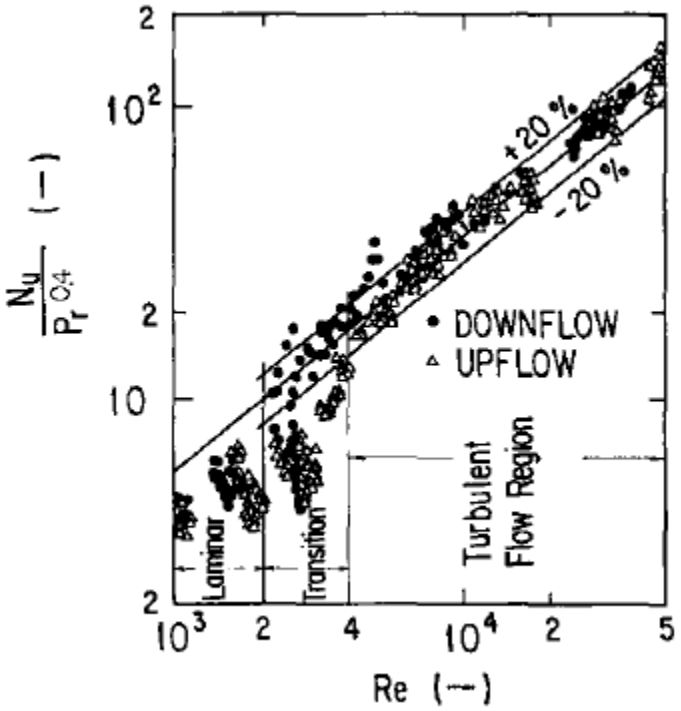

Figure 76: Single Phase Heat Transfer Results from the Study by Sudo et al. for a Geometry Heated on Two Sides. The spread of the data makes it difficult to draw firm conclusions with respect to the adequacy of circular tube predictions. *Source: Ref. [52]*.

conclusions with respect to circular tube predictions. Therefore, Sudo recommends use of the Dittus-Boelter equation (the McAdams correlation, equation (73)) for predicting turbulent single phase heat transfer in such channels.

Table 30: Summary of Studies Investigating Various Heat Transfer Phenomena In Narrow Rectangular Channels for MTR Applications.

Institution/ Reactor	Year	Geometry	*Re*	*P, T*	Parameter Studied	Result	Ref.
GE & KAPL	1959	Rectangular channel; t_{gap}= 0.1"; L×w: 2.5"×18"/36"; Vertical flow	6000-200,000	4.5-13.8 bar; 20-134 °C	$h_{1\phi}$, CHF	$h_{1\phi}$ 15%-45% less than c.t. correlations; CHF values 1/3 of those predicted by c.t. correlations	[47]
ORNL/ HFIR	1961	Rectangular channel; t_{gap}= 0.043"-0.0057"; L×w: 18"×1.06"; Upflow	9000-270,000	1.0-39.5 bar	f, $h_{1\phi}$, CHF	$h_{1\phi}$ 10%-20% greater than Sieder-Tate eqn; CHF accurately predicted by Zenkevich-Subbotin correlation	[48]
MIT/ MITR	1969	Rectangular channel; t_{gap}= 0.090" L×w: 2.5"×24"; Upflow	6500-20,000	MITR conditions	$h_{1\phi}$	$h_{1\phi}$ 12% greater than modified Colburn correlation	[49]
MIT/ MITR	1974	Rectangular channel; t_{gap}= 0.11" L×w: 2.18"×24"; Upflow	N/A	MITR conditions	$h_{1\phi}$	Inconclusive due to design- failure of insulator	[50]
MIT/ MITR	1975	Rectangular channel; D_{hyd} = 2.16 mm; Upflow	~2200-~14,000	MITR conditions	$h_{1\phi}$	No smooth channel results	[51]
JAERI/ JRR-3	1984	Rectangular channel; t_{gap}=2.25mm L×w: 50 mm×750mm; Upflow/Downflow	~100-50,000	<42 °C	$h_{1\phi}$	***Turbulent flow***: Large spread in $h_{1\phi}$ (+/-20% spread), but recommends Dittus-Boelter; ***Laminar flow***: New correlation	[52]

The results of studies investigating turbulent single-phase heat transfer specifically for materials test reactor coolant channel geometries are summarized in Table 30 on the preceding page. Note that with the exception of the data presented by Levy and Sudo, the measured turbulent single-phase heat transfer coefficient is greater than that predicted by circular tube correlations. However, the Reynolds and Prandtl number ranges were limited in the studies listed in Table 30, making it difficult to develop a robust correlation for the narrow geometries.

While many other studies have investigated heat transfer in rectangular channels, few approach aspect ratios as high as that of the MITR or have heating conditions and Prandtl numbers prototypical of the MITR. Much of the work done in rectangular channels has been done for air, with $Pr<1$. A study by Sparrow and Cur [113] investigated mass transfer in a rectangular channel with $\alpha^*=0.0556$ and $10{,}000<Re<45{,}000$. The gap of the channel was approximately 2 cm, significantly larger than that in this study. Although the working fluid was a naphthalene-air system, studies were conducted at a fixed Schmidt number of $Sc=2.5$. For heating on both sides (uniform wall temperature conditions), they found that:

$$Sh = 0.0500Re^{0.76} \tag{82}$$

The Chilton-Colburn analogy relates the Sherwood number to *Nu* [114], giving us:

$$j_h = \frac{Nu}{RePr^{1/3}} = j_{\mathcal{M}} = \frac{Sh}{ReSc^{1/3}} \tag{83}$$

In the original paper by Chilton and Colburn, equation (83) is stated as being valid for $0.7\leq Pr\leq 1000$, though more recent sources list different applicable ranges ($Pr\geq 0.5$ [115], or $0.6<Pr<60$ [116]). Using the Chilton-Colburn analogy, we can infer from the results of Sparrow and Cur a relation for the Nusselt number at the fixed Prandtl number of $Pr=2.5$:

$$Nu = 0.0500Re^{0.76} \tag{84}$$

If we assume the dependence of the Nusselt number on the Prandtl number to be similar to the Colburn correlation (i.e., $Nu\sim Pr^{1/3}$), then a general correlation for a high aspect ratio rectangular channel heated on both sides with isothermal wall conditions can be formulated as:

$$Nu = 0.036Re^{0.76}Pr^{1/3} \tag{85}$$

Note that equation (85) is based on mass transfer measurements for a naphthalene-air system at a single Schmidt number. Also note that the wall conditions were isothermal (unlike in this study), and for a channel with a substantially larger gap than in MTR's, so equation (85) should be used with caution.

While data for rectangular channels at relevant Reynolds and Prandtl numbers is sparse, turbulent heat transfer studies with parallel plates are more abundant. As noted in chapter 1, parallel plate studies (where $\alpha^* \rightarrow 0$) should be applicable to heat transfer in MTR-type coolant channels away from the channel edges. Bhatti and Shah [117] summarize expected heat transfer results for parallel plates, noting that in the range $10{,}000 < Re < 30{,}000$ and $0.5 < Pr < 100$, the Nusselt number is up to 1.23 times that predicted by circular tube correlations, as shown in Table 31.

Table 31: Comparison of Nusselt Numbers from Circular Tube Predictions (Gnielinski) versus Expected Values for Flat Ducts. *Source: Ref. [117].*

***Pr* Range**	***Re* Range**	$Nu_{flat\ duct}/Nu_{c.t.}$
$0.5 < Pr < 100$	$10^4 < Re < 3\times10^4$	Up to 1.23
$0.5 < Pr < 100$	$3\times10^4 < Re < 10^6$	0.911 to 0.925
$Pr = 1000$	$10^4 < Re < 10^6$	Down to 0.77
$0 < Pr < 0.003$	$10^4 < Re < 10^6$	0.945 to 1.57

A number of analytical and semi-analytical studies have been conducted for the parallel plate geometry. In 1961 Barrow [118] published analytical results for the case of turbulent flow between parallel plates with each wall having unequal, but uniform heat fluxes. For the case of symmetric heating, the Nusselt number calculated by Barrow is:

$$Nu = \frac{0.1986Re^{7/8}Pr}{5.03Re^{1/8} + 9.74(Pr - 1)} \tag{86}$$

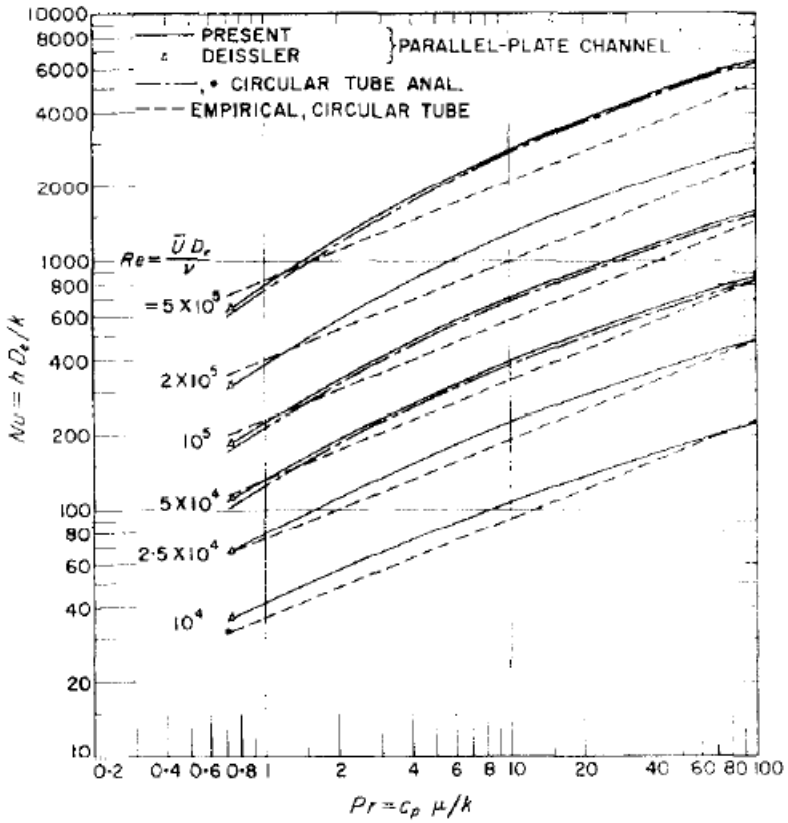

Figure 77: Analytical Solution to Turbulent Heat Transfer in Parallel Plates with Uniform Heat Flux at Both Walls Presented by Sparrow and Lin. The dashed lines represent the predictions of the Dittus-Boelter (McAdams) correlation, equation (73). *Source: Ref. [119].*

Barrow claims his theoretical analysis is valid for *Pr* greater than about 0.7, as he assumes that turbulent eddy conductivity is constant in his analysis. Barrow also assumes that the thickness of the viscous sublayer is negligible compared with the channel gap for his analysis. From the estimates of the sublayer thickness for the test section in this study, this assumption may not be valid. Sparrow and Lin [119] also perform an analytical study for a parallel plate configuration with *Pr* from 0.7 to 100 and *Re* from 10,000 to 500,000. Sparrow and Lin present their results graphically, which are shown in Figure 77. They also note that from their solution, the Nusselt number dependence on the Prandtl number is more complex than a simple power law, which is that typically encountered in empirical correlations. Note from the figure, that for Prandtl numbers relevant to this study, the analytic solution of Sparrow and Lin predicts Nusselt numbers higher than those by equation (73). A numerical solution to the parallel plate problem with the boundary conditions of uniform wall temperatures is proposed by Sakakibara and Endo

[120]. They provide the necessary constants and eigenvalues for different *Pr* and *Re* in a tabular format.

Despite the number of correlations available, it is difficult to assess from the literature which correlation is best suited for application to the MITR, especially if accurate prediction in the transition regime is desired. The existing correlations provide a wide range of values in the turbulent regime at conditions relevant to the MITR, with the correlation of Sieder and Tate predicting the highest Nusselt number, and the modified Colburn correlation predicting the lowest. Therefore, a driver for the single-phase experimental campaign is to provide data that may either enable a more informed selection of an existing correlation or support the development of a new correlation for the MITR operating conditions and proposed unfinned geometry.

4.2. Heater Surface Preparation

The surface finish of the channel was carefully controlled, with the heater plate prepared to match the roughness expected on actual MTR cladding (refer to section 6.1). While it was not possible to exactly replicate the texture of MTR cladding due to the different fabrication process, the objective was to obtain an arithmetic surface roughness, R_a, equivalent to that measured for MTR cladding surfaces. While the maximum roughness, R_z, was also measured, this value can be more difficult to replicate. Coupons of 316 stainless steel, with the same nominal starting finish as the heater plate, were wet-sanded using varying grits for sandpaper. The coupons were analyzed using confocal microscopy to determine which surface treatment yielded a roughness greater than or equal to that measured for MTR cladding. The surface finishing techniques were shown to be very repeatable by roughness measurements at various locations on different coupons prepared in a nominally identical fashion. The technique ultimately selected involved wet-sanding of the as-received surface with 120-grit SiC sandpaper using a figure-eight pattern, resulting in a uniform surface free of gouges or deep scratches. The resulting finish had an R_a of about 0.5 μm (detailed results are provided in section 6.2). Before installation into the flow facility, the heater surface was sonicated in acetone for 15 minutes to remove any remaining grit, rinsed with ethanol, wiped with non-scratching delicate task wipes, followed by a final rinse with DI water and blown dry with clean, compressed nitrogen. A photo of the surface following finishing, compared with a test coupon, is shown in Figure 78 and Figure 79.

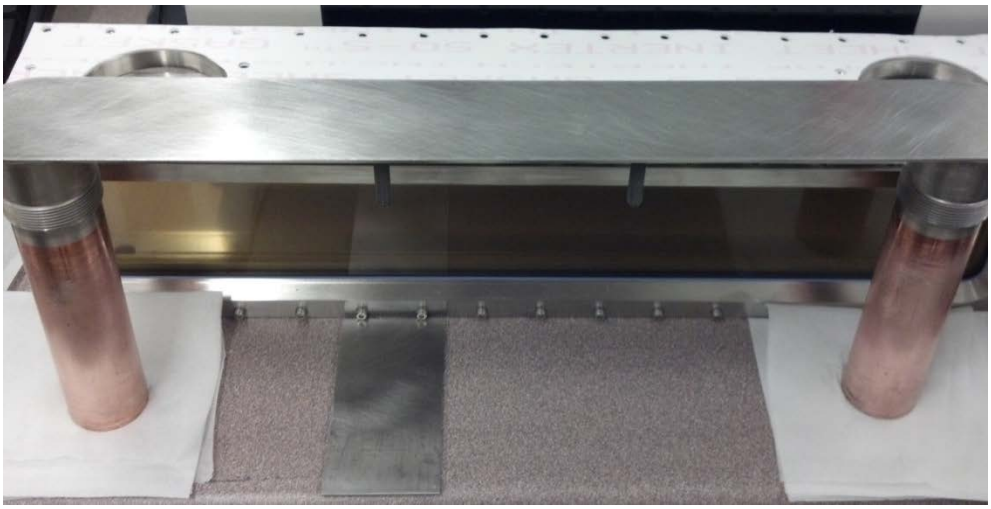

Figure 78: Photograph of Heater Plate Following Surface Finishing with Sample Coupon on Table.

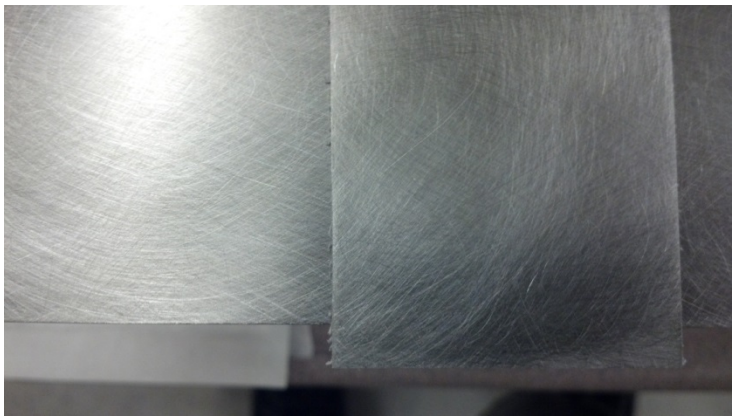

Figure 79: Close-up Comparing Heater Plate Surface (left) to Sample Coupon Surface (right).

In general, the surface roughness of the plate is not expected to have an influence on single-phase heat transfer as long as it can be considered hydraulically smooth, such that the characteristic roughness of the surface is small compared to the thickness of the viscous sublayer. Typically, the root-mean-square roughness, $R_{rms,}$ is used as the characteristic length scale for this comparison. For the heater plate, R_{rms}~0.7 μm. From section 4.1, we can estimate that $\delta_v << R_{rms}$, so the flow can be treated as hydraulically smooth. Similarly, the Moody diagram [121] may be referenced, showing that an RMS roughness of 0.7 μm would not be expected to have an appreciable effect on the friction factor and therefore should have little effect on the heat transfer coefficient.

4.3. Single-Phase Measurement Considerations

As mentioned in the introduction, determination of an appropriate hydraulic diameter for high aspect ratio rectangular channels is important when presenting data or predicting heat transfer from correlations. Unfortunately, there is inconsistency in choice of the hydraulic diameter for such channels, leading to small, but non-negligible differences in results. Treating the dependence of the Nusselt number on Reynolds number as $Nu \sim Re^{0.8}$, then the heat transfer coefficient would be expected to vary with the hydraulic diameter as:

$$h \propto D_{hyd}^{-0.2} \tag{87}$$

For this study, most temperature measurements are situated at the center of the channel, away from the edges. Also, considering that the aspect ratio is very large (α^*=0.035), it has already been argued that the parallel plate hydraulic diameter should be used. However, past studies have used various forms of the hydraulic diameter, with Spurgeon [49] and others at MIT using the standard formula given in equation (1).

In studying turbulent friction factors, Jones postulates that the standard hydraulic diameter may not be the correct dimension to obtain geometric similarity between round and rectangular ducts [122]. Jones points to the example of the effect of increasing aspect ratio on the measured friction factor, which is not captured by the standard hydraulic diameter. Using an analytic comparison between circular and rectangular geometries in laminar flow, and empirical data for turbulent flow, Jones introduces a modified Reynolds number and laminar equivalent diameter:

$$Re^* = \phi^* Re_{D_{hyd}} \tag{88}$$

$$D_L = \phi^* D_{hyd} \tag{89}$$

where D_{hyd} is the standard hydraulic diameter, calculated by equation (1), and ϕ^* is a geometry function, which is exactly equal to:

$$\phi^* = \frac{2}{3}\left(1+\frac{t_{gap}}{w}\right)^2 \times\left[1-\frac{192t_{gap}}{\pi^5 w}\sum_{n=0}^{\infty}\frac{1}{(2n+1)^5}\,tanh\left\{\frac{(2n+1)\pi w}{2t_{gap}}\right\}\right] \tag{90}$$

Equation (90) may be approximated within 2% for all aspect ratios by:

$$\phi^* \approx \frac{2}{3}+\frac{11}{24}\times\frac{t_{gap}}{w}\left(2-\frac{t_{gap}}{w}\right) \tag{91}$$

A comparison of the different equivalent diameters and the expected effect on the calculated heat transfer coefficient for this study is provided in Table 32. As seen in the table, the expected difference in the heat transfer coefficient between using the hydraulic diameter for parallel plates compared to the standard formula is small, while the difference with respect to the laminar equivalent diameter is significant. This is not surprising since velocity and temperature profiles in laminar flow are generally more sensitive to channel geometry and boundary conditions.

Table 32: Comparison of Different Equivalent Diameters and the Effect on the Calculated Heat Transfer Coefficient

	Duct	**Parallel Plates**	**Laminar Equivalent Diameter**
Formula	$\frac{4A_{flow}}{P_w}$	$2t_{gap}$	$\phi^*\frac{4A_{flow}}{P_w}$
Equivalent Diameter for this Study	3.78 mm	3.91 mm	2.64 mm
$\boldsymbol{D_{eq}/\left(\frac{4A_{flow}}{P_w}\right)}$	1	1.034	0.698
Heat Transfer Coefficient Ratio	1	0.993	1.075

Another important measurement consideration involves treatment of temperature effects on fluid properties, primarily viscosity. First, the bulk temperature may vary significantly with axial position within the test section. Therefore, parameters are calculated at each axial thermocouple position, reflecting local properties. In addition, property variation between the wall and the bulk of the fluid may be significant enough to affect calculated heat transfer coefficients. For this reason, single-phase tests were conducted with the expected wall-to-bulk temperature difference being kept at 10 °C or less for most test conditions. This allows for reasonable correlation using bulk fluid properties. Note that this is also representative of the conditions in the MITR under normal steady-state operation, where wall-to-bulk temperature differences are typically small. During loss of flow or other transients, the temperature difference may be higher. However, use of a correlation based on bulk fluid properties provides a lower conservative bound on the heat transfer coefficient value, since an increase in the wall-to-bulk temperature difference leads to a decreased wall viscosity, and therefore a higher heat transfer coefficient.

An important issue, mentioned in chapter 2 in regard to the test section design, is the effect of one-sided versus two-sided heating on single-phase heat transfer. Fuel assemblies in the MITR consists of both “full channels,” heated on both sides, and “side channels” at the ends, which can be heated on one side only if next to a support plate. In most cases, the side channels are limiting in terms of power peaking. As it was only possible in this study to test a channel heated on one side, it is important to consider the potential effects of one-sided versus two-sided heating on heat transfer.

Consider the schematic of flow between parallel plates in Figure 80. The heating condition at each wall imposes a boundary condition on the problem. Therefore, it is expected that altering the boundary condition will affect the solution to the temperature profile. Consider, first, the case of the velocity profile. If the velocity profile is not coupled to the temperature profile, then the thermal boundary conditions will have no effect on the solution for velocity, resulting in a symmetric profile, with no difference whether there is no heating, heating on one side, or heating on both sides. In reality, the fluid properties change with temperature, which will have a small effect on the velocity profile.

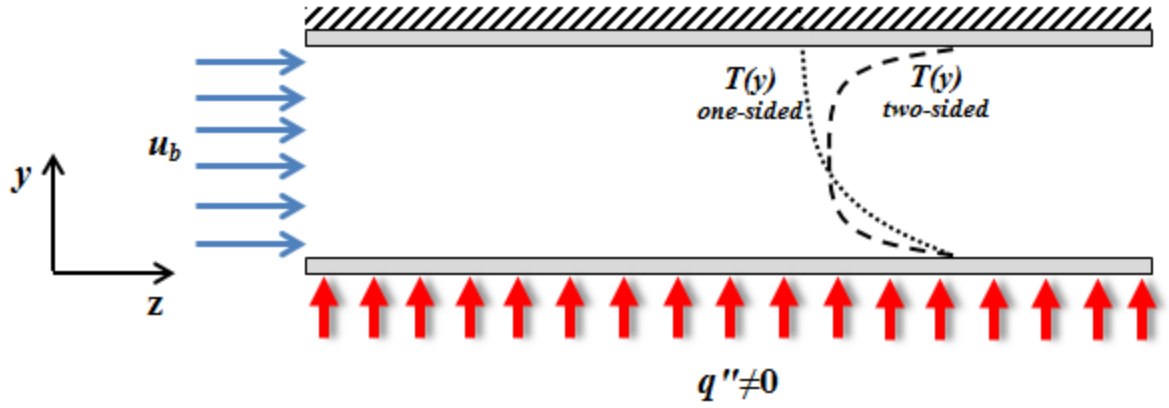

Figure 80: Influence of One-sided versus Two-sided Heating on the Temperature Profile in the Fluid. Effect of boundary conditions on temperature profile is exaggerated in this drawing.

Therefore, it can be said for turbulent flow that if the velocity boundary layer is thicker than the thermal boundary layer, then the heat transfer process is dominated by advection (i.e. $\delta_{th} > \delta_{hyd}$, or $Pr>1$), and the influence of one-sided versus two-sided heating should be small. The same cannot be said for laminar or buoyancy driven flows, where the effect of one-sided versus two-sided heating may be significant, as demonstrated by Sudo [52].

Empirical results for turbulent flow in narrow channels support that the effect of one-sided versus two-sided heating on turbulent heat transfer is small for $Pr>>1$. Referring again to the mass transfer study of Sparrow and Cur [113], and also relying on the Chilton-Colburn analogy, their results for $Sc=2.5$ indicate that the Nusselt number will be about 8% lower for one-sided versus two-sided heating when $Pr=2.5$. For his turbulent heat transfer results, Sudo [52] is not able to distinguish any difference between one-sided and two-sided heating in his prototypic MTR channel. In a semi-empirical study of flow in annular spaces, Kays and Leung [123] analytically extend their experimental results for heated annuli to the case of parallel plates, reaching a similar finding, with Nusselt numbers being about 10% less for parallel plates heated on one side only versus both sides.

The semi-analytical results of Kays and Leung are tabulated for parallel plates at different Reynolds and Prandtl numbers. Using these tabulated solutions, it is possible to plot the ratio of Nusselt numbers for one-sided heating to two-sided heating, under otherwise similar conditions. These results are plotted in Figure 81, showing the trend with Prandtl number for a range of Reynolds numbers. As expected, the ratio converges to unity with increasing Prandtl number,

due to the increasing thickness of the velocity boundary layer relative to the thermal boundary layer. Though not shown in the graph, note that for very small Prandtl numbers, i.e. $Pr<0.1$, the ratio approaches the asymptotic value of 0.53. Recall that the expected Prandtl number range in the MITR during normal operation is $2.98<Pr<4.15$. Therefore, one would expect the single-phase heat transfer coefficient to be ~10% lower for the case of one-sided versus two-sided heating, which is consistent with that found in other studies. More importantly, the values for single-phase heat transfer reported in this study can therefore be considered as a conservative lower bound for the full channels in the MITR.

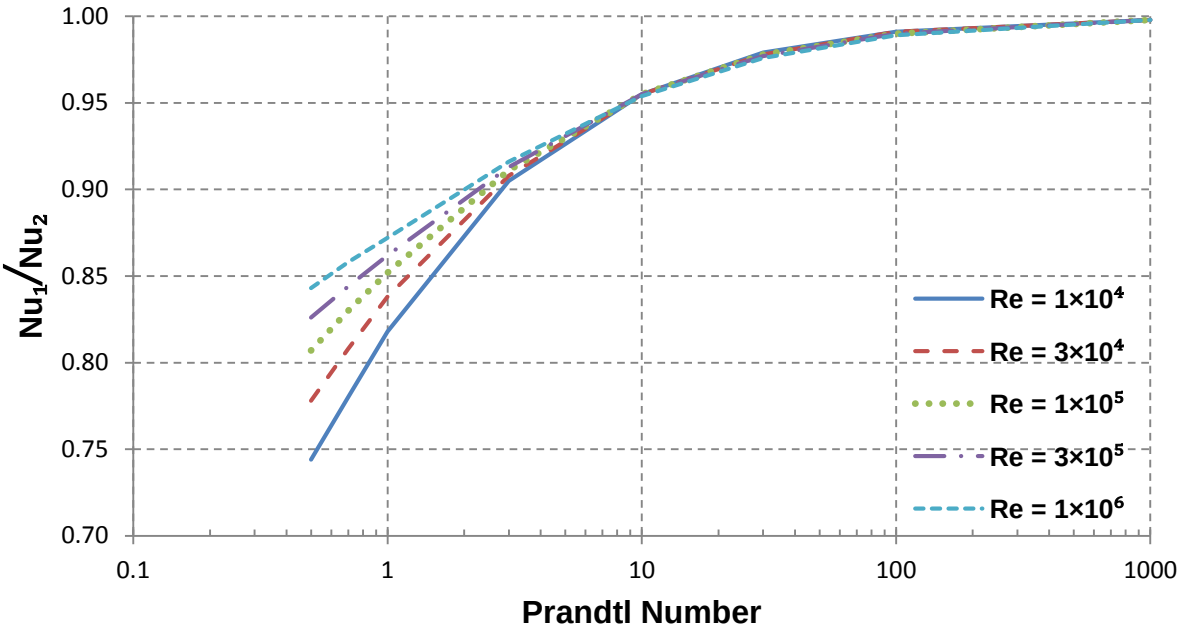

Figure 81: Expected Effect of One-Sided versus Two-Sided Heating for Parallel Plates. Expressed as the ratio of the Nusselt numbers for one-sided heating (Nu_1) and two-sided heating (Nu_2). *Adapted from the tabular results based off the numerical solution of Ref. [123].*

4.4. Experimental Results

All single-phase experiments were conducted using deionized water, with a measured electrical resistivity of ρ>15 MΩ-cm. The water and surface were degassed prior to taking measurements. Tests were conducted for each bulk fluid temperature condition by increasing the mass flux in a step-wise fashion. At each mass flux, sufficient time was taken for the temperature of the system to achieve steady-state conditions. Measurements were recorded for five minutes at each steady-state condition. The local conditions at each thermocouple along the center of the channel were calculated using the methods described in section 3.6. It was noted that for thermocouples near the inlet and outlet of the test section, higher values of the heat transfer coefficient were usually observed, with behavior also being less consistent compared to the middle of the channel. This is likely due to flow development and disturbance near the inlet and outlet, discussed in the following sections. All time-averaged, local heat transfer data for thermocouples displaying fully developed flow behavior are provided in Appendix C.

4.4.1. Friction Pressure Drop

The friction pressure drop along a channel may be expressed as:

$$-\left(\frac{dP}{dz}\right)_{friction} = {}^{1}/_{2}\, f \frac{\rho u_b^2}{D_{hyd}} \tag{92}$$

where f is the Darcy friction factor. In laminar flow, an exact solution for the velocity profile, and therefore the friction factor, is available for circular tubes, parallel plates, and rectangular channels. For circular tubes, the Darcy friction factor for fully developed, laminar flow is:

$$f = \frac{64}{Re} \tag{93}$$

and for parallel plates it equal to:

$$f = \frac{96}{Re} \tag{94}$$

In the case of rectangular channels, the aspect ratio is a relevant parameter in laminar flow, with the analytical solution for the fully developed friction factor being [124]:

$$f = \frac{96}{(1+1/\alpha^*)^2\left[1-\frac{192}{\pi^5\alpha^*}\sum_{n=1,3,\ldots}^{\infty}\frac{1}{n^3}\tanh\left(\frac{n\pi\alpha^*}{2}\right)\right]Re} \tag{95}$$

In our case, the inverse aspect ratio, α^*, is 0.035, and the friction factor for laminar flow is therefore:

$$f = \frac{91.67}{Re} \tag{96}$$

For turbulent flow, circular tube correlations are typically used with the hydraulic diameter in place of the tube diameter. In 1912, Blasius provided the following relation for the fully developed, turbulent friction factor in a smooth tube [125]:

$$f = 0.3164Re^{-0.25} \tag{97}$$

with equation (97) being applicable for turbulent flow with Re>3000.

As noted in section 3.3.2, single-phase friction pressure drop for turbulent flow in rectangular channels may deviate from circular tube predictions significantly, due to the sharp corners found in such channels and the presence of secondary flows. Figure 82 shows an example of the secondary flow profile in a rectangular channel. As discussed in the preceding section, Jones [122] notes that the standard hydraulic diameter does not capture the effect of increasing aspect ratio on friction pressure drop. The turbulent friction factor is known to increase monotonically with increasing aspect ratio when the Reynolds number and hydraulic diameter are kept constant. Jones recommends correlating turbulent friction pressure drop data for rectangular channels with a laminar equivalent diameter and Reynolds number, which are provided in equation (88) and equation (89).

The pressure drop across the channel was measured using the differential pressure transducer. When accounting for the gravity head, the difference between the absolute transducers was in excellent agreement with the differential transducer. The measured friction

factor, based upon measurements with the differential transducer, is plotted in Figure 83. The correlations plotted for laminar and turbulent flow utilize *Re**. Note that the use of 64/*Re** for laminar flow yields an equivalent result to equation (96). The length over which pressure drop was measured likely included the region of developing flow, which may have influenced the results.

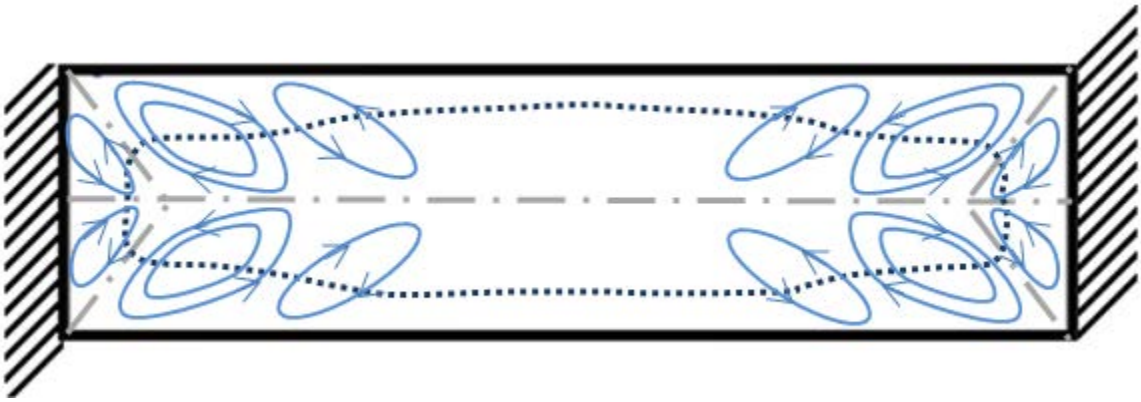

Figure 82: Typical Secondary Flow Profile in a Rectangular Channel. The dark dotted blue line represents an isovelocity line of the primary flow profile (flowing into the page). The light blue lines represent secondary flows, with the flow direction perpendicular to the primary flow.

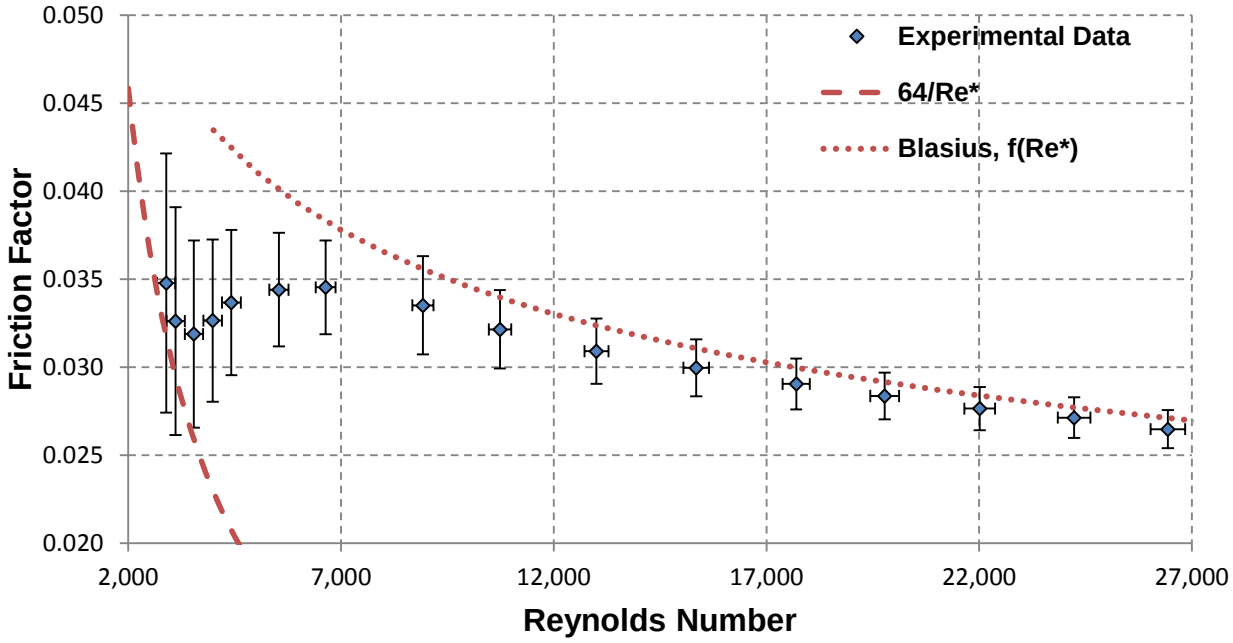

Figure 83: Experimental Friction Factor as a Function of Reynolds Number. The corresponding prediction for laminar flow (analytic result) and turbulent flow (Blasius equation), calculated using *Re, are plotted for comparison.**

4.4.2. Developing Flow (the Entrance Region)

As discussed in chapter 2, few data exist in regards to developing flows in narrow rectangular channels. For hydrodynamic entry lengths in the laminar flow regime, Han [126] approaches the problem analytically, determining a strong dependence of entry length on aspect ratio. From his graphical result, we may infer that for our aspect ratio (α*=0.035) under laminar flow, the hydrodynamic entry length will be:

$$\frac{L_{hyd}}{D_{hyd}} = 0.0133Re \tag{98}$$

Thermal entry lengths for laminar flow also depend on the Prandtl number, and may be significantly greater for the conditions of this study. The thermal entry length for laminar flow is typically related using the dimensionless distance z*, which is defined as:

$$z^* = \frac{z_H/D_{hyd}}{RePr} \tag{99}$$

For thermally developing laminar flow between parallel plates (that is fully developed hydrodynamically) the dimensionless thermal entry length will be:

$$\frac{L_{th}}{D_{hyd}} = 0.01154RePr \tag{100}$$

where the uniform heat flux boundary condition is assumed. Therefore, at a Prandtl number of 5.4 and Reynolds number of 2000, the thermal entry length is estimated to be 125 L/D_{hyd} from the start of heating. The local Nusselt number for thermally developing laminar flow with the uniform heat flux boundary condition may be estimated using the following empirical equations [127]:

$$Nu(z) = \begin{cases} 1.490z^{*-1/3} & for\ z^* \le 2\times10^{-4} \\ 1.490z^{*-1/3} - 0.4 & for\ 2\times10^{-4} < z^* \le 1\times10^{-3} \\ 8.235 + 8.68[10^3 z^*]^{-0.506}e^{-164z^*} & for\ z^* > 1\times10^{-3} \end{cases} \tag{101}$$

For turbulent flow, Levy [47] noted thermal entry lengths of 40 to 60 L/D_{hyd} in his experiments, which is similar to the circular tube prediction.

In this study, it was not possible to measure values very close to start of heating. In addition, the developing length is strongly dependent on the inlet configuration and heating boundary condition (e.g. uniform heat flux, uniform temperature). Therefore, results for thermal developing lengths for the experimental facility may not be directly applicable to the MITR coolant channel, for reasons previously discussed. Nonetheless, measurements were made to estimate the developing length for laminar, transition, and fully turbulent flow. It should be noted that in addition to an entry length, an "exit length" was also observed, likely due to flow disturbance at the end of the channel due to the transition between the narrow rectangular channel and circular tubing.

As the vortex meter is not functional at low flows, flow rate for laminar conditions was measured by diverting flow through the dissolved oxygen measurement loop and taking a visual reading off the rotameter. Therefore, laminar heat transfer tests were limited to low bulk fluid temperature and the resulting uncertainty in the flow rate, and in turn the Reynolds number, is high. Results of one such experiment are provided in Figure 84, illustrating the long thermal development length under laminar flow conditions, even at low Reynolds number. The fully developed Nusselt number values for laminar flow between parallel plates are:

$$Nu = \begin{cases} 5.385 & for\ q_1'' = const., q_2'' = 0 \\ 8.235 & for\ q_1'' = q_2'' = const. \end{cases} \quad (102)$$

where the subscripts 1 and 2 denote wall 1 and 2, respectively. Since the flow configuration in this study is vertically upward, natural convection may contribute to overall heat transfer at very low Reynolds numbers, leading to mixed convection. This may explain the slightly higher than expected Nusselt number values reported in Figure 84.

Flow development at the lower end of the transition regime is depicted in Figure 85. For the turbulent flow regime (Figure 86), flow appears fully developed by about 50 L/D_{hyd}. Recall that heat transfer under fully developed conditions is most limiting and independent of inlet configuration, and is therefore the desired value in this study. The channel pressure drop is increased by the entrance region, requiring additional pumping power, but once again is specific to the inlet configuration.

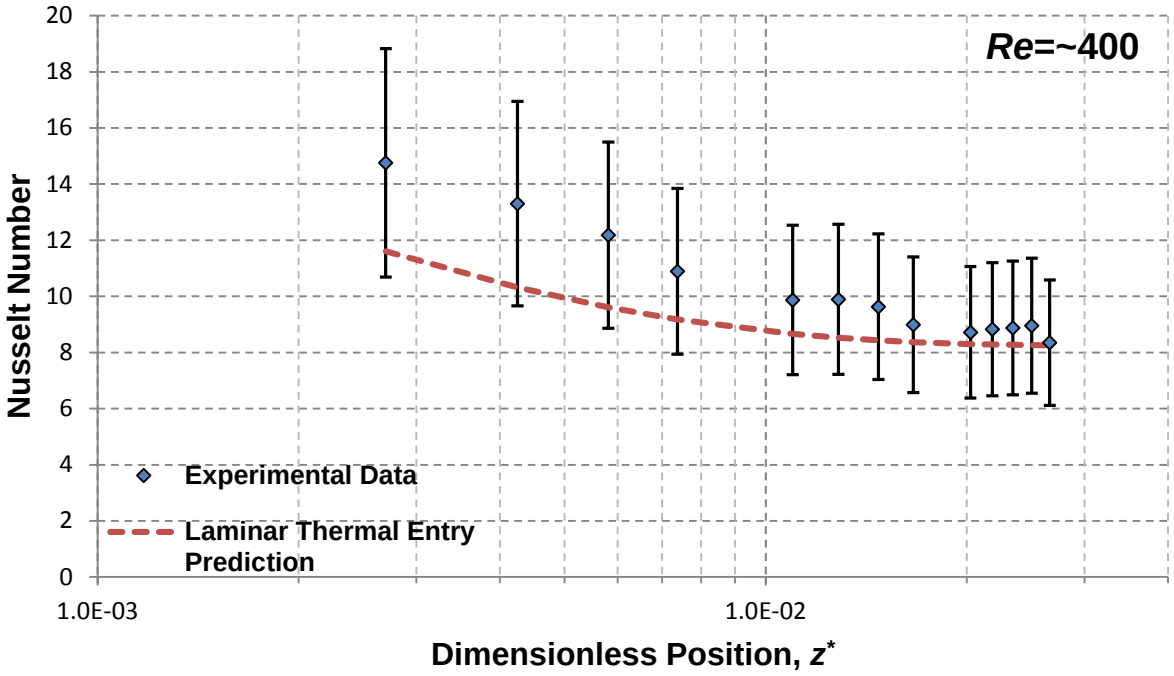

Figure 84: Local Nusselt Number versus Dimensionless Position from Start of Heating for Laminar Flow. The Reynolds number is estimated by diverting flow through the DO Loop and using the rotameter for flow measurement. The prediction plotted is from equation (101).

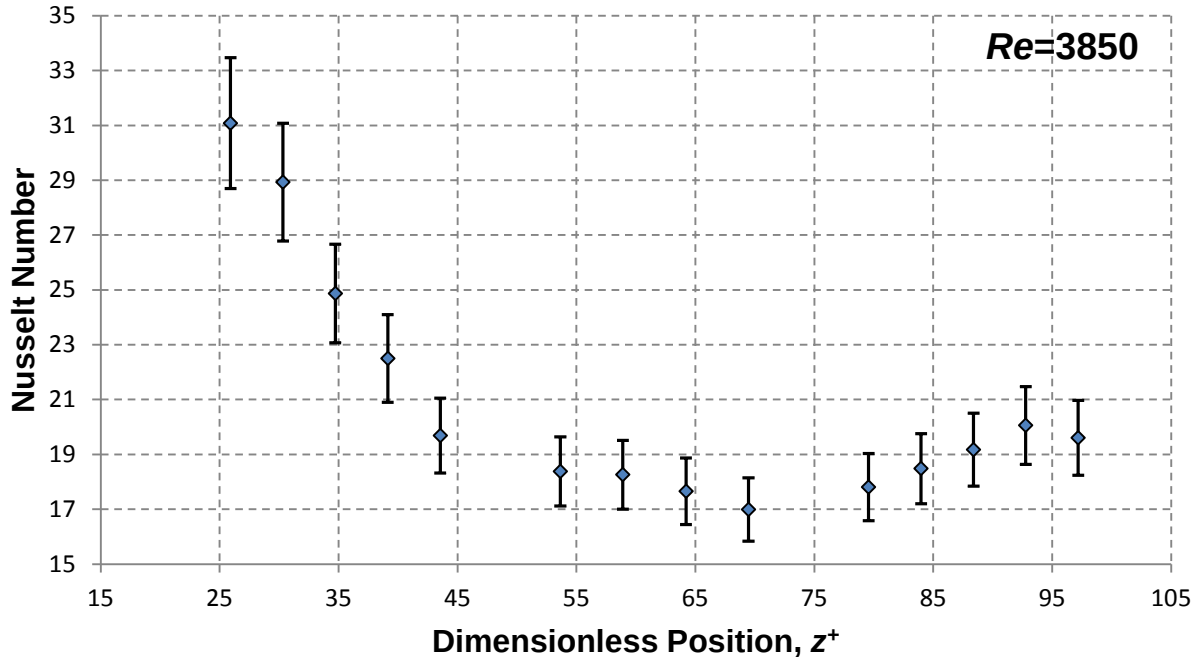

Figure 85: Local Nusselt Number versus Dimensionless Position from Channel Inlet for Re_{avg}=3850 and Pr_{avg}=5.44.

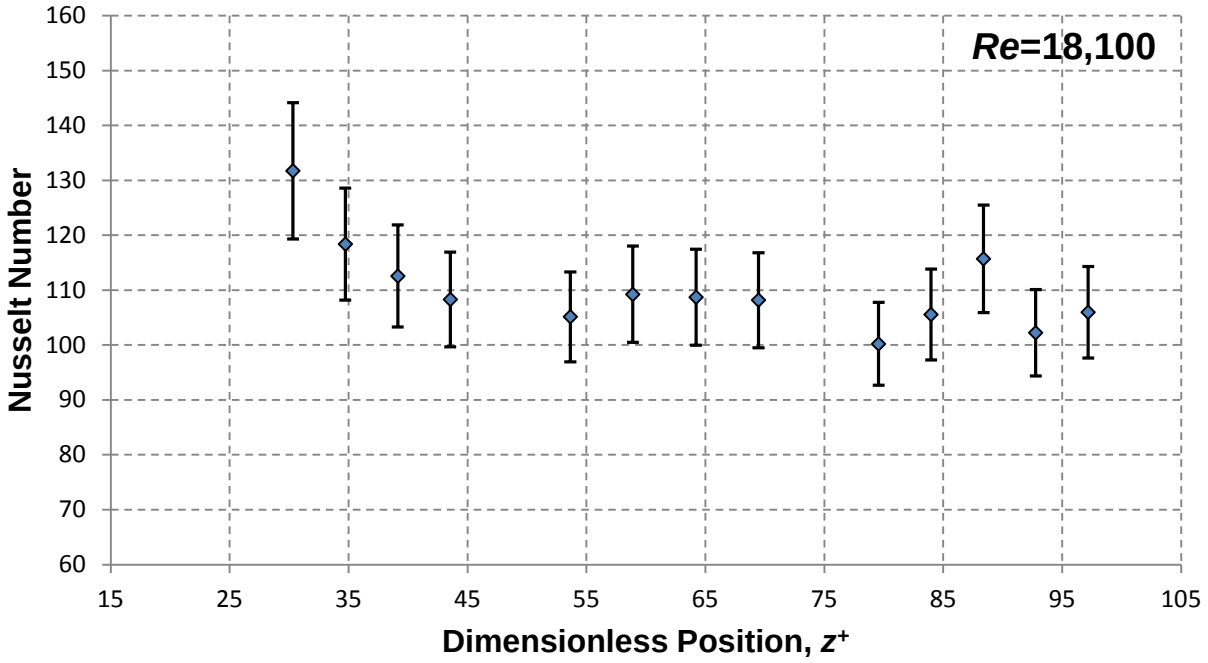

Figure 86: Local Nusselt Number versus Dimensionless Position from Channel Inlet for Re_{avg}=18,100 and Pr_{avg}=4.37. No conclusions can be drawn in regard to the entry length, though the flow appears to be fully developed by the middle of the channel.

4.4.3. Low Reynolds Number (Re<10,000) Results

Under normal operating conditions, flow in the MITR for both the existing finned and proposed unfinned channels is expected to be fully turbulent, with *Re*>13,500, based upon the total core flow rate and flow area provided in the Safety Analysis Report [17]. However, lower flow conditions (*Re*<10,000) are relevant to transients, such as loss of flow (LOF) accidents. The critical Reynolds number, below which the flow remains laminar, depends on a number of factors in rectangular channels, including aspect ratio and entrance configuration. Reported lower limits of the critical Reynolds number from the literature are listed in Table 33. Note that flow may remain laminar to much higher *Re* under appropriate conditions, and Table 33 represents measured lower limits from the literature. The configuration of the experimental test section in this study most closely corresponds to the smooth entrance, whereas an actual channel in the MITR corresponds to the abrupt entrance.

Table 33: Lower Limits of the Critical Reynolds Number for Rectangular Channels. Note that α^*=0 corresponds to parallel plates. Recall that for this study, α^*=0.035. *Adapted from Ref. [73].*

Entrance Configuration	α^*	Re_{crit}
Smooth Entrance	0	3400
	0.1	4400
	0.2	7000
Abrupt Entrance	0	3100
	0.01	2920
	0.2	2500

For this study, measurements with *Re*<2200 were not practical due to range limitations of the flow meter. However, measurements were obtained for flows as low as *Re*≈3800 for the heat transfer coefficient and ≈2900 for the friction factor. From the friction factor data in Figure 83, the critical Reynolds number in this study falls between 3500 and 4000, or:

$$Re_{crit} = 3500\ to\ 4000 \tag{103}$$

which is consistent with the values reported in Table 33. The friction factor data also indicate that flow does not become fully turbulent until *Re*≳7000.

The fully developed, single-phase heat transfer results for *Re*<10,000 are summarized in Figure 87 for the range of Prandtl numbers tested in this study. Even at the low end of the flow range, measured Nusselt numbers were quite repeatable. The Gnielinski correlation, which is considered applicable as low as *Re*=2100, is also plotted for comparison at the highest and lowest Prandtl number. Note that the measured values in this range are, on average, 10.3% higher than that predicted by the Gnielinski correlation. Below *Re*=4000, the Gnielinski correlation for *Pr*=5.4 (top curve) over predicts the Nusselt number by about 40% possibly indicating that the flow is still laminar in this region. Therefore, for conservatism, the laminar flow heat transfer prediction for rectangular channels should be used for *Re*<4000, while the Gnielinski correlation may be used as a conservative estimate for 4000<*Re*<10,000.

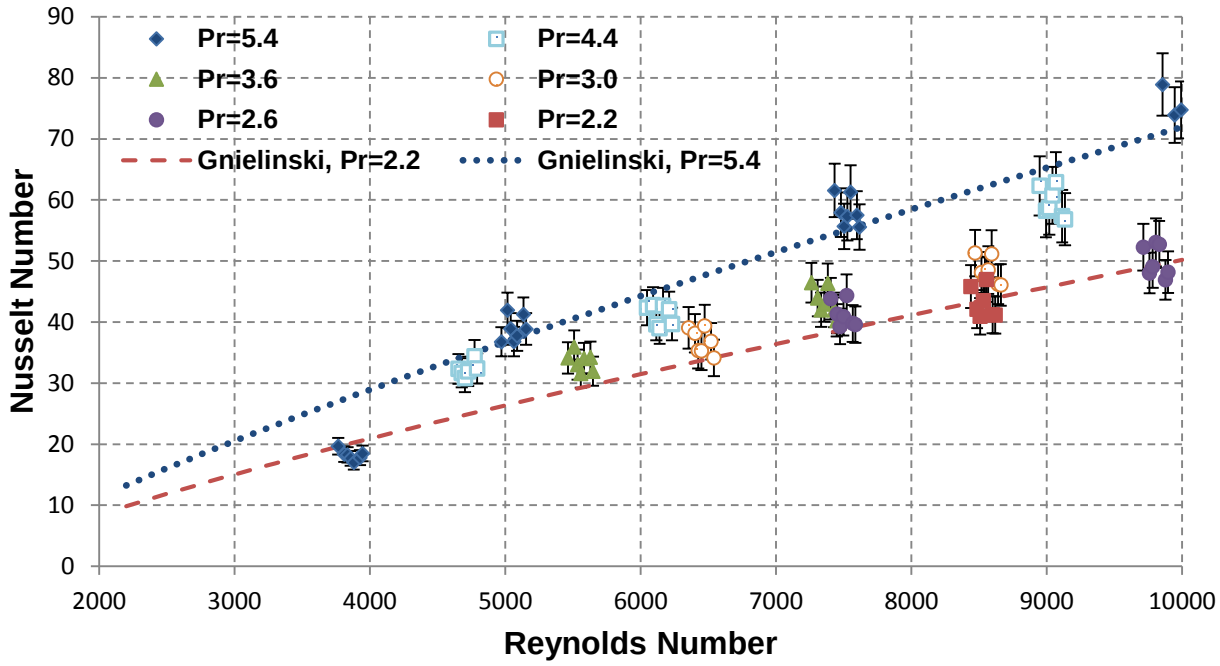

Figure 87: Local Fully Developed Nusselt Number Results in the High Aspect Ratio, Narrow Rectangular Channel Heated on One Side for *Re*<10,000.

4.4.4. Fully Turbulent Flow, Re>10,000

Results are presented below in Figure 88 through Figure 93 for all cases with *Re* is greater than 10,000. Each data point represents the average Nusselt number of locations experiencing fully developed flow conditions. Error bars represent 95% confidence limits for each measurement. Uncertainty in the Reynolds number was also accounted for, but is small and not shown for clarity. Six bulk temperature conditions were tested, consisting of Pr_{avg}=5.4 (T_b≈30 °C), Pr_{avg}=4.4 (T_b≈40 °C), Pr_{avg}=3.6 (T_b≈50 °C), Pr_{avg}=3.0 (T_b≈60 °C), Pr_{avg}=2.6 (T_b≈70 °C), and Pr_{avg}=2.2 (T_b≈80 °C). Recall that under normal operation, the typical *Pr* number in the MITR is between 2.98 and 4.15.

Up to a Reynolds number of 30,000, the measured Nusselt number is consistently higher than that predicted by the Dittus-Boelter equation, by ~5-10%. However, this trend decreases as Prandtl number decreases (increasing fluid temperature), likely due to the larger influence of one-sided versus two-sided heating, as described earlier in Figure 81 for the case of parallel plates. It is also important to note that most data collected for *Re*>30,000 was for lower Prandtl numbers, due to the viscosity reduction resulting in a higher Reynolds number for a given mass

flux. The uncertainty in the measured Nusselt number was also higher at these conditions, due to the smaller temperature rise from the inlet to the outlet and between the bulk fluid and the surface.

Nonetheless, the trend of a lower Nusselt number above *Re*=30,000 is consistent with that reported in Table 31, if the one-sided heating condition is taken into account. The analytic study of Barrow [118] determines a similar trend with respect to the Dittus-Boelter equation for *Re*>30,000. This may also explain the recommendation of the Phillips Reactor Safeguard Committee to use the modified Colburn equation in the Materials Testing Reactor, and its adoption for the High Flux Beam Reactor's safety analysis. The average coolant channel velocity in the Materials Testing Reactor and High Flux Beam Reactor were 30 ft/sec (9.14 m/sec) and 35 ft/sec (10.67 m/sec), respectively [128, 129].

While most channels in the MITR are heated on both sides, the side channels, heated on one side only, are often limiting in that they experience peak flux values. Therefore, these single-phase results represent the limiting case. When estimating turbulent single-phase heat transfer rates for a similar channel heated on both sides, Figure 81 should be consulted, with the Prandtl number taken into account.

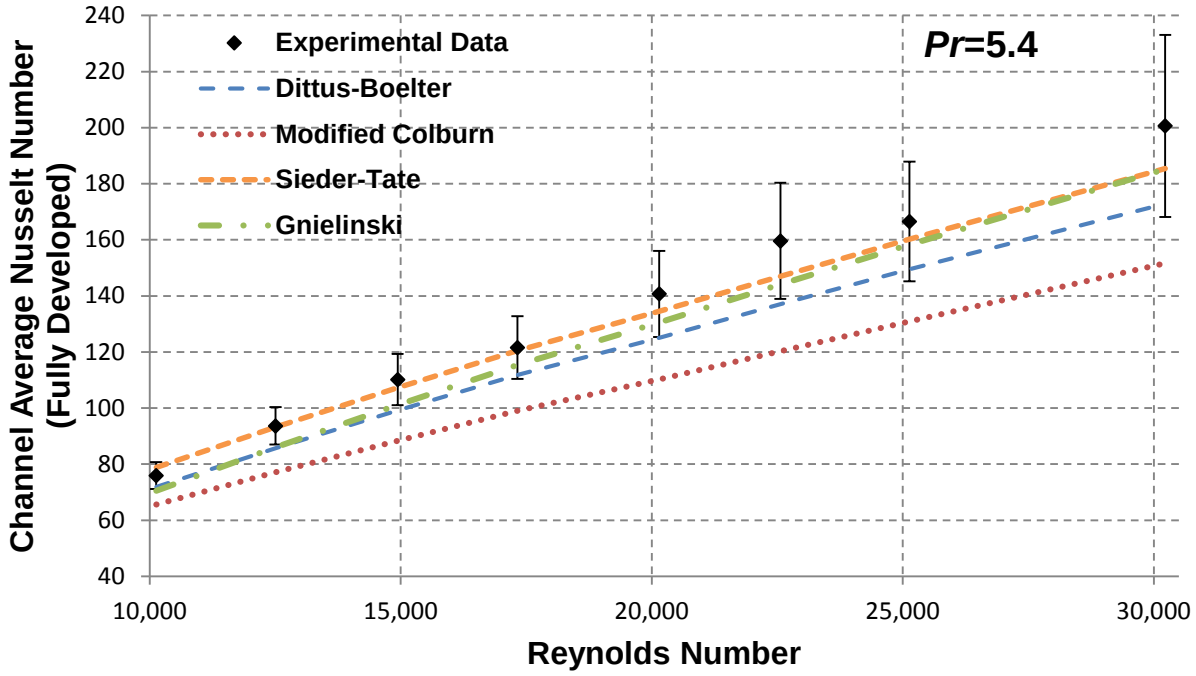

Figure 88: Fully Developed, Average Channel Nusselt Numbers for *Pr*=5.4 in a High Aspect Ratio, Narrow Rectangular Channel Heated on One Side.

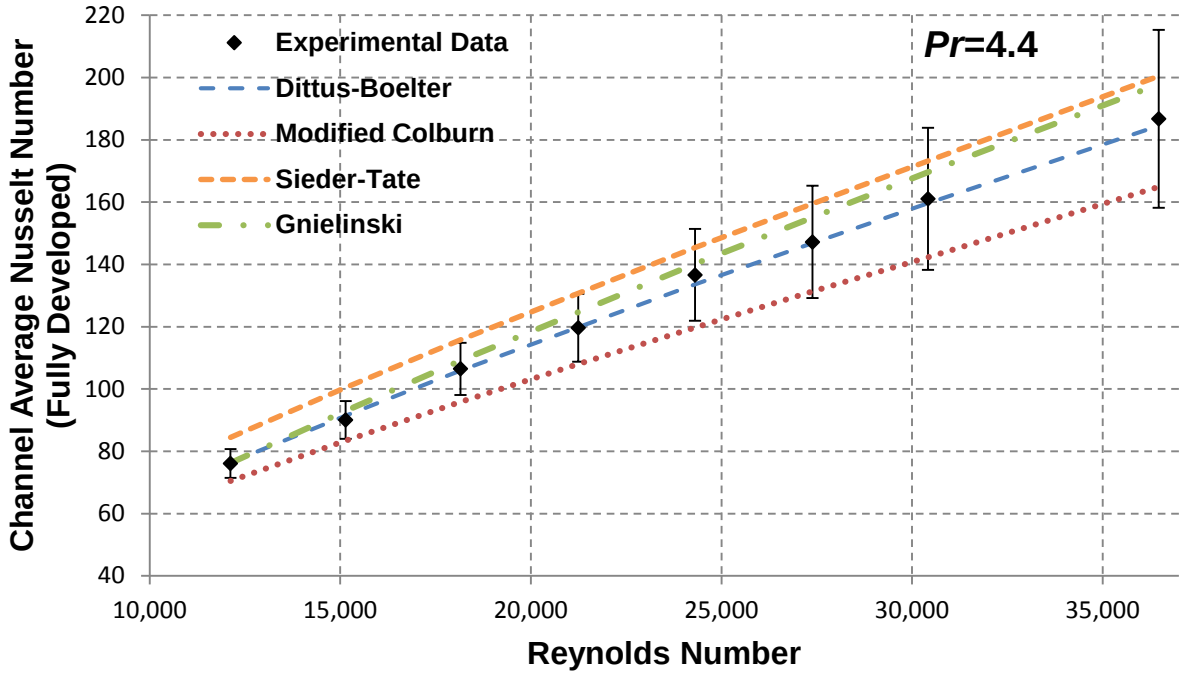

Figure 89: Fully Developed, Average Channel Nusselt Numbers for *Pr*=4.4.

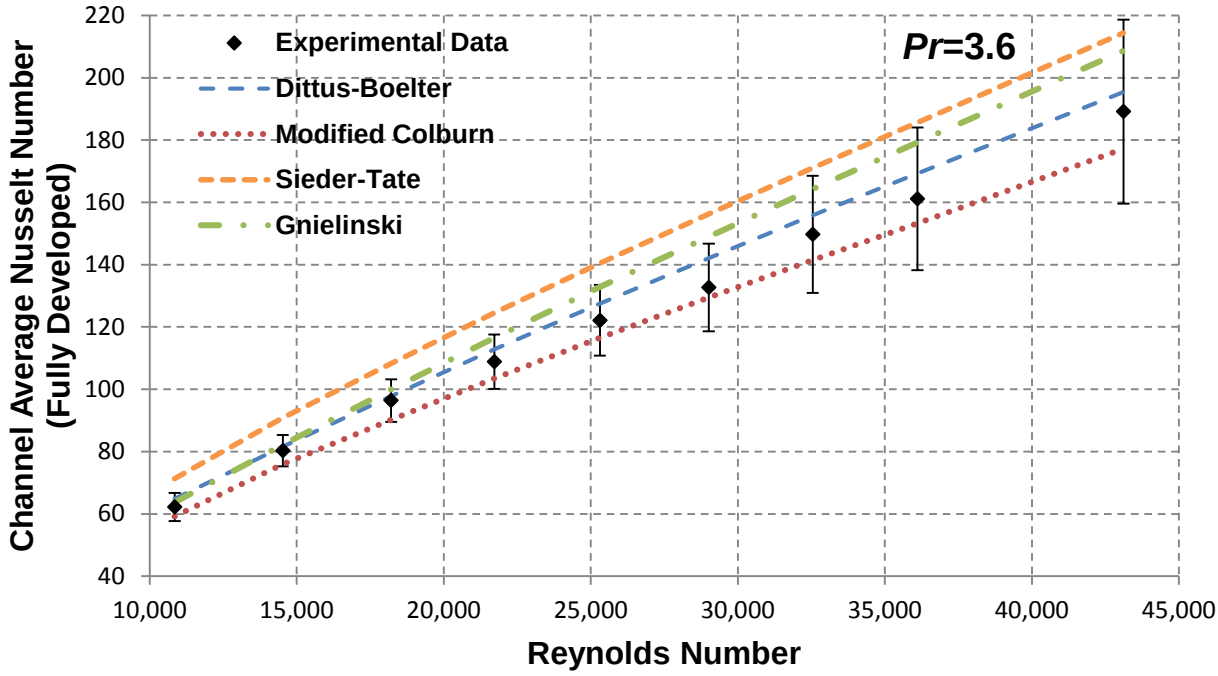

Figure 90: Fully Developed, Average Channel Nusselt Numbers for *Pr*=3.6.

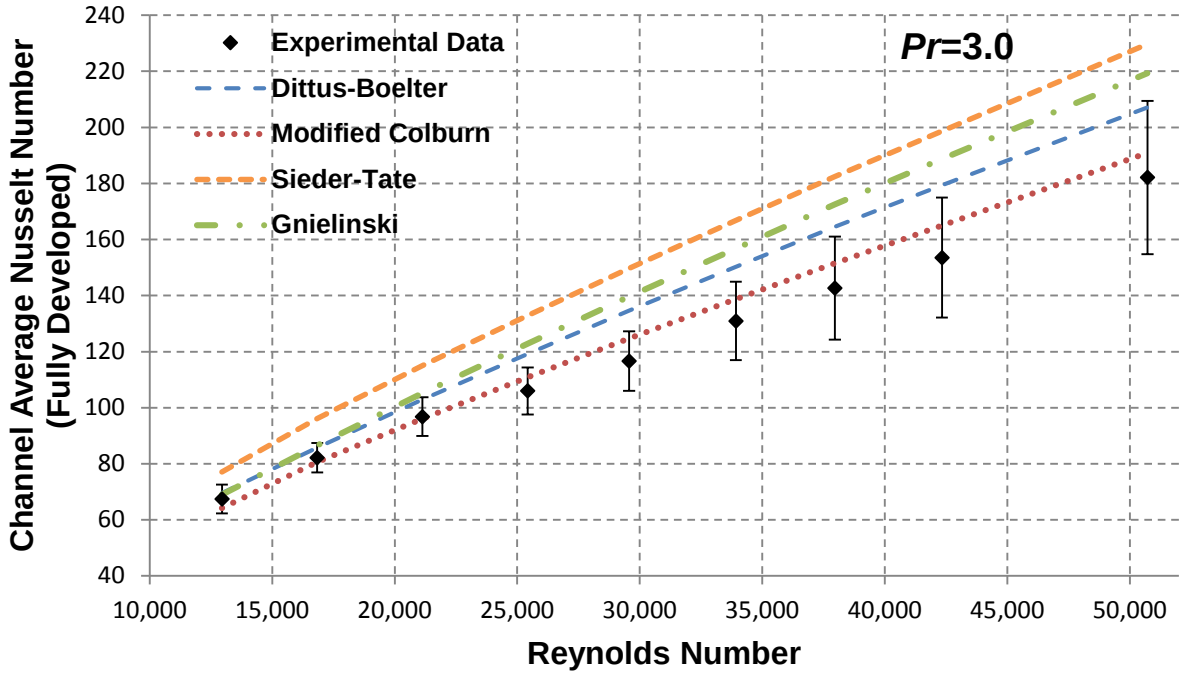

Figure 91: Fully Developed, Average Channel Nusselt Numbers for *Pr*=3.0.

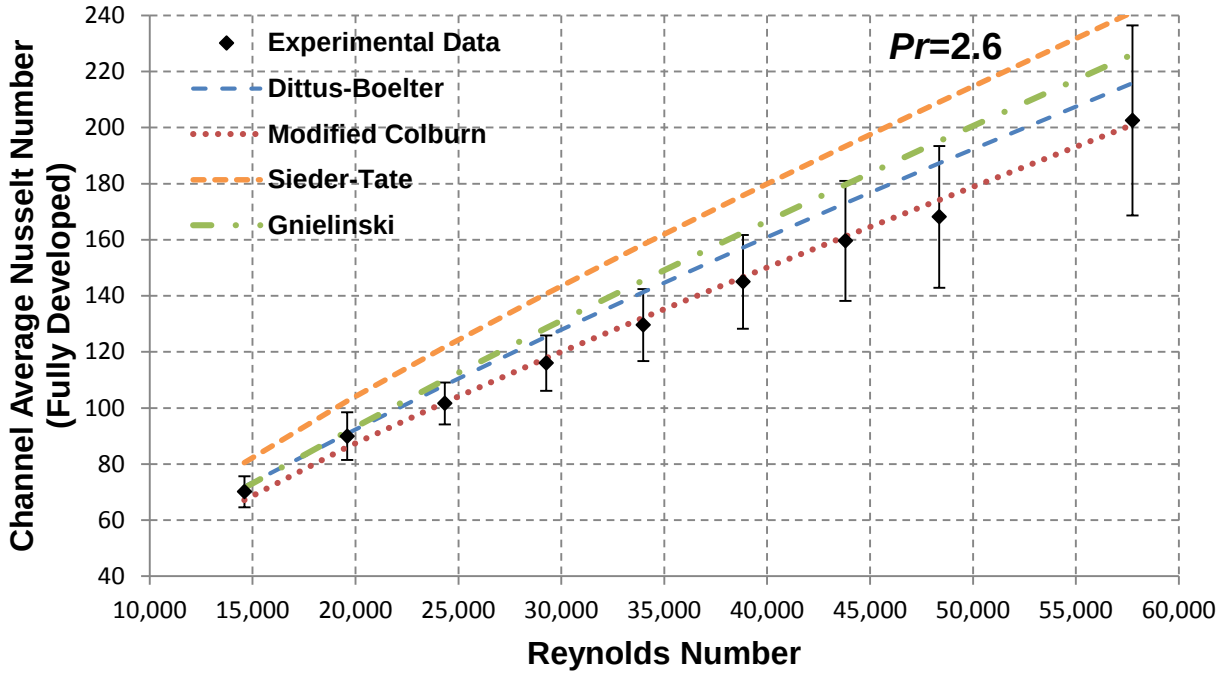

Figure 92: Fully Developed, Average Channel Nusselt Numbers for *Pr*=2.6.

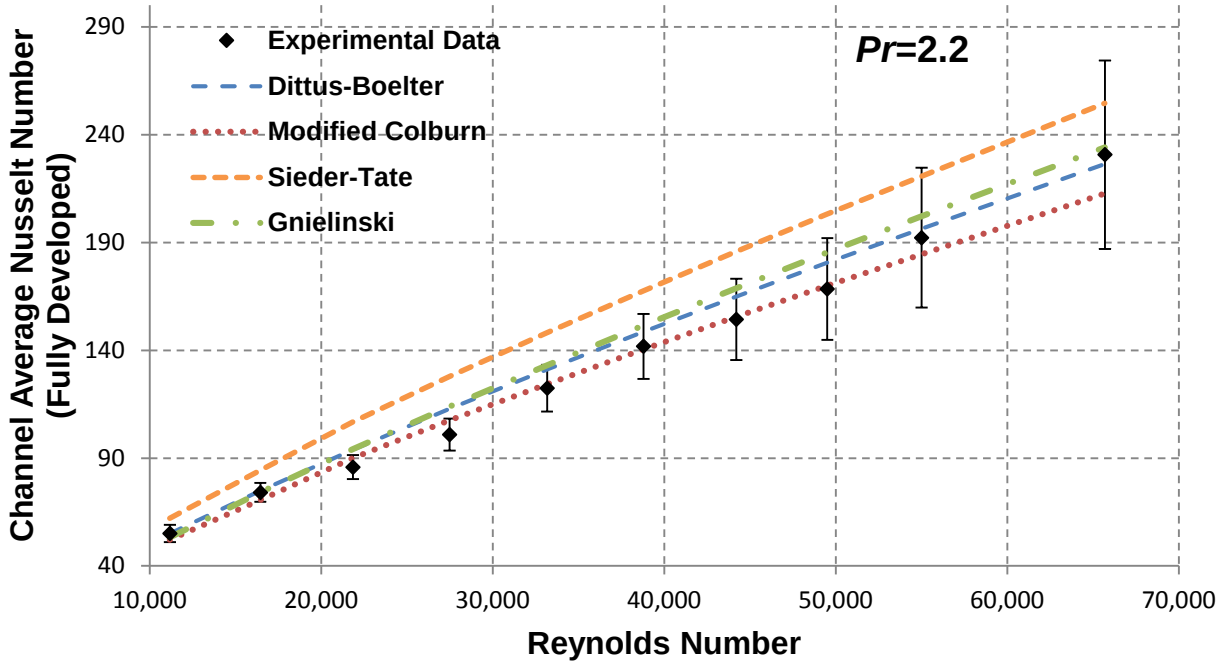

Figure 93: Fully Developed, Average Channel Nusselt Numbers for *Pr*=2.2.

While the relationship between the Nusselt number and Prandtl number is complicated by the asymmetric heating condition, it is still useful to summarize all data relative to the Dittus-Boelter equation, which has been the default single-phase heat transfer correlation for calculation in the MITR. All data for fully developed conditions with Re>10,000 are plotted in Figure 94, normalized by $Pr^{0.4}$.

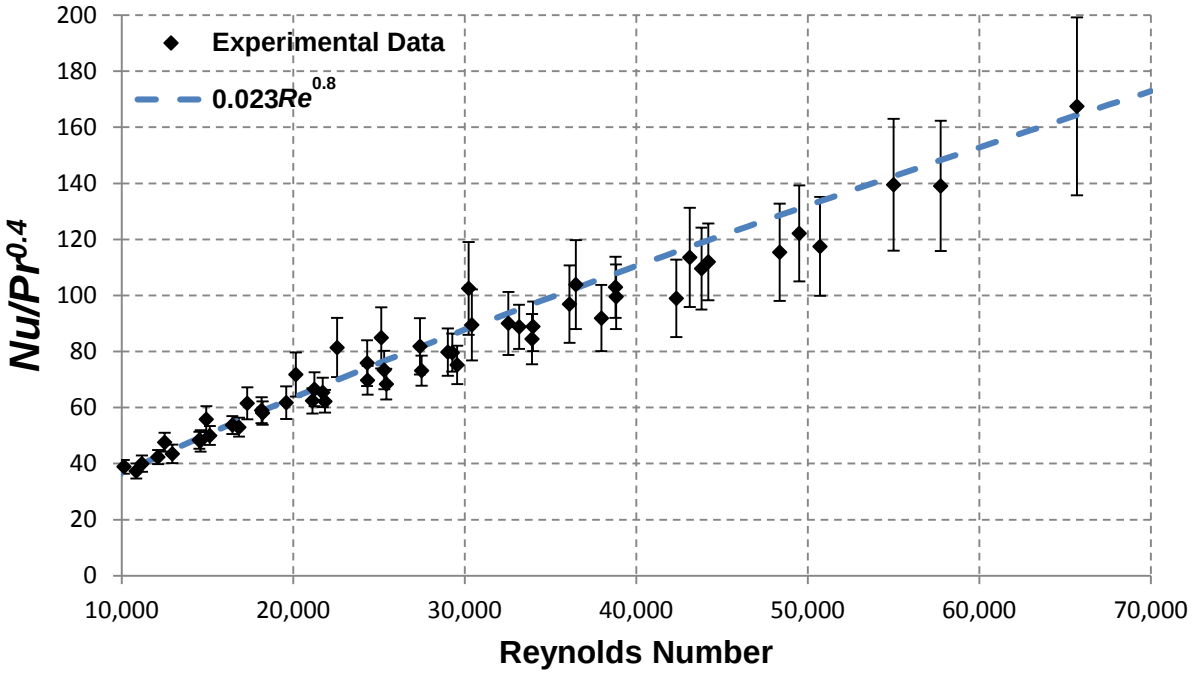

Figure 94: Summary of Experimental Data for Re>10,000 Normalized by $Pr^{0.4}$. The Dittus-Boelter equation is plotted for comparison. Note that prior studies for parallel plates indicate that the behavior with Prandtl number is more complicated than $Pr^{0.4}$, and that the asymmetric (one-sided) heating in this study influences the Prandtl number dependence.

4.5. Development of a Single-Phase Heat Transfer Correlation

The expected Reynolds number range for the proposed unfinned coolant channels in the MITR is 13,500 to 26,700 under normal operating conditions. Therefore, there is utility in developing a single-phase heat transfer correlation for this range. For simplicity, any correlation relying on bulk properties alone is considered more desirable; therefore any dependence on the film temperature or wall viscosity is omitted. While modern single-phase heat transfer correlations have moved away from simple power law dependencies on the Reynolds and Prandtl numbers, the correlation being considered here is only intended for application over a narrow range. Therefore, a power law relation is utilized. Considering that for one-sided heating the behavior of the Nusselt number with Prandtl number is somewhat complex, neither a $Pr^{1/3}$ nor a $Pr^{0.4}$ dependence are assumed. Therefore, a two-dimensional fit to data is required to determine the constants *a*, *b*, and *c* such that:

$$Nu = cRe^{a}Pr^{b} \tag{104}$$

The method of weighted least squares can be applied in two-dimensions, where an appropriate weight must be assigned to each measurement. The uncertainty in *Re* and *Pr* will be treated as small compared to that in *Nu*. While the inverse of the variance is typically used as the weighting factor in statistics, here individual measurements are used to construct the fitted surface, where variances for each individual measurement are not well defined. Therefore, the relative weights associated with each measurement, Nu_i, will be defined using the measurement uncertainty of that datum, such that:

$$w_i = \frac{1}{\left(\varepsilon_{Nu_i}/_{Nu_i}\right)} \tag{105}$$

Therefore, a datum with lower associated fractional measurement uncertainty will more heavily influence the fit. For example, any two measurements with the same fractional uncertainty, say 10% of the measured value, will weigh equally in the fitted correlation, whereas a measurement

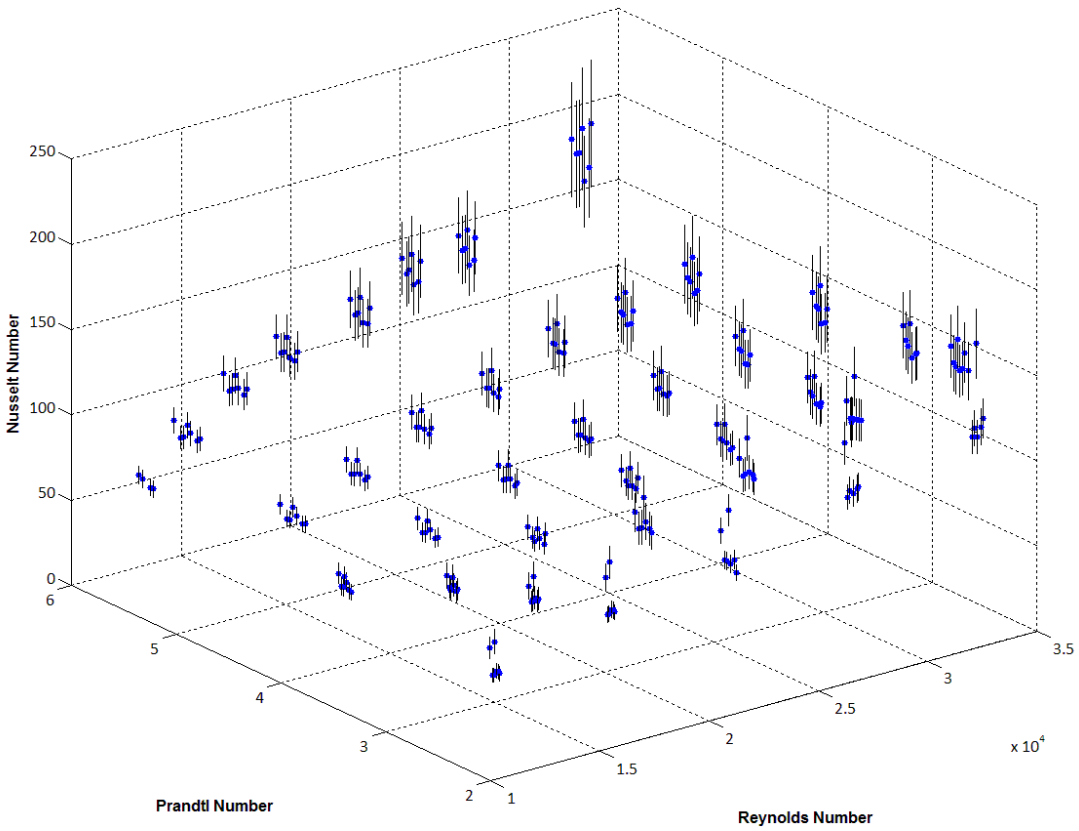

Figure 95: Data Used for Fitting the Single-Phase Correlation with Measurement Error Provided.

with 20% uncertainty will carry half the weight of the measurements with 10% uncertainty. Though this addresses the issue of data of varying quality, it does not remedy the issue of outliers. Here an outlier is described as a datum showing an unusual deviation from similar measurements that is not explained by the measurement uncertainty. Least squares methods are highly sensitive to outliers, since the objective is to minimize the square of the residual. The statistical test proposed by Peirce [130] is one method to quantitatively identify outliers, but it was not used here.

Instead, a robust least squares regression method was utilized to reduce the effect of outlying data. A three-dimensional plot of the data used for the fit, with error bars representing measurement uncertainty (95% confidence) is shown in Figure 95. A surface fit to the data yields the following correlation:

$$Nu = 0.0242 Re^{0.775} Pr^{0.548} \tag{106}$$

for $10{,}000 \leq Re \leq 35{,}000$ and $2.2 \leq Pr \leq 5.5$

which is applicable for fully developed flow at the center of a rectangular channel with $\alpha^* \approx 0.35$, heated on one side with uniform heat flux. Equation (106) should not be used outside of the specified *Re* and *Pr* range for which it was fit, since the data here and in other studies in the literature indicate a simple power law is not adequate for describing the behavior of *Nu* over a broader range in such channels. The surface of equation (106) with corresponding data is shown in Figure 96, and a contour plot is shown in Figure 97. The residuals are plotted in Figure 98.

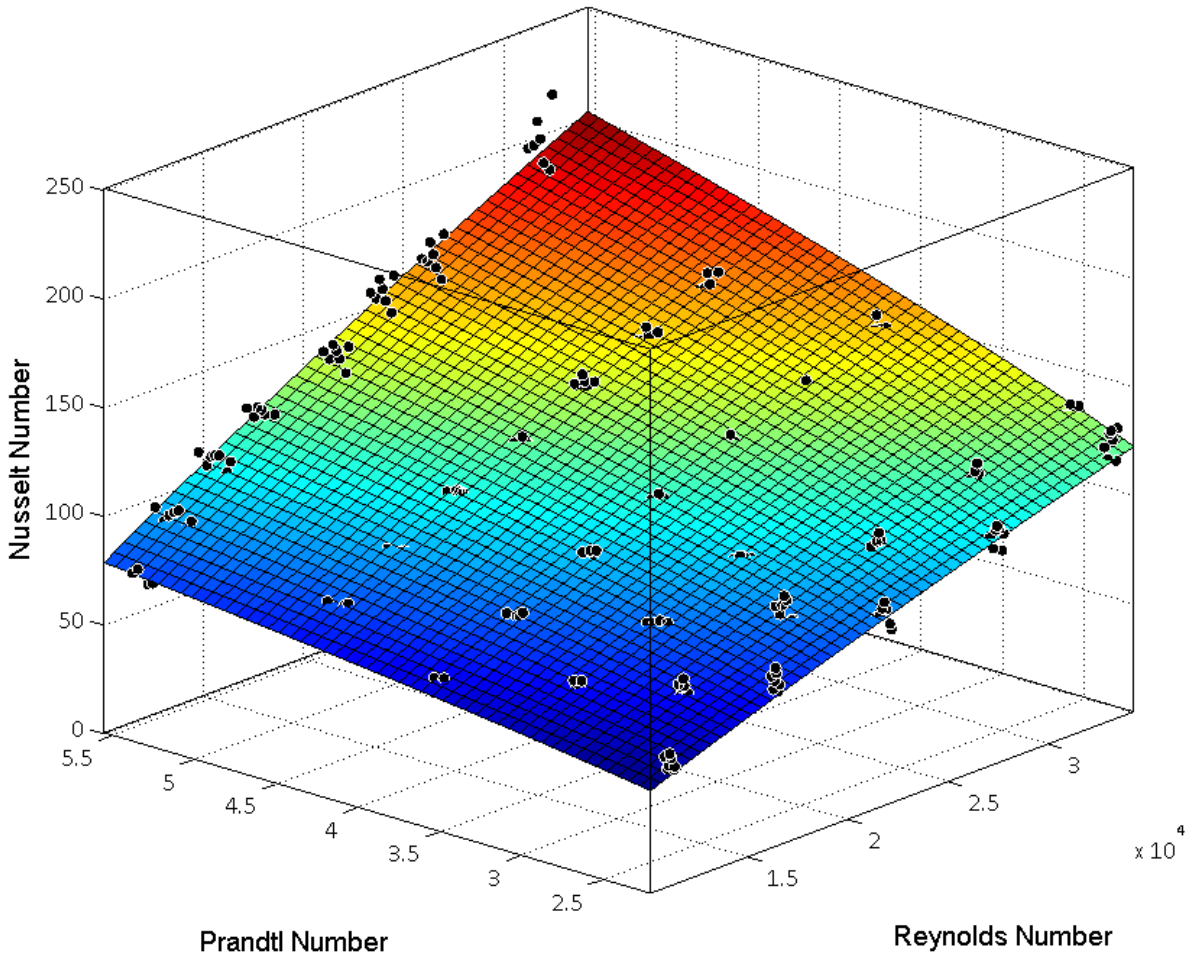

Figure 96: Fitted Surface to Experimental Data for a Fully Developed Flow in a High Aspect Ratio Channel Heated on One Side with Constant Heat Flux Surface Condition. The fitted surface is represented by the equation $Nu=0.0242Re^{0.775}Pr^{0.548}$. The corresponding data range is $10{,}000 \le Re \le 35{,}000$ and $2.2 \le Pr \le 5.5$. The fit was performed using the method of weighted least squares, with the associated coefficient of determination being $R^2=0.9997$.

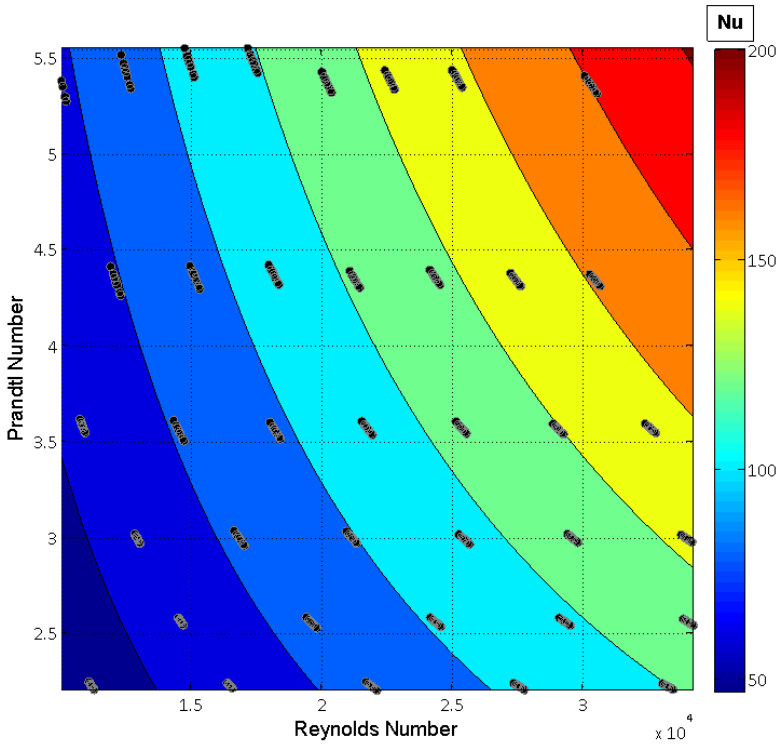

Figure 97: Contour Plot of Nusselt Number versus Reynolds and Prandtl Numbers. Each contour line represents a change in the Nusselt number of 10.

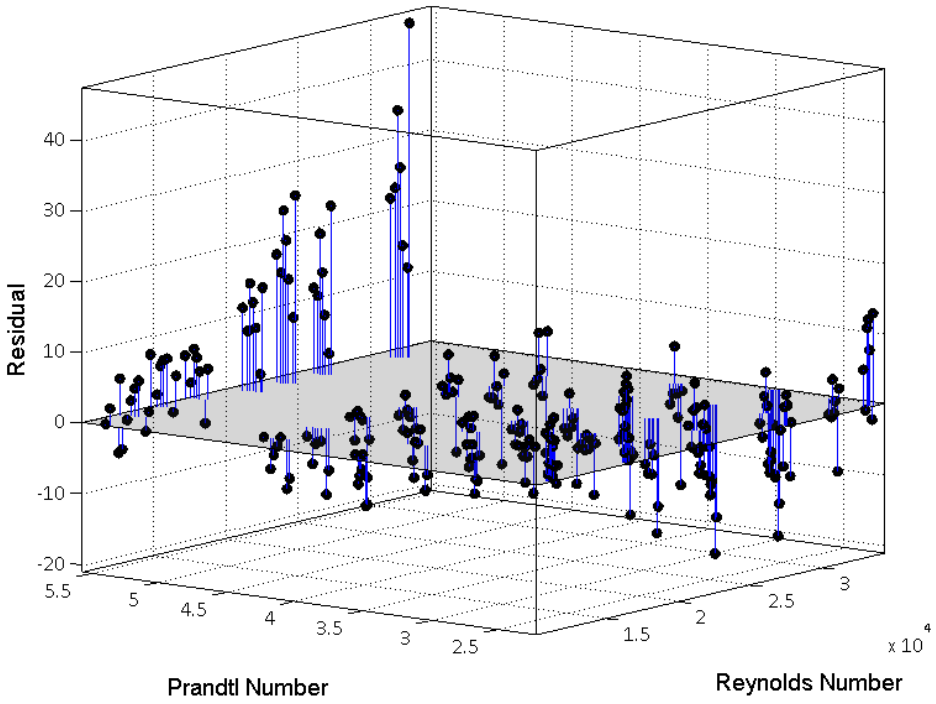

Figure 98: Plot of Residuals for the Fitted Curve in Figure 96.

In order to determine the relative performance of single-phase heat transfer correlations for the channel in this study, the mean absolute error (MAE) percentage can be used as a basis for comparison. The mean absolute error percentage for the single-phase data will be defined as:

$$MAE(\%) = \frac{1}{N}\sum_{i=1}^{N}\frac{\left|Nu_{i,expt} - Nu_{i,corr}\right|}{Nu_{i,expt}} \times 100 \tag{107}$$

where *N* is the number of data points. Note that this does not account for the weights associated with the data. Using the averaged data at each Reynolds and Prandtl number, the proposed correlation shown in equation (106) yields a mean absolute error of 3.6%. The results for all correlations are summarized in Table 34.

As seen in the Table the next best performer is the Petukhov correlation, followed by the Gnielinski correlation. However, the Gnielinski correlation is also applicable through the transition region, and conservatively predicts the Nusselt number down to *Re*=4000 (refer to Figure 87). Therefore, the Gnielinski correlation appears to be an adequate choice for predicting single-phase heat transfer in the case of one-sided heating with uniform heat flux from $4000 \leq Re \leq 35{,}000$ if use of an existing correlation is preferred.

While data was only collected for the case of one-sided (asymmetric) heating with uniform surface heat flux, there is desire to extend the empirical result to the case of two-sided heating. As discussed in section 4.3, the case of one-sided heating is expected to yield a lower Nusselt number than if both sides were heated with uniform heat flux. Therefore, it may be more appropriate to formulate the Nusselt number as:

$$Nu = \boldsymbol{f}(Re, Pr, \gamma) \tag{108}$$

where γ is the surface heat flux ratio at the boundaries of the channel. The surface heat flux ratio is defined relative to a reference wall such that:

$$\gamma = \frac{q''_w}{q''_{w,ref}} \tag{109}$$

Table 34: Summary of Mean Absolute Errors of Various Correlations in Predicting the Single-Phase Data of This Study. The range of *Re* and *Pr* for which the MAE is calculated is provided.

CORRELATION	EQ.	*Re* RANGE	*Pr* RANGE	MAE
Dittus-Boelter (McAdams)	(73)	10,000-35,000	2.2-5.5	6.0%
Modified Colburn	(77)	10,000-35,000	2.2-5.5	8.6%
Sieder and Tate	(78)	10,000-35,000	2.2-5.5	13.6%
Petukhov	(79)	10,000-35,000	2.2-5.5	10.3%
Gnielinski	(81)	10,000-35,000	2.2-5.5	7.1%
Sparrow and Cur	(85)	10,000-35,000	2.2-5.5	6.5%
Barrow	(86)	10,000-35,000	2.2-5.5	10.8%
Fitted Empirical Correlation	(106)	10,000-35,000	2.2-5.5	3.6%
Analytically Derived Correlation	(151)	10,000-35,000	2.2-5.5	4.5%

By definition, the Nusselt number of the specified wall is:

$$Nu_w = \frac{q''_w D_{hyd}}{k(T_w - T_b)} \tag{110}$$

It is important to recall that the bulk fluid temperature, T_b, is the mean temperature based upon the energy balance, such that:

$$T_b = \frac{\int \rho u c_p T dA_{flow}}{\bar{\rho} u_b \bar{c_p} A_{flow}} \tag{111}$$

and if the flow is incompressible, then the bulk, or mean, flow velocity in the axial direction is simply:

$$u_b = \frac{\int u dA_{flow}}{A_{flow}} \tag{112}$$

For flow at high Reynolds numbers, the thermal boundary layer may be characterized in a manner similar to the velocity boundary layer, with distinct regions near the wall. The thermal wall layer will only display universal properties if it is within the velocity wall layer, which is the case when $Pr \gtrapprox 0.5$ [131]. In determining the temperature profile in the wall layer, Schlichting uses an analogy to the friction relation for the wall layer to obtain the following result for the Stanton number [132]:

$$St = \frac{Nu}{RePr} = \frac{C_f/2}{\kappa/_{\kappa_\theta} + \sqrt{C_f/2}\psi_\theta(Pr)} \tag{113}$$

The Nusselt number may therefore be written as:

$$Nu = \frac{\frac{1}{2}C_f RePr}{\kappa/_{\kappa_\theta} + \sqrt{C_f/2}\psi_\theta(Pr)} \tag{114}$$

Here C_f is the skin friction coefficient, which is defined as:

$$C_f = \frac{\tau_w}{\frac{1}{2}\rho u_b^2} \tag{115}$$

The Darcy friction factor is simply four times the skin friction coefficient:

$$f = 4C_f \tag{116}$$

The von Kármán constant, κ, has been empirically determined from numerous experiments and is considered to be universal, with:

$$\kappa = 0.41 \tag{117}$$

The constant κ_θ is unnamed but is the thermal wall layer analog to the von Kármán constant in the friction law, with the value of 0.47 being typical. The turbulent Prandtl number, Pr_t, is defined as the ratio of the eddy diffusivity for momentum to the eddy diffusivity of heat:

$$Pr_t = \frac{\varepsilon_M}{\varepsilon_H} \tag{118}$$

In turbulence models which treat Pr_t as constant, the following relationship may be obtained for the overlap layer when Pr>0.5:

$$Pr_t = \frac{\kappa}{\kappa_\theta} \tag{119}$$

The Nusselt number can be written as:

$$Nu = \frac{\frac{1}{8} f Re Pr}{Pr_t + \sqrt{f/8}\psi_\theta(Pr)} \tag{120}$$

The function $\psi_\theta(Pr)$ depends on the thermal boundary condition and requires a specific turbulence model to compute it. Therefore, the effect of one-sided versus two-sided heating is captured solely by $\psi_\theta(Pr)$. If Pr_t is constant, $\psi_\theta(Pr)$ will have no dependence on the velocity profile [132].

It is therefore desirable to elucidate the form of $\psi_\theta(Pr)$ in the case of constant wall heat flux with one side heated (asymmetric heating) and both sides heated (symmetric heating). Rather than focus on a specific turbulence model, a more fundamental approach will be taken. For incompressible flow, we know that:

$$\nabla \cdot \vec{\mathbf{v}} = 0 \tag{121}$$

Treating radiative heat transfer as negligible, the energy equation for incompressible flow may be written:

$$\rho c_p \frac{DT}{Dt} = \nabla \cdot k\nabla T + q''' + \mu\Phi \tag{122}$$

where Φ is the dissipation function. For steady, fully developed, turbulent flow, this may be expressed as:

$$u\frac{\partial T}{\partial z} + \mathrm{v}\frac{\partial T}{\partial y} = \alpha\nabla^2 T - \left[\frac{\partial}{\partial z}(\overline{u'T'}) + \frac{\partial}{\partial y}(\overline{\mathrm{v}'T'})\right] \tag{123}$$

where the prime denotes a fluctuating quantity, *u* denotes the axial component of the velocity (z-direction), v denotes the y-component of the velocity, and the following assumptions have been made:

- Axial conduction in the primary flow direction is dwarfed by advection. This is valid for $Pe \gg 1$.
- Free convection is negligible compared to forced convection. This is valid for:

$$\frac{\sqrt{Gr}}{Re} \ll 1 \tag{124}$$

- Viscous dissipation is negligible, i.e. $\Phi \approx 0$. This is valid when $Br \ll 1$. The Brinkmann number is defined as:

$$Br = EcPr = \frac{\mu u^2}{k(T_s - T_b)} \tag{125}$$

- No internal heat generation in the fluid. This is valid when there are no chemical/nuclear reactions or ionizing radiation interactions in the fluid.
- Thermal transport and turbulent mixing in the transverse direction is negligible. This is valid about the center of the channel. Away from the center, secondary flows in the transverse direction will affect transport phenomena. Far away from the center, the channel edges will also have an effect.
- The velocity and energy equations are uncoupled, such that flow properties are constant. This will be important later, as it allows us to assume that the velocity profile is symmetrical regardless of the heating condition.

It has already been mentioned that the thermal boundary layer displays a layered structure near the wall analogous to the velocity boundary layer. Using Prandtl's approach, equation (123) may be re-written for the region near the wall as:

$$u\frac{\partial T}{\partial z} + \mathrm{v}\frac{\partial T}{\partial y} = \frac{\partial}{\partial y}\left[\left(\frac{\nu}{Pr} + \frac{\nu_t}{Pr_t}\right)\frac{\partial T}{\partial y}\right] \tag{126}$$

where ν_t is the kinematic eddy viscosity, which is an analog to the kinematic viscosity in Newton's law of friction for the turbulent shear stress. This can be re-written as:

$$u\frac{\partial T}{\partial z} + \mathrm{v}\frac{\partial T}{\partial y} = \frac{\partial}{\partial y}\left[(\alpha + \varepsilon_H)\frac{\partial T}{\partial y}\right] \tag{127}$$

The v component of the velocity is small near the wall, so we can assume that v=0, so the energy equation may finally be written as:

$$u\frac{\partial T}{\partial z} = \frac{\partial}{\partial y}\left[(\alpha + \varepsilon_H)\frac{\partial T}{\partial y}\right] \tag{128}$$

Ultimately, the temperature drop in each layer is desired. The velocity boundary layer will be modeled as consisting of a laminar sublayer and a turbulent overlap layer that extends into the turbulent core, with the buffer layer essentially being neglected.

In the laminar sublayer, it is assumed that thermal conduction is the dominant mode of heat transfer and eddy diffusivity is negligible (i.e. $k>>\varepsilon_h$), such that for the reference wall:

$$q''_w = -k\frac{\Delta T}{\Delta y} = -k\frac{(T_w - T_1)}{y_1} \tag{129}$$

where the subscript 1 denotes the outer boundary of the laminar sublayer. In the laminar sublayer, the universal law of the wall states:

$$u^+ = y^+ \tag{130}$$

with u^+, y^+, and the friction velocity defined as:

$$u^+ = \frac{u}{u_\tau} \tag{131}$$

$$y^+ = \frac{y u_\tau}{\nu} \tag{132}$$

$$u_\tau = \sqrt{\frac{\tau_w}{\rho}} \tag{133}$$

where the maximum value of y^+ for the laminar sublayer corresponds to position y_1, the outer boundary of the sublayer. In many instances, y^+=5 is a good choice for the limit of the laminar sublayer. The dimensionless thickness of the laminar sublayer will be defined as:

$$\delta_\nu^+ = \frac{y_1 u_\tau}{\nu} \tag{134}$$

The temperature drop across the laminar sublayer may be written as:

$$(T_w - T_1) = \frac{\delta_\nu^+ \nu q''_w}{k u_\tau} = \frac{\delta_\nu^+ q''_w Pr}{\rho c_p u_\tau} \tag{135}$$

Neglecting the buffer layer and proceeding directly to the turbulent overlap layer, the Reynolds analogy gives:

$$\frac{(T_b - T_1)}{u_b - u_1} = \frac{q''_w}{c_p \tau_w} \tag{136}$$

However, the Reynolds analogy is only valid when both the velocity and temperature profiles have similar shapes (i.e., they are symmetric). In the case of asymmetric heating, we will return to equation (128). The heat balance for a differential axial element per unit width of the channel yields

$$(q''_{w1} + q''_{w2}) = \rho c_p u_b t_{gap} \frac{\partial T_b}{\partial z} \tag{137}$$

If the heat transfer coefficient is constant axially (fully developed temperature profiles), then the following assumption can be made:

$$\frac{\partial T_b}{\partial z} = \frac{\partial T_w}{\partial z} = \frac{\partial T}{\partial z} \tag{138}$$

Using this, and the definition of γ from equation (109), equation (137) may be written as:

$$\frac{\partial T}{\partial z} = \frac{(q''_w - \gamma q''_w)}{\rho c_p t_{gap} u_b} \tag{139}$$

where q''_w is the heat flux at the reference wall, and γ= -1 corresponds to the case of symmetric heating, γ=0 corresponds to one-sided heating with the other wall adiabatic, and γ=1 corresponds to heating at one wall with constant heat flux and cooling at the opposite wall.

Taking an approach similar to that employed by Barrow [118] in determining an overall analytical heat transfer solution for the case of turbulent flow between parallel plates, we will treat the viscous sublayer thickness as small compared to the channel gap, such that $t_{gap} \approx t_{gap}$-$2y_1$,

and approximating the velocity as uniform across the turbulent core and equal to the bulk velocity, u_b, the energy equation for the turbulent overlap layer can be written as:

$$\rho c_p u_b \frac{\partial T}{\partial z}\left(t_{gap} - y - y_1\right) = -\rho c_p(\alpha + \varepsilon_H)\frac{\partial T}{\partial y} - \gamma q''_w \tag{140}$$

If the bulk temperature is treated as equivalent to the mean temperature in the turbulent core, and the thickness of the laminar sublayer, y_1, is treated as negligible compared to the thickness of the turbulent core, then the thermal resistance with respect to the reference wall will be:

$$\frac{(T_1 - T_b)}{q''_w} \approx \frac{(2+\gamma)t_{gap}}{6\rho c_p(\alpha + \varepsilon_H)} \tag{141}$$

In the overlap layer and turbulent core, $\varepsilon_H >> \alpha$. Additionally, Barrow [118] derives the following relation from the Reynold's analogy, which should be valid regardless of the asymmetry of the boundary condition:

$$\frac{u_b - u_1}{c_p \tau_w} \approx \frac{t_{gap}}{6\rho c_p \varepsilon_H} \tag{142}$$

This allows equation (141) to be expressed as:

$$(T_1 - T_b) \approx \frac{q''_w(2+\gamma)(u_b - u_1)}{c_p \tau_w} \tag{143}$$

Therefore, the total temperature drop between the bulk fluid and the reference wall is:

$$(T_w - T_b) \approx \frac{\delta_v^+ q''_w Pr}{\rho c_p u_\tau} + \frac{q''_w(2+\gamma)(u_b - u_1)}{\rho c_p u_t^2} \tag{144}$$

The shear stress at the wall, and, in turn, the friction velocity may be related to the friction factor by:

$$\tau_w = \frac{f}{8}\rho u_b^2 \tag{145}$$

$$u_\tau = u_b\sqrt{\frac{f}{8}} \tag{146}$$

It was shown earlier that use of *Re** (equation (91)) with the Blasius correlation (equation (97)) correlates friction pressure drop data well. Therefore, the friction velocity can be expressed as:

$$u_\tau = u_b\sqrt{0.0396[\phi^* Re]^{-0.25}} \tag{147}$$

Recall that ϕ^*, defined in equation (90) and (91), only depends on the aspect ratio of the channel. Substituting this relation for the friction velocity into the temperature drop, and also realizing that the velocity at the inner boundary of the overlap layer is equivalent to that on the outer part of the sublayer:

$$u_1 = u_\tau \delta_\nu^+ \tag{148}$$

Noting the relation of the Stanton number to the Nusselt number in equation (113) and using the definition of the heat transfer coefficient, Reynolds number, and Prandtl number, the following relation can be written:

$$Nu = \frac{q_w'' RePr}{\rho c_p u_b (T_w - T_b)} \tag{149}$$

Combining this with equation (144), the following analytical solution for the Nusselt number may be written, which accounts for asymmetric heating and the aspect ratio of the channel:

$$Nu = \frac{0.199 Re^{7/8} Pr}{\delta_\nu^+ [Pr - (\gamma + 2)]\phi^{*1/8} + 5.025 Re^{1/8}(\gamma + 2)\phi^{*1/4}} \tag{150}$$

The above equation is intended for the center of the channel, away from the edges. In the form derived here, the dimensionless laminar sublayer thickness may be specified independently if a value other than δ_v^+=5 is desired. Due to the approximations made, the equation is only valid for $Pr \gtrapprox 1.0$. Note that for one-sided heating, γ=0, and for both sides heated, γ=-1. This is the solution for the reference wall; the solution fort the $\gamma q_w''$ wall is easily derived from this.

Despite the substantial approximations made in the boundary layer analysis to derive this purely analytical solution, equation (150) yields a mean absolute error of 4.1% in predicting experimental data within this study when 10,000<*Re*<35,000. In addition, the analytical solution derived above correctly predicts the behavior of the Nusselt number for *Re*>30,000. Re-plotting the experimental data and normalizing by the Prandtl number, it is clear that the analytic solution captures the effect of one-sided heating for the low Prandtl, high Reynolds number data, as seen in Figure 101.

The predicted effect of channel aspect ratio using equation (150) is shown in Figure 99. Note that α*=0 corresponds to the situation of parallel plates, whereas α*=1 corresponds to a square duct. For the channel tested in this study, α*=0.035. The analytical correlation correctly predicts the expected trend in the Nusselt number with the aspect ratio. Increasing aspect ratio,

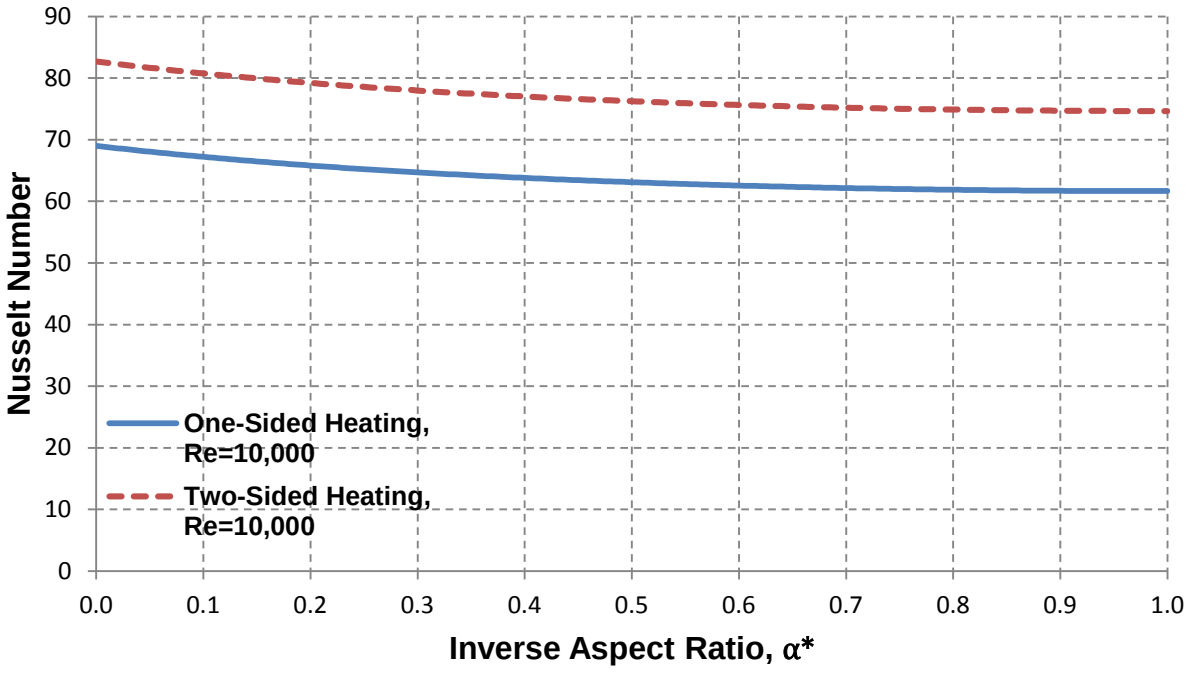

Figure 99: Effect of Channel Aspect Ratio and One versus Two-Sided Heating on the Nusselt Number as Predicted by the Semi-Analytical Equation for *Pr*=4.4 and *Re*=10,000. *α=0 for parallel plates. The trend of the Nusselt number with aspect ratio is predicted correctly by the correlation.**

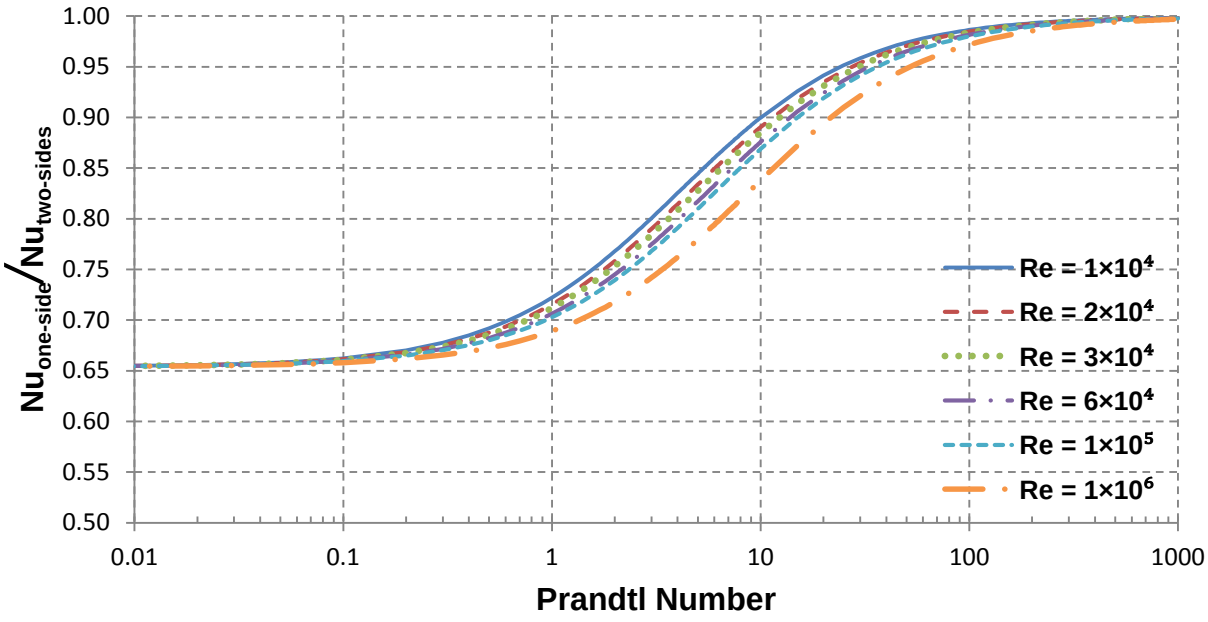

Figure 100: Nusselt Number Ratio for One-Sided versus Two-Sided Heating as Predicted by the Analytical Correlation. While the Nusselt number for one-sided heating is accurately predicted, the effect of two-sided heating appears to be overestimated.

corresponding to a smaller inverse aspect ratio, results in a stronger effect from secondary flows, improving the heat transfer in the channel. The Nusselt number ratio for one versus two-sided heating as a function of the Prandtl and Reynolds number is shown in Figure 100. While the predicted Nusselt number for one-sided heating is accurate and the trends predicted for two-sided heating are correct, it would appear that the effect of two-sided heating is overestimated. Therefore, further work and experimental data are required for the two-sided heating case so the heating symmetry factor, γ, can be modified appropriately.

Returning to the case of one-sided heating (γ=0), for 4000<*Re*<10,000, the purely analytical correlation overpredicts the experimental data somewhat, with a mean absolute error of 7.3%. It is possible to modify equation (150) to better account for the transition regime without significantly affecting the prediction when *Re*>10,000. In a somewhat similar manner to Gnielinski's modification of the Petukhov correlation [112], the Reynolds number term can be modified slightly. In addition, comparison to the limited studies investigating one versus two-sided heating, it is clear that the analysis, though accurately predicting the Nusselt number for one-sided heating, will overcompensate for two-sided heating. Therefore, re-writing the

equation just for the one-sided heating case and modifying the Reynolds term to improve accuracy in the transition region, the equation may be written as:

$$Nu = \frac{0.199(Re - 600)^{7/8} Pr}{5[Pr - 2]\phi^{*1/8} + 10.05(Re - 600)^{1/8}\phi^{*1/4}} \tag{151}$$

This semi-analytic correlation predicts the experimental data for one-sided heating in the transition regime with a mean absolute error of 4.2%. The mean absolute error for the entire range, i.e. 4000<*Re*<70,000 and 2.2<*Pr*<5.5, is less than 4.9%. A summary of all experimental data where *Re*>10,000, normalized to $Pr^{0.4}$, is plotted along with the Dittus-Boelter (McAdams) equation in Figure 101. The semi-analytical correlation proposed in equation (151) is also plotted for the upper and lower bounds of the Prandtl number explored in experiments.

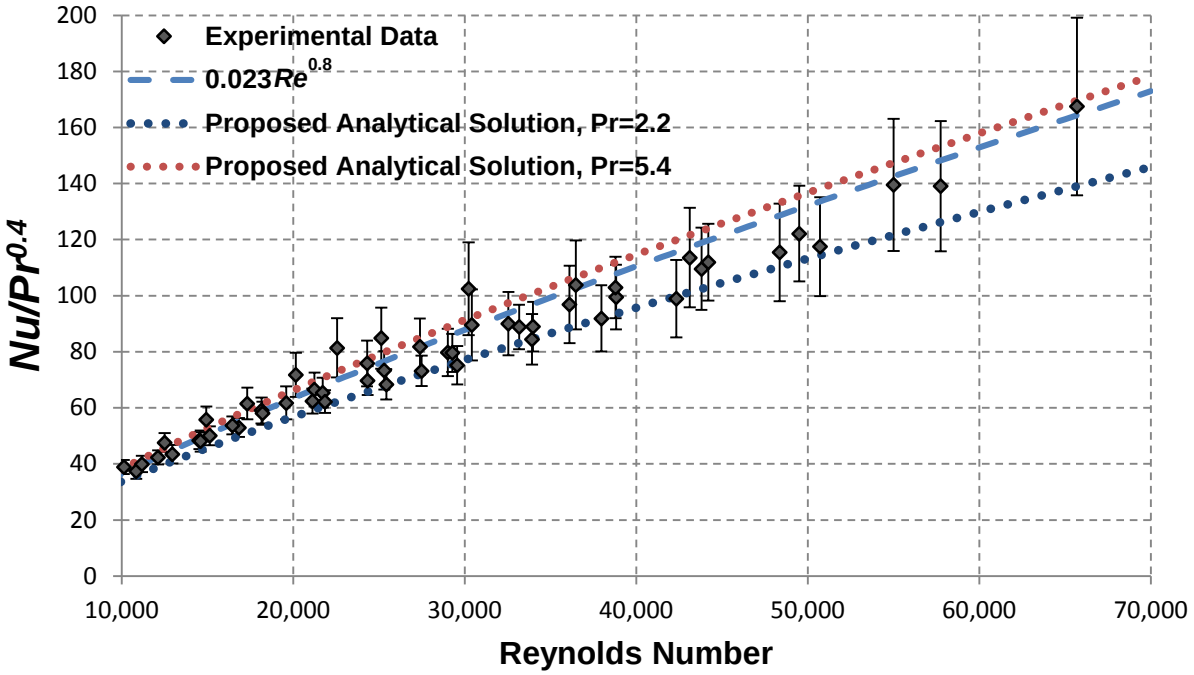

Figure 101: Summary of Experimental Data for *Re*>10,000 Normalized by $Pr^{0.4}$. The newly derived semi-analytical solution is plotted along with the Dittus-Boelter equation for the highest and lowest Prandtl numbers explored in this study.

4.6. Chapter Summary

Accurate prediction of the surface temperature on MITR cladding during normal operation is necessary for predicting the margin to the onset of nucleate boiling. While flow remains fully turbulent during normal operation, a loss of flow transient (LOFA) will result in a decrease in flow through the transition and laminar flow regions until natural circulation is established. Existing predictions rely on correlations developed for circular tubes, and the most appropriate correlation is not readily obvious. Therefore, the applicability of several existing single-phase correlations to the narrow rectangular channel has been explored in this chapter. The correlation of Sieder and Tate predicts the largest heat transfer coefficient for MITR conditions, whereas the modified Colburn correlation predicts the lowest value. The only correlation that is suitable for the transition regime is that proposed by Gnielinski.

Friction pressure drop and single-phase heat transfer data were collected for the narrow rectangular channel (α^*=0.035) heated on one side. The conditions ranged from $2.2<Pr<5.4$ and $Re<70{,}000$. Friction pressure drop was well-correlated by the Blasius equation, as long as the laminar equivalent diameter concept is utilized. The critical Reynolds number for the test channel was between 3500 and 4000, higher than the typical Reynolds number of 2200 expected for circular tubes. The higher critical Reynolds number is supported by the literature. The transition regime also extends to a higher Reynolds number than that typically expected in circular tubes.

Experimental results for the single-phase heat transfer coefficient indicate that Prandtl number dependence is more complex than a simple power law. From a literature review, it was expected that the more complicated dependence was a result of the asymmetric (one-sided) heating, and this was confirmed using a boundary layer analysis. The analysis also led to a purely analytical solution for the Nusselt number, though a slight modification was made to better account for heat transfer in the transition region. The proposed semi-analytical correlation in equation (151) is valid for $Pr \gtrapprox 1.0$, $Re>4000$, and one-sided heating with uniform heat flux. The proposed correlation predicts the experimental results with a mean absolute error of less than 4.9% for data in the range of $2.2<Pr<5.4$ and $4000<Re<70{,}000$. Empirical data for two-sided heating and/or further analysis is required to extend the correlation to the case of two-sided heating, as the current analysis overestimates the increase in Nusselt number for the two-sided heating.

Chapter 5

Two-Phase Heat Transfer Experiments

5.1. Introduction

Boiling incipience may be classified as homogeneous or heterogeneous. In homogeneous nucleation, bubble nucleation occurs within the bulk of a superheated liquid. In water at atmospheric pressure, superheats on the order of 200 °C are required to achieve homogeneous nucleation. In real heat transfer systems, nucleation occurs at interfaces, typically a solid surface. This form of nucleation is called heterogeneous nucleation. On ideal surfaces which are clean, very smooth, and free of dust, the superheat required for nucleation can still be quite high [133]. However, on practical engineering surfaces, the wall temperature needed for incipience is typically in the range of a few degrees to tens of degrees. Research in the field of boiling heat transfer indicates that entrapped gas in cavities on these practical surfaces leads to the initial nucleation process [134]. Therefore, cavities that are not completely flooded by liquid water can promote bubble nucleation at lower wall superheats. On an idealized boiling surface, whether a cavity will be flooded depends on the groove angle, 2γ, and the contact angle of the liquid with the side of the cavity. The situation can be treated as a liquid front advancing over the cavity, and therefore, the relevant parameters for initial entrapment of gas in the cavity will be the dynamic advancing contact angle [135, 136, 137]. This situation is shown in Figure 102. Therefore, the higher advancing contact angle, the higher the initial radius of the nucleus. The presence of an initial vapor embryo will lead to a lower initial activation temperature, resulting in lower wall superheats at boiling incipience.

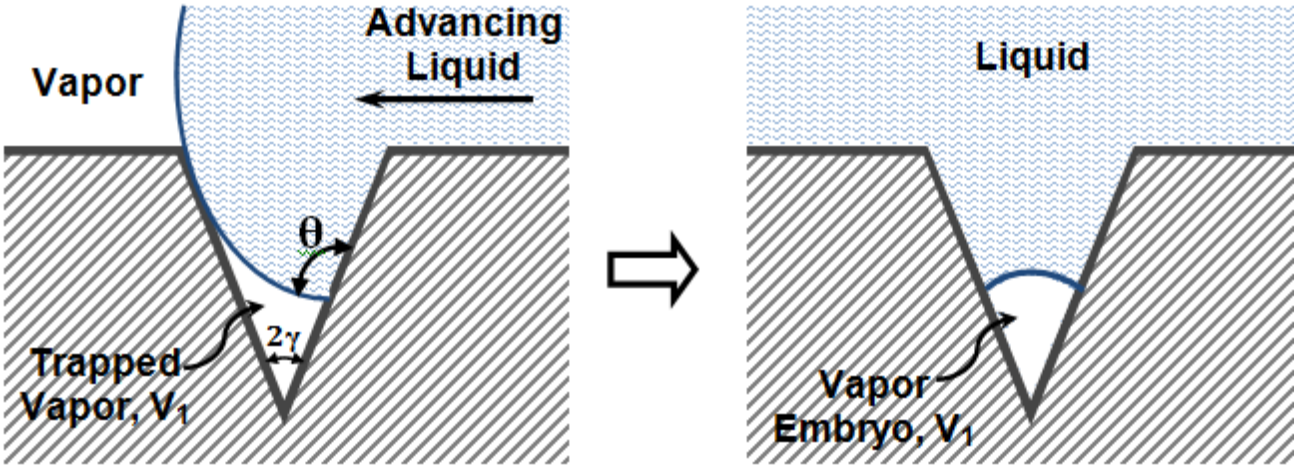

Figure 102: Idealized Cavity on a Boiling Surface. Here *θ* represents the advancing contact angle.

The surface condition will therefore influence the temperature and heat flux at which boiling incipience occurs. While exact surface texture and features such as cavities are difficult to carefully characterize, the surface roughness provides some indication of whether vapor-trapping cavities may be present on a surface. Chemical constituency is also an important parameter, as it will influence the contact angle that the liquid makes with the surface. Experimental results are presented in this chapter for onset of boiling under forced convection from unoxidized and oxidized 316 stainless steel surfaces. The methods used to identify incipience will also affect the result, and are discussed in detail in this chapter. Two-phase phenomena beyond onset of nucleate boiling, including the onset of flow instability, are also studied, with results presented in section 5.6. In the following section, the theoretical criteria for incipience, along with various models for the case of forced convection, are provided.

5.1.1. Review of Theory for the Onset of Nucleate Boiling

The superheat required to sustain a vapor bubble may be derived from the Young-Laplace and Clausius-Clapeyron equations. The Young-Laplace equation describes the pressure difference between two interfaces with curvature to maintain mechanical equilibrium, such as that between a vapor bubble and the surrounding liquid:

$$P_{\mathrm{v}} - P_l = \frac{2\sigma}{r} \tag{152}$$

where r is the radius of curvature of the interface, assumed spherical. The Clausius-Clapeyron equation may be written as:

$$\frac{dP}{dT} = \frac{h_{fg}}{\Delta v T} \tag{153}$$

where Δv is the specific volume change between liquid and vapor. If the vapor can be treated as an ideal gas and $\Delta v \approx v_{\mathrm{v}}$, then the above equation may be written as:

$$\frac{dP}{dT} = \frac{h_{fg} P}{R T^2} \tag{154}$$

where R is the specific gas constant. Taking $T_l = T_{sat}$, equation (154) can be integrated between (P_l, T_l) and $(P_{\mathrm{v}}, T_{\mathrm{v}})$:

$$T_{\mathrm{v}} - T_{sat} = \frac{R T_{\mathrm{v}} T_{sat}}{h_{fg}} ln\left(\frac{P_{\mathrm{v}}}{P_l}\right) \tag{155}$$

and substituting in equation (152) gives the resultant superheat equation required to sustain a vapor bubble of radius r_{ve} in equilibrium with the surrounding liquid:

$$T_{\mathrm{v}} - T_{sat} = \frac{R T_{\mathrm{v}} T_{sat}}{h_{fg}} ln\left(1 + \frac{2\sigma}{r_{\mathrm{ve}} P_l}\right) \tag{156}$$

At low superheats or higher pressure (but still well below the critical point), the superheat equation may be simplified to:

$$T_{\mathrm{v}} - T_{sat} = \frac{2\sigma T_{sat}}{r_{\mathrm{ve}} h_{fg} \rho_{\mathrm{v}}} \tag{157}$$

Hsu and Graham [138] expand upon this criteria for stable bubble formation to identify the condition required for bubble growth out of a cavity in pool boiling. Their basic requirement is that heat must be transferred to the bubble for it to grow. Therefore, Hsu and Graham infer that the temperature in the thermal layer surrounding this bubble must be greater than or equal to the bubble temperature for growth to occur. In the model of Hsu and Graham, a thermal layer at this temperature must have a thickness which is at least the height of the bubble. Hsu also develops a transient model to account for the change in thickness of this thermal layer during pool boiling [139]. Investigations of incipience under forced convection are largely based on Hsu's original model, though in some respects they are simpler as they usually assume steady-state conditions.

For incipience under forced convection, models usually deal with a single, isolated bubble such that the thermal layer is within the laminar sublayer and can be treated as having a uniform and non-varying thickness temporally. Heat transfer in the laminar sublayer is usually treated as occurring via conduction only, such that the temperature drop from the wall is linear:

$$T_l(y) = T_w - \frac{q''_w y}{k_l} \tag{158}$$

where k_l is the thermal conductivity of the liquid in the laminar sublayer. The condition for incipience will vary depending on what assumption is taken for the bubble shape and the required thickness of the thermal layer. Figure 103 shows an illustration of different bubble models at incipience. As seen in the figure, the selection of bubble shape will affect the maximum height of the bubble above the heated surface. The superheated thermal layer meets the minimum superheat requirement of equation (157) such that at the outer edge of the superheated thermal layer:

$$T_l|_{y=\delta_{crit}} - T_{sat} = \frac{2\sigma T_{sat}}{r_{ve} h_{fg} \rho_v} \tag{159}$$

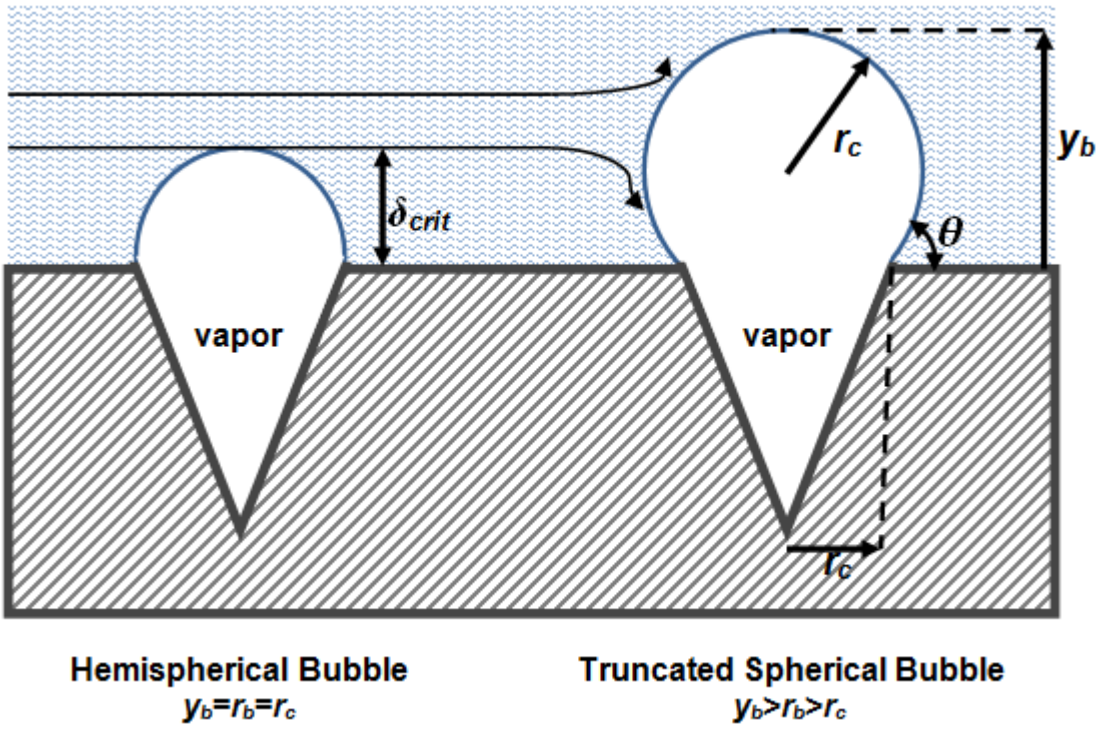

Figure 103: Hemispherical Bubble Model (left) and Truncated Sphere Model (right). The choice of bubble shape, along with the required thickness of the thermal layer meeting the requirement of equation (157), δ_{crit}, will influence the criterion for incipience of boiling. The truncated spherical bubble reduces to the hemispherical case when θ=90°.

The required thickness, δ_{crit}, for incipience depends on the criterion chosen with regard to the bubble height. In the original model of Hsu and Graham, this superheated thermal layer must be at least as thick as the bubble height, or $\delta_{crit}=y_b$. However, one can imagine that a streamline at a certain height would be deflected around the bubble, and the thermal layer thickness might therefore only need to reach this height. Several approaches have dealt with the issue of incipience under forced convection, and covered below, with most building upon the model of Hsu and Graham.

Bergles and Rohsenow

In their 1962 work, Bergles and Rohsenow [18] treat the bubble shape as hemispherical, noting that the bubble must pass through this state before growing outside the cavity. This state also matches that of the minimum radius of curvature, and the radius of the bubble can be considered equal to the cavity radius, such that:

$$r_b = r_c \tag{160}$$

In their model, Bergles and Rohsenow assume that the bubble will grow when the superheat requirement is met at the top of the hemispherical bubble, or at $y=r_b=r_c$ from the nominal surface, though they note that this likely represents an upper limit. They acknowledge that if the liquid superheat criteria is met at a distance somewhat less than the bubble height (r_b in this case), then there is net heat transfer to the bubble and it should still grow. Another important assumption taken by Bergles and Rohsenow is that a practical engineering surface will have a wide range of cavities, such that the optimum cavity size will be available for a given set of conditions. They approximate the analytical result by using a graphical solution method, arriving at the following expression:

$$q''_{ONB} = 1083P^{1.156}[1.8(T_w - T_{sat})]^{2.16/P^{0.0234}} \tag{161}$$

where all variables are in SI units except for P which is in bar. Equation (161) was determined for water over a pressure range of 1 bar<P<138 bar. Bergles and Rohsenow conduct experimental tests with de-gassed water in a small diameter stainless steel tube (2.39 mm inner diameter) and an annulus to verify their analytical result, with good agreement found between the prediction and measured values.

Satō and Matsumura

Satō and Matsumura [140] approach the issue of incipience under forced convection analytically, initially assuming a complete sphere (not a truncated sphere) sitting on the surface. They select the height of the centerline of the spherical bubble as the required thickness for superheated layer meeting the condition of equation (159). In their analysis, they define the thickness of the entire superheated layer as:

$$\delta_{shl} = \frac{k_l(T_w - T_{sat})}{q''_w} \tag{162}$$

The range of bubble sizes that can be supported at a given set of conditions will be:

$$\frac{\delta_{shl}}{2} - \frac{1}{2}\sqrt{\delta_{shl}^2 - \frac{8k_l T_{sat}(\nu_v - \nu_l)}{q''_w h_{fg}}} \leq r_b \leq \frac{\delta_{shl}}{2} + \frac{1}{2}\sqrt{\delta_{shl}^2 - \frac{8k_l T_{sat}(\nu_v - \nu_l)}{q''_w h_{fg}}} \tag{163}$$

The starting point of boiling is taken to be that requiring the minimum superheated layer, resulting in the following for the spherical bubble model:

$$q''_{ONB} = \frac{k_l h_{fg}}{8\sigma A T_{sat}(\nu_v - \nu_l)}(T_w - T_{sat})^2 \tag{164}$$

where *A* is the "heat equivalent of work" (equal to 1 when SI units employed). Satō and Matsumura also consider the case of a hemispherical bubble, where here they use the height corresponding to the position of "the center of gravity of the critical bubble" for the superheated layer thickness, resulting in the following expression:

$$q''_{ONB} = \frac{k_l h_{fg}}{3\sigma A T_{sat}(\nu_v - \nu_l)}(T_w - T_{sat})^2 \tag{165}$$

The former expression in equation (164) is that typically referenced from the work of Satō and Matsumura. The latter assumption used for equation (165) predicts incipient boiling at about 40% lower superheat.

Satō and Matsumura also collect experimental data to support their analysis using a 10 mm × 7 mm stainless steel rectangular channel heated on two opposing sides. They perform tests with de-aerated water for flow velocities ranging from 0.6 m/sec to 4.1 m/sec and subcoolings from 3 °C to 70 °C, finding reasonable agreement with results predicted from their analysis with a spherical bubble (equation (164)).

Davis and Anderson

Davis and Anderson [141] also approach the problem of incipience under forced convection analytically, assuming the following:

- The bubble cavity, which develops at a surface cavity, has the shape of a truncated sphere.
- Equilibrium theory can be used to predict the superheat required to satisfy a force balance on the bubble (equation (157)).
- A bubble nucleus will grow if the temperature of the fluid at a distance from the wall equal to the bubble height is greater than the superheat required for bubble equilibrium in equation (159).
- The bubble nucleus does not alter the temperature profile in the surrounding liquid.
- Due to their small size, the bubble nuclei are found entirely within the laminar sublayer and the temperature profile in the liquid can be determined from equation (158).

Davis and Anderson point out that the choice of streamline location is somewhat arbitrary, and that selection at the top of the bubble, as both Hsu and Bergles and Rohsenow did, results in the limiting (maximum) superheat case for onset of boiling on a practical surface. They note that in their analysis, the bubble shape reduces to the hemispherical bubble when the contact angle is 90°, and also that the bubble may not grow much beyond the hemispherical bubble anyway, due to the strong shear forces which may act to sweep it from the wall [141]. Therefore, they consider the hemispherical bubble to have the greatest stability.

In the analysis, Davis and Anderson calculate the height of the bubble, bubble radius, and cavity radius to be related to the contact angle by:

$$y_b = r_b[1 + cos(\theta)] \tag{166}$$

$$r_c = r_b sin(\theta) \tag{167}$$

Assuming that the optimum surface cavity size is present, and also simplifying the problem by assuming a system at high pressure or fluid with low surface tension, Davis and Anderson arrive at the following relation between the heat flux and saturation superheat at the onset of nucleate boiling:

$$q''_{ONB} = \frac{k_l h_{fg} \rho_v}{8\sigma T_{sat}[1+\cos(\theta)]}(T_w - T_{sat})^2 \tag{168}$$

Note that when a contact angle of 90° is assumed, equation (168) essentially reduces to Satō's prediction assuming a perfectly spherical bubble sitting on the surface (equation (164)). Note, however, that the bubble contact angle of 90° implies a hemispherical bubble, but the same end result is obtained to the choice of different streamline locations.

Davis and Anderson compare their prediction to the data of prior studies and reach several interesting conclusions. They note that inconsistencies between theoretical analyses and empirical data are primarily due to characteristics of the heat transfer surface. Specifically, they note that some studies used very smooth surfaces which likely lacked cavities of the optimum size or active cavities altogether, thereby leading to higher superheats for initial nucleation. In addition, they note that the method for identifying incipience will affect the result, stating that inaccuracies will likely result from visual identification techniques. They also point out that since the optimum cavity sizes under normal circumstances can be on the order of one micron, which is below the magnitude that can be studied with optical instruments, that considerable difficulty may be associated with studying active cavities and bubble nuclei on heat transfer surfaces.

Kandlikar

A more recent study by Kandlikar et al. [142, 143] reviews several models for boiling incipience under forced convection and proposes one where the necessary thickness of the superheated liquid layer must be greater than or equal to the height of the stagnation point. Kandlikar states that the relevant contact angle in Figure 103 is the receding contact angle. In his review, he reminds us that Hsu used a streamline at the top of a truncated spherical bubble, and

that Hsu assumed that y_b=1.6r_b, which essentially equates to a receding contact angle of 53.1°. Kandlikar, however, assumes that a streamline can be taken at a lower point on the bubble, arguing that any streamlines above a stagnation point will be deflected above and around the bubble. For receding contact angles from 20° to 60°, Kandlikar states that the height of the stagnation point, y_{stag}, will be:

$$y_{stag} = 1.1 r_b = 1.1 \frac{r_c}{sin(\theta_r)} \tag{169}$$

According to Kandlikar's model, the range of active cavity sizes on a surface that can support nucleation for a given set of conditions will be:

$$\begin{aligned} \{r_{c,min}, r_{c,max}\} &= \frac{\delta_{th,eq} sin(\theta_r)}{2[1+cos(\theta_r)]} \left(\frac{T_w - T_{sat}}{T_w - T_b}\right) \\ &\times \left[1 \mp \frac{1}{2}\sqrt{1 - \frac{8.8 T_{sat}(T_w - T_b)}{\rho_v h_{fg} \delta_{th,eq} (T_w - T_{sat})^2}}\right] \end{aligned} \tag{170}$$

It is important to note that the thermal layer thickness, $\delta_{th,eq}$, used by Kandlikar is not the thickness of the superheated layer, as in equation (162), but rather, an equivalent thickness of the entire thermal layer assuming a linear temperature profile such that:

$$\delta_{th,eq} = \frac{k_l}{h} = \frac{k_l (T_w - T_b)}{q''_w} \tag{171}$$

where h is the heat transfer coefficient for forced convection prior to incipience. While this assumption of a linear temperature profile for the entire thermal layer is not accurate for transition and turbulent flows, it can be seen in equation (170) that this thermal layer thickness can be reduced to the superheated layer thickness by combining with the wall superheat terms. The final relation between wall superheat and surface heat flux at the point of incipience for Kandlikar's model is:

$$q''_{ONB} = \frac{k_l sin(\theta_r)}{1.1 r_c}\left[(T_w - T_{sat}) - \frac{2\sigma T_{sat} sin(\theta_r)}{\rho_v h_{fg} r_c}\right] \quad (172)$$

Experimental studies were carried out by Kandlikar et al. in a 3 mm × 40 mm rectangular channel with a 10 mm diameter circular heater flush with the lower wall. Tests were conducted at essentially atmospheric pressure with distilled water that was thoroughly degassed. It should be noted that given the small size of the heater, flow was not likely fully developed thermally in their tests. They measure the onset of nucleate boiling with wall temperature and also attempt to identify incipience visually using a high speed video camera/microscope setup. However, tests are conducted at relatively low flows, with a maximum Reynolds number of 5068 and mass flux of 355 kg/m^2-sec. Therefore, the flow velocities of their study are about 1/10th that relevant to conditions in the MITR during steady state operation.

Nonetheless, the experimental study yields useful information regarding visual identification of incipience. At a subcooling of about 40 °C and Reynolds number of 1267, bubbles reach a maximum diameter of 78 μm before departure, while at *Re*=2280, the maximum departure diameter was only 56 μm. At a subcooling of about 20 °C and Reynolds number of 1664, observed bubble departure diameters ranged from 80 μm to 90 μm. They also observe bubble growth rates, noting that the influence of subcooling and flow rate are quite complex. A decrease in the subcooling leads to higher growth rates, which they note makes it quite difficult to capture bubble growth when the subcooling is less than 20 °C. For a subcooling of 20 °C and *Re*=1664, Kandlikar et al. observe bubble growth times of 22 msec. At higher flow rates, the bubble growth period is even more rapid, and they note frame rates in excess of 100,000 Hz might be required to capture the rapid bubble growth and departure of very small bubbles. They conclude that under certain conditions, bubble growth is so strongly dependent on subcooling and mass flux that bubble activity could not be captured, despite heat transfer data indicating the presence of nucleation. They hypothesize the possibility of small bubbles (5 μm to 10 μm in diameter) being ejected from cavities at high speeds, in excess of 6000 bubbles per second at a given nucleation site, and therefore go undetected by visual measurement techniques.

Other Studies

A number of other relevant studies have been conducted for the onset of nucleate boiling under forced convection. In a 1986 study supporting a power uprate of the JRR-3 following conversion to LEU fuel, Sudo et al. [53] investigate the onset of nucleate boiling in the same test apparatus used for an earlier work [52] and discussed in Chapter 2. The 2.25 mm by 50 mm narrow rectangular channel is intended to simulate the coolant channel of a materials test reactor. They collect data for upflow with "pure" water at 1.2 bar and inlet temperature of 34.85 °C. The maximum flow velocity where onset of boiling is measured for their configuration is 1.48 m/sec. Sudo et al. state that the Bergles-Rohsenow correlation gives a good estimate of onset of nucleate boiling, corresponding to the lower limits of measured onset of nucleate boiling. They also observe no difference in boiling onset for upflow or downflow at the conditions tested. Lastly, they claim there is no significant hysteresis in the boiling curve with operational history, i.e. whether the heat flux is increasing or decreasing. The study by Sudo et al. has been the motivation for continued usage of the Bergles-Rohsenow correlation for the MITR, and is cited in the current Safety Analysis Report [17].

Several recent studies investigate onset of nucleate boiling in narrow annuli [144] and narrow rectangular channels [145, 146], but flow is limited to low flow velocities, with mass fluxes in these studies being below 840 kg/m^2-sec, 603 kg/m^2-sec, and 145 kg/m^2-sec, respectively. In one of the studies [145], thermocouples are welded directly to the current-carrying heater plate. Even if ungrounded, welding the thermocouple sheath to the plate will affect the local temperature measurement. Results are reported for onset of boiling using both visual identification and temperature measurement with surprisingly good agreement between the two methods for the conditions tested. This is in stark contrast to results reported elsewhere indicating the difficulty and inaccuracy in measuring incipience using visual techniques.

5.2. Heater Surface Preparation

5.2.1. Nominal Surface

The heater plate used in the onset of boiling tests from the nominal surface was the same as that used for the single-phase heat transfer experiments and prepared in the same manner, as described in section 4.2. This method of preparation yields a uniformly textured surface with an arithmetic roughness, R_a, of about 0.5 μm. Details of the surface characteristics are provided in Chapter 6. Before every boiling test, the surface was thoroughly cleaned by wiping with ultra-pure reagent grade ethanol and rinsing with deionized water. This helped to prevent buildup of electrochemical corrosion products or contaminant deposits that may have formed on the heater during the prior test. In addition, the surface was periodically refreshed by wet sanding with 120-grit SiC sandpaper and cleaned in the same manner described in Chapter 4.2.

5.2.2. Oxidized Surface

The heater plate to be used for the oxidized surface studies was fabricated in the same manner as that for the nominal surface studies, except that the full length of the electrodes were nickel plated to mitigate copper corrosion during the oxidation treatment. The boiling surface was prepared by initially finishing the 316 stainless steel heater in the same manner as the nominal surface, i.e. wet-sanding with 120-grit SiC paper in a figure-eight pattern with the appropriate cleaning and drying procedure. The entire heater was then placed in a ThermoScientific ThermoLyne box furnace, which was preheated to 600 °C. The plate was heated in air at atmospheric pressure for four hours, at which point it was removed from the furnace. The 316 stainless steel heater surface exhibited a blue/brown tint after removal (refer to Figure 104), as a result of the thin-film interference of the thin oxide film formed on the surface. Prior to final installation in the test section, the heater surface was cleaned with acetone, ethanol, and water in the usual manner. Between every boiling test with the oxidized heater plate, the surface was wiped down with ultra-pure ethanol and rinsed with DI water.

Figure 104: Heater Plate Following Surface Finishing Followed by Oxidation in Air at 600 °C.

5.3. Measurement Considerations and Criteria for the Onset of Nucleate Boiling

The onset of nucleate boiling is the point on a heated surface when a vapor embryo is able to grow above the surface (outside of a cavity) and be sustained in equilibrium with the surrounding liquid. The method used to experimentally identify this point will have a significant effect on the heat flux and superheat reported. Several techniques exist, and depending on the conditions, may yield drastically different results for onset of nucleate boiling. Even using the same technique between experiments may yield significantly different results depending on the exact criteria used. In general, methods for identifying onset of nucleate boiling will rely on at least one of the methods discussed below.

Temperature

Techniques relying on temperature measurement attempt to determine the point of boiling incipience by analyzing the change in the surface heat transfer coefficient. As bubbles grow on the surface, they may collapse (due to condensation heat transfer) and result in a new bubble being formed at the same location. The heat transfer coefficient will be improved due to the latent heat required to form the vapor bubble, the increased convective motion at the surface, and the quenching effect required to heat the subcooled liquid that replaces the vapor bubble. Surface temperature measurement using thermocouples typically only provides local information at or about where the thermocouple is placed, with infrared thermometry being the only means to achieve full-field temperature measurements. Therefore, the point at which a detectable change in the heat transfer coefficient occurs will likely be slightly beyond the onset of nucleate boiling. This is because many sites must become active, and the bubble must grow large enough to either collapse or depart to result in a noticeable effect on the heat transfer coefficient. Most prior studies use some form of temperature measurement to determine the onset of nucleate boiling point. However, the criteria are not always clearly stated, leading to inconsistencies between studies. For example, identifying incipience as the point at which the heat transfer coefficient changes by 5% will yield a different result than requiring a 10% change in the heat transfer coefficient. Simply identifying the point on the boiling curve where a significant change in slope occurs may not be adequate, as the “knee” of the boiling curve may extend over a wide range of superheat, especially at higher mass fluxes. Lastly, the uncertainty in the surface temperature

and heat flux measurement must be carefully accounted for, to ensure that the change in the heat transfer coefficient at the expected point of onset is statistically significant.

Pressure

Phase change in a heated channel will influence the pressure drop of the system by altering the friction factor friction and an increase in the acceleration pressure drop. Therefore, pressure drop measurements are one possible way of determining onset of nucleate boiling. In tests to measure the onset of flow instability, Kennedy et al. [147] state that on the characteristic pressure drop versus flow rate curve, the point at which the gradients for the heated and unheated curves become noticeably different should correspond to the onset of nucleate boiling. However, gradual changes in liquid properties with heating, along with dimensional changes which may be non-negligible for very narrow channels, will also result in changes in the pressure drop as the heat flux is increased in the channel. The relative effect of boiling on pressure drop will also depend on the subcooling and flow conditions. For high subcooling where the bubbles collapse immediately and do not depart, the relative effect on pressure drop is more subdued. Similarly, at high mass fluxes where inertia forces dominate, the relative effect of boiling on pressure drop will be at first less noticeable. Therefore, at onset of boiling, there will not be a sharp rise in the pressure drop, but more of a gradual transition, meaning that there is also some subjectivity in applying this technique.

In conducting experiments, it was noted in many cases that the rise in pressure drop with increasing heat flux was so gradual as to preclude objectively identifying onset of boiling using this method. However, the pressure drop signal was measured with time, at approximately 50 msec intervals. A sharp increase in the relative standard deviation of the pressure drop signal with time was noted at the onset of boiling. This method of identifying incipience appeared to work equally well regardless of subcooling, providing a global measurement for first onset of boiling in the channel, even if it occurred at a location without temperature measurement, such as at the very exit of the channel. The increased oscillation in the pressure signal with time is likely due to the rapid growth and collapse of bubbles at the surface.

Visual

Visual measurement techniques, in which a sight glass or viewing window on the heated flow section allows for optical equipment or the experimentalist to physically see bubbles on the surface, have been used, or at least attempted, in a number of studies, including the current one. In principal, the technique should be quite simple, with the appearance of a bubble growing outside of a cavity indicating the incipience point. However, in practice, visual identification methods are neither reliable nor consistent. Under relevant conditions in water, the optimum cavity size for nucleation is on the order of several microns. Therefore, on a practical engineering surface which possesses cavities in this range, these will be the first cavities to nucleate. Assuming a hemispherical bubble, as did Bergles and Rohsenow, the bubble diameter will be the same as the cavity diameter, or several microns wide. Therefore, the optical system must have a spatial resolution that is even smaller than 2-3 μm. The theoretical spatial limit for optical techniques, defined by the diffraction limit (which is set by the wavelength of light), is about 0.25 μm. In practice, the best optical systems for high speed visualization might be able to achieve spatial resolutions of a few microns, which is still not adequate for the expected bubble diameter and height at the exact moment of incipience.

According to Collier and Thome, when bubbles are visible, a much higher heat flux (two and one-half times) is required to permit visual detection than to cause an improvement in the heat transfer coefficient at the same point [148]. Under such circumstances at incipience, bubbles at the wall are likely too small to see even with the best optical setup. This would tend to explain the recent studies using visual means reporting onset of nucleate boiling occurring at much higher temperatures and heat fluxes than predicted by Bergles and Rohsenow. And while one of the test sections used in the original study by Bergles and Rohsenow was a Pyrex annulus, presumably to permit visual identification of incipience, no visual characterization is mentioned in their paper [18]. A detailed report for the Air Force Office of Scientific Research [149] explains that visual identification of incipience was not possible, even at high magnifications.

In fact, in this study it was confirmed that incipience was practically impossible to view at mass fluxes greater than 750 kg/m^2-sec and subcoolings greater than 25 °C. In this study, the spatial resolution of the optical setup was about 20 μm per pixel, and at least several pixels are required to resolve a single bubble. When voiding was visible, it was at much greater heat fluxes and shortly before the onset of flow instability. At the lowest mass flux of this study (750

kg/m^2-sec) and a subcooling of 25 °C, dispersed bubble sizes following onset of boiling were on the order of 80 μm in diameter. Increases in mass flux and subcooling will make the bubble size near the incipient heat flux substantially smaller, and well below the optical resolution for visualization.

Audible

Audible measurement techniques have been proposed for determining the onset of nucleate boiling in subcooled flow boiling. Kennedy et al. [147] note that an easily audible whistle-like sound emanated from their test section, attributing it to the occurrence of the onset of nucleate boiling. Bouré et al. [150] mention a study by A.A. Bishop where a microphone in water detected audible frequency oscillations in the range of 1000 Hz to 10,000 Hz for flow boiling, resulting in an audible whistling noise.

In the present study, a loud crackling noise could be heard clearly from the test section even when no boiling was visible, likely coming from the rapid growth and collapse of micro-bubbles at the surface below the visualization threshold. However, the intensity of the crackling noise depended strongly on subcooling, and at low subcoolings was barely audible (typically under circumstances where bubbles could be visualized). Given the inconsistent audible output with subcooling and mass flux, along with the high background noise from the pump and power supply, this was determined not to be a reliable or consistent means of identifying the onset of nucleate boiling.

Ultimately, the identification of the onset of nucleate boiling using temperature measurements is expected to be most reliable. In addition, when comparing results to existing correlations, the least amount of bias will result if the same identification technique is used as that employed by the original researcher. In most (but not all) cases correlation developers used temperature measurement to when their correlation was supported with empirical values. Visual techniques are only possible with very high resolution equipment at certain flow conditions, and are still subject to the experimentalist's bias. Audible techniques are expected to be inconsistent and dependent on subcooling, among other factors, with the experimentalist's bias once again being an issue. Measurement of the pressure fluctuation has the potential to provide a more

quantitative assessment and yield a "global" measurement, but the main drawback is it does not provide an associated wall temperature, and it will likely be sensitive to edge effects.

5.3.1. The Criteria of Bergles and Rohsenow

As the current MITR safety analysis relies upon the correlation proposed by Bergles and Rohsenow, it is important to understand how the onset of nucleate boiling was identified in their experiments, which supported their analytical correlation. They use temperature measurements to identify incipience, and while visual identification was originally intended to support this, it was found that incipient boiling occurred below the visual threshold. It is also critical to understand the exact temperature criteria used to identify incipience; otherwise a direct comparison to their results is not possible. While the journal publication [18] does not go into great detail, their report for the Air Force [149] describes the approach in depth. Forced convection data were collected, and the resultant boiling curves (refer to Figure 105) were partitioned into the forced convection single-phase and boiling heat flux components (refer to Figure 106). The single-phase component of the heat flux was determined from a fit to their single-phase data. While Bergles and Rohsenow do not explicitly specify a set breakpoint for choosing the onset of nucleate boiling, it would appear from the figure that when the boiling component of the heat flux exceeds ~7.5%, boiling incipience is declared to occur. Bergles and Rohsenow themselves note that exact determination of the onset of nucleate boiling under forced convection is a matter of judgment, with incipience occurring over a spread of at least 5 degrees in the wall superheat.

Inconsistent results in the literature may well be attributed to different techniques and criteria used to identify the onset of nucleate boiling, as well as different surface conditions. Most studies do not provide details regarding surface condition. In addition, operating procedures for experiments to measure the incipience point may differ between studies. Dissolved gas content is known to affect boiling incipience [80, 151, 152] and is difficult to control. Substantial amounts of dissolved gas in the fluid and cavities in the heating surface can lead to "pseudo-boiling," where a surface may off-gas non-condensable gas bubbles as its temperature increases, even if the surface is below the saturation temperature, e.g. upon opening a bottle of champagne or during the heat up of aerated water. This bubbling of non-condensable

gases from the surface could potentially be mistaken for actual boiling. In the study of Bergles and Rohsenow, their system water was degassed to less than 1.5 cubic centimeters of air per liter for all runs, such that they did not expect this premature "boiling" due to gas release to occur. Operational history and whether the onset of boiling point is measured while ramping the heat flux up or decreasing it may also affect the measured heat flux and superheat at which incipience occurs. Details of the experimental approach for the current study are provided in the next section.

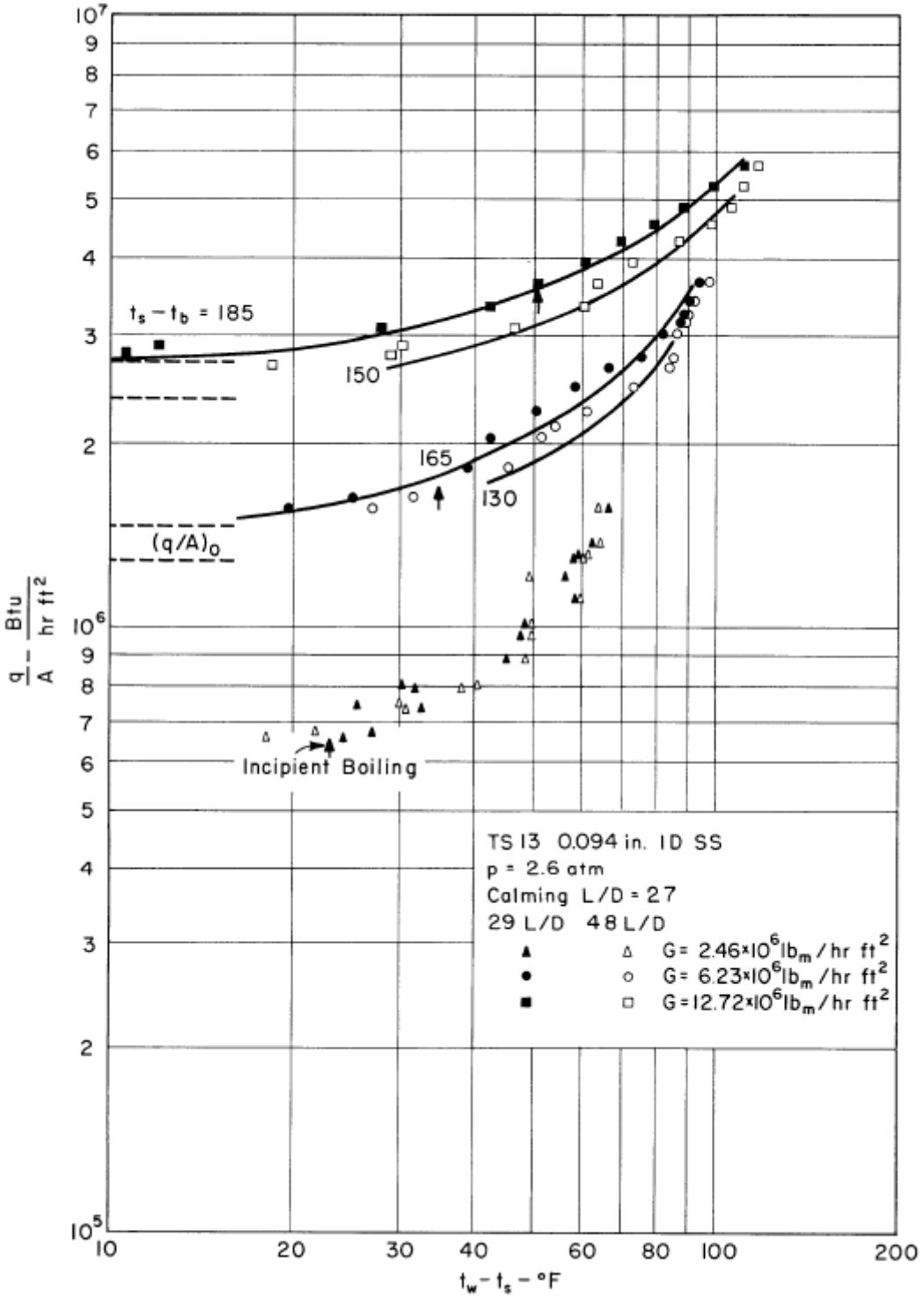

Figure 105: Forced Convection Boiling Curves of Bergles and Rohsenow [149]. Note that the axes are in British units.

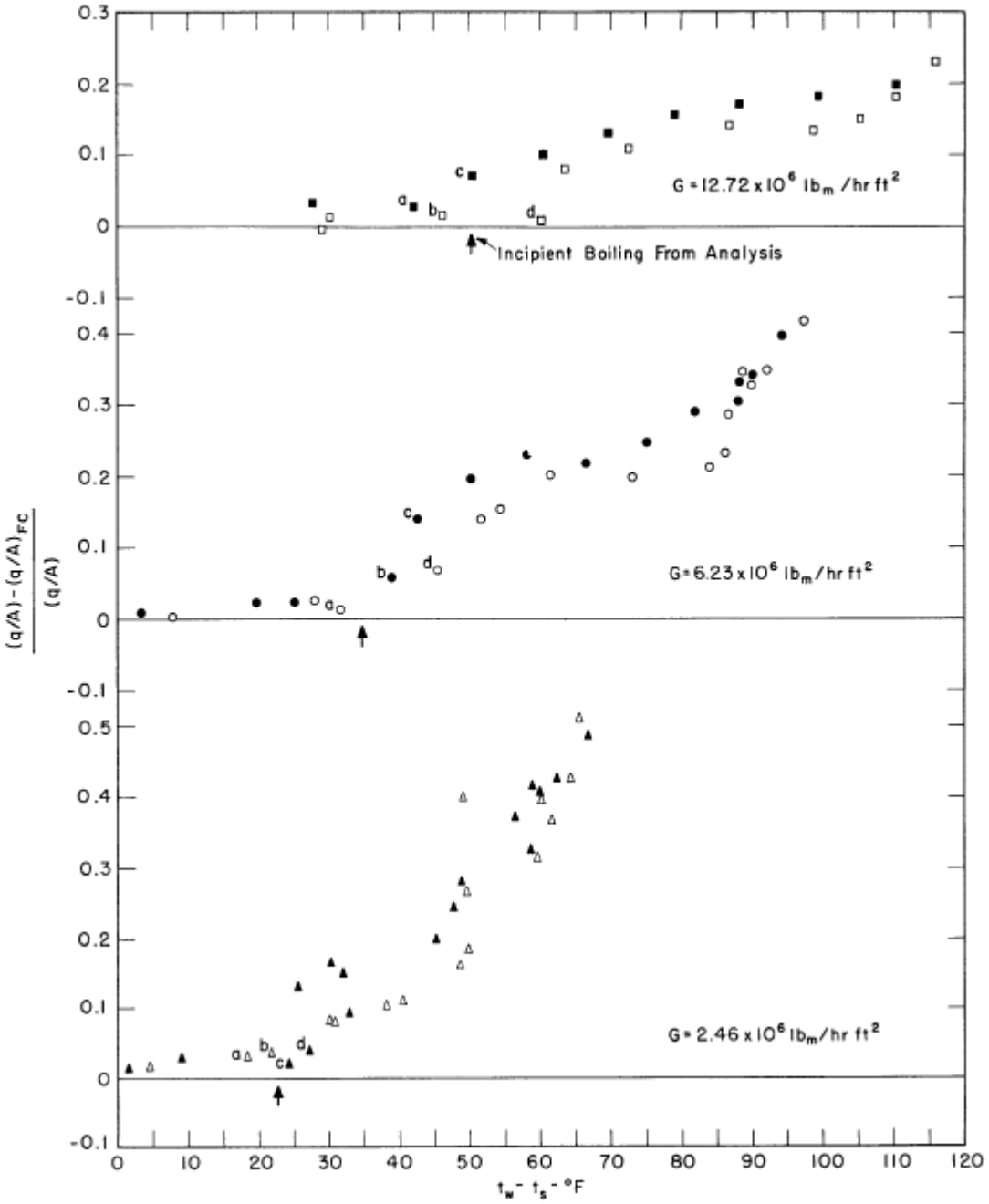

Figure 106: The approach used by Bergles and Rohsenow to determine onset of nucleate boiling under forced convection [149]. Partition Heat Flux (*y*-axis) versus Wall Saturation Superheat (*x*-axis).

5.4. Experimental Results for the Onset of Nucleate Boiling

The intent of this study was to assess the suitability of the Bergles and Rohsenow correlation in predicting the onset of nucleate boiling in an MITR coolant channel geometry under prototypic conditions, and if it was not adequate, to potentially develop an improved correlation. Therefore, it was important to emulate as closely as possible the methods used by Bergles and Rohsenow, since their study is the basis for current prediction. All tests were conducted with deionized water, where the measured resistivity was greater than 15 MΩ-cm. Water was degassed by reducing the system pressure and heating to 80 °C for several hours. The heater surface was degassed prior to every test by boiling vigorously for at least 30 minutes at reduced pressure, with non-condensable gases being frequently vented from the system. The system pressure was increased and the fluid temperature decreased following degassing to collapse any entrapped vapor on the heater surface. The dissolved oxygen content of the water was measured at the end of each test by diverting the full flow through the dissolved oxygen measurement loop, and was typically around 4.0 ppm or less. Dissolved oxygen measurements were taken at a fixed flow rate as specified by the meter.

Onset of nucleate boiling tests were conducted by maintaining a fixed mass flux through the test section while increasing the heat flux in a step-wise manner. Tests were conducted by keeping the test section outlet pressure at a fixed value and maintaining the test section inlet temperature at a fixed value, similar to the actual conditions in the MITR. Therefore, as the heat flux was increased, the bulk fluid temperature rise along the test section would increase, thereby resulting in a higher bulk outlet temperature with each step. The heat flux was held at each step long enough to reach equilibrium conditions (typically around 30 minutes). Local backside temperatures were measured at five second intervals, and the pressure drop was measured at 50 msec intervals.

Data were first collected at lower heat fluxes such that the single-phase component of the heat flux could be determined for each test at each location by fitting a line to the this data where the wall temperatures were below the saturation temperature. The total heat flux at each thermocouple location was partitioned into single-phase forced convection and boiling components. The inception of first significant boiling was identified in the empirical studies as the first point which met all of the following criteria:

1) The calculated surface temperature is greater than the local saturation temperature.
2) The partitioned boiling heat flux is greater than 7% to 8% (approximate value assumed by Bergles and Rohsenow from inspection of their graphs).
3) The measurement uncertainty in the heat flux at that point is less than the partitioned boiling heat flux.

The local pressure at each thermocouple location (which is necessary to determine the local saturation temperature) was determined using a linear interpolation between pressure taps, in the same manner as Bergles and Rohsenow. However, given the large pressure drop typically observed in the channel, boiling could take place toward the end of the channel, while the region closer to the entrance could remain in the single-phase heat transfer regime. Under these circumstances, a linear pressure drop model is no longer valid. Therefore, the thermocouple location closest to the outlet of the channel that experienced fully developed flow (in this case, TC13, located 27.2 cm from the channel inlet, or $z/D_{hyd}\approx 70$), was typically considered to yield the most reliable result. The results for forced convection boiling tests for mass fluxes ranging from 750 kg/m^2-sec to 3000 kg/m^2-sec and subcoolings from 15 °C to 40 °C are reported in the following sections.

5.4.1. Nominal Surface

Partial forced convection boiling curves were plotted from measured data at each thermocouple location using local conditions. Several curves are shown in Figure 107 at the lowest mass flux condition of 750 kg/m^2-sec, with error bars for TC13 indicating 95% bounds of the measurement uncertainty and representing values typical for the other thermocouple locations. Figure 108 shows a partial forced convection boiling curve for G=3000 kg/m^2-sec with an inlet bulk temperature of 80 °C. All tests were conducted with a channel outlet pressure of 1.3 bar, similar to that in the MITR.

The dimensionless axial position from the channel inlet (hydrodynamic) for the thermocouple at position 9 is z^+=43.6, whereas for the thermocouple at position 13, z^+=69.5. At the conditions plotted in Figure 107, the maximum pressure difference between TC9 and TC13 is only about 0.02 bar, resulting in the saturation temperature being about 0.5 °C higher at TC9. Additionally, at the maximum heat flux condition, the local bulk temperature at TC13 is as much as 5 °C higher than at TC9. Therefore, boiling is most likely to begin toward the end of the

channel, where the pressure is lower (leading to a lower saturation temperature) and the bulk fluid temperature is higher. In theory, this should enable collection of numerous boiling curves at different conditions. However, as mentioned earlier, once boiling initiates at one location, the assumption of linear pressure drop becomes less accurate. In addition, at the higher mass flux conditions, like that depicted in Figure 108, the pressure difference can be greater than 0.1 bar, leading to local saturation temperatures differing by more than several degrees Celsius. Therefore, it was possible to have boiling toward the outlet of the channel, with incipience not having occurred further upstream. Under some conditions, it was possible to have a significant amount of voiding at the channel exit, leading to onset of flow instability, with regions upstream not having reached the onset of nucleate boiling. Lastly, at very high heat fluxes, slight deflection of the heater plate led to unreliable temperature measurement at some locations. Therefore, thermocouple locations toward the outlet of the channel that experienced fully developed flow (i.e., that were not in the "exit length" region) were used to determine the onset of nucleate boiling point.

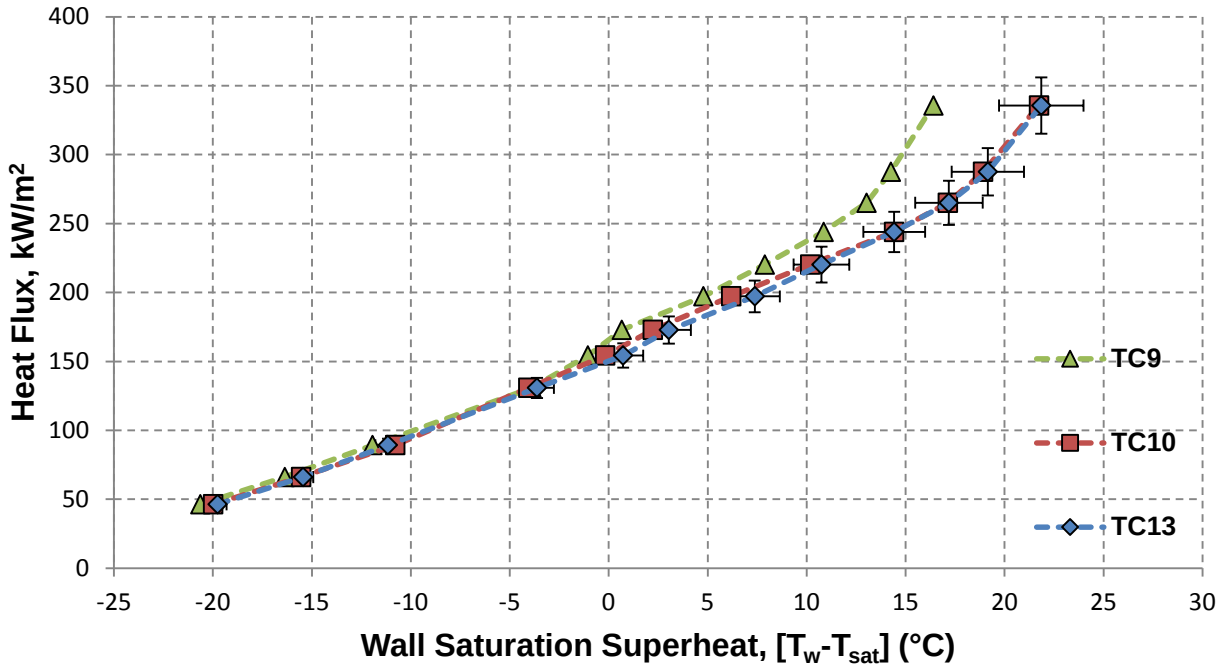

Figure 107: Partial Boiling Curves Based On Local Temperature Measurements for G=750 kg/m²-sec, and $T_{b,in}$=80 °C. Local conditions and saturation temperatures were used for each curve due to the large variation in saturation temperature and pressure axially along the channel. The pressure at the channel outlet 1.3 bar, the same as the nominal outlet pressure at the exit of the MITR fuel assemblies. Error bars are shown for TC13 only, and represent typical measurement uncertainty.

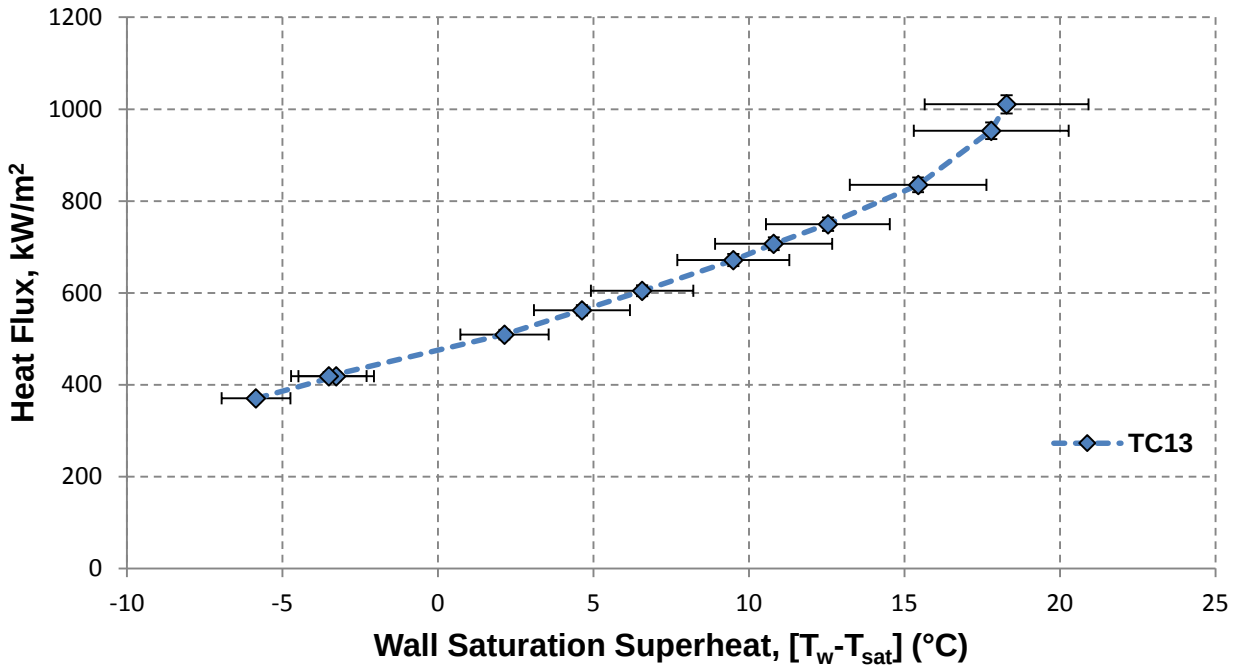

Figure 108: Partial Forced Convection Boiling Curve for G=3000 kg/m^2-sec and $T_{b,in}$=80 °C. The high pressure gradient and bulk temperature difference resulted in locations further upstream not reaching onset of nucleate boiling.

The onset of nucleate boiling point was determined using the method of Bergles and Rohsenow, as outlined in the preceding section, and is demonstrated in Figure 109. The same metric was consistently applied for all test conditions. As is demonstrated in Figure 109, a slight change in the partition heat flux may lead to a substantially different assessment for the onset of nucleate boiling, indicating that the uncertainty in ONB identification is much larger than the measurement uncertainty in the heat flux. Therefore, the 95% uncertainty in the onset of nucleate boiling heat flux was estimated by using neighboring data points where the heat flux partition differed by at least ±2.5%. This uncertainty accounts for both the error induced by a finite heat flux step size and also attempts to account for the underlying uncertainty in the partition method. Considering the measurement criteria and that a change of ±2.5% in the partition may not lead to the same increase or decrease in the onset of nucleate boiling heat flux, the estimated uncertainty in the ONB heat flux was not necessarily symmetric about the determined value.

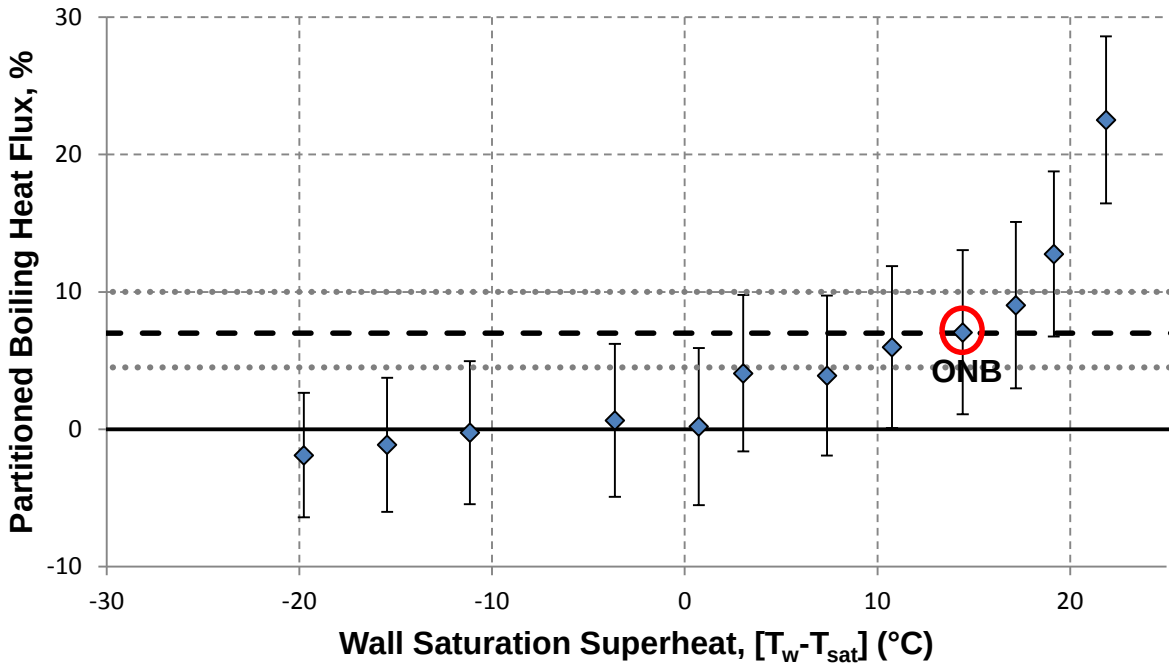

Figure 109: Partitioned Boiling Heat Flux for TC13 from the forced convection boiling curve in Figure 107. A boiling heat flux partition of about 7.5% was used as the breakpoint to determine the onset of nucleate boiling. This is the estimated value used by Bergles and Rohsenow from inspection of their graphs.

Results for all conditions where the temperature measurement criteria was applied (i.e., the partition heat flux method) are summarized in Figure 110. Complete data are provided in Appendix D. Note that repeatability tests were carried out at some conditions to demonstrate that the measured heat flux at the onset of nucleate boiling was consistent, as seen in Figure 110. The local surface temperature at the incipient point was also recorded in order to calculate the saturation superheat required for nucleation. These results are plotted in Figure 111, along with several models described previously. The error bars in this figure represent the measurement uncertainty for the heat flux and saturation superheat. Note that a small change in the surface heat flux will lead to a change of the surface temperature of a few degrees or more, which represents a large change in the saturation superheat. Therefore, the experimentally determined saturation superheat at the point of ONB is very sensitive to the exact selection criteria for boiling incipience (i.e. the partition heat flux criteria) and the inherent uncertainty associated with this method. Nonetheless, the experimentally determined saturation superheat at the point

of incipience is in reasonable agreement with the Bergles-Rohsenow model, except at the lowest mass flux condition when G=750 kg/m^2-sec.

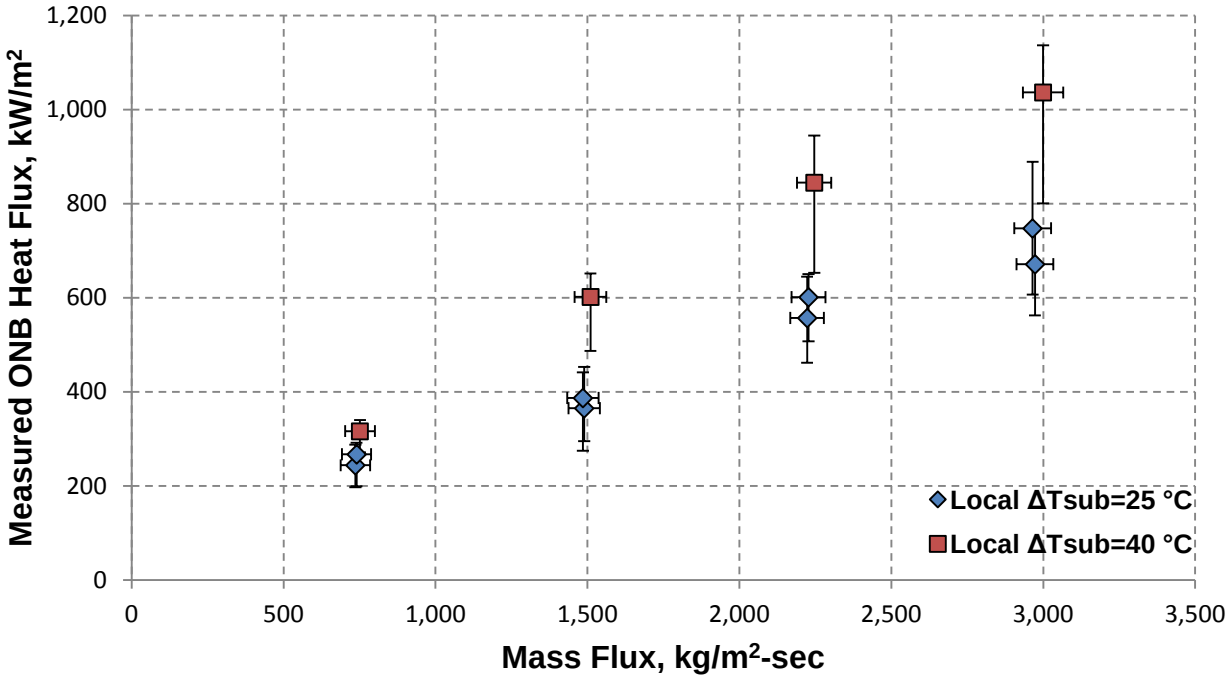

Figure 110: Measured Heat Flux at the Onset of Nucleate Boiling, Determined Using Local Temperature Measurement and the Partition Heat Flux Method. Error bars on the *x*-axis represent the 95% measurement uncertainty in the mass flux, whereas error bars on the *y*-axis represent the experimentalist's best estimate of the 95% uncertainty associated with the partition heat flux criteria. For the 25 °C subcooling, two nominally identical tests were run on separate days after cleaning and/or refreshing the surface to demonstrate the repeatability in the onset of nucleate boiling measurement.

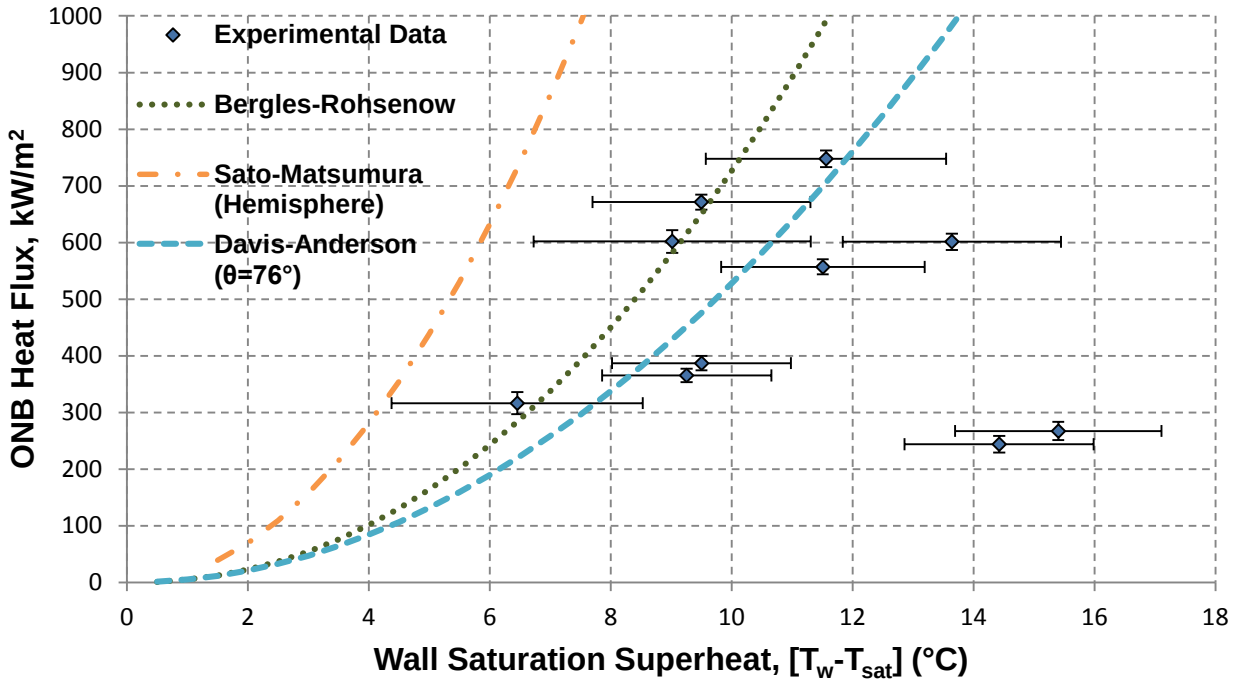

Figure 111: Measured Heat Flux versus Saturation Superheat at the Onset of Nucleate Boiling in a Narrow Rectangular Channel Heated on One Side. The heat flux predictions (using the experimental saturation superheat) for Bergles-Rohsenow, Davis and Anderson (using the measured equilibrium contact angle following testing), and Sato and Matsumura (hemispherical bubble) models are plotted for comparison. Error bars represent the measurement uncertainty in the heat flux and saturation superheat, and not the overall uncertainty resulting from the method of ONB determination.

In typical applications, the surface temperature is unknown, and must be predicted using an appropriate single-phase heat transfer correlation in combination with the chosen model for the onset of nucleate boiling. In most cases, the result is a transcendental equation that cannot be solved explicitly, but rather the solution can be found through an iterative scheme. As this is the calculation method for the MITR, it may be more appropriate to compare the measured heat flux at the onset of nucleate boiling to that predicted with the incipience model in combination with the single-phase heat transfer correlation. Figure 112 provides the comparison of the ONB heat flux data obtained with temperature measurements to values predicted with Bergles-Rohsenow and the Dittus-Boelter (McAdams) equation. As seen in the figure, several of the measured values at higher mass flux conditions and higher subcoolings fall short of the predicted value. Recall from Chapter 4 that the Dittus-Boelter equation tends to slightly overpredict the heat transfer coefficient at higher mass fluxes in the case of one-sided heating, thereby predicting a

lower wall temperature than actually exists at a given heat flux. Assuming the model of Bergles and Rohsenow is correct, this would lead to an overprediction in the heat flux at which the onset of nucleate boiling occurs. For comparison, the same measured data is plotted in against that predicted with the Bergles-Rohsenow model in combination with the semi-analytic correlation introduced in equation (151). Note that the wall viscosity factor of equation (52) was multiplied by equation (151) for the single-phase prediction due to the high bulk-to-wall temperature difference. The resulting agreement is slightly better than that achieved with the Dittus-Boelter equation. The error bars in both comparisons represent the estimated total uncertainty associated with the heat flux partition method used to identify incipience.

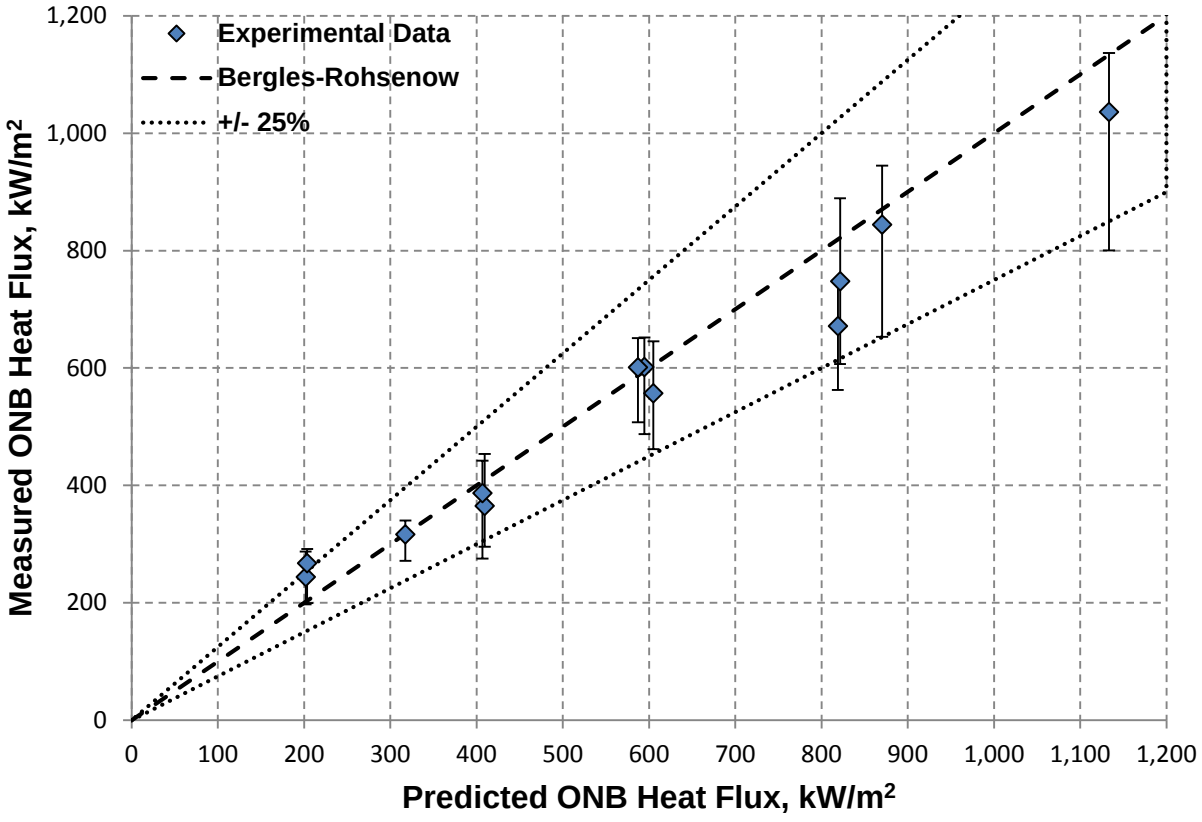

Figure 112: Measured Heat Flux at the Onset of Nucleate Boiling versus that Predicted from the Model of Bergles and Rohsenow (equation (161)) in combination with the Dittus-Boelter Equation (equation (73)). Experimental data were determined from temperature measurements using the heat flux partition method employed by Bergles and Rohsenow. Error bars represent the experimentalist's best estimate of the 95% uncertainty associated with the partition heat flux criteria.

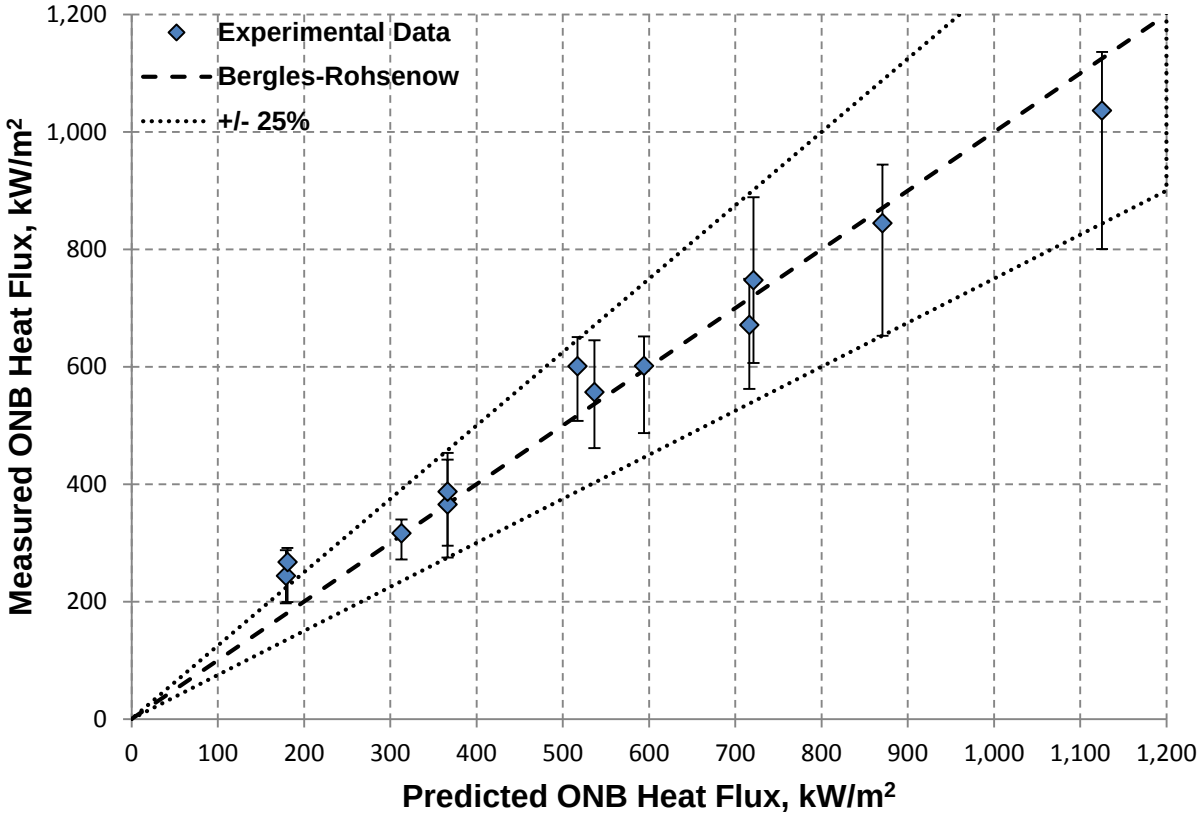

Figure 113: Measured Heat Flux at the Onset of Nucleate Boiling versus that Predicted from the Model of Bergles and Rohsenow (equation (161)) in combination with the Semi-Analytic Equation introduced in Chapter 4 (equation (151)). The wall viscosity factor was used in the single-phase prediction due to the high bulk-to-wall temperature difference. Experimental data were determined from temperature measurements using the heat flux partition method employed by Bergles and Rohsenow. Error bars represent the experimentalist's best estimate of the 95% uncertainty associated with the partition heat flux criteria.

As previously mentioned, pressure measurements could also be used to determine the heat flux at which the onset of nucleate boiling occurs. The change in the pressure drop at the onset of nucleate boiling was typically quite small, which is expected, especially under subcooled conditions. Therefore, the time-averaged pressure drop at each heat flux was not a suitable criterion for determining the ONB heat flux in the channel. However, as the heat flux increased, the fluctuation in the pressure signal with time became significant, and can therefore be used as the means for identifying first ONB in the channel. An example of the measured pressure drop at each heat flux step, along with the associated fluctuation in the pressure drop

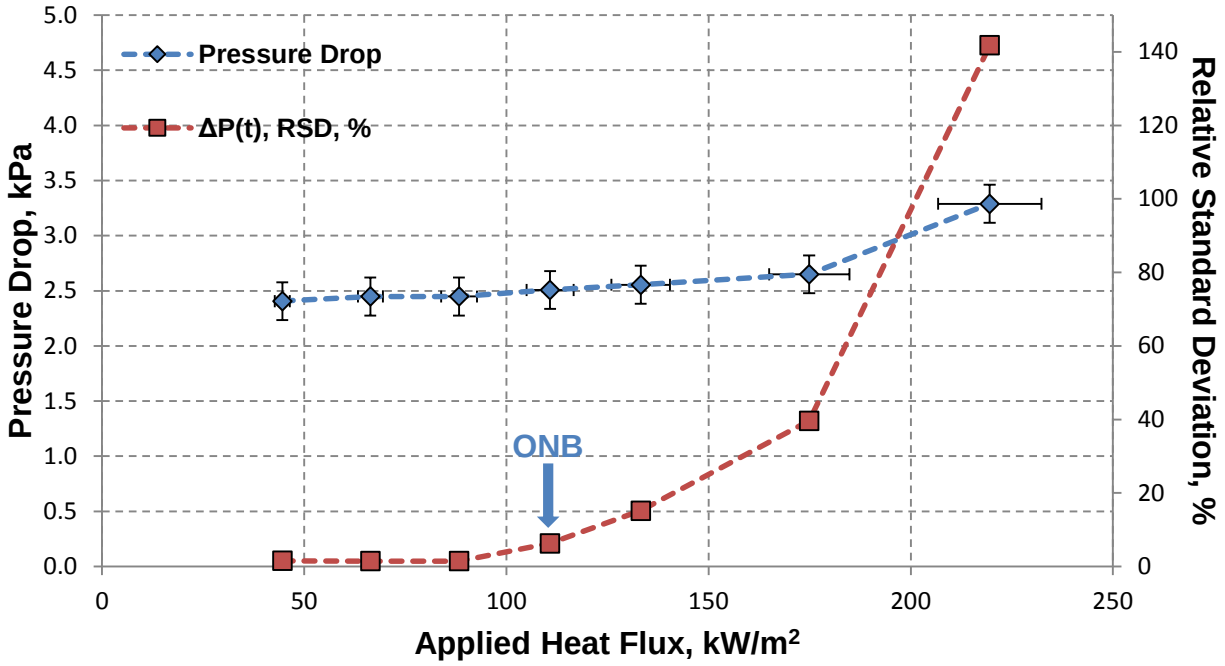

Figure 114: Channel Pressure Drop and Relative Standard Deviation of Pressure Drop-Time Signal for G=750 kg/m^2-sec and $T_{b,in}$=90 °C.

signal, is provided in Figure 114. The relative standard deviation of the pressure signal with time was used as a measure of the pressure signal fluctuation. The advantage of this approach is that it offers a means of determining first onset of boiling in the channel and is not tied to a specific thermocouple position. Therefore, if incipience were to occur first at the channel exit, which is generally expected, or at any other location where the thermocouples could not be placed (such as away from the axial centerline), the pressure fluctuation method would be able to capture the occurrence. However, the serious drawback of this method is that the local wall temperature at the onset of boiling cannot be assessed. It is the superheat itself, and not the heat flux, which leads to incipience on the surface. However, as discussed previously, the measured saturation superheat at the onset of boiling is highly sensitive to the ONB selection criteria and subject to large uncertainty. Therefore, the value of correlating the onset of nucleate boiling heat flux using the experimental wall temperature is somewhat diminished. Instead, the surface temperature can be predicted using the appropriate single-phase correlation and the comparison of data can be made in this manner.

Figure 115 summarizes all measured heat fluxes at the onset of nucleate boiling using the pressure fluctuation method. Note that at the lowest subcooling, where the bulk inlet

temperature was about 90 °C, onset of boiling always started at the channel exit, where thermocouples could not be installed due to the electrode clamp. The low subcooling condition was associated with flow instabilities shortly following ONB at the channel exit, leading to the inability to measure ONB upstream at thermocouple locations via temperature. The results using the pressure fluctuation method cannot be compared directly to those with the temperature measurement method, as the conditions may differ substantially due to the difference in axial position. Rather, the ONB heat flux can be compared to that predicted with Bergles-Rohsenow and the semi-analytical single-phase correlation, as was done in Figure 113 for the temperature measurement method. For the pressure fluctuation approach, property values for the predictions were evaluated using the properties at the channel exit, where ONB is expected to first occur. Results are plotted in Figure 116. A direct comparison between the onset of nucleate boiling identified with pressure oscillation and temperature measurement is not appropriate, since they are first detecting the phenomenon in different parts of the channel where the conditions (pressure and subcooling) can be significantly different. A comparison of the measured versus expected values (i.e., Figure 114 compared to Figure 116) is the most appropriate way to compare the results obtained with the two methods.

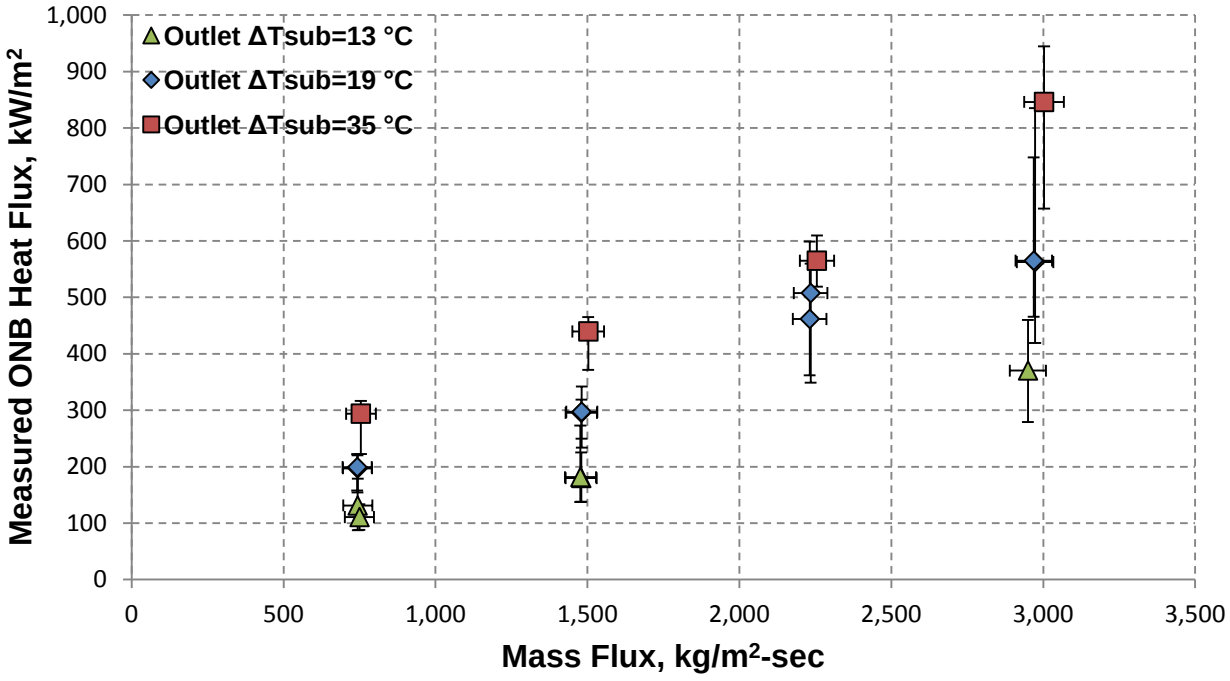

Figure 115: Onset of Nucleate Boiling Heat Flux for Channel as Determined from Pressure Measurement Fluctuations. Generally, onset of boiling is expected to start at the channel outlet, so the subcoolings reported are for the channel exit.

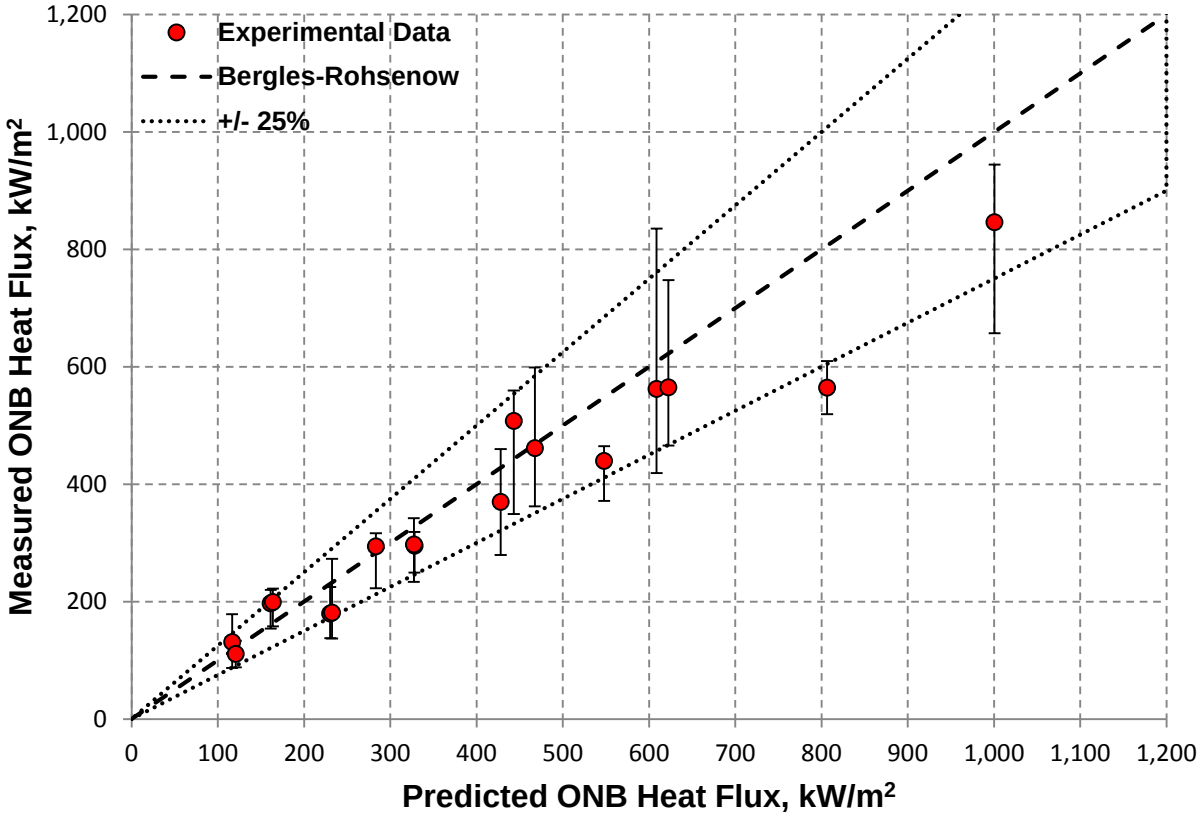

Figure 116: Measured ONB Heat Flux from Pressure Measurement Fluctuations versus Value Predicted for Outlet Conditions Using the Model of Bergles and Rohsenow and the Semi-Analytic Single-Phase Correlation with Wall Viscosity Factor Multiplier.

Using the pressure fluctuation approach to identify the ONB heat flux results in a slightly larger deviation from predicted values than with the temperature measurement (heat flux partition) method. Measured values tend to fall lower than predicted, possibly due to the detection of boiling at the edge of the heater. At the very edge of the heater, the influence of the side walls results in a lower fluid velocity, and edge effects from the interface between the heater plate and insulator may play a role in initial nucleation. Whereas the thermocouples, which are located at the axial centerline of the heater, are sufficiently removed not to be affected by edge effects, the pressure fluctuation method is sensitive to boiling anywhere in the channel. Predicted values are based upon the heater centerline and may not completely account for conditions at the heater edge. Therefore, the somewhat lower measured value of the ONB heat flux is expected due to the probable influence of boiling at the heater edges. The pressure fluctuation method might best be characterized as a "global" ONB detection technique.

It was generally not possible to visualize vapor bubbles at or shortly after incipience under most flow conditions for reasons previously described in section 5.3. For these tests, flow appeared to transition from single-phase to slug/churn flow almost immediately, though pressure and temperature measurements clearly indicated that boiling was occurring prior to reaching this point. However, in the test cases at the lowest mass fluxes, bubbles were visible near incipience, where they departed with some fraction surviving for a short time in the flow before collapsing.

Table 35: Summary of Visual Observations of the Onset of Nucleate Boiling Using High Speed Video Recordings. Under most conditions, vapor bubbles could not be visualized at or near the point of incipience.

MASS FLUX (kg/m^2-sec)	SUBCOOLING (°C)	ONB HEAT FLUX, Heat Flux Partition (kW/m^2)	ONB HEAT FLUX, Visual Observation (kW/m^2)
740	10.7	Not Measured	220
740	21.2	267 [199, 292]*	246
750	39.6	317 [272, 340]	272
1460	10.7	Not Measured	Not Visible
1480	22.8	442 [387, 497]	Not Visible
1510	40.7	602 [487, 652]	Not Visible
2220	24.6	557 [462, 645]	Not Visible
2230	23.4	651 [508, 794]	Not Visible
2970	26.1	748 [607, 889]	Not Visible
3000	43.0	1036 [801, 1136]	Not Visible

*Values in brackets indicate the experimentalist's 95% confidence interval estimate.

It is important to once again note that the working fluid and surface were degassed prior to conducting these tests. Using water with high dissolved gas content may lead to the erroneous visual identification of nucleation due to off-gassing of non-condensables during surface heating. Bubbles which are seen leaving the surface may consist entirely of non-condensable gases or a mix of gas and vapor, and therefore are not indicative of actual boiling, but rather, "pseudo-boiling," as pointed out by McAdams [80] and later Bergles and Rohsenow [149]. This was in fact observed during surface degassing prior to testing, with some bubbles forming and departing from the surface even when the surface was below the saturation temperature, clearly indicating that they were composed of non-condensable gas and not vapor. Keep in mind, however, that the MITR system is open to air, and the water should therefore be air-saturated.

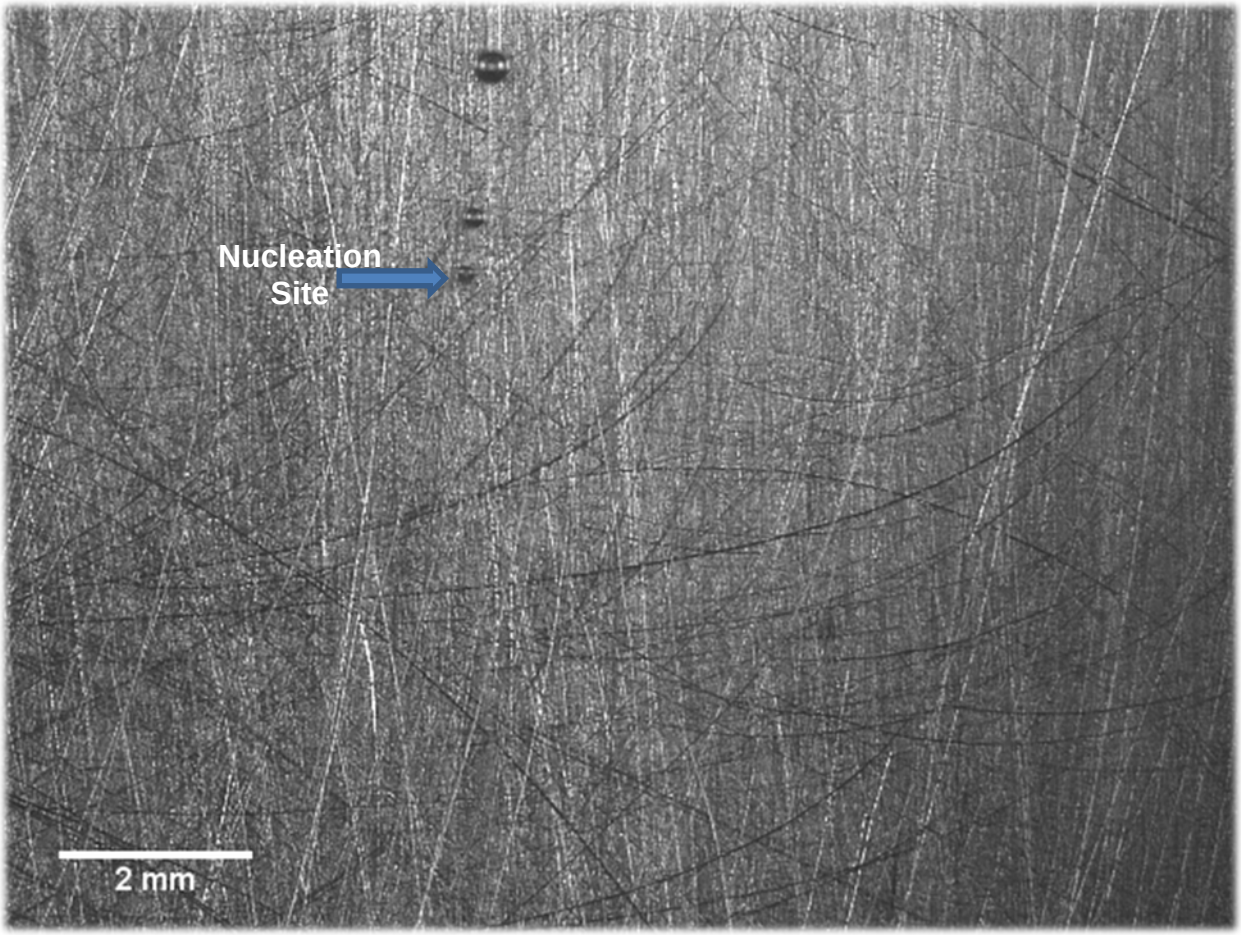

Figure 117: G=750 kg/m^2-sec, $T_{b,in}$=90 °C, z^+=79.56, center of channel. Several bubbles and an active nucleation site are visible at the ONB heat flux identified using temperature measurements.

In the few test cases where vapor bubbles were visible at or near the incipience point, the bubbles were rather small and nearly impossible to visualize without video playback (i.e. they were not distinguishable in still frames). In only one case at the lowest subcooling (10.7 °C) and mass flux (740 kg/m^2-sec) tested could an actual nucleation site be visualized shortly after the point of incipience. This is shown in Figure 117. At heat fluxes beyond initial incipience, bubbles in the free stream were greater in number and larger in size, as seen in Figure 118, though this occurrence shortly preceded the onset of flow instability. The flow regime can best be described as bubbly about the center of the channel, with vapor slugs becoming more prominent at the channel edges as heat flux was increased (refer to Figure 119), likely indicating direct evaporation was taking place at the edges. Toward the outlet of the channel as heat flux was increased further, vapor engulfed a significant fraction of the channel (refer to Figure 120), with the flow regime best being described as slug/churn flow. Flow instabilities were observable at this point, with visual discontinuity in the flow captured using high speed video and accompanied by large fluctuations in the measured channel pressure drop. Flow instabilities in narrow channels are discussed further in section 5.5.

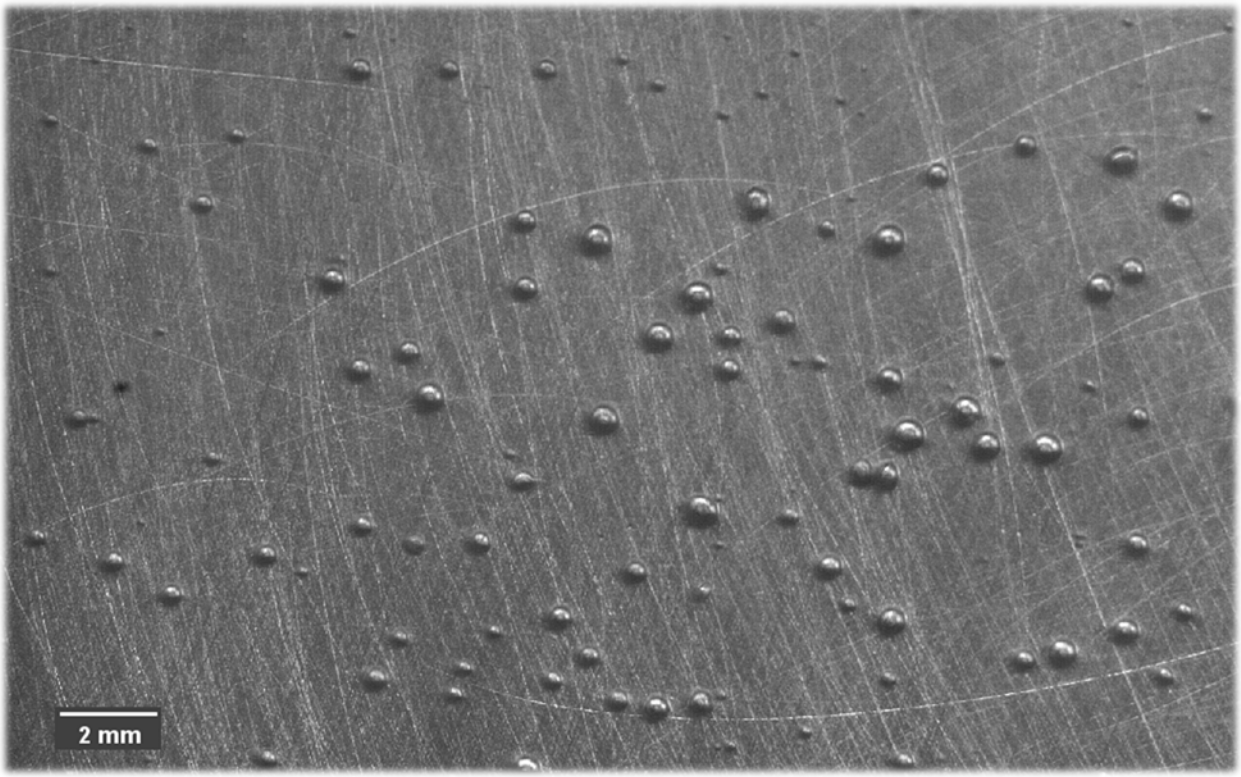

Figure 118: Bubbly Flow in Center of Channel. G=750 kg/m^2-sec. $T_{b,in}$=90 °C. The bubbles become larger in diameter with an increase in the heat flux and associated decrease in the local subcooling.

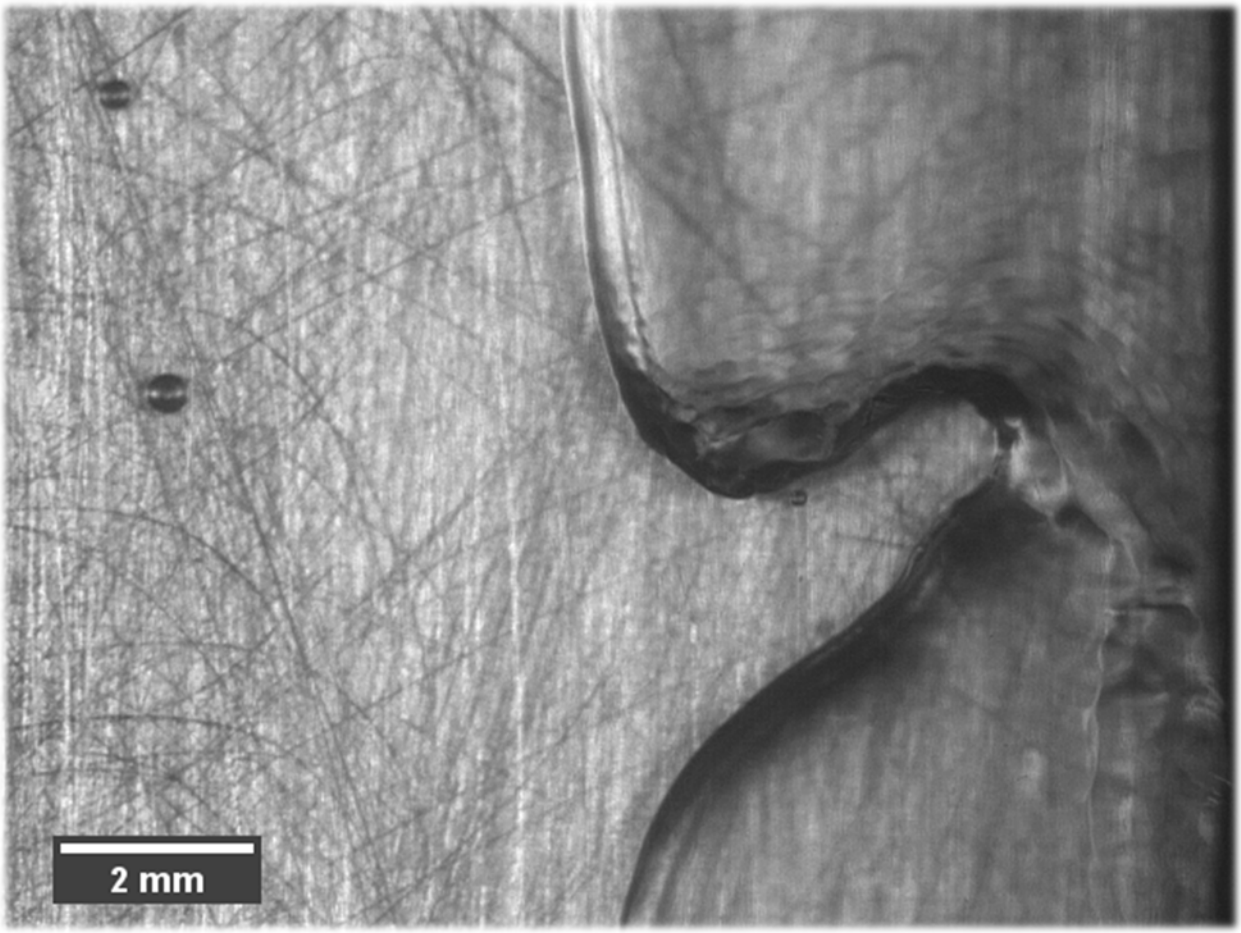

Figure 119: Channel Outlet, Right Edge. Slug flow at edges with bubbly flow in center of channel. G=750 kg/m^2-sec. $T_{b,in}$=90 °C.

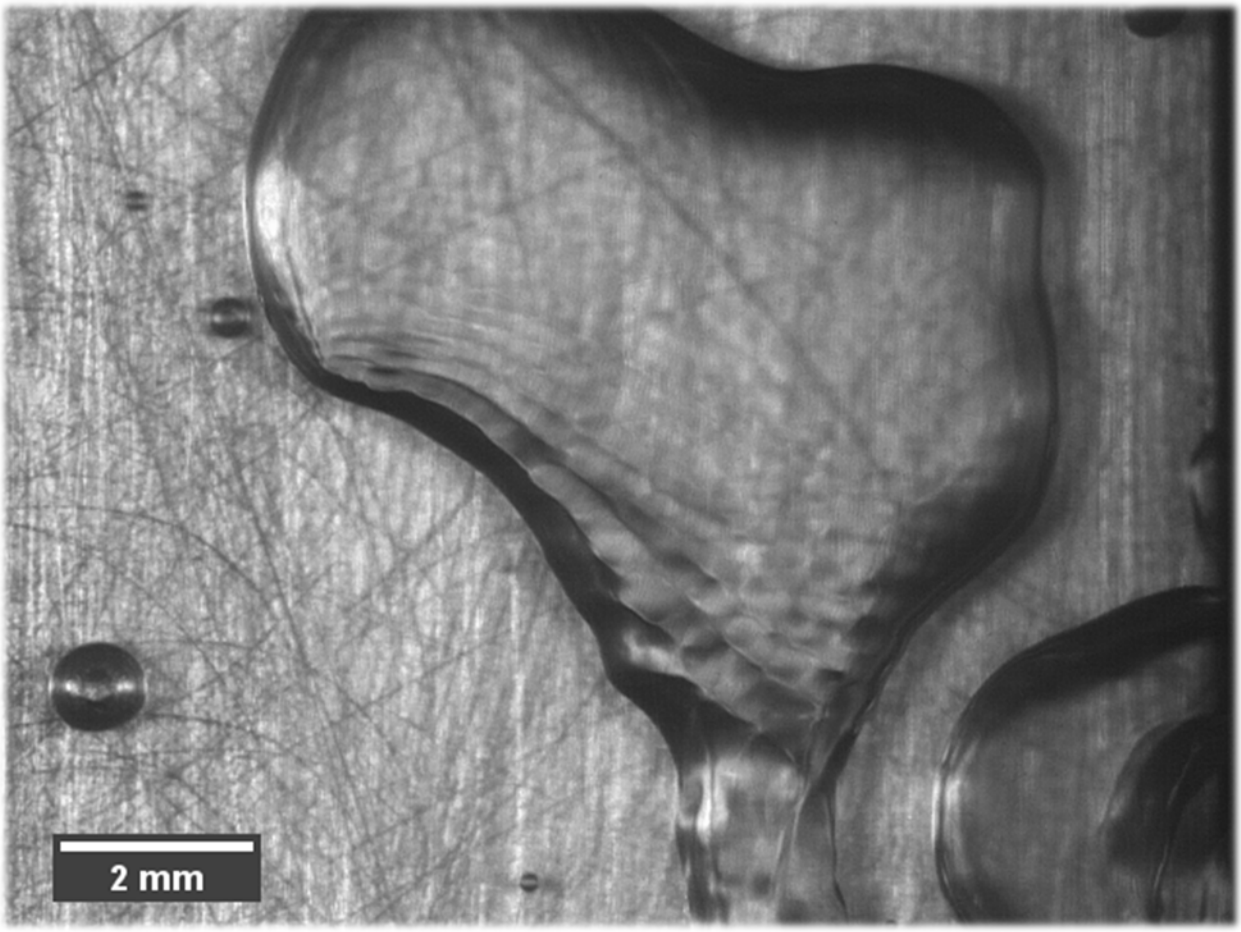

Figure 120: Slug/churn flow at channel outlet. G=750 kg/m^2-sec. $T_{b,in}$=90 °C. Vapor occupied a substantial fraction of the channel at the outlet, and flow instabilities were readily detected, with large accompanying fluctuation in the channel pressure drop.

For the lowest mass flux condition, the different flow regimes observed are illustrated in Figure 121. The flow regimes differed both axially along the channel and transversely across the channel, likely due to the large differences in local conditions. At very high heat fluxes, the entire outlet of the channel appeared to be enveloped by vapor, though high speed video showed shifting fingers of vapor and liquid. Additionally, while to the unaided eye the edges of the channel appeared to be occupied by continuous vapor jets, they were in fact rapidly moving, discontinuous vapor slugs which often collapsed.

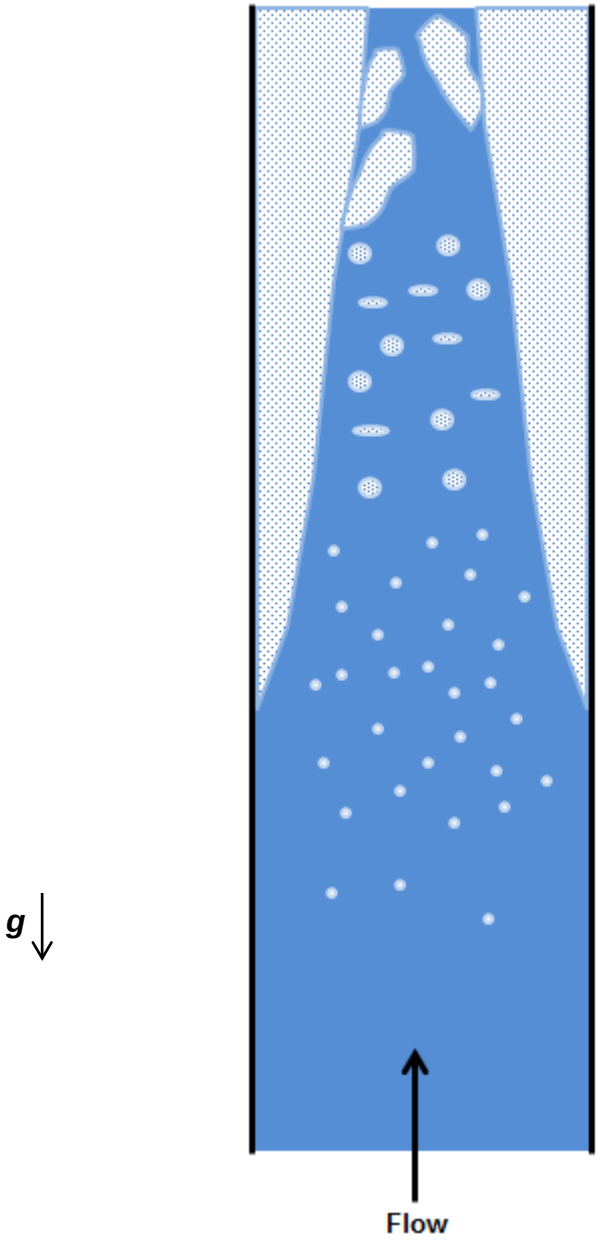

Figure 121: Illustration Summarizing Subcooled Boiling Flow Regimes for Vertical Upflow in the Narrow Channel at Low Velocities (u_{lo}<1 m/sec). The backside is heated with uniform heat flux for the entire channel length pictured.

At higher mass fluxes, the bubbly flow regime was not visible, though temperature and pressure measurements indicated boiling was occurring in the center of the channel. An audible crackling also indicated the presence of boiling. It is suspected that bubbles did exist at the center of the channel but departed and collapsed quickly and were well below the visualization threshold for the setup (20 μm/pixel with a few pixels required to resolve a bubble). At higher heat fluxes, spherical bubbles did appear during slug/churn flow at the edges due to the breakup of larger vapor slugs, as seen in Figure 122. An illustration of how the channel appeared during boiling at high flow velocities is provided in Figure 123. Once again, while thermocouples placed at the center of the channel indicated boiling was occurring, departing bubbles were not visible for most conditions where u_{lo}>1 m/sec, likely due to the small size.

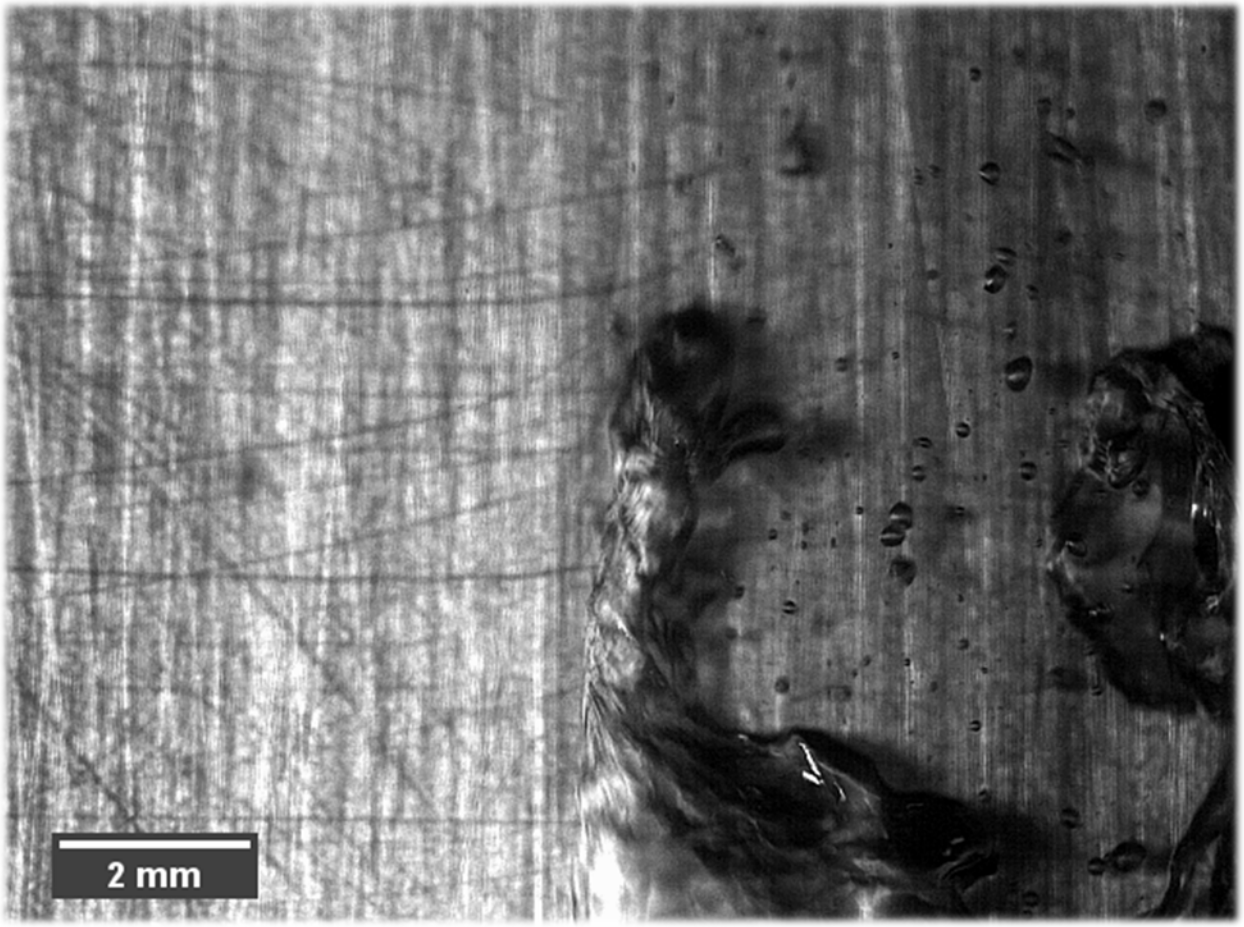

Figure 122: Breakup of Vapor Slug Producing Smaller Spherical Bubbles at the Channel Exit. G=3000 kg/m^2-sec, $T_{b,in}$=80 °C, q''=1000 kW/m^2.

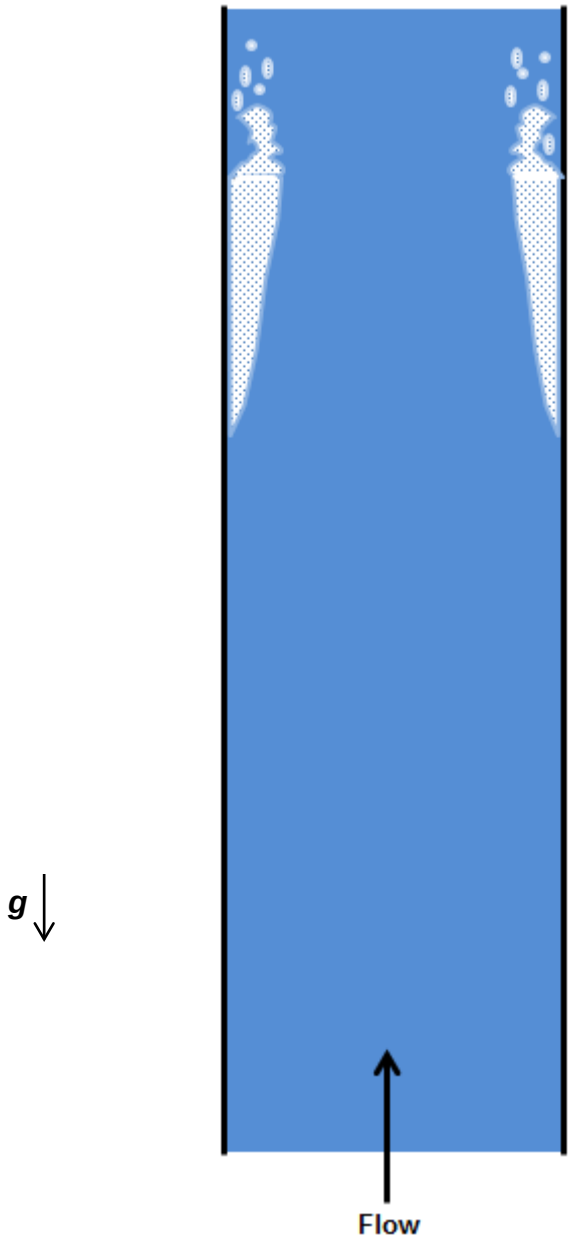

Figure 123: Illustration Depicting Subcooled Boiling for Vertical Upflow in the Narrow Channel at High Velocities (u_{lo}>1 m/sec). The backside is heated with uniform heat flux for the entire channel length pictured. Vapor slugs appeared to breakup just prior to the end of the heated length. While vapor bubbles were not visible in the center of the channel, thermocouples positioned there indicated boiling was occurring.

5.4.2. Oxidized Surface

After installation of the oxidized heater plate, tests were conducted to determine the isothermal heat loss and contact resistance of the newly installed thermocouples. As a means of verifying the heater installation and ensuring that no other channel conditions were altered beyond the oxide characteristics on the surface, single-phase heat transfer tests were conducted for the channel at a few select conditions. Considering that the oxidation process on stainless steel made a negligible change in the surface roughness, the single-phase heat transfer coefficient should be essentially unaffected. The channel average Nusselt numbers for fully developed conditions with *Pr*=3.0 and *Pr*=2.2 are plotted in in Figure 124 and Figure 125, respectively, with comparison to single-phase measurements for the nominal surface from chapter 4.

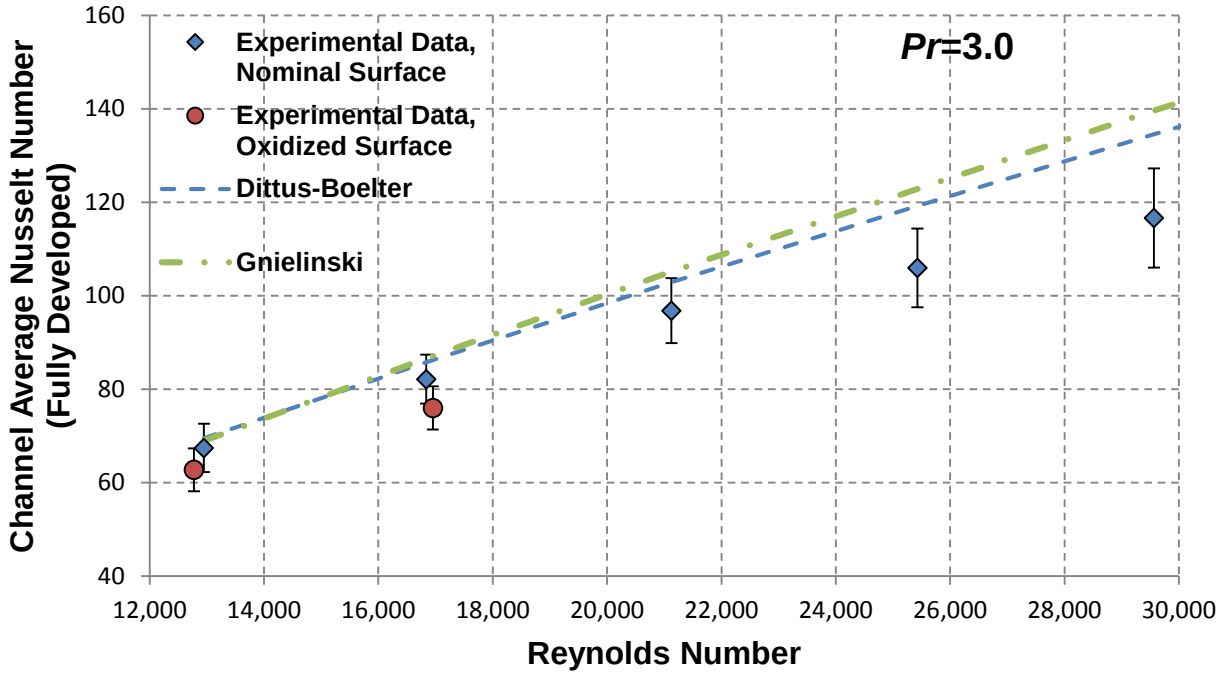

Figure 124: Channel Average Nusselt Number for Fully Developed, Single-Phase Conditions at a Prandtl Number of 3.0 (T_b≈60 °C). The data at the two flow conditions measured for the oxidized surface agree (within the experimental uncertainty) with values measured for the unoxidized surface.

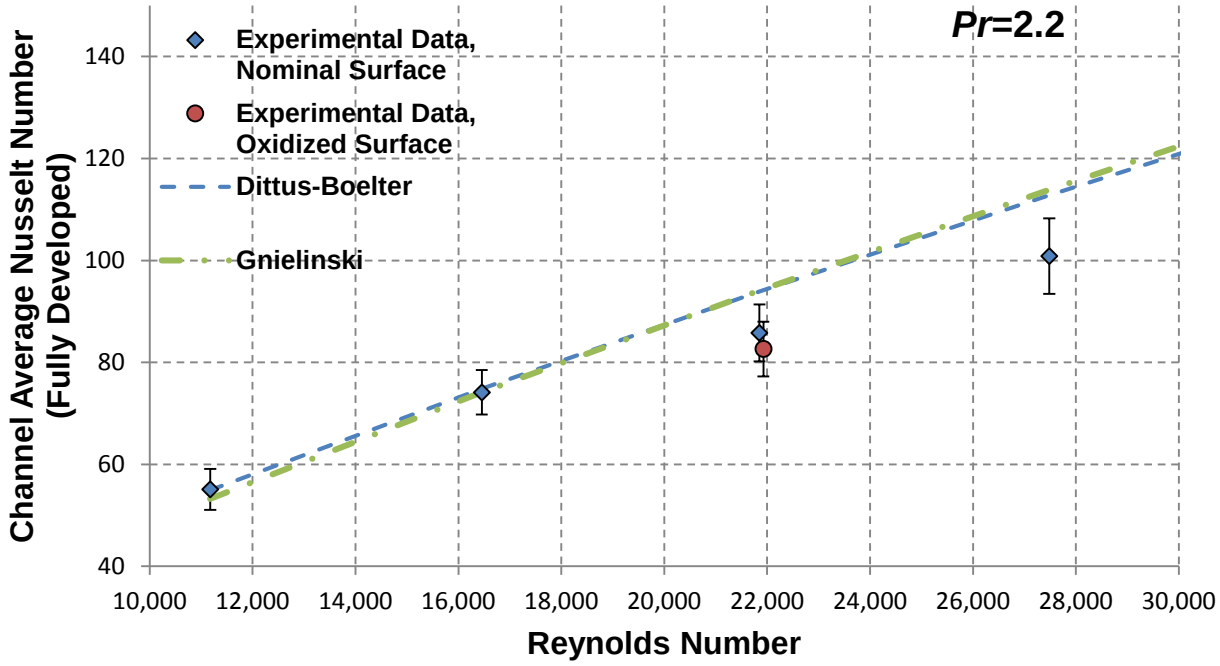

Figure 125: Channel Average Nusselt Number for Fully Developed Conditions at a Prandtl Number of 2.2 (T_b≈80 °C). The data at the single flow condition measured for the oxidized surface agree reasonably well with values measured for the unoxidized surface.

As an additional verification, the local single-phase heat transfer coefficient used for the heat flux partition in ONB tests was also compared at similar test conditions for the oxidized and unoxidized surfaces. These heat transfer coefficients were determined from the single-phase portion of boiling curves when $T_w<T_{sat}$. Therefore, repeatable values are indicative of similar conditions and enable direct comparison of the onset of nucleate boiling between the oxidized and unoxidized surfaces. Results are plotted in Figure 126, demonstrating good agreement for similar conditions, indicating that the channel and surface roughness remained essentially the same for the oxidized heater surface installation.

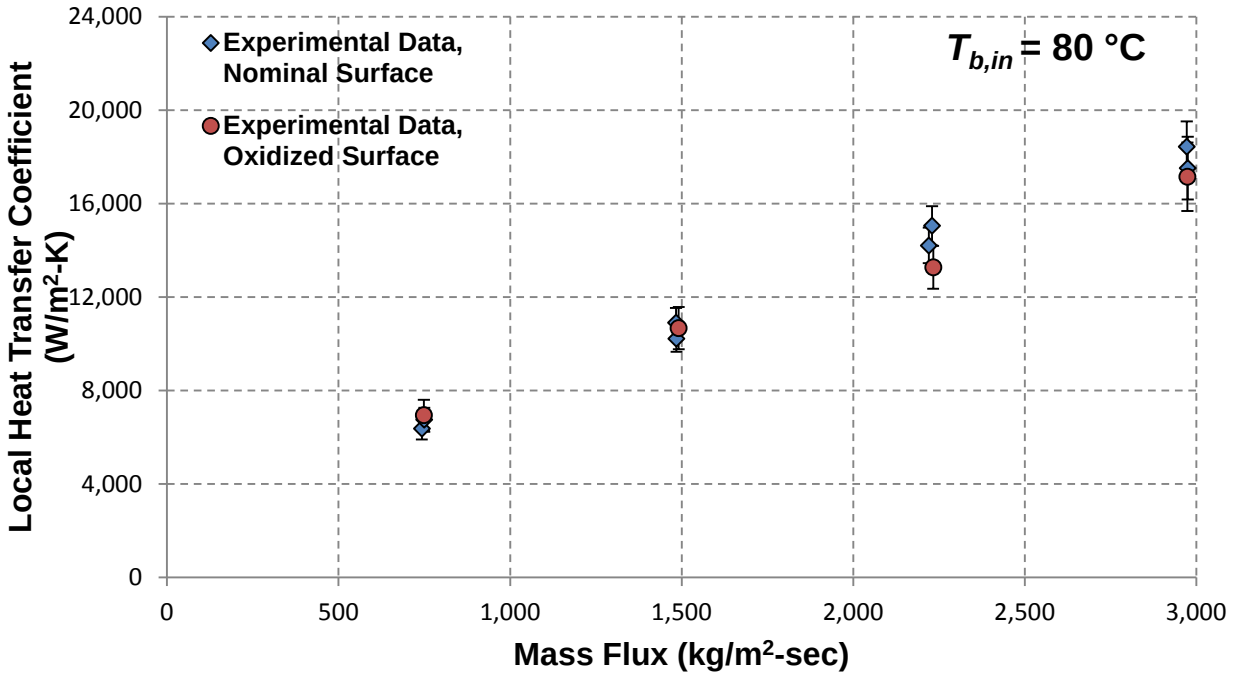

Figure 126: Local Heat Transfer Coefficients Based Upon the Single-Phase Region of Boiling Curves (where $T_w<T_{sat}$), which were Subsequently Used in the Heat Flux Partition to Determine the ONB Heat Flux. As seen in the figure, the values were very similar between the oxidized and nominal surface, indicating that the channel and surface roughness remained essentially unchanged with the new installation.

Partial boiling curves were obtained from the oxidized surface for an inlet temperature condition of 80 °C. All tests were conducted by fixing the outlet pressure at 1.3 bar, similar to that at the outlet of a channel in the MITR. The mass fluxes tested ranged from 750 kg/m^2-sec to 3000 kg/m^2-sec. All tests were conducted with deionized water, which was degassed to 4 ppm of O_2 or less. The tests were conducted, and the onset of nucleate boiling identified in the same manner as for the nominal surface. A comparison of partial boiling curves for the lowest mass flux condition is provided in Figure 127. Figure 128 summarizes the results for the oxidized surface as a function of mass flux.

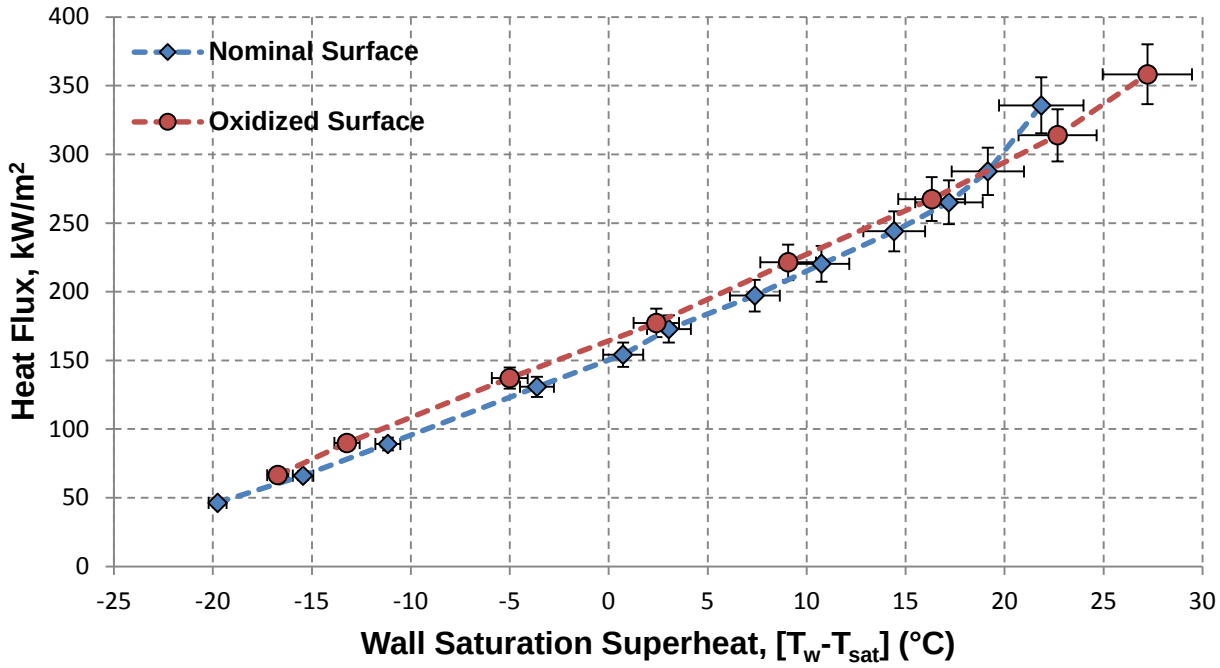

Figure 127: Partial Boiling Curves for Nominal Surface and Oxidized Surface Recorded at Same Axial Location (z^+=69.5). The mass flux, inlet temperature, and outlet pressure for both tests were G=750 kg/m²-sec, $T_{b,in}$=80 °C, and P_{out}=1.3 bar. Local conditions were used to create the curves.

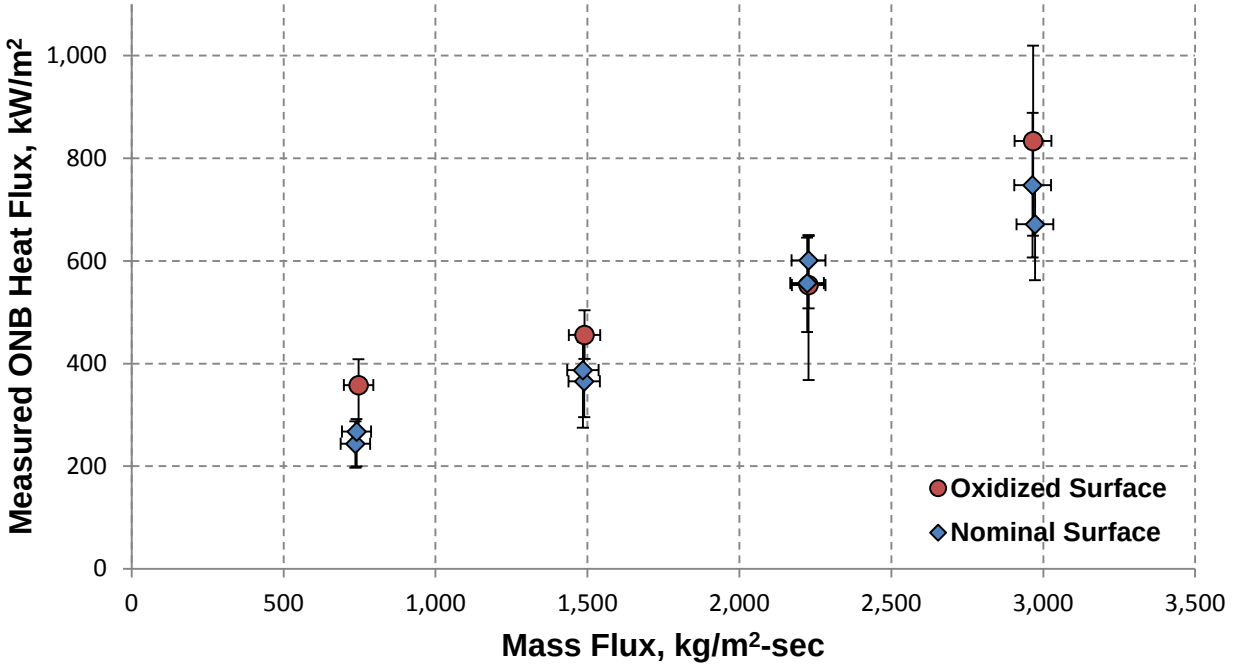

Figure 128: Comparison of the Measured Onset of Nucleate Boiling Heat Flux for the Oxidized and Unoxidized Surfaces as a Function of Mass Flux. All tests listed are for an inlet temperature of 80 °C, and an outlet pressure of 1.3 bar.

While the sensitivity in the saturation superheat measurement is rather high for reasons previously described, it is still useful to plot the measured heat flux at the onset of nucleate boiling against this parameter, since the superheat beyond saturation is what leads to incipience. A comparison between the nominal surface and oxidized surface is provided in Figure 129, where only tests for an inlet temperature of 80 °C are compared for clarity. The Davis-Anderson correlation (equation (168)) is plotted for the measured equilibrium contact angles on the nominal and oxidized surfaces. While Kandlikar advocates the use of the receding contact angle, in the Davis-Anderson prediction the equilibrium contact angle is most appropriate, as their analysis was conducted for a static bubble on the heated surface. As seen in the figure, while the Davis-Anderson correlation correctly predicts the trend with decreasing contact angle, the prediction is rather far off, either due to lack of optimum cavity sizes where incipience was measured or due to the large sensitivity in the saturation superheat determination. The tests conducted at the lowest mass flux (750 kg/m^2-sec), where Re<10,000, which potentially falls in

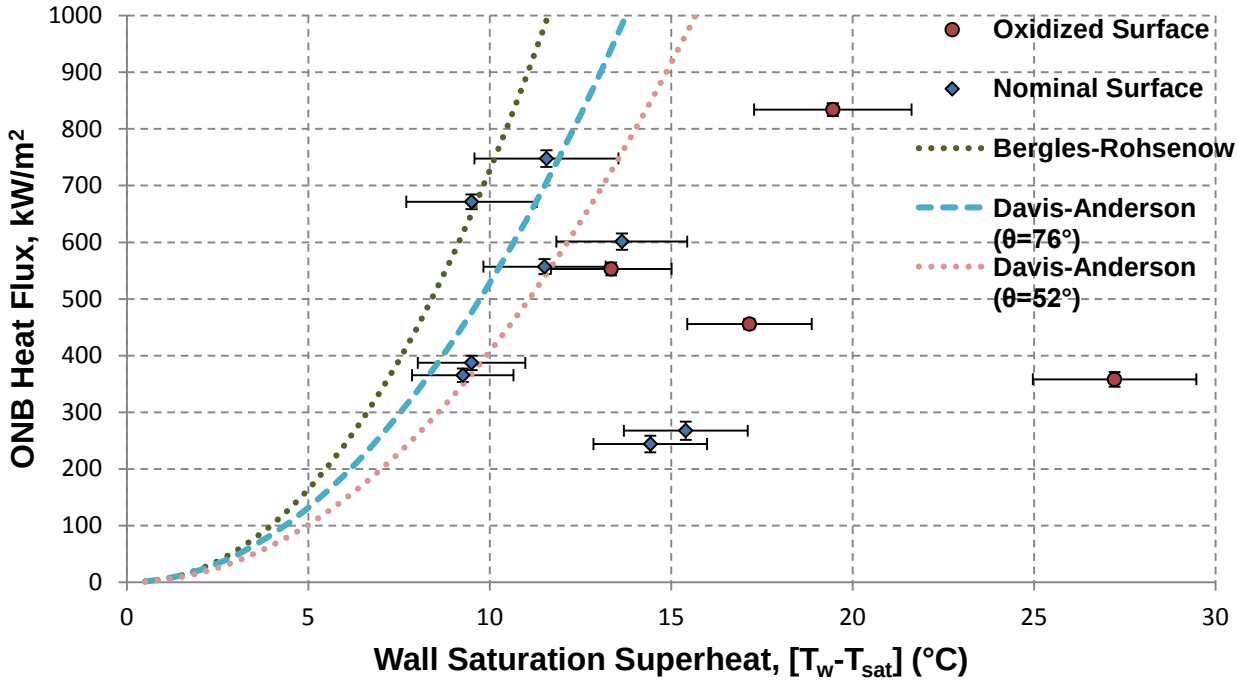

Figure 129: Onset of Nucleate Boiling Heat Flux versus Wall Saturation Superheat for All Tests Conducted with $T_{b,in}$=80 °C. In this plot, the Davis-Anderson correlation is shown using the two different equilibrium contact angles measured on the nominal and oxidized surfaces.

the transition regime for this channel, displayed the highest superheats at incipience. This could either be related to the transition flow behavior and varying boundary layer thickness or simply an aberration in the measurement, once again owing to the high sensitivity in the saturation superheat to the heat flux.

A summary of the measured onset of nucleate boiling heat flux for all conditions with both the nominal surface and oxidized surface are plotted in Figure 130 against the predicted value using the Bergles-Rohsenow correlation coupled with the semi-analytical expression for single-phase heat transfer presented in chapter 4 using the wall viscosity factor. Note that the prediction is based entirely upon the single-phase heat transfer correlation and the Bergles and Rohsenow correlation, so there is no dependence on the measured superheats shown in Figure 129. This is the method of prediction in the MITR, since cladding surface temperature measurement is not practical. As seen in the figure, the oxidized surface, on average, results in a modest increase in the onset of nucleate boiling heat flux. The contact angle reduction of about 30°, discussed in detail in chapter 6, is the probable cause of the delayed incipience.

While the measured onset of nucleate boiling heat flux for the oxidized surface was, on average, higher than that for the nominal surface, the same cannot be said for the pressure fluctuation measurement technique. As seen in the data provided in Appendix D, the pressure fluctuation method showed no change in the incipience point between the nominal and oxidized surface, with the heat fluxes being comparable for equivalent conditions. This supports the initial suspicion that the pressure fluctuation method first detects incipience at the edges of the channel, along the interface with the insulator. While the plate was oxidized, this would have little effect on bubble growth at the interface between heater plate and insulator. Therefore, incipience measured using the heat flux partition with temperature measurement should be considered more reliable, and a better means of comparing incipience between the oxidized and unoxidized surfaces.

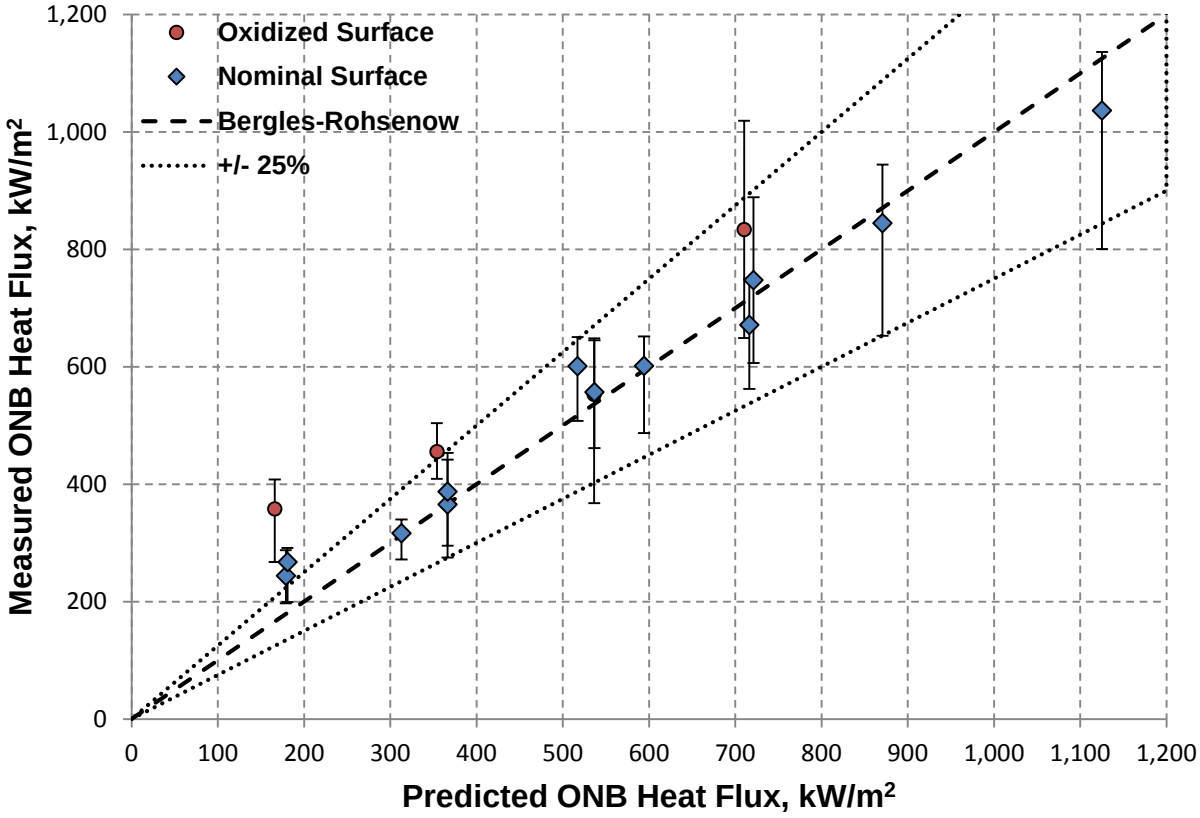

Figure 130: Measured Onset of Nucleate Boiling Heat Flux versus that Predicted Using the Bergles-Rohsenow Correlation Along with the Semi-Analytical Correlation for Single-Phase Heat Transfer Developed in Chapter 4. The wall viscosity multiplier of Sieder and Tate has been used in the single-phase prediction.

5.5. Flow Instabilities in Narrow Channels

While the onset of nucleate boiling is chosen as the criterion for the LSSS derivation in the MITR, this is established to provide substantial margin between normal operating conditions and actual safety limits. The ultimate safety limits are established to maintain integrity of the fuel clad, with the softening point of aluminum (about 450 °C) being the relevant temperature for the MITR. The critical heat flux is typically used as the criterion at which fuel and clad overheating is expected. However, flow in narrow channels at low pressure is susceptible to instabilities when significant voiding occurs. Flow instabilities will likely occur before the predicted CHF, potentially leading to reduced flow rates in the hot channel and consequently reducing the CHF below that predicted for normal flow in the channel. In the MITR, both CHF and the onset of flow instability (OFI) are calculated, with the safety limits being determined by whichever occurs first under a given set of conditions [17]. Therefore, flow instabilities are relevant phenomena in such channels, and were investigated in this study.

5.5.1. Review of Theory for Flow Instabilities

Two major classes of flow instabilities exist: static instabilities and dynamic instabilities. In nuclear systems such as the MITR, the potential for neutronic feedback may result in a compound thermal hydraulic/neutronic instability, but this will not be discussed here. Of the static instabilities, the excursive instability has been studied most, first being investigated by Ledinegg in 1938 [150], and is the most relevant static instability for flow in loop-type systems operating at low pressures such as the MITR. The excursive, or Ledinegg-type instability is characterized by a sudden, large amplitude excursion to a new stable operating condition. The Ledinegg-type instability is best described using the heated channel characteristic curve shown in Figure 131. In the figure, the "S-curve" (ΔP_{int}) represents the heated channel characteristic, with all-liquid and all-vapor lines for an adiabatic channel shown for comparison. The heated channel characteristic deviates from the adiabatic all-liquid curve in the single-phase region due to the higher film temperature from heating, leading to a reduction in the liquid viscosity near the surface. Moving from right to left (i.e., decreasing the flow rate), the onset of nucleate boiling occurs shortly before the local minimum in the curve. Further reduction in the flow rate in the

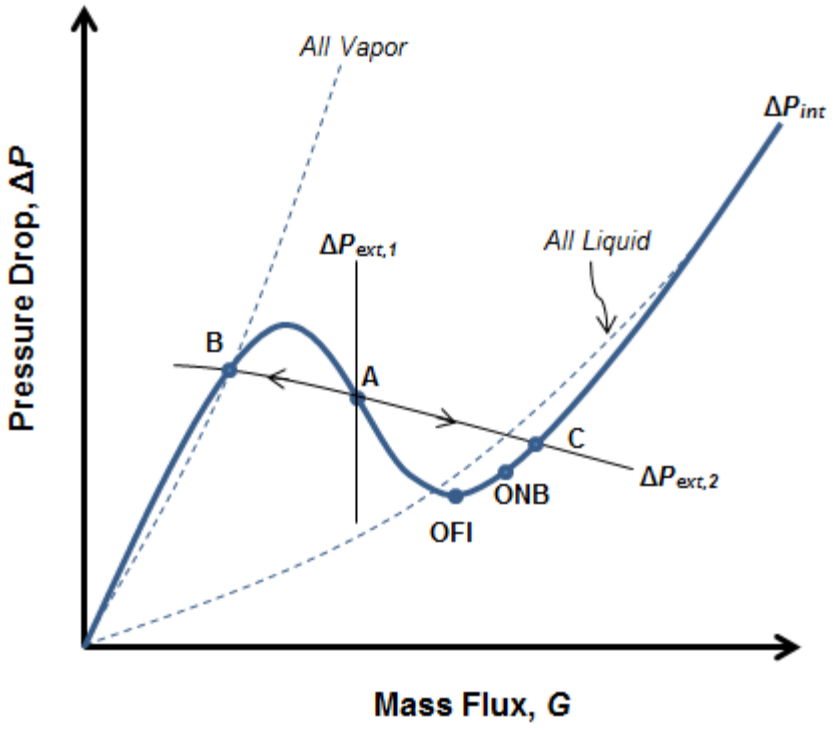

Figure 131: Pressure-drop vs. Mass Flux Characteristic Curve for a Heated Channel. The "S-curve" represents the pressure drop characteristic of the heated channel, with all-liquid and all-vapor curves shown for comparison. The external pressure drop curves represent the pump characteristic, with curve 1 representing a positive displacement-type pump (e.g. a piston pump) and curve 2 being representative of a centrifugal-type pump, such as that used in this study.

channel results in significant voiding, leading to a higher pressure drop even as flow rate is reduced further. The basic criterion required for the excursive instability is:

$$\left.\frac{\partial \Delta P}{\partial G}\right|_{int} \leq \left.\frac{\partial \Delta P}{\partial G}\right|_{ext} \tag{173}$$

A negative slope in the channel characteristic curve, such as the encountered between the minima and maxima in Figure 131, does not by itself imply an unstable operating point. For example, if the external pressure is supplied by a positive displacement-type pump (e.g. a piston pump), with $\Delta P_{ext,1}$ representing an idealized characteristic curve for such a device, operation in the negatively-sloped region will be stable. However, operation with a centrifugal pump

displaying the characteristic curve represented by $\Delta P_{ext,2}$ will result in unstable operation at point *A*, with a slight disturbance resulting in an excursion to either point *B* or point *C*, both of which are stable operating points. A flow excursion to point *B* would likely result in CHF.

The Ledinegg instability is particularly troubling in a parallel channel system such as the MITR, since the externally imposed pressure drop across all fuel channels is constant, or nearly so, due to the potential for redistribution of flow between channels. As a result, the external pressure drop characteristic for a given channel in the system will be a horizontal line. In this case, the local minimum in Figure 131 will meet the criterion for the excursive flow instability. Whittle and Forgan, in a 1967 study related to a power uprate for the 15 MW PLUTO test reactor, confirmed experimentally that the excursive flow instability did in fact occur at the minimum in the S-curve for a parallel channel system [153]. In their study, they constructed a narrow, heated rectangular channel with a large unheated hydraulic bypass in parallel to simulate the hot channel and rest of the core, respectively. Their test conditions are highly relevant to the MITR, with exit pressures from 17 to 27 psia (1.17-1.86 bar), flow velocities of 2 to 30 feet/sec (0.61-9.14 m/sec), and inlet temperatures ranging from 35 °C to 75 °C. Whittle and Forgan note that the minima in the S-curves can be related to the channel outlet subcooling ratio, *R*:

$$R = \frac{\left(T_{b,out} - T_{b,in}\right)_{OFI}}{\left(T_{sat,out} - T_{b,in}\right)} \tag{174}$$

Using data for several narrow rectangular channels with different aspect ratios and dimensionless lengths, they determine that the value of *R* at the minima of the S-curves can be correlated by:

$$R = \begin{cases} 0.697 + 0.00063\left(\frac{L_H}{D_H}\right), & 100 < \left(\frac{L_H}{D_H}\right) < 200 \\ \frac{1}{1 + 25\left(\frac{D_H}{L_H}\right)}, & \left(\frac{L_H}{D_H}\right) < 100 \end{cases} \tag{175}$$

where D_H is the heated equivalent diameter, not the hydraulic equivalent diameter. Note that the MITR Safety Analysis Report simply indicates the equivalent diameter, which is not correct.

Whittle and Forgan note that the value of *R* at the minimum point is about 5% lower for circular tubes. For a constant and uniform channel power input, the mass flux at which the local minimum in the pressure drop occurs can be determined from an energy balance for the channel:

$$G_{OFI} = \frac{\dot{Q}}{Rc_p A_{flow}\left[T_{sat}(P_{out}) - T_{b,in}\right]} = \frac{4q'' L_H}{Rc_p D_H\left[T_{sat}(P_{out}) - T_{b,in}\right]} \tag{176}$$

where D_H is once again the equivalent heated diameter and $\dot{Q}$ is the channel power. This will be the mass flux at which the excursive instability is expected for a parallel channel system, though Whittle and Forgan stress that this conclusion is only valid for low pressure systems, where the liquid-to-vapor density ratio is very large. Systems are less susceptible to the Ledinegg instability at high pressures, and the assumption of the minimum in the S-curve corresponding to the flow excursion point becomes less accurate as system pressure increases.

Whittle and Forgan conducted tests with and without an unheated hydraulic bypass, and the location of the minimum in the S-curve remained unchanged. This signifies that experiments could be conducted using a single channel, and as long as the pressure drop characteristics of the channel (including form losses at the inlet and outlet) are the same as the channel of interest in the parallel system, the correct point of the minimum in the S-curve should be obtainable. Kennedy et al. [147] arrive at a similar conclusion in their experiments, where they measure the onset of flow instability in both parallel and single microchannels. They arrive at the following purely empirical relations for determining the heat flux (for a constant mass flux) and mass flux (for a constant heat flux) at which the excursive instability will occur:

$$q''_{OFI} = 0.9 q''_{sat} \tag{177}$$

$$G_{OFI} = 1.11 G_{sat} \tag{178}$$

where q''_{sat} and G_{sat} are the heat flux and mass flux, respectively, required to yield saturated conditions at the channel outlet when other conditions are held constant. These parameters are defined as:

$$q''_{sat} = \frac{GA_{flow}\left(h_f - h_{in}\right)}{P_H L_H} \tag{179}$$

$$G_{sat} = \frac{q'' P_H L_H}{A_{flow}\left(h_f - h_{in}\right)} \tag{180}$$

While the above expressions utilize the surface heat flux, it is in fact the total channel power that influences the onset of flow instability, which is accounted for by using the heated perimeter and heated length. The onset of flow instability is a global, not a local, phenomenon, and therefore the total channel power must be considered. This is especially important in the case of side channels which may only be heated on one side.

The Ledinegg instability can be countered by increasing the system pressure, as mentioned before, or by installing a large form loss at the channel entrance, such that the pressure drop at the channel inlet is far greater than that at the outlet. However, in systems like the MITR, it is not practical to raise the system pressure, and throttling the inlet of channels would be counterproductive as the flow is limited by the pumping power. Therefore, the Ledinegg instability is largely unavoidable in the MITR, and is the determining factor for the ultimate safety limit under most operating conditions.

Dynamic flow instabilities display a temporal dependence, where feedback effects play an integral role in the process. As such, they are typically periodic in nature, and can be characterized by the frequency of oscillation observed in the flow and channel pressure drop. Acoustic instabilities are the result of resonance of pressure waves in the fluid resulting from vapor collapse, and typically result in high frequency oscillations ranging from 10 Hz to 1000 Hz. Acoustic oscillations are in many cases nothing more than a curiosity, though large amplitude vibrations in channel pressure drop have been observed. While acoustic instabilities will not be discussed further in this study, a thorough review is provided by Bouré et al. [150].

The other fundamental dynamic flow instability is the density wave oscillation. Density waves are a result of multiple regenerative feedbacks between flow rate, vapor generation rate, and channel pressure drop, resulting in sustained oscillatory behavior in the channel flow and pressure drop. As such, density wave oscillations have also been referred to as “flow-void

feedback instabilities" and "time-delay oscillations" [150]. As the mechanism is tied to the physical transit of the fluid through the channel, the period density wave instabilities is approximately one to two times the transit time of the channel [150]. For a 3.5 m long channel in a light water reactor, this corresponds to a density wave oscillation frequency of about 1 Hz [154]. Ishii [155] formulated a stability analysis for a boiling channel assuming thermal equilibrium and introduced the two following non-dimensional groupings:

$$N_{pch} = \frac{q'' L_H P_H \left(\rho_f - \rho_g\right)}{\rho_f \rho_g h_{fg} A_{flow} u_{in}} \tag{181}$$

$$N_{sub} = \frac{\left(h_f - h_{in}\right)\left(\rho_f - \rho_g\right)}{h_{fg}\rho_g} \tag{182}$$

The phase change number (equation (181)) effectively scales the rate of phase change to the heat rate in the channel. The subcooling number (equation (182)) accounts for time lag effects in the liquid region due to subcooling at the inlet. The simplified stability criterion of Ishii, which assumes thermal equilibrium, is applicable for high subcooling number such that $N_{sub} > \pi$:

$$N_{pch} - N_{sub} \leq \frac{2\left[K_{in} + \frac{f_m L_H}{2D_{hyd}} + K_{out}\right]}{1 + \frac{1}{2}\left[\frac{f_m L_H}{2D_{hyd}} + 2K_{out}\right]} \tag{183}$$

Here K_{in} and K_{out} represent the inlet and exit form losses for the channel and f_m is the two-phase mixture friction factor. However, the assumption of thermal equilibrium, as pointed out by Saha [156], excludes the possibility of net vapor generation in the subcooled boiling region. In the current study, nearly all experiments were carried out with the bulk fluid remaining well below saturation in the entirety of the channel. Despite this, significant voiding was observed at high heat fluxes, indicating that the thermal equilibrium assumption is not valid for the narrow channel.

Saha, Ishii, and Zuber [157] performed experiments to investigate the stability of boiling channels and compared results to the stability analysis using both equilibrium and nonequilibrium theory. According to the study, the nonequilibrium theory predicts a less stable system at high subcooling number compared to that predicted by assuming thermal equilibrium, which agrees with their experimental data. Todreas and Kazimi also provide a succinct comparison of stability boundaries using homogeneous-equilibrium, homogeneous-nonequilibrium, nonhomogeneous-equilibrium, and nonhomogeneous-nonequilibrium two-phase flow models [154].

5.5.2. Experimental Results

While the experimental setup was a single-channel, not a parallel channel system as in the MITR and no bypass was installed in parallel with the test section, it was thought that useful information regarding the excursive instability could still be garnered by conducting tests to obtain the channel characteristic pressure drop curve as a function of mass flux. The minimum in the S-curve corresponds to the excursive flow instability point for a system at low pressure with a flat external pressure characteristic (i.e., a parallel channel system). Recall that Whittle and Forgan [153] and Kennedy et al. [147] indicate the minimum in the S-curve will be unchanged for a single channel or parallel channel as long as all other channel pressure drop characteristics are the same. Therefore, tests were conducted where the heat flux, outlet pressure, and inlet temperature were held at constant values, with the mass flux being decreased in a step-wise fashion, starting at a sufficiently high enough mass flux such that the entire channel was in the single-phase region. However, significant oscillations were encountered in both the flow and pressure drop before reaching the minimum in the S-curve. Figure depicts one such attempt at obtaining the characteristic curve for the channel. It is clear that as the mass flux decreases, and hence the inlet velocity decreases, the phase change number increases to a point where the channel is operating in the unstable region from the standpoint of density wave oscillations. Dynamic instabilities such as the density wave oscillation are associated with the positive-sloped

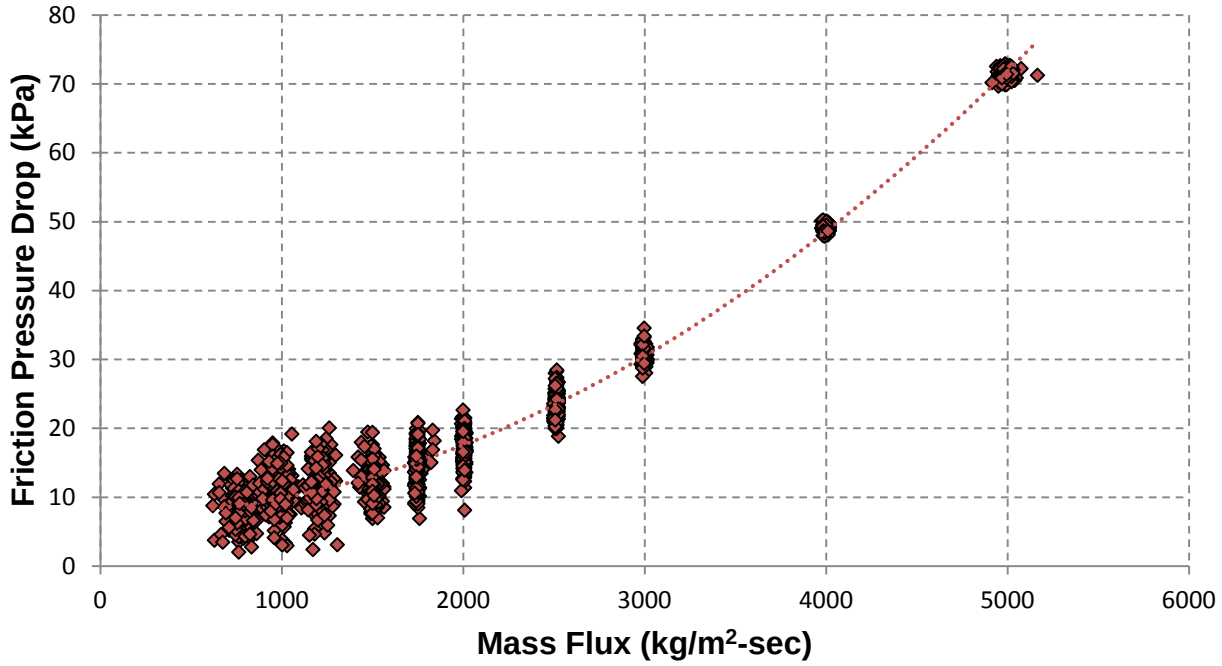

Figure 132: Partial Channel Characteristic Curve for the Narrow Rectangular Channel. $T_{b,in}$=90 °C, P_{out}=1.3 bar, q''=440 kW/m^2. The test was conducting by fixing inlet temperature and outlet pressure and decreasing the flow rate at a constant heat flux. As early as G=3000 kg/m^2, significant oscillations in the channel pressure drop were observed. As the slope approached zero, the large amplitude oscillation in the pressure drop and channel flow rate prevented further reduction of the mass flux. The large oscillations prior to reaching the minima are likely due to the density wave oscillation.

regions of the channel characteristic curve [158]. Therefore, it should not come as a surprise that the density wave oscillation is encountered prior to reaching the local minima. Throttling the inlet would likely reduce the oscillation and facilitate acquisition of the channel characteristic curve.

Examples of the pressure drop signal with time are shown in Figure 133 through Figure 135. In Figure 133 the wall temperature is below saturation and the water in the channel is entirely within the single-phase regime. In Figure 134, the channel is well past the onset of boiling, with voiding clearly visible, and the oscillation is suspected to be a result of the density wave instability. In Figure 135, higher order oscillations from the density wave instability are likely present. Higher order instabilities are possible beyond the initial stability line for conditions at high subcooling number as the phase change number is increased (i.e. as heat flux

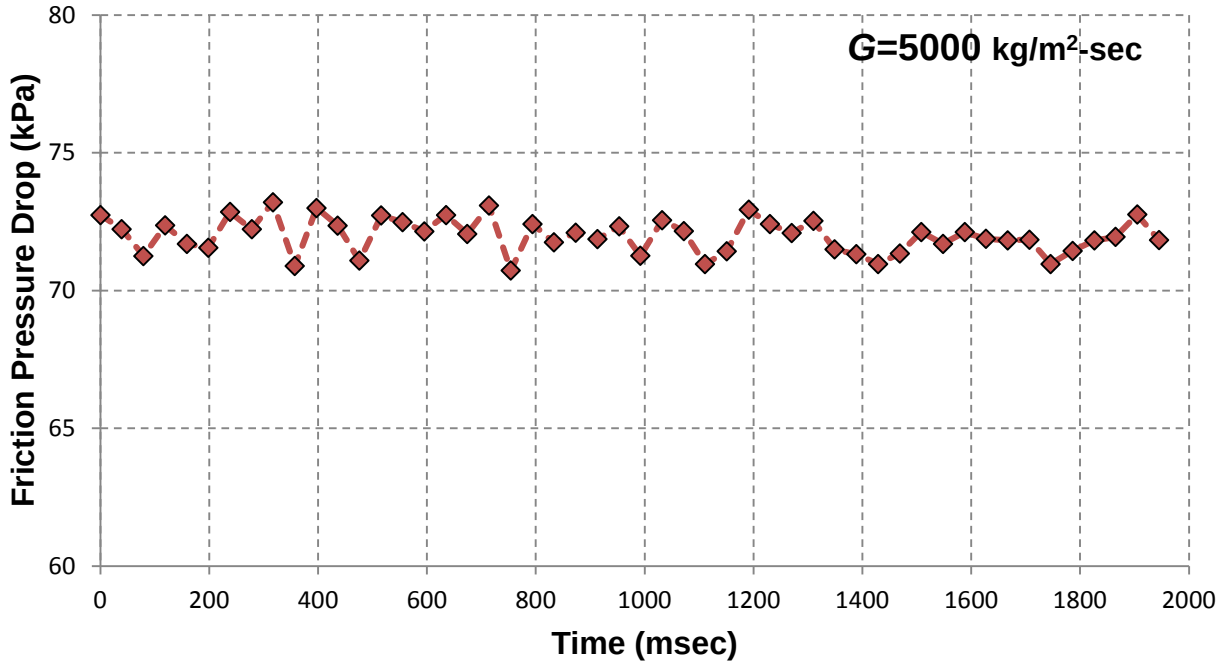

Figure 133: Pressure Drop Signal with Time. G=5000 kg/m²-sec, $T_{b,in}$=90 °C, P_{out}=1.3 bar, q''=440 kW/m².

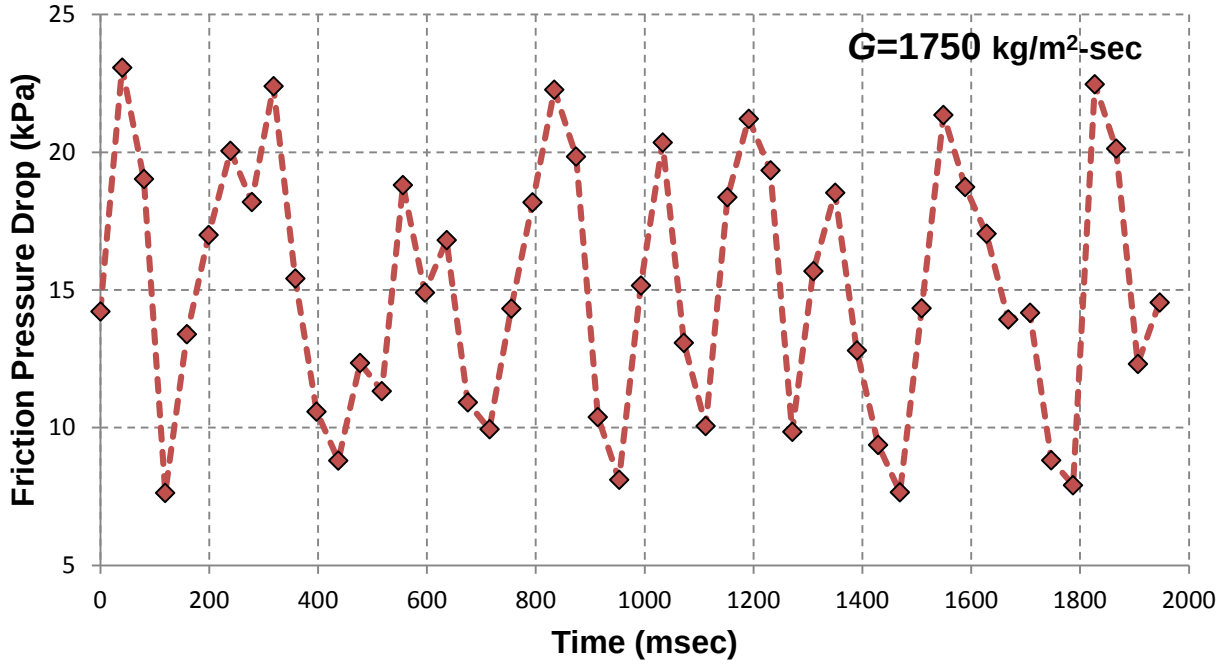

Figure 134: Pressure Drop Signal with Time. G=1750 kg/m²-sec, $T_{b,in}$=90 °C, P_{out}=1.3 bar, q''=440 kW/m². The periodic oscillation is readily apparent at this point on the demand curve, still well before the zero-slope point where the excursive instability would be expected for a parallel channel setup.

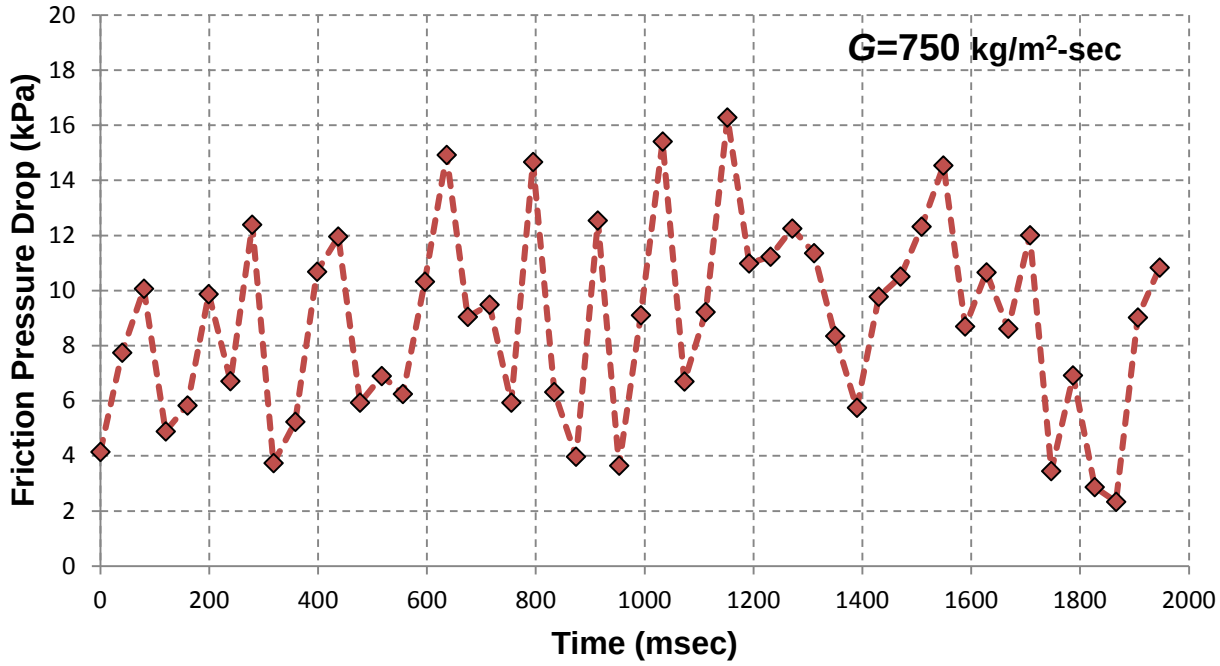

Figure 135: Pressure Drop Signal with Time. G=750 kg/m²-sec, $T_{b,in}$=90 °C, P_{out}=1.3 bar, q''=440 kW/m². Higher order oscillations may also be present.

is increased or inlet velocity is decreased), as noted in the analysis of Saha [156]. An example of higher order stability lines obtained in Saha's analysis for Freon-113 is shown in Figure 136. Follow up experiments by Saha, Zuber, and Ishii were unable to confirm the presence of higher order oscillations [157], though they admit the power input to the channel (and hence the phase change number) was limited to avoid damaging the experimental apparatus. However, Yadigaroglu and Bergles [159] had already previously demonstrated the presence of higher order density wave oscillations in their experiments

To confirm that the pressure fluctuations observed in the current study were in fact a result of the density wave oscillation, a frequency analysis was performed on the pressure drop signal as a function of time. The sampling rate for the differential pressure signal was limited by the data acquisition system, with a minimum period of 40 msec, which corresponds to a sampling rate of 25 Hz. The Nyquist frequency, which is half the sampling frequency, sets frequency threshold at which signals can be resolved. If a component of the sampled signal has a frequency component higher than the Nyquist frequency, signal aliasing will result. Therefore, if

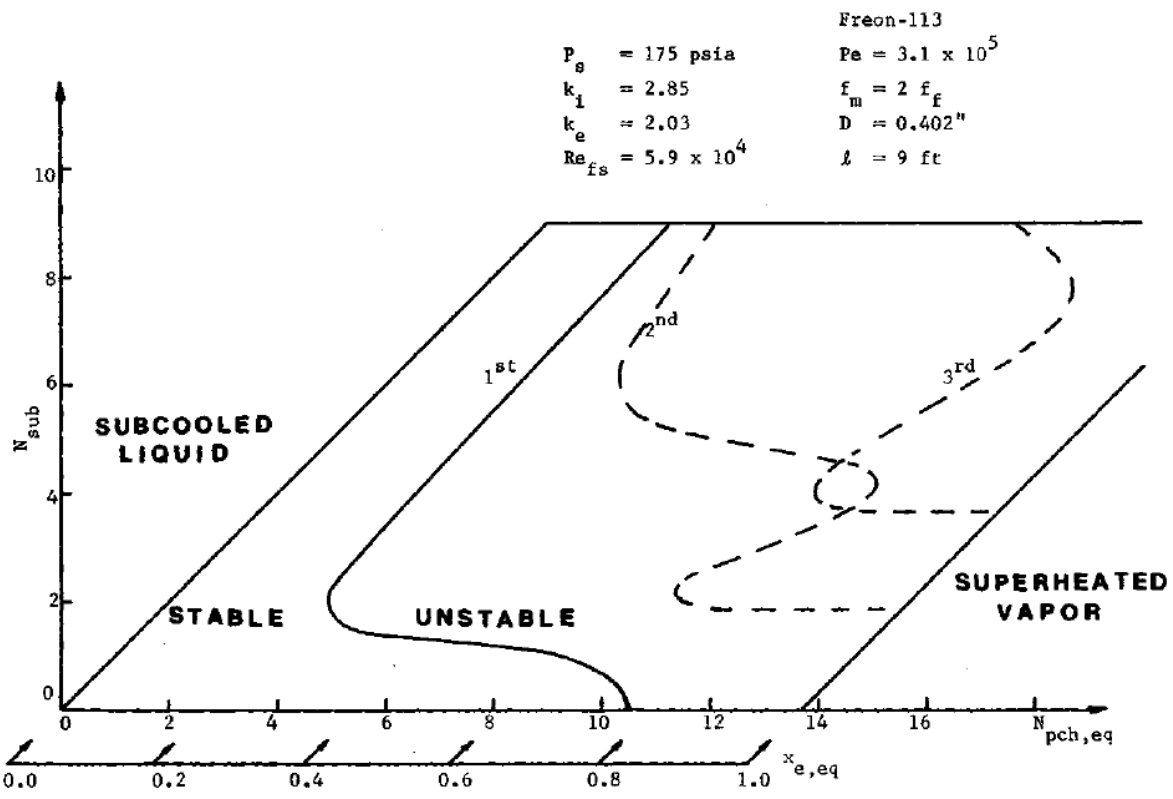

Figure 136: Stability Map Formulated by Saha for Freon-113 with Higher Order Stability Lines Shown. At high subcoolings, higher order density-wave instabilities are possible as the phase change number is increased. *Source: Ref. [156].*

acoustic oscillations were present during flow testing they would be indistinguishable from lower frequency oscillation and alias the sampled signal.

The spectral analysis of the pressure drop data was performed using the Signal Processing Toolbox in MATLAB. The "detrend" function was used to first remove the non-oscillating (steady-state or 0 Hz) component of the signal. The frequency analysis was performed using different methods, starting with a discrete Fourier Transform using the fast Fourier Transform algorithm. However, it was suspected that there was some aliasing of the sampled signal, either due to acoustic oscillations or random noise with a frequency component higher than the Nyquist frequency. Therefore, the Yule-Walker autoregressive method was also used to provide a correlated spectral estimate with a smoother result. An example of the spectral analysis for one set of conditions where the instability was present is shown in Figure 137 and Figure 138 using the FFT and Yule-Walker AR methods, respectively.

Yadigaroglu and Bergles report a period of oscillation in the density wave instability as approximately twice the transit time for their channel. It is important to note that they define the transit time as the sum of one half the residence time of a fluid particle in the single-phase region plus the vapor transit time in the two-phase region. Bouré et al. indicate a period of approximately one to two times the channel transit time [150]. Saha, Ishii, and Zuber [157] experimentally determine that the period of oscillation for the density wave instability was on the order of the transit time of the kinematic wave, which they estimate as:

$$\tau_{transit} = \frac{L_H}{u_{l,in}} \tag{184}$$

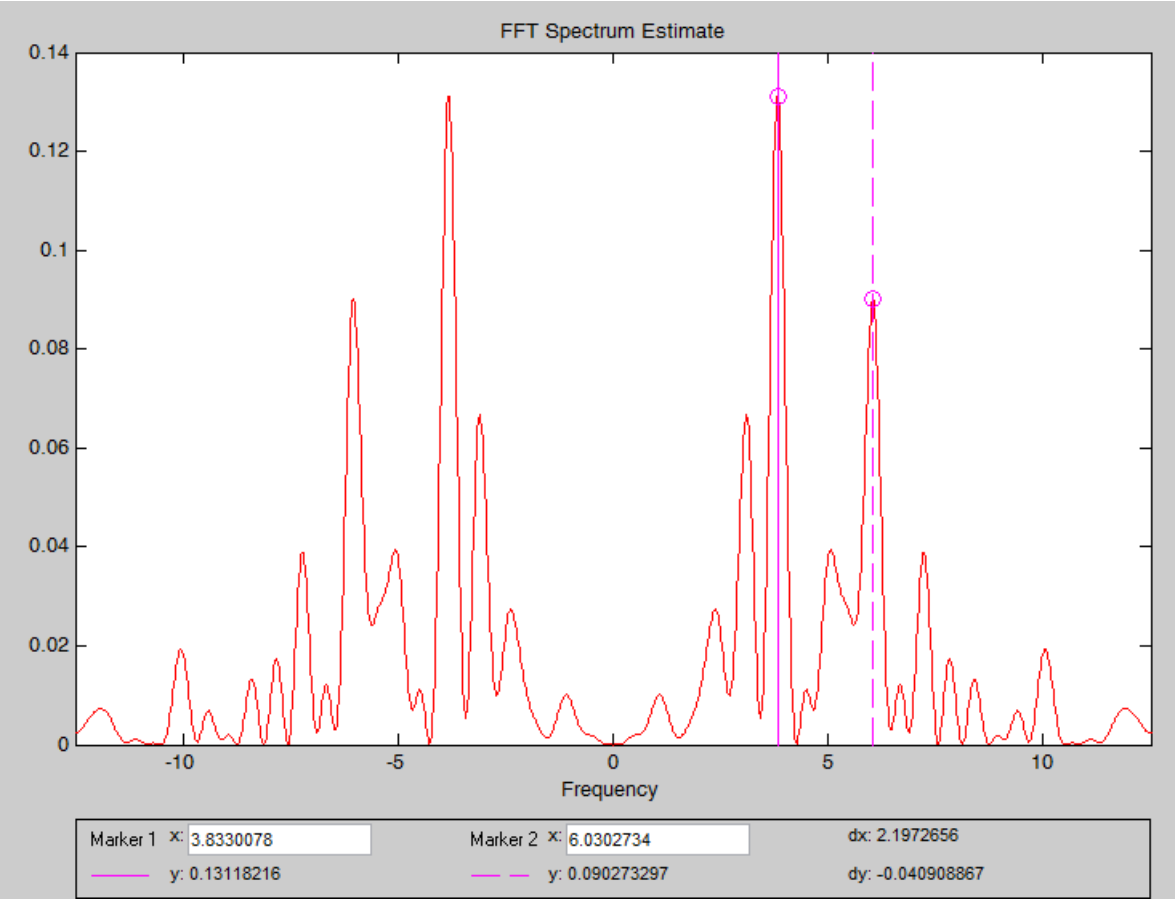

Figure 137: Power Spectral Density of Data in Figure 134 Using the Fast Fourier Transform. In this case, where G=1750 kg/m^2-sec, the inverse transit time for the channel is $1/\tau_{transit}$=5.94 sec^{-1}.

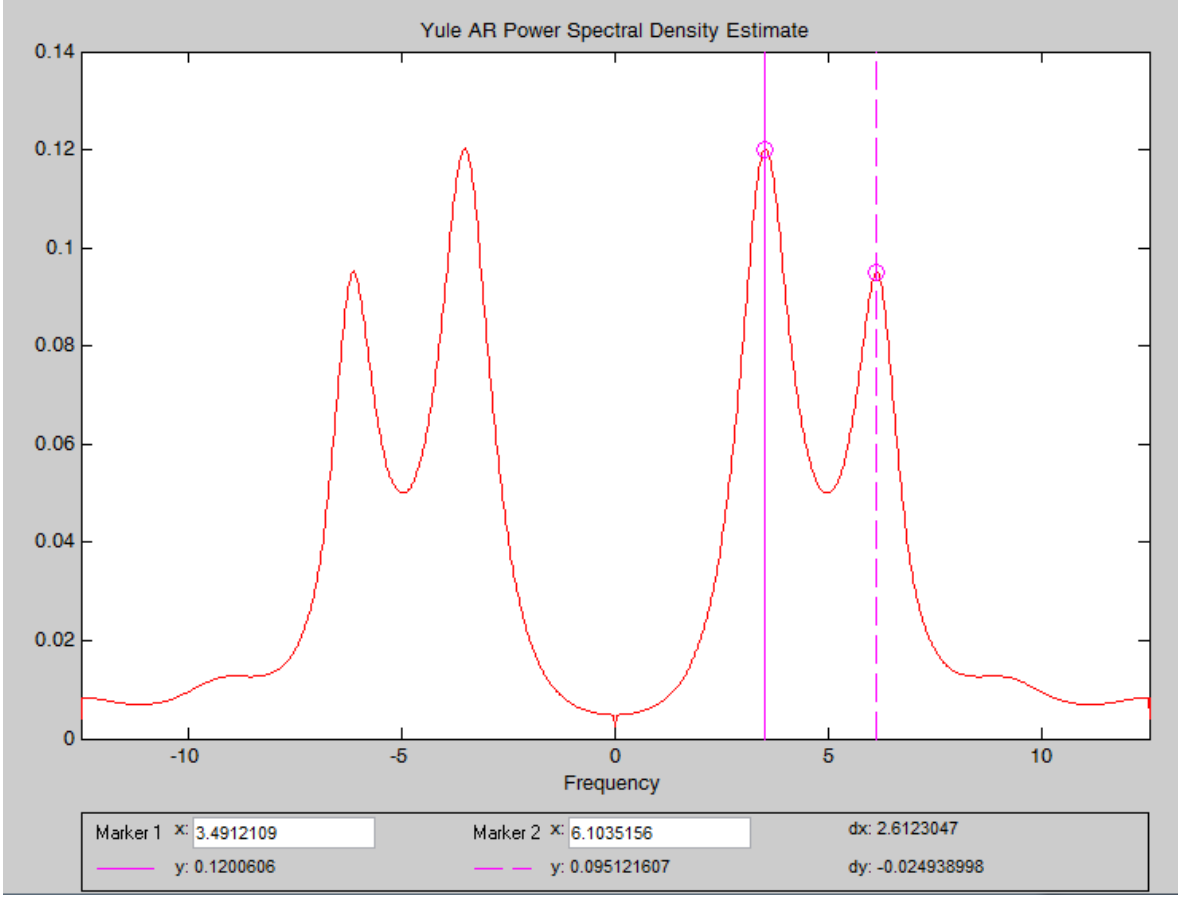

Figure 138: Power Spectral Density of Data in Figure 134 Using the Yule-Walker Autoregressive Estimate. In this case, where G=1750 kg/m^2-sec, the inverse transit time for the channel is $1/\tau_{transit}$=5.94 sec^{-1}.

The measured oscillation periods appear to be on the order of the fluid transit time for the channel. At even higher phase change number (heat flux held constant while inlet velocity reduced), an additional oscillation mode would appear to be present, as shown in Figure 139. And while the presence of the density wave oscillation has been confirmed to occur prior to the expected excursive instability point in the prototypic MITR unfinned channel, it is important to stress that these experiments were carried out for a single-channel. Channels in the MITR have a different external pressure boundary condition due to the parallel channel setup, which could result in a compounded density wave/parallel channel instability. In addition, the inlet and exit form loss factors have a direct effect on channel instability, and they have not been replicated in the experimental setup. Therefore, while the experimental results here confirm a large area of instability in the positive-sloping region of the channel pressure drop characteristic curve, the

results may not be directly applicable to a flow channel in the MITR. Further investigation is needed, however, as the current MITR Safety Analysis Report only addresses the Ledinegg instability, and does not consider the either the density wave instability or the potential for a compounded dynamic parallel channel instability in the core.

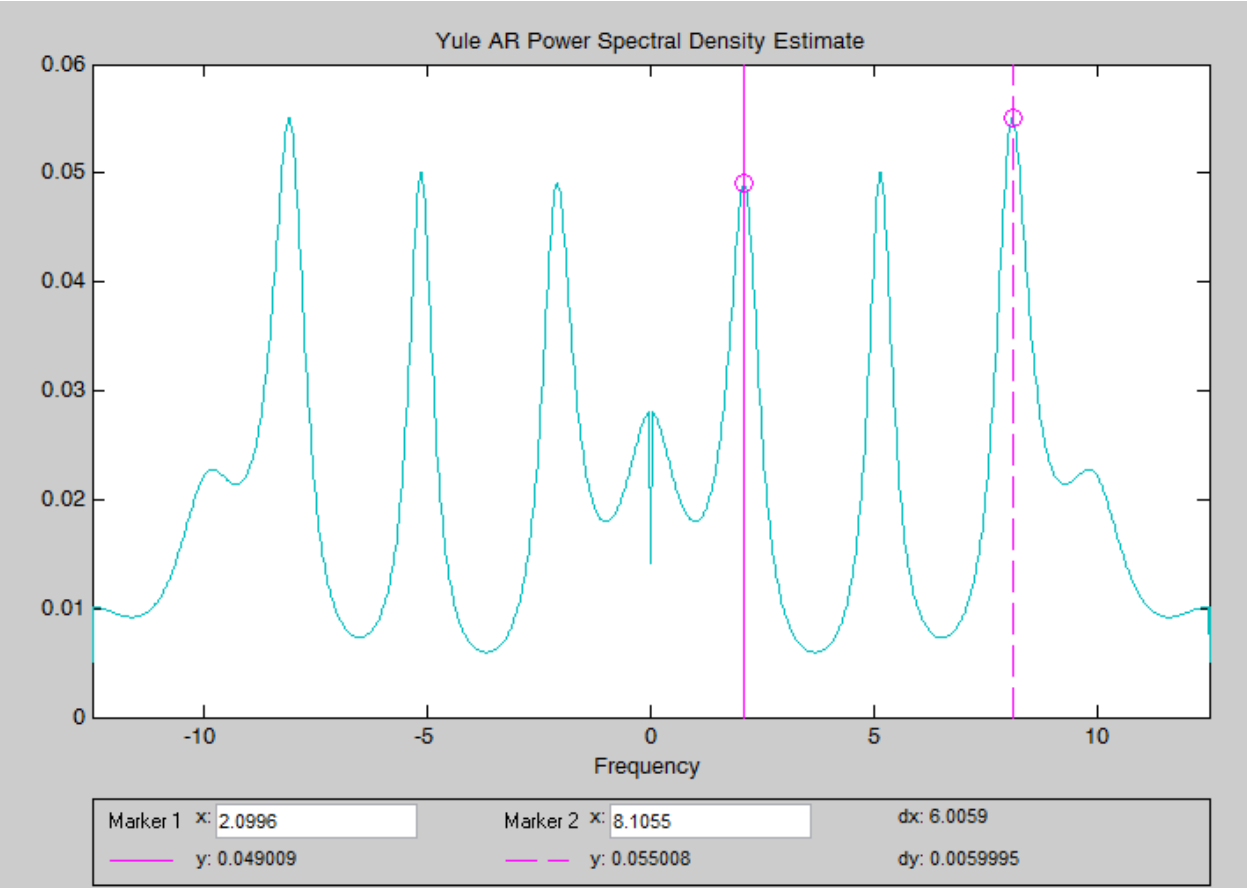

Figure 139: Power Spectral Density of Data in Figure 135 Using the Yule-Walker Autoregressive Estimate. In this case, where G=750 kg/m^2-sec, the inverse transit time for the channel is $1/\tau_{transit}$=2.62 sec^{-1}. Higher order oscillations were confirmed in the channel at the increased phase change number.

5.6. Chapter Summary

This chapter has explored two-phase heat transfer in the narrow rectangular channel, with onset of nucleate boiling tests being performed on unoxidized and oxidized stainless steel heaters. Analytical correlations to predict the incipience point under forced convection are based upon Hsu's model developed for pool boiling, but in most cases are actually simpler since steady-state conditions are assumed. The bubble model (hemispherical, truncated sphere, spherical, etc.) along with the required height of the thermal layer (tip of bubble, stagnation point, etc.) are the two major parameters that differ between models. Some models, such as that Davis and Anderson or Kandlikar, account for contact angle due to its effect on the bubble height.

The experimental program indicated that the incipience point during testing is not clear-cut, and the technique used can significantly affect the result. Overall, the temperature measurement techniques using a heat flux partition produced the most reliable and consistent results across all subcooling and mass fluxes, and is that recommended for future comparison. From the nominal unoxidized surface, results indicate that the Bergles and Rohsenow correlation adequately predicts the onset of nucleate boiling heat flux to within +/-25% as long as the appropriate single-phase heat transfer correlation is used in predicting the surface temperature in the single-phase regime. However, the oxidized surface, displaying a reduction in the contact angle of about 30°, similar to that for prefilmed boehmite cladding, showed an increase in the ONB heat flux ranging from 18% to 40%, depending on the mass flux. This increase is not captured by the Bergles and Rohsenow correlation, though correlations accounting for contact angle do predict this trend.

Lastly, flow instabilities were investigated in the single channel to identify the type and conditions under which they occurred. A frequency analysis confirmed that the instabilities were a result of density wave oscillations, and higher order instabilities modes were detected with increasing phase change number.

Some of the key conclusions from the two-phase experimental program are:

- Forced convection incipience models such as those of Bergles and Rohsenow, Davis and Anderson, and Satō and Matsu assume the optimum cavity size is available on the surface. For practical engineering and industrial surfaces, this is often a reasonable assumption. However, it should not be assumed for all surfaces. There are many

industrial surface finishing techniques that will yield a very smooth surface lacking the optimum cavity size.

- The experimentally determined incipience point depends heavily on the identification technique. Temperature measurement using the heat flux partition provides a reliable means of identifying incipience, as long as a consistent metric is applied.
    - Visual measurement techniques are not reliable due to the inability to spot incipience at high flow velocities or subcoolings. Visual techniques may significantly over estimate the onset of nucleate boiling heat flux. In this study, where the spatial resolution of the optical setup was 20 μm/pixel, it was nearly impossible to visualize vapor bubbles at incipience when the flow velocity was greater than 1 m/sec.
    - Pressure fluctuation techniques enable "global" detection of incipience in the channel, but are sensitive to edge effects.
- Much of the variation in ONB reported in the literature is likely either due to inconsistent identification techniques or not properly accounting for surface condition.
- The correlation of Bergles and Rohsenow is appropriate for predicting incipience from a practical, unoxidized metal surface ($\theta \approx 75°$ to $90°$) as long as the optimum cavity size is available and the appropriate single-phase correlation is used in conjunction.
- Substantial surface oxidation can increase the heat flux and therefore the superheat required for incipience due to the reduction in the contact angle.

Chapter 6

Surface Science Measurements in Support of Heat Transfer Experiments

The influence of surface parameters on two-phase heat transfer phenomena has long been recognized, but is not well understood. The large number of variables influencing the surface-fluid interaction, along with the difficulty of controlling surface features across all length scales, makes precise determination of surface effects on liquid-vapor phase change phenomena incredibly challenging. Surface morphology and chemical constituency can have a profound impact on boiling incipience, the critical heat flux, and the Leidenfrost transition.

Advanced surface characterization techniques were largely unavailable when many landmark studies in the field of two-phase heat transfer were conducted, leading to observations on the importance of the surface-fluid interaction without adequate elaboration on the mechanism of effect. For example, in his classic pool boiling study, Nukiyama notes that changes to the surface from electrolysis affected the boiling curves [160]. As noted by Griffith in 1958 [161], models for nucleate boiling typically relied on fluid properties alone with the role of surface condition being captured by fitted coefficients. Rohsenow's semi-empirical model for pool boiling is one such example [162], where the fitted surface-fluid interaction constant, $C_{s,f}$, is noted to be directly related to the bubble contact angle on the surface. The dimensional analysis performed in 1948 by Kutateladze for the critical heat flux, which was later further developed by Zuber using a hydrodynamic stability analysis [163] derives no analytical dependence of the

critical heat flux on surface effects. However, as early as 1964, Costello [164] and Gambill [165] noted the importance of capillary wicking, wettability, and deposit formation on burnout.

As discussed in Chapter 5, boiling incipience is strongly dependent on surface effects, particularly the surface morphology, available cavity size, and wettability. Wettability is commonly quantified using the static equilibrium contact angle of a liquid on a solid surface, as shown in Figure 140. From a force balance, the intrinsic contact angle may be related using the following expression, which was first described qualitatively by Young in 1805 [166]:

$$cos\theta_I = \frac{\gamma_{sv} - \gamma_{sl}}{\sigma} \tag{185}$$

where γ_{sv} is the solid-vapor interfacial tension (sometimes referred to as the surface tension of the solid in equilibrium with the vapor), γ_{sl} is the solid-liquid interfacial tension, and σ is the surface tension of the liquid (liquid-vapor interfacial tension). γ_{sv}-γ_{sl} is often referred to as the adhesion tension of the liquid/vapor/solid combination. However, if a surface is not perfectly flat, one must account for the surface roughness, as described by Wenzel [167], in order to determine the apparent contact angle:

$$cos\theta = rcos\theta_I \tag{186}$$

Here r is the roughness factor, which Wenzel defined as the total surface area divided by the projected area, and θ is the macroscopic, or apparent, contact angle. Note that, in the absence of

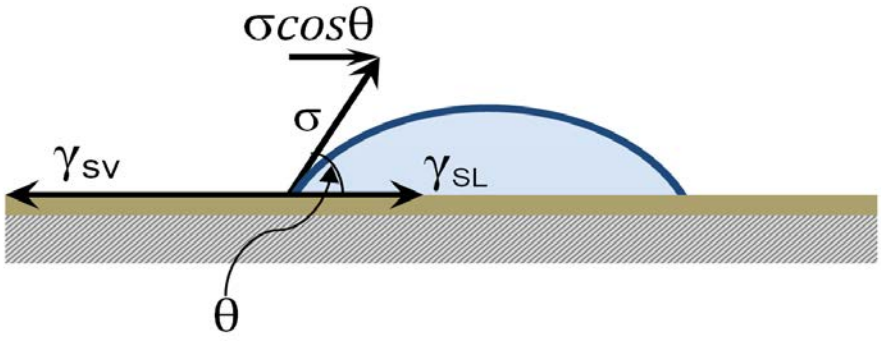

Figure 140: Two-Dimensional Representation of the Interfacial Forces Acting On a Sessile Drop. Here σ is the surface tension (or liquid-vapor interfacial tension).

line tension, the local contact angle on a rough surface will be exactly equal to the intrinsic contact angle for that material. In other words, if one were to observe the three-phase contact line microscopically, the contact angle relative to the local surface feature will be equivalent to the intrinsic contact angle. Neumann [168] has shown that below a roughness scale of 0.1 μm, the surface roughness does not affect the contact angle. In the Wenzel regime, a small contact angle hysteresis (below perhaps 8°), would indicate that the surface is very smooth and fits closely with the assumption of an ideal surface [169]. However, on real surfaces, the surface will have blemishes, or local variations in the chemical constituency due to oxidation, contamination, etc. which will result in variability in the measured contact angle.

Wenzel's model is applicable to the case of homogeneous wetting, where the liquid comes in direct contact with the entire surface. In the case of heterogeneous wetting, i.e. when a liquid sits atop surface features, Wenzel's model is no longer adequate and the model of Cassie and Baxter [170] must be used. Wetting in the Cassie-Baxter regime is typified by minimal contact angle hysteresis with droplets displaying high mobility (roll-off tendency). Surfaces exhibiting Cassie-Baxter wetting are of practical importance in condensation heat transfer applications, but typically not desirable in other two-phase heat transfer systems due to the degradation of the critical heat flux. All of the surfaces investigated in this study fall in the Wenzel regime, and the Cassie-Baxter model is therefore not considered. It is important to note that the Wenzel regime can include hydrophobic or superhydrophobic surfaces, but the three-phase contact line will display pinning behavior with a notable hysteresis in the contact angle, where droplets will have more difficulty rolling off the surface.

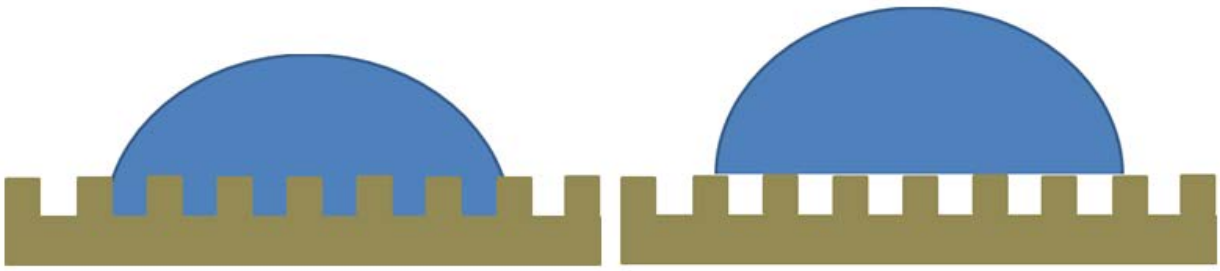

Figure 141: Wetting in the Wenzel State (left) and in the Cassie-Baxter State (right). In the Wenzel regime, a liquid droplet impregnates surface features, typically resulting in contact line pinning, contact angle hysteresis, and roll-off resistance. In the Cassie-Baxter regime, air pockets remain below the liquid droplet, resulting in a higher roll-off tendency.

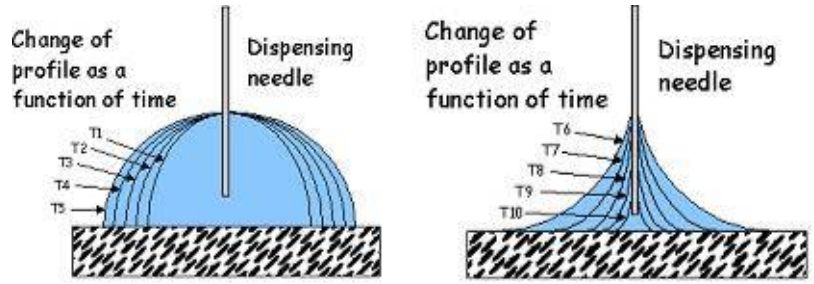

Figure 142: Technique for Measuring Static Advancing Contact Angle (Left) and Static Receding Contact Angle (Right). The static advancing and static receding contact angles are the apparent angles immediately prior to motion of the three-phase contact line. *Source: Ref. [171].*

Equation (185) and equation (186) pertain to static, or equilibrium, contact angles. However, bubble nucleation, CHF, and the Leidenfrost transition are dynamic processes, so dynamic advancing and receding contact angles are more appropriate in relating wettability to the boiling processes. Bernardin et al. concisely covers the distinct differences between dynamic and static angles in two-phase heat transfer [172]. Unfortunately, measurement of the dynamic advancing and dynamic receding contact angles is not as straightforward as static measurements, and depends on the velocity of the three-phase contact line. Dynamic wetting also has a strong dependence on the surface texture and contact angle hysteresis (difference between advancing and receding angles). Tilting plate methods are common for measuring true advancing and receding contact angles. The static advancing (advanced) and static receding (receded) contact angles may be used to approximate the advancing and receding angles, respectively, and can be measured with a stationary setup. The dispensing/withdrawing droplet measurement technique may be used to obtain these values, and is shown in Figure 142.

It is useful to note that the static equilibrium contact angle is expected to fall between the static receding contact angle and static advancing contact angle [173]:

$$\theta_R < \theta_{eqm} < \theta_A \tag{187}$$

Tadmor attempts to analytically relate the equilibrium contact angle to the maximal advancing and minimal receding angles, arriving at the following expression:

$$\theta_{eqm} = \arccos\left[\frac{\Gamma_A\cos(\theta_A) + \Gamma_R\cos(\theta_R)}{\Gamma_A + \Gamma_R}\right] \tag{188}$$

with Γ_A and Γ_R being defined as:

$$\Gamma_A = \left[\frac{\sin^3(\theta_A)}{2 - 3\cos(\theta_A) + \cos^3(\theta_A)}\right]^{1/3} \tag{189}$$

$$\Gamma_R = \left[\frac{\sin^3(\theta_R)}{2 - 3\cos(\theta_R) + \cos^3(\theta_R)}\right]^{1/3} \tag{190}$$

Surface roughness, in addition to influencing the macroscopic contact angle as seen in Wenzel's equation, is important for the initial nucleation process. As noted in Chapter 5, the presence of cavities on a heated surface act as nucleation sites for boiling. The presence of roughness alone does not guarantee that the necessary cavities will be present on a surface. The overall surface morphology and texture are required to truly determine micro-scale geometric effects on boiling phenomena including incipience, as demonstrated by O'Hanley et al. [174]. However, as roughness standards are well-defined and utilized across disciplines, these are the metrics used to typify heat transfer surfaces. Additionally, it can generally be said that for practical engineering surfaces, a rougher surface will possess more cavities to support nucleation, with a higher probability of optimally-sized cavities being found on the surface. Therefore, rougher surfaces are expected to experience onset of nucleate boiling at a lower heat flux and wall superheat than a smooth surface.

Numerous definitions for roughness exist, many of which are defined in ISO 4287:1997 [175]. The arithmetic mean surface roughness, R_a, is often reported in modern heat transfer studies, being defined as:

$$R_a = \frac{1}{L}\int_0^L |y(x)|dx \qquad (191)$$

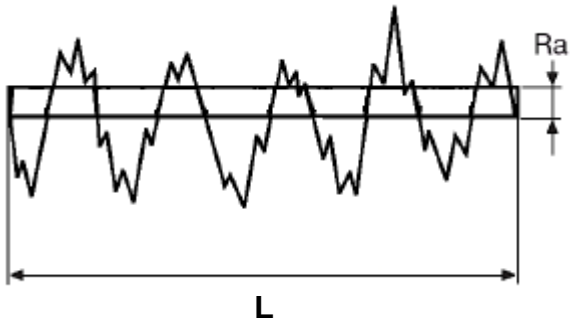

The maximum height, R_z, is also relevant, which is defined as the maximum peak height plus the maximum valley depth over a sampling length. The ten-point mean roughness, R_{zJIS}, is often encountered in place of R_z defined in the ISO standard. R_{zJIS} is a Japanese Industrial Standard defined as the average of the difference between the five highest peaks and five lowest valleys on the surface [176]:

$$R_{z,JIS} = \frac{1}{5}\sum_{i=1}^{5}(Y_{peak,\max} + Y_{valley,\max}) \qquad (192)$$

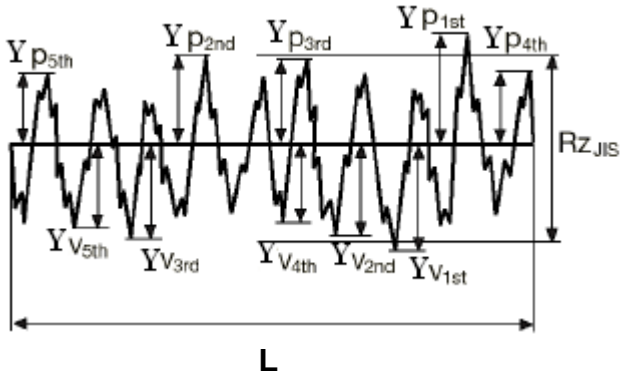

Another roughness parameter encountered in heat transfer literature is the Glättungstiefe, or R_p, literally meaning "smoothing depth." It is defined by the defunct German standard DIN 4762 [177]. However, due to the widespread use of R_p for correlating nucleate boiling heat transfer data in the 1960's through the 1980's, it is still commonly encountered in the literature, with little or no description of its meaning. Details regarding its interpretation, along with typical values on 6061 aluminum, can be found in reference [178].

Given the importance of surface effects on boiling incipience, there was interest in characterizing the surfaces of actual cladding as a basis for comparison to the heat transfer surfaces employed in this study. In fact, the heat transfer surfaces were prepared such that they had a similar R_a value to that of actual cladding. Test reactor cladding coupons, pre-filmed with

boehmite, were procured for surface characterization. While the existing HEU fuel surface in the MITR is not pre-filmed, there is interest in pre-filming the cladding of the LEU fuel to control oxidation growth. The results of the pre-filmed cladding surface characterization are provided in section 6.1. The heat transfer surfaces used in this study were also carefully characterized, with results presented in section 6.2. Lastly, the effects of contamination and oxidation on 6061 aluminum and zirconium, a potential alternative cladding material for test reactors, were explored. Quantitative determination of the relationship between contaminant thickness and contact angle were performed using angle-resolved X-ray photoelectron spectroscopy (AR-XPS), with results provided in Appendix E.

6.1. Test Reactor Cladding Coupons

Five test reactor cladding samples, composed of 6061 aluminum and pre-filmed with boehmite, were received at the MIT Nuclear Reactor Laboratory from Babcock & Wilcox. Table 36 describes the samples received from B&W. The expected surface finish was ~32 μin (0.81 μm) or smoother [179].

Table 36: Summary of Boehmite Pre-filmed, Aluminum 6061 Cladding Samples obtained from B&W.

Designation	Side 2 Marking	Dimensions (*w* x *h*)	Measured Thickness
XA-761TNB	*62-071*	2.17” x 3.05”	0.049”
XA-763TNB	*62-071*	2.17” x 3.06”	0.049”
XA783-TNB	*62-071*	2.17” x 3.05”	0.050”
XA-789T	*61-066*	2.12” x 3.05”	0.079”
XA-817T	*61*	2.12” 3.03”	0.079”

The boehmite (γ-AlO(OH)) pre-filming process forms a highly protective surface layer on the aluminum substrate. The formation of the boehmite film is performed by heating the substrate in de-ionized water at 180 °C and holding it there for 18 to 24 hours. An amorphous, gelatinous layer of boehmite initially forms, which must age to fully crystallize. The pH of the de-ionized water is held between 5 and 6.2 to form extremely thin, highly protective layers. Thicker layers may be formed by raising the pH above 6.2 [180]. While the current fuel in the MITR is not pre-filmed with boehmite, there is incentive to implement pre-filmed cladding on the LEU fuel to help control oxidation growth. Therefore, characterization of these cladding samples is pertinent to the MITR conversion project and the experimental heat transfer component of this study.

After receipt, all samples were cleaned by sonicating in reagent grade acetone for 15 minutes. Samples were then rinsed with pure, reagent grade ethanol followed by a rinse with de-ionized water. Samples blown dry with high purity compressed nitrogen. The surfaces were characterized using various means, as described in the following sections.

6.1.1. Surface Analysis Using Optical Microscopy

Cladding samples were viewed under an optical microscope at 10x, 20x, and 50x magnifications. The images shown in Figure 143 through Figure 145 are representative of all the samples observed. The spotted features were found on both sides of each cladding sample, and were relatively uniformly distributed across the surface. These spots are actually raised, not recessed, features on the surface, and are made of boehmite, as demonstrated using EDS in section 6.1.6.

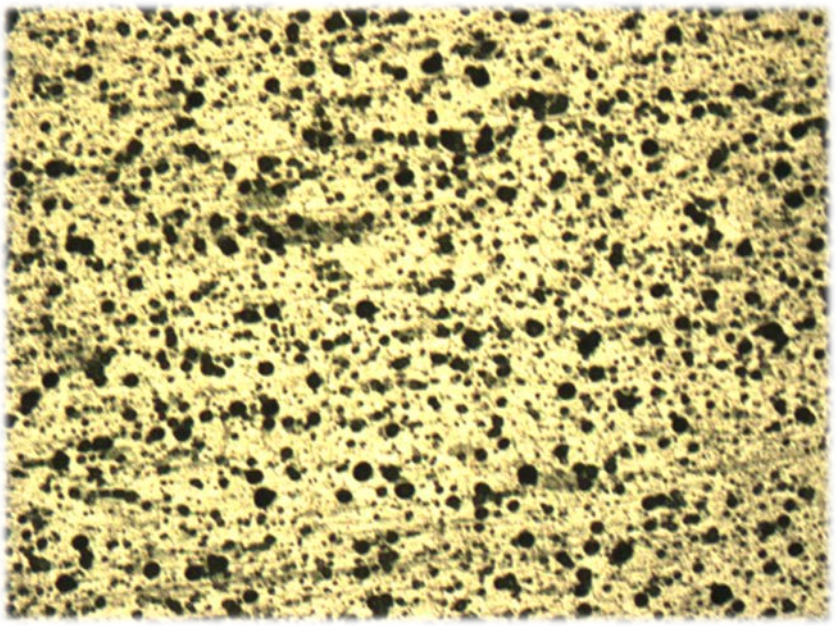

Figure 143: Optical Images of the Cladding Surface at 10x Magnification.

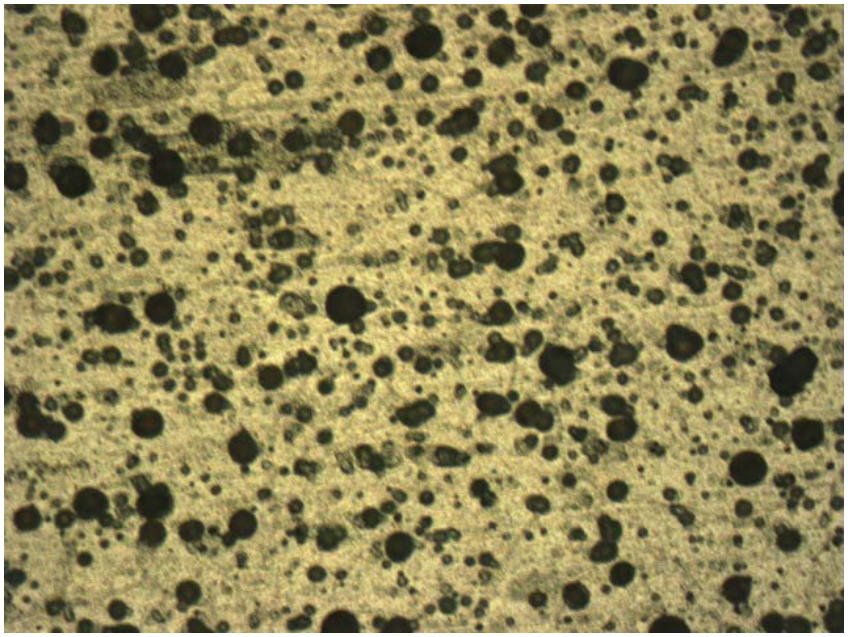

Figure 144: Optical Images of the Cladding Surface at 20x Magnification.

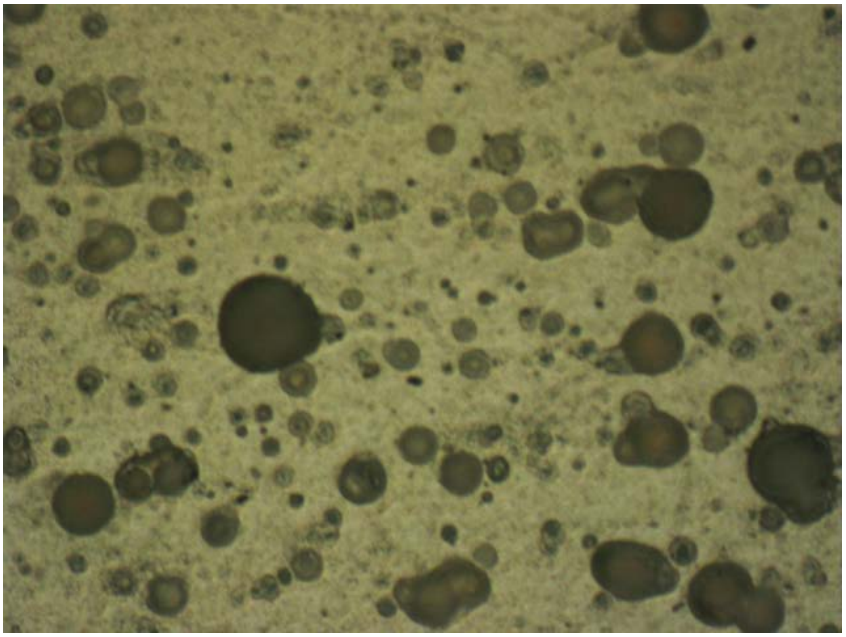

Figure 145: Optical Images of the Cladding Surface at 50x Magnification.

6.1.2. Surface Roughness Using Confocal Microscopy

An Olympus LEXT OLS3000 Confocal Scanning Laser Microscope was used to measure surface morphology and roughness of cladding samples. Although it is difficult to strictly apply roughness standards to the optical techniques used here due to the smaller scan lengths, the measured roughness parameters most closely conform to those earlier specified (ISO 4287:1997 [175]).

The measurements are summarized in Table 37. The reported values are determined from the entire surface area, not from line scans. Typical scan areas were 256 µm x 256 µm. Representative confocal micrographs of the surfaces are shown in Figure 146 through Figure 148.

Table 37: Summary of Surface Roughness Measurements Using Confocal Microscopy.

Sample	R_a (µm)	R_z (µm)
XA-763TNB		
Side 1:	0.466	9.924
Side 2:	0.533	9.798
XA-783TNB		
Side 1:	0.509	9.462
Side 2:	0.506	9.524
XA-789T		
Side 1:	0.536	12.836
Side 2:	0.603	9.927
XA-817T		
Side 1:	0.505	8.143
Average:	**0.523 ±0.042**	**9.945 ±1.416**

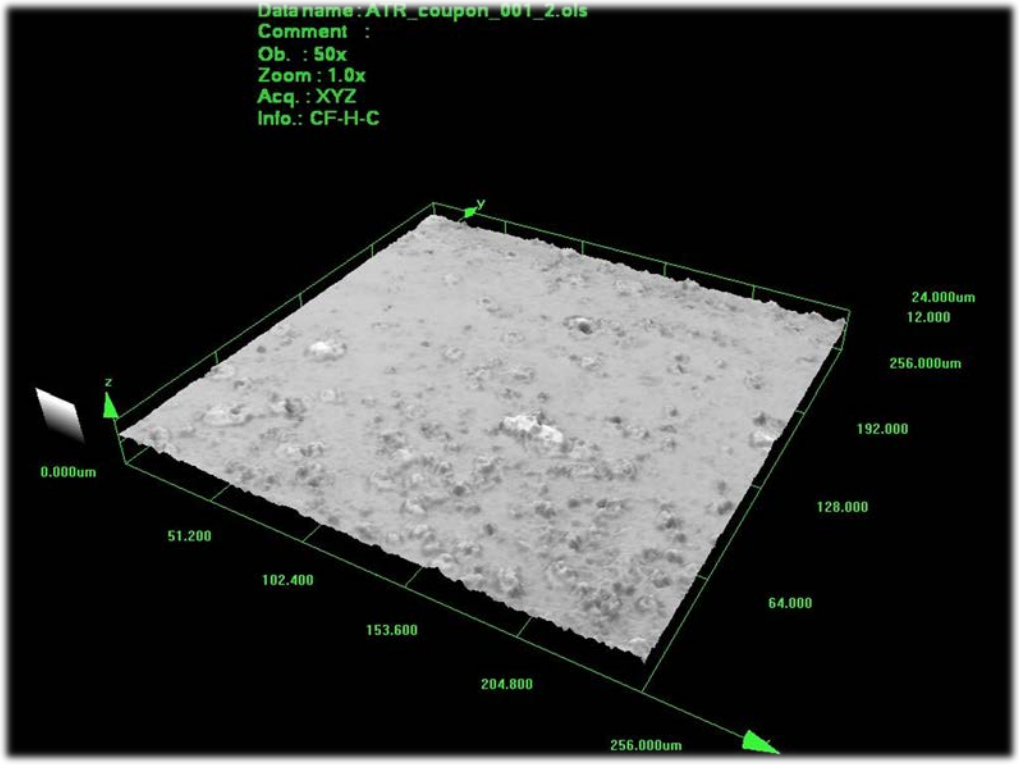

Figure 146: Confocal Micrograph of Cladding Surface Showing Raised Features.

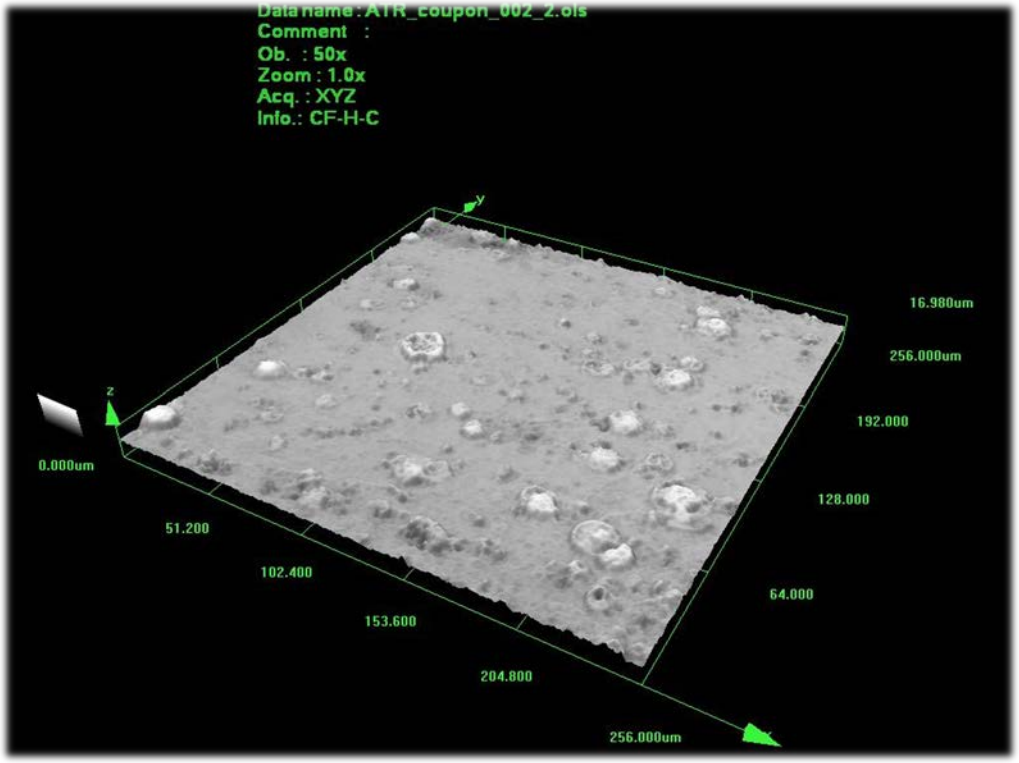

Figure 147: Confocal Micrograph of Cladding Surface.

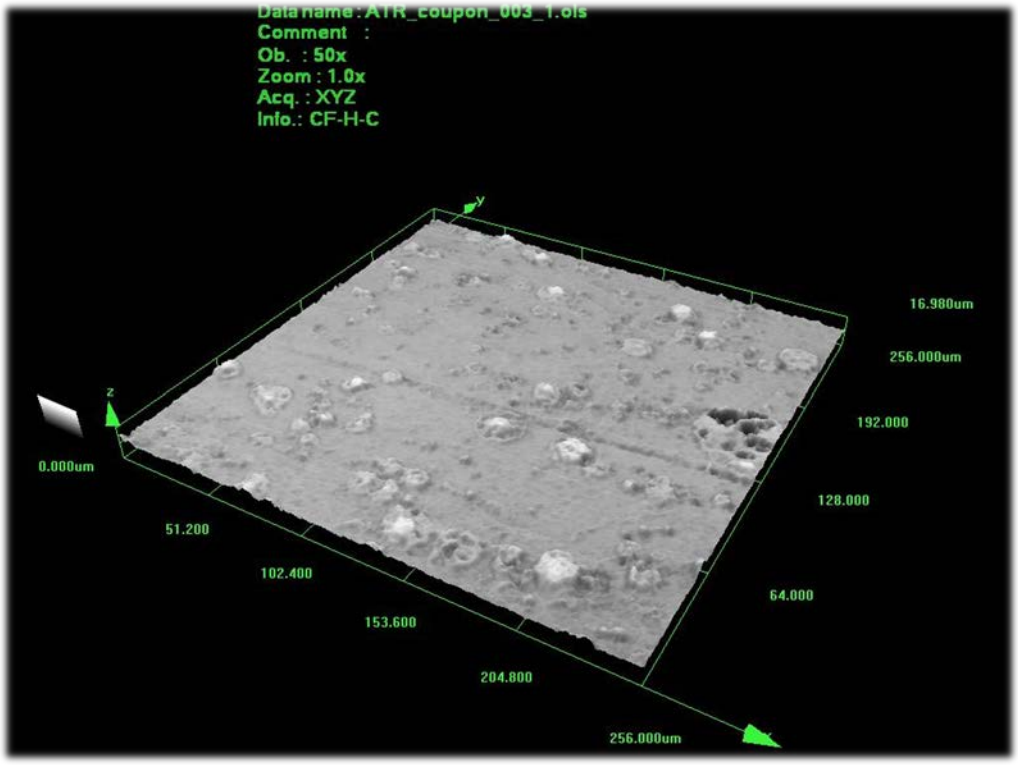

Figure 148: Confocal Micrograph of Cladding Surface. While the surface features were predominantly raised, there were some noted depressions, as seen here.

6.1.3. Surface Roughness Using Non-contact Profilometry

A Nanovea PS50 non-contact profilometer was also used to measure surface roughness on the cladding samples. The results are summarized in Table 38. Typical scan areas were 1 mm x 1 mm. Two scans were performed for each of the coupons listed, with reported values being determined from four random line measurements, 256 µm in length, for comparison against the confocal microscope measurements. A representative scan is shown in Figure 149. Recall that the average R_a from the confocal scans on other samples was 0.526 µm, which is very similar to the 0.507 µm value measured using the profilometer. The smaller R_z value measured the Nanovea is likely due to the fact that the measurements are based off line values, not the entire area as was the case with the confocal microscope.

Table 38: Summary of Roughness Measurements on the Test Reactor Cladding Coupons Using a Non-Contact Profilometer.

Sample	R_a (µm)	R_z (µm)
XA-761TNB	0.585 ±0.152	3.395 ±0.914
XA-763TNB	0.493 ±0.078	3.563 ±0.661
XA-783T	0.573 ±0.203	3.664 ±1.272
XA-817T	0.377 ±0.058	2.601 ±0.416
Average:	**0.507 ±0.162**	**3.305 ±0.985**

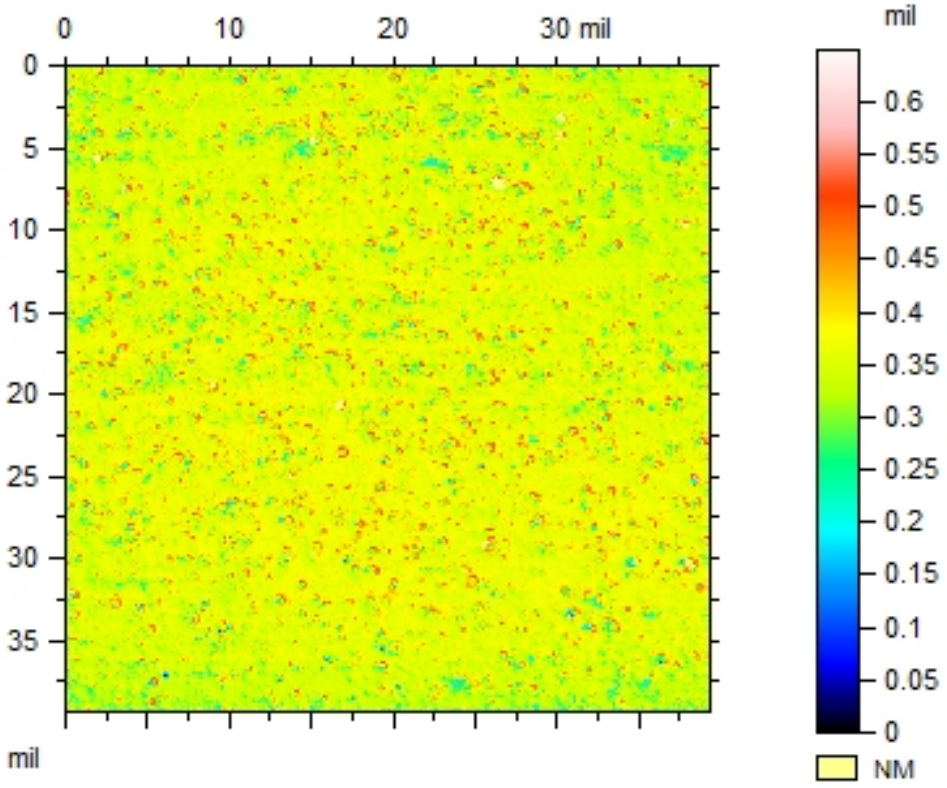

Figure 149: Typical Surface Profile Obtained with the Nanovea PS50 Profilometer. Note the scan area here is 1 mm x 1 mm (the scale shown is in "mil," or thousandths of an inch).

6.1.4. Surface Wettability Using Contact Angle Measurements

Contact angle measurements were performed using a KSV Instruments CAM 101 system, consisting of a goniometer, camera, and light source. Figure 150 shows the setup used to measure contact angles. A Hamilton 500 μL GasTight series syringe with a 22 gauge needle was used to dispense droplets of DI water onto the test surface. For equilibrium contact angles, a droplet of approximately 2.5 to 5 μL in volume was used. Gravity may affect the measurement when larger droplets are used, and evaporation effects may be non-negligible for small droplets. When surface roughness is present, contact angle depends heavily on the liquid drop size. In a study by Drelich [181], an increase in the sessile drop receding contact angle of over 40° was noted as the liquid drop base diameter was increased from 1.5 mm to 6.5 mm for water on a rough polymer surface. However, no contact angle dependence on drop size was observed when very smooth and homogenous surfaces were prepared.

Temperature may also affect the measured contact angle. However, contact angle seems to vary little with temperature and pressure when the temperature of the surface is below 120°C. This corresponds with reports by Bernardin et al. [172] that contact angle decreases about 0.1°

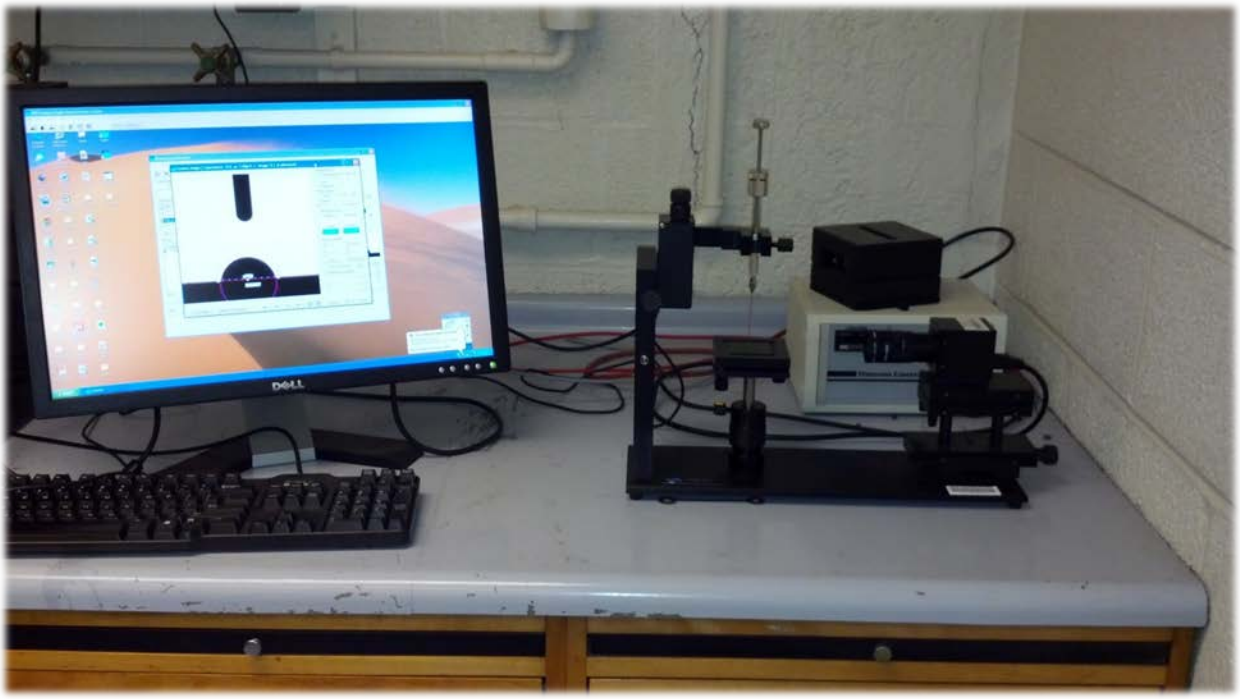

Figure 150: Contact Angle System Used to Measure Contact Angles on Test Reactor Cladding Surfaces.

per 1 K decrease in temperature for temperatures between 5 and 100°C. Relative humidity, although less frequently cited in terms of its effect on wettability, may also influence contact angles. Gledhill [182] noted that the surface energy of steel decreases as relative humidity increases. Relative humidity may also have an effect on the rate of surface oxidation. For glass surfaces, high relative humidity levels cause a layer of adsorbed water to form on the surface that is thick enough to have the same properties of bulk water. While effects of temperature and relative humidity were not investigated in this study, they were kept constant and recorded to ensure consistency of measurements.

The typical uncertainty quoted for contact angle measurement is 1° to 5°. For practical surfaces, local variations in the chemical constituency and morphology may lead to a noticeably larger spread in measured values. Therefore, contact angle measurements reported in this study are provided with the standard deviation of a set of expectedly identical measurements. A still image was recorded with the KSV software ten to fifteen seconds after the drop came in contact with the surface. This allowed the droplet to settle while not being long enough for evaporation to influence the measurement.

Measurement of the contact angle on each pre-filmed cladding coupon was performed at four locations on each side of the coupon. The results are summarized in Table 39. In some instances, it was observed that contact angles were higher when measured perpendicular to the roll marks on the coupons. This is likely due to pinning of the three-phase contact line at these features. As a comparison, the expected contact angle is between 60° and 90° for a smooth 6061 aluminum surface with the native surface oxide, as reported in section 6.2.

Table 39: Summary of Contact Angle Measurements on the Test Reactor Cladding Coupons.

Sample	Equilibrium Contact Angle		Static Adv. Contact Angle	Static Receding Contact Angle
	Side 1	Side 2	Side 1	Side 1
XA-761TNB	48.3° ±5.4°	48.3° ±5.4°	-	-
XA-763TNB	42.7° ±3.9°	43.9° ±7.8°	85.4° ±4.2°	9.8° ±0.9°
XA-783TNB	35.9° ±4.4°	56.8° ±6.3°	-	-
XA-789T	48.4° ±5.4°	62.6° ±6.3°	-	-
XA-817T	52.2° ±7.7°	45.1° ±5.1°	-	-
Average:	**48.4° ±7.9°**		**85.4° ±4.2°**	**9.8° ±0.9°**

6.1.5. Surface Morphology Using Scanning Electron Microscopy

Cladding samples were imaged using both a JEOL NeoScope JCM-5000 scanning electron microscope and a JOEL 5910 General Purpose scanning electron microscope. Particular attention was paid to the spotted features, which were determined to be elevated above the rest of the surface. Results are shown in Figure 151 through Figure 154.

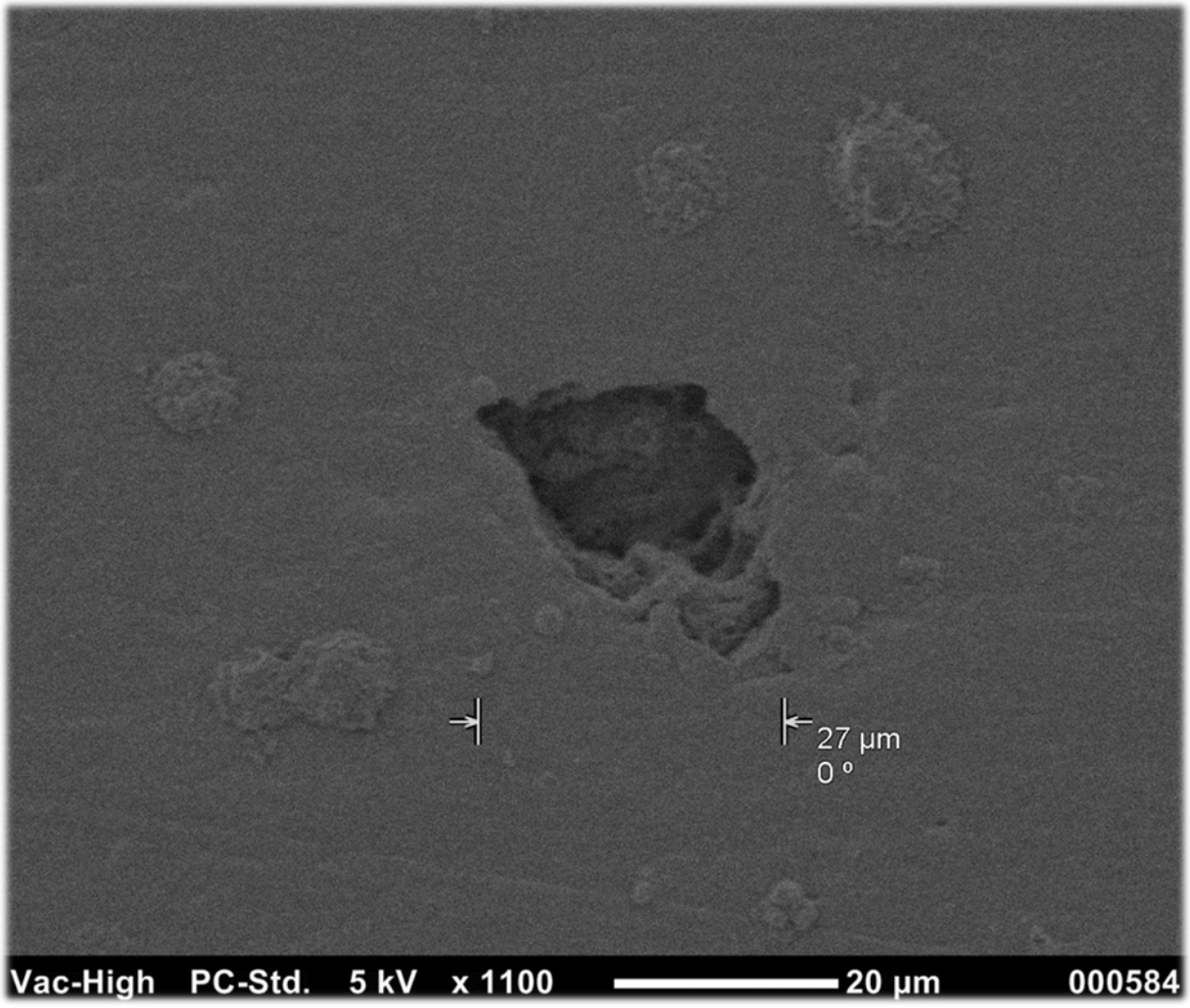

Figure 151: A Large Cavity on the Cladding Surface.

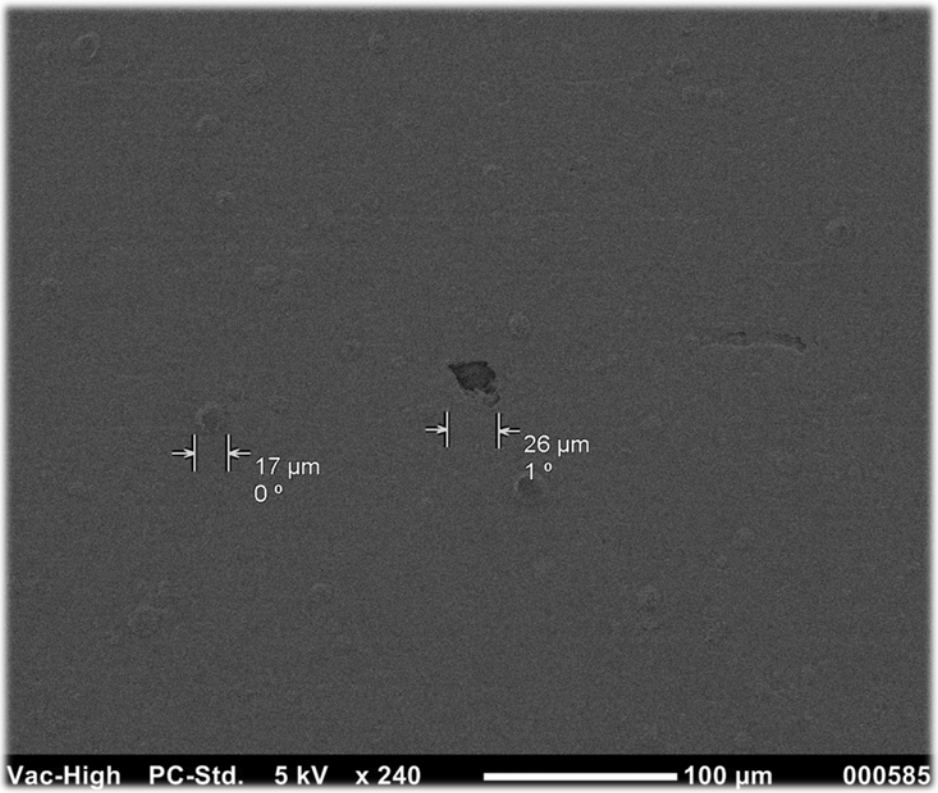

Figure 152: Typical Dimensions and Distribution of Features on the Cladding Surface.

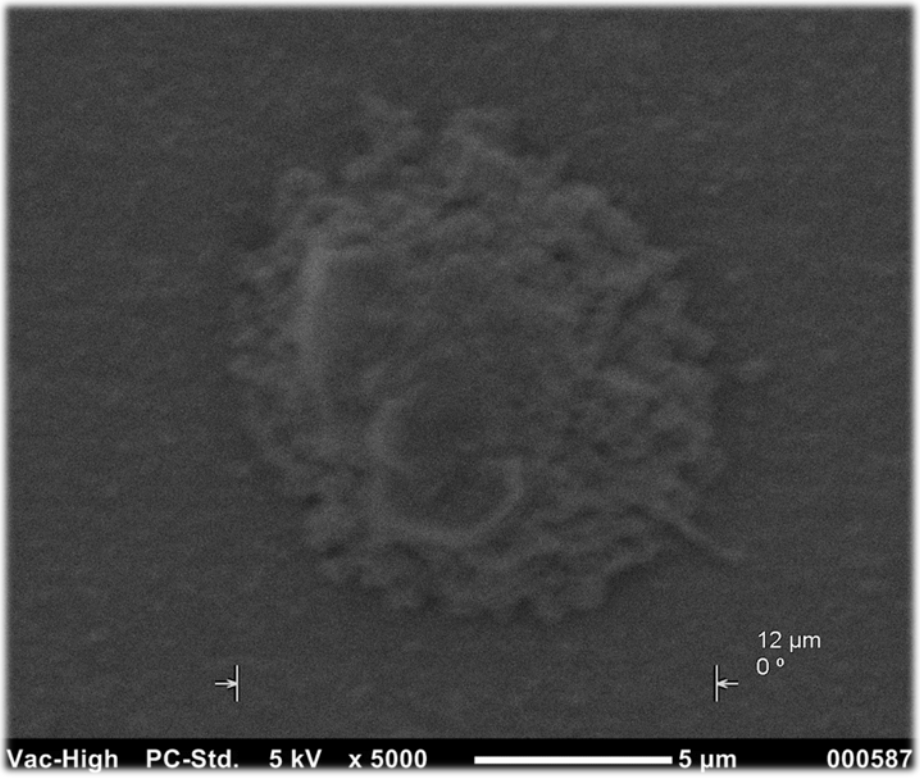

Figure 153: Close-up View of a Typical Raised Feature Observed on the Surface.

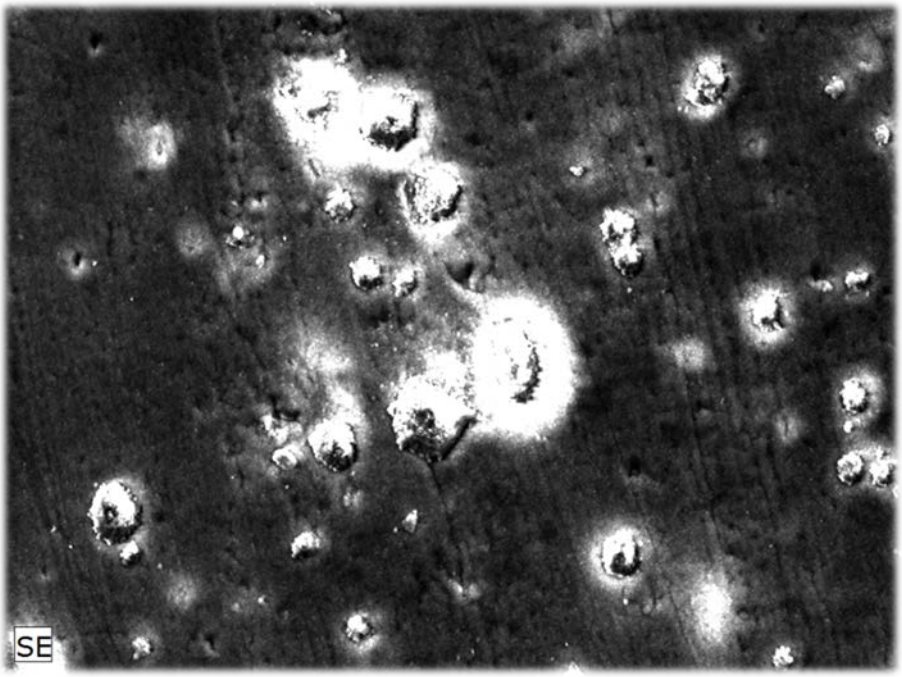

Figure 154: The Raised Features Exhibited Added Charging Compared to the Surrounding Sample. This may either be attributed to beam geometry effects or the added thickness of oxide at these locations.

6.1.6. Surface Composition Using Energy Dispersive X-Ray Spectroscopy

The JOEL 5910 General Purpose SEM was also capable of performing elemental characterization of the cladding surface via energy dispersive X-ray spectroscopy using an X-ray detector. Incident electrons from the electron gun result in ejection of inner shell electrons from atoms in the sample. As outer shell electrons fill inner shell vacancies, characteristic X-rays are emitted, which may be used to determine the elemental composition of the sample. The spectroscopy revealed that both the nominal surface and the raised features primarily consisted of aluminum and oxygen. Note that other elements typically found in 6061 aluminum were not readily detectable, likely due to the limited penetration of the EDS measurement coupled with the thickness of the boehmite film. This indicates that the boehmite film covers the entire surface. The results are shown in Figure 155 and Figure 156. The exact cause of these outgrowths is unknown, but likely occurs during the prefilming process.

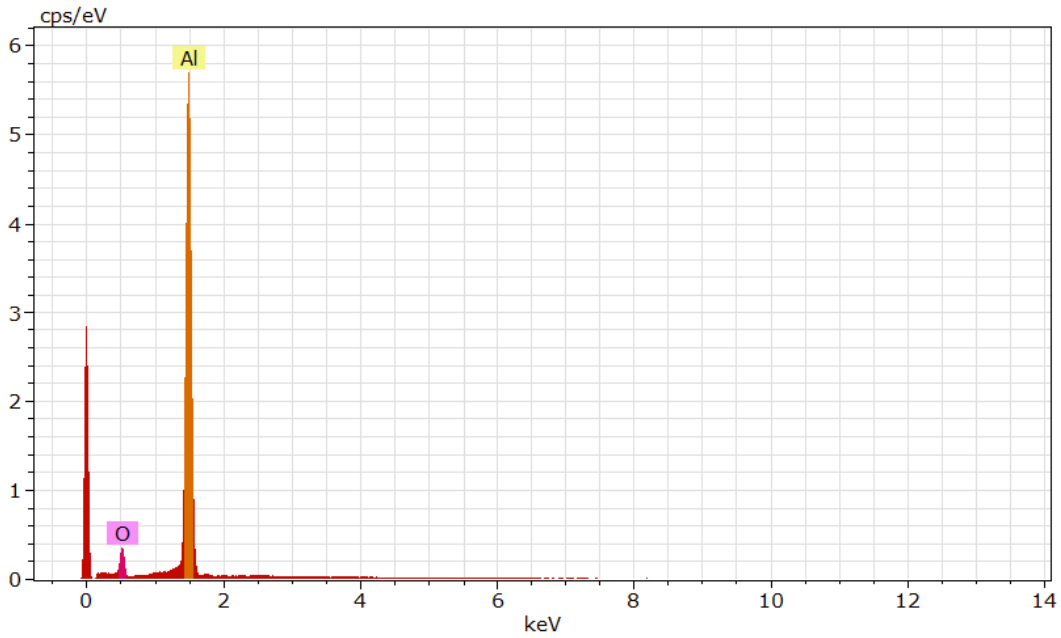

Figure 155: Energy Spectrum of Emitted X-rays from the Sample Indicating the Presence of Aluminum and Oxygen in the Surface Layers.

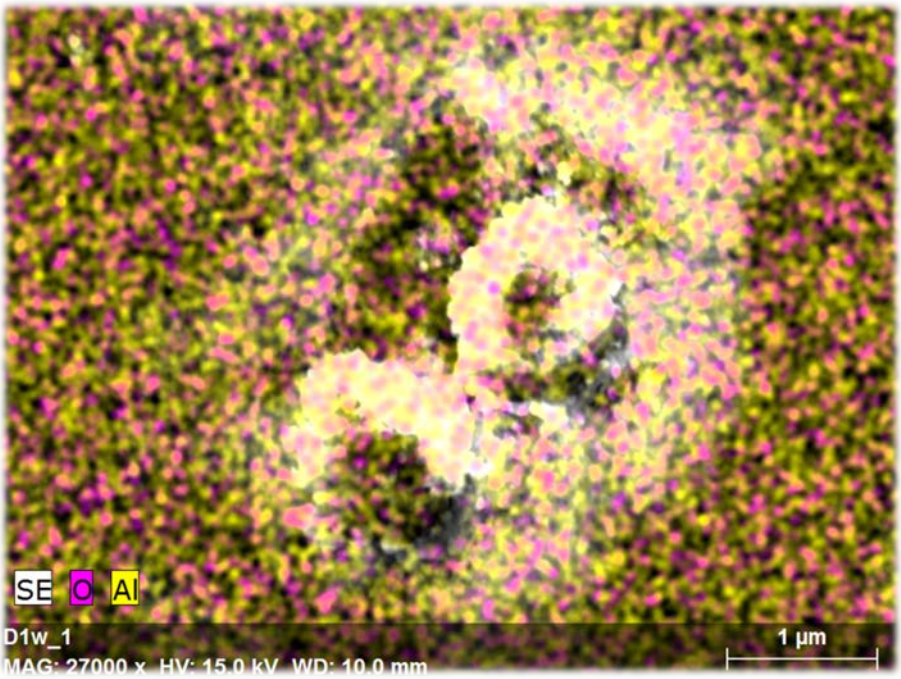

Figure 156: Elemental Map Overlay of the Surface Showing Presence of Aluminum and Oxygen on Both the Nominal Surface and On the Raised Features.

6.2. Heater Plate Characterization

In chapter 2, it was pointed out that the heater plate material in this study (316 stainless steel) is different from the actual cladding material in the MITR and similar MTR's (6061 aluminum). As long as the roughness is comparable, this will have no effect on the single-phase heat transfer. For very thin heaters or heaters with non-uniform heat generation, the thermal diffusivity of the heater, which depends on the material, will affect the ultimate heat flux distribution at the surface and can also influence the transient temperature response during ebullition cycles or during hot-spot formation immediately prior to CHF. However, the heater in this study is sufficiently thick to avoid this effect, and it was already shown in chapter 2 that the surface heat flux profile is essentially uniform. Therefore, the surface material should only influence onset of nucleate boiling by virtue of different contact angles on the surfaces (due to different surface chemistry and specific surface features).

However, as will be shown here, the wettability on practical stainless steel and aluminum surfaces with their native oxide is quite similar. In fact, it is shown in section 6.3.2 that 300 series stainless steel and 6061 aluminum exhibit similar affinities for surface contaminants, resulting in comparable surface contaminant profiles on practical surfaces. The resulting surface energy, and therefore the contact angle, is similar for as-received 6061 aluminum and 300 series stainless steel when cleaned with solvents. While pre-filmed 6061 aluminum leads to stable low contact angle behavior, it is still not certain whether this process will be employed for LEU fuel cladding in the MITR. Existing cladding in the MITR undergoes a brief nitric acid etch, prior to swaging of fuel plates in the assembly. After assembly, the exterior elements are wiped with alcohol and the entire assembly is rinsed with DI water, as described in the next section. The existing cleaning process likely results in a surface similar to the as-received surfaces of this study with a mild solvent clean.

In order to compare the wettability of practical stainless steel and aluminum surfaces, the contact angle was measured on surfaces of different roughness. Contact angles were measured using the KSV CAM 101 system described in section 6.1.4. Roughness was measured using the confocal microscope described in section 6.1.2. Surface finishes ranged from #8 mirror finishes (from the mill) to surfaces lapped with 310 μm paste. Any surfaces which were mechanically refinished were allowed to sit over night to reform their native surface oxides and nominal surface contaminant profiles. Immediately prior to contact angle measurement, surfaces were

cleaned by sonicating in ACS reagent grade acetone for 10 minutes, followed by a rinse with ultra-pure ethanol, followed by a final rinse with de-ionized water, and then blown dry with ultra-high purity compressed nitrogen. The results of equilibrium (static, sessile drop) contact angle measurements are listed in Table 40. Note that with the #8 mirror finish, the R_a for both surfaces is ~0.1 μm. Therefore, the measured contact angles for these surfaces should be approximately equivalent to the intrinsic contact angle with the given surface chemistry [168]. Note that Wenzel's equation is ineffective for predicting effects of roughness on the apparent contact angle when the intrinsic contact angle is close to 90°.

Table 40: Comparison of Equilibrium Contact Angles for As-received 316 Stainless Steel and 6061 Aluminum Surfaces following a Solvent Clean. Increasing surface roughness results in a lower apparent contact angle. A minimum of three contact angle measurements were made for each condition, with the standard deviation listed.

Material	Finish	Equilibrium Contact Angle	R_a (μm)	Roughness Ratio, *r*
316 Stainless Steel	*#8 Mirror*	88.9° ± 1.4°	0.108	1.003
	25 μm lapped	55.5° ± 6.8°	0.906	1.456
	109 μm lapped	36.4° ± 4.0°	2.008	1.328
	310 μm lapped	36.6° ± 3.7°	3.426	1.399
6061 Aluminum	*#8 Mirror*	86.1° ± 2.4°	0.094	1.003
	25 μm lapped	59.9° ± 6.4°	1.51	1.381
	109 μm lapped	16.3° ± 3.4°	4.084	1.534
	310 μm lapped	19.7° ± 1.3°	6.716	1.705

Figure 157 plots the measured equilibrium contact angles as a function of the surface roughness for 6061 aluminum and 316 stainless steel. The value for the 6061 aluminum cladding surface pre-filmed with boehmite, which was characterized in the preceding section, is included for comparison. Both the nominal and well-wetting 316 stainless steel heater plates prepared for this study are also listed. Note that all surfaces were cleaned and dried with the standard solvent cleaning procedure immediately prior to making measurements.

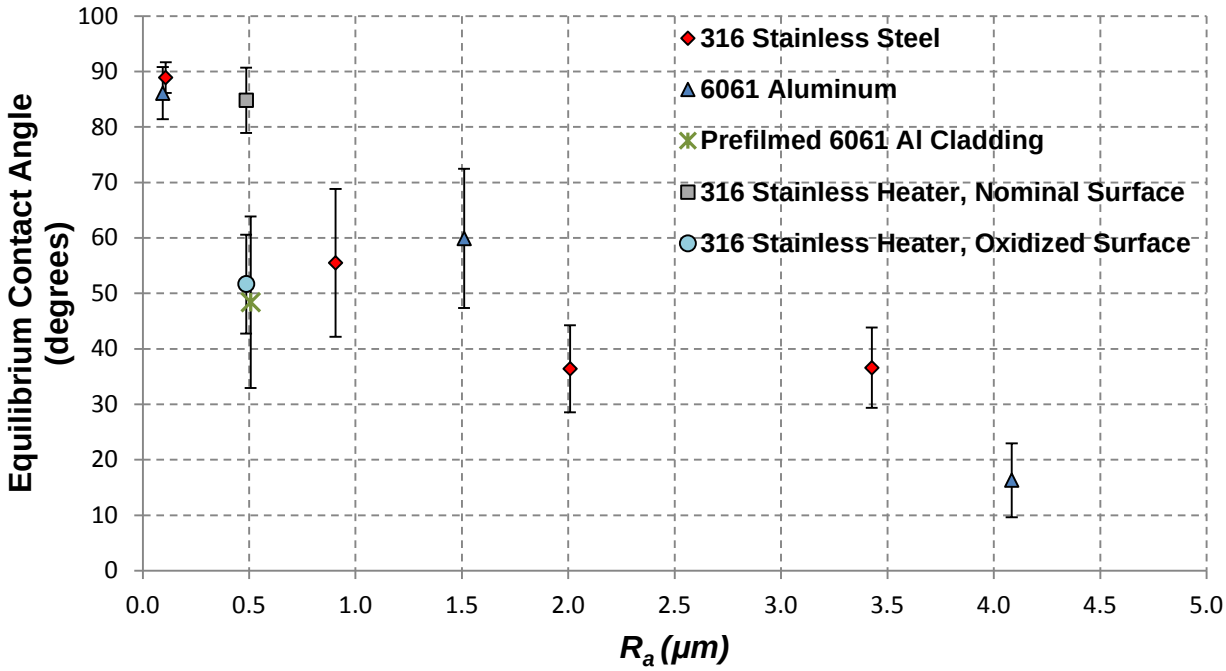

Figure 157: Measured Equilibrium (Apparent) Contact Angle versus Arithmetic Roughness for 316 Stainless Steel and 6061 Aluminum Surfaces. The surfaces possess their native oxides, except for the pre-filmed cladding surface, which has a protective boehmite layer, and the oxidized 316 surface, which was heated in air at 600 °C. Note that the "intrinsic" contact angle for 6061 aluminum and 316 stainless steel with their native oxides and associated hydrocarbon contaminant overlayers are nearly identical. All surfaces were cleaned using the standard solvent cleaning procedure immediately prior to contact angle measurements. Error bars represent 1.96× the standard deviation of each set of measurements.

6.2.1. Nominal Surface

The preparation procedure for the nominal 316 stainless steel surface is described in Section 4.2. The surface was prepared to have an arithmetic roughness, R_a, comparable to that measured for the pre-filmed cladding coupons characterized in section 6.1 ($R_a \approx 0.5$ μm). A trial-and-error approach was taken until the appropriate finish was achieved. The same heater surface was utilized for the single-phase heat transfer experiments and for the two-phase experiments with the standard surface. Roughness was measured using the profilometer described in section 6.1.3. The results were consistent across each surface and on various test coupons finished in the same manner. The average arithmetic roughness and standard deviation from eight separate measurements was $R_a = 0.486 \pm 0.111$ μm. The maximum roughness was $R_z = 2.587 \pm 0.737$ μm.

Surface wettability was characterized by measuring equilibrium, advanced, and receded contact angles with de-ionized water. Measurements were made using the setup described in section 6.1.4, and advanced and receded angles were determined using the technique discussed at the beginning of this chapter. Representative contact angles measured prior to boiling are depicted in Figure 158 and Figure 159. All results are summarized in Table 41, and the equilibrium contact angle is plotted in Figure 157 for comparison to the other measurements made on 316 stainless steel and 6061 aluminum. Equilibrium contact angles were also measured following onset of nucleate boiling tests, and were found to decrease slightly from pre-test values to an average of 75.6 ° ± 1.7 °.

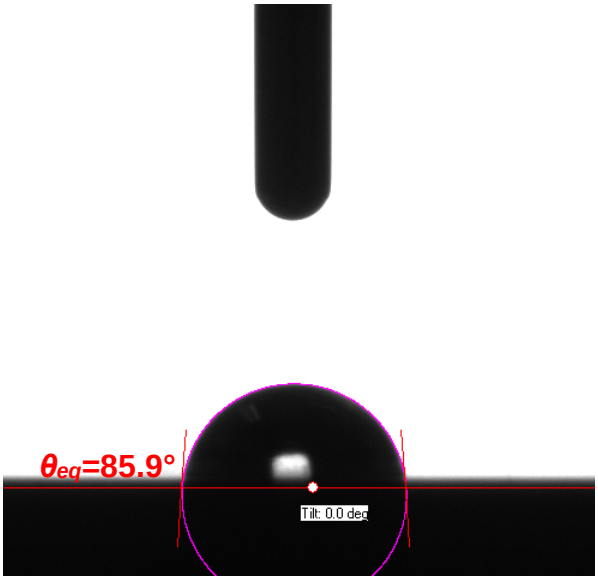

Figure 158: Equilibrium Contact Angle of De-ionized Water on Nominal 316 Stainless Steel Heater Surface.

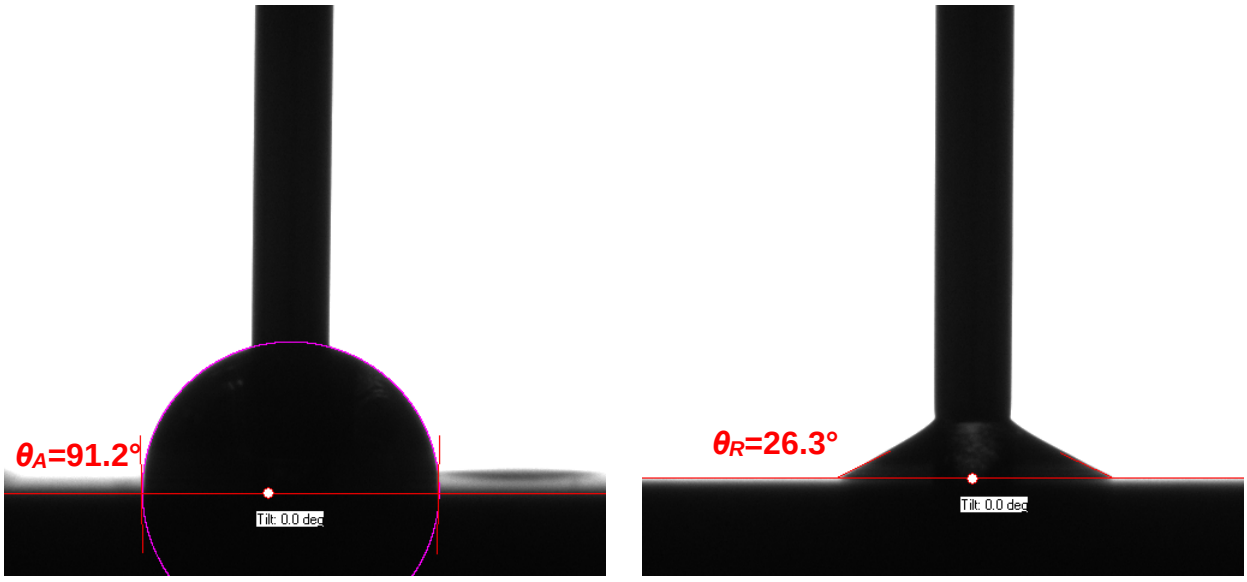

Figure 159: Static Advancing Contact Angle (left) and Static Receding Contact Angle (right) on Nominal 316 Stainless Steel Heater Surface.

6.2.2. Oxidized Surface

The oxidized surface was prepared in the same manner as the nominal surface, except following surface finishing and cleaning, it was heated in a furnace in air at 600 °C, as described in section 5.1.3. Following heating, a blue/brown tint was observed on the surface, which is a result of the thin-film interference caused by the formation of the thin oxide layer. "Tempering colors" are well-characterized for many metals and are a rough indicator of how high a certain metal has been heated. Immediately after removal from the furnace (and being allowed to cool to room temperature), the surface displayed nearly perfect wetting. The surface was allowed to age overnight (i.e. accumulate the stable contaminant overlayer), as the heat transfer testing would not take place immediately after removal from the furnace. Solvent cleaning was performed immediately before measuring the equilibrium, advanced, and receded contact angles, which are shown in Figure 160 and Figure 161. Values are listed in Table 41.

Figure 160: Equilibrium Contact Angle of De-ionized Water on Well-wetting (Oxidized) 316 Stainless Steel Heater Surface.

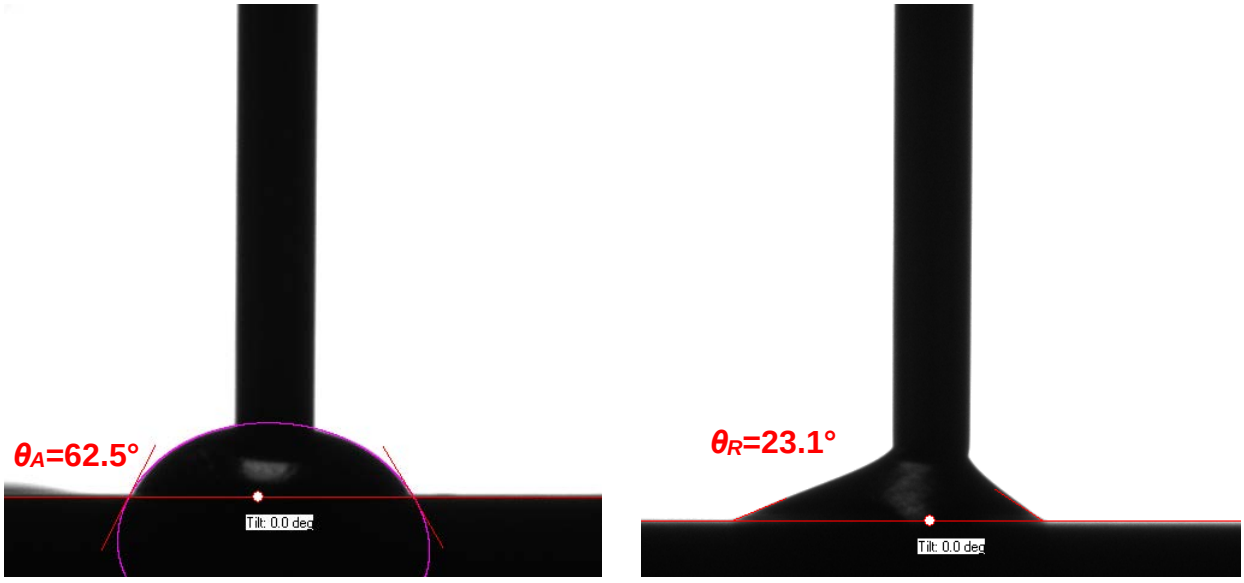

Figure 161: Static Advancing Contact Angle (left) and Static Receding Contact Angle (right) on Well-wetting (Oxidized) 316 Stainless Steel Heater Surface.

Table 41: Summary of Contact Angles for the 316 Stainless Steel Heater Surfaces in This Study.

	Nominal 316 Stainless Steel Surface	Well-wetting (Oxidized) 316 Stainless Steel Surface
Equilibrium	84.8° ± 3.0°	51.7° ± 4.6°
Static Advancing	95.4° ± 2.9°	57.9° ± 6.4°
Static Receding	23.9° ± 2.6°	21.5° ± 1.5°

From the measurements, it is clear that the oxidation treatment results in a modest reduction in the contact angle. This contact angle reduction is the suspected cause of the delay in incipience reported for the oxidized heater in Chapter 5. Therefore, the prefilmed cladding, which exhibits a contact angle very similar to that of the oxidized stainless steel, would be expected to have a higher onset of nucleate boiling heat flux than the aluminum cladding with the native oxide. However, as explored in Appendix E, issues such as surface contamination and aging also have a role in wettability on the surfaces, and will influence the contact angle on plain and oxidized surfaces.

6.3. Chapter Summary

Surface characteristics have a crucial role in two-phase surface phenomena, including boiling incipience. For this reason, careful surface characterization was carried out on prefilmed cladding coupons and on the heater plates used in the experimental program. Roughness, texture, elemental composition, and surface wettability were investigated to provide a better understanding of how these parameters influence the onset of nucleate boiling. An independent study was carried out and is reported in Appendix E on the influence of surface contamination and oxidation on wettability, with results being quite pertinent to the investigation of the onset of nucleate boiling. The important findings in this chapter are summarized below:

- 6061-T6 aluminum cladding coupons display a reduced equilibrium contact angle compared to that on aluminum with the native surface oxide. The average equilibrium contact angle was 48.2°.
- The surface preparation method for the heaters used in the investigation of the onset of nucleate boiling yielded an average arithmetic roughness 0.486 μm, intentionally similar to the roughness value measured for the prefilmed aluminum cladding coupons.
- The equilibrium contact angle on stainless steel with the native surface oxide is comparable to that for aluminum with the native surface oxide, as long as the roughness is similar.
- The oxidized stainless steel surface used in the two-phase experiments had an equilibrium contact angle of 51.7°, very similar to that of the prefilmed aluminum cladding surface.
- Considering the similarity in wettability, the onset of nucleate boiling results obtained for the nominal and oxidized stainless steel surfaces should be applicable to the plain aluminum and prefilmed aluminum surfaces, respectively.
- Surface contamination can have a profound impact on wettability, with deposited hydrocarbons only a few nanometers thick resulting in decreased surface energies and therefore higher contact angles.
- Hydrocarbon surface contamination is unavoidable outside a clean room environment, and standard solvent cleaning methods fail to remove several nanometers of hydrocarbon.

- Alternative cleaning treatments investigated for fuel and cladding surfaces have the ability to create cleaner surfaces showing stable reductions in the contact angle.

Chapter 7

Conclusion

Thermal hydraulic characteristics of narrow rectangular mini-channels are relevant to materials test reactors, which have historically adopted plate-type fuel design. Single-phase heat transfer, onset of nucleate boiling, flow instabilities, and the critical heat flux have not been as thoroughly studied in these channels as they have been in other geometries. In the MITR, the Limiting Safety System Setting is established such that the onset of nucleate boiling may not occur anywhere in the core during normal operation. The planned conversion of the MITR to LEU fuel to reduce proliferation risk, and the associated power uprate that will be sought, motivates the need for a better understanding of thermal hydraulic phenomena in these systems. Better estimates of the single-phase heat transfer coefficient and onset of nucleate boiling are necessary to support future power uprates.

A full-scale, 75 kW two-phase test facility has been designed and built at MIT that incorporates a test section with geometry and characteristics resulting in one-to-one hydrodynamic similarity with a coolant channel in the MITR. The facility is capable of operating at the flow conditions, temperatures, and pressures encountered in the MITR. After careful design and construction an experimental program was undertaken to investigate single-phase heat transfer, the onset of nucleate boiling, and the single-channel flow instability. The summary of major findings is provided in section 7.1. A list of major contributions resulting from this study is provided in section 7.2. Lastly, several recommendations are made for future work.

7.1. Summary of Findings

The summary of key findings are broken into four areas: those involving single-phase fluid flow and heat transfer, those involving two-phase heat transfer, those involving surface science measurements, and general conclusions.

Single-Phase Fluid Flow and Heat Transfer

- The friction pressure drop in high aspect ratio, narrow rectangular channels is well-predicted using the Blasius equation as long as the laminar equivalent diameter concept is used, which accounts for the increase in the friction factor due to the presence of secondary flows.
- The measured critical Reynolds number for the experimental channel was:

$$Re_{crit} = 3500\ to\ 4000$$

  The friction factor data also indicate that flow does not become fully turbulent until $Re \gtrsim 7000$. It is important to note that these findings depend on inlet configuration as well as aspect ratio, and therefore may not be equivalent in the MITR due to its inlet plenum configuration and fuel element nozzle design.
- Measured single-phase heat transfer coefficients in the transition flow regime for the narrow channel, which was heated on one side with uniform heat flux, were about 10% higher than predictions using the Gnielinski correlation. All other existing correlations overestimated heat transfer when the Reynolds number was below 10,000 in the narrow channel.
- The Prandtl number dependence of the Nusselt number in the fully turbulent region could not be adequately described by a simple power law. This may be in part due to the one-sided heating, which was confirmed using a boundary layer analysis.
- A new semi-analytical correlation (equation (151)) is developed that accounts for the heating asymmetry and aspect ratio of the channel. The correlation is extended down to the transition regime, and predicts experimental data in the range of $2.2<Pr<5.4$ and $4000<Re<70{,}000$ with a mean absolute error of less than 4.9%.

Two-Phase Heat Transfer

- Models for incipience under forced convection often assume the existence of the optimum cavity size on the heated surface. This is often true for practical engineering and industrial surfaces, but should not always be assumed. Higher superheats will be required to nucleate from very smooth surfaces lacking cavities in the optimum size range.
- Experimental determination of the incipience point is influenced by the identification technique employed by the experimentalist. Temperature measurement techniques relying on a heat flux partition allow for local identification and appear to be the most reliable and consistent across subcoolings and mass fluxes, and was the method used by Bergles and Rohsenow in their experimental program. Measurement of the fluctuation in pressure or pressure drop is a global method, but is sensitive to edge effects and does not provide surface temperature data at the incipience point.
- Visual identification of incipience is unreliable at higher flow velocities and subcoolings due to bubble sizes falling below the visualization threshold for many optical setups. In this study, a high speed video system with a spatial resolution of 20 μm/pixel and temporal resolution of up to 20,000 Hz was unable to capture vapor bubbles at the incipient point for v>1 m/sec. Much higher heat fluxes are likely required until vapor can be visualized, leading to the potential for overestimating the onset of nucleate boiling point if this technique is relied upon.
- For the stainless steel surface tested, which had similar roughness and wettability to 6061 aluminum with the native oxide, the Bergles and Rohsneow correlation adequately predicted the onset of nucleate boiling heat flux as long as it was used in conjunction with the appropriate single-phase heat transfer correlation, which in this case was the newly developed semi-analytical correlation.
- Oxidized stainless steel surfaces were also tested which had similar contact angles to boehmite prefilmed 6061 aluminum cladding coupons. The effect of reducing contact angle on the incipience point was confirmed, with the measured ONB heat flux being 18% to 40% higher on the oxidized surface than on the nominal surface.
- The presence of the density wave instability was confirmed for high phase change numbers in the experimental channel by performing a spectral analysis. Results are

not directly applicable to the MITR due to different entrance and exit form loss coefficients and different external pressure boundary conditions (single-channel vs. parallel channel).

Surface Science Measurements

- Measured contact angles measured on 6061 cladding coupons prefilmed with boehmite were, on average, 48.7°. This is about 30° lower than values measured on 6061 of similar roughness with the native surface oxide.
- The arithmetic roughness, R_a, and contact angle on the nominal stainless steel surface were similar to those measured for a plain 6061-T6 surface. This means the onset of nucleate boiling measured on the reference surface should be similar to the plain 6061 surface.
- The arithmetic roughness, R_a, and contact angle on the oxidized stainless steel surface were similar to those measured for a 6061 cladding surface prefilmed with boehmite. Once again, this means the onset of nucleate boiling measured on the oxidized surface should be similar to the boehmite pre-filmed surface.
- The effect of surface contamination on contact angle has been determined quantitatively. Hydrocarbon thicknesses of only a few nanometers can have a drastic effect on wettability, with thicker contaminant layers leading to lower surface energies and higher contact angles.
- Solvent cleaning alone leaves 4-6 nm of hydrocarbon on a surface. Alternative cleaning techniques may be used to impart stable reductions in the contact angle on cladding.

General Conclusions

- The prefilming of boehmite on 6061 cladding reduces the contact angle, leading to higher heat fluxes at which the onset of nucleate boiling occurs. Such treatment could therefore not only be beneficial to future MITR fuel by reducing pitting corrosion, but also by improving onset of nucleate boiling margin.
- Surface conditions such as roughness and cleanliness can have a significant impact on the onset of nucleate boiling. More careful control of surface roughness through fuel fabrication specifications could potentially improve margin to the onset of nucleate boiling by reducing cavities available for nucleation. Cleaning treatments explored in this study can produce cladding surfaces with reduced contact angles that are stable, i.e. they remain at lower values.

7.2. Major Contributions

The major contributions of this study include:

(1) ***The design and construction of a 75 kW test facility with a full-scale Materials Test Reactor coolant channel for studying heat transfer phenomena in narrow channels with the aid of high speed visualization.***

(2) ***Collection of single-phase friction pressure drop and heat transfer data over a wide range of conditions applicable to the MITR.***

(3) ***The development of a new semi-analytical correlation to predict single-phase heat transfer in narrow rectangular channels.*** The correlation is derived using a boundary layer analysis and supported by experimental results. The aspect ratio and heating asymmetry are accounted for in the correlation, and it has been modified to extend it down to the transition regime. It predicts experimental data in the range of $2.2<Pr<5.4$ and $4000<Re<10{,}000$ with a mean absolute error of less than 4.9%.

$$Nu = \frac{0.199(Re-600)^{7/8}Pr}{5[Pr-2]\phi^{*1/8} + 10.05(Re-600)^{1/8}\phi^{*1/4}}$$

(4) ***The systematic classification of different techniques for experimentally identifying the onset of nucleate boiling.***

(5) ***Confirmation of the suitability of the correlation of Bergles and Rohsenow in predicting the onset of nucleate boiling under forced convection for plain metal surfaces with a wide range of available cavities for nucleation.***

(6) ***Determination of the effect of surface oxidation and wettability on boiling incipience in high aspect ratio rectangular mini-channels.***

(7) ***Direct quantification of the effect of surface contamination and oxidation on the wettability and surface energy of cladding materials.***

7.3. Recommendations for Future Work

The results of this study have set the stage for future work in at least three key areas of research. These areas include single-phase heat transfer, two-phase heat transfer, and safety analyses for the MITR and other research and test reactors. While the study provided comprehensive results in a number of areas, it led to several questions which would be prime areas for future research.

Recommended Future Work in Single-Phase Heat Transfer

- Further experimental investigation into the effect of one versus two-sided heating to extend the results of this study to channels heated on both sides.
- Investigation of natural and mixed convection regimes in the narrow channel experimental setup.

Recommended Future Work in Two-Phase Heat Transfer

- Parametric investigation of surface roughness and texture effects on boiling incipience in the high aspect ratio channel.

Recommended Future Work in Safety Analyses for Research and Test Reactors

- Application of new correlations to RELAP5 for MITR steady-state and transient analysis.

Appendix A

A Primer on Nuclear Weapons Proliferation as it Pertains to HEU-Fueled Research and Test Reactors

The threat of nuclear weapons proliferation is the primary driver for controlling nuclear technology and limiting access to special nuclear material. Whether the proliferant is a nation or a non-state actor, it is generally viewed as a major detriment to global security should any new entity acquire a nuclear weapons capability. In the past decade, the public focus has largely shifted to non-state actors, though, to date, proliferation has only occurred among nation-states. The added fears surrounding non-state actors are, in some respects, justified, since traditional deterrence may not apply to such entities [183]. While there is an inexorable link between civilian nuclear technology and nuclear weapons technology, the actual risk of proliferation, especially to non-state actors, is difficult to quantify, which has led to significant speculation on the issue. The probability of a terrorist nuclear attack being successfully carried out against a population center is even more difficult to estimate, though one political scientist has suggested the probability to be as high as 29% in the next decade, with others claiming a likelihood as high as 50% over the next decade [184]. While such conjecture is clearly not based in reality, dismissal of the threat would be even more dangerous than some of the alarmist suppositions being made. The purpose here is not to provide a precise estimate, but rather provide basic background on the threat of nuclear proliferation, especially as it pertains to high enriched uranium in the civilian nuclear fuel cycle.

In terms of modern commercial power production, the link between nuclear weapons and civilian reactors primarily lies in uranium enrichment, plutonium breeding, and plutonium separation technologies. The most notable example is the theft and the subsequent dissemination of gas centrifuge designs and technology from URENCO by Abdul Qadeer Khan [185]. Nuclear material from commercial light water reactors (LWR's) themselves are a rather poor avenue for proliferation, due to complications arising with the weaponization of reactor-grade plutonium, the difficulty of diverting fissile material while the reactor is on-line, and the effectiveness of safeguards for item counting. In fact, the once-through LWR fuel cycle has become a benchmark for nonproliferation criteria, which is often referred to as the "spent fuel standard" [186]. A 1979 DOE report summarizes the issue, stating:

> All nuclear fuel cycles would entail some proliferation risks; there is no technical "fix." Nevertheless, the light-water reactor fuel cycle with spent fuel discharged to interim storage does not involve directly weapons-usable material in any part of the fuel cycle and is a more proliferation-resistant nuclear power fuel cycle than other fuel cycles which involve highly enriched uranium or pure plutonium [187].

To date, no nuclear weapons program has relied on plutonium extracted from spent fuel taken from the commercial fuel cycle, though the possibility is not excluded in the future.

In the case of research and test reactors, the proliferation risk due to diversion or theft of material is much more credible. For test reactors operating with natural uranium or uranium at otherwise low enrichment levels, the concern lies in the potential for separating weapons-grade or fuel-grade plutonium from the irradiated fuel. North Korea constructed a graphite-moderated, natural uranium-fueled 5 MW(e) (around 20 to 25 MW thermal) reactor near Yongbyon under the guise that it was for research purposes. However, the North Korean regime has used the reactor to produce plutonium for its nuclear weapons program. From the viewpoint of safeguards, the IAEA is particularly concerned about research reactors with a thermal power of 25 MW or more because, as a general rule, they can produce one or more significant quantities of plutonium annually [188]. With respect to research and test reactors fueled by high enriched uranium, the concern primarily lies with diversion or theft of the fuel itself, either before or after irradiation. HEU-fueled research reactors are actually less desirable for plutonium production, due to the higher production of plutonium-238 with increasing uranium enrichment. Plutonium-238 has a very high neutron generation rate (2.59×10^6 neutrons/kg-sec) due to spontaneous

fission and a very high rate of heat generation (570 W/kg) due to alpha decay. These factors can significantly complicate use of the plutonium for weapons purposes. Increasing burnup will lead to a higher isotopic content of plutonium-240, which is once again undesirable for weaponizing plutonium due to a high neutron generation rate. Separating plutonium-239 from the less desirable plutonium isotopes is at least as difficult as enriching uranium, and would be further complicated by the increased radiation dose.

Several grades of uranium and plutonium isotopes that could potentially be used to construct a nuclear weapon are listed in Table A1. Uranium-233, neptunium-237, and some other higher actinides are alternative isotopes that could theoretically be used to achieve a nuclear yield, but are not discussed here. At this point, it is necessary to distinguish between two general classes of designs for achieving a nuclear yield. A gun-type design entails launching an annular subcritical projectile of fissile material down a barrel toward a subcritical cylindrical target, to create a supercritical mass that generates a nuclear yield. Assembly velocities are typically about 200 m/sec, but could be as high as 1000 m/sec [189]. An implosion-type design involves the compression of a pit of fissile material using explosive lenses to increase the physical density of the pit to a point where it becomes supercritical. Implosion-type weapons can achieve much higher assembly velocities, and therefore shorter assembly times, than gun-type designs. This also leads to higher efficiencies and therefore increased yields with the implosion design. Both gun-type and implosion-type designs can suffer from pre-detonation, but the choice of fissile material and design flaws will exacerbate the issue. Plutonium, even with high purity of ^{239}Pu, is usually considered impractical for a gun-type weapon as neutron generation rates are still high enough to make pre-detonation unavoidable. Therefore, plutonium is only suitable for implosion-type weapons, with high enriched uranium being suitable for either gun-type or implosion-type designs. It is important to keep in mind that in either design, the fission reactions must occur on a very short time scale (on the order of "shakes," where one shake equals 10^{-8} sec), prior to explosive pressure forcing the fissile material apart. Therefore, the assembly must not just be critical, but very supercritical (close to two critical masses), and be supercritical on fast neutrons alone.

In modern nuclear weapons employed by advanced states, weapons are often multi-stage thermonuclear devices, where the primary stage relies on an implosion configuration, with plutonium typically being favored. While plutonium is favored by advanced states for its lower

Table A1: Grades of Uranium and Plutonium Relevant to Nuclear Weapons. Definition of material grades derived from Reference [190].

MATERIAL	CONTENT	USABILITY IN WEAPONS
Weapons-Grade Uranium	≥90% enrichment in ^{235}U	Suited for gun-type or implosion design. Often considered most desirable material for non-state actors.
High Enriched Uranium (HEU)	≥20% enrichment in ^{235}U	Difficult for lower enrichments, especially if in non-metallic form or alloyed with other materials. The lower the enrichment, the higher the critical mass and higher chance of pre-detonation.
Super-Grade Plutonium	<3% ^{240}Pu ≥95% ^{239}Pu	Usable in implosion-type weapons, but even small fractions of ^{240}Pu precludes use in gun-type weapons due to pre-detonation.
Weapons-Grade Plutonium	≥93% ^{239}Pu	Same as super-grade plutonium.
Reactor-Grade Plutonium	<25% ^{240}Pu ≥60% ^{239}Pu	Though possible to make an implosion-type device, larger critical mass, lower assured yield, and more fizzling issues due to internal heat generation and increased probability of pre-detonation.

critical mass and compactness in modern nuclear weapon designs, the general assumption in the nuclear policy community is that implosion-type weapons require greater sophistication and skill to design and construct than gun-type designs. The logic following this is that any low technology states or non-state actors seeking a nuclear weapon would favor gun-type designs due to their perceived simplicity compared to implosion designs, and therefore high enriched uranium would be the most desirable material unless an already functioning nuclear device could be stolen or purchased. The potential avenues for a non-state actor to acquire a nuclear capability are summarized in Figure A1.

To date, no non-state actor has acquired a nuclear capability, so it is unknown what scenario would be most probable. Some low technology states, such as North Korea, have actually started their programs based on plutonium, and therefore have developed implosion weapons (though North Korea did have some trouble, with its first nuclear test resulting in a

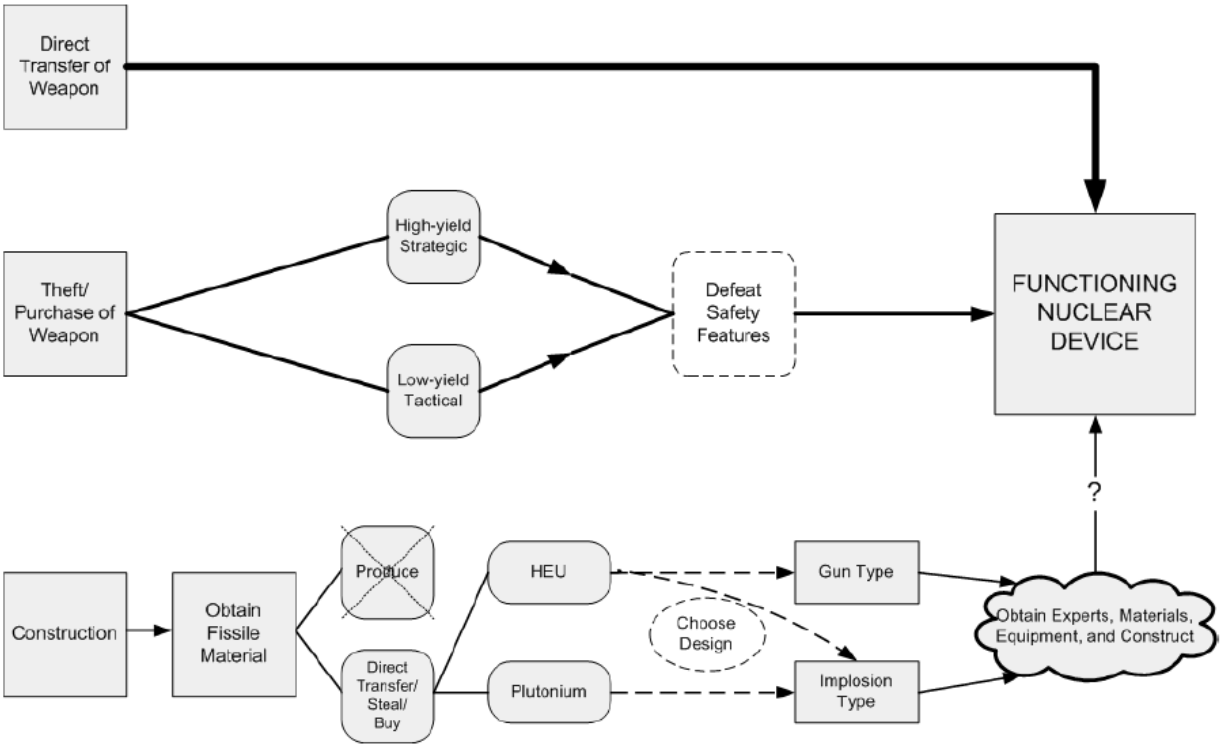

Figure A1: Possible Pathways Leading to Terrorist Acquisition of a Functioning Nuclear Device. Terrorists could obtain a weapon through direct transfer (the easiest from the standpoint of the terrorist), through theft, though some devices have integrated security features, or through construction of a device. Construction of a nuclear device by terrorists has the most uncertainty in the result- even with investment and organization, the device might fail to produce an appreciable yield.

fizzle yield by most accounts). The second major assumption in the nuclear policy arena involves the ease with which non-state actors could construct a functioning nuclear device. The term "crude nuclear explosive" [191] has found its way into numerous policy discussions, which tends to trivialize the associated challenges in making a nuclear device with an appreciable yield. South Africa, which developed a limited nuclear capability of six HEU gun-type weapons, provides a real-world example that can be used to gauge the difficulties facing non-state actors in developing even a simple nuclear capability. South African efforts involved around 400 personnel working on the project, exclusive of uranium enrichment efforts, to build low-yield (10 to 20 kT) gun-type nuclear weapons. The conclusion that Frost makes is [192]:

> The crucial point about the South African programme is that it took at least three years, from 1974 to 1977, for a relatively wealthy state with an existing nuclear infrastructure, years of friendly international exchange of nuclear technology and

> knowledge and high levels of domestic expertise to build a simple gun-type device that could have produced a nuclear yield.

Yet, significant disagreement still exists over the difficulty that non-state actors might have in constructing a functioning nuclear device of appreciable yield. While few seem to doubt that it is theoretically possible for non-state actors to achieve such a feat, the debate is essentially unconstrained, with little distinction between what is possible and what is probable. Other elements leading to disagreement likely stem from a failure to recognize the difference between schematics and actual design drawings. Stephen Younger, former director of the Defense Threat Reduction Agency, takes a pragmatic approach, stating that while construction of a nuclear weapon by terrorists is possible, it is unlikely, and that other avenues (such as direct transfer) are more probable [193].

Lastly, the entire concept of risk involves both the probability of an occurrence and the potential consequence of that occurrence. Therefore, it is important to differentiate between a 0.5 kT fizzle yield, a 20 kT detonation, or a 330 kT detonation, as the probabilities of these events occurring at the hands of a non-state actor are not all equivalent. The theft of only HEU would unlikely give the proliferant the capability to develop a 330 kT nuclear device; additional technology for a multistage weapon would be required. While any nuclear yield would have dire consequences in a population center, the effects would be drastically different, where effects can be calculated and total damage and loss of life estimated. The classic text by Glasstone is appropriate for reviewing the relevant effects of nuclear weapons and the scaling of these effects with yield [194].

It is incredibly difficult, if not impossible, to provide an accurate determination of the quantitative risk posed by the use of high enriched uranium in research and test reactors. However, this material has been identified as the most attractive to low technology states and non-state actors for constructing a nuclear weapon, and is therefore viewed as a desirable target for theft or diversion. While there is considerable uncertainty as to whether non-state actors could successfully steal a significant quantity of HEU and then successfully construct a nuclear device with an appreciable yield, the potential consequences are sufficiently dire to warrant further action by the United States and other governments. Increased physical security at research and test reactor sites where HEU is present can reduce the probability of theft, but without knowing the overall risk, it is difficult to determine what level of security is ultimately

appropriate. Conversion of research and test reactors to LEU fuel provides the opportunity for permanent threat reduction.

Appendix B

Calculated Parameters and Uncertainties

Calculated parameters, along with their propagated total uncertainties that are not listed in Table 28, are provided in this appendix. Total uncertainties represent 95% confidence bounds, unless otherwise noted. Calculated parameters not listed in this appendix or in Table 28 either had negligible uncertainties (<0.1%) or were not used in further analysis.

-Mass Flow Rate (kg/sec)

$$\dot{m} = Q \times \rho(P,T) \times \frac{1}{60} \times \frac{1}{264.172} \tag{B1}$$

where Q is in gpm.

$$\varepsilon_{\dot{m}} = \varepsilon_{Q} \times \rho(P,T) \times \frac{1}{60} \times \frac{1}{264.172} \tag{B2}$$

-Mass Flux (kg/m^2-sec)

$$G = \frac{\dot{m}}{A_{flow}} \tag{B3}$$

$$\varepsilon_{G} = \sqrt{\left(\frac{1}{A_{flow}}\varepsilon_{\dot{m}}\right)^2 + \left(\frac{\dot{m}}{A_{flow}^2}\varepsilon_{A_{flow}}\right)^2} \tag{B4}$$

-Pressure at Axial Location, z_p (Pa)

Treating the axial pressure change, *dP*/*dz*, as constant for the single-phase flow, the pressure at a given axial location may be written as:

$$P(z) = P_{in} - \frac{(P_{in} - P_{out})}{L_P} z_P \tag{B5}$$

$$\varepsilon_{P(z)} = \varepsilon_P \sqrt{1 + 2\left(\frac{z_P}{L_P}\right)^2} \tag{B6}$$

-Darcy Friction Factor

$$f = \frac{2\rho}{G^2} \frac{D_{hyd}}{L_{PT}} \Delta P \tag{B7}$$

$$\varepsilon_f = \sqrt{\left(\frac{2\rho\Delta P}{L_{PT}G^2}\varepsilon_{D_{hyd}}\right)^2 + \left(\frac{2\rho D_{hyd}}{L_{PT}G^2}\varepsilon_{DP}\right)^2 + \left(\frac{4\rho D_{hyd}\Delta P}{L_{PT}G^3}\varepsilon_G\right)^2} \tag{B8}$$

-Specific Enthalpy Rise (J/kg)

$$\Delta h = h_{out} - h_{in} \tag{B9}$$

$$\varepsilon_{\Delta h} = h_{out}\left(T + \varepsilon_{\Delta T_{RTD}}, P\right) - h_{out}(T, P) \tag{B10}$$

-Thermal Power (W)

With a constant linear heat rate, treating the axial pressure change as equivalent to the friction pressure loss (i.e., $(dP/dz) \approx \tau_w P_w / A_{flow}$), and accounting for the isothermal heat loss, the energy equation yields:

$$\dot{Q}_{th} = \dot{m} \times \Delta h + \dot{Q}_{iso} \tag{B11}$$

$$\varepsilon_{\dot{Q}_{th}} = \sqrt{(\Delta h \varepsilon_{\dot{m}})^2 + (\dot{m}\varepsilon_{\Delta h})^2 + \left(\varepsilon_{\dot{Q}_{iso}}\right)^2} \tag{B12}$$

-Thermal Heat Flux (W/m^2)

$$q''_{th} = \frac{\dot{Q}_{th}}{A_{heat}} \tag{B13}$$

$$\varepsilon_{q''_{th}} = \sqrt{\left(\frac{1}{A_{heat}}\varepsilon_{\dot{Q}_{th}}\right)^2 + \left(\frac{\dot{Q}_{th}}{A_{heat}^2}\varepsilon_{A_{heat}}\right)^2} \tag{B14}$$

-Electric Power (W)

$$\dot{Q}_{elec} = I_P V_{E,plate} \tag{B15}$$

$$\varepsilon_{\dot{Q}_{elec}} = \sqrt{\left(V_{E,plate}\varepsilon_{I_P}\right)^2 + \left(I_P \varepsilon_{V_{E,plate}}\right)^2} \tag{B16}$$

-Volumetric Heat Generation in Heater Plate (W/m^3)

$$q'''_{elec} = \frac{\dot{Q}_{elec}}{V_{heat}} \tag{B17}$$

$$\varepsilon_{q'''_{elec}} = \sqrt{\left(\frac{1}{V_{heat}}\varepsilon_{\dot{Q}_{elec}}\right)^2 + \left(\frac{\dot{Q}_{elec}}{V_{heat}^2}\varepsilon_{V_{heat}}\right)^2} \tag{B18}$$

-Bulk Temperature at Axial Position, z_h (°C)

$$T_b(z) = T_{in} + \frac{\Delta T}{L_{heat}} z_h \tag{B19}$$

The maximum change in c_p between the inlet and outlet was <0.05% for the single-phase tests and <0.26% for the onset of nucleate boiling tests, making equation B19 a reasonable assumption for calculation of the local bulk temperature in both cases. Note that the covariance between T_{in} and ΔT was small enough to be neglected in the uncertainty propagation.

$$\varepsilon_{T_b} = \sqrt{\varepsilon_{T_b}^2 + \left(\frac{z}{L_{heat}}\varepsilon_{\Delta T}\right)^2 + \left(\frac{z(T_{out} - T_{in})}{L_{heat}^2}\varepsilon_{L_{heat}}\right)^2} \tag{B20}$$

-Wall Temperature (°C)

$$T_w = T_{back} - q'''_{elec}\frac{t_{plate}^2}{2k_{ss}} + \frac{t_{plate}}{k_{ss}}\left(q'''_{elec}t_{plate} - q''_{th}\right) \tag{B21}$$

$$\begin{aligned}\varepsilon_{T_w} = \Bigg[&\varepsilon_{T_{back}}^2 + \left(\frac{t_{plate}^2}{2k_{ss}}\varepsilon_{q'''_{elec}}\right)^2 + \left(\frac{t_{plate}}{k_{ss}}\varepsilon_{q''_{th}}\right)^2 \dots \\ &+ \left(\frac{q'''_{elec}t_{plate} - q''_{th}}{k_{ss}}\varepsilon_{t_{plate}}\right)^2 \dots \\ &+ \left(\frac{t_{plate}(q'''_{elec}t_{plate} - 2q''_{th})}{2k_{ss}^2}\varepsilon_{k_{ss}}\right)^2\Bigg]^{1/2}\end{aligned} \tag{B22}$$

-Heat Transfer Coefficient (W/m^2-K)

$$h = \frac{q''_{th}}{T_w - T_b} \tag{B23}$$

Here the uncertainty with the thermal heat flux is correlated to both the surface temperature uncertainty and the bulk fluid temperature uncertainty, making the situation a little more complicated. In this case, if the uncertainties of the terms in equation (B21) are to be used directly in calculating the uncertainty of the heat transfer coefficient, the covariance for each correlated pair of uncertainties must be taken into account in the uncertainty propagation. In this case, the uncertainty in *h* will be:

$$\varepsilon_h = \left[\left(\frac{\partial h}{\partial q''_{th}}\right)^2 \varepsilon^2_{q''_{th}} + \left(\frac{\partial h}{\partial T_w}\right)^2 \varepsilon^2_{T_w} + \left(\frac{\partial h}{\partial T_b}\right)^2 \varepsilon^2_{T_b} \ldots + 2\left(\frac{\partial h}{\partial q''_{th}}\right)\left(\frac{\partial h}{\partial T_w}\right)\varepsilon_{q''_{th}T_w} \ldots + 2\left(\frac{\partial h}{\partial q''_{th}}\right)\left(\frac{\partial h}{\partial T_b}\right)\varepsilon_{q''_{th}T_b}\right]^{1/2} \quad \text{(B24)}$$

The terms $\varepsilon_{q''_{th}T_w}$ and $\varepsilon_{q''_{th}T_b}$ represent 1.96 times the covariance of the subscript variables, respectively. The result is therefore:

$$\varepsilon_h = \left[\left(\frac{1}{T_w - T_b}\right)^2 \varepsilon^2_{q''_{th}} + \left(\frac{q''_{th}}{(T_w - T_b)^2}\right)^2 \varepsilon^2_{T_w} + \left(\frac{q''_{th}}{(T_w - T_b)^2}\right)^2 \varepsilon^2_{T_b} \ldots - 2\left(\frac{1}{T_w - T_b}\right)\left(\frac{q''_{th}}{(T_w - T_b)^2}\right)\varepsilon_{q''_{th}T_w} \ldots + 2\left(\frac{1}{T_w - T_b}\right)\left(\frac{q''_{th}}{(T_w - T_b)^2}\right)\varepsilon_{q''_{th}T_b}\right]^{1/2} \quad \text{(B25)}$$

-Reynolds Number

$$Re = \frac{G D_{hyd}}{\mu} \quad \text{(B26)}$$

$$\varepsilon_{Re} = \sqrt{\left(\frac{D_{hyd}}{\mu}\varepsilon_G\right)^2 + \left(\frac{G}{\mu}\varepsilon_{D_{hyd}}\right)^2} \quad \text{(B27)}$$

-Nusselt Number

$$Nu = \frac{h D_{hyd}}{k} \quad \text{(B28)}$$

$$\varepsilon_{Nu} = \sqrt{\left(\frac{D_{hyd}}{k}\varepsilon_h\right)^2 + \left(\frac{h}{k}\varepsilon_{D_{hyd}}\right)^2} \tag{B29}$$

Appendix C

Single-Phase Heat Transfer Data

All local, fully developed single-phase heat transfer data collected in this study are provided in Table C1. Channel average pressure (P_{avg}), channel average mass flux (G), channel average surface heat flux (q''), dimensionless axial position (z^+), local bulk temperature ($T_{b,loc}$), and local surface temperature ($T_{w,loc}$) are provided. In addition, calculated parameters, such as the local bulk fluid Prandtl number (Pr), the local bulk fluid Reynolds number (Re), and the local Nusselt number (Nu) are given. The calculated uncertainties for the Reynolds number (ε_{Re}) and Nusselt number (ε_{Nu}) are listed at 95% confidence levels. Nusselt number values represent those for the center (transverse) of the channel. Each datum represents the time average of a measurement over 30 minutes, and is grouped by mass flux with decreasing Prandtl number (increasing bulk temperature). Refer to chapter 4 for details on the experiments.

Table C1: Local Single-Phase Heat Transfer Data for Fully Developed Flow Conditions.

P_{avg} (bar)	G (kg/m^2-sec)	q'' (kW/m^2)	z^+	$T_{b,loc}$ (°C)	$T_{w,loc}$ (°C)	Pr	Re	ε_{Re}	Nu	ε_{Nu}
1.19	784	96.50	43.5	28.89	60.22	5.57	3,765	240	19.68	1.37
1.19	784	96.50	53.6	29.44	62.95	5.49	3,810	242	18.38	1.26
1.19	784	96.50	58.9	29.72	63.43	5.46	3,833	244	18.26	1.25
1.19	784	96.50	64.2	30.01	64.85	5.42	3,857	245	17.65	1.21
1.19	784	96.50	69.5	30.29	66.47	5.38	3,880	247	16.99	1.16

P_{avg} (bar)	G (kg/m^2-sec)	q'' (kW/m^2)	z^+	$T_{b,loc}$ (°C)	$T_{w,loc}$ (°C)	Pr	Re	ε_{Re}	Nu	ε_{Nu}
1.19	784	96.50	79.6	30.84	65.32	5.31	3,925	250	17.80	1.22
1.19	784	96.50	84.0	31.08	64.28	5.28	3,945	251	18.48	1.28
1.20	1023	97.56	43.5	29.45	46.38	5.49	4,971	248	36.77	2.39
1.20	1023	97.56	53.6	29.87	44.70	5.44	5,016	250	41.96	2.87
1.20	1023	97.56	58.9	30.09	46.08	5.41	5,040	251	38.89	2.58
1.20	1023	97.56	64.2	30.32	47.20	5.38	5,064	252	36.81	2.40
1.20	1023	97.56	69.5	30.54	47.00	5.35	5,087	254	37.74	2.48
1.20	1023	97.56	79.6	30.96	46.01	5.30	5,133	256	41.25	2.82
1.20	1023	97.56	84.0	31.15	47.11	5.27	5,153	257	38.87	2.59
1.22	1538	98.18	43.5	29.21	39.39	5.52	7,433	260	61.56	4.39
1.22	1538	98.18	53.6	29.49	40.31	5.48	7,479	262	57.92	3.97
1.22	1538	98.18	58.9	29.64	40.89	5.47	7,502	262	55.68	3.73
1.22	1538	98.18	64.2	29.79	40.72	5.45	7,526	263	57.30	3.91
1.22	1538	98.18	69.5	29.94	40.15	5.43	7,550	264	61.30	4.36
1.22	1538	98.18	79.6	30.23	41.10	5.39	7,596	266	57.49	3.94
1.22	1538	98.18	84.0	30.35	41.60	5.37	7,616	266	55.58	3.73
1.23	2028	191.69	43.5	29.46	44.97	5.49	9,855	277	78.90	5.10
1.23	2028	191.69	53.6	29.89	46.43	5.43	9,945	279	73.90	4.57
1.23	2028	191.69	58.9	30.11	46.45	5.41	9,992	281	74.75	4.66
1.23	2028	191.69	64.2	30.33	46.18	5.38	10,039	282	77.06	4.92
1.23	2028	191.69	69.5	30.55	45.92	5.35	10,086	283	79.39	5.17
1.23	2028	191.69	79.6	30.98	47.61	5.30	10,177	286	73.29	4.56
1.23	2028	191.69	84.0	31.16	47.65	5.27	10,217	287	73.91	4.65

P_{avg} (bar)	G (kg/m^2-sec)	q'' (kW/m^2)	z^+	$T_{b,loc}$ (°C)	$T_{w,loc}$ (°C)	Pr	Re	ε_{Re}	Nu	ε_{Nu}
1.20	2545	193.25	43.5	29.27	42.06	5.51	12,317	294	96.47	7.01
1.20	2545	193.25	53.6	29.61	43.18	5.47	12,408	296	90.84	6.30
1.20	2545	193.25	58.9	29.79	42.94	5.45	12,455	297	93.68	6.66
1.20	2545	193.25	64.2	29.97	42.87	5.42	12,503	299	95.49	6.91
1.20	2545	193.25	69.5	30.15	42.88	5.40	12,550	300	96.67	7.05
1.20	2545	193.25	79.6	30.49	44.21	5.36	12,641	302	89.68	6.23
1.20	2545	193.25	84.0	30.64	43.92	5.34	12,681	303	92.56	6.60
1.21	3063	194.16	43.5	29.03	40.04	5.55	14,747	313	112.64	9.48
1.21	3063	194.16	53.6	29.31	40.88	5.51	14,838	315	107.16	8.66
1.21	3063	194.16	58.9	29.46	40.60	5.49	14,885	316	111.28	9.28
1.21	3063	194.16	64.2	29.61	40.65	5.47	14,933	317	112.21	9.45
1.21	3063	194.16	69.5	29.76	40.77	5.45	14,981	318	112.48	9.47
1.21	3063	194.16	79.6	30.05	41.82	5.41	15,072	320	105.07	8.44
1.21	3063	194.16	84.0	30.17	41.39	5.40	15,112	321	110.29	9.25
1.20	3565	192.15	43.5	29.02	38.88	5.55	17,161	334	124.48	11.66
1.20	3565	192.15	53.6	29.26	39.42	5.52	17,251	336	120.83	11.04
1.20	3565	192.15	58.9	29.39	39.15	5.50	17,298	336	125.61	11.87
1.20	3565	192.15	64.2	29.52	39.37	5.48	17,345	337	124.46	11.68
1.20	3565	192.15	69.5	29.64	39.64	5.47	17,392	338	122.60	11.35
1.20	3565	192.15	79.6	29.89	40.50	5.43	17,483	340	115.42	10.19
1.20	3565	192.15	84.0	29.99	39.94	5.42	17,522	341	123.14	11.50
1.18	4069	193.09	43.5	29.95	38.54	5.43	19,983	363	143.43	15.93
1.18	4069	193.09	53.6	30.17	38.94	5.40	20,074	365	140.26	15.28

P_{avg} (bar)	G (kg/m^2-sec)	q'' (kW/m^2)	z^+	$T_{b,loc}$ (°C)	$T_{w,loc}$ (°C)	Pr	Re	ε_{Re}	Nu	ε_{Nu}
1.18	4069	193.09	58.9	30.28	38.64	5.38	20,121	366	147.06	16.72
1.18	4069	193.09	64.2	30.39	38.91	5.37	20,170	367	144.43	16.17
1.18	4069	193.09	69.5	30.50	39.23	5.36	20,217	367	140.90	15.43
1.18	4069	193.09	79.6	30.72	39.85	5.33	20,309	369	134.51	14.16
1.18	4069	193.09	84.0	30.81	39.18	5.32	20,349	370	146.77	16.71
1.22	4565	194.02	43.5	29.90	37.54	5.43	22,394	386	162.03	21.26
1.22	4565	194.02	53.6	30.09	37.84	5.41	22,486	388	159.59	20.66
1.22	4565	194.02	58.9	30.19	37.53	5.39	22,534	388	168.43	22.91
1.22	4565	194.02	64.2	30.30	37.82	5.38	22,582	389	164.25	21.85
1.22	4565	194.02	69.5	30.40	38.18	5.37	22,630	390	158.80	20.49
1.22	4565	194.02	79.6	30.59	38.63	5.34	22,722	392	153.54	19.25
1.22	4565	194.02	84.0	30.67	37.90	5.33	22,762	392	170.83	23.61
1.27	5089	194.14	43.5	29.89	37.23	5.43	24,963	411	168.74	21.98
1.27	5089	194.14	53.6	30.07	37.44	5.41	25,055	413	167.73	21.80
1.27	5089	194.14	58.9	30.16	37.16	5.40	25,103	414	176.57	24.15
1.27	5089	194.14	64.2	30.25	37.48	5.39	25,151	415	171.12	22.54
1.27	5089	194.14	69.5	30.34	37.83	5.38	25,199	415	165.15	21.13
1.27	5089	194.14	79.6	30.51	38.24	5.35	25,292	417	159.86	19.35
1.27	5089	194.14	84.0	30.59	37.43	5.34	25,332	418	180.74	24.63
1.39	6090	242.57	43.5	30.12	37.75	5.40	30,016	464	202.52	32.97
1.39	6090	242.57	53.6	30.30	37.87	5.38	30,132	466	204.16	33.50
1.39	6090	242.57	58.9	30.40	37.58	5.37	30,192	467	215.14	37.08
1.39	6090	242.57	64.2	30.49	37.95	5.36	30,254	468	207.14	34.49

P_{avg} (bar)	G (kg/m^2-sec)	q'' (kW/m^2)	z^+	$T_{b,loc}$ (°C)	$T_{w,loc}$ (°C)	Pr	Re	ε_{Re}	Nu	ε_{Nu}
1.39	6090	242.57	69.5	30.59	38.46	5.34	30,314	469	196.18	31.04
1.39	6090	242.57	79.6	30.77	38.76	5.32	30,431	471	193.19	30.21
1.39	6090	242.57	84.0	30.85	37.62	5.31	30,482	471	227.77	41.56
1.21	780	94.09	43.5	39.11	61.95	4.42	4,607	294	25.74	1.84
1.21	780	94.09	53.6	39.64	57.80	4.37	4,653	297	32.33	2.45
1.21	780	94.09	58.9	39.91	58.44	4.35	4,677	298	31.67	2.39
1.21	780	94.09	64.2	40.19	59.21	4.32	4,702	300	30.83	2.31
1.21	780	94.09	69.5	40.46	58.81	4.30	4,726	301	31.94	2.41
1.21	780	94.09	79.6	40.98	58.00	4.25	4,772	304	34.42	2.68
1.21	780	94.09	84.0	41.21	59.27	4.23	4,792	305	32.41	2.48
1.20	1019	94.76	43.5	39.39	53.35	4.40	6,045	302	42.36	2.89
1.20	1019	94.76	53.6	39.79	53.61	4.36	6,091	304	42.77	2.93
1.20	1019	94.76	58.9	40.00	54.91	4.34	6,115	305	39.63	2.63
1.20	1019	94.76	64.2	40.21	55.36	4.32	6,140	306	38.99	2.57
1.20	1019	94.76	69.5	40.42	54.25	4.30	6,164	307	42.69	2.93
1.20	1019	94.76	79.6	40.82	54.83	4.27	6,210	310	42.12	2.88
1.20	1019	94.76	84.0	41.00	55.86	4.25	6,231	311	39.69	2.65
1.21	1522	95.72	43.5	38.88	48.48	4.44	8,947	315	62.31	4.84
1.21	1522	95.72	53.6	39.15	49.42	4.42	8,994	316	58.23	4.33
1.21	1522	95.72	58.9	39.30	49.48	4.40	9,018	317	58.69	4.39
1.21	1522	95.72	64.2	39.44	49.28	4.39	9,042	318	60.74	4.66
1.21	1522	95.72	69.5	39.58	49.08	4.38	9,067	319	62.89	4.92
1.21	1522	95.72	79.6	39.85	50.27	4.35	9,113	321	57.33	4.29

P_{avg} (bar)	G (kg/m^2-sec)	q'' (kW/m^2)	z^+	$T_{b,loc}$ (°C)	$T_{w,loc}$ (°C)	Pr	Re	ε_{Re}	Nu	ε_{Nu}
1.21	1522	95.72	84.0	39.97	50.48	4.34	9,134	321	56.84	4.26
1.20	2016	189.64	43.5	39.21	54.24	4.41	11,922	336	78.84	4.88
1.20	2016	189.64	53.6	39.63	55.51	4.37	12,016	338	74.51	4.43
1.20	2016	189.64	58.9	39.84	55.29	4.35	12,065	340	76.56	4.64
1.20	2016	189.64	64.2	40.06	55.25	4.33	12,115	341	77.84	4.78
1.20	2016	189.64	69.5	40.28	55.21	4.32	12,164	342	79.19	4.92
1.20	2016	189.64	79.6	40.70	57.08	4.28	12,259	345	72.08	4.20
1.20	2016	189.64	84.0	40.88	56.91	4.26	12,301	346	73.63	4.36
1.22	2529	188.75	43.5	39.17	51.90	4.42	14,946	358	92.61	6.36
1.22	2529	188.75	53.6	39.50	52.76	4.39	15,040	360	88.87	5.91
1.22	2529	188.75	58.9	39.68	52.51	4.37	15,088	361	91.76	6.26
1.22	2529	188.75	64.2	39.85	52.63	4.35	15,138	362	92.13	6.31
1.22	2529	188.75	69.5	40.02	52.78	4.34	15,187	363	92.24	6.32
1.22	2529	188.75	79.6	40.35	54.21	4.31	15,281	366	84.86	5.46
1.22	2529	188.75	84.0	40.50	53.81	4.30	15,322	367	88.29	5.87
1.23	3040	190.06	43.5	39.14	50.10	4.42	17,957	382	108.29	8.65
1.23	3040	190.06	53.6	39.41	50.70	4.39	18,051	384	105.13	8.19
1.23	3040	190.06	58.9	39.56	50.41	4.38	18,100	385	109.26	8.80
1.23	3040	190.06	64.2	39.70	50.61	4.37	18,150	386	108.71	8.72
1.23	3040	190.06	69.5	39.85	50.81	4.35	18,199	387	108.17	8.64
1.23	3040	190.06	79.6	40.12	51.95	4.33	18,294	389	100.21	7.54
1.23	3040	190.06	84.0	40.24	51.46	4.32	18,336	390	105.57	8.30

P_{avg} (bar)	G (kg/m^2-sec)	q'' (kW/m^2)	z^+	$T_{b,loc}$ (°C)	$T_{w,loc}$ (°C)	Pr	Re	ε_{Re}	Nu	ε_{Nu}
1.15	3540	190.44	43.5	39.47	49.31	4.39	21,042	410	120.82	11.05
1.15	3540	190.44	53.6	39.71	49.71	4.37	21,137	412	118.82	10.72
1.15	3540	190.44	58.9	39.83	49.43	4.36	21,186	413	123.81	11.57
1.15	3540	190.44	64.2	39.96	49.71	4.34	21,236	414	121.75	11.22
1.15	3540	190.44	69.5	40.08	49.91	4.33	21,285	415	120.85	11.07
1.15	3540	190.44	79.6	40.32	50.88	4.31	21,380	417	112.35	9.69
1.15	3540	190.44	84.0	40.42	50.36	4.30	21,422	417	119.40	10.86
1.20	4060	191.37	43.5	39.41	48.12	4.39	24,105	438	137.14	14.81
1.20	4060	191.37	53.6	39.62	48.40	4.37	24,201	440	136.03	14.59
1.20	4060	191.37	58.9	39.73	48.16	4.36	24,250	440	141.68	15.76
1.20	4060	191.37	64.2	39.84	48.46	4.35	24,300	441	138.48	15.10
1.20	4060	191.37	69.5	39.95	48.69	4.35	24,350	442	136.52	14.70
1.20	4060	191.37	79.6	40.16	49.47	4.33	24,445	444	128.15	13.08
1.20	4060	191.37	84.0	40.25	48.87	4.32	24,487	445	138.39	15.12
1.24	4563	191.46	43.5	39.59	47.72	4.38	27,185	468	147.01	17.94
1.24	4563	191.46	53.6	39.78	47.90	4.36	27,281	470	147.04	17.95
1.24	4563	191.46	58.9	39.87	47.68	4.35	27,331	470	153.00	19.36
1.24	4563	191.46	64.2	39.97	48.00	4.34	27,381	471	148.78	18.37
1.24	4563	191.46	69.5	40.07	48.23	4.33	27,431	472	146.22	17.77
1.24	4563	191.46	79.6	40.26	48.91	4.32	27,527	474	137.90	15.94
1.24	4563	191.46	84.0	40.34	48.25	4.31	27,569	475	150.73	18.87
1.29	5066	191.99	43.5	39.65	47.15	4.37	30,217	498	159.94	22.44
1.29	5066	191.99	53.6	39.82	47.27	4.36	30,313	500	160.77	22.67

P_{avg} (bar)	G (kg/m^2-sec)	q'' (kW/m^2)	z^+	$T_{b,loc}$ (°C)	$T_{w,loc}$ (°C)	Pr	Re	ε_{Re}	Nu	ε_{Nu}
1.29	5066	191.99	58.9	39.91	47.06	4.35	30,363	501	167.40	24.49
1.29	5066	191.99	64.2	40.00	47.38	4.34	30,414	501	162.29	23.10
1.29	5066	191.99	69.5	40.09	47.63	4.33	30,464	502	158.61	22.11
1.29	5066	191.99	79.6	40.26	48.20	4.32	30,560	504	150.63	20.09
1.29	5066	191.99	84.0	40.33	47.46	4.31	30,603	505	167.82	24.68
1.41	6069	240.16	43.5	39.68	47.83	4.37	36,217	560	183.86	27.64
1.41	6069	240.16	53.6	39.86	47.87	4.35	36,339	562	186.87	28.52
1.41	6069	240.16	58.9	39.95	47.62	4.34	36,402	563	195.18	31.02
1.41	6069	240.16	64.2	40.04	48.01	4.34	36,466	564	188.07	28.89
1.41	6069	240.16	69.5	40.14	48.40	4.33	36,529	565	181.09	26.86
1.41	6069	240.16	79.6	40.31	48.95	4.31	36,651	567	173.29	24.73
1.41	6069	240.16	84.0	40.39	47.91	4.31	36,704	568	199.00	32.29
1.20	776	92.67	43.5	48.91	65.56	3.64	5,462	348	34.13	2.56
1.20	776	92.67	53.6	49.41	65.22	3.61	5,508	351	35.90	2.74
1.20	776	92.67	58.9	49.67	66.85	3.59	5,532	353	33.03	2.45
1.20	776	92.67	64.2	49.93	67.91	3.57	5,557	354	31.55	2.31
1.20	776	92.67	69.5	50.19	66.85	3.56	5,581	356	34.03	2.55
1.20	776	92.67	79.6	50.69	67.24	3.52	5,628	359	34.22	2.59
1.20	776	92.67	84.0	50.91	68.63	3.51	5,648	360	31.95	2.37
1.20	1030	93.87	43.5	49.02	61.41	3.63	7,261	357	46.43	3.24
1.20	1030	93.87	53.6	49.40	62.49	3.61	7,308	360	43.92	2.98
1.20	1030	93.87	58.9	49.59	63.28	3.60	7,332	361	42.01	2.80
1.20	1030	93.87	64.2	49.79	63.18	3.58	7,357	362	42.94	2.89

P_{avg} (bar)	G (kg/m^2-sec)	q'' (kW/m^2)	z^+	$T_{b,loc}$ (°C)	$T_{w,loc}$ (°C)	Pr	Re	ε_{Re}	Nu	ε_{Nu}
1.20	1030	93.87	69.5	49.99	62.38	3.57	7,381	363	46.36	3.24
1.20	1030	93.87	79.6	50.37	64.04	3.54	7,428	365	41.99	2.81
1.20	1030	93.87	84.0	50.54	64.79	3.53	7,449	367	40.28	2.65
1.20	1518	95.29	43.5	49.27	58.20	3.62	10,749	378	65.42	4.89
1.20	1518	95.29	53.6	49.53	59.05	3.60	10,797	379	61.32	4.39
1.20	1518	95.29	58.9	49.67	59.00	3.59	10,821	380	62.53	4.54
1.20	1518	95.29	64.2	49.81	58.99	3.58	10,846	381	63.52	4.67
1.20	1518	95.29	69.5	49.94	58.83	3.57	10,871	382	65.63	4.93
1.20	1518	95.29	79.6	50.20	60.17	3.56	10,919	384	58.47	4.08
1.20	1518	95.29	84.0	50.32	60.25	3.55	10,939	384	58.71	4.11
1.19	2019	187.62	43.5	49.37	63.23	3.61	14,320	401	82.95	5.32
1.19	2019	187.62	53.6	49.77	64.27	3.58	14,417	404	79.20	4.91
1.19	2019	187.62	58.9	49.98	64.01	3.57	14,468	406	81.83	5.20
1.19	2019	187.62	64.2	50.19	64.24	3.56	14,519	407	81.72	5.20
1.19	2019	187.62	69.5	50.40	64.10	3.54	14,570	408	83.73	5.42
1.19	2019	187.62	79.6	50.80	66.04	3.52	14,667	411	75.24	4.51
1.19	2019	187.62	84.0	50.98	65.77	3.51	14,710	412	77.48	4.75
1.21	2532	188.82	43.5	49.53	61.29	3.60	18,007	429	98.34	7.08
1.21	2532	188.82	53.6	49.85	61.97	3.58	18,105	432	95.37	6.70
1.21	2532	188.82	58.9	50.02	61.65	3.57	18,156	433	99.34	7.21
1.21	2532	188.82	64.2	50.19	62.01	3.56	18,207	434	97.74	7.01
1.21	2532	188.82	69.5	50.35	61.96	3.55	18,258	435	99.48	7.24
1.21	2532	188.82	79.6	50.68	63.44	3.52	18,356	438	90.42	6.11

P_{avg} (bar)	G (kg/m^2-sec)	q'' (kW/m^2)	z^+	$T_{b,loc}$ (°C)	$T_{w,loc}$ (°C)	Pr	Re	ε_{Re}	Nu	ε_{Nu}
1.21	2532	188.82	84.0	50.82	63.08	3.52	18,399	439	94.09	6.56
1.19	3031	189.38	43.5	49.40	59.94	3.61	21,512	457	110.15	8.93
1.19	3031	189.38	53.6	49.67	60.40	3.59	21,610	459	108.12	8.63
1.19	3031	189.38	58.9	49.82	60.07	3.58	21,661	460	113.03	9.37
1.19	3031	189.38	64.2	49.96	60.50	3.57	21,713	461	109.94	8.91
1.19	3031	189.38	69.5	50.10	60.53	3.56	21,764	462	111.11	9.08
1.19	3031	189.38	79.6	50.37	61.62	3.54	21,862	465	102.95	7.91
1.19	3031	189.38	84.0	50.48	61.34	3.54	21,905	465	106.71	8.46
1.22	3534	189.92	43.5	49.45	58.94	3.60	25,103	488	122.67	11.42
1.22	3534	189.92	53.6	49.68	59.24	3.59	25,202	490	121.70	11.26
1.22	3534	189.92	58.9	49.80	58.91	3.58	25,253	491	127.75	12.33
1.22	3534	189.92	64.2	49.93	59.38	3.57	25,305	492	122.99	11.49
1.22	3534	189.92	69.5	50.05	59.40	3.57	25,356	493	124.31	11.72
1.22	3534	189.92	79.6	50.28	60.37	3.55	25,455	495	115.15	10.19
1.22	3534	189.92	84.0	50.38	60.04	3.54	25,498	496	120.19	11.05
1.19	4044	189.76	43.5	49.62	58.34	3.59	28,805	523	133.36	14.16
1.19	4044	189.76	53.6	49.82	58.49	3.58	28,903	525	134.07	14.30
1.19	4044	189.76	58.9	49.93	58.22	3.57	28,955	526	140.10	15.54
1.19	4044	189.76	64.2	50.04	58.68	3.57	29,006	527	134.36	14.37
1.19	4044	189.76	69.5	50.14	58.93	3.56	29,058	528	132.17	13.93
1.19	4044	189.76	79.6	50.34	59.79	3.55	29,156	529	122.87	12.18
1.19	4044	189.76	84.0	50.43	59.24	3.54	29,199	530	131.72	13.88

P_{avg} (bar)	G (kg/m^2-sec)	q'' (kW/m^2)	z^+	$T_{b,loc}$ (°C)	$T_{w,loc}$ (°C)	Pr	Re	ε_{Re}	Nu	ε_{Nu}
1.23	4540	190.77	43.5	49.62	57.43	3.59	32,338	557	149.64	18.69
1.23	4540	190.77	53.6	49.80	57.53	3.58	32,437	559	151.16	19.05
1.23	4540	190.77	58.9	49.90	57.29	3.58	32,488	559	157.90	20.71
1.23	4540	190.77	64.2	49.99	57.71	3.57	32,540	560	151.26	19.10
1.23	4540	190.77	69.5	50.08	57.98	3.56	32,592	561	147.93	18.30
1.23	4540	190.77	79.6	50.27	58.69	3.55	32,691	563	138.50	16.20
1.23	4540	190.77	84.0	50.35	58.03	3.55	32,734	564	151.79	19.27
1.28	5032	191.00	43.5	49.73	57.02	3.59	35,902	593	160.32	22.65
1.28	5032	191.00	53.6	49.89	57.07	3.58	36,001	594	162.78	23.32
1.28	5032	191.00	58.9	49.98	56.87	3.57	36,053	595	169.51	25.20
1.28	5032	191.00	64.2	50.06	57.27	3.56	36,105	596	162.23	23.19
1.28	5032	191.00	69.5	50.15	57.52	3.56	36,157	597	158.46	22.17
1.28	5032	191.00	79.6	50.31	58.18	3.55	36,256	598	148.51	19.64
1.28	5032	191.00	84.0	50.38	57.42	3.54	36,299	599	166.02	24.29
1.39	6029	239.49	43.5	49.50	57.39	3.60	42,851	663	185.89	28.45
1.39	6029	239.49	53.6	49.67	57.39	3.59	42,977	665	189.94	29.65
1.39	6029	239.49	58.9	49.76	57.12	3.58	43,042	666	199.27	32.53
1.39	6029	239.49	64.2	49.85	57.56	3.58	43,108	667	190.07	29.72
1.39	6029	239.49	69.5	49.94	57.94	3.57	43,174	668	183.23	27.69
1.39	6029	239.49	79.6	50.11	58.40	3.56	43,300	670	176.97	25.98
1.39	6029	239.49	84.0	50.19	57.57	3.56	43,355	671	198.69	32.47
1.20	768	91.99	43.5	59.00	73.20	3.05	6,353	408	39.07	2.99
1.20	768	91.99	53.6	59.48	74.01	3.02	6,400	411	38.16	2.89

P_{avg} (bar)	G (kg/m^2-sec)	q'' (kW/m^2)	z^+	$T_{b,loc}$ (°C)	$T_{w,loc}$ (°C)	Pr	Re	ε_{Re}	Nu	ε_{Nu}
1.20	768	91.99	58.9	59.73	75.42	3.01	6,424	412	35.32	2.60
1.20	768	91.99	64.2	59.98	75.69	3.00	6,449	414	35.27	2.60
1.20	768	91.99	69.5	60.23	74.31	2.99	6,473	415	39.35	3.02
1.20	768	91.99	79.6	60.71	75.73	2.96	6,520	418	36.86	2.77
1.20	768	91.99	84.0	60.92	77.12	2.95	6,540	420	34.15	2.50
1.21	1026	93.08	43.5	58.84	69.79	3.06	8,471	416	51.30	3.73
1.21	1026	93.08	53.6	59.20	70.87	3.04	8,518	419	48.12	3.38
1.21	1026	93.08	58.9	59.39	71.27	3.03	8,542	420	47.23	3.29
1.21	1026	93.08	64.2	59.59	71.14	3.02	8,567	421	48.53	3.43
1.21	1026	93.08	69.5	59.77	70.73	3.01	8,592	422	51.18	3.72
1.21	1026	93.08	79.6	60.14	72.27	2.99	8,639	425	46.19	3.20
1.21	1026	93.08	84.0	60.30	72.46	2.98	8,660	426	46.09	3.19
1.19	1539	93.86	43.5	59.56	67.63	3.02	12,850	445	70.06	5.50
1.19	1539	93.86	53.6	59.80	68.25	3.01	12,898	446	66.96	5.09
1.19	1539	93.86	58.9	59.93	68.23	3.00	12,922	447	68.08	5.23
1.19	1539	93.86	64.2	60.06	68.34	2.99	12,947	448	68.20	5.26
1.19	1539	93.86	69.5	60.18	68.23	2.99	12,972	449	70.22	5.53
1.19	1539	93.86	79.6	60.42	69.35	2.98	13,019	450	63.29	4.65
1.19	1539	93.86	84.0	60.53	69.17	2.97	13,040	451	65.35	4.92
1.20	2003	186.35	43.5	59.20	72.69	3.04	16,627	467	83.32	5.37
1.20	2003	186.35	53.6	59.59	73.29	3.02	16,727	470	81.97	5.22
1.20	2003	186.35	58.9	59.80	73.29	3.01	16,779	472	83.20	5.36
1.20	2003	186.35	64.2	60.00	73.71	3.00	16,832	473	81.91	5.22

P_{avg} (bar)	G (kg/m^2-sec)	q'' (kW/m^2)	z^+	$T_{b,loc}$ (°C)	$T_{w,loc}$ (°C)	Pr	Re	ε_{Re}	Nu	ε_{Nu}
1.20	2003	186.35	69.5	60.21	73.51	2.99	16,884	474	84.36	5.49
1.20	2003	186.35	79.6	60.60	75.18	2.97	16,984	477	76.91	4.69
1.20	2003	186.35	84.0	60.77	74.20	2.96	17,028	479	83.53	5.43
1.23	2516	187.45	43.5	59.27	70.85	3.03	20,916	499	97.55	7.01
1.23	2516	187.45	53.6	59.58	71.24	3.02	21,016	502	96.85	6.92
1.23	2516	187.45	58.9	59.74	71.15	3.01	21,068	503	99.00	7.20
1.23	2516	187.45	64.2	59.91	71.54	3.00	21,120	504	97.08	6.95
1.23	2516	187.45	69.5	60.07	71.53	2.99	21,173	505	98.56	7.15
1.23	2516	187.45	79.6	60.39	72.83	2.98	21,273	508	90.70	6.17
1.23	2516	187.45	84.0	60.52	72.03	2.97	21,317	509	98.03	7.11
1.24	3020	187.71	43.5	59.57	70.06	3.02	25,216	535	107.89	8.67
1.24	3020	187.71	53.6	59.83	70.43	3.01	25,316	538	106.67	8.49
1.24	3020	187.71	58.9	59.97	70.17	3.00	25,369	539	110.84	9.12
1.24	3020	187.71	64.2	60.10	70.71	2.99	25,421	540	106.62	8.50
1.24	3020	187.71	69.5	60.24	70.57	2.99	25,473	541	109.37	8.90
1.24	3020	187.71	79.6	60.50	71.99	2.97	25,574	543	98.38	7.36
1.24	3020	187.71	84.0	60.62	71.67	2.97	25,618	544	102.18	7.90
1.24	3518	186.11	43.5	59.53	68.97	3.02	29,354	571	118.73	10.93
1.24	3518	186.11	53.6	59.75	69.19	3.01	29,453	573	118.72	10.93
1.24	3518	186.11	58.9	59.86	68.99	3.00	29,505	574	122.82	11.65
1.24	3518	186.11	64.2	59.98	69.52	3.00	29,557	575	117.49	10.74
1.24	3518	186.11	69.5	60.10	69.59	2.99	29,609	576	118.11	10.83
1.24	3518	186.11	79.6	60.32	70.71	2.98	29,708	578	107.82	9.19

P_{avg} (bar)	G (kg/m^2-sec)	q'' (kW/m^2)	z^+	$T_{b,loc}$ (°C)	$T_{w,loc}$ (°C)	Pr	Re	ε_{Re}	Nu	ε_{Nu}
1.24	3518	186.11	84.0	60.42	70.33	2.98	29,752	579	113.03	10.04
1.19	4034	186.87	43.5	59.62	68.11	3.02	33,712	611	132.64	14.28
1.19	4034	186.87	53.6	59.82	68.26	3.01	33,811	613	133.30	14.42
1.19	4034	186.87	58.9	59.92	68.05	3.00	33,863	614	138.39	15.47
1.19	4034	186.87	64.2	60.02	68.59	3.00	33,915	615	131.31	14.03
1.19	4034	186.87	69.5	60.12	68.72	2.99	33,967	616	130.94	13.95
1.19	4034	186.87	79.6	60.31	69.49	2.98	34,067	618	122.65	12.39
1.19	4034	186.87	84.0	60.40	69.24	2.98	34,111	619	127.30	13.29
1.22	4525	187.33	43.5	59.51	67.38	3.02	37,753	650	143.45	18.44
1.22	4525	187.33	53.6	59.68	67.46	3.01	37,852	651	145.18	18.83
1.22	4525	187.33	58.9	59.77	67.21	3.01	37,904	652	151.68	20.44
1.22	4525	187.33	64.2	59.86	67.75	3.00	37,956	653	143.02	18.40
1.22	4525	187.33	69.5	59.95	67.90	3.00	38,008	654	141.99	18.10
1.22	4525	187.33	79.6	60.13	68.59	2.99	38,108	656	133.37	16.32
1.22	4525	187.33	84.0	60.20	68.25	2.99	38,152	657	140.20	17.97
1.28	5037	187.57	43.5	59.67	67.04	3.01	42,122	694	153.34	21.31
1.28	5037	187.57	53.6	59.82	67.06	3.01	42,222	695	156.13	22.05
1.28	5037	187.57	58.9	59.90	66.88	3.00	42,274	696	161.97	23.64
1.28	5037	187.57	64.2	59.99	67.34	3.00	42,326	697	153.68	21.42
1.28	5037	187.57	69.5	60.07	67.45	2.99	42,378	698	153.01	21.23
1.28	5037	187.57	79.6	60.22	68.09	2.99	42,478	699	143.53	18.87
1.28	5037	187.57	84.0	60.29	67.66	2.98	42,522	700	153.23	21.37

P_{avg} (bar)	G (kg/m^2-sec)	q'' (kW/m^2)	z^+	$T_{b,loc}$ (°C)	$T_{w,loc}$ (°C)	Pr	Re	ε_{Re}	Nu	ε_{Nu}
1.50	6022	241.66	43.5	59.78	67.85	3.01	50,443	780	180.42	26.76
1.50	6022	241.66	53.6	59.95	67.81	3.00	50,574	782	185.21	28.14
1.50	6022	241.66	58.9	60.04	67.58	3.00	50,642	783	192.88	30.43
1.50	6022	241.66	64.2	60.13	68.04	2.99	50,711	784	183.79	27.75
1.50	6022	241.66	69.5	60.22	68.41	2.99	50,779	785	177.57	25.97
1.50	6022	241.66	79.6	60.39	68.98	2.98	50,910	787	169.36	23.79
1.50	6022	241.66	84.0	60.46	68.30	2.97	50,968	788	185.51	28.34
1.23	771	90.72	43.5	69.22	81.53	2.59	7,404	470	43.82	3.42
1.23	771	90.72	53.6	69.66	82.71	2.58	7,450	473	41.32	3.13
1.23	771	90.72	58.9	69.89	83.61	2.57	7,473	475	39.28	2.92
1.23	771	90.72	64.2	70.12	83.29	2.56	7,497	476	40.92	3.10
1.23	771	90.72	69.5	70.35	82.50	2.55	7,521	478	44.34	3.48
1.23	771	90.72	79.6	70.79	84.33	2.53	7,566	481	39.77	2.99
1.23	771	90.72	84.0	70.98	84.59	2.53	7,586	482	39.57	2.98
1.18	1010	90.97	43.5	69.37	79.72	2.59	9,713	482	52.28	3.82
1.18	1010	90.97	53.6	69.71	80.96	2.58	9,759	484	48.04	3.34
1.18	1010	90.97	58.9	69.88	80.90	2.57	9,782	485	49.09	3.46
1.18	1010	90.97	64.2	70.06	80.25	2.56	9,806	487	53.05	3.92
1.18	1010	90.97	69.5	70.24	80.49	2.56	9,830	488	52.71	3.87
1.18	1010	90.97	79.6	70.58	82.09	2.54	9,876	490	46.93	3.25
1.18	1010	90.97	84.0	70.73	81.94	2.54	9,896	491	48.18	3.40
1.22	1505	92.42	43.5	69.50	77.11	2.58	14,506	509	72.13	5.75
1.22	1505	92.42	53.6	69.72	77.87	2.57	14,552	510	67.48	5.12

P_{avg} (bar)	G (kg/m^2-sec)	q'' (kW/m^2)	z^+	$T_{b,loc}$ (°C)	$T_{w,loc}$ (°C)	Pr	Re	ε_{Re}	Nu	ε_{Nu}
1.22	1505	92.42	58.9	69.84	77.60	2.57	14,576	511	70.82	5.57
1.22	1505	92.42	64.2	69.96	77.30	2.57	14,600	512	74.89	6.16
1.22	1505	92.42	69.5	70.08	77.75	2.56	14,624	513	71.68	5.70
1.22	1505	92.42	79.6	70.31	78.68	2.55	14,670	515	65.61	4.91
1.22	1505	92.42	84.0	70.41	78.46	2.55	14,690	515	68.23	5.27
1.22	2014	188.86	43.5	69.37	81.70	2.59	19,381	540	91.10	8.59
1.22	2014	188.86	53.6	69.75	82.57	2.57	19,484	543	87.59	8.01
1.22	2014	188.86	58.9	69.95	82.21	2.57	19,537	544	91.55	8.63
1.22	2014	188.86	64.2	70.15	81.86	2.56	19,591	546	95.82	9.39
1.22	2014	188.86	69.5	70.35	82.29	2.55	19,644	547	94.01	8.98
1.22	2014	188.86	79.6	70.73	83.96	2.54	19,747	550	84.80	7.91
1.22	2014	188.86	84.0	70.90	84.12	2.53	19,792	551	84.81	8.04
1.23	2504	189.03	43.5	69.45	80.45	2.59	24,122	575	102.14	7.54
1.23	2504	189.03	53.6	69.76	81.08	2.57	24,224	578	99.19	7.15
1.23	2504	189.03	58.9	69.92	80.67	2.57	24,277	579	104.42	7.86
1.23	2504	189.03	64.2	70.08	80.45	2.56	24,331	580	108.29	8.41
1.23	2504	189.03	69.5	70.24	80.95	2.56	24,384	582	104.83	7.92
1.23	2504	189.03	79.6	70.54	82.28	2.54	24,487	584	95.66	6.73
1.23	2504	189.03	84.0	70.68	82.28	2.54	24,532	585	96.78	6.88
1.24	3015	189.74	43.5	69.48	79.23	2.58	29,052	615	115.78	9.78
1.24	3015	189.74	53.6	69.74	79.64	2.57	29,154	618	113.91	9.49
1.24	3015	189.74	58.9	69.87	79.29	2.57	29,207	619	119.71	10.41
1.24	3015	189.74	64.2	70.01	79.16	2.56	29,261	620	123.15	10.99

P_{avg} (bar)	G (kg/m^2-sec)	q'' (kW/m^2)	z^+	$T_{b,loc}$ (°C)	$T_{w,loc}$ (°C)	Pr	Re	ε_{Re}	Nu	ε_{Nu}
1.24	3015	189.74	69.5	70.14	79.66	2.56	29,315	621	118.45	10.21
1.24	3015	189.74	79.6	70.39	80.73	2.55	29,417	623	109.04	8.80
1.24	3015	189.74	84.0	70.51	80.57	2.55	29,462	624	111.99	9.25
1.28	3498	188.39	43.5	69.62	78.29	2.58	33,769	657	129.22	12.76
1.28	3498	188.39	53.6	69.84	78.53	2.57	33,871	659	128.83	12.68
1.28	3498	188.39	58.9	69.95	78.29	2.57	33,923	660	134.18	13.69
1.28	3498	188.39	64.2	70.06	78.71	2.56	33,977	661	129.51	12.83
1.28	3498	188.39	69.5	70.18	78.71	2.56	34,029	662	131.17	13.13
1.28	3498	188.39	79.6	70.39	79.62	2.55	34,131	664	121.31	11.40
1.28	3498	188.39	84.0	70.49	78.90	2.55	34,175	665	133.02	13.56
1.30	3994	189.14	43.5	69.70	77.47	2.58	38,606	702	144.87	16.68
1.30	3994	189.14	53.6	69.89	77.65	2.57	38,708	704	144.90	16.69
1.30	3994	189.14	58.9	69.99	77.41	2.56	38,760	705	151.46	18.16
1.30	3994	189.14	64.2	70.09	77.87	2.56	38,814	706	144.60	16.65
1.30	3994	189.14	69.5	70.19	78.08	2.56	38,866	706	142.44	16.17
1.30	3994	189.14	79.6	70.38	78.67	2.55	38,968	708	135.60	14.80
1.30	3994	189.14	84.0	70.47	77.90	2.55	39,012	709	151.04	18.16
1.35	4506	189.65	43.5	69.77	76.90	2.57	43,589	750	158.06	20.91
1.35	4506	189.65	53.6	69.94	77.01	2.57	43,690	751	159.30	21.23
1.35	4506	189.65	58.9	70.03	76.81	2.56	43,743	752	166.07	22.99
1.35	4506	189.65	64.2	70.11	77.19	2.56	43,796	753	159.30	21.25
1.35	4506	189.65	69.5	70.20	77.34	2.56	43,849	754	157.88	20.88
1.35	4506	189.65	79.6	70.37	77.99	2.55	43,950	756	147.84	18.49

P_{avg} (bar)	G (kg/m^2-sec)	q'' (kW/m^2)	z^+	$T_{b,loc}$ (°C)	$T_{w,loc}$ (°C)	Pr	Re	ε_{Re}	Nu	ε_{Nu}
1.35	4506	189.65	84.0	70.44	77.12	2.55	43,995	757	168.77	23.80
1.28	4977	188.03	43.5	69.77	76.41	2.57	48,150	795	168.37	25.27
1.28	4977	188.03	53.6	69.92	76.55	2.57	48,250	796	168.52	25.32
1.28	4977	188.03	58.9	70.00	76.25	2.56	48,302	797	178.74	28.34
1.28	4977	188.03	64.2	70.08	76.79	2.56	48,355	798	166.43	24.75
1.28	4977	188.03	69.5	70.15	76.81	2.56	48,407	799	167.86	25.12
1.28	4977	188.03	79.6	70.31	77.67	2.55	48,507	801	151.60	20.78
1.28	4977	188.03	84.0	70.37	76.73	2.55	48,551	801	175.64	27.52
1.52	5942	237.81	43.5	69.76	76.81	2.57	57,477	891	200.54	33.11
1.52	5942	237.81	53.6	69.93	76.94	2.57	57,606	893	201.70	33.48
1.52	5942	237.81	58.9	70.01	76.60	2.56	57,674	894	214.59	37.74
1.52	5942	237.81	64.2	70.10	77.06	2.56	57,742	895	203.00	33.93
1.52	5942	237.81	69.5	70.18	77.36	2.56	57,810	896	196.89	31.96
1.52	5942	237.81	79.6	70.35	77.86	2.55	57,940	898	188.09	29.38
1.52	5942	237.81	84.0	70.42	77.05	2.55	57,996	899	213.16	37.42
1.24	771	90.62	43.5	79.21	90.85	2.25	8,440	534	45.81	3.53
1.24	771	90.62	53.6	79.63	92.28	2.24	8,485	536	42.12	3.11
1.24	771	90.62	58.9	79.85	92.87	2.23	8,508	538	40.92	2.99
1.24	771	90.62	64.2	80.07	92.31	2.23	8,531	539	43.50	3.28
1.24	771	90.62	69.5	80.29	91.63	2.22	8,555	541	46.95	3.66
1.24	771	90.62	79.6	80.71	93.62	2.21	8,600	544	41.22	3.05
1.24	771	90.62	84.0	80.89	93.82	2.20	8,619	545	41.16	3.05
1.35	4506	189.65	84.0	70.44	77.12	2.55	43,995	757	168.77	23.80

P_{avg} (bar)	G (kg/m^2-sec)	q'' (kW/m^2)	z^+	$T_{b,loc}$ (°C)	$T_{w,loc}$ (°C)	Pr	Re	ε_{Re}	Nu	ε_{Nu}
1.25	1012	91.75	43.5	79.29	88.56	2.25	11,095	546	58.21	4.38
1.25	1012	91.75	53.6	79.61	89.88	2.24	11,141	549	52.53	3.70
1.25	1012	91.75	58.9	79.78	89.75	2.24	11,164	550	54.09	3.89
1.25	1012	91.75	64.2	79.95	89.00	2.23	11,188	551	59.56	4.56
1.25	1012	91.75	69.5	80.12	89.49	2.23	11,211	552	57.54	4.30
1.25	1012	91.75	79.6	80.44	90.78	2.22	11,257	554	52.12	3.69
1.25	1012	91.75	84.0	80.58	90.59	2.21	11,277	555	53.86	3.90
1.27	1490	93.00	43.5	79.49	86.60	2.24	16,373	576	76.88	4.70
1.27	1490	93.00	53.6	79.71	87.40	2.24	16,418	578	71.05	4.06
1.27	1490	93.00	58.9	79.82	87.14	2.23	16,442	579	74.76	4.49
1.27	1490	93.00	64.2	79.94	86.71	2.23	16,465	580	80.78	5.18
1.27	1490	93.00	69.5	80.05	87.02	2.23	16,489	580	78.49	5.00
1.27	1490	93.00	79.6	80.27	88.07	2.22	16,534	582	70.05	3.68
1.27	1490	93.00	84.0	80.37	87.83	2.22	16,554	583	73.22	3.93
1.24	1977	187.48	43.5	79.24	92.14	2.25	21,667	609	85.46	5.52
1.24	1977	187.48	53.6	79.62	92.38	2.24	21,769	612	86.33	5.63
1.24	1977	187.48	58.9	79.81	92.11	2.23	21,823	614	89.59	6.01
1.24	1977	187.48	64.2	80.01	91.94	2.23	21,877	615	92.34	6.36
1.24	1977	187.48	69.5	80.21	92.58	2.22	21,930	617	89.06	5.95
1.24	1977	187.48	79.6	80.58	93.95	2.21	22,034	620	82.36	5.21
1.24	1977	187.48	84.0	80.75	94.56	2.21	22,079	621	79.73	4.95
1.27	2485	188.32	43.5	79.44	90.21	2.25	27,299	652	102.82	7.67
1.27	2485	188.32	53.6	79.74	91.07	2.24	27,401	654	97.72	6.99

P_{avg} (bar)	G (kg/m^2-sec)	q'' (kW/m^2)	z^+	$T_{b,loc}$ (°C)	$T_{w,loc}$ (°C)	Pr	Re	ε_{Re}	Nu	ε_{Nu}
1.27	2485	188.32	58.9	79.90	90.32	2.23	27,455	656	106.19	8.13
1.27	2485	188.32	64.2	80.05	90.31	2.23	27,509	657	107.88	8.39
1.27	2485	188.32	69.5	80.21	90.60	2.22	27,563	658	106.45	8.17
1.27	2485	188.32	79.6	80.51	91.98	2.21	27,666	661	96.46	6.87
1.27	2485	188.32	84.0	80.64	91.26	2.21	27,711	662	104.11	7.91
1.31	2998	190.18	43.5	79.56	88.52	2.24	32,982	698	124.84	11.23
1.31	2998	190.18	53.6	79.81	89.19	2.23	33,085	701	119.13	10.30
1.31	2998	190.18	58.9	79.94	88.48	2.23	33,139	702	130.79	12.26
1.31	2998	190.18	64.2	80.07	88.53	2.23	33,193	703	132.09	12.51
1.31	2998	190.18	69.5	80.20	88.95	2.22	33,247	704	127.72	11.73
1.31	2998	190.18	79.6	80.45	89.92	2.22	33,350	706	117.96	10.16
1.31	2998	190.18	84.0	80.56	88.96	2.21	33,395	707	132.97	12.73
1.35	3507	191.08	43.5	79.62	87.43	2.24	38,608	748	143.92	15.44
1.35	3507	191.08	53.6	79.84	87.93	2.23	38,711	750	138.74	14.41
1.35	3507	191.08	58.9	79.95	87.32	2.23	38,764	751	152.38	17.21
1.35	3507	191.08	64.2	80.06	87.39	2.23	38,818	752	153.16	17.40
1.35	3507	191.08	69.5	80.17	87.78	2.22	38,872	753	147.59	16.20
1.35	3507	191.08	79.6	80.38	88.58	2.22	38,975	755	136.98	14.14
1.35	3507	191.08	84.0	80.48	87.59	2.21	39,020	756	157.82	18.50
1.41	3995	189.65	43.5	79.68	86.78	2.24	44,019	798	157.02	19.46
1.41	3995	189.65	53.6	79.87	87.22	2.23	44,121	800	151.54	18.19
1.41	3995	189.65	58.9	79.96	86.83	2.23	44,173	800	162.30	20.72
1.41	3995	189.65	64.2	80.06	87.54	2.23	44,227	801	148.88	17.62

P_{avg} (bar)	G (kg/m^2-sec)	q'' (kW/m^2)	z^+	$T_{b,loc}$ (°C)	$T_{w,loc}$ (°C)	Pr	Re	ε_{Re}	Nu	ε_{Nu}
1.41	3995	189.65	69.5	80.15	87.05	2.22	44,280	802	161.54	20.54
1.41	3995	189.65	79.6	80.34	87.91	2.22	44,381	804	147.16	17.30
1.41	3995	189.65	84.0	80.42	86.75	2.22	44,426	805	175.82	24.28
1.46	4477	190.08	43.5	79.68	86.21	2.24	49,326	849	171.30	24.32
1.46	4477	190.08	53.6	79.85	86.62	2.23	49,428	850	165.05	22.65
1.46	4477	190.08	58.9	79.93	86.18	2.23	49,480	851	178.71	26.38
1.46	4477	190.08	64.2	80.02	86.43	2.23	49,534	852	174.23	25.15
1.46	4477	190.08	69.5	80.10	86.44	2.23	49,586	853	176.25	25.69
1.46	4477	190.08	79.6	80.27	87.21	2.22	49,688	855	160.84	21.65
1.46	4477	190.08	84.0	80.34	86.12	2.22	49,732	856	193.24	30.80
1.56	4970	190.95	43.5	79.77	85.49	2.24	54,822	903	196.45	33.77
1.56	4970	190.95	53.6	79.92	85.89	2.23	54,923	905	187.86	30.98
1.56	4970	190.95	58.9	80.00	85.32	2.23	54,976	906	210.99	38.76
1.56	4970	190.95	64.2	80.07	85.88	2.23	55,029	907	193.13	32.73
1.56	4970	190.95	69.5	80.15	85.77	2.22	55,081	908	199.69	34.86
1.56	4970	190.95	79.6	80.30	86.37	2.22	55,183	909	184.84	30.18
1.56	4970	190.95	84.0	80.36	85.40	2.22	55,227	910	222.70	43.24
1.48	5934	238.94	43.5	79.78	85.77	2.24	65,457	1013	234.45	45.00
1.48	5934	238.94	53.6	79.94	86.09	2.23	65,587	1015	228.31	42.74
1.48	5934	238.94	58.9	80.02	85.57	2.23	65,655	1016	252.89	52.12
1.48	5934	238.94	64.2	80.10	85.29	2.23	65,724	1017	270.74	59.57
1.48	5934	238.94	69.5	80.19	86.13	2.22	65,792	1018	236.35	45.72
1.41	3995	189.65	69.5	80.15	87.05	2.22	44,280	802	161.54	20.54

P_{avg} (bar)	G (kg/m^2-sec)	q'' (kW/m^2)	z^+	$T_{b,loc}$ (°C)	$T_{w,loc}$ (°C)	Pr	Re	ε_{Re}	Nu	ε_{Nu}
1.48	5934	238.94	79.6	80.34	86.62	2.22	65,922	1020	223.73	41.31

Appendix D

Onset of Nucleate Boiling Data

Onset of nucleate boiling data collected for this study is provided in the following tables. Local subcooling, local pressure, local saturation temperature, mass flux, dimensionless position from inlet, measured heat flux, and the experimentalist's 95% confidence interval on the ONB heat flux are provided. For ONB determined using temperature measurement, the local saturation superheat at ONB is also provided, along with the measurement uncertainty. For the ONB heat flux determination via fluctuations in the pressure signal, the outlet conditions are provided as first incipience in the channel is generally to occur at this location. Results are provided for both the nominal surface and oxidized surface. While ONB was also measured visually, this was only possible at a limited set of conditions and is not provided here. Refer to Chapter 5 for details regarding the visualization of incipience.

Nominal Surface

Table D1: Onset of Nucleate Boiling Data from Heat Flux Partition (Temperature Measurement) for Nominal Surface.

$\Delta T_{sub,loc}$ (°C)	P_{loc} (bar)	$T_{sat,loc}$ (°C)	G (kg/m^2-sec)	z^+	q''_{ONB} (kW/m^2)	95% Conf. Int. (kW/m^2)	$\Delta T_{sat,ONB}$ (°C)	$\varepsilon_{\Delta T_{ONB}}$ (°C)
21.15	1.32	107.48	736	69.5	243.99	[197, 288]	14.42	1.56
21.20	1.35	108.14	740	69.5	267.44	[199, 292]	15.40	1.71
23.64	1.37	108.58	1489	69.5	365.45	[295, 453]	9.26	1.40
23.56	1.38	108.78	1485	69.5	387.21	[275, 442]	9.50	1.48
24.60	1.43	109.82	2223	69.5	557.05	[462, 645]	11.51	1.68
23.50	1.40	109.22	2227	69.5	601.27	[508, 651]	13.64	1.80
25.82	1.46	110.62	2973	69.5	671.47	[562, 750]	9.50	1.80
26.08	1.50	111.38	2965	69.5	747.86	[607, 889]	11.56	1.99
39.62	1.34	108.07	751	69.5	316.57	[272, 340]	6.45	2.08
40.68	1.37	108.67	1510	69.5	601.92	[487, 652]	9.02	2.29
42.65	1.42	109.73	2246	69.5	844.65	[653, 945]	7.30	2.53
43.01	1.45	110.39	2999	69.5	1036.49	[801, 1136]	5.29	2.74

Table D2: Onset of Nucleate Boiling Data from Pressure Fluctuation (Pressure Drop Measurement) for Nominal Surface.

$\Delta T_{sub,outlet}$ (°C)	P_{outlet} (bar)	$T_{sat,outlet}$ (°C)	G (kg/m^2-sec)	z^+	q''_{ONB} (kW/m^2)	95% Conf. Int. (kW/m^2)
12.46	1.32	107.52	744	113.5	131.34	[87, 179]
12.85	1.29	106.97	750	113.5	110.80	[88, 133]
13.48	1.30	107.14	1479	113.5	179.79	[138, 225]
13.68	1.32	107.45	1477	113.5	181.42	[137, 273]
13.47	1.32	107.47	2949	113.5	370.23	[279, 460]
18.35	1.28	106.60	743	113.5	197.17	[154, 220]
18.96	1.31	107.23	742	113.5	199.36	[158, 222]
20.57	1.30	107.11	1480	113.5	295.39	[250, 319]
20.74	1.31	107.32	1481	113.5	297.35	[234, 342]
20.61	1.32	107.62	2231	113.5	461.72	[362, 599]
19.33	1.30	107.17	2234	113.5	507.66	[349, 560]
20.75	1.31	107.26	2973	113.5	562.48	[419, 835]
21.52	1.34	108.08	2969	113.5	565.07	[466, 748]
34.55	1.32	107.47	754	113.5	293.95	[223, 317]
37.31	1.31	107.34	1503	113.5	439.54	[372, 465]
38.57	1.32	107.46	2255	113.5	564.74	[519, 610]
37.11	1.29	107.00	3003	113.5	846.21	[657, 945]

Oxidized Surface

Table D3: Onset of Nucleate Boiling Data from Heat Flux Partition (Temperature Measurement) for Nominal Surface.

$\Delta T_{sub,loc}$ (°C)	P_{loc} (bar)	$T_{sat,loc}$ (°C)	G (kg/m^2-sec)	z^+	q''_{ONB} (kW/m^2)	95% Conf. Int. (kW/m^2)	$\Delta T_{sat,ONB}$ (°C)	$\varepsilon_{\Delta T_{ONB}}$ (°C)
18.78	1.35	108.22	747	69.5	358.25	[267, 408]	27.22	2.25
22.47	1.36	108.49	1491	69.5	455.72	[409, 504]	17.15	1.72
24.63	1.42	109.71	2228	69.5	553.07	[368, 649]	13.35	1.66
25.69	1.51	111.45	2966	69.5	834.06	[649, 1020]	19.45	2.17

Table D4: Onset of Nucleate Boiling Data from Pressure Fluctuation (Pressure Drop Measurement) for Nominal Surface.

$\Delta T_{sub,outlet}$ (°C)	P_{outlet} (bar)	$T_{sat,outlet}$ (°C)	G (kg/m^2-sec)	z^+	q''_{ONB} (kW/m^2)	95% Conf. Int. (kW/m^2)
17.98	1.31	107.31	752	113.5	221.39	[137, 267]
22.06	1.34	107.96	1491	113.5	271.91	[228, 317]
20.72	1.33	107.69	2227	113.5	464.59	[368, 553]
21.58	1.33	107.81	2974	113.5	558.96	[464, 743]

Appendix E

Influence of Contamination and Oxidation on the Wettability of MTR Fuel[*]

Surface cleanliness is known to affect surface wettability of water on metals. Results by Mantel show a strong dependence of surface energy on organic contaminant thickness on stainless steels [195]. As wettability influences heat transfer parameters relevant to Materials Test Reactors, including onset of nucleate boiling and the critical heat flux, any excess surface contamination or oxidation remaining on the exterior of fuel plate surfaces could have a significant effect on fuel performance. For example, oil or cutting fluid remaining on the outer cladding surface could lead to significantly lower onset of nucleate boiling and even premature critical heat flux.

This component of the study quantitatively relates varying degrees of surface cleanliness with wettability, primarily focusing on 6061 aluminum, the outer clad material of the LEU fuel plates. Wettability on zirconium surfaces is also characterized, as zirconium or zircaloy could be considered in the near future as an alternative cladding material for the LEU fuel. Coupons of 90% depleted uranium/10% Mo clad in zirconium from a co-rolling process were also studied.

The surface conditions and various cleaning procedures are described in detail in the lists on the following pages.

[*] The data within this appendix was collected by the author at Los Alamos National Laboratory and is derived from "Surface Science and Bond Strength Measurements Supporting U10Mo Fuel Fabrication," approved for public release under LA-UR-11-04972.

For each surface, the following levels of cleanliness were examined:

1) *As-received with solvent clean only*.
2) *LANL-cleaned.* LANL-prescribed cleaning treatment for each material is used.
3) *Mild contamination.* Following LANL-prescribed cleaning treatment, surfaces are coated with light hydrocarbon-based oil which is wiped clean with a dry KimWipe.
4) *Heavy contamination.* Following LANL-prescribed cleaning treatment, oil is drained by leaning vertically for approximately 3 hours.

Shell Vitrea 46, a highly refined mineral oil, was used to contaminate the samples. For mild contamination, the oil was applied to surfaces with a saturated KimWipe, and then wiped dry with a clean KimWipe. For the heavily contaminated samples, oil was applied by full immersion. Oil was allowed to drain by leaning vertically for three hours, with intermittent removal of oil pooling at the bottom of samples. The "solvent clean only" process is characterized by:

<u>Solvent Clean Process</u>

1) Immersion in ultrasonic bath of acetone for 10 minutes.
2) Rinse with ethanol.
3) Rinse with DI water.
4) Dry with clean compressed nitrogen.

The LANL-prescribed cleaning treatment is summarized below, and described in detail in Reference [196]:

Aluminum Sheet

1) Ultrasonic Blue Gold Cleaner for 10 seconds
2) DI water rinse
3) 50% nitric acid plus 2% ammonium bifluoride (NH_4HF_2) soak for 10 seconds
4) DI water rinse
5) Etch in 10% sodium hydroxide at 70 °C for 30 seconds
6) DI water rinse
7) 50% nitric acid plus 2% ammonium bifluoride soak for 15 seconds
8) DI water rinse
9) 50% nitric acid soak for 30 seconds to one minute
10) DI water rinse
11) Dry with clean compressed air or nitrogen

Zirconium Foil

1) Ultrasonic Blue Gold Cleaner for two minutes
2) DI water rinse
3) 50% nitric acid plus 2% ammonium bifluoride soak for two minutes
4) DI water rinse
5) Dry with clean compressed nitrogen

For comparison, the current cleaning process for MITR fuel elements is provided below [197]:

1) Clean or pickle individual plates and side plate in Nitric acid (~ 5-30 sec soak time). The parts are then rinsed in DI water. Then the parts are dried with compressed air. OP-25000 and OP-0006109.
2) The plates are then visually inspected for surface contaminants. If contaminants are found in visual inspection, clean / pickle may be performed again using same method used in step 1 above. OP-006309
3) Plates and side plates are assembled and swaged to form the assembly. End adapters and welded on and assembly is machined. Final inspection is completed.
4) Assembly is cleaned by alcohol wipe on outside surfaces (i.e. plates 1 & 15).
5) Assembly is washed with DI water then dried with compressed air in vertical tank. OP-0006105
6) Final assembly is visually inspected and re-cleaned (steps 4 & 5) as necessary.
7) The clean final assembly is placed in a bag for shipment.

E.1. AR-XPS Measurements to Quantify Contaminant and Oxide Thickness

The effect of both surface contamination and oxidation were investigated in this component of the study. Composition and thickness of contaminant and oxide layers were determined quantitatively using angle resolved X-ray photoelectron spectroscopy (AR-XPS). XPS relies on the photoelectric effect, in which an incident photon results in ejection of an electron from its orbital. Samples are irradiated with soft monoenergetic X-rays, with Mg Kα or Al Kα typically being used [198]. The kinetic energy of the photoelectron is measured, from which the binding energy may be calculated by the following:

$$BE = h\nu - KE - \phi_s \tag{E1}$$

where $h\nu$ is the incoming photon energy, KE is the measured kinetic energy of the ejected photon, and ϕ_s is the spectrometer work function. XPS can therefore determine elemental composition and concentration at the surface, along with the chemical state which is indicated by slight shifts in the binding energy. Angle resolved XPS allows for measurement of surface layer thicknesses, typically on the order of 100 Å or less. By varying the sample angle (90°, 45°, and 15° are typical), depth profiling may be performed. The technique is detailed in Reference [199].

Auger Electron Spectroscopy (AES) is another common technique for measuring composition and thickness of surface layers. The Auger process occurs when an incident particle or photon ejects an inner shell electron. As a higher shell electron fills the vacancy, the Auger electron is simultaneously emitted from an outer shell due to transfer of the relaxation energy. The Auger process competes with X-ray fluorescence (XRF), in which a photon instead of an electron carries away the relaxation energy. Typical Auger instruments utilize an electron beam for sample irradiation. As with XPS, the binding energy may be inferred, resulting in a characteristic spectrum which may be used to identify elemental composition, concentration, and chemical state. The Auger technique is only sensitive to 10's of Ångstroms. However, ion sputter depth profiling, usually relying on Argon ions to etch away the surface, allows for chemical characterization to greater depths and also provides for a means of quantifying thickness of surface layers.

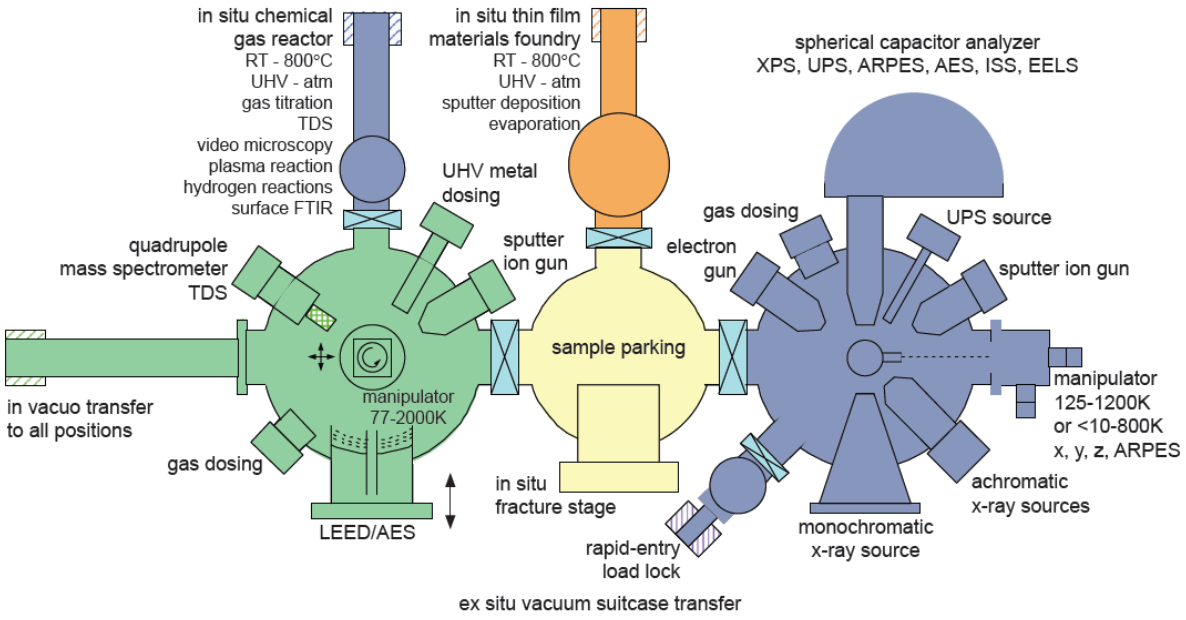

Figure E1: Integrated Surface Science Measurement Facility in MST-6 at Los Alamos National laboratory. XPS and AES measurements are performed in the vacuum chamber on the right. ***Source: Ref. [200].***

Surface measurements for the contamination study were taken using the facility shown in Figure E1, located in the Materials Science Laboratory at Los Alamos National Laboratory. For the heavily contaminated samples, thickness estimations were made using weight gain measurements, as AR-XPS and AES sputter depth profiling would have been insufficient due to the overall thickness of the hydrocarbon layer.

For the aluminum samples, AR-XPS measurements were recorded at three take-off angles (90°, 45°, 20°). For the contaminated zirconium coupons, measurements were only taken at 90° and 45°, since the expected signal from the underlying layers at 20° would have been too low to measure. High resolution scans using the standard aluminum X-ray source were obtained for carbon and the respective metal and metal oxide peaks. Typical acquisition time was 60 minutes. These spectra, along with selected survey spectra, are shown in the following figures. Note that the intensity (area under peak relative to background) should be used as a basis for comparison between measurements. In Figure E2, note the distinct difference in surface composition achieved with various cleaning treatments on aluminum 6061. While 6061 is alloyed with magnesium and silicon, the large presence of these elements at the surface, giving a higher signal than aluminum itself, seems to indicate the presence of a protectant or contaminant from the production process, which solvent cleaning does not remove. Although not shown, it

was also discovered during this study that as-received zirconium foil possessed sub-stoichiometric surface oxides, along with the possible presence of zirconium carbide on the surface. Only the LANL cleaning process removed these layers and fostered the formation of a stoichiometric, passive oxide layer on the zirconium surface.

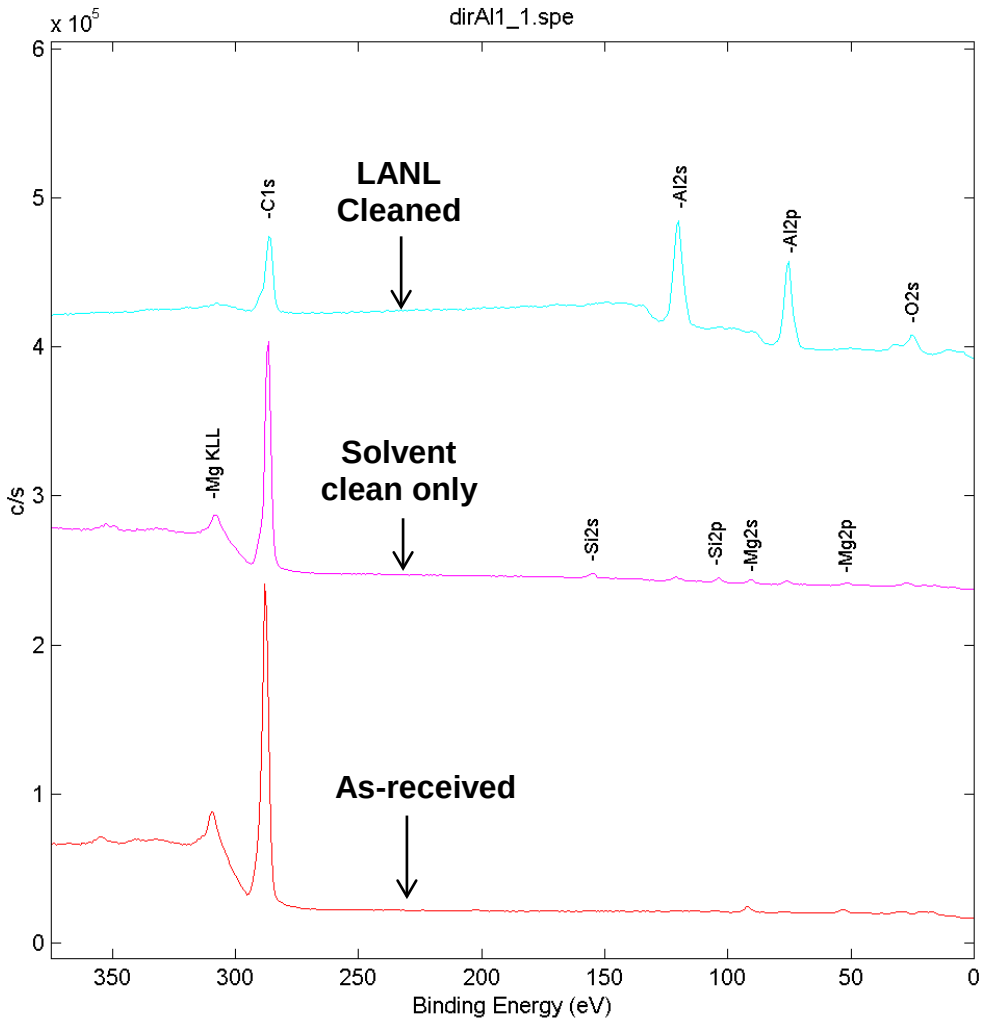

Figure E2: XPS Survey Spectra of 6061 Foils Using Al Monochromatic Source at TOA=45°. Bottom (red): As-received; Middle (purple): As-received with solvent clean only; Turquoise (top): LANL cleaned. Note that the solvent clean still leaves a significant amount of hydrocarbon on the surface.

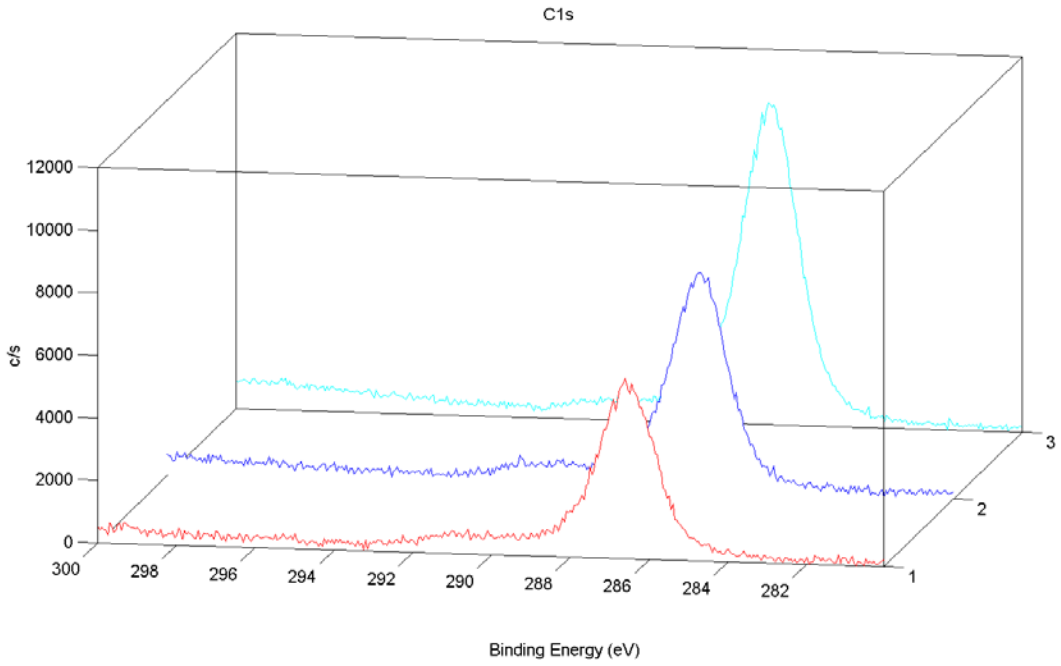

Figure E3: Carbon Peaks for Al 6061 Foil As-received with Solvent Clean Only. Red: 90° TOA; Blue: 45° TOA; Turquoise: 20° TOA.

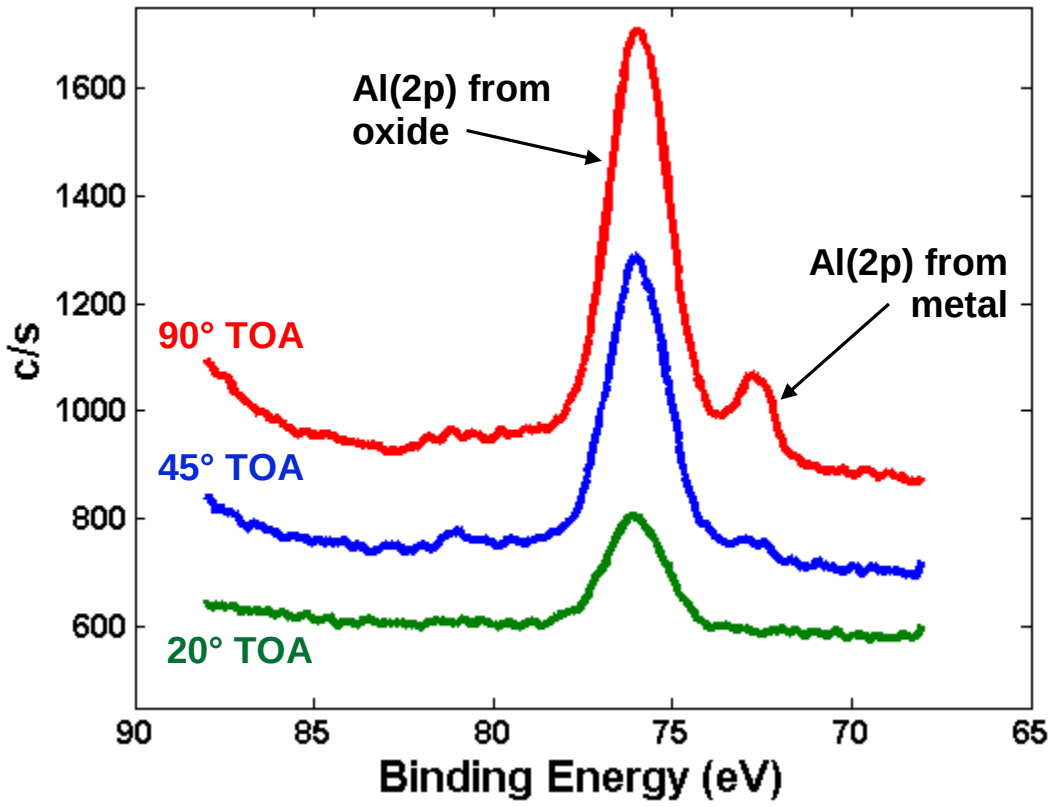

Figure E4: Aluminum Metal and Oxide Peaks for Al 6061 Foil as-received with Solvent Clean Only.

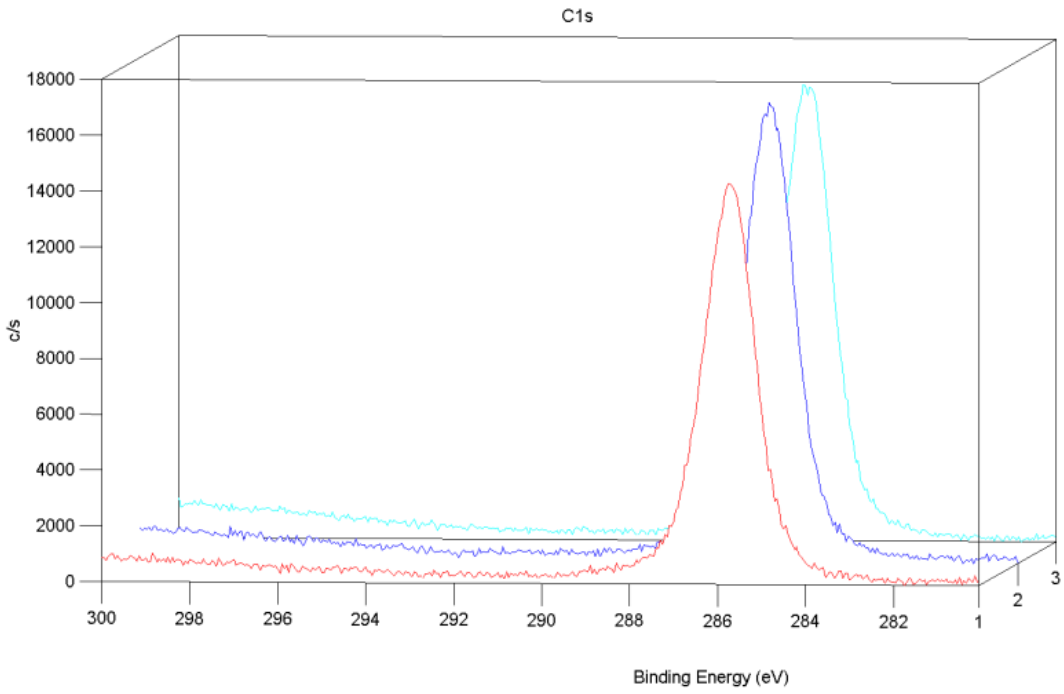

Figure E5: Carbon Peaks for Mildly Contaminated Al 6061 Foil. Red: 90° TOA; Blue: 45° TOA; Turquoise: 20° TOA.

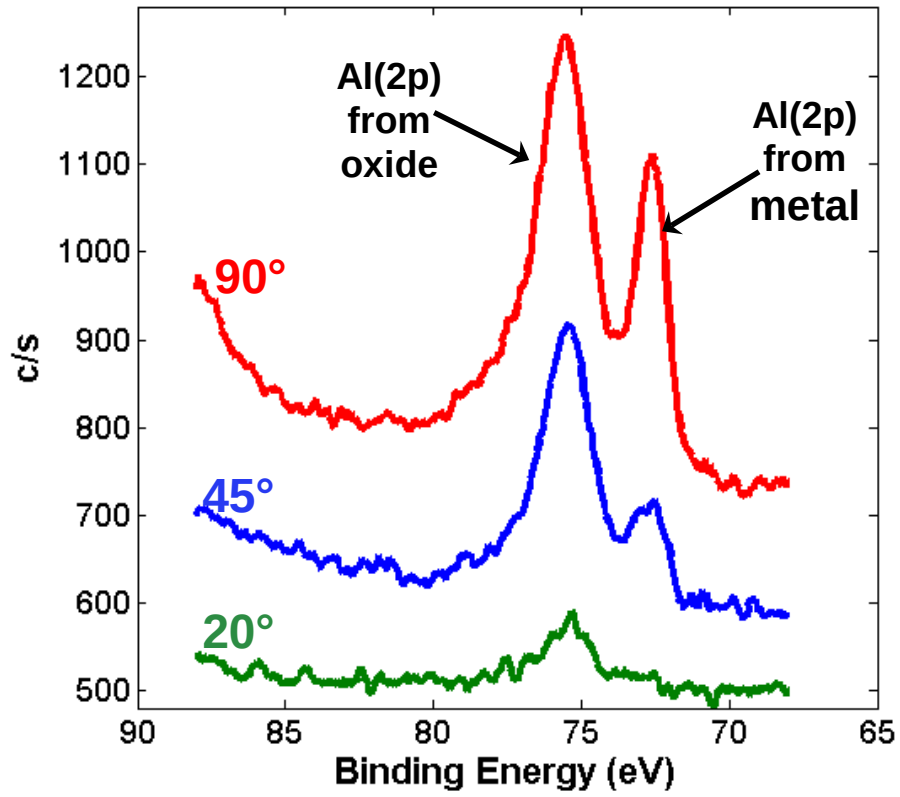

Figure E6: Aluminum Metal and Oxide Peaks for Mildly Contaminated Al 6061 Foil.

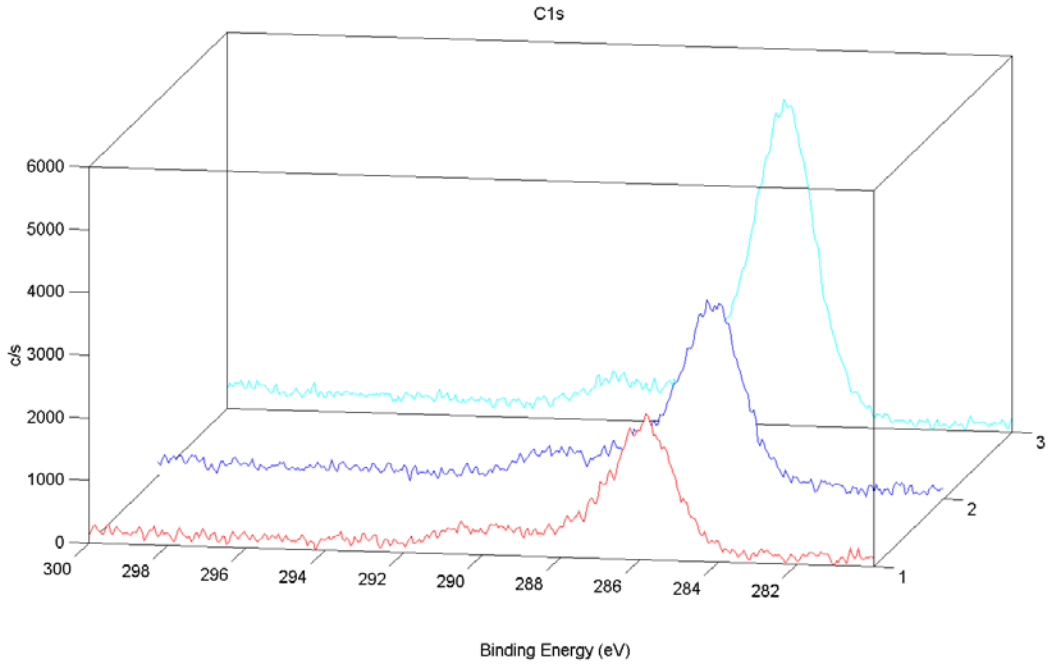

Figure E7: Carbon Peaks for Mildly Contaminated Al 6061 Foil with Subsequent Solvent Clean. Red: 90° TOA; Blue: 45° TOA; Turquoise: 20° TOA.

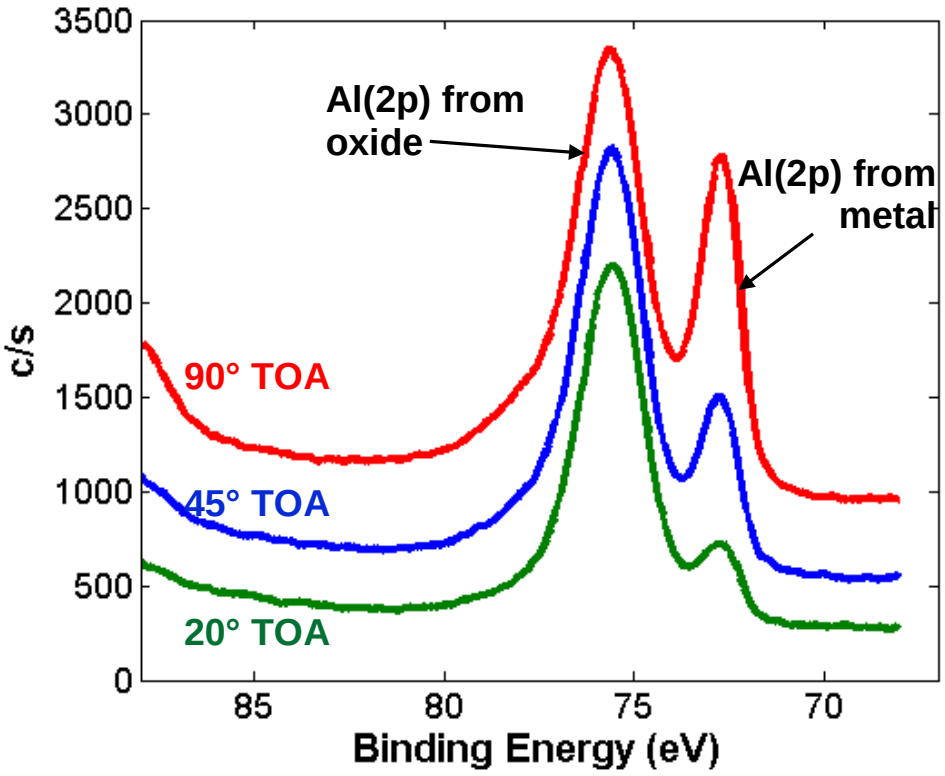

Figure E8: Aluminum Metal and Oxide Peaks for Mildly Contaminated Al 6061 Foil with Subsequent Solvent Clean.

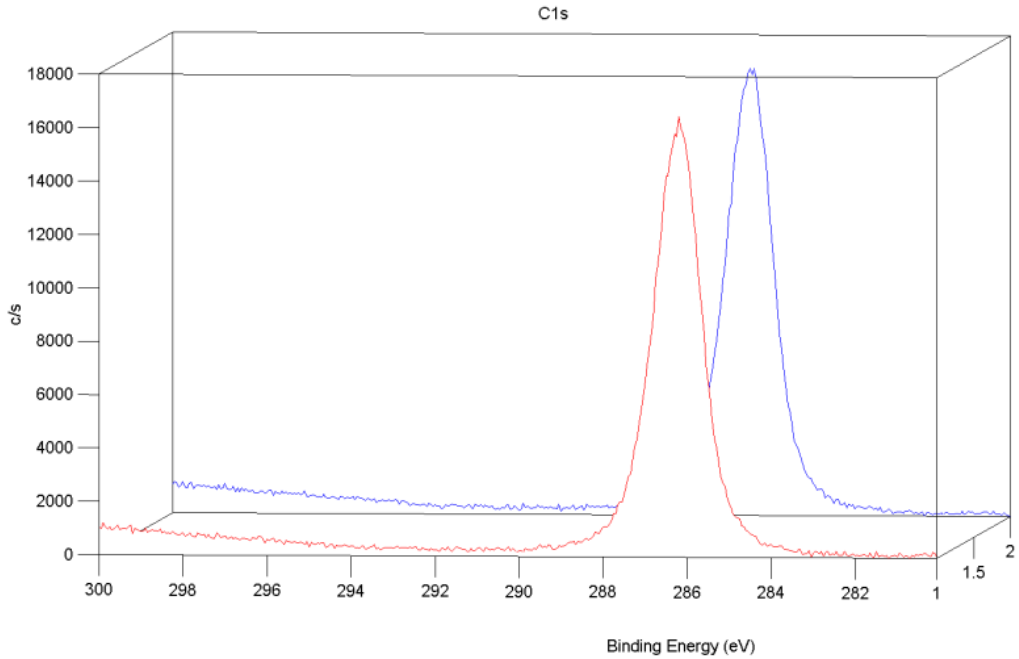

Figure E9: Carbon Peaks for Mildly Contaminated Zr Foil. Red: 90° TOA; Blue: 45° TOA.

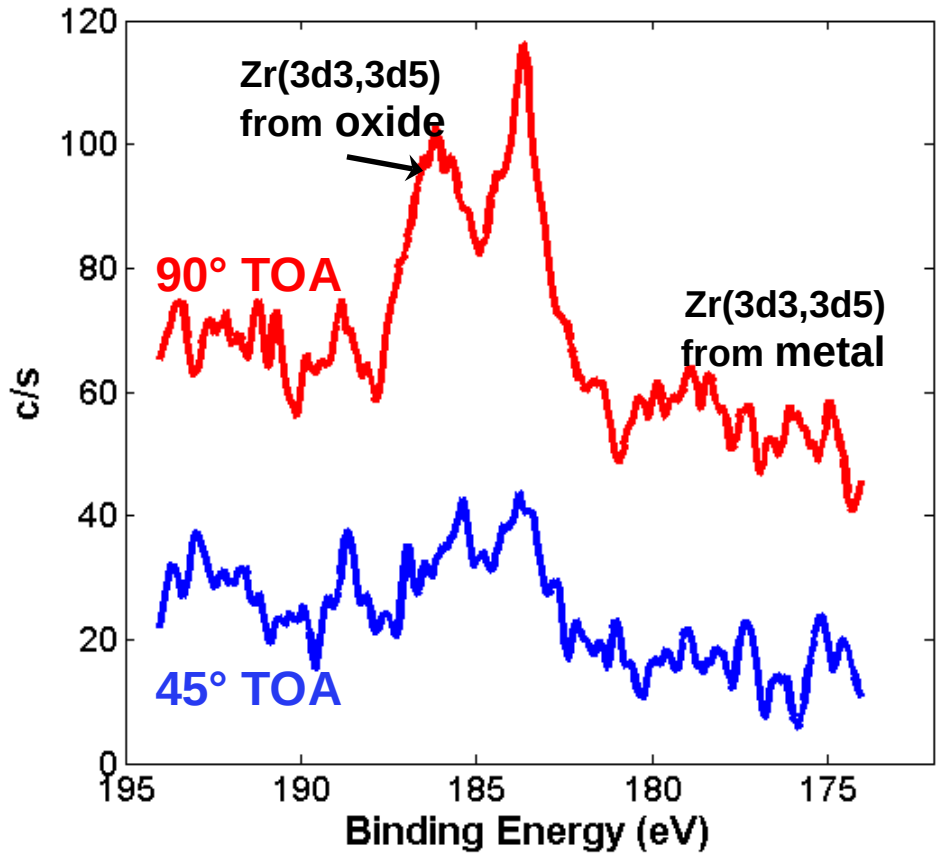

Figure E10: Zirconium Metal and Oxide Peaks for Mildly Contaminated Zirconium Foil.

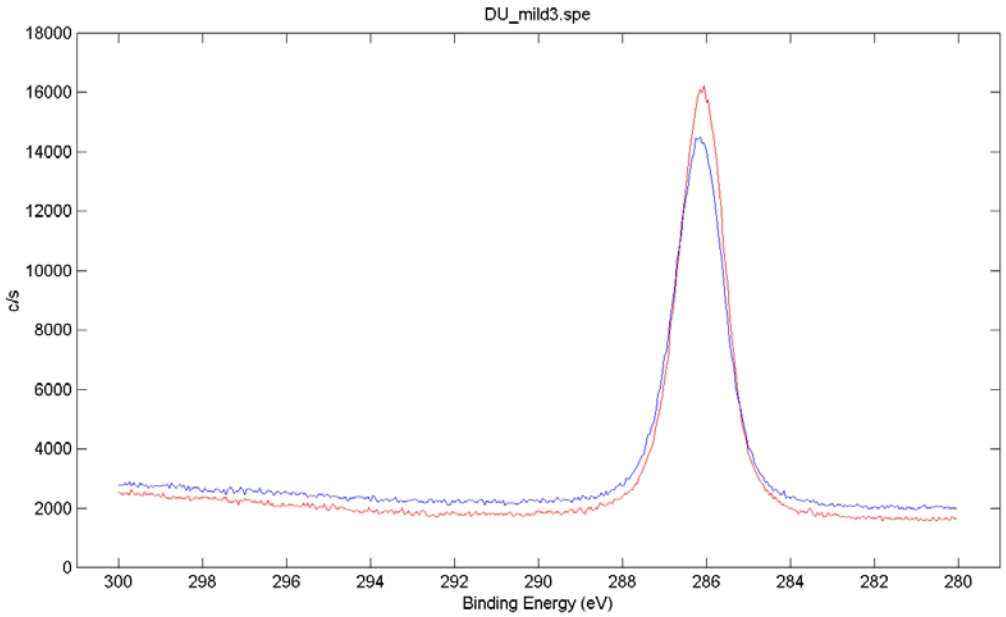

Figure E11: Carbon Peaks for Mildly Contaminated Zr-clad DU-10Mo Foil. Red: 90° TOA; Blue: 45° TOA.

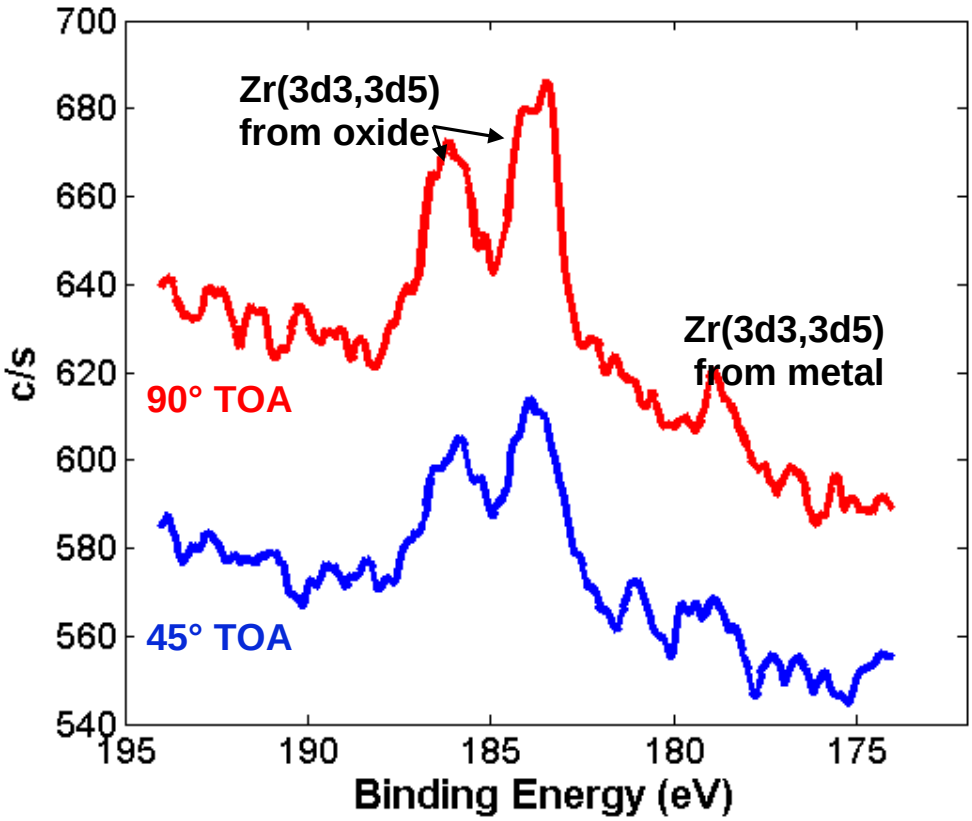

Figure E12: Zirconium Metal and Oxide Peaks for Mildly Contaminated Zr-clad DU-10Mo Foil.

Peak areas from the above spectra were calculated using the Physical Electronics MultiPak software. Curve fits for carbon were obtained using a Gauss-Lorentz model with ~80% Gaussian. Metal peaks were fit using an asymmetric model to account for the characteristic tail of such peaks. Metal oxide peaks were fit using the Gauss-Lorentz model with ~70%-80% Gaussian. Results of peak intensity calculations are listed in Table E1 through Table E5.

Table E1: Measured Intensity for Al 6061, As-received with Solvent Clean Only.

θ_N	*TOA*	I_{Carbon} (c/sec)	I_{Al} (c/sec)	I_{Al2O3} (c/sec)
0°	**90°**	11,586	334	1644
45°	**45°**	14,133	78†	1254
70°	**20°**	20,112	6†	473

†*Subject to significant uncertainty due to poor signal to noise ratio.*

Table E2: Measured Intensity for Al 6061 with Mild Contamination.

θ_N	*TOA*	I_{Carbon} (c/sec)	I_{Al} (c/sec)	I_{Al2O3} (c/sec)
0°	**90°**	21,713	489	1193
45°	**45°**	25,374	175	659
70°	**20°**	25,622	6†	140

†*Subject to significant uncertainty due to poor signal to noise ratio.*

Table E3: Measured Intensity for Al 6061 with Mild Contamination and Subsequent Solvent Clean.

θ_N	*TOA*	I_{Carbon} (c/sec)	I_{Al} (c/sec)	I_{Al2O3} (c/sec)
0°	**90°**	5202	2280	5721
45°	**45°**	7095	1253	5567
70°	**20°**	11,982	491	4404

Table E4: Measured Intensity for Zirconium with Mild Contamination.

θ_N	*TOA*	I_{Carbon} (c/sec)	I_{Al} (c/sec)	I_{Al2O3} (c/sec)
0°	**90°**	23,797	15†	177
45°	**45°**	24,560	2†	70†
70°	**20°**	-	-	-

†*Subject to significant uncertainty due to poor signal to noise ratio.*

Table E5: Measured Intensity for Zr-Clad DU-10Mo with Mild Contamination.

θ_N	*TOA*	I_{Carbon} (c/sec)	I_{Al} (c/sec)	I_{Al2O3} (c/sec)
0°	**90°**	20,700	55†	290
45°	**45°**	21,330	12†	147
70°	**20°**	-	-	-

†*Subject to significant uncertainty due to poor signal to noise ratio.*

Weight gain measurements were performed on the heavily contaminated samples, as the contaminant layer was too thick to measure with AR-XPS. The foil dimensions were measured at each end using calipers, with the average dimension being used for calculations. Hydrocarbon thickness was calculated assuming that the mineral oil covered the surface uniformly. Additionally, the edges of the foils were neglected. Knowing that the density of Vitrea 46 oil at room temperature is 0.873 g/cm^3, the contaminant layer was calculated by:

$$t_{oil} = \frac{m_{oil}}{\rho_{oil} A_{surf}} \tag{E2}$$

Measurement results are listed in Table E6. Uncertainty on all mass measurements is taken to be ±0.0001 g. Uncertainty on the final oil thickness is calculated using error propagation.

Table E6: Measurement Parameters for Estimating Hydrocarbon Thickness on Heavily Contaminated Foils.

	Tare	Gross	Net (m_{oil})	Foil Length	Foil Width
Al 6061	0.5990 g	0.6028 g	3.8 ±0.14 mg	0.987±0.007 in. (2.507±0.018 cm)	1.418±0.015 in. (3.602±0.038 cm)
Zirconium	1.4467 g	1.4493 g	2.6 ±0.14 mg	1.019±0.009 in. (2.588±0.023 cm)	1.439±0.001 in. (3.655±0.003 cm)
Zr-clad DU-10Mo	7.5003 g	7.5100 g	9.7 ±0.14 mg	1.018±0.002 in. (2.586±0.005 cm)	1.997±0.003 in. (5.072±0.008 cm)

For all other samples, surface layer thickness was calculated using the AR-XPS intensity data with the three-layer model shown in Figure E13. Mean free paths of the electrons through the materials of interest were obtained from the NIST Standard Reference Database 71, "Electron Inelastic Mean Free Paths" [201], and are listed in Table E7. Varying the TOA yields different path lengths, allowing for calculation of layer thickness from relative peak intensities due to attenuation. Layer thickness was calculated using the QUASES-ARXPS software. Figure E14 shows an example of the graphical user interface and fit obtained. Thicknesses were

calculated by minimizing the RMS error between the model and measured data. The calculated thicknesses are listed in Table E8.

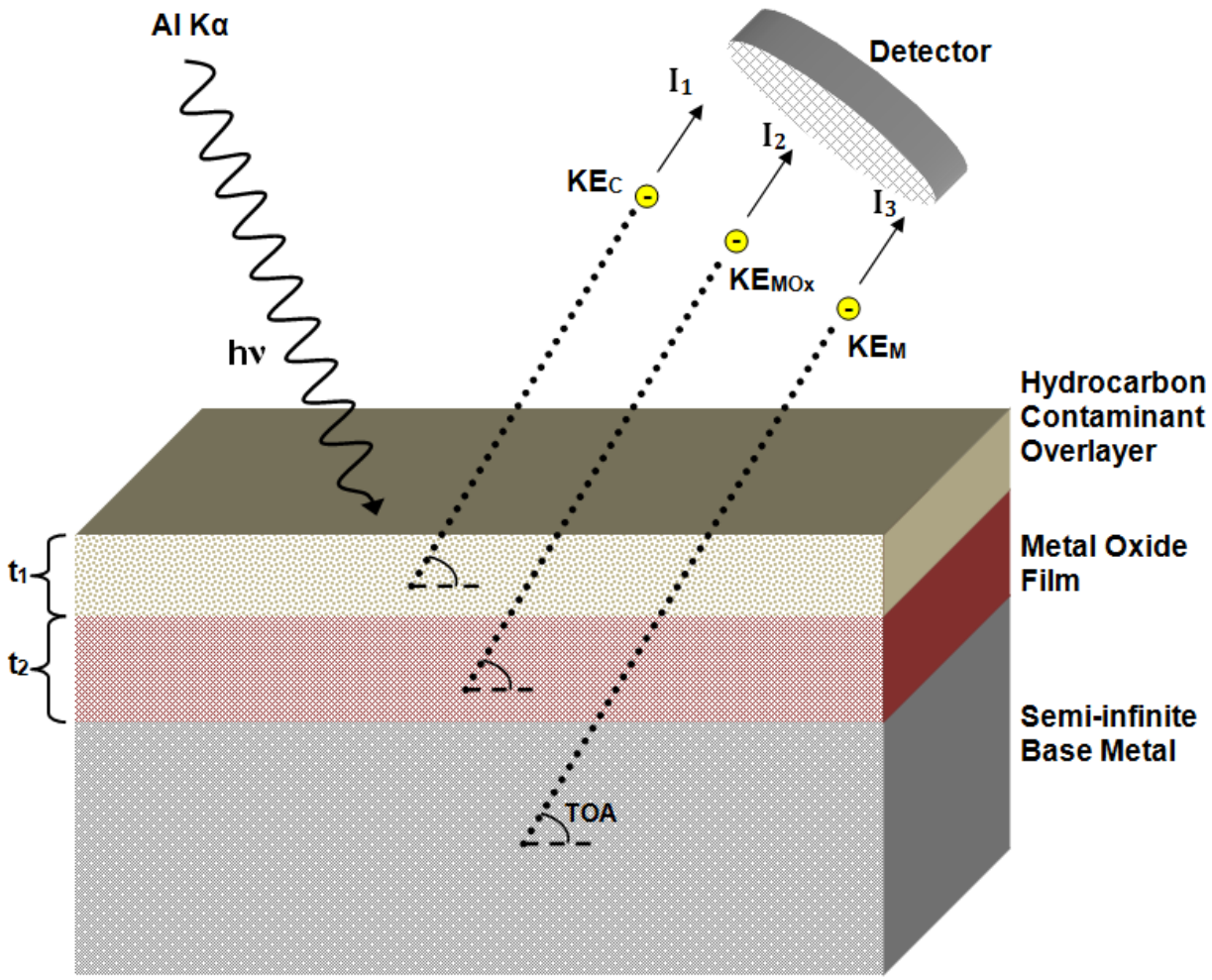

Figure E13: Three-Layer Model Used to Compute Thickness of Oxide and Contaminant Overlayers.

Table E7: Mean Free Paths of Photoelectrons in Materials of Interest.

	KE = 1202 eV	KE = 1305 eV	KE = 1410 eV
λ_{Al}	-	-	25.7 Å
λ_{Al2O3}	-	-	27.5 Å
λ_{Zr}	-	25.4 Å	-
λ_{ZrO2}	-	26.3 Å	-
λ_{C} (Paraffin equivalent)	40.1 Å	42.9 Å	45.6 Å

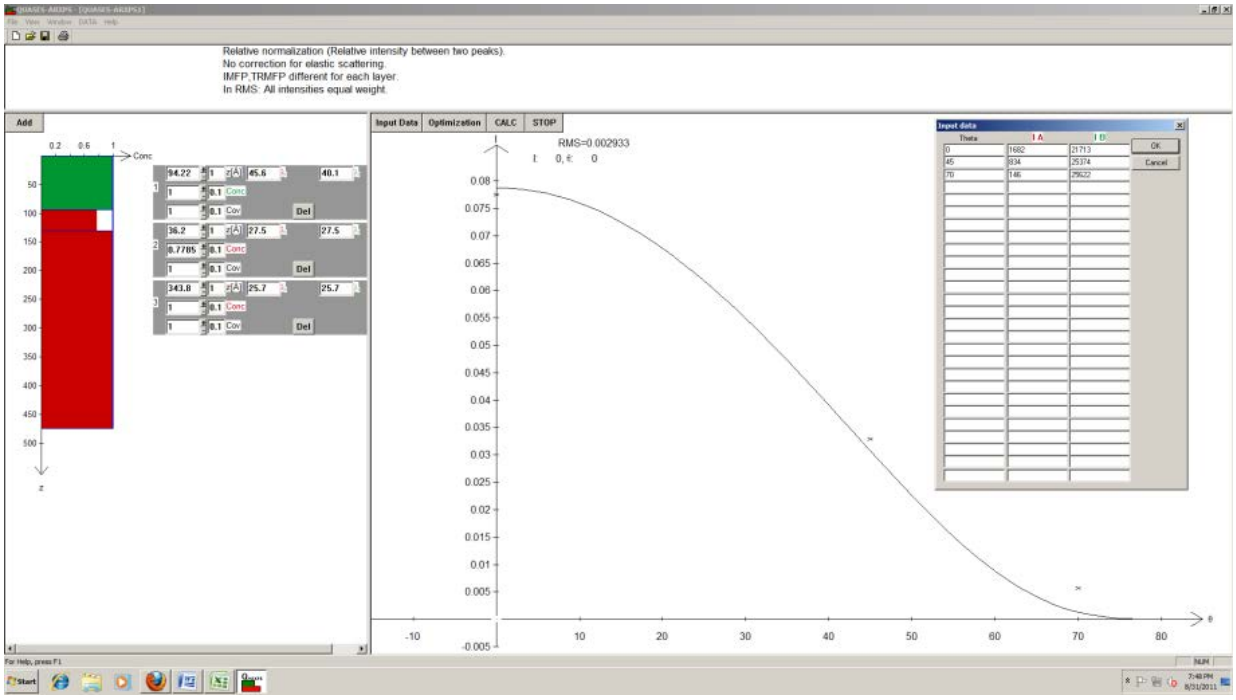

Figure E14: QUASES-ARXPS Graphical Interface Showing Example of Layer-Thickness Calculations.

Table E8: Summary of Oxide Layer and Hydrocarbon Layer Thicknesses Calculated for Surface Cleaning Study.

SPECIMEN	OXIDE THICKNESS (Al_2O_3 or ZrO_2)	HYDROCARBON THICKNESS
Al 6061, As Received with Solvent Clean Only	51±4 Å	54±2 Å
Al 6061, LANL Cleaned	45±3Å	4.8±0.3 Å
Al 6061, Mild Contamination	36±3 Å	94±2 Å
Al 6061, Heavy Contamination	Not Measured	2.41±0.09 μm
Al 6061, Mild Contamination followed by solvent clean	37±1 Å	13±0.4 Å
Zr, LANL Cleaned	57±1Å	8.5±0.5 Å
Zr, Mild Contamination	77±3 Å	170±19 Å
Zr, Heavy Contamination	Not Measured	1.57±0.09 μm
Zr-clad DU-10Mo, LANL Cleaned	37±1 Å	16±2 Å
Zr-clad DU-10Mo, Mild Contamination	57±2 Å	140±16 Å
Zr-clad DU-10Mo, Heavy Contamination	Not Measured	4.24±0.06 μm

E.2. Measurement of Surface Wettability Using Contact Angle Measurements

Wettability was characterized on the aluminum and zirconium surfaces using contact angle measurement. An analyzer with a camera and software was unavailable, so equilibrium contact angle measurements were performed using the manual goniometer shown in Figure E15. The manual measurements proved to be quite repeatable, though measurement of advanced and receded angles was not possible Sessile drop measurements were obtained for the side of each droplet. Results are summarized for the 6061 aluminum and zirconium surfaces in Table E9 and Table E10, respectively. Unfortunately, contact angle measurements could not be performed on the Zr-Clad U-10Mo samples as the samples were mildly radioactive and not cleared to be brought to that particular laboratory.

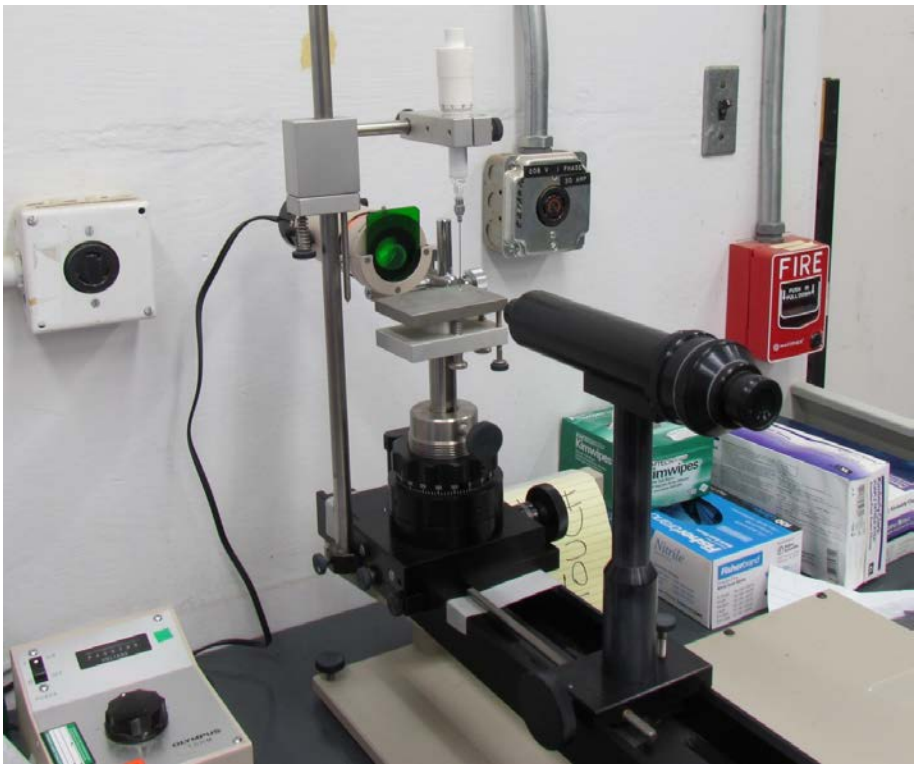

Figure E15: Goniometer for Performing Contact Angle Measurements. Although no optical software was available, accurate results were achievable with the "manual" setup for sessile drop measurements.

Table E9: Measured Sessile Drop Contact Angles for 6061 Aluminum with Different Hydrocarbon Contaminant Layer Thicknesses. Two independent measurements were performed for each surface.

		LANL Cleaned	As-Received with Solvent Clean	Mild Cont. with Solvent Clean	Mild Cont.	Heavy Cont.
1	**Left:**	33°	64°	45°	80°	79°
	Right:	33°	66°	44°	83°	80°
2	**Left:**	30°	71°	41°	83°	83°
	Right:	32°	67°	48°	84°	81°
AVERAGE:		**32.0°**	**67.0°**	**44.5°**	**82.5°**	**80.8°**
Standard Deviation:		1.4°	2.9°	2.9°	1.7°	1.7°

Table E10: Measured Sessile Drop Contact Angles for Zirconium with Different Hydrocarbon Contaminant layer Thicknesses. Two independent measurements were performed for each surface.

		LANL Cleaned	As-Received with Solvent Clean	Mild Cont. with Solvent Clean	Mild Cont.	Heavy Cont.
1	**Left:**	52°	71°	57°	90°	80°
	Right:	46°	73°	61°	92°	81°
2	**Left:**	46°	75°	58°	96°	80°
	Right:	49°	76°	58°	98°	78°
AVERAGE:		**48.3°**	**73.8°**	**58.5°**	**94.0°**	**79.8°**
Standard Deviation:		2.9°	2.2°	1.7°	3.7°	1.3°

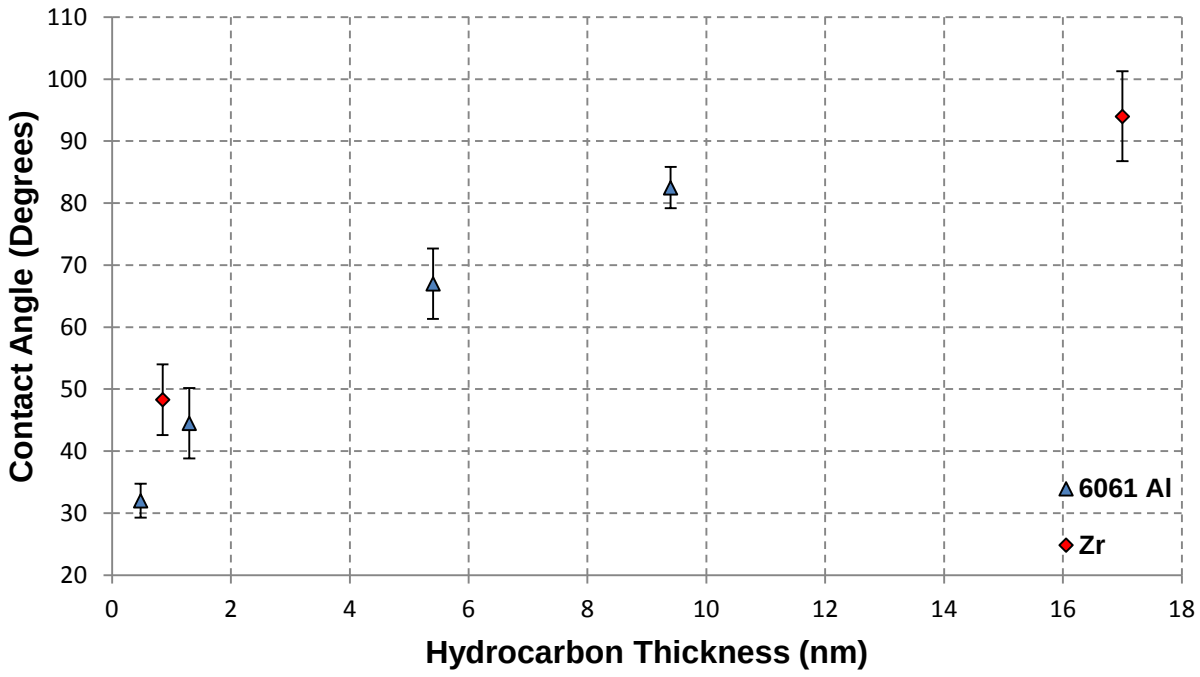

Figure E16: Contact Angle of Water on 6061 Aluminum and Zirconium Surfaces as a Function of Hydrocarbon Contaminant Overlayer Thickness. The error bars represent 1.96× the standard deviation of each set of measurements.

The trend of contact angle with hydrocarbon contaminant thickness is illustrated in Figure E16 for the 6061 aluminum and zirconium surfaces. Note that contact angle increases (wettability decreases) for increasing contaminant layer thickness. This relates to a decrease in the surface energy of the solid with increasing hydrocarbon contaminant layer thickness. High surface energies are typically associated with clean metals, inorganic compounds such as metal oxides, intermetallic oxides, diamond, etc. Low surface energies are usually associated with polymers and hydrocarbons. By virtue of their high surface energy, clean metals will not remain clean when exposed to the environment due to the spontaneous adsorption of organic contaminants of low surface energy onto the high surface energy substrate to minimize the surface free energy of the system [202].

The work by Athanase Dupré on adhesion between two immiscible liquids [203] resulted in the following relation:

$$W_{AB} = \gamma_A + \gamma_B - \gamma_{AB} \tag{E3}$$

where the subscripts *A* and *B* denote each liquid. Dupré's result may be combined with equation (185) to obtain what is commonly referred to as the Young-Dupré equation:

$$W_{sl} = \sigma[1 + \cos(\theta)] \tag{E4}$$

where W_{sl} is the work of adhesion per unit surface area, and the spreading pressure, $\pi=\gamma_s-\gamma_{sv}$ has been neglected, i.e. $\gamma_s=\gamma_{sv}$ and $\gamma_l=\gamma_{lv}=\sigma$. Note that the units of surface energy (mJ/m^2) are equivalent to that of surface tension (mN/m). The work of adhesion for water at room temperature and atmospheric pressure on the surfaces studied here is plotted in Figure E17.

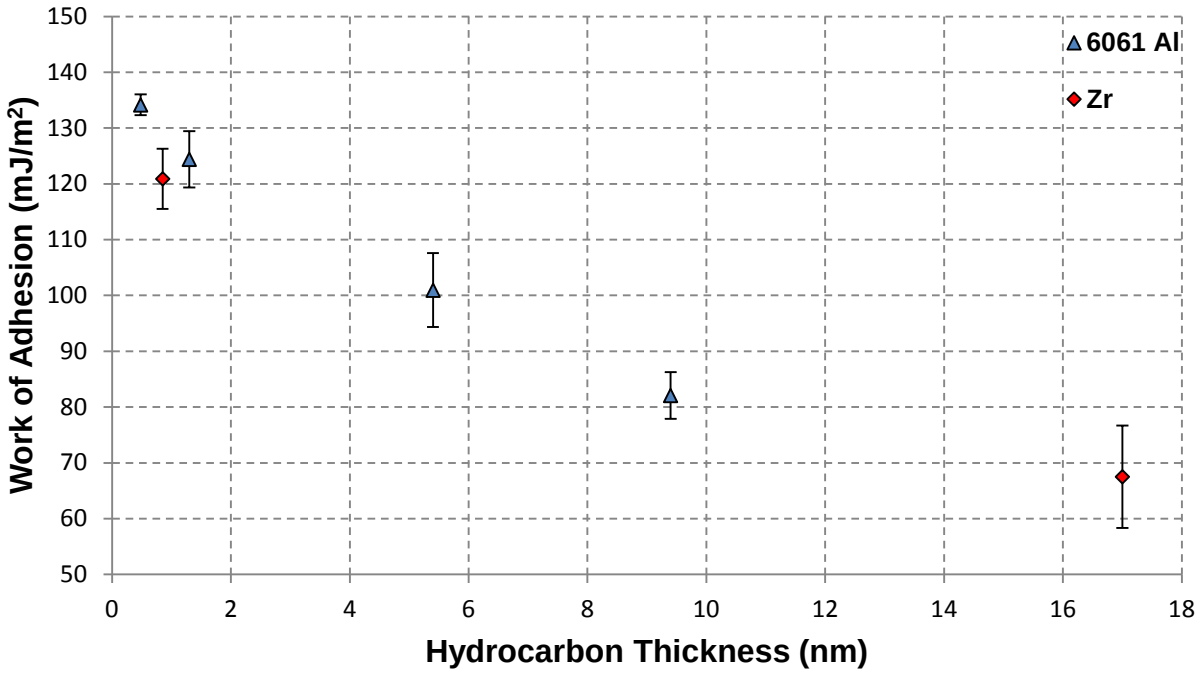

Figure E17: Work of Adhesion versus Hydrocarbon Contaminant Thickness for Al 6061 and Zr Surfaces.

The force components of the surface tensions, or surface energies, may be broken into two components: the dispersive element representing the effect of London dispersive forces and the non-dispersive element represents polar interactions [204]:

$$\gamma = \gamma^D + \gamma^{ND} \tag{E5}$$

The equation for work of adhesion can be substituted into an equation provided by Mantel and Wightman when the spreading pressure is negligible [195] to yield the following relation:

$$\frac{W_{sl}}{2\sqrt{\gamma_l^D}} = \left(\frac{\gamma_l^{ND}}{\gamma_l^D}\right)^{1/2} \sqrt{\gamma_s^{ND}} + \sqrt{\gamma_s^D} \tag{E6}$$

where for water at room temperature and atmospheric pressure, γ_l=72.6 mJ/m^2, γ_l^D=21.6 mJ/m^2, and γ_l^{ND}=51.0 mJ/m^2. One method of determining the relation between dispersive and non-dispersive solid surface tension is to perform contact angle measurements using different liquids. However, measurements were only performed for water in this study, so a further simplifying assumption will be made, which was not made by Mantel. The non-dispersive component of the surface energy will be treated as equal to the dispersive component, such that $\gamma_s^{ND} \approx \gamma_s^D \approx ½\gamma_s$. This is approximately valid when the separation distance is very small. Doing some algebra, equation (E6) can be re-written in terms of the surface energy of the solid, $E_s = \gamma_s$, such that:

$$E_s = \frac{W_{sl}^2 \left[\frac{1}{2}(\gamma_l^D + \gamma_l^{ND}) - \sqrt{\gamma_l^D \gamma_l^{ND}}\right]}{(\gamma_l^D - \gamma_l^{ND})^2}, \quad \delta_{HC} \text{ small} \tag{E7}$$

From equation (E4) and equation (E7), it is clear that a solid interface with a high surface energy will have a low contact angle (i.e. have good wettability) and a solid interface with low surface energy will have a high contact angle (i.e. display poor wettability). Typical surface energies for contaminant layers on a metal surface are provided in Table E11.

Using equation (E4) and equation (E7), the surface energy for zirconium and aluminum investigated in this study can be plotted against the hydrocarbon contaminant layer thickness based off the contact angle and AR-XPS measurements. The estimates are plotted in Figure E18. The fitted equation from the empirical results of Mantel's study is shown for comparison [195]. Note that the fitted equation from Mantel's study is for 304 stainless steel, and that no approximation was taken in calculating the dispersive and non-dispersive component of the solid surface tension (they were calculated explicitly). In the $\lim_{\delta_{HC}} \to \infty$, the empirical equation from Mantel's study predicts a surface energy of 11 mJ/m^2, which is about equivalent to the surface energy of a typical organic hydrocarbon, as seen in Table E11.

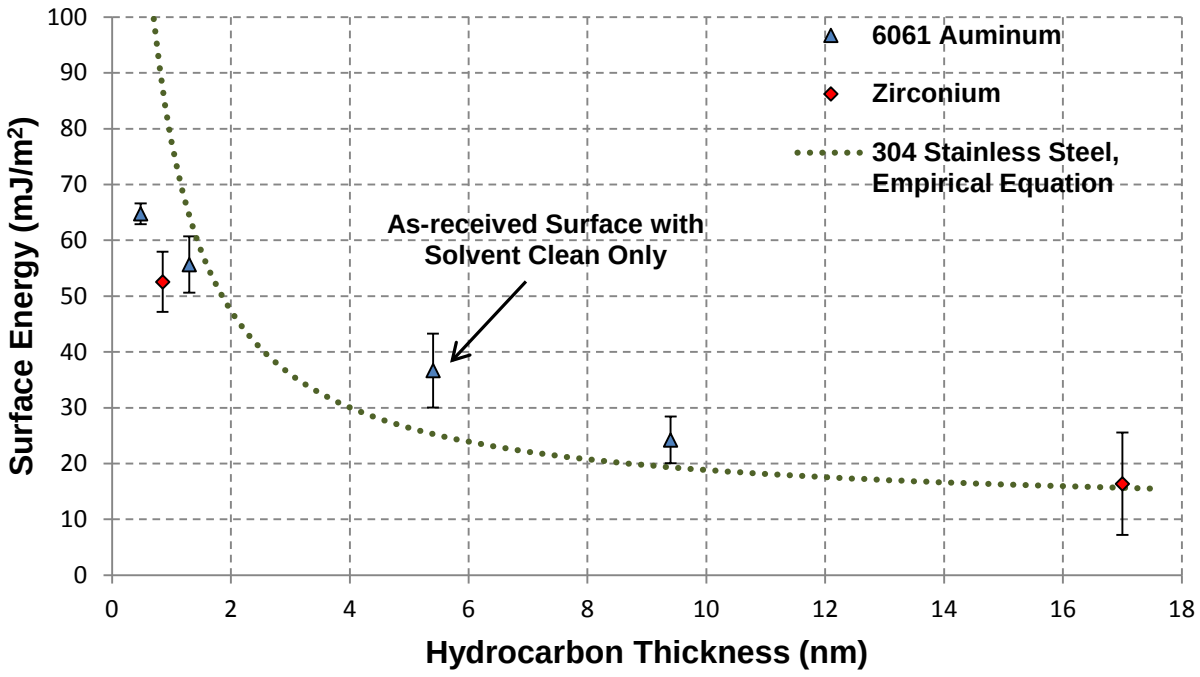

Figure E18: Estimated Surface Energy of 6061 Aluminum and Zirconium with Varying Degrees of Cleanliness Investigated in this Study. The fitted equation from the empirical results of Mantel [195] for 304 stainless steel is also shown.

Table E11: Typical Surface Free Energies Corresponding to Contaminant Layers on a Metal Surface. *Adapted from Ref. [205]*.

SURFACE	SURFACE FREE ENERGY (mJ/m^2)
Organic Hydrocarbons	~20
Organic Polymers	~20-30
Metal Oxides	200-300
Metals	1000-5000

E.3. Summary and Conclusion

From the results of this substudy, a number of relevant observations and conclusions can be drawn in in regard to the effect of surface contamination on wettability, and in turn, onset of boiling and two-phase heat transfer in general:

- Regardless of the underlying metal or metal oxide, as the hydrocarbon contaminant layer becomes thick enough, it will dominate the surface-fluid interaction.
- In the case of 6061 aluminum, zirconium, and 300 series stainless steel (study by Mantel), the effect of hydrocarbon contamination on surface energy is comparable. A similar effect is expected for most metals which form a thin protective metal oxide.
- It is clear that only a thin contaminant layer can have a profound effect on the surface energy, and in turn, the wettability, such that, for $\delta_{HC} \gtrapprox 8$ nm, the surface energy has fallen to that of a typical hydrocarbon.
- The solvent cleaning process on as-received surfaces leaves at least several nanometers of hydrocarbon contaminant overlayer. The majority of two-phase heat transfer studies rely on solvent cleaning alone prior to testing.
- Each specific metal, metal oxide, and associated surface treatment likely result in a different affinity for the adsorption of atmospheric contaminants onto the surface. This is exemplified with the LANL cleaning process, for which solvent cleaning after re-contamination proves far more effective than on the as-received surface. Surface morphology may also play a role in the adsorption phenomenon of atmospheric contaminants on the surface.
- The contaminant adsorption process appears to be time-dependent, with the thickness reaching a steady-state value over the course of hours to several days.
- Storage in plastic bags or foil does not appear to completely prevent the adsorption of contaminants. Surfaces would need to be prepared in a clean room, and vacuum sealed in a clean room-grade container.
- A common misconception is that metals are not well-wetting. In reality, clean metals, where $\delta_{HC} \approx 0$, have very high surface energies, and display almost perfect wetting with water. Reference [172] has typical values of water contact angles on clean gold, silver, aluminum, brass, copper, magnesium, nickel, stainless steel, zinc, rhodium,

palladium, platinum, titanium, and cadmium. The higher values typically reported (~60°-80°) in the heat transfer literature are likely for surfaces with a native oxide and a contaminant overlayer.

- In the heat transfer literature, "oxidized" surfaces typically display better wettability for two reasons. First, heat treatments are usually performed to obtain such oxides, which will disrupt or decompose the hydrocarbon contaminant layer. This was observed for the heat treated 316 stainless steel described in section 6.2. The oxidized 316 stainless steel surface displayed almost perfect wetting immediately after being removed from the furnace and cooling to room temperature. Second, it is hypothesized that clean metals have a higher affinity for low energy atmospheric contaminants. Therefore, a thicker oxide leads to less adsorption of hydrocarbons on the surface, and a thinner "permanent" hydrocarbon contaminant layer on the surface.
- There is no guarantee that the surface layers on metals and metal oxides display the same characteristics at elevated temperatures. In addition to the temperature dependence of surface energies, conditions in power reactors (~300 °C) likely lead to degradation/decomposition of the hydrocarbon contaminant overlayer. Radiation effects and coolant chemistry may also affect the composition of the contaminant overlayers at the interface with the coolant. Thus, in-situ contact angle measurements would be most useful, although they may prove extremely difficult to perform.

Many studies of surface wettability outside of the field of heat transfer have arrived at similar results, indicating that not only does contamination from organic constituents have an effect, but it is also very difficult to avoid. Aronov [206] states, "It is generally known that when exposed to the atmosphere, contamination occurs very rapidly at the surface. Also, dust particles may accumulate at the solid surface due to settling and electrostatic interaction." Mantel further states that, "A study of organic contamination on different metal oxides' leads to the suggestion of an adsorption phenomenon, where each of the metal oxides has its own characteristic rate and amount of adsorption [195]."

It is important to understand that any practical boiling surface will have atmospheric contamination, so inclusion of these effects is most representative of the end application. The MITR is a tank-type reactor, and therefore exposed to the atmosphere of the containment.

Surfaces in pressurized Materials Test Reactors are exposed to contaminants, as even de-ionized water will contain atmospheric contaminants. Attempting to achieve a Class 1 clean room-type setting, even in a heat transfer laboratory, would prove quite difficult. As Bernardin and Mudawar [172] state, "It is apparent that even under highly controlled conditions, ideal surfaces are very difficult to produce and maintain. Moreover, it is extremely difficult and impractical to conduct boiling heat transfer experiments with perfectly clean and ideal surfaces such as those found in surface chemistry laboratories." Nonetheless, surface cleanliness should not be neglected all together. Solvent cleaning is effective at removing oils and loose contaminants on a surface, which could severely degrade heat transfer. In addition, while solvent cleaning is unable to remove a hydrocarbon layer several nanometers thick on an otherwise untreated surface, it is fairly consistent and repeatable, with contact angles on practical boiling surfaces typically measuring between 60° and 90°.

However, as noted above, aluminum surfaces, either cleaned using the LANL-prescribed cleaning treatment, or pre-filmed with boehmite, display lower contact angles than as-received aluminum with the native surface oxide, even when exposed to atmospheric contaminants. Therefore, such surfaces may allow for improved heat transfer in the MITR by delaying the onset of boiling. The mechanism of certain surface treatments in providing better wettability that is stable on practical heat transfer surfaces should be investigated further. In particular, the exact influence of surface chemistry needs to be explored, especially in relation to expected deposits and contaminants in a reactor environment. This substudy has clearly demonstrated that only monolayer levels of hydrocarbons, on the order of Ångstroms thick, dominate the wetting process on a practical heat transfer surface. Therefore, in addition to the cleaning and surface treatments already mentioned, other surface treatments which counteract or limit the adsorption of atmospheric contaminants while improving wettability, such as application of nanoparticle thin-films, should be further explored for applications in Materials Test Reactors.

References

[1] International Atomic Energy Agency. *IAEA Safeguards Glossary, 2001 Edition*. International Nuclear Verification Series, No. 3. Vienna, Austria: IAEA, 2002.

[2] Glaser, A. "On the Proliferation Potential of Uranium Fuel for Research Reactors at Various Enrichment Levels." *Science and Global Security*, 12 (2006): 1-24.

[3] International Atomic Energy Agency. "Management of High Enriched Uranium for Peaceful Purposes: Status and Trends." IAEA-TECDOC-1452. June 2005.

[4] Office of the General Counsel. "Nuclear Regulatory Legislation." NUREG-0980, Vol.3, No. 10. U.S. Nuclear Regulatory Commission.

[5] Congressional Record- House. "Conference Report on H.R. 776. Comprehensive National Energy Policy Act." H12103. October 5, 1992.

[6] "Nuclear Terrorism FAQ." *The Washington Post*. September 26, 2007.

[7] Allison, G. "A Failure to Imagine the Worst." *Foreign Policy*. January 26, 2010.

[8] Staples, P., D. Burkes, and M. MacQuigg. "An Overview of the Global Threat Reduction Initiative Research Reactor Conversion Program. *Proceedings of the Institute for Nuclear Materials Management 51st Annual Meeting*. Baltimore, MD. July 2010.

[9] Argonne National Laboratory. "RERTR." Available: http://www.rertr.anl.gov.

[10] International Atomic Energy Agency. "Production Technologies for Molybdenum-99 and Technetium-99m." IAEA-TECDOC-1065. Vienna, Austria. February 1999.

[11] Wachs, D.M. "RERTR Fuel Development and Qualification Plan." INL/EXT-05-01017. January 2007.

[12] Dupuy, J.P., G. Perotto, G. Ithurrdale, C. Leydier, and X. Bravo. "Jules Horowitz Reactor General Layout, Main Design Options Resulting from Safety Options, Technical Performances and Operating Constraints." *TRTR-2005/IGORR-10 Joint Meeting*. Gaithersburg, MD. September 12-16, 2005.

[13] Bagleitto, E. Personal communication. MIT Department of Nuclear Science and Engineering. January 29, 2013.

[14] Kew, P.A. and K. Cornwell. "Correlations for the Prediction of Boiling Heat Transfer in Small-Diameter Channels." *Applied Thermal Engineering*, 17, Nos. 8-10 (1997): 705-715.

[15] Kandlikar, S.G. and W.J. Grande. "Evolution of Microchannel Flow Passages-Thermohydraulic Performance and Fabrication Technology." *Heat Transfer Engineering*, 24, No. 1 (2003): 3-17.

[16] Kandlikar, S.G. *Heat Transfer and Fluid Flow in Minichannels and Microchannels*. p. 3 Amsterdam, Netherlands: Elsevier, 2006.

[17] MITR Staff. "Safety Analysis Report for the MIT Research Reactor." 2011.

[18] Bergles, A.E. and W.M. Rohsenow. "The Determination of Forced-Convection Surface-Boiling Heat Transfer." *Journal of Heat Transfer*, 86 (1964): 365-372.

[19] Thompson, T.J. and T. Cantwell. MITR: The MIT Research Reactor." *Nucleonics*, 15, No. 1 (1957): 38-40.

[20] Carpenter, D., G. Kohse, and L.W. Hu. "MITR User's Guide, Revision 3." Massachusetts Institute of Technology Nuclear Reactor Laboratory. July 2012.

[21] Peacock, H.B. "Properties of U_3O_8-Aluminum Cermet Fuel." WSRC-RP-89-981. Westinghouse Savannah River Company. October 1989.

[22] Muranaka, R.G. "Conversion of Research Reactors to Low-Enrichment Uranium Fuels." *IAEA Bulletin*, 25, No. 1: 18-21.

[23] Klein, J.L. "Uranium and Its Alloys." *Nuclear Reactor Fuel Elements: Metallurgy and Fabrication*. A.R. Kaufmann, Ed. pp. 31-91. New York, NY: John Wiley & Sons, 1962.

[24] Huffman, J.R. "The Materials Testing Reactor Design." IDO-16121-PPCo. Phillips Petroleum Company- Atomic Energy Division. October 1953.

[25] Stahl, D. "The Status and Development Potential of Plate-Type Fuels for Research and Test Reactors." ANL-79-11. Argonne National Laboratory. March 1979.

[26] Thurber, W.C., J.H. Erwin, and R.J. Beaver. The Application of a Nominal 48 wt% U-Al Alloy to Plate-Type Aluminum Research Reactor Fuel Elements." ORNL-2351. Oak Ridge National Laboratory. February 1958.

[27] Adamson, Jr., G.M. "Fabrication of Research Reactor Fuel Elements." ORNL-TM-2197. Oak Ridge National Laboratory. June 1968.

[28] Vatulin, A.V., A.V. Morozov, V.B. Suprun, Y.I Petrov, and Y.I. Trifonov. "High-Density U-Mo Fuel for Research Reactors." *Metal Science and Heat Treatment*, 46, Nos. 11-12 (2004): 484-489.

[29] Mid-Atlantic Region National Park Service. "Historic American Engineering Record-Shippingport Atomic Power Station." HAER No. PA-81. Department of the Interior. 1985.

[30] Todreas, N.E. Personal communication. MIT Department of Nuclear Science and Engineering. February 15, 2014.

[31] Grossenbacher, J. and C.E. Behrens. *Energy: Nuclear*. p. 195. Alexandria, VA: TheCapitol.Net, Inc., 2010.

[32] Gupta, C.K. *Extractive Metallurgy of Molybdenum*. p. 51. Boca Raton, FL: CRC Press, 1992.

[33] Wimett, T.F. "Fast Burst Reactors in the U.S.A." SM 62/53. Los Alamos Scientific Laboratory. May 1965.

[34] Rienecker, F. and W.H. Moran. "Uranium-Molybdenum Alloy for Use in a Prompt-Burst Reactor." *Journal of Basic Engineering, Transactions of the ASME*, 87, No. 4 (1965): 865-870.

[35] Bosworth, G.H. and W.E. Parkins. "Designs for Large Organic Reactor Power Plants." *Transactions of the American Institute of Electrical Engineers, Part I: Communication and Electronics*, 78, No. 6 (1960): 964-973).

[36] Crawford, R.M. and E.E. Garrett. "Fabrication of Uranium Alloy Fuel Elements for the OMRE Fourth Core." NAA-SR-8412. Atomics International. July 1963.

[37] Schulz, W.W., R.E. Burns, and E.M. Duke. "Nitric Acid Dissolution of Uranium-Molybdenum Alloy Reactor Fuels." *I&EC Process Design and Development*, 1, No. 2 (1962): 156-160.

[38] Buker, L., R. Halsey, K. Jessen, D. Mantooth. "Evaluation Report Summary: SEC-00126, Piqua Organic Moderated Reactor" SEC-00126. National Institute of Occupational Safety and Health. April 27, 2009.

[39] International Atomic Energy Agency. "Research Reactor Core Conversion Guidebook, Volume 4: Fuels." IAEA-TECDOC-643. April 1992.

[40] McDaniel, W.N., O.E. Homeister, and D.O. Leeser. "Development of Core Elements for the Enrico Fermi Power Reactor." *Second U.N. International Conference on the Peaceful Uses of Atomic Energy*. October 1958.

[41] Gelles, S.H. "Interactions Between Core and Cladding." *Nuclear Reactor Fuel Elements: Metallurgy and Fabrication*. A.R. Kaufmann, Ed. p. 257-269. New York, NY: John Wiley & Sons, 1962.

[42] Pemsler, J.P. "Cladding Materials." *Nuclear Reactor Fuel Elements: Metallurgy and Fabrication*. A.R. Kaufmann, Ed. p. 239. New York, NY: John Wiley & Sons, 1962.

[43] Clark, C.A., J.F. Jue, G.A. Moore, N.P. Hallinan, and B.H. Park. "Update on Monolithic Fuel Fabrication Methods." *Proceedings of the 28thInternational Meeting on reduced Enrichment for Research and Test Reactors*. Cape Town, South Africa. October 29-November 3, 2006.

[44] Moore, G.A., B.H. Rabin, J.F. Jue, C.R. Clark, N.E. Woolstenhulme, B.H. Park, S.E. Steffler, M.D. Chapple, M.C. Marshall, J.J. Green, and B.L. Mackowiak. "Development Status of U10Mo Monolithic Fuel Foil Fabrication at the Idaho National Laboratory." *Proceedings of the 32nd International Meeting on Reduced Enrichment for Research and Test Reactors*. Lisbon, Portugal. October 10-14, 2010.

[45] Loh, N.L. and K.Y. Sia. "An Overview of Hot Isostatic Pressing." *Journal of Materials Processing Technology*, 30 (1992): 45-65.

[46] Moore, G.A. and M.C. Marshall. "Co-Rolled U10Mo/Zirconium-Barrier-Layer Monolithic Fuel Foil Fabrication Process." INL/EXT-10-17774. Idaho National Laboratory. January 2010.

[47] Levy, S., R.A. Fuller, and R.O. Niemi. "Heat Transfer to Water in Thin Rectangular Channels." *Journal of Heat Transfer*, 81, No. 2 (1959): 129-143.

[48] Gambill, W.R. and R.D. Bundy. "HFIR Heat-Transfer Studies of Turbulent Water Flow in Thin Rectangular Channels." ORNL-3079. Oak Ridge National Laboratory. June 1961.

[49] Spurgeon, D. "Preliminary Design Studies for a High Flux MIT Reactor." Nuclear Engineer Thesis, Department of Nuclear Engineering. Massachusetts Institute of Technology. June 1969.

[50] Hollenberg, T. "The Design of an Experiment to Investigate In-Channel Thermocouples, Heat Transfer Coefficient, and Fin Effectiveness for the MITR-II Fuel Plates." Bachelor of Science Thesis, Department of Mechanical Engineering. Massachusetts Institute of Technology. June 1974.

[51] Szymczak, W.J. "Experimental Investigation of Heat Transfer Characteristics of MITR-II Fuel Plates, In-Channel Thermocouple Response and Calibration." Master of Science Thesis, Department of Nuclear Engineering. Massachusetts Institute of Technology. September 1975.

[52] Sudo, Y., K. Miyata, H. Ikawa, M. Ohkawara, and M. Kaminaga. "Experimental Study of Differences in Single-Phase Heat Transfer Characteristics Between Upflow and Downflow for Narrow Rectangular Channel." *Journal of Nuclear Science and Technology*, 22, No. 3 (1985): 202-212.

[53] Sudo, Y., K. Miyata, H. Ikawa, and M. Kaminaga. "Experimental Study of Incipient Nucleate Boiling in Narrow Vertical Rectangular Channel Simulating Subchannel of Upgraded JRR-3." *Journal of Nuclear Science and Technology*, 23, No. 1 (1986): 73-82.

[54] Belhadj, M., T. Aldemir, and R.N. Christensen. "Onset of Nucleate Boiling in Research Reactors with Thin Rectangular Channels Under Low-Velocity Upward Flow Conditions." *Nuclear Technology*, 82 (1988): 330-340.

[55] Hong, G., X. Yan, Y.H. Yang, S. Liu, and Y.P. Huang. "Experimental Study of Onset of Nucleate Boiling in a Narrow Rectangular Channel Under Static and Heaving Conditions." *Annals of Nuclear Energy*, 39 (2012): 26-34.

[56] Wang, J., Y. Huang, Y. Wang. "Visualized Study on Specific Points on Demand Curves and Flow Patterns in a Single-Side Heated Narrow Rectangular Channel." *International Journal of Heat and Fluid Flow*, 32 (2011): 982-992.

[57] Kandlikar, S.G. "Heat Transfer Mechanisms During Flow Boiling in Microchannels." *Journal of Heat Transfer*, 126 (2004): 8-16.

[58] Lienhard IV, J.H. and J.H. Lienhard V. *A Heat Transfer Textbook, 4th Edition*. p. 356. Cambridge, MA: Phlogiston Press, 2012.

[59] Hartnett, J.P, J.C.Y. Koh, and S.T. McComas. "A Comparison of Predicted and Measured Friction Factors for Turbulent Flow Through Rectangular Channels." *Journal of Heat Transfer*, 84, No. 1 (1962): 82-88.

[60] Bhatti, S. and R.K. Shah. "Turbulent and Transition Flow Convective Heat Transfer In Ducts." *Handbook of Single-Phase Convective Heat Transfer*. S. Kakaç, R. Shah, and W. Aung, eds. p. 4.83. New York, NY: John Wiley & Sons, Inc., 1987.

[61] Zhi-qing, W. "Study on Correction Coefficients of Laminar and Turbulent Entrance Region Effect in Round Pipe." *Applied Mathematics and Mechanics*, 3, No. 3 (1982): 433-446. (Original article published in 1960)

[62] Todreas, N.E. and M.S. Kazimi. *Nuclear Systems I: Thermal Hydraulic Fundamentals*. p. 448. New York, NY: Taylor and Francis Group, 1990.

[63] Melly, J.P. "Characteristics and Application of Electric Resistance Heaters." *Handbook of Applied Thermal Design*. E.C. Guyer and D.L. Brownell, eds. p. 8-13. New York, NY: McGraw Hill Book Company, 1989.

[64] Occupational Safety and Health Administration. "Extremely Low Frequency Radiation." U.S. Department of Labor. 2006. https://www.osha.gov/SLTC/elfradiation/index.html. Accessed September 7, 2013.

[65] International Commission on Non-Ionizing Radiation Protection. "Guidelines on Limits of Exposure to Static Magnetic Fields." *Health Physics*, 96, No. 4 (2009): 504-514.

[66] Institute of Electrical and Electronics Engineers (IEEE). "IEEE PC95.6-2002 Standard for Safety Levels with Respect to Human Exposure to Electromagnetic Fields, 0 to 3 kHz." Institute of Electrical and Electronics Engineers, Inc. 2002.

[67] Pentair Ltd. "Berkeley SSCX Series Centrifugal Pumps." B2022BK. November 2012.

[68] Lipták, B.G. *Instrument Engineers' Handbook, Volume 1: Process Measurement and Analysis*. 4th Edition. Boca Raton, FL: CRC Press, 2003.

[69] OMEGA Engineering, Inc. "Flow and Level Measurement." *Transactions in Measurement and Control, Vol. 4*. p. 44. Putnam Publishing Company, 2001.

[70] Holman, J.P. *Experimental Methods for Engineers, 7th Edition*. p. 312. New York, NY: McGraw-Hill, 2001.

[71] Shaw, R. "The Influence of Hole Dimensions on Static Pressure Measurements." *Fluid Mechanics*, 7 (1959): 550-564.

[72] Wong, S.Y. "Friction Pressure Drop Measurements and Flow Distribution Analysis for LEU Conversion Study of MIT Research Reactor." Master of Science Thesis, Department of Nuclear Science and Engineering, Massachusetts Institute of Technology, September 2008.

[73] Bhatti, S. and R.K. Shah. "Turbulent and Transition Flow Convective Heat Transfer In Ducts." *Handbook of Single-Phase Convective Heat Transfer*. S. Kakaç, R. Shah, and W. Aung, eds. pp. 4.62-4.63., 4.74-4.77. New York, NY: John Wiley & Sons, Inc., 1987.

[74] Bhattacharya, P., R. Fornari, and H. Kamimura, Eds. *Comprehensive Semiconductor Science and Technology, Volume 1*. p. 336. Amsterdam, Netherlands: Elsevier Science, 2011.

[75] Burns, G.W. and M.G. Scroger. "The Calibration of Thermocouples and Thermocouple Materials." *NIST Special Publication 250-35*. Gathersburg, MD: National Institute of Standards and Technology, April 1989.

[76] Holman, J.P. *Experimental Methods for Engineers, 7th Edition*. p. 374. New York, NY: McGraw-Hill, 2001.

[77] ASTM Committee E20 on Temperature Measurement. *Manual on the Use of Thermocouples in Temperature Measurement, Fourth Edition*. p. 46. Philadelphia, PA: ASTM. 1993.

[78] Bentley, R.E. *Handbook of Temperature Measurement, Volume 3: The Theory and Practice of Thermoelectric Thermometry*. Singapore: Springer-Verlag Singapore Pte. Ltd., 1998.

[79] Rohsenow, W.M. "Boiling." *Annual Review of Fluid Mechanics*, 3 (1971): 211-236.

[80] McAdams, W.H., W.E. Kennel, C.S. Minden, R. Carl, P.M. Picornell, and J.E. Dew. "Heat Transfer at High Rates to Water with Surface Boiling." *Industrial and Engineering Chemistry*, 41, No. 9 (1949): 1945-1953.

[81] Current & Voltage Sensors Department, ABB France. "Technical Catalog: Current Sensors/Voltage Sensors." ABB. 2013.

[82] Mandel, J. *The Statistical Analysis of Experimental Data*. New York, NY: Dover Publications. 1984.

[83] Working Group 1 of the Joint Committee for Guides in Metrology. "Evaluation of Measurement Data- Guide to the Expression of Uncertainty in Measurement." JCGM 100:2008- GUM 1995 with Minor Corrections. ISO, BIPM, IEC, IFCC, ILAC, IUPAC, and OIML. September 2008.

[84] "Measurement Uncertainty." ANSI/ASME PTC 19.1- 1985 Part I. 1986.

[85] Kim, J.H., T.W. Simon, and R. Viskanta. "Editorial- Journal of Heat Transfer Policy on Reporting Uncertainties in Experimental Measurements and Results." *Journal of Heat Transfer*, 115, No. 1 (1993): 5-6.

[86] Taylor, J.R. *An Introduction to Error Analysis: The Study of Uncertainties in Physical Measurements*. p. 110. Sausalito, CA: University Science Books, 1997.

[87] Kline, S.J. and F.A. McClintock. "Describing Uncertainties in Single-Sample Experiments." *Mechanical Engineering*, 75 (1953): 3-8.

[88] Kandlikar, S.G. "Critical Heat Flux in Subcooled Flow Boiling- An Assessment of Current Understanding and Future Directions for Research." *Multiphase Science and Technology*, 13 (2001): 207-232.

[89] Crowe, C.T. *Multiphase Flow Handbook*. p. 3-27. CRC Press, 2006.

[90] Preston-Thomas, H. "The International Temperature Scale of 1990." *Metrologia*, 27 (1990): 3-10.

[91] Wagner, W. and H.J. Kretzschmar. *International Steam Tables: Properties of Water and Steam Based on the Industrial Formulation IAPWS-IF97, Second Edition*. Berlin, Germany: Springer-Verlag, 2008.

[92] Taylor, J.R. *An Introduction to Error Analysis: The Study of Uncertainties in Physical Measurements*. p. 190. Sausalito, CA: University Science Books, 1997.

[93] Mikic, B.B. and W.M. Rohsenow. "Thermal Contact Resistance." Report No. DSR 74542-41. Massachusetts Institute of Technology Engineering Projects Laboratory. September 1966.

[94] Incropera, F.P., D.P. DeWitt, T.L. Bergman, and A.S. Lavine. *Fundamentals of Heat and Mass Transfer, Sixth Edition*. p. 103. Hoboken, NJ: John Wiley & Sons, 2007.

[95] Adiutori, E.F. "Origins of the Heat Transfer Coefficient." *Mechanical Engineering* (August 1990): 46-50.

[96] Fourier, J. *The Analytic Theory of Heat*. Translated by A. Freeman. Cambridge, England: The University Press, 1878. (English Translation of *Théorie Analytique de la Chaleur*, 1822).

[97] Prandtl, L. "Über Flüssigkeitsbewegung bei Sehr Kleiner Reibung." *Verhandlungen des Dritten Internationalen Mathematiker-Kongresses*. pp. 484-491. Heidelberg, German Empire. August 8-August 13, 1904. (Proceedings published in 1905).

[98] Blasius, H. "The Boundary Layers in Fluids with Little Friction." National Advisory Committee for Aeronautics, Technical Memorandum 1256. February 1950. (English Translation of "Grenzschichten in Flüssigkeiten mit Kleiner Reibung." *Zeitschrift für Mathematik und Physik* 56, No. 1, 1908).

[99] Tani, I. "History of Boundary-Layer Theory." *Annual Reviews in Fluid Mechanics* 9 (1977): 87-111.

[100] Lienhard IV, J.H. and J.H. Lienhard V. *A Heat Transfer Textbook, 4th Edition*. pp. 271-341. Cambridge, MA: Phlogiston Press, 2012.

[101] Schlichting, H. and K. Gersten. *Boundary-Layer Theory, 8th English Edition*. Translated by K. Mayes. Berlin, Germany: Springer-Verlag, 2000.

[102] Dittus, F.W. and L.M.K. Boelter. "Heat Transfer in Automobile Radiators of the Tubular Type." *University of California Publications in Engineering*, 2, No. 13 (October 1930): 443-461. (Reprint from *International Communications in Heat and Mass Transfer*, 12 (1985): 3-22.

[103] McAdams, W.H. *Heat Transmission, 2nd Edition*. p. 167-168. New York, NY: McGraw-Hill Book Company, Inc., 1942.

[104] R. Winterton, "Where Did the Dittus and Boelter Equation Come From?," *International Journal of Heat and Mass Transfer*, 41, Nos. 4-5 (1998): 809-810.

[105] Colburn, A.P. "A Method of Correlating Forced Convection Heat Transfer Data and a Comparison with Fluid Friction." *Transactions of the American Institute of Chemical Engineers*, 29 (1933): 174-209.

[106] Stoever, H.J. "Heat Transfer: Conduction, Radiation and Convection." *Chemical & Metallurgical Engineering*, 51 (May 1944): 98-107.

[107] Nertney, R.J. "Calculated Surface Temperatures for Nuclear Systems and Their Uncertainties." The First Report of the Heat Transfer Subcommittee of the Phillips Reactor Safeguard Committee. AEC Research and Development Report IDO 16343. Phillips Petroleum Co., Atomic Energy Division. June 1, 1957.

[108] Hendrie, J.M. "Final Safety Analysis Report on the Brookhaven High Flux Beam Reactor, Vol I." BNL 7661. p. 4-40. Brookhaven National Laboratory, U.S. Atomic Energy Commission. April 1964.

[109] Sieder, E.N. and G.E. Tate. "Heat Transfer and Pressure Drop of Liquids in Tubes." *Industrial and Engineering Chemistry*, 28, No. 12 (1936): 1429-1435.

[110] McAdams, W.H. *Heat Transmission, 3nd Edition*. p. 219. New York, NY: McGraw-Hill Book Company, Inc., 1954.

[111] Petukhov, B.S. "Heat Transfer in Turbulent Pipe Flow with Variable Physical Properties." *Advances in Heat Transfer*, 6 (1970): 503-564.

[112] Gnielinski, V. "New Equations for Heat and Mass Transfer in Turbulent Pipe and Channel Flow." *International Chemical Engineering*, 16 (1976): 359-368.

[113] E. Sparrow, N. Cur, "Turbulent Heat Transfer in a Symmetrically or Asymmetrically Heated Flat Rectangular Duct With Flow Separation at Inlet," *Journal of Heat Transfer*, 104 (1982): 82-89.

[114] Chilton, T.H. and A.P. Colburn. "Mass Transfer (Absorption) Coefficients: Prediction from Data on Heat Transfer and Fluid Friction." *Industrial and Engineering Chemistry* 26, No. 11 (1934): 1183-1187.

[115] Incropera, F.P., D.P. DeWitt, T.L. Bergman, and A.S. Lavine. *Fundamentals of Heat and Mass Transfer, Sixth Edition*. p. 385. Hoboken, NJ: John Wiley & Sons, 2007.

[116] Lienhard IV, J.H. and J.H. Lienhard V. *A Heat Transfer Textbook, 4th Edition*. p. 326. Cambridge, MA: Phlogiston Press, 2012.

[117] Bhatti, S. and R.K. Shah. "Turbulent and Transition Flow Convective Heat Transfer In Ducts." *Handbook of Single-Phase Convective Heat Transfer*. S. Kakaç, R. Shah, and W. Aung, eds. p. 4.64. New York, NY: John Wiley & Sons, Inc., 1987.

[118] Barrow, H. "Convection Heat Transfer Coefficients for Turbulent Flow Between Parallel Plates with Unequal Heat Fluxes." *International Journal of Heat and Mass Transfer*, 1 (1961): 306-311.

[119] Sparrow, E.M. and S.H. Lin. "Turbulent Heat Transfer in a Parallel-Plate Channel." *International Journal of Heat and Mass Transfer*, 6, No. 3 (1963): 248-249.

[120] Sakakibara, M. and K. Endo. "Analysis of Heat Transfer for Turbulent Flow Between Parallel Plates." *International Chemical Engineering*, 16, No. 4 (1976): 728-733.

[121] Moody, L. "Friction Factors for Pipe Flow." *Transactions of the ASME*, 66, No. 8 (1944): 671-684.

[122] Jones Jr., O.C. "An Improvement in the Calculation of Turbulent Friction in Rectangular Ducts." *Journal of Fluids Engineering*, 98, No.2 (1976): 173-180.

[123] Kays, W. and E. Leung. "Heat Transfer in Annular Passages- Hydrodynamically Developed Turbulent Flow with Arbitrarily Prescribed Heat Flux." *International Journal of Heat and Mass Transfer*, 6 (1963): 537-557.

[124] Shah, R.K. and A.L. London. "Laminar Flow Forced Convection Heat Transfer and Flow Friction in Straight and Curved Ducts- A Summary of Analytical Solutions." Office of Naval Research, Technical Report No. 75, NR-090-342. November 1971.

[125] Blasius, Von H. "Das Aehnlichkeitsgesetz bei Reibungvorgängen." *Zeitschrift des Vereines Deutscher Ingenieure*, 639 (1912): 1-5.

[126] Han, L.S. "Hydrodynamic Entrance Lengths for Incompressible Laminar Flow in Rectangular Ducts." *Journal of Applied Mechanics*, 27, No. 3 (1960): 403-409.

[127] Shah, R.K. and M.S. Bhatti. "Laminar Convective Heat Transfer in Ducts." *Handbook of Single-Phase Convective Heat Transfer*. S. Kakaç, R. Shah, and W. Aung, eds. p. 3.40. New York, NY: John Wiley & Sons, Inc., 1987.

[128] Buck, J.H. and C.F. Leyse. "Materials Testing Reactor Project Handbook." Contract No. W-7405. P. 477. Oak Ridge National Laboratory, Carbide and Carbon Chemical Company. May 1951.

[129] Hendrie, J.M. "Final Safety Analysis Report on the Brookhaven High Flux Beam Reactor, Vol I." BNL 7661. p. 1-4. Brookhaven National Laboratory, U.S. Atomic Energy Commission. April 1964.

[130] Peirce, B. "Criterion for the Rejection of Doubtful Observations." *The Astronomical Journal*, 2, No. 45 (1852): 161-163.

[131] Schlichting, H. and K. Gersten. *Boundary-Layer Theory, 8th English Edition*. Translated by K. Mayes. pp. 604-605. Berlin, Germany: Springer-Verlag, 2000.

[132] Schlichting, H. and K. Gersten. *Boundary-Layer Theory, 8th English Edition*. Translated by K. Mayes. pp. 551-552. Berlin, Germany: Springer-Verlag, 2000.

[133] Witharana, S., B. Phillips, S. Strobel, H.D. Kim, T. McKrell, J.B. Chang, J. Buongiorno, K.K. Berggren, L. Chen, and Y. Ding. "Bubble Nucleation on Nano- to Micro-Size Cavities and Posts: An Experimental Validation of Classical Theory." *Journal of Applied Physics*, 112 No. 064904 (2012): 1-5.

[134] Carey, Van P. *Liquid-Vapor Phase-Change Phenomena*. pp.210-226. New York City, New York: Taylor & Francis Group, 2007.

[135] Bankoff, S.G. "Entrapment of a Gas in the Spreading of a Liquid Over a Rough Surface." *A.I.Ch.E. Journal*, 4 (1958): 24-26.

[136] Jones, S.F., G.M. Evans, and K.P. Galvin. "Bubble Nucleation from Gas Cavities- A Review." *Advances in Colloid and Interface Science*, 80 (1999): 27-50.

[137] Eddington, R.I. and D.B.R. Kenning. "The Effect of Contact Angle on Bubble Nucleation." *International Journal of Heat and Mass Transfer*, 22 (1979): 1231-1236.

[138] Hsu, Y.Y. and W. Graham. "An Analytical and Experimental Study of the Thermal Boundary Layer and Ebullition Cycle in Nucleate Boiling." NASA Technical Note D-594. May 1961.

[139] Hsu, Y.Y. "On the Size Range of Active Nucleation Cavities on a Heating Surface," *Journal of Heat Transfer*, 84 (1962): 207-216.

[140] Satō, T. and H. Matsumura. "On the Conditions of Incipient Subcooled-Boiling with Forced Convection." *Bulletin of the Japan Society of Mechanical Engineers*, 7 (1964): 329-398.

[141] Davis, E.J. and G.H. Anderson. "The Incipience of Nucleate Boiling in Forced Convection Flow." *A.I.Ch.E. Journal*, 12, No. 4 (1966): 774-780.

[142] Kandlikar, S.G. *Heat Transfer and Fluid Flow in Minichannels and Microchannels*. pp. 175-181. Amsterdam, Netherlands: Elsevier, 2006.

[143] Kandlikar, S.G., V. Mizo, M. Cartwright, E. Ikenze. "Bubble Nucleation and Growth Characteristics in Subcooled Flow Boiling of Water." HTD-Vol. 342, *National Heat Transfer Conference*, Vol. 4 (1997): 11-18.

[144] Hong, G., X. Yan, Y.H. Yang, S. Liu, and Y.P. Huang. "Experimental Study of Onset of Nucleate Boiling in a Narrow Rectangular Channel Under Static and Heaving Conditions." *Annals of Nuclear Energy*, 39 (2012): 26-34.

[145] Wang, J., Y. Huang, Y. Wang. 'Visualized Study on Specific Points on Demand Curves and Flow Patterns in a Single-Side Heated Narrow Rectangular Channel." *International Journal of Heat and Fluid Flow*, 32 (2011): 982-992.

[146] Wu, Y.W., G.H. Su, B.X. Hu, and S.Z Qiu. "Study of Onset of Nucleate Boiling in Bilaterally Heated Narrow Annuli." *International Journal of Thermal Sciences*, 49 (2010): 741-748.

[147] Kennedy, J.E., G.M. Roach, Jr., M.F. Dowling, S.I. Abdel-Khalik, S.M. Ghiaasiaan, S.M. Jeter, and Z.H. Quershi. "The Onset of Flow Instability in Uniformly Heated Horizontal Microchannels." *Journal of Heat Transfer*, 122 (2000): 118-125.

[148] Collier, J.G. and J.R. Thome. *Convective Boiling and Condensation, 3rd Edition*. p. 196. Oxford: Clarendon Press, 1994.

[149] Bergles, A.E. and W.M. Rohsenow. "Forced Convection Surface-Boiling Heat Transfer and Burnout In Tubes of Small Diameter." Report No. 8767-21. Air Force Contract AF 19(604)-7344. Massachusetts Institute of Technology. May 1962.

[150] Bouré, J.A., A.E. Bergles, and L.S. Tong. "Review of Two-Phase Flow Instability." *Nuclear Engineering and Design*, 25 (1973): 165-192.

[151] You, S.M., T.W. Simon, and A. Bar-Cohen. "Effects of Dissolved Gas Content on Pool Boiling of a Highly Wetting Fluid." *Journal of Heat Transfer*, 117 (1995): 687-692.

[152] Rainey, K.N., S.M. You, and S. Lee. "Effect of Pressure, Subcooling, and Dissolved Gas on Pool Boiling Heat Transfer From Microporous Surfaces in FC-72." *Journal of Heat Transfer*, 125 (2003): 75-83.

[153] Whittle, R.H., and R. Forgan. "A Correlation for the Minima in the Pressure Drop Versus Flow-Rate Curves for Sub-Cooled Water Flowing in Narrow Heated Channels." *Nuclear Engineering and Design*, 6 (1967): 89-99.

[154] Todreas, N.E. and M.S. Kazimi. *Nuclear Systems I: Thermal Hydraulic Fundamentals, Second Edition*. pp. 679-696. Boca Raton, FL: Taylor and Francis Group, 2012.

[155] Ishii, M. "Thermally Induced Flow Instabilities in Two-Phase Mixtures in Thermal Equilibrium." Doctoral Thesis, School of Mechanical Engineering. Georgia Institute of Technology. June 1971.

[156] Saha, P. "Thermally Induced Two-Phase Flow Instabilities, Including the Effect of Thermal Non-Equilibrium Between the Phases." Doctoral Thesis, School of Mechanical Engineering. Georgia Institute of Technology. June 1974.

[157] Saha, P., M. Ishii, and N. Zuber. "An Experimental Investigation of the Thermally Induced Flow Oscillations in Two-Phase Systems." *Journal of Heat Transfer*, 98, No. 4 (1976): 616-622.

[158] Narayanan, S., B. Srinivas, S. Pushpavanam, and S.M. Bhallamudi. "Non-linear Dynamics of Two Phase Flow System in an Evaporator: The Effects of (i) a Time

Varying Pressure Drop (ii) an Axially Varying Heat Flux." *Nuclear Engineering and Design*, 178 (1997): 279-294.

[159] Yadigaroglu, G. and A.E. Bergles. "An Experimental and Theoretical Study of Density-Wave Oscillations in Two-Phase Flow." Report No. DSR 74629. Office of Naval Research Contract Nonr-3963 (15). Massachusetts Institute of Technology. December 1969.

[160] Nukiyama, S. "The Maximum and Minimum Values of the Heat Q Transmitted From Metal to Boiling Water Under Atmospheric Pressure." *International Journal of Heat and Mass Transfer*, 9 (1966): 1419-1433. (Reprint from *Journal of Japanese Society of Mechanical Engineers*, 37 (1934): 367-374.

[161] Griffith, P. and J.D. Wallis. "The Role of Surface Conditions in Nucleate Boiling." Office of Naval Research, Technical Report No. 14, NONR-1848(39). December 1958.

[162] Rohsenow, W.M. "A Method of Correlating Heat-Transfer Data for Surface Boiling of Liquids." *Transactions of the ASME,* 74 (1952): 969-976.

[163] Zuber, N. "Hydrodynamic Aspects of Boiling Heat Transfer." United States Atomic Energy Commission, AECU-4439. June 1959.

[164] Costello, C.P. and W.J. Frea. "The Roles of Capillary Wicking and Surface Deposits in the Attainment of High Pool Boiling Burnout Heat Fluxes." *A.I.Ch.E. Journal*, 10, No. 3 (1964): 393-398.

[165] Gambill, W. An Experimental Investigation of the Inherent Uncertainty in Pool Boiling Critical Heat Fluxes to Saturated Water." *A.I.Ch.E. Journal*, 10, No. 4 (1964): 502-508.

[166] Young, T. "An Essay on the Cohesion of Fluids." *Philosophical Transactions of the Royal Society of London*, 95 (1805): 65-87.

[167] Wenzel, R.N. "Resistance of Solid Surfaces to Wetting by Water." *Industrial and Engineering Chemistry*, 28 (1936): 988-94.

[168] Neumann, A.W. and R.J. Good. "Thermodynamics of Contact Angles I. Heterogeneous Solid Surfaces." *Journal of Colloid and Interface Science*, 38, No. 2 (1972): 341-358.

[169] Amirfazli, A., D.Y. Kwok, J. Gaydos, and A.W. Neumann. "Line Tension Measurements Through Drop Size Dependence of Contact Angle." *Journal of Colloid and Interface Science*, 205 (1998): 1-11.

[170] Cassie, A.B.D. and S. Baxter. "Wettability of Porous Surfaces." *Transactions of the Faraday Society*, 40 (1944): 546-551.

[171] KSV Instruments. "Dynamic Contact Angles." KSV Instruments Ltd., 2009. Available: http://www.ksvltd.com/content/index/keydca.

[172] Bernardin, J.D., I. Mudawar, C.B. Walsh, and E.I. Franses. "Contact Angle Temperature Dependence for Water Droplets on Practical Aluminum Surfaces." *International Journal of Heat and Mass Transfer*, 40 (1997): 1017-1033.

[173] Starov, V.M., M.G. Velarde, and C.J. Radke. "Wetting and Spreading Dynamics." *Surfactant Science Series*, Vol. 138. CRC Press, 2007.

[174] O'Hanley, H., C. Coyle, J. Buongiorno, T. McKrell, L.W. Hu, M. Rubner, and R. Cohen. "Separate Effects of Surface Roughness, Wettability, and Porosity on the Boiling Critical Heat Flux." *Applied Physics Letters*, 103, No. 024102 (2013): 1-5.

[175] International Organization for Standardization. "Geometrical Product Specifications (GPS)- Surface Texture: Profile Method- Terms, Definitions and Surface Texture Parameters." ISO 4287:1997.

[176] Japanese Standards Association. "Geometrical Product Specifications (GIS)- Indication of Surface Texture in Technical Product Documentation." JIS B 0031:2003.

[177] "Erfassung der Gestaltabweichungen 2. bis 5. Ordnung an Oblerflächen an Hand von Oberflächenschnitten." DIN 4762, Part 1, August 1960.

[178] Forrest, E., L.W. Hu, J. Buongiorno, T. McKrell. "Pool Boiling Heat Transfer Performance of a Dielectric Fluid with Low Global Warming Potential." *Heat Transfer Engineering*, 34, No. 15 (2013): 1262-1277.

[179] Wight, J. Babcock & Wilcox Nuclear Operations Group, Inc. Personal Communication. January 17, 2012.

[180] Shaber, E.L. Idaho National Laboratory. Personal Communication. February 18, 2011.

[181] Drelich, J., J. D. Miller, and R. J. Good. "The Effect of Drop (Bubble) Size on Advancing and Receding Contact Angles for Heterogeneous and Rough Solid Surfaces as Observed with Sessile-Drop and Captive-Bubble Techniques." *Journal of Colloid and Interface Science*, 179, No. 1 (1996): 37-50.

[182] Gledhill, R.A., A.J. Kinloch, and S.J. Shaw(1977). "Effect of Relative Humidity on the Wettability of Steel Surfaces." *The Journal of Adhesion*, 9 (1) (1977): 81-85.

[183] Robinson, C.P. "Is There a Purpose for Deterrence After the Cold War?" Sandia National Laboratories. Presented to the Project On Nuclear Issues of the Center for Strategic and International Studies. June 10, 2004.

[184] Bunn, M. "A Mathematical Model of the Risk of Nuclear Terrorism." *Annals of the American Academy of Political and Social Science*, 607 (2006): 103-120.

[185] Doyle, J.E. *Nuclear Safeguards, Security, and Nonproliferation: Achieving Security with Technology and Policy*. pp. 561-574. Boston, MA: Butterworth-Heinemann, 2008.

[186] Committee on International Security and Arms Control. "Management and Disposition of Excess Weapons Plutonium." National Academy of Sciences, 1994.

[187] United States Department of Energy. "Nuclear Proliferation and Civilian Nuclear Power: Report of the Nonproliferation Alternative Systems Assessment Program." DOE/NE-0001. December 1979.

[188] Powers, J.A. "Safeguarding Research Reactors." STR-118. International Atomic Energy Agency. March 1983.

[189] Reed, B.C. *The Physics of the Manhattan Project*. pp. 58-59. Berlin, Germany: Springer, 2011.

[190] "The Plutonium Challenge: Avoiding Nuclear Weapons Proliferation." *Los Alamos Science*, 26 (2000): 28-35.

[191] Bunn, M. and A. Wier. "Terrorist Nuclear Weapon Construction: How Difficult?" *Annals of the American Academy of Political and Social Science*, 607 (2006): 133-149.

[192] Frost, R.M. *Nuclear Terrorism After 9/11*. Abingdon, UK: Routledge for the International Institute for Strategic Studies, 2005.

[193] Mueller, J. "The Atomic Terrorist: Assessing the Likelihood." Paper prepared for presentation at the Program on International Security Policy. University of Chicago. January 15, 2008.

[194] Glasstone, S. and P.J. Dolan. *The Effects of Nuclear Weapons, Third Edition*. Washington, D.C.: U.S. Government Printing Office, 1977.

[195] Mantel, M. and J.P. Wightman. "Influence of the Surface Chemistry on the Wettability of Stainless Steel." *Surface and Interface Analysis*, 21 (1994): 595-605.

[196] Edwards, R., M.A. Hill, and R.K. Schulze. "Mid-year Report FY2011 Convert Program LEU Fabrication Process Cleaning Study Process Certification for Material Surface Cleaning for Bonded LEU Fuel Composite Including AFIP-7 LEU Coupons." LA-UR-11-02854. May 2011.

[197] Wight, J. Babcock & Wilcox Nuclear Operations Group, Inc. Personal Communication. January 26, 2012. Available in work document PPO-5010029.

[198] Moulder, J.F., W.F. Stickle, P.E. Sobol, and K. Bomben. *Handbook of X-ray Photoelectron Spectroscopy, 2nd Edition*. Eden Prairie, MN: Perkin-Elmer Corporation, 1992.

[199] Edwards, R., M.A. Hill, and R.K. Schulze. "Mid-year Report FY2011 Convert Program LEU Fabrication Process Cleaning Study Process Certification for Material Surface Cleaning for Bonded LEU Fuel Composite Including AFIP-7 LEU Coupons." LA-UR-11-02854. May 2011.

[200] "Integrated Instrument Available for Surface Science, Materials Research." Materials Science and Technology Division Facility Focus. LALP-07-018. Spring 2007.

[201] National Institute of Standards and Technology. "NIST Electron Inelastic-Mean-Free-Path Database: Version 1.2." Available: http://www.nist.gov/srd/nist71.cfm.

[202] Ebnesajjad, E. *Handbook of Adhesives and Surface Preparation: Technology, Applications and Manufacturing*. p. 23. Burlington, MA: Elsevier, 2011.

[203] Dupré, M.A. *Théorie Mécanique de La Chaleur*. Paris, France: Gauthier-Villars, Imprimeur Libraire de L'École Polytechnique, 1869.

[204] Somasundaran, P., Ed. *Encyclopedia of Surface and Colloid Science, Volume 1, Second Edition*. pp. 115-116. CRC Press, 2006.

[205] Castle, J.E. "The Composition of Metal Surfaces After Atmospheric Exposure: An Historical Perspective." *The Journal of Adhesion*, 84 (2008): 368-388.

[206] Aronov, D., and G. Rosenman. "Wettability Study of Modified Silicon Dioxide Surface Using Environmental Scanning Electron Microscopy." *Journal of Applied Physics*, 101 (2007): 1-5.